Journal of Applied Mechanics

Published Bimonthly by ASME

VOLUME 76 • NUMBER 5 • SEPTEMBER 2009

Transactions of the ASME, Journal of Applied Mechanics (ISSN 0021-8936) is published bimonthly (Jan., Mar., May, July, Sept., Nov.) by The American Society of Mechanical Engineers, Three Park Avenue, New York, NY 10016. Periodicals postage paid at New York, NY and additional mailing offices. POSTMASTER: Send address changes to Transactions of the ASME, Journal of Applied Mechanics, c/o THE AMERICAN SOCIETY OF MECHANICAL ENGINEERS, 22 Law Drive, Box 2300, Fairfield, NJ 07007-2300.
CHANGES OF ADDRESS must be received at Society headquarters seven weeks before they are to be effective. Please send old label and new address.
STATEMENT from By-Laws. The Society shall not be responsible for statements or opinions advanced in papers or printed in its publications (B7.1, Para. 3).

PREFACE

RESEARCH PAPERS

ADVANCES IN IMPACT ENGINEERING

This journal is printed on acid-free paper, which exceeds the ANSI Z39.48-1992 specification for permanence of paper and library materials. ∞™
♲ 85% recycled content, including 10% post-consumer fibers.

Journal of Applied Mechanics Volume 76, Number 5 SEPTEMBER 2009

TECHNICAL BRIEFS

ERRATA

The ASME Journal of Applied Mechanics is abstracted and indexed in the following:

Alloys Index, Aluminum Industry Abstracts, Applied Science & Technology Index, Ceramic Abstracts, Chemical Abstracts, Civil Engineering Abstracts, Compendex (The electronic equivalent of Engineering Index), Computer & Information Systems Abstracts, Corrosion Abstracts, Current Contents, EEA (Earthquake Engineering Abstracts Database), Electronics & Communications Abstracts Journal, Engineered Materials Abstracts, Engineering Index, Environmental Engineering Abstracts, Environmental Science and Pollution Management, Fluidex, Fuel & Energy Abstracts, GeoRef, Geotechnical Abstracts, INSPEC, International Aerospace Abstracts, Journal of Ferrocement, Materials Science Citation Index, Mechanical Engineering Abstracts, METADEX (The electronic equivalent of Metals Abstracts and Alloys Index), Metals Abstracts, Nonferrous Metals Alert, Polymers Ceramics Composites Alert, Referativnyi Zhurnal, Science Citation Index, SciSearch (Electronic equivalent of Science Citation Index), Shock and Vibration Digest, Solid State and Superconductivity Abstracts, Steels Alert, Zentralblatt MATH

Journal of Applied Mechanics

Preface

Special Issue on Advances in Impact Engineering

It is now established that computational tools are indispensable to augment experimental techniques for the analysis of complex structures under dynamic loading. Many new computational techniques are currently being developed and new applications in the fields of impact and shock loadings are emerging. In this special issue of *Journal of Applied Mechanics*, we have assembled a number of recent studies in the field of impact engineering. The present issue attempts to provide a glimpse into the wide range of engineering problems in the field of *Impact Engineering* that mainly can be dealt with by employing computational techniques. A brief overview of each article published in this special issue is provided here.

In "Dynamic Fracture of Shells Subjected to Impulsive Loads," Song and Belytschko present a novel numerical model based on the extended finite element method for the simulation of dynamic cracks in thin shells. The capability of the proposed model is demonstrated by comparing the numerical results with the elasto-plastic crack propagation experiments involving quasi-brittle fracture.

In "Fluid-Structure and Shock-Bubble Interaction Effects During Underwater Explosions Near Composite Structures," Young et al. investigate the role of fluid-structure interaction and shock-bubble interaction in the response of composite structures during underwater explosions using a 2D Eulerian–Lagrangian numerical method. A systematic study is carried out to highlight the effect of Taylor's FSI, the bending/stretching deformation, the core compression, and the boundary condition, on the response of composite structures.

In "Finite Element Analysis of Plugging in Steel Plates Struck by Blunt Projectiles," Kane et al. investigate the fracture of various steel structures impacted by blunt projectiles using the explicit solver of a non-linear finite element code, which incorporates a thermoelastic-thermoviscoplastic constitutive model with coupled or uncoupled ductile damage.

In "The Crushing Characteristics of Square Tubes With Blast-Induced Imperfections: Part 1—Experiments" and "The Crushing Characteristics of Square Tubes With Blast-Induced Imperfections: Part II—Numerical Simulations," Yuen and Nurick study the crushing characteristics of square tubes, with blast-induced imperfections, subjected to axial load. In the experimental part of the study, different imperfection types are created on opposite sides at mid-length of a square tube by means of localized blast loads. In the numerical part, the response of tubes with imperfection is modeled under dynamic axial loading using the finite element method. The work provides insight into the role of imperfection on energy absorption characteristics and deformation mechanisms of the tube.

In "Computational Modelling of Damage Development in Composite Laminates Subjected to Transverse Dynamic Loading," Forghani and Vaziri present a robust computational model for the response of composite laminates to high intensity transverse dynamic loading using a cohesive type tie-break interface for modeling delamination. The proposed model also simulates intra-laminar damage mechanisms within the sub-laminates in a smeared manner using a strain-softening plastic-damage model. The validity of the developed model is assessed by comparing the results with experiments and its capabilities are highlighted by providing several numerical examples.

In "The Influence of Material Properties and Confinement on the Dynamic Penetration of Alumina by Hard Spheres," Wei et al. study the roles of plasticity and micro-cracking on penetration resistance of alumina using the computational protocol devised by Deshpande and Evans. The results provide significant insight into the behavior of alumina and new avenues for building structures and materials for applications that require high penetration resistance.

In "Integrated Experimental, Atomistic, and Microstructurally-Based Finite-Element Investigation of the Dynamic Compressive Behavior of 2139 Aluminum," Elkhodary et al. study the microstructural mechanisms related to the high strength and ductile behavior of 2139-Al using three interrelated approaches. In the computational part, a specialized microstructurally-based finite-element analysis and a dislocation-density based multiple-slip formulation are conducted. The numerical simulations and experimental observations provide fundamental insight into the microstructural mechanisms of shear strain localization in 2139-Al behavior due to dynamic compressive loads.

In "Energy and Momentum Transfer in Air Shocks," Hutchinson presents a series of one-dimensional studies to reveal basic aspects of momentum and energy transfer to plates in air blasts. A simple conjecture, backed by numerical simulations, is put forward related to the momentum transmitted to massive plates and dimensionless parameters are selected to highlight the most important groups of parameters that govern the energy and momentum transfer in air shocks.

Guest Editors:

Ashkan Vaziri
Department of Mechanical and Industrial Engineering,
Northeastern University, Boston, MA
e-mail: vaziri@coe.neu.edu

Zhenyu Xue
Schlumberger Reservoir Completions, Rosharon, TX
e-mail: zxue@rosharon.oilfield.slb.com

Vikram S. Deshpande
Engineering Department,
University of Cambridge, Cambridge, UK
e-mail: vsd@eng.cam.ac.uk

Horacio D. Espinosa
Department of Mechanical Engineering,
Northwestern University, Evanston, IL

Comparison and Validation of Two Models of Netting Deformation

F. G. O'Neill
Fisheries Research Services Marine Laboratory,
375 Victoria Road,
Aberdeen AB11 9DB, Scotland

D. Priour
IFREMER,
BP 70,
Pointe du Diable,
29280 Plouzane Cedex, France

The predictions of two numerical models of the deformation of fishing netting are compared. Analytical solutions are found to the differential equations that govern one of these models, and these solutions are used to evaluate the accuracy of both. There is very good agreement between the numerical solutions and the corresponding analytical values. The models are also applied to the deformation of networks where there is an in-plane shear resistance. Although there are no analytical solutions available, the similarity of the numerical solutions gives confidence in both methods. [DOI: 10.1115/1.3112737]

1 Introduction

In recent years a number of numerical models of the deformation of fishing netting have been developed and applied to the design of fishing gears (Fig. 1) and fish farming cages. These can be broadly categorized as either lumped mass models [1–4], linear finite element models [5–8], or triangular finite element models [9]. Although developed independently, these models can be viewed as numerical counterparts of the general theories of "pure" networks. Steigmann and Pipkin [10] reviewed the theories of networks formed by two families of twines. For networks where the twines are fixed at their point of intersection they define pure networks to be those where there is no resistance to change in the angle between twines and "reinforced" networks to be those where there is some shear resistance. Rivlin [11] and Kuznetsov [12,13] developed theories of the large scale deformation of pure networks where the twines are inextensible, and Pipkin [14] examined reinforced networks. O'Neill [15] derived equations governing the deformation of pure axisymmetric networks (Fig. 2) and extends these to include rigid networks in Ref. [16].

While the convergence of the above numerical models will presumably have been tested during their development, investigations of their accuracy have been limited to comparing their predictions with data collected experimentally in flume or towing tanks or during full scale trials at sea. Consequently there can be experimental measurement error and errors due to inaccurate modeling of the hydrodynamic and mechanical forces acting on the netting. Often, the accuracy and convergence of numerical models are verified using simplified problems for which analytical solutions are available. In this paper, we find two such analytic solutions using the differential equations of Ref. [15]. The first of these, the tractrix, is a complete solution to the problem of inextensible diamond mesh netting held under tension between two circular rings. The second is an upper bound on the maximum radius of inextensible diamond mesh netting subject to a constant internal pressure. These analytical solutions can be used to test the accuracy of any of the models cited above assuming appropriate descriptions of the forces acting on the netting are used.

Here, we compare the predictions of the models of O'Neill [15] and Priour [9] with these analytical solutions. These two models are very different in both derivation and structure. That of O'Neill uses an iterative finite difference scheme to solve the governing set of differential equations that have been derived by considering the limiting case of the force balance on an infinitesimal mesh (Fig. 3), whereas the model of Priour discretizes the netting surface using triangular elements (Fig. 4), establishes the force balance at the nodes of each element, and finds the equilibrium position of the nodes using an iterative Newton–Raphson method.

We also compare the predictions of these two models when they are applied to reinforced networks. Increasingly, some sectors of the fishing industry have begun to use thicker and stiffer twines and the need to consider reinforced networks has become more apparent. To deform these types of networks, the individual twine elements (between two points of intersection) have to be deformed. This can lead to large local curvature of the twine elements (Fig. 5), which manifests itself as a shear resistance. Depending on the magnitude of the twine bending stiffness, this can have a considerable effect on the large scale deformation of the network. The model of O'Neill is extended in Ref. [16] to account for this by considering the case where arbitrary membrane forces f and g act longitudinally and transversely, in the plane of the network surface. Having arbitrary membrane forces permits the introduction of constitutive-type relationships between the membrane forces and the in-plane deformation of the network. Priour [17] accounted for the shear resistance by having a couple acting between the individual twine elements.

O'Neill [18] derived an asymptotic solution for the singularly perturbed equations that govern the deformation of a twine under tension. Here we employ these results to describe (i) the in-plane membrane forces and (ii) the bending couple, and use the models of O'Neill [15] and Priour [9] to investigate the influence of twine bending stiffness on the deformation of fishing netting.

2 Equations Governing The Deformation of Axisymmetric Networks

Let the x-axis be the axis of symmetry, y be the vertical (and radial) distance from the x-axis to the netting, and a be the distance along the profile (Fig. 2). O'Neill [16] showed that the equations governing the geometry of an axisymmetric diamond mesh network subject to a constant pressure force P acting normally to the netting surface are

$$\frac{d^2y}{da^2} = \frac{2\pi}{\sqrt{\mu^2N^2M^2 - 4\pi^2y^2}}\left(1 - \left(\frac{dy}{da}\right)^2\right)\frac{g(a)}{f(a)} - \frac{2\pi yP}{Nf(a)}\left(1 - \left(\frac{dy}{da}\right)^2\right)^{0.5} \quad (1)$$

$$Nf\frac{dx}{da} - \pi y^2 P = \text{const} \quad (2)$$

Contributed by the Applied Mechanics Division of ASME for publication in the Journal of Applied Mechanics. Manuscript received January 14, 2008; final manuscript received January 26, 2009; published online June 16, 2009. Review conducted by Edmundo Corona.

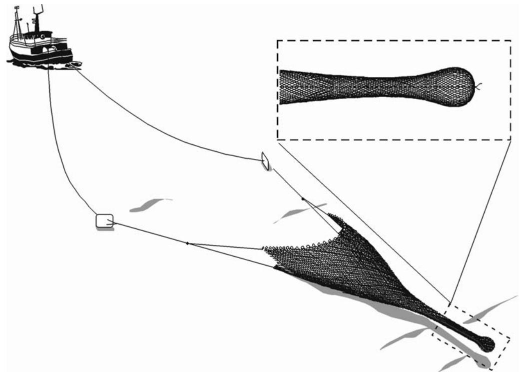

Fig. 1 A demersal otter trawl with the axisymmetric cod-end, at the back of the fishing gear, magnified

$$\frac{dx}{da}=\left(1-\left(\frac{dy}{da}\right)^2\right)^{0.5} \tag{3}$$

$$\int_0^{a_{r+1}}\frac{N/r}{\sqrt{\mu^2N^2M^2-4\pi^2y^2}}da=1 \tag{4}$$

where N is the number of meshes around the circumference, M is twice the length of each twine element, μ is a coefficient of extension/contraction, f and g are twice the longitudinal and transverse forces that act at the end of each twine element (Figs. 3 and 5), and a_{r+1} is the value of a at the $(r+1)$th node (i.e., the right hand side of the rth mesh). These equations are fully determined if we have additional relationships specifying mesh deformation (characterized by y and μ) in terms of f and g.

3 Analytical Solutions

The case where the netting twine is inextensible and has no bending stiffness is considered in Ref. [15]. Under these circumstances the twine tensions are the only membrane forces and the corresponding equations can be derived by setting $\mu=1$ and $g/f=\tan\varphi=2\pi y/(N^2M^2-4\pi^2y^2)^{0.5}$. The first equation above becomes

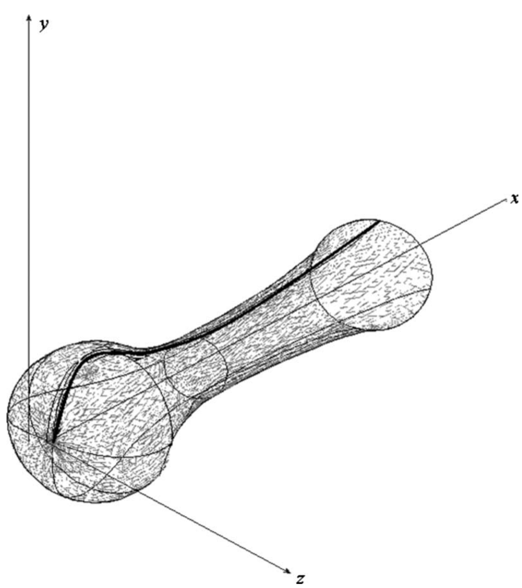

Fig. 2 The coordinate system and the strip of meshes under consideration along the profile of the axisymmetric cod-end

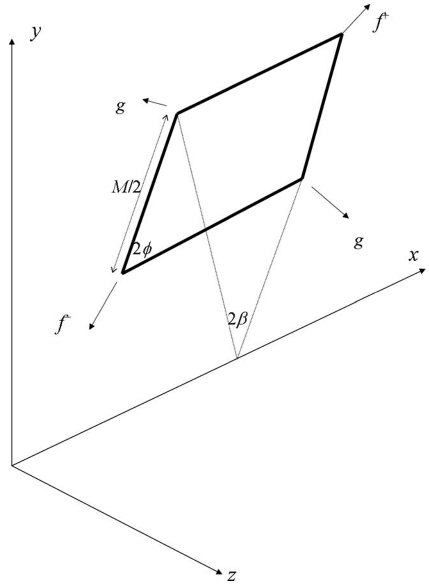

Fig. 3 The coordinate system and the in-plane membrane forces acting on one of the meshes along the network profile

$$\frac{d^2y}{da^2}=\frac{4\pi^2y}{N^2M^2-4\pi^2y^2}\left(1-\left(\frac{dy}{da}\right)^2\right)-\frac{2\pi yP}{Nf(a)}\left(1-\left(\frac{dy}{da}\right)^2\right)^{0.5} \tag{5}$$

(inextensible diamond mesh netting held between two circular rings).

By putting $P=0$ we derive the equation governing inextensible diamond mesh netting held under tension between two circular rings. It is shown in the Appendix that this can be solved by

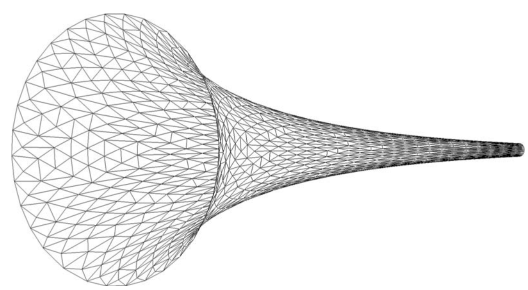

Fig. 4 The triangular finite elements that discretize the netting in Priour's model

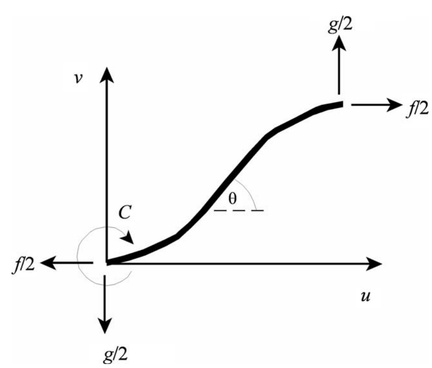

Fig. 5 The forces and bending couple acting on a twine element of a reinforced network

$$y(a) = A \cosh na + B \sinh na$$

where $n=2\pi/(N^2M^2+4\pi^2B^2-4\pi^2A^2)^{0.5}$ and A and B are determined from the boundary conditions. Kuznetsov [19] recognized that diamond mesh netting stretched between two rings forms a pseudosphere. Pseudospheres are surfaces of constant negative Gaussian curvature where the Gaussian curvature of a surface is the product of the two principle curvatures. Given that our surfaces are generated by revolution of $y(a)$, we can demonstrate directly that they have a Gaussian curvature equal to $-n^2$. For the special case where $A=-B$ the problem is that of netting attached to a ring of radius A at the origin, which has radius 0 at infinity. This curve is the tractrix or pursuit curve [20]. In terms of the arc length a it is

$$y(a) = Ae^{-na}$$

where now $n=2\pi/NM$. We show in the Appendix that we can find a complete analytical solution to this problem and also derive

$$x(a) = \frac{1}{n}\tanh^{-1}\sqrt{1-n^2A^2e^{-2na}} - \frac{1}{n}\sqrt{1-n^2A^2e^{-2na}} + \text{const} \quad (6)$$

$$t(a) = \frac{T}{2N(1-n^2A^2e^{-2na})} \quad (7)$$

where the constant in the equation for x ensures that $x(0)=0$, t is the tension in an individual twine element, and T is the axial force acting on the circular ring at the boundary. We also show that the position of the $(r+1)$th point of intersection along the netting profile is given by

$$a_{r+1} = -\frac{1}{2n}\ln\left(\frac{1-\tanh^2(nrM+\tanh^{-1}\sqrt{1-n^2A^2})}{n^2A^2}\right) \quad (8)$$

(inextensible diamond mesh netting subject to a constant internal pressure force).

Although we are unable to find an analytic solution to the problem of inextensible diamond mesh netting subject to a constant internal pressure force, it is possible to determine an analytic expression for an upper bound on the maximum diameter that such an axisymmetric network will have [21].

In general, y will have a local maximum where $dy/da=0$ and $d^2y/da^2\leq 0$. When the pressure is positive and constant it is reasonable to expect that for a given set of boundary conditions there will be an upper bound on the maximum value y can take. Consider the case where $y(0)$, $f(0)$, and the boundary slope are fixed and there is a local maximum, y_m, which due to insufficient netting along the axial direction is less than the upper bound. If we increase the number of meshes, L, along this direction, y_m will increase until it approaches its upper bound. Further increases in L will lead to a region around x_m where y approaches it maximum, $dy/da\to 0$ and $d^2y/da^2\to 0$. By setting $dy/da=0$ and $d^2y/da^2=0$ above we get

$$6\pi^2y^2 - N^2M^2 - 2\pi\left(\pi y_0^2 - \frac{Nf_0}{P}\left.\frac{dx}{da}\right|_0\right) = 0 \quad (9)$$

which can be solved to give

$$y_{up} = \sqrt{\frac{N^2M^2}{6\pi^2} + \frac{y_0^2}{3} - \frac{Nf_0}{3\pi P}\left.\frac{dx}{da}\right|_0} \quad (10)$$

With regard to fishing gears the most important case is where $y_0=0$ and $dy/da|_0=0$ to give

$$y_{up} = \frac{NM}{\pi\sqrt{6}} \quad (11)$$

These are the conditions that apply at the rearmost end of a trawl gear where the netting is tied closed and where the catch accumulates (Figs. 1 and 2). Half the angle between twines can be shown to be $\tan^{-1}\sqrt{2}$, which is the same as the result given in Ref. [13] for the case of a pressurized woven hose with unrestrained ends.

4 Axisymmetric Networks With Twine Bending Stiffness

To include the influence of twine bending stiffness in the formulation of O'Neill (Eqs. (1)–(4)) we must be able to relate mesh deformation to f and g, the in-plane membrane forces. To deform a mesh we must deform each of the four component twines, which we assume here are all identical and have fixed slope angles at their points of intersection. Thus we need to be able to relate the deformation of the twine elements to the forces acting on them. If we assume that the bending moment of a deformed twine is proportional to its curvature and that there is no twine extension then the equations of moment equilibrium of a twine element are

$$EI\frac{d\theta}{ds} = c + vf/2 - ug/2 \quad (12)$$

$$\frac{du}{ds} = \cos\theta \quad (13)$$

$$\frac{dv}{ds} = \sin\theta \quad (14)$$

where θ is the slope angle of a twine element, u and v are local Cartesian coordinates, s is the arc length along a twine element, EI is the twine bending stiffness, $f/2$ and $g/2$ are the tensile components acting at each end of the twine, and c is a counteracting couple (Fig. 5). For the problem of interest here we usually have $u(0)=v(0)=0$ and $\theta(0)=\theta(M/2)=\lambda$, say. We will also know two of the following four quantities: $u(M/2)$, $v(M/2)$, f, and g, and can accordingly calculate the other two and c.

These equations are singularly perturbed and are solved asymptotically in Ref. [18]. The form of the solution that interests us here is the following, which expresses the position of the twine boundary and the counteracting couple in terms of the applied forces:

$$u(M/2) = \frac{M}{2}\cos\beta_o + 2M\varepsilon\left\{\cos\left(\frac{\lambda+\beta_o}{2}\right) - \cos\beta_o\right\} + O(\varepsilon^2) \quad (15)$$

$$v(M/2) = \frac{M}{2}\sin\beta_o + 2M\varepsilon\left\{\sin\left(\frac{\lambda+\beta_o}{2}\right) - \sin\beta_o\right\} + O(\varepsilon^2) \quad (16)$$

$$c = 2\sqrt{EIt}\sin\left(\frac{\beta_o-\lambda}{2}\right) + O(\varepsilon^2) \quad (17)$$

where $\varepsilon^2=4EI/NM^4Pt$, $\beta_o=\tan^{-1} g/f$, and here $t=0.5\sqrt{(f^2+g^2)}$.

Mesh deformation at any point along the network can, thus, be related to the in-plane forces f and g as follows:

$$y(a) = \frac{N}{\pi}v(M/2)$$

$$\mu(a) = \frac{2}{M}\sqrt{u^2(M/2)+v^2(M/2)}$$

where the first expression is derived by dividing the network circumference by the number of meshes around the circumference and the second from the length of the dashed line of Fig. 5. These two expressions couple the two sets of differential equations (1)–(4) and (12)–(14), which together with appropriate boundary conditions govern the geometry of an axisymmetric network of twines with bending stiffness subject to a constant pressure force P.

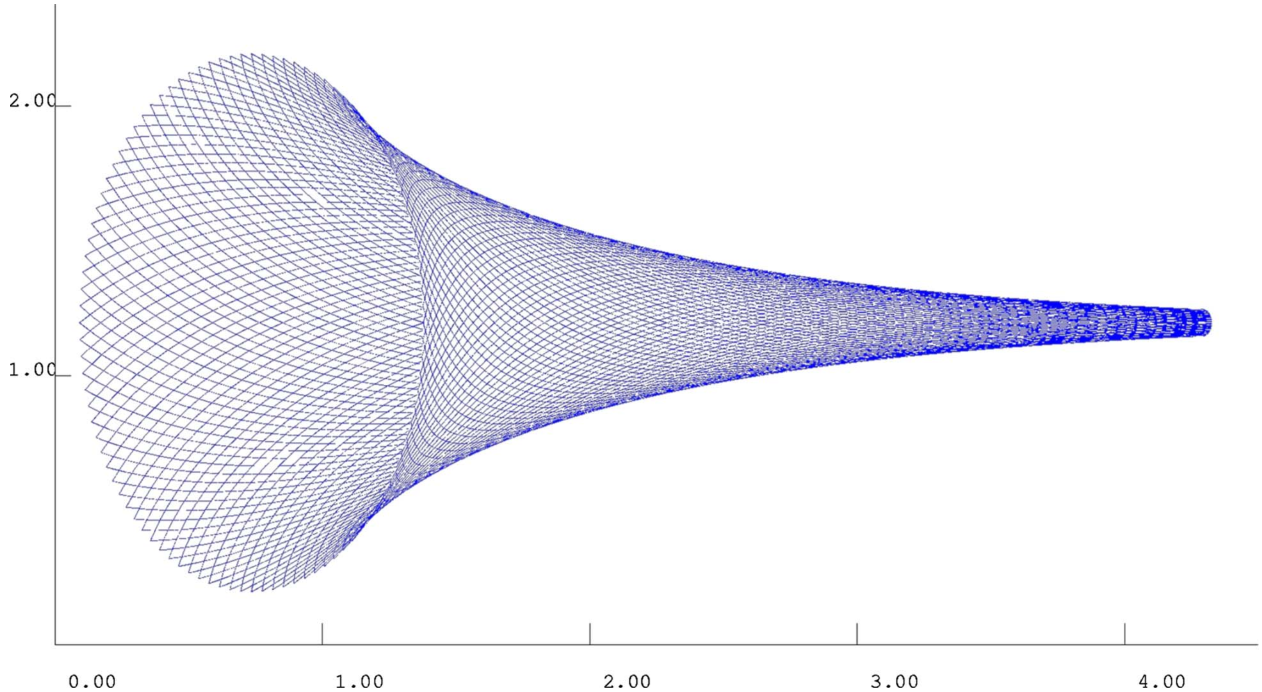

Fig. 6 Tractrix calculated by Priour's model. The radii of the boundary rings are 1 m and 0.048599 m. The distance between them is 4.6473 m. The mesh size of the netting is M=0.1 m, the number of meshes around N=100, and the number of meshes between the rings is L=50.

The asymptotic solutions (15)–(17) are shown in Ref. [18] to be very accurate for $\varepsilon < 0.2$, and such values are typical of the netting materials used by the North East Atlantic demersal fleets.

5 Numerical Models

5.1 O'Neill's Model. O'Neill [15] found numerical solutions to a more general form of Eqs. (1)–(4) using an iterative finite difference scheme employing three-point central differences except at the boundaries where three-point forward and backward differences are used. Integrations are carried out using the trapezoidal rule. This approach is used below to obtain numerical predictions to the above analytic solutions where there is no twine bending stiffness.

To solve the cases where the twine elements have bending stiffness a zero finding routine was used during each iteration to find the g that satisfied Eq. (16) for given f and y. In the examples presented below it has been assumed that $\lambda=0$ and accordingly the expression for the counteracting couple is

$$c_o = 2\sqrt{EIt}\,\sin\left(\frac{\beta_o}{2}\right)$$

5.2 Priour's Model. The model of Priour [9] uses a very different approach. This model assumes that the netting twine is isotropic and elastic and discretizes the netting surface using contiguous triangular elements. Each element is made up of a number of meshes, which can be characterized by two parallel families of twine. It is assumed that twines from the same family remain parallel and consequently, for a given element, it is possible to establish a relationship between the forces applied to each node and its position. The final equilibrium position of the nodes is then found using Newton–Raphson iteration.

This model is extended in Ref. [17], using the principle of virtual work, to account for the case where a couple, c_p, acts between each twine element. The couple is assumed to be proportional to the angle between twines, $\beta_p=\tan^{-1} v/u$. In this formulation the twine elements themselves do not bend and β_p and β_o above are equal only in the limiting case of no bending stiffness. If we choose the constant of proportionality to be $\sqrt{(EIt)}$ then the counteracting couple

$$c_p = \sqrt{EIt}\beta_p$$

which, for small ε, is a good approximation to c_o (at the maximum mesh opening $2\sin(\beta/2)$ differs from β by only 4%) and allows us to compare both models.

6 Numerical Predictions of Analytic Solutions

6.1 Tractrix Solution. Consider a cylindrical piece of 100 mm mesh size netting, 100 meshes in circumference and 50 meshes in length, that is attached to a circular ring of radius 1.0 m at the origin, i.e., $M=0.1$ m, $N=100$, $L=50$, and $A=1.0$ m where L is the number of meshes along the length of the cod-end. If we set $r=50$ in Eq. (8) we get $a_{51}=4.813073$ m which, from Eq. (6), gives a radius of 0.048599 m at this point. Hence, if we attach the other end of the piece of netting described above to a circular ring with this radius, the solution is a tractrix.

Figure 6 presents the solution to this problem while Table 1 displays the analytic solution at a number of equally spaced points along the netting profile and the corresponding numerical predictions of the models of both O'Neill and Priour obtained at these points where the resolution of the numerical procedure is successively increased. It is clear that both methods provide good predictions, which are increasingly accurate as the number of nodes is increased.

6.2 Maximum Radius of Netting Subject to a Constant Internal Pressure Force. Equation (11) provides an upper bound on the radius of a diamond mesh axisymmetric network. Hence the maximum possible radius where $M=0.1$ m and $N=100$ is $y_{up}=1.299495$ m. As the area over which the constant pressure force acts is increased, the maximum radius ($y_{\max}$) should increase toward this value (assuming there are sufficient numbers of meshes along the length). Figure 7 presents the solution of the case where

Table 1 Analytical solution of the tractrix and the corresponding predictions of the models of O'Neill and Priour for several resolutions

	O'Neill's model					Priour's model			
No. of nodes x	11	21	41	81	Analytic y	662	298	84	32
0	1	1	1	1	1	1	1	1	1
0.403501	0.740757	0.7395	0.739173	0.739091	0.739032	0.739158	0.740672	0.749615	0.731177
0.844094	0.548568	0.546819	0.546366	0.546252	0.546168	0.546159	0.54723	0.552714	0.53157
1.303628	0.406168	0.404321	0.403846	0.403725	0.403636	0.403594	0.404185	0.407713	0.39635
1.773173	0.30068	0.298944	0.298498	0.298385	0.2983	0.298292	0.298861	0.302777	0.291388
2.248093	0.222536	0.221017	0.220627	0.220528	0.220453	0.220415	0.220829	0.223283	0.215256
2.725923	0.164639	0.163387	0.163065	0.162984	0.162922	0.162865	0.163171	0.164585	0.157114
3.205334	0.121724	0.120761	0.120515	0.120453	0.120404	0.120315	0.120615	0.121574	0.117079
3.685607	0.089886	0.089227	0.089058	0.089016	0.088983	0.088883	0.089138	0.08953	0.086114
4.166349	0.066229	0.065888	0.0658	0.065778	0.065761	0.065664	0.065867	0.065915	0.064538
4.647348	0.048599	0.048599	0.048599	0.048599	0.048599	0.048599	0.0486	0.048604	0.048601
	→ Increasing accuracy					← Increasing accuracy			

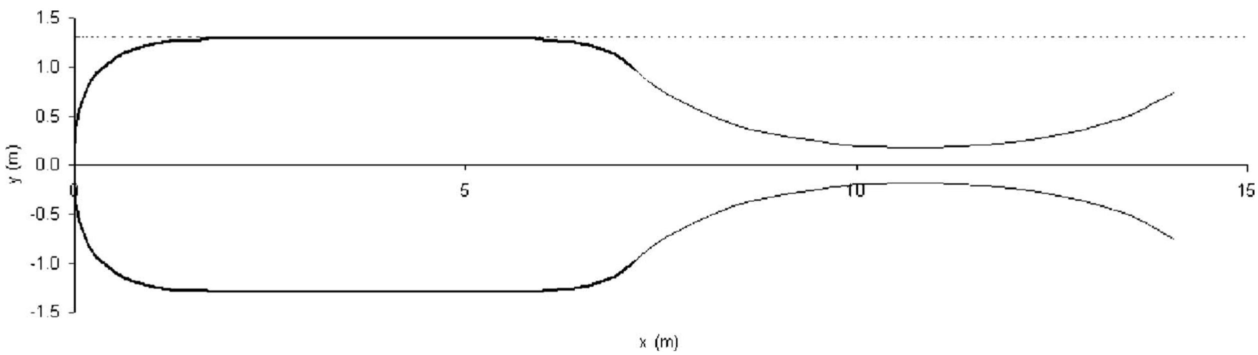

Fig. 7 The profile of a cod-end (axisymmetric network) subject to a constant internal pressure force acting over the first 8 m of the cod-end profile. The bold part of the curve identifies the region where the pressure acts. The cod-end specification is $M=0.1$ m, $N=100$, and $L=200$. The horizontal line is the upper bound on the radius.

$M=0.1$ m, $N=100$, $L=200$, and the pressure force acts over the first 8 m of the network profile. The horizontal line is the upper bound on the radius.

Figure 8 contains the predictions for both models of the maximum radii as the region over which the pressure force acts on the above network increases from 3 m to 12 m. While, both sets of results tend toward y_{up}, in these simulations those of O'Neill are always less than y_{up} whereas Priour's oscillate around the upper bound.

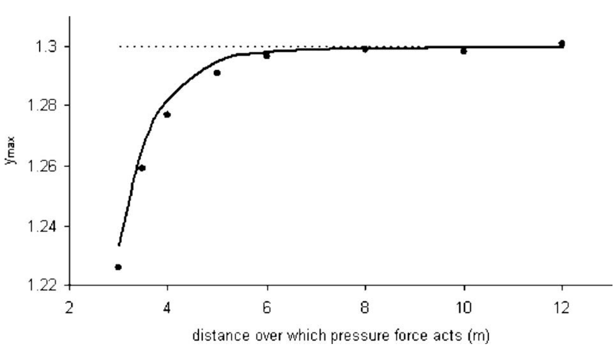

Fig. 8 The maximum radius of a cod-end with $M=0.1$ m, $N=100$, and $L=200$, where the pressure force acts over a range from 3 m to 12 m. The solid line and the points are the predictions of the models of O'Neill and Priour, respectively. The dashed line is the analytical upper bound.

6.3 Geometry of a Diamond Mesh Cod-End With Twine Bending Stiffness. Figure 9 contains the profile predicted by models of O'Neill and Priour of a cod-end where $y(0)=0$, $y(a_{\max})=0.5$ m, $M=0.1$ m, $N=100$, $L=60$, $\lambda=0$, and the internal pressure acts from the left hand boundary to $a=2.5$ m (the bold part of each curve), after which there are no applied forces acting on the network surface (the thin part of each curve). The outer curve is the solution for the case where the individual twine elements do not have twine bending stiffness, i.e., $EI/NM^4P=0$. It is not possible to demonstrate graphically any difference between the predictions of either model.

The inner curves are the model predictions where the twine elements have twine bending stiffness, $EI=10^{-4}$ N m^2, $P=100$ N m^{-2}, and $EI/NM^4P=10^{-4}$. In this case there is a difference between the two models. In the region of the applied forces the difference is less than 0.5% and again cannot be seen graphically; however, in the region where the netting necks and is at its narrowest there is about a 5% difference.

7 Discussion

There is very good agreement between the numerical solutions of the two models examined here and the corresponding analytical values. The accuracy of the models increases as the number of nodes employed increases and both converge to the analytical solutions. It may be argued that this is what would be expected of O'Neill's model as it is based on finding numerical solutions to the differential equations from which the analytical solutions are

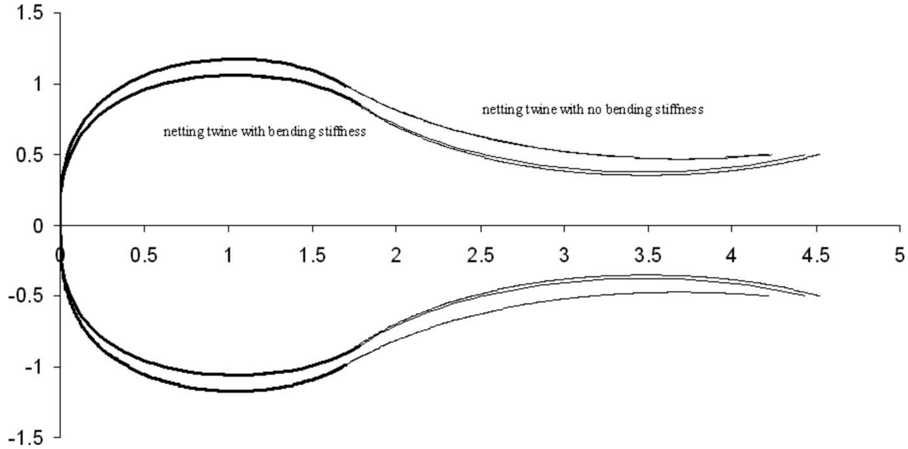

Fig. 9 The profiles predicted by models of O'Neill and Priour of a cod-end subject to a constant internal pressure. The bold part of each curve identifies the region where the pressure acts. The outer curve is the solution predicted by both models for the case there is no twine bending stiffness and cannot be differentiated graphically. The inner curves are the predictions where there is bending stiffness, which differs by about 5% where the cod-end necks.

derived. Nevertheless, the numerical approach has to be tested and these results are very encouraging and give confidence in both methods.

The similarity of the predictions of the reinforced networks is also very encouraging, especially when one considers how different the models are in terms of both derivation, structure, and numerical methodology. O'Neill's used iterative finite differences to solve the governing differential equations and introduced twine bending stiffness via a constitutive relationship between the membrane forces and the in-plane deformation of the network. Whereas, the model of Priour discretizes the netting surface using triangular elements, establishes the force balance at the nodes of each element, and finds the equilibrium position of the nodes using an iterative Newton–Raphson method.

The model of O'Neill converges more quickly, but this is primarily due to its assumption of axisymmetry. While this makes it less adaptable, it is still very useful and has been employed successfully to predict the geometry of commercial cod-ends and in a predictive model of cod-end selection to estimate the extent to which fish are retained by a fishing gear [22]. The cod-end is the rearmost part of a towed fishing gear; it is where fish accumulate, from where they escape, and, to a very good approximation, axisymmetric (Fig. 2).

Priour's model can examine three-dimensional netting structures; hence it is more versatile and, in addition to cod-ends, has been used to model the geometry of whole fishing gears (Fig. 1) and aquaculture cages.

The two analytical solutions presented will also be very useful to test the accuracy of the other numerical models of the deformation of netting material that have been developed in recent years. Up to now the only way to validate these models has been to compare their predictions with experimental measurements where there have often been difficulties associated with measurement error and/or accurate specification of the problem.

Appendix

The equations governing diamond mesh netting made of inextensible flexible twine stretched between two circular rings can be found by putting $P=0$ in Eq. (5) to give

$$\frac{d^2y}{da^2} = \frac{4\pi^2 y}{N^2M^2 - 4\pi^2y^2}\left(1 - \left(\frac{dy}{da}\right)^2\right) \tag{A1}$$

We can show that $y(a)=A\cosh na + B\sinh na$ solves this equation where $n=2\pi/(N^2M^2+4\pi^2B^2-4\pi^2A^2)^{0.5}$ and the unknown constants, A and B, are determined from the boundary conditions. This is most easily done by first showing that this form of y solves

$$1 - \left(\frac{dy}{da}\right)^2 = \frac{n^2}{4\pi^2}(N^2M^2 - 4\pi^2y^2)$$

after which it is clear that it also solves what remains of Eq. (A1). From Eq. (3) we then get

$$\frac{dx}{da} = \frac{n}{2\pi}(N^2M^2 - 4\pi^2y^2)^{0.5}$$

and accordingly that the tension in each twine element is

$$t = \frac{cM}{n(N^2M^2 - 4\pi^2y^2)}$$

where $t=f/\cos\varphi$ and c is a constant that depends on the axial tensile force applied to the circular rings.

For the case where $A=-B$, $y(a)=Ae^{-na}$ and the equation for dx/da can be expressed as

$$\frac{dx}{da} = (1 - n^2A^2e^{-2na})^{0.5} = (1 - n^2A^2e^{-2na})^{-0.5} - n^2A^2e^{-2na}(1 - n^2A^2e^{-2na})^{-0.5}$$

which can be integrated using standard tables of integrals [23] to give

$$x(a) = \frac{1}{n}\tanh^{-1}\sqrt{1 - n^2A^2e^{-2na}} - \frac{1}{n}\sqrt{1 - n^2A^2e^{-2na}} + \text{const}$$

Similarly Eq. (4) becomes

$$\int_0^{a_{r+1}} \frac{1}{rM\sqrt{1 - n^2A^2e^{-2na}}}da = 1$$

which on integration gives

$$a_{r+1} = -\frac{1}{2n}\ln\left(\frac{1 - \tanh^2(nrM + \tanh^{-1}\sqrt{1 - n^2A^2})}{n^2A^2}\right)$$

References

[1] Lee, C.-W., Lee, J.-H., Cha, B.-J., Kim, H.-Y., and Lee, J.-H., 2005, "Physical Modeling for Underwater Flexible Systems Dynamic Simulation," Ocean Eng., **32**, pp. 331–347.

[2] Takagi, T., Shimizu, T., Suzuki, K., Hiraishi, T., and Yamamoto, K., 2004,

"Validity and Layout of 'NaLa': A Net Configuration and Loading Analysis System," Fish. Res., **66**, pp. 235–243.
[3] Theret, F., 1993, "Etude de l'´equilibre de surfaces r'eticul'ees plac'ees dans un courant uniforme;application aux chalets," Ph.D. thesis, Ecole Centrale de Nantes, Nantes, France.
[4] Bessonneau, J. S., and Marichal, D., 1998, "Study of the Dynamics of Submerged Supple Nets (Applications to Trawls)," Ocean Eng., **25**(7), pp. 563–583.
[5] Tsukrov, I., Eroshkin, O., Fredriksson, D. W., Swift, M. R., and Celikkol, B., 2003, "Finite Element Modeling of Net Panels Using a Consistent Net Element," Ocean Eng., **30**, pp. 251–270.
[6] Hu, F., Shiode, D., Wan, R., and Tokai, T., 2006, "Accuracy Evaluation of Numerical Simulation of Mid-Water Trawl Nets," *Contributions on the Theory of Fishing Gears and Related Marine Systems*, Vol. 4, C.-W. Lee, ed., Pukyong National University Press, Busan, Korea.
[7] Niedzwiedz, G., and Hopp, M., 1998, "Rope and Net Calculations Applied to Problems in Marine Engineering and Fisheries Research," Arch. Fish. Mar. Res., **46**, pp. 125–138.
[8] Le Dret, H., Priour, D., Lewandowski, R., and Chagneau, F., 2004, "Numerical Simulation of a Cod End Net Part 1: Equilibrium in a Uniform Flow," J. Elast., **76**(2), pp. 139–162.
[9] Priour, D., 1999, "Calculation of Net Shapes by the Finite Element Method With Triangular Elements," Commun. Numer. Methods Eng., **15**(10), pp. 755–763.
[10] Steigmann, D. J., and Pipkin, A. C., 1991, "Equilibrium of Elastic Nets," Philos. Trans. R. Soc. London, Ser. A, **335**, pp. 419–454.
[11] Rivlin, R. S., 1958, "The Deformation of a Membrane Formed by Inextensible Cords," Arch. Ration. Mech. Anal., **2**, pp. 447–476.
[12] Kuznetsov, E. N., 1986, "Kinetoelastostatics of Axisymmetric Nets," ASME J. Appl. Mech., **53**, pp. 891–896.
[13] Kuznetsov, E. N., 1991, *Underconstrained Structural Systems*, Springer, New York.
[14] Pipkin, A. C., 1980, "Some Developments in the Theory of Inextensible Networks," Q. Appl. Math., **38**, pp. 343–355.
[15] O'Neill, F. G., 1997, "Differential Equations Governing the Geometry of a Diamond Mesh Cod-End of a Trawl Net," ASME J. Appl. Mech., **64**(1), pp. 7–14.
[16] O'Neill, F. G., 1999, "Axisymmetrical Trawl Cod-Ends Made From Netting of Generalized Mesh Shape," IMA J. Appl. Math., **62**, pp. 245–262.
[17] Priour, D., 2001, "Introduction of Mesh Resistance to Opening in a Triangular Element for Calculation of Nets by the Finite Element Method," Commun. Numer. Methods Eng., **17**(4), pp. 229–237.
[18] O'Neill, F. G., 2002, "The Bending of Twines and Fibres Under Tension," J. Text. Inst., Part 1, **93**, pp. 1–10.
[19] Kuznetsov, E. N., 1982, "Axisymmetric Static Nets," Int. J. Solids Struct., **18**, pp. 1103–1112.
[20] Kuznetsov, E. N., 1997, private communication.
[21] O'Neill, F. G., 2004, "The Influence of Bending Stiffness on the Deformation of Axisymmetric Networks," 23rd International Conference on Offshore Mechanics and Artic Engineering.
[22] O'Neill, F. G., and Herrmann, B., 2007, "PRESEMO—A Predictive Model of Cod-End Selectivity–A Tool for Fisheries Managers," ICES J. Mar. Sci., **64**, pp. 1558–1568.
[23] Gradshteyn, I. S., and Ryzhik, I. M., 1965, *Table of Integrals, Series and Products*, Academic, New York.

Validation of Nonlinear Viscoelastic Contact Force Models for Low Speed Impact

Yuning Zhang
e-mail: yuning.zhang@mail.mcgill.ca

Inna Sharf
e-mail: inna.sharf@mcgill.ca

Department of Mechanical Engineering,
McGill University,
Montreal, QC, H3A 2K6, Canada

Compliant contact force modeling has become a popular approach for contact and impact dynamics simulation of multibody systems. In this area, the nonlinear viscoelastic contact force model developed by Hunt and Crossley (1975, "Coefficient of Restitution Interpreted as Damping in Vibroimpact," ASME J. Appl. Mech., ***42****, pp. 440–445) over 2 decades ago has become a trademark with applications of the model ranging from intermittent dynamics of mechanisms to engagement dynamics of helicopter rotors and implementations in commercial multibody dynamics simulators. The distinguishing feature of this model is that it employs a nonlinear damping term to model the energy dissipation during contact, where the damping coefficient is related to the coefficient of restitution. Since its conception, the model prompted several investigations on how to evaluate the damping coefficient, in turn resulting in several variations on the original Hunt–Crossley model. In this paper, the authors aim to experimentally validate the Hunt–Crossley type of contact force models and furthermore to compare the experimental results to the model predictions obtained with different values of the damping coefficient. This paper reports our findings from the sphere to flat impact experiments, conducted for a range of initial impacting velocities using a pendulum test rig. The unique features of this investigation are that the impact forces are deduced from the acceleration measurements of the impacting body, and the experiments are conducted with specimens of different yield strengths. The experimental forces are compared with those predicted from the contact dynamics simulation of the experimental scenario. The experiments, in addition to generating novel impact measurements, provide a number of insights into both the study of impact and the impact response.* [DOI: 10.1115/1.3112739]

1 Introduction

Over the past several decades, important advances have been made in the area of contact and impact dynamics modeling with new models and solution approaches developed [1–6]. Significantly less attention, however, has been directed toward the experimental studies of contact and more specifically to the validation of the proposed models. One approach to contact *force* modeling, which has gained significant popularity, is the *compliant* contact force model [7–11] in which the contact force between two objects is defined explicitly as a continuous function of local deformation and its rate. The oldest model in this category is due to Hertz [1], developed in the context of quasistatic contact analysis of elastic bodies. Hertz's model defines the normal contact force as

$$F = kx^n \tag{1}$$

where k and n are the stiffness coefficient and power exponent, respectively, computed from material and geometric properties by using elastostatic theory. The utility of Hertz's model is limited to contacts involving elastic deformation and the model does not allow for energy dissipation. In spite of the fact that Hertzian model has been in existence for over a century, experimental validation of the *force response* predicted by Hertz theory is rare in literature. The relevant references are Refs. [1,12,13], where low-velocity head-on impact experiments between a steel sphere and a bar (lead in Refs. [1,12] and aluminum in Ref. [13]) are implemented and good agreement is demonstrated between the experimental and theoretical results.

With the view to using the compliant model for impact scenarios, Hunt and Crossley [2] augmented Hertz's model with a nonlinear viscoelastic term as follows:

$$F = kx^n + \lambda x^n \dot{x} \tag{2}$$

To ensure that the energy dissipated during impact is consistent with the energy loss subsumed in the coefficient of restitution e, several researchers proposed approximate and exact relationships between λ of Eq. (2) and e [7,8,14–18], thereby giving rise to several types of Hunt–Crossley models. In spite of their numerous applications [2,15,16,19,20], an important question remains to be answered: do the existing nonlinear models reflect the real impact force response during impact? To the authors' knowledge, no experimental validation of any of the Hunt–Crossley models proposed to date is available. Thus, the principal objective of the present work is to conduct an experimental impact study aiming to validate the models of the form (2) and furthermore to compare the experimental results to the model predictions obtained with different values of the damping coefficient λ as proposed in Refs. [2,7,8,14–18].

There is another aspect of contact force modeling defined by Eq. (2) that is addressed in the present investigation. As alluded earlier, these models apply to what is commonly referred to in literature as "*elastic*"[1] impacts since they preclude the possibility of any permanent (plastic) deformation. Yet, as noted by Johnson in Ref. [21] and discussed in Sec. 3 of this paper, even at relatively small impact velocities, the stresses in the impacting region may exceed the yield stress of the material, resulting in plastic deformation. Therefore, another question of significant impor-

Contributed by the Applied Mechanics Division of ASME for publication in the JOURNAL OF APPLIED MECHANISM. Manuscript received February 22, 2008; final manuscript received January 11, 2009; published online June 16, 2009. Review conducted by Kenneth M. Liechti.

[1]This term is a misnomer since, in fact, energy dissipation does occur in these impacts. However, since it is the standard terminology in the field, it is adhered to in this paper.

Table 1 Existing expressions for damping coefficient

Researchers	Damping coefficient
Hunt and Crossley [2] Marhefka and Orin [7,8]	$\lambda_{HC}=\lambda_{MO}=\frac{3}{2}\alpha k$
Herbert and McWhannell [14]	$\lambda_{HM}=\frac{6(1-e)}{[(2e-1)^2+3]}\frac{k}{v_i}$
Lee and Wang [15]	$\lambda_{LW}=\frac{3}{4}\alpha k$
Lankarani and Nikravesh [16]	$\lambda_{LN}=\frac{3k(1-e^2)}{4v_i}$
Gonthier et al. [17] Zhang and Sharf [18]	$k\ln\left[\frac{\lambda_E v_i+k}{-\lambda_E(1-\alpha v_i)v_i+k}\right]-2\lambda_E v_i+\alpha\lambda_E v_i^2=0$

Table 2 Material properties of impacting bodies

Impacting bodies	Young's modulus (GPa)	Poisson's ratio	Yield strength (MPa)	Yield contact force (N)
Cylinder specimen 1, C1 (PD613)[a]	213	0.29	1815	6674
Cylinder specimen 2, C2 (4150)[b]	205	0.29	330	42
Ball	210	0.30	2050	-

[a]Specimen C1 (PD613) is a special mold steel produced by Daido Steel (Japan) Co. Ltd. and heat treated at Kai Lai (China) Mold Co.
[b]Specimen C2 (4150) complies with ASTM designations.

tance, which has not been addressed in literature, is as follows: can the nonlinear viscoelastic impact models in Eq. (2) be used to predict the force response for impacts with some plastic deformation? The relevant previous research, although not directly addressing the above question, is by Tsuji et al. [22] and Mishra [23], where simulations are presented with the damping term used to account for the energy dissipated by the plastic deformation. Johnson [21] presented a comprehensive analysis of elastic and inelastic impacts under different conditions. For inelastic impacts at moderate speeds and using quasistatic assumptions, Johnson derived formulas for the coefficient of restitution, the time of plastic indentation and the time of elastic rebound; we will revisit these in Sec. 7.

In Sec. 2, a brief overview of Hunt–Crossley type of nonlinear compliant contact force models is presented. This is followed by the description of the experimental setup in Sec. 3. Section 4 is devoted to the experimental procedures for the velocity and force measurements and Sec. 5 presents the experimental results, including the measured and postprocessed experimental data. Then in Sec. 6, the impact simulation results using the nonlinear compliant models for the experimental scenario are presented, followed by their comparison to the experimental results in Sec. 7.

2 Compliant Contact Force Models

Much of the research based on the Hunt–Crossley nonlinear contact force model of Eq. (2) revolved around the issue of how to determine the damping parameter λ, and more specifically, how λ can be related to the coefficient of restitution e. The resulting methods developed to evaluate the damping coefficient can be categorized in two groups. Those in the first category are best described as the "energy-based" approaches, such as Hunt and Crossley's [2] and Lankarani and Nikravesh's [16], and are characterized by the application of the work-energy principle in the derivation of λ. Methods in the second group directly tackle the equation of motion based on Eq. (2) and include the approximate solutions by Herbert and McWhannell [14], Lee and Wang [15], Marhefka and Orin [7,8], as well as the *exact* solution by Gonthier et al. [17] and Zhang and Sharf [18].

Examination of the aforementioned references reveals five distinct expressions for the damping coefficient λ, which we summarize in Table 1. There, α is an empirical coefficient obtained from a linear fit of the experimental data for e as a function of impact velocity v_i, that is,

$$e=1-\alpha v_i \tag{3}$$

From the analytical standpoint, all "models" for λ appear reasonable as they all generate qualitatively similar force responses. From the practical viewpoint, the different models for λ may result in significant differences in the impact responses, as illustrated in Ref. [18] for an impact scenario with $e=0.6$.

Of relevance to this paper, however, is the fact that all models in Table 1 yield nearly identical results for impacts with coefficient of restitution close to 1. Moreover, it is for this same category of impacts that the assumption of elastic impact, i.e., negligible permanent deformation, applies as enforced by the Hunt and Crossley type models. These factors make the experimental validation of different models for λ a particularly difficult task. For the experiments presented in this manuscript, two materials were employed for the impacted flat, giving the measured coefficients of restitution in the ranges 0.95–0.97 and 0.76–0.92, respectively.

3 Experimental Samples, Setup, and Instrumentation

To capture the main characteristics of impact within the constraints of using a relatively simple experimental test rig and inexpensive instrumentation, our experiments make use of a steel ball impacting the top flat of a cylindrical specimen. In this section, the selection of the specimens and the variables measured in the experiments are discussed, followed by the description of two test rigs—the drop-weight tower and the pendulum test rigs—and the instrumentation employed.

3.1 Selection of Ball and Surface Specimens. Although our ideal experimental scenario would involve a ball impacting a massive stationary flat surface, it was not possible to accommodate a large metal bulk within the geometric and instrumentation constraints of the drop-weight tower and pendulum test rigs employed in this experimental study. Accordingly, the impacting surface used in our experiments was comprised of a cylindrical specimen. The height or thickness of the specimen was chosen based on the experimental results reported in Ref. [1] where it is shown that the coefficient of restitution for impact between steel spheres and a glass plate converges as the plate thickness approaches 2.54 cm. Combining this conclusion with the geometric features of our test rigs, we chose the thickness of the specimen as $h=5.08$ cm.

For a given initial impact velocity, the mass and diameter of the impacting ball directly affect the magnitude of the impact force and therefore, these parameters were selected to produce signals to cover the full range of the instrumentation employed in the experiments. It is also noted that according to Hertzian theory, the size of the ball determines the stresses produced in the impact region.

With the above considerations, we chose the 5.08 cm diameter chrome-steel ball and two cylindrical specimens, C1 and C2, 5.08 cm in diameter and thickness, made of steels with different yield strength values, respectively. The material properties of our impacting bodies are tabulated in Table 2 where the last column includes the value of the contact force F_{yield} to initiate plastic deformation in the specimen. An expression for the latter is given in Ref. [24] and for the ball/massive surface contact scenario it reduces to[2]

$$F_{\text{yield}} = 23.214 p^3 R^2 (q_1 + q_2)^2 \tag{4}$$

where p is the smaller yield strength of the materials of the two impacting bodies, R is the radius of the ball and the subscripted q can be written as $q=(1-\upsilon^2)/E$ with E and υ as Young's modulus and Poisson's ratio of the impacting body (1 or 2). The value of F_{yield} for C2 specimen is particularly low, indicating that plastic deformation may occur even for very small initial impacting velocities.

Last, we take note of the time it takes for the elastic stress waves to propagate the length of our specimens. Setting the longitudinal (bar) wave speed c_0 to be an average of the values for the ball and the two specimens, $c_0=5170$ m/s,[3] the time for the stress pulse to traverse the length of the cylindrical specimen (or the diameter of the ball) away from and back to the impact surface is calculated as [21]

$$T_{\text{wave}} = 2h/c_0 = 1.97 \times 10^{-5} \text{ s}$$

For the range of impact speeds considered in our experiments, the resulting wave propagation time constitutes 7–10% of the duration of impact and therefore, we may expect some energy loss due to elastic waves in the impacting bodies.

3.2 Measured Variables. The measured variables in the impact experiments fall into two categories: the variables measured for direct comparison with the model predictions and the quantities measured in order to determine the parameters required by the model. The experimental impact force between the ball and the surface specimen is the primary quantity required for comparison with the contact force profiles predicted by the models of Sec. 2. As for the model parameters, we assume that the "spring" parameters k and n in the Hunt–Crossley model (Eq. (2)) can be accurately determined based on Hertzian theory, given the geometric and material properties of the impacting bodies. However, the evaluation of the damping coefficient, according to all of the models discussed in Sec. 2, requires the value of the coefficient of restitution e (or the value of α in Eq. (3)). Thus, the initial (pre-impact) and final (postimpact) velocity measurements are employed to determine the coefficient of restitution as per Newton's (kinematic) model of restitution. With the value of e in hand, we can calculate the corresponding parameter α in Eq. (3) and the damping coefficients as per Table 1. Accordingly, two types of experiments are designed: (i) to measure the impact force profile in the impact force experiments and (ii) to measure the initial and final velocities of the ball in the coefficient of restitution experiments.

3.3 Experimental Test Rigs. Majority of the experimental impact studies reported in literature were conducted on a drop tower [25–29] or a pendulum test rig [12,30–32]. In the experimental impact study reported here, the impact force experiments were conducted using the pendulum test rig, while the drop-weight tower was employed to obtain *velocity* measurements for the coefficient of restitution estimation.[4] A detailed description of the test rigs and experimental procedures can be found in Ref. [33].

The experimental setup for impact force measurements (see Fig. 1) is composed of a massive iron base to house the cylindrical

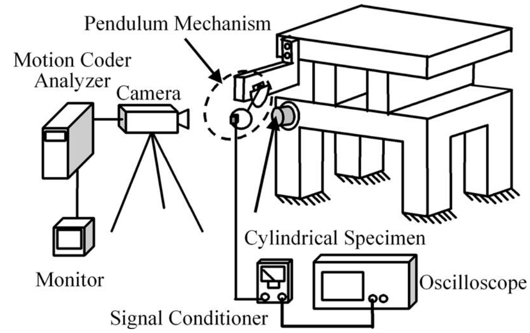

Fig. 1 Experimental setup for force measurement using pendulum test rig (not to scale)

specimen, a pendulum mechanism to enable impact of the ball on the specimen, and the video camera system to record the orientation of the accelerometer (as described in Sec. 4.1). The cylindrical specimen is glued using Loctite metal adhesive to a flattened and polished area on one side of the iron base. The main components of the pendulum mechanism are illustrated in Fig. 2; the mechanism is fixed to a steel hanger mounted on top of the iron bulk. The angle scale is calibrated so that the 90 deg orientation coincides with the line of the pendulum in static equilibrium under gravity.

The steel ball, initially held manually, is released from a particular angle, and falls on the free surface of the cylindrical specimen to make a central direct impact. The vertical position of the cylindrical specimen is such that the ball impacts the center of its free surface. It is also noted that when hung freely, the steel ball of the pendulum is just touching the cylindrical specimen. The steel ball is instrumented with an accelerometer (PCB 352C23), which is glued to a circular flat on the ball, as illustrated in Fig. 2(*a*). The accelerometer is powered by a signal conditioner (PCB 480C02) and the data from it is collected by a digital oscilloscope (TEK TDS3052B) (see Fig. 1). The range of the accelerometer allowed impact force experiments with the pre-impact velocities of $v_i \leq 0.5$ m/s.

The coefficient of restitution experiments to obtain velocity measurements are conducted on a drop-weight tower, which is an iron structure composed of a base, an upper frame, and a releasing mechanism, as shown in Fig. 3. The center of the releasing mechanism is above the center of the top surface of the base cylinder, with the alignment guaranteed by the two vertical steel poles mounted on the base. Mounted on top of the releasing part is a pointer toward the steel ruler for measuring the height of the releasing mechanism.

For the velocity measurements, the specimen (C1 or C2) is centered on the top surface of the base cylinder and is tightly constrained to it with four steel plates, as illustrated in Fig. 3. The steel ball, released from a certain height (adjustable by a dc winch), impacts the top surface of the specimen, followed by a number of rebounds. The resulting motion is imaged by Kodak Motion Corder Analyzer composed of a processor and a video

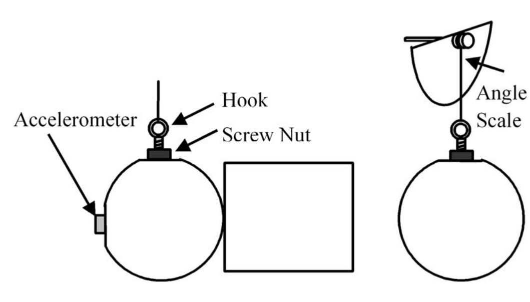

Fig. 2 Pendulum mechanism

[2]Equation (6.10) from Johnson [21] yields a slightly lower coefficient of 21.167 in Eq. (4).

[3]The dilatational wave speed c_1 may be more appropriate for the geometries considered here; however, the corresponding value is higher than c_0 resulting in a lower value of T_{wave}. Therefore, the result obtained here provides a conservative estimate.

[4]The pendulum test rig cannot be used to accurately measure the postimpact velocity because of the vibration of the pendulum string and the ball after impact.

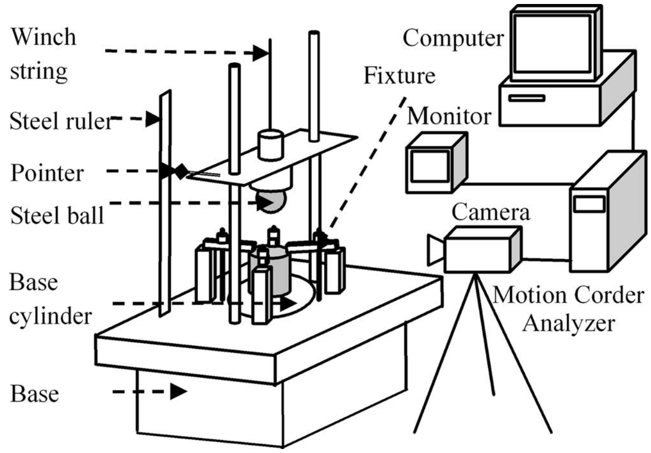

Fig. 3 Experimental setup for velocity measurement (not to scale)

camera with a frame rate of a 1000 frames/s. The camera is mounted horizontally on a tripod, with the camera lens at the height of the impact, approximately 25 cm away. The images captured by the camera are transmitted to the processor and then downloaded to a computer as image frames for further processing.

4 Experimental Procedures

4.1 Force Measurement Procedures. As noted earlier, the pendulum test rig is utilized for the impact force experiments to measure the impact force profiles. In these experiments, the steel ball, initially held manually, is released from an angle indicated by the pendulum string against the angle scale. The geometry of the pendulum is illustrated in Fig. 4 where point A is the origin of the angle scale, point O is the pivot point of the pendulum, r is the radius of the angle scale, d is the distance between points O and A, and L is the distance between points O and C. Referring to Fig. 4, application of energy conservation to the pendulum ball yields a relationship between the pre-impact velocity v_i and the pendulum angle β:

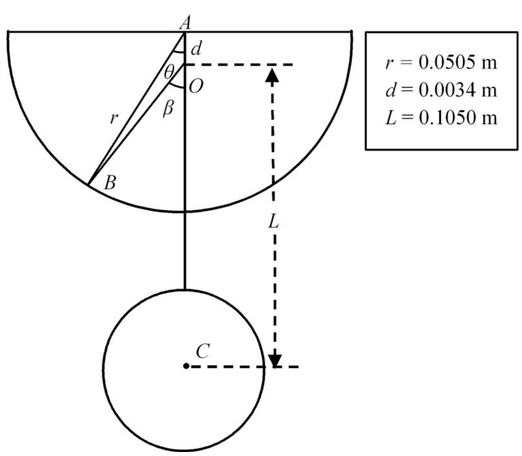

Fig. 4 Geometry of angle scale

$$v_i = \sqrt{10gL^3\left(\frac{1-\cos\beta}{2R^2+5L^2}\right)} \tag{5}$$

where R is the radius of the steel ball and the other geometric parameters are indicated in Fig. 4. It is noted that the possible error in v_i calculated with Eq. (5) from the effect of aerodynamics on the ball is negligible. From the same figure, we can also deduce the relationship between the releasing angle β and the measured angle θ as

$$\beta = \arctan\left(\frac{r\sin\theta}{r\cos\theta - d}\right) \tag{6}$$

It was mentioned in Sec. 1 that our experimental study is partly dedicated to nearly elastic impacts with negligible permanent deformation and therefore, very low impacting velocities are desirable. However, the lowest impact velocity attainable with acceptable accuracy is approximately 0.1 m/s, corresponding to the releasing angle of 5 deg. Hence, in the force measurement with the pendulum test rig, the following initial impact velocities v_i are targeted: 0.1 m/s, 0.15 m/s, 0.2 m/s, 0.3 m/s, 0.4 m/s, and 0.5 m/s. The corresponding releasing angles θ rounded to the nearest integer and their corresponding initial impact velocities are tabulated in Table 3.

When impact occurs between the ball and the specimen, the acceleration signal generated by the accelerometer on the ball in the form of a voltage profile is acquired by the oscilloscope at a sampling frequency of 5 MHz. The acquisition process is triggered by the acceleration signal itself when the signal value exceeds the trigger level set in the oscilloscope. A pre-trigger value is also defined for complete data acquisition over a certain period ahead of the triggering instant. The acceleration profiles of the ball are obtained by multiplying the voltage data with the calibrated sensitivity coefficient. Finally, the impact force on the ball is determined from Newton's second law as $F=ma$, m being the mass of the ball and a being the measured acceleration along the line of impact.

Possible sources of error in the force measurement corresponding to the calculated initial impact velocity are the additional centripetal acceleration measured by the accelerometer on the surface of the ball and the inaccuracies induced by the manual operation of the ball. The latter may induce rotation of the ball about the pendulum string, which would produce a deviation of the accelerometer from the desired orientation along the line of impact. This deviation, if it occurred, was identified by visual inspection of the images obtained with the video camera and the corresponding tests were discarded from the data postprocessing. In this manner, a total of 6 "good" sets of test data are obtained for each v_i. We also point out that the specimens (C1 and C2) were grounded down and polished between experiments to minimize the effects from prior impacts, for example, residual deformations and strain hardening, on subsequent tests.

The additional centripetal acceleration mentioned above arises from the rotation of the ball, which in turn results from two factors: (1) from the rotation of the ball about the pin joint of the pendulum right before the impact and (2) from the friction force generated at the impact point, and acting throughout the impact process. Fortunately, the two effects produce rotations in opposite directions of the same order of magnitude and therefore result in only a very small additional acceleration ($<0.1\%$ of peak measured acceleration).

Table 3 Releasing angles and corresponding initial impact velocities

Releasing angle θ (deg)	5	8	11	16	21	27
v_i (m/s)	0.0938	0.1500	0.2060	0.2989	0.3910	0.5000
Desired v_i (m/s)	0.1	0.15	0.2	0.3	0.4	0.5

4.2 Velocity Measurement Procedure. As noted earlier, the pre- and postimpact velocities required to determine the coefficient of restitution are measured using the video camera system with the drop-weight tower test rig. These experiments are carried out for pre-impact velocity ranges of $0.15\ \mathrm{m/s} \leq v_i \leq 0.8\ \mathrm{m/s}$ for specimen C1 and $0.15\ \mathrm{m/s} \leq v_i \leq 0.5\ \mathrm{m/s}$ for specimen C2. For lower impact velocities, $v_i \leq 0.5\ \mathrm{m/s}$, the following procedure is employed to achieve the most accurate results. The ball is dropped from a certain height H and the repetitive impacts and rebounds of the impact process are captured with the video camera. The resulting image sequences are processed manually, frame by frame, to evaluate the pre- and postimpact velocities for each impact other than the first. For example, the two images corresponding to the first two consecutive impacts can be identified and the time Δt_1 elapsed between them determined from the camera frame rate and the frame numbers. Thus, the pre-impact velocity for the second impact is obtained by using the free-fall relations $v_{i2}=g\Delta t_1/2$. Similarly the pre-impact velocity for the third impact can be obtained from $v_{i3}=g\Delta t_2/2$ with Δt_2 as the time interval between the second and the third impacts. Under the free-fall conditions, the pre-impact velocity of the third impact is equal in magnitude to the postimpact velocity of the second impact, i.e., $v_{f2}=-g\Delta t_2/2$. In this fashion, we can obtain pre- and postimpact velocities for all the following impacts.

For higher impact velocities for specimen C1 ($v_i > 0.5\ \mathrm{m/s}$), the initial impact velocity v_i can be evaluated accurately from $v_i = \sqrt{2gH}$, while the velocity of the ball after impact is determined using a similar estimation procedure as described above.

Possible sources of error in the velocity measurement procedures are the effect of aerodynamics on the ball, which was again ascertained to be negligible. Other effects include the small inaccuracies introduced during the manual release of the ball, relevant when the pre-impact velocities are determined directly from the releasing height, and the effect caused by any permanent deformation from the previous impacts on the top of the cylindrical specimen when the velocities are determined from multiple rebounds. To minimize the influence of these errors, all experiments are repeated to obtain at least ten sets of data and appropriate averaging of the results is used for the calculation of the coefficient of restitution in Sec. 5.1.

It is noted that the accuracy of the above velocity estimation and the corresponding coefficient of restitution degrades significantly for very low impact velocities ($v_i \leq 0.1\ \mathrm{m/s}$), and hence the lower bound of $v_i = 0.15\ \mathrm{m/s}$ is used in the coefficient of restitution experiments. The values of e for impact velocities lower than 0.15 m/s, if required, are obtained from the curve fit of the measured results.

5 Experimental Results: Measurements and Postprocessing

5.1 Coefficient of Restitution. As described in Sec. 4.2, the images captured by the camera system from the coefficient of restitution experiments are processed to extract the pre- and postimpact velocities for each nominal impact velocity. Then the coefficient of restitution is obtained as

$$e = -v_f/v_i \tag{7}$$

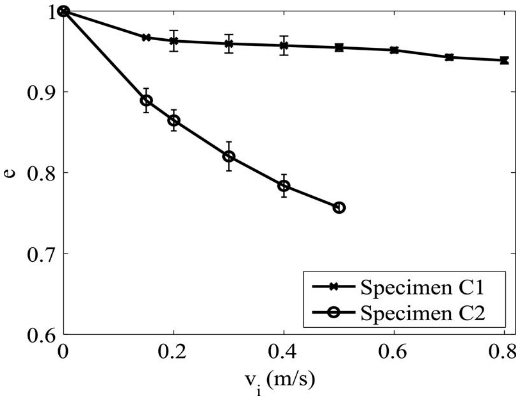

Fig. 5 e as a function of v_i for the two specimens

It is noted that the postimpact velocities for a particular pre-impact velocity show good precision as demonstrated by the error bars in Fig. 5 where the coefficient of restitution e is plotted as a function of v_i, with the experimental results indicated by crosses for specimen C1 and circles for specimen C2. These results confirm the expected decrease in e with increasing pre-impact velocity, as well as the significantly lower values for the specimen with the lower yield strength (C2). Relative to the results for a steel sphere impacting a cast iron plate reported in Ref. [1], our experimental setup produces values of e 20–30% higher for specimen C1 and slightly higher for specimen C2 for the same range of impact velocities.

The plots in Fig. 6 include a linear fit (dashed line) and a nonlinear (dotted line) fit of the experimental data for each specimen, obtained with the nonlinear least-squares curve-fitting algorithm in MATLAB. The general form of the linear fit was stated previously in Eq. (3) while the nonlinear approximation is formulated as

Table 4 Identified parameters of the linear and nonlinear approximations for e

Parameters	Specimens	
	C1	C2
α (Eq. (3))	0.0888	0.5436
α_n (Eq. (8))	0.0626	0.3860
β_n (Eq. (8))	0.3637	0.6475

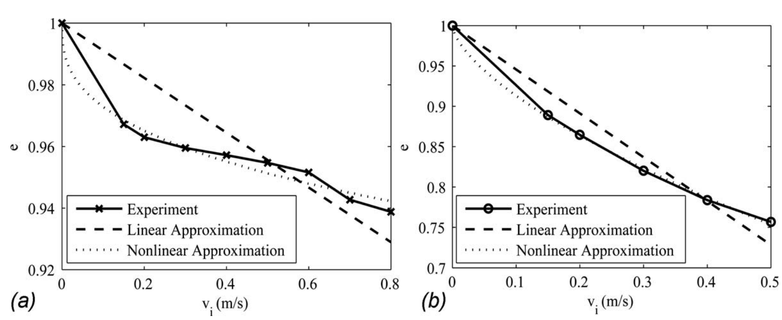

Fig. 6 Approximations of e as a function of v_i: (*a*) specimen C1 and (*b*) specimen C2

Table 5 Coefficient of restitution for the pre-impact velocities in the impact force experiments

	v_i (m/s)					
Specimens	0.0938	0.1500	0.2060	0.2989	0.3910	0.5000
C1	0.9735	0.9672	0.9647	0.9596	0.9555	0.9547
C2	0.9166	0.8892	0.8612	0.8234	0.7899	0.7568

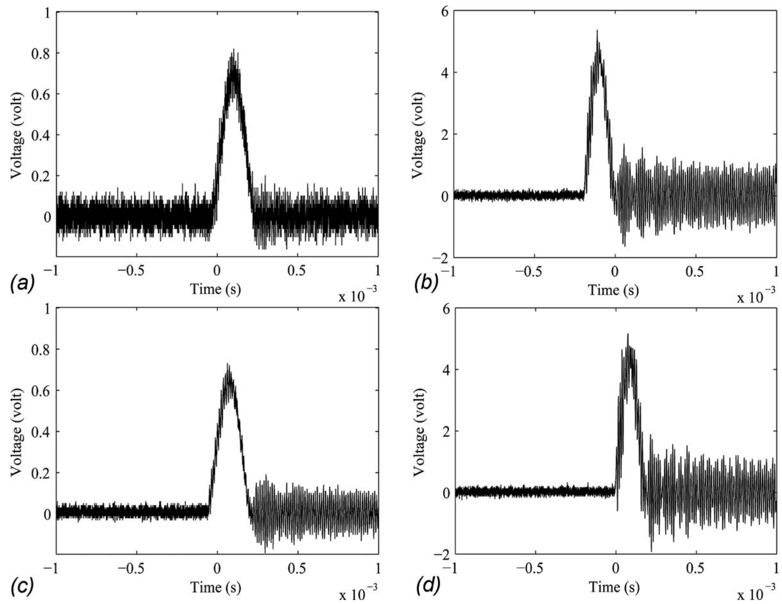

Fig. 7 Acceleration waveforms: (*a*) specimen C1: v_i=0.0938 m/s, (*b*) specimen C1: v_i=0.5 m/s, (*c*) specimen C2: v_i=0.0938 m/s, and (*d*) specimen C2: v_i=0.5 m/s

$$e = 1 - \alpha_n v_i^{\beta_n} \tag{8}$$

The calculated values of α, α_n, and β_n for the two specimens are tabulated in Table 4. Figure 6 also demonstrates that the nonlinear fit provides a slightly better approximation of the experimental data and is therefore employed to estimate the coefficient of restitution at intermediate impact velocity values as required. The coefficients of restitution for the two specimens at the velocities employed in the impact force experiments are tabulated in Table 5.

5.2 Impact Force Estimation. We now present the impact acceleration results obtained from the pendulum test-rig experiments along with the data processing procedure. From the post-processed acceleration profiles, the impact forces are determined directly as described in Sec.4.1.

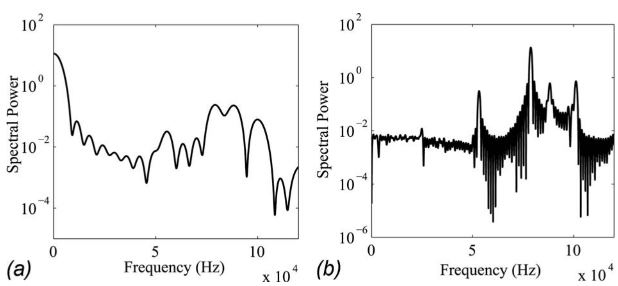

Fig. 8 Frequency spectrum of acceleration signal for specimen C1 at v_i=0.5 m/s: (*a*) during impact and (*b*) after impact

5.2.1 Impact Acceleration Results. The acceleration signals measured with the accelerometer in the pendulum experiments with both types of specimens are plotted in Fig. 7 for the smallest and highest impact velocities employed. In these plots, the triggering instant corresponds to time 0.0 in the impact process, so that the time values in advance of this (starting from the pretrigger instant) are represented by negative values in all time responses.

As observed from Fig. 7, the acceleration signals are characterized by significant oscillations due to the resonance induced by the impact. The power spectra of the acceleration signals were obtained in the frequency range from dc up to the Nyquist frequency. Details in the low-frequency range (up to 120 kHz) are displayed in Fig. 8 for impact of Fig. 7(*b*) with measurements during and after impact.

The power spectrum of the acceleration signal during impact (Fig. 8(*a*)) has the strongest peak at low frequency, two significant secondary peaks near 79 kHz and 88 kHz and two tertiary peaks near 55 kHz and 99 kHz. It is important to point out that the four "extraneous" peaks appear in all the power spectra of the acceleration signals for both specimens and different pre-impact velocities. The 79 kHz component coincides with the specified resonance frequency of the accelerometer, this being further confirmed by the Fast Fourier Transform (FFT) results of the postimpact acceleration signal (Fig. 8(*b*)). We conjecture that the other three secondary peaks correspond to the frequencies of elastic wave propagation[5] and/or the resonances inside the steel ball, as the same peaks appear in Fig. 8(*b*), after the impact.

[5]We estimate the frequencies corresponding to the longitudinal and dilatational waves to be 51 kHz and 57 kHz, respectively.

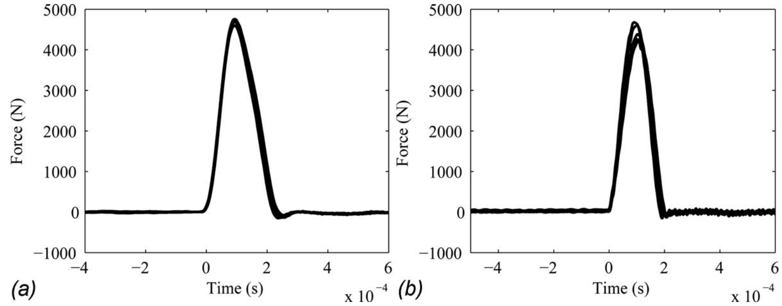

Fig. 9 All impact force profiles with v_i=0.5 m/s: (*a*) specimen C1 and (*b*) specimen C2

Table 6 Standard deviation of peak impact forces (%)

	v_i (m/s)					
Specimens	0.0938	0.15	0.2060	0.2989	0.3910	0.5
C1	2.8	0.9	0.8	3.4	2.1	1.5
C2	5.4	2.9	4.5	4.5	2.4	4.7

5.2.2 Impact Forces. The impact forces can be determined directly from the acceleration signals but first the latter are filtered by using a digital low-pass filter. Here, we make use of the popular Butterworth filter from the signal processing toolbox in MATLAB because of its flat passband characteristics. Based on the results of the FFT analysis, the cutoff frequency is selected at 20 kHz and we use the third order filter. Thus, the six sets of acceleration data, obtained from the six experiments for each pre-impact velocity v_i, are filtered, respectively, and averaged, and the results are used to calculate the impact force between the ball and the cylinder specimen, as discussed in Sec. 4.1.

In Fig. 9 we illustrate all six impact force profiles for the impact scenario with v_i=0.5 m/s for both specimens. As can be seen, the force responses at this impact velocity are in excellent agreement for specimen C1. They are also in very good agreement during compression and restitution phases for specimen C2, however, exhibit a more noticeable spread near the peak impact force. The variations in the peak force values for the impact velocities considered are measured by the standard deviation as percentage of the average peak impact force and are tabulated in Table 6 for both specimens.

6 Impact Model and Simulations

Validation of the nonlinear compliant contact force models must be done by comparing the simulated impact force response from the models to the experimentally observed results. This section is devoted to the modeling of the pendulum impact scenario and the corresponding results obtained with different Hunt–Crossley type models.

6.1 Impact Model for Pendulum Test Rig. The impact system in the pendulum setup is composed of the steel ball and the cylindrical specimen (C1 or C2) glued to the massive iron bulk and thus constitutes a 1DOF dynamics system, as illustrated in Fig. 10. Employing Hunt–Crossley modeling to represent the impact force, we can write down the equation of motion for the steel ball during impact as

$$F_c = -m\ddot{d} = d^n(k + \lambda\dot{d}) \tag{9}$$

where d is the impact penetration between the steel ball and the fixed surface, which also represents the displacement of the center of mass of the steel ball. The result of numerical integration of Eq. (9) for the penetration d and its rate can be substituted into the Hunt–Crossley model to calculate the simulated impact force between the steel ball and the cylindrical specimen.

The parameters of the model are the mass of the steel ball, m =0.54 kg, the power exponent n, and the stiffness and damping coefficients of the compliant contact force model, k and λ. Here, n and k are defined in accordance with the Hertzian theory so that n=1.5, $k=2.4614\times10^{10}$ N/s^n for specimen C1 and $k=2.4144\times10^{10}$ N/s^n for specimen C2, while λ is obtained as per Table 1 for the five compliant contact force models (see Table 7). We note that α, involved in Hunt and Crossley's and Lee and Wang's definitions of damping coefficient, is obtained from the linear fit of the coefficient of restitution, i.e., α in Table 4. On the other hand, the models by Herbert and McWhannell [14], Lankarani and Nikravesh [16], Zhang and Sharf [18], and Gonthier et al. [17] employ the coefficient of restitution directly to define their respective λ, in which case e is taken from Table 5.

6.2 Simulation Results. The dynamics equations (9) for the pendulum impact have been simulated in MATLAB with the ODE45 solver for the initial impact velocities used in the experiments. For conciseness, only the simulation results corresponding to two "extreme" velocities, i.e., 0.0938 m/s and 0.5 m/s, are illustrated in this section. The simulated force profiles obtained from the five Hunt–Crossley type contact force models discussed in Sec. 2—LW, LN, HC, HM, and ZS—are presented in Figs. 11 and 12 where the plots on the right-hand side show the zoom-ins near the peak force values to demonstrate more clearly the differences between the models. Also included in Figs. 11 and 12 are the simulated results obtained with the Hertz model of contact (Hz), per Eq. (1), to allow a more clear demonstration of the effect of the

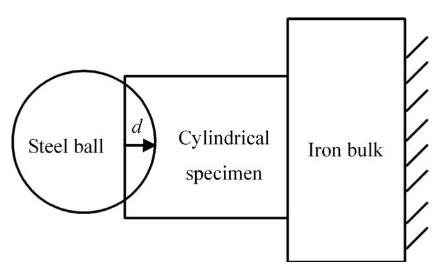

Fig. 10 Model of pendulum impact system

Table 7 Damping coefficients λ (×10[10]) employed in simulations for specimens C1 and C2

Models		v_i (m/s)					
		0.0938	0.15	0.2060	0.2989	0.3910	0.50
Lee and Wang(LW)	C1	0.164	0.164	0.164	0.164	0.164	0.164
	C2	0.984	0.984	0.984	0.984	0.984	0.984
Lankarani and Nikravesh (LN)	C1	1.029	0.794	0.622	0.489	0.411	0.327
	C2	3.086	2.527	2.271	1.951	1.742	1.547
Hunt and Crossley (HC)	C1	0.328	0.328	0.328	0.328	0.328	0.328
	C2	1.969	1.969	1.969	1.969	1.969	1.969
Herbert and McWhannell (HM)	C1	1.071	0.834	0.655	0.519	0.439	0.350
	C2	3.487	2.968	2.772	2.504	2.333	2.159
Zhang and Sharf (ZS)	C1	1.072	0.835	0.656	0.520	0.440	0.350
	C2	3.510	3.004	2.827	2.589	2.450	2.310

damping term on the impact force profiles. The results in these figures reveal the following:

(1) An obvious and not surprising observation is that for a particular impact velocity, the differences between the models are more pronounced for the specimen with lower yield strength (C2), while for a particular specimen, the differences are more significant for higher impact velocities.

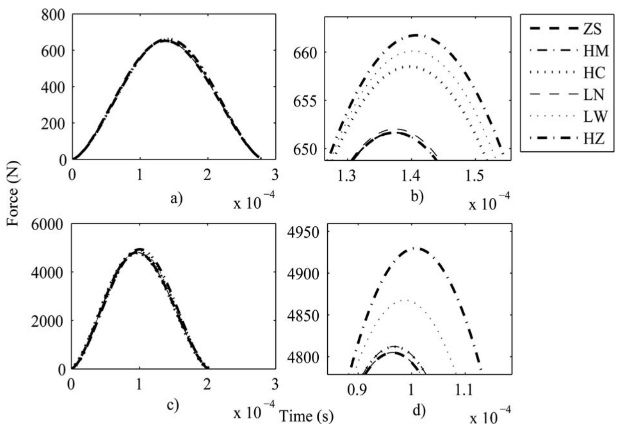

Fig. 11 Simulated impact force profiles for specimen C1: (*a*) v_i=0.0938 m/s (original), (*b*) v_i=0.0938 m/s (zoomed in), (c) v_i=0.5 m/s (original), and (d) v_i=0.5 m/s (zoomed in)

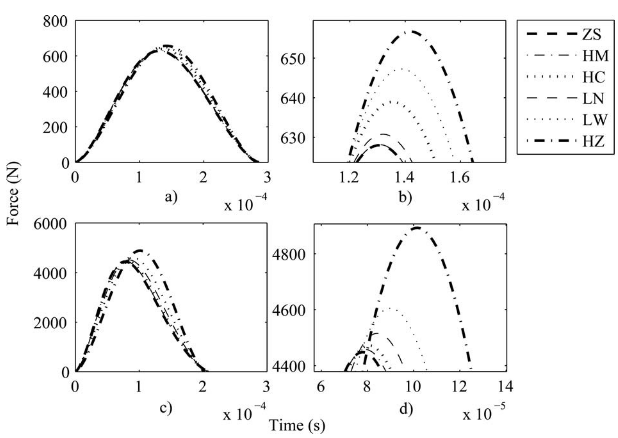

Fig. 12 Simulated impact force profiles for specimen C2: (*a*) v_i=0.0938 m/s (original), (*b*) v_i=0.0938 m/s (zoomed in), (*c*) v_i=0.5 m/s (original), and (*d*) v_i=0.5 m/s (zoomed in)

(2) For specimen C1 and the velocities considered, the differences between Hunt–Crossley series of models are not significant, which renders accurate differentiation between them impossible. By contrast, for specimen C2 with lower coefficients of restitution, there is a visible discrepancy between the five damped models for all velocities. At the highest experimental velocity considered here, there is a substantial disagreement between the Hunt–Crossley type models, both individually and between them as a group and the predictions based on Hertz model. Interestingly, all models are very consistent in predicting the duration of impact.

(3) Hunt–Crossley series of models tend to be in better agreement during the compression phase, with the differences becoming more pronounced during the restitution phase.

(4) The ZS model, which recall is considered to be the most accurate in the series of Hunt–Crossley models, tends to produce lowest peak forces and shortest compression phases. Its predictions tend to be furthest away from the Hertzian nondissipative response.

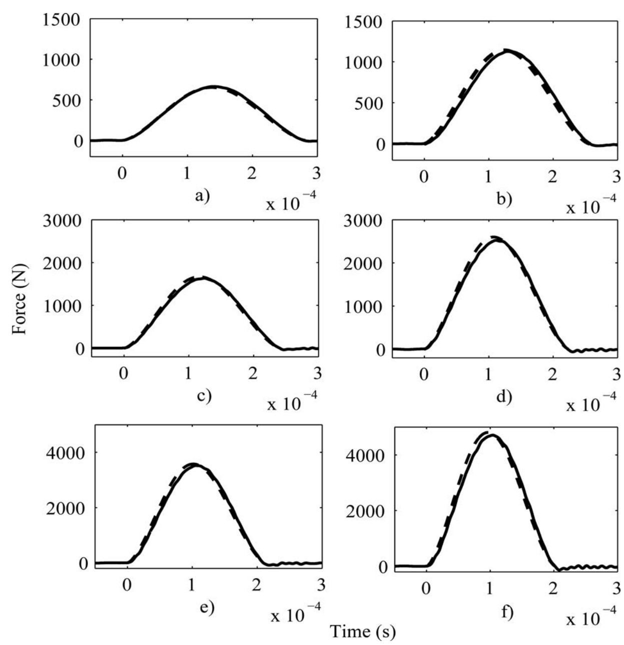

Fig. 13 Comparison of impact force profiles for specimen C1 between simulation (dash line) and experimental results (solid line): (*a*) v_i=0.0938 m/s, (*b*) v_i=0.15 m/s, (*c*) v_i=0.2060 m/s, (*d*) v_i=0.2989 m/s, (*e*) v_i=0.3910 m/s, and (*f*) v_i=0.50 m/s.

Table 8 Comparison of maximum impact forces for specimen C1 in the pendulum experiments

v_i (m/s)	0.0938	0.15	0.2060	0.2989	0.3910	0.50
F_{max} Simulation (N)	651.6	1140.7	1666.8	2598.3	3578.6	4804.8
F_{max} Experiment (N)	663.0	1126.9	1633.6	2521.4	3519.7	4709.6
Difference (N)	−11.4	13.8	33.2	76.9	58.9	95.2
% error	−1.7	1.2	2.0	3.1	1.7	2.0

(5) Figure 12(*c*) provides a vivid picture of the effect of the nonlinear damping term on the impact force response: compared with Hertzian response, the damping term introduces a substantial asymmetry in the force profile between the compression and restitution phases. We shall return to this observation shortly when comparing the simulated and experimental results.

7 Comparison Between Simulation and Experimental Results

In this section, the simulation results are compared with the experimental results. Given the rather small differences between the contact force models for specimen C1, only the nonlinear energy-consistent impact force model (ZS) results are presented in the comparison for this specimen. For specimen C2, however, we also include the Hertz model predictions.

7.1 Specimen C1. For the impact scenarios with specimen C1, the simulated impact force profiles are illustrated against the experimental results with the initial impact velocity ranging from 0.0938 m/s to 0.5 m/s in Fig. 13. As expected, the impact forces predicted by the model and observed experimentally rise with the increase in the impact velocity; this accompanied by the shrinking impact durations from 0.28 ms to 0.21 ms. We also observe that during both the compression and the restitution phases, the simulation results are in very good agreement with the experiments in that the two exhibit similar slopes of the force profiles, although the experimental responses slightly lag the simulation.

The peak forces are overall in very good agreement with maximum discrepancy of 3.1% occurring at $v_i=0.2989$ m/s (see Table 8). Recall that the estimated force value to initiate permanent deformation during impact for specimen C1 is 6674 N (see Table 2). Therefore, all impact scenarios with this specimen are expected to fall in the "elastic" impact category and we attribute the small energy dissipation ($e \in [0.95, 0.97]$) to the elastic wave propagation.

The results in Fig. 13 also exhibit excellent agreement between the model prediction and the experimental data for the duration of impact. A more detailed analysis of the component phases—compression and restitution—indicates that both simulation and experiment exhibit slightly shorter compression time[6] than the restitution time for a specific impact velocity. The model predictions underestimate the compression times and overestimate the restitution times: the two effects nearly cancel, thereby yielding excellent agreement in the overall impact time (within 2%).

7.2 Specimen C2. For the impact scenario with specimen C2, the two simulated impact force profiles—that obtained with ZS Hunt–Crossley type model and that predicted with Hertz's model—are illustrated against the experimental results in Fig. 14. Inspection of these plots reveals some interesting observations.

Similarly to the results for specimen C1, the experimental force profiles display a slower rise time compared with the Hunt–Crossley (ZS) simulation results. Much more drastic, however, are the discrepancies in the slopes of the force profiles, both during the compression and restitution phases. The experimental results exhibit a nearly symmetrical profile about the peak force instant, similar to the Hertzian profiles. However, the ZS model predicts a substantially faster compression and slower restitution, while, as for specimen C1, the total impact duration is still predicted very accurately (within 5%). A more detailed analysis of the compression and restitution times (T_c and T_r) is presented in Table 9 for simulated and experimental responses. In particular, we calculate the ratios T_r/T_c and compare both the simulated and experimental results to the theoretical ratio of the time of plastic indentation to the time of elastic rebound. An approximation for the latter is derived by Johnson [21] as $1.2e$, based on the assumptions of fully plastic indentation and elastic rebound governed by Hertz theory. The results in Table 9 demonstrate complete divergence between the simulated ratios from the Hunt–Crossley energy-consistent model and the theoretical ratios of Ref. [21]. By contrast, the experimental results show the same general trend as theory and are reasonably close to the theoretical values.

Finally, the peak force predictions of the Hunt–Crossley model are still in very good agreement (within 5%) as shown in Table 10, while the Hertzian responses display substantially higher peak forces than observed experimentally. Note that the maximum impact forces exceed the value required to initiate permanent deformation (42 N) as per our previous analysis in Sec. 3.1 and therefore, according to the criteria in Ref. [24], all impact scenarios considered for specimen C2 fall into the elastoplastic category of

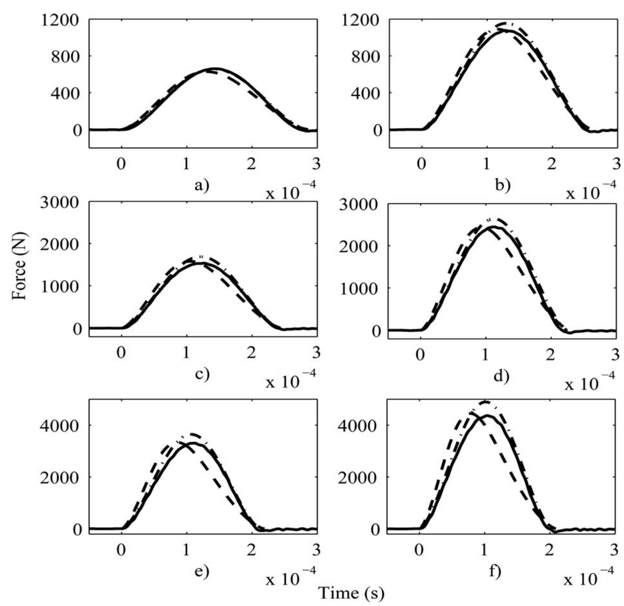

Fig. 14 Comparison of impact force profiles for specimen C2 between simulation (ZS: dash line; Hertz: dash-dot line), and experimental (solid line) results: (*a*) $v_i=0.0938$ m/s, (*b*) $v_i=0.15$ m/s, (*c*) $v_i=0.2060$ m/s, (*d*) $v_i=0.2989$ m/s, (*e*) $v_i=0.3910$ m/s, and (*f*) $v_i=0.50$ m/s

[6]The compression time is measured as the time to peak force. Results in Fig. 16 confirm that this is a very accurate approximation of the compression time (time to maximum deformation).

Table 9 Comparison of time variables for specimen C2

v_i (m/s)	Simulation T_c (10^{-4} s)	Simulation T_r (10^{-4} s)	Simulation T_r/T_c	Expt. T_c (10^{-4} s)	Expt. T_r (10^{-4} s)	Expt. T_r/T_c	Theor. 1.2e
0.0938	1.31	1.56	1.1908	1.44	1.32	0.9167	1.0999
0.15	1.16	1.46	1.2586	1.29	1.23	0.9535	1.0670
0.2060	1.05	1.41	1.3429	1.26	1.13	0.8968	1.0334
0.2989	0.94	1.37	1.4574	1.18	1.05	0.8898	0.9881
0.3910	0.85	1.35	1.5882	1.14	0.96	0.8421	0.9479
0.50	0.78	1.32	1.6923	1.12	0.95	0.8482	0.9082

Table 10 Comparison of peak impact forces for specimen C2

v_i (m/s)	0.0938	0.15	0.2060	0.2989	0.3910	0.50
$F_{\max}$ ZS model (N)	628.0	1089.9	1577.5	2435.4	3332.7	4448.0
$F_{\max}$ Experiment (N)	660.2	1076.6	1533.1	2447.9	3303.3	4364.6
Difference (N)	−32.2	13.3	44.4	−12.5	29.4	83.4
% error	−4.9	1.2	2.9	−0.5	0.9	1.9

impact. Incidentally, we note that plastic deformation on the cylindrical specimen surface starts to be visible for $v_i=0.15$ m/s.

7.3 Comparison of Two Specimens. Since the pendulum impact experiments involved two specimens with different yield strength values and were conducted under the same conditions, we are in a unique position to juxtapose the results for the two specimens and offer further insights into the impact phenomenon. In Fig. 15, we display the experimental force profiles for the two specimens for the six impact velocities tested in the pendulum experiments. These results demonstrate that the ordering of the peak impact forces for the particular pre-impact velocity is $(F_{\max})_{C1} > (F_{\max})_{C2}$, in accordance with the ordering of the yield strength of the two specimens. We suggest that this can be attributed to the significant permanent deformation that occurs on the specimen with the lower yield strength (C2), which is also supported by the fact that the difference in the peak impact forces between the two specimens is very small at $v_i=0.0938$ m/s and increases (in relative terms) for higher impact velocities.

Additional insight can be gained by inspecting the force versus penetration and velocity versus penetration diagrams for the two specimens. These are presented in Figs. 16 and 17, respectively, for impact velocities of 0.0938 m/s ((a) plots) and 0.5 m/s ((b) plots), where the velocity and penetration data for the impact process were generated by integrating the accelerations collected from the pendulum test rig experiments. Though the accuracy of these results is limited by the numerical integration of the acceleration signal, we deem them sufficiently accurate for the qualitative analysis presented here.

The force-penetration plots in Fig. 16 exhibit the presence of significant plastic deformation for the C2 specimen and show that

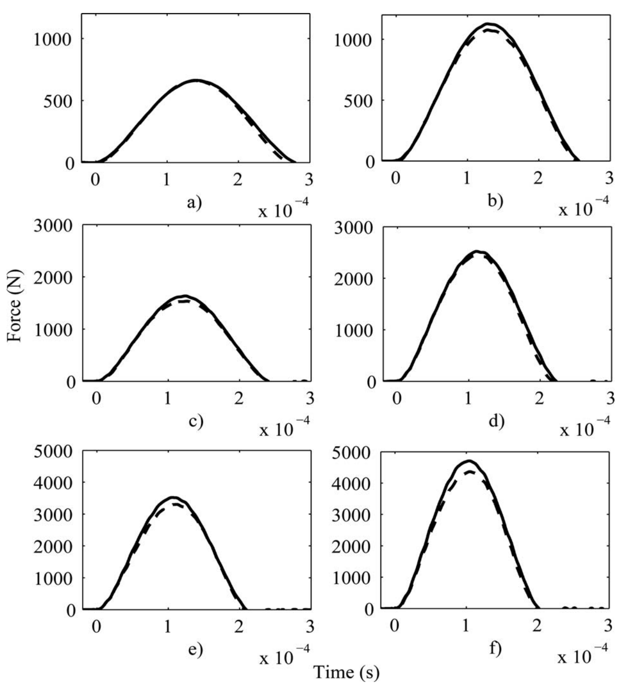

Fig. 15 Comparison of impact force profiles between specimens C1 (solid line) and C2 (dotted line): (*a*) v_i=0.0938 m/s, (*b*) v_i=0.15 m/s, (*c*) v_i=0.2060 m/s, (*d*) v_i=0.2989 m/s, (*e*) v_i=0.3910 m/s, and (*f*) v_i=0.50 m/s

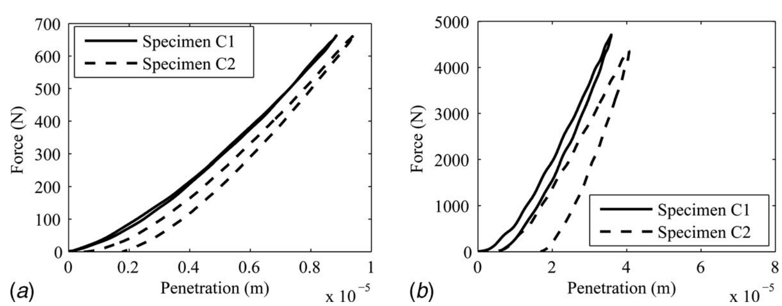

Fig. 16 Experimental impact force versus penetration diagrams: (*a*) for v_i=0.0938 m/s and (*b*) for v_i=0.5 m/s

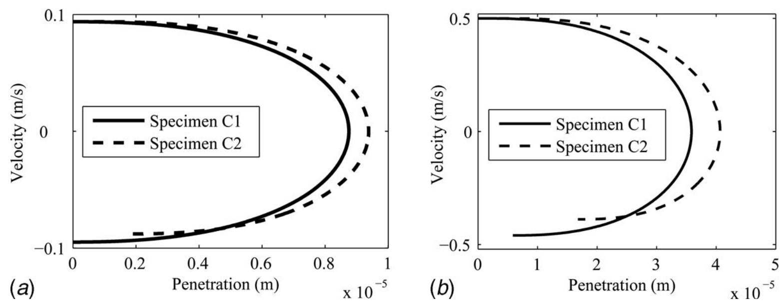

Fig. 17 Experimental velocity versus penetration diagrams: (*a*) for $v_i = 0.0938$ m/s and (*b*) for $v_i = 0.5$ m/s

for the same penetration, its response is consistently characterized by lower impact forces and from Fig. 17, higher velocities during the compression phase than those observed for C1 specimen. This correlates with the intuitive notion of plastic deformation, the effect of which is a "softening" of the material. Further inspection of the plots in Fig. 17 indicates that impact of the "softer" specimen is accompanied by somewhat larger maximum deformation and the velocity profile demonstrates a significant asymmetry about the zero-velocity line, particularly visible for the higher impact velocity. Note that for $v_i = 0.5$ m/s, the postprocessed results in Figs. 16 and 17 also show a small residual deformation in the C1 specimen.

In spite of the clear presence of hysteresis and asymmetries in the phase plots of the impact response for specimen C2, the force-time profiles of Fig. 15 retain their symmetrical shape for the lower yield specimen. This is in stark contrast to the predictions of all Hunt–Crossley models, which introduce a clear asymmetry in the force responses.

8 Conclusions

In this paper, impact experiments involving a spherical ball impacting two specimens of different yield strengths were conducted to validate the Hunt–Crossley series of models. In the experiments, the coefficient of restitution and impact force profiles were measured, the latter compared with the simulation results from the models and the former used as the input to the model. Based on these results, we can make the following conclusions.

1. For nearly elastic impacts, those characterized by coefficients of restitution larger than approximately 0.95, the Hunt–Crossley nonlinear models provide excellent predictions of the impact force response, in particular, the peak impact forces, the slopes during restitution and compression phases, the corresponding times, and the total impact duration, but underestimate the compression time and overestimate the restitution time. For these same conditions, however, there are insignificant differences between the five Hunt–Crossley models discussed in this manuscript and it is therefore virtually impossible to differentiate between them, given practical limitations of the experimental measurements and instrumentation. Furthermore, at these conditions, the Hunt–Crossley models do not deviate substantially from the Hertz's model predictions ($<2\%$ discrepancies in peak forces, for example).
2. For impacts that exhibit non-negligible energy dissipation, for example, through plastic deformation, even on a micro-scale, the results of our research beg for a more cautious use of Hunt–Crossley type models. In these cases, the energy-consistent model developed in Refs. [17,18] provides a good estimate of the peak force and the duration of impact. Yet, as observed for all five damped models, addition of the nonlinear damping term significantly skews the force-time responses—a result that was not confirmed by the experimental measurements for the lower yield specimen.

In summary, Hunt–Crossley type models, which explicitly represent viscoelastic impacts, perform very well in nearly elastic impact scenarios ($e > 0.95$). Since the models do not account for the mechanism of permanent deformation, their predictions of impact force profiles are not as accurate when plastic deformation becomes more significant, although they still produce excellent estimates of the peak impact force values and the total impact duration. Further experimental investigations with a broader range of materials and impact velocities would be beneficial to provide a more comprehensive database of impact force measurements. We also suggest that new compliant models need to be developed to properly capture the effects of plastic deformation on the contact force response, by considering the analysis of plastic deformation in Ref. [21] and the more recent finite element analysis in Ref. [34].

References

[1] Goldsmith, W., 1960, *Impact: The Theory and Physical Behavior of Colliding Solids*, Edward Arnold, London, UK.
[2] Hunt, K. H., and Crossley, F. R. E., 1975, "Coefficient of Restitution Interpreted as Damping in Vibroimpact," ASME J. Appl. Mech., **42**, pp. 440–445.
[3] Dubowsky, S., and Freudenstein, F., 1971, "Dynamics Analysis of Mechanical Systems With Clearances—Part 1: Formation of Dynamical Model," ASME J. Eng. Ind., **93**, pp. 305–309.
[4] Brach, R. M., 1989, "Rigid Body Collisions," ASME J. Appl. Mech., **56**, pp. 133–138.
[5] Stronge, W. J., 1990, "Rigid Body Collisions With Friction," Proc. R. Soc. London, Ser. A, **431**, pp. 169–181.
[6] Han, I., and Gilmore, B. J., 1993, "Multi-Body Impact Motion With Friction—Analysis, Simulation and Experimental Validation," ASME J. Mech. Des., **115**, pp. 412–422.
[7] Marhefka, D. W., and Orin, D. E., 1996, "Simulation of Contact Using a Nonlinear Damping Model," *Proceedings of the 1996 IEEE International Conf. on Robotics and Automation*, Minneapolis, MN, pp. 1662–1668.
[8] Marhefka, D. W., and Orin, D. E., 1999, "A Compliant Contact Model With Nonlinear Damping for Simulation of Robotic Systems," IEEE Trans. Syst. Man Cybern., Part A. Syst. Humans, **29**, pp. 566–572.
[9] Fregly, B. J., 1999, "A Three-Dimensional Compliant Contact Model for Dynamic Simulation of Total Knee Replacements," *Proceedings of the Seventh International Symposium on Computer Simulation in Biomechanics*, University of Calgary, Calgary, AL, pp. 10–13.
[10] Howard, W. S., and Kumar, V., 1993, "A Minimum Principle for the Dynamics Analysis of Systems With Frictional Contacts," *Proceedings of the 1993 IEEE International Conference on Robotics and Automation*, Vol. 1, pp. 437–442.
[11] Mirza, K., Hanes, M. D., and Orin, D. E., 1993, "Dynamic Simulation of Enveloping Power Grasps," *Proceedings of the 1993 IEEE International Conference on Robotics and Automation*, Vol. 1, pp. 430–435.
[12] Crook, A. W., 1952, "A Study of Some Impacts Between Metal Bodies by a Piezo-Electric Method," Proc. R. Soc. London, Ser. A, **212**, pp. 377–390.
[13] Schiehlen, W., and Seifried, R., 2004, "Three Approaches for Elastodynamic Contact in Multibody Systems," Multibody Syst. Dyn., **12**, pp. 1–16.
[14] Herbert, R. G., and McWhannell, D. C., 1977, "Shape and Frequency Composition of Pulses From an Impact Pair," ASME J. Eng. Ind., **99**, pp. 513–518.
[15] Lee, T. W., and Wang, A. C., 1983, "On the Dynamics of Intermittent-Motion Mechanisms—Part 1: Dynamic Model and Response," ASME J. Mech., Transm., Autom. Des., **105**, pp. 534–540.
[16] Lankarani, H. M., and Nikravesh, P. E., 1990, "A Contact Force Model With Hysteresis Damping for Impact Analysis of Multi-Body Systems," ASME J. Mech. Des., **112**, pp. 369–376.
[17] Gonthier, Y., McPhee, J., Lange, C., and Piedboeuf, J., 2002, "A Regularized Contact Model With Asymmetric Damping and Dwell-Time Dependent Friction," Forum 2002, SCGM Queen's University, Kingston, ON.

[18] Zhang, Y., and Sharf, I., 2004, "Compliant Force Modeling for Impact Analysis," *Proceedings of the 2004 ASME International Design Technical Conference*, Salt Lake City, UT, Paper No. DETC2004–57220.
[19] Bottasso, C. L., and Bauchau, O. A., 2001, "Multibody Modeling of Engage and Disengage of the Helicopter Rotors," J. Am. Helicopter Soc., **46**, pp. 290–300.
[20] Cole, M. O. T., Keogh, P. S., and Burrows, C. R., 2002, "The Dynamic Behavior of a Rolling Element Auxiliary Bearing Following Rotor Impact," ASME J. Tribol., **124**, pp. 406–413.
[21] Johnson, K. L., 1985, *Contact Mechanics*, Cambridge University Press, Cambridge.
[22] Tsuji, Y., Kawaguchi, T., and Tanaka, T., 1993, "Discrete Particle Simulation of Two-Dimensional Fluidized Bed," Powder Technol., **77**, pp. 79–87.
[23] Mishra, B. K., 1995, "Ball Charge Dynamics in a Planetary Mill," Kona, **13**, pp. 151–158.
[24] Stronge, W. J., 2000, *Impact Mechanics*, Cambridge University Press, Cambridge.
[25] Shivaswamy, S., and Lankarani, H. M., 1997, "Impact Analysis of Plates Using Quasi-Static Approach," ASME J. Mech. Des., **119**, pp. 376–381.
[26] Cross, R., 1999, "The Bounce of a Ball," Am. J. Phys., **67**, pp. 222–227.
[27] Ahmed, S., Lankarani, H. M., and Pereira, M., 1999, "Frictional Impact Analysis in Open-Loop Multibody Mechanical Systems," J. Mech. Des., **121**, pp. 119–127.
[28] Carre, M. J., James, D. M., and Haake, S. J., 2004, "Impact of a Non-Homogeneous Sphere on a Rigid Surface," J. Mech. Eng. Sci., **218**, pp. 273–281.
[29] Falcon, E., Laroche, C., Fauve, S., and Coste, C., 1998, "Behavior of One Inelastic Ball Bouncing Repeatedly Off the Ground," Eur. Phys. J. B, **3**, pp. 45–57.
[30] Osakue, E. E., and Rogers, R. J., 2001, "An Experimental Study of Friction During Planar Elastic Impact," ASME J. Pressure Vessel Technol., **123**, pp. 493–500.
[31] Doyle, J. F., 1987, "Determining the Contact Force During the Transverse Impact of Plates," Exp. Mech., **27**, pp. 68–72.
[32] Lewis, A. D., and Rogers, R. J., 1988, "Experimental and Numerical Study of Forces During Oblique Impact," J. Sound Vib., **125**, pp. 403–412.
[33] Zhang, Y., 2007, "Contact Dynamics for Rigid Bodies: Modeling and Experiments," Ph.D. thesis, McGill University, Montreal, QC.
[34] Kogut, L., and Etsion, I., 2002, "Elastic-Plastic Contact Analysis of a Sphere and a Rigid Flat," ASME J. Appl. Mech., **69**, pp. 657–662.

Local Damage Evolution of Double Cantilever Beam Specimens During Crack Initiation Process: A Natural Boundary Condition Based Method

Zhenyu Ouyang

Guoqiang Li[1]
e-mail: guoli@me.lsu.edu

Department of Mechanical Engineering,
Louisiana State University,
Baton Rouge, LA 70803

Cohesive zone models are being increasingly used to simulate fracture and debonding processes in metallic, polymeric, and ceramic materials and their composites. The crack initiation process as well as its actual stress and damage distribution beyond crack tip are important for understanding fracture of materials and debonding of adhesively bonded joints. In the current model, a natural boundary condition based method is proposed, and thus the concept of extended crack length (characteristic length l) is no longer required and more realistic and natural local deformation beyond crack tip can be obtained. The new analytical approach, which can consider both crack initiation and propagation as well as local deformation and interfacial stress distribution, can be explicitly obtained as a function of the remote peel load P with the given bilinear cohesive laws. An intrinsic geometric constraint condition is then used to solve the remote peel load P. The nonlinear response in both the ascending and descending stages of loading is accurately predicted by the current model, as evidenced by a comparison with both experimental results and finite element analysis results. It is found that the local deformation and interfacial stress beyond crack tip are relatively stable during crack propagation. It is also found that, when the cohesive strength is low, it has a significant effect on the critical peel load and loadline deflection. In principle, the approach developed in the current study can be extended to multilinear cohesive laws, although only bilinear cohesive law is presented in this work as an example. [DOI: 10.1115/1.3112742]

Keywords: CZM, bonded joint, crack initiation, local damage, FRP, analytical solution

1 Introduction

Fracture studies are usually carried out under several idealized conditions, as in the case of linear elastic fracture mechanics or the case of small scale yielding. In such cases, the details of the stress-strain around the crack tip are uniquely characterized by a single macroscopic parameter such as the stress intensity factor. These global parameters are related to the corresponding material properties typically the fracture toughness that determines the critical conditions of crack initiation and growth. When the crack tip experiences inelastic damage, the above concepts based purely on the theory of elasticity are not valid. Further, for cracks along bimaterial interfaces, the crack tip will no longer be embedded in a square-root singular stress field, leading to a condition that stress intensity factor may either be zero or infinity [1]. As an alternative approach to this singularity driven fracture approach, the origins of the concept of cohesive zone model (CZM) go back to the work of Barenblatt [2] and Dugdale [3].

CZM has evolved as a preferred method to analyze fracture problems in monolithic and composite material systems not only because it avoids the singularity but also because it can be easily implemented in a numerical method of analysis such as in finite element modeling. Therefore, various CZMs have been proposed to investigate the fracture process in a number of material systems including fiber reinforced polymer composites, metallic materials, ceramic materials, cementitious or concrete materials, and bimaterial systems. All of them start from the assumption that one or more interfaces can be defined, where crack propagation is allowed by the introduction of a possible discontinuity in the displacement field. The fundamental calculations by Rose et al. [4] suggest a universal exponential form of stress-separation law for most common interfaces.

The polynomial and exponential types of traction-separation law were first proposed by Needleman [5,6] to simulate particle debonding in metal matrices. Tvergaard [7] developed a quadratic traction-displacement relation to analyze interfacial fracture. Tvergaard and Hutchinson [8] used a trapezoidal shape of the traction-separation model to calculate the crack growth resistance in elastoplastic materials. Xu and Needleman [9] further used exponential types of traction-separation law to study the fast crack growth in brittle materials under dynamic crack growth along the interface of bimaterials. Camacho and Ortiz [10] employed a linear softening cohesive fracture model to investigate multiple cracks along arbitrary paths during impact damage in brittle materials. Hilleborg et al. [11] developed a cohesive zone model to simulate the crack formation and growth in concrete. Fundamentally, their model is bilinear type. Geubelle and Baylor [12] used bilinear CZM to simulate spontaneous initiation and propagation of transverse matrix cracks in composite plates subjected to low-

[1]Corresponding author.

Contributed by the Applied Mechanics Division of ASME for publication in the Journal of Applied Mechanics. Manuscript received April 29, 2008; final manuscript received November 4, 2008; published online June 16, 2009. Review conducted by Kenneth M. Liechti.

velocity impact. The main difference between these models lies in the shape of the traction-displacement response and the parameters used to describe that shape. It is generally accepted that CZMs can be described by two or three independent parameters [13]. These parameters may be the fracture toughness (the area under the traction-displacement curve, which is typically obtained from experimental test), the cohesive strength σ_f, and/or the characteristic separation length δ_1 at which the cohesive traction reaches its maximum.

However, the analytical effort by applying CZMs to study fracture process faced some challenges, especially for the fracture process under Mode I (normal separation) or mixed fracture mode, because the fracture process under these loading conditions is governed by fourth or higher-order differential equations. Fortunately, the general solution of fourth or higher-order differential equations is available for cohesive laws with linear or multilinear type traction-separation relation. Kanninen [14] and Williams [15] modeled the elastic deformation beyond the crack tip in a debonding cantilever. In their models, the local deformation beyond the crack tip was computed using a beam on a linear elastic foundation with effective interfacial stiffness k_e. Kinloch et al. [16] developed the concept of correction factors to analyze the debonding of adhesively bonded joints under peel loading. The correction factor method extends the crack length a by a characteristic length l beyond the physical crack tip. With the corrected crack length $(a+l)$, the classical beam theory can be readily applied and well compensated for the local deformation beyond the crack tip. As an extension of the root correction factor method, Williams and Hadavinia [17] further analytically investigated the debonding process with other nonlinear type of separation-traction laws, such as linear damage and bilinear cohesive laws.

Although the previous studies helped significantly in modeling and understanding the fracture and debonding process, they are limited because (1) most previous analytical solutions of Mode I peel specimen in the literature are based on root rotation correction method, which is basically an equivalent method. In the current work, the concept of extended crack length (characteristic length l) is no longer required. This modeling method seems more natural and physically meaningful than the traditional root correction based equivalent method, which requires that all deformations must be simultaneously equal to zero at the location of the characteristic length l beyond the crack tip. The natural boundary condition based approach is developed to obtain a simple solution of peel specimen with bilinear cohesive laws. (2) Few analytical models considered the local damage evolution beyond crack tip during the crack initiation process. There is a need to develop an analytical model that can consider the entire process of crack initiation and propagation. For mixed mode loading, the critical normal cohesive separation δ is generally less than its final cohesive separation δ_f under pure Mode I loading. The understanding of crack initiation process $(0<\delta<\delta_f)$ under pure Mode I loading might help solve the mixed mode problem. (3) For the crack initiation and propagation process, the real local deformation and interfacial stress distribution provide fundamental information for understanding the distribution of the local damage and softening size in the cohesive zone. This helps in understanding fracture of materials and debonding of adhesively bonded joints. In this study, the local deformation and interfacial stress beyond the physical crack tip are solved in a simple and explicit form as a function of the remote peel load P. Furthermore, an intrinsic geometric constraint condition is found in the current study, which provides a concise governing equation for solving the remote peel load P. In principle, the method developed in the current study can be extended to multilinear cohesive laws, although only bilinear cohesive laws are presented in this work as an example.

2 Theoretical Background

Based on the classical Euler–Bernoulli beam theory and J-integral theory, Olsson and Stigh [18] and Andersson and Stigh [19] theoretically solved an inverse problem for the double cantilever beam (DCB) specimen (Fig. 1). According to their derivation, for the given initial elongation w of the adhesive layer, the applied force P and the rotation θ_P at the loadline are correlated with J-integral as below:

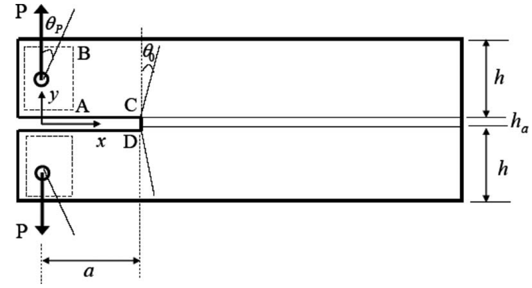

Fig. 1 Double cantilever beam specimen under peel loading

$$2P \cdot \theta_P = b \cdot J(2\delta) \tag{1}$$

where b is the width of the beam.

It is noted that instead of defining the cohesive stress $\sigma(2\delta)$ as a cohesive function of the relative separation 2δ between the two beams, we define a cohesive law for each single beam as

$$\sigma = \sigma(\delta) \tag{2}$$

The fracture energy is shared by the two single cantilever beam (SCB) equally as

$$J_{\mathrm{DCB}}(w) = J_{\mathrm{DCB}}(2\delta) = 2J_{\mathrm{SCB}}(\delta) \tag{3}$$

Note that the function of J_{DCB} for $J(2\delta)$ is different from the function of J_{SCB} for $J(\delta)$, where 2δ is the relative separation of the two beams in the DCB specimen, and δ is the separation of each beam with respect to its original position. Therefore, Eq. (1) can be rewritten as

$$\theta_P \cdot P = \frac{J_{\mathrm{DCB}}(2\delta)\cdot b}{2} = J_{\mathrm{SCB}}(\delta)\cdot b \tag{4}$$

Note that $J(\delta)$ in Eq. (4) is equal to half of the J-integral of the DCB system $J_{\mathrm{DCB}}(2\delta)$. It is given by Rice [20]

$$J(\delta) = \int_0^{\delta} \sigma(\delta) d\delta \tag{5}$$

and

$$\sigma(\delta) = \frac{\partial J_{\mathrm{SCB}}(\delta)}{\partial(\delta)} \tag{6}$$

The cohesive law for the relative separation of the two beams can be expressed as

$$\sigma_{\mathrm{DCB}}(2\delta) = \frac{\partial J_{\mathrm{DCB}}(2\delta)}{\partial(2\delta)} = \frac{\partial[J_{\mathrm{SCB}}(\delta)+J_{\mathrm{SCB}}(\delta)]}{\partial(\delta)}\cdot\frac{\partial\delta}{\partial(2\delta)} = \sigma(\delta) \tag{7}$$

From Eq. (7), it can be seen that with the definition of the cohesive law for a single beam, the cohesive law for the relative separation of the two beams in the DCB can be readily obtained. Namely, if the separation is δ, the cohesive stress is $\sigma(\delta)$, and the cohesive energy is $J(\delta)$ for a single beam, then the relative separation is 2δ, the cohesive fracture is $2J(\delta)$, while the cohesive stress is still $\sigma(\delta)$ for the two beams. This means that the cohesive law for a single beam is a shrunk cohesive law with respect to that of the two beam system. The separation is twice as much as the single beam cohesive law, while the interfacial stress σ remains the same, as illustrated in Fig. 2. We use $J(\delta)$ and $\sigma(\delta)$ for an individual beam in the following text for the purpose of clarity.

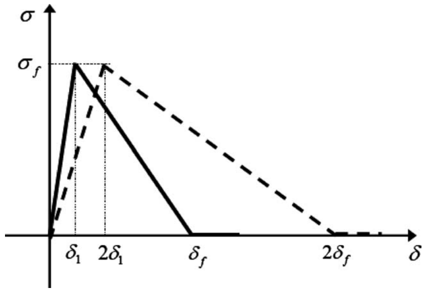

Fig. 2 CZM for double cantilever beam specimen and single cantilever beam specimen

3 Local Deformation and Interfacial Stress During Crack Initiation Process

In order to examine the real cohesive zone size, instead of the equivalent characteristic cohesive length, we need to solve fourth-order differential equations. However, the full field solution of the fourth-order differential equation is generally not available when a nonlinear cohesive law is adopted. One solution is through the multilinear cohesive zone model to approximate the nonlinear cohesive law. In the current study, a methodology is developed to obtain a simple and explicit solution for the local deformation and stress field with the obtained remote peel load P. The idea is to first express all solution coefficients as a function of the remote peel load P. Then the size of the elastic zone can be expressed as a function of the remote peel load P. Further, we use the size of the elastic region to express the size of the softening zone. Consequently, the elastic zone and softening zone are derived as an explicit function of the remote peel load P. Finally, by applying the intrinsic geometric constraint condition, the remote peel load P can be determined. With the determined remote peel load P, the softening and elastic zone size beyond crack tip can be simply and explicitly obtained. For the sake of simplicity, the shear deformation in the beam is not considered, and the classical Euler–Bernoulli beam theory is applied.

A typical bilinear cohesive law is shown in Fig. 3. For most CZMs in the literature, the traction-separation laws are such that with increasing interfacial separation, the traction across the interface reaches a maximum, then decreases, and eventually vanishes. This typical bilinear separation-traction law has three segments: (a) elastic stage when the normal interfacial separation $\delta \le \delta_1$, including negative separation (compression). The normal interfacial stress increases linearly with separation; (b) elastic softening stage when $\delta_1 \le \delta \le \delta_f$. The normal interfacial stress decreases linearly with separation; and (c) complete debonding stage. There is no interfacial stress when $\delta \ge \delta_f$. The interfacial constitutive law is described as follows:

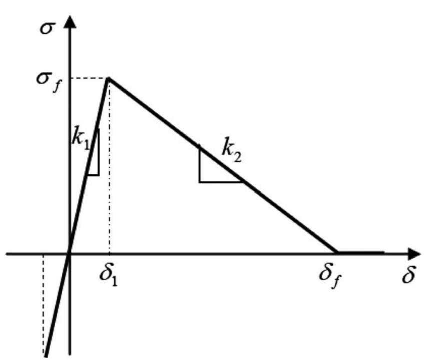

Fig. 3 Separation-stress relation for a typical bilinear CZM

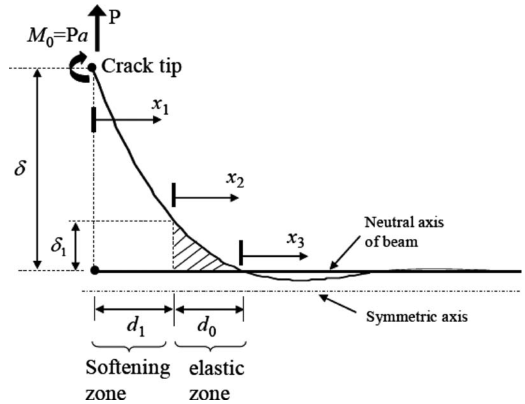

Fig. 4 Schematic of local deformation beyond crack tip

$$\sigma(x) = \begin{cases} -k_1 \cdot \delta(x), & \delta(x) \le \delta_1 \\ -[\delta_f - \delta(x)] \cdot k_2, & \delta_1 \le \delta(x) \le \delta_f \\ 0, & \delta(x) \ge \delta_f \end{cases} \tag{8}$$

Let us consider the local deformation beyond the crack tip, as shown in Fig. 4. When the crack tip separation δ is smaller than δ_1, one can readily use linear elastic model [14] to obtain the explicit solution for the range $(0 \le \delta \le \delta_1)$. Since the elastic separation limit δ_1 is normally small compared with its final separation δ_f, let us focus on the crack initiation process when the crack tip separation δ is within the softening region $(\delta_1 \le \delta \le \delta_f)$. Namely, the crack tip separation δ is larger than δ_1 (the characteristic separation for linear elastic cohesive stress), as shown in Fig. 4.

The governing equation for the descending branch (softening region) in the bilinear CZM, as shown in Fig. 3, is given by

$$\frac{d^4 w(x_1)}{dx^4} = 4\beta^4\{w(x_1) - \delta_f\} \quad (0 \le x_1 \le d_1) \tag{9}$$

The general solution of Eq. (9) can be written as

$$w(x_1) = \delta_f + C_1 \cos(\sqrt{2}\beta x_1) + C_2 \sin(\sqrt{2}\beta x_1) + C_3 \cosh(\sqrt{2}\beta x_1) + C_4 \sinh(\sqrt{2}\beta x_1) \tag{10}$$

The governing equation for the ascending branch (elastic region) in the bilinear CZM, as shown in Fig. 3, is given by

$$\frac{d^4 w(x_3)}{dx_3^4} = -4\alpha^4 w(x_3) \tag{11}$$

Fixing the origin of the coordinate x_3 at the first zero-deflection cross section as illustrated in Fig. 4, the general solution of Eq. (11) can be simply written as

$$w(x_3) = \frac{-\delta_1 \exp(-\alpha x_3)}{\exp(\alpha d_0)\sin(\alpha d_0)}\sin(\alpha x_3) \quad (x_3 \ge -d_0) \tag{12}$$

where

$$\beta = \sqrt[4]{\frac{bk_2}{4EI}}, \quad \alpha = \sqrt[4]{\frac{bk_1}{4EI}} \tag{13}$$

and k_1 and k_2 are the interfacial stiffnesses for the elastic and softening regions, respectively.

When the crack tip separation is equal to δ, and consider the equilibrium at the cross section at $x_1 = d_1$ ($x_3 = -d_0$ or $x_2 = 0$), we can readily obtain

$$\delta_1 - \delta_f = C_1 \cos(\sqrt{2}\beta d_1) + C_2 \sin(\sqrt{2}\beta d_1) + C_3 \cosh(\sqrt{2}\beta d_1) + C_4 \sinh(\sqrt{2}\beta d_1) \tag{14}$$

$$\frac{w_1'}{\sqrt{2}\beta} = [-C_1 \sin(\sqrt{2}\beta d_1) + C_2 \cos(\sqrt{2}\beta d_1) + C_3 \sinh(\sqrt{2}\beta d_1) + C_4 \cosh(\sqrt{2}\beta d_1)] \quad (15)$$

$$\frac{w_1''}{2\beta^2} = [-C_1 \cos(\sqrt{2}\beta d_1) - C_2 \sin(\sqrt{2}\beta d_1) + C_3 \cosh(\sqrt{2}\beta d_1) + C_4 \sinh(\sqrt{2}\beta d_1)] \quad (16)$$

$$\frac{w_1'''}{2\sqrt{2}\beta^3} = [C_1 \sin(\sqrt{2}\beta d_1) - C_2 \cos(\sqrt{2}\beta d_1) + C_3 \sinh(\sqrt{2}\beta d_1) + C_4 \cosh(\sqrt{2}\beta d_1)] \quad (17)$$

where C_1, C_2, C_3, and C_4 will be determined by the boundary conditions in terms of the rotation, peel force, moment, and cohesive separation, and w_1', w_1'', and w_1''' are the first, second, and third derivatives with respect to x_1 at $x_1 = d_1$ ($x_3 = -d_0$ or $x_2 = 0$), respectively.

On the other hand, from the governing equation of the ascending branch of the bilinear CZM (see Fig. 3), we can readily express w_1', w_1'', and w_1''' at $x_3 = -d_0$ ($x_1 = d_1$ or $x_2 = 0$) as follows:

$$w_1' = -\delta_1 \alpha [1 + \cot(\alpha d_0)] \quad (18)$$

$$w_1'' = 2\delta_1 \alpha^2 \cot(\alpha d_0) \quad (19)$$

$$w_1''' = -2\delta_1 \alpha^3 [\cot(\alpha d_0) - 1] \quad (20)$$

It is noted that d_0 is used to denote the elastic zone size, which is the length between the cross section with $\delta = \delta_1$ and the cross section with $\delta = 0$ (the first zero-deflection cross section), as shown in Fig. 4. How to determine the unknown coefficients and the actual softening and elastic zone's sizes beyond crack tip in the crack initiation process, instead of an equivalent characteristic cohesive length [16], is one of the primary purposes of the current study.

From Eqs. (15) and (17), it can be derived that

$$2C_1 \sin(\sqrt{2}\beta d_1) - 2C_2 \cos(\sqrt{2}\beta d_1) = \frac{w_1'''}{2\sqrt{2}\beta^3} - \frac{w_1'}{\sqrt{2}\beta} \quad (21)$$

From Eqs. (14) and (16), it can be obtained that

$$2C_1 \cos(\sqrt{2}\beta d_1) + 2C_2 \sin(\sqrt{2}\beta d_1) = (\delta_1 - \delta_f) - \frac{w_1''}{2\beta^2} \quad (22)$$

From Eqs. (15) and (17), it can also be derived that

$$2C_3 \sinh(\sqrt{2}\beta d_1) + 2C_4 \cosh(\sqrt{2}\beta d_1) = \frac{w_1'''}{2\sqrt{2}\beta^3} + \frac{w_1'}{\sqrt{2}\beta} \quad (23)$$

From Eqs. (14) and (16), it can also be found that

$$2C_3 \cosh(\sqrt{2}\beta d_1) + 2C_4 \sinh(\sqrt{2}\beta d_1) = (\delta_1 - \delta_f) + \frac{w_1''}{2\beta^2} \quad (24)$$

Obviously, from Eqs. (21) and (22), we have

$$\left[(\delta_1 - \delta_f) - \frac{w_1''}{2\beta^2}\right]^2 + \left[\frac{w_1'''}{2\sqrt{2}\beta^3} - \frac{w_1'}{\sqrt{2}\beta}\right]^2 = 4[C_1^2 + C_2^2] \quad (25)$$

It can be observed from Fig. 3 and Eq. (13) that

$$\frac{\delta_f - \delta_1}{\delta_1} = \frac{k_1}{k_2} = \frac{\alpha^4}{\beta^4} = \eta^4 \quad (26)$$

We use $\eta = \alpha/\beta$ to represent the ratio of the interfacial stiffness for the bilinear CZM. Substituting Eqs. (18)–(20) into Eq. (25) yields

$$\frac{\{\eta[1 + \cot(\alpha d_0)] + \eta^3[1 - \cot(\alpha d_0)]\}^2}{2} + \left\{\eta^2 \cot(\alpha d_0) + \left(\frac{\delta_f - \delta_1}{\delta_1}\right)\right\}^2 = \frac{4[C_1^2 + C_2^2]}{\delta_1^2} \quad (27)$$

Using a similar method for coefficients C_3 and C_4, it can be derived as

$$\frac{\{\eta[1 + \cot(\alpha d_0)] + \eta^3[\cot(\alpha d_0) - 1]\}^2}{2} - \left\{\eta^2 \cot(\alpha d_0) - \left(\frac{\delta_f - \delta_1}{\delta_1}\right)\right\}^2 = \frac{4[C_4^2 - C_3^2]}{\delta_1^2} \quad (28)$$

When the separation at the crack tip is δ, the displacement, moment, and shear force boundary conditions at the crack tip ($x_1 = 0$) are given by

$$w(x_1)|_{x_1=0} = \delta, \quad w''(x_1)|_{x_1=0} = \frac{Pa}{EI}, \quad w'''(x_1)|_{x_1=0} = \frac{P}{EI} \quad (29)$$

From these boundary conditions, the coefficients can be readily expressed as

$$C_1 = \frac{\delta - \delta_f}{2} - \frac{Pa}{4\beta^2 EI}, \quad C_3 = \frac{\delta - \delta_f}{2} + \frac{Pa}{4\beta^2 EI}$$

$$C_4 - C_2 = \frac{P}{2\sqrt{2}\beta^3 EI} = \frac{\sqrt{2}\beta \cdot P}{bk_2} \quad (30)$$

$$(C_2 + C_4) \cdot \sqrt{2}\beta = \left.\frac{dw}{dx}\right|_{x_1=0} = -\theta_0$$

$$C_2 = \frac{1}{2}\left[\frac{-\sqrt{2}\beta \cdot P}{bk_2} - \frac{\theta_0}{\sqrt{2}\beta}\right], \quad C_4 = \frac{1}{2}\left[\frac{\sqrt{2}\beta \cdot P}{bk_2} - \frac{\theta_0}{\sqrt{2}\beta}\right]$$

As discussed in Sec. 2, the crack tip rotation θ_0 can be conveniently expressed as a function of the remote peel load P and crack tip separation δ as follows:

$$\theta_0 = \frac{bJ(\delta)}{P} - \frac{Pa^2}{2EI}, \quad J(\delta) = \Gamma - \frac{k_2}{2}(\delta_f - \delta)^2 \quad (31)$$

where $J(\delta)$ is the area under the given cohesive law corresponding to the separation δ, and Γ is the interfacial toughness. When $\delta = \delta_f$, $J(\delta) = \Gamma$, and crack starts to propagate.

Adding Eq. (27) to Eq. (28), we can obtain a quadric function of the variable $\cot(\alpha d_0)$. By solving the quadric equation, the positive root is derived as follows:

$$\cot(\alpha d_0) = \frac{2\sqrt{C_1^2 + C_2^2 - C_3^2 + C_4^2}}{\eta\sqrt{\delta_1 \delta_f}} - 1 \quad (32)$$

It is noted that only the positive root is physically meaningful ($\cot(\alpha d_0) > 0$). First, the elastic zone size d_0 has to be larger than zero, obviously. At the same time, it should be noted that αd_0 must be less than $\pi/2$. Otherwise, the second derivative of Eq. (12) can be zero at a certain cross section within the region $0 < x_2 < d_0$ (see Fig. 4). This means that the beam's internal bending moment at a certain cross section in this region can be zero. Evidently, this is physically impossible under peel loading, as illustrated in Fig. 4. Therefore, the upper bound of the elastic zone size d_0 must be less than $\pi/2\alpha$. Since $0 < \alpha d_0 < \pi/2$, one can readily see that $\cot(\alpha d_0) > 0$ (the positive root).

Equation (32) gives the general explicit expression of the elastic region size d_0 for the crack initiation process. For the condition when $\delta = \delta_f$ (crack propagation process), it is noted that $C_1 = -C_3$, as implied by Eq. (30). Thus, Eq. (32) can be further reduced to

$$\cot(\alpha d_0) = \frac{2\sqrt{C_2^2 + C_4^2}}{\eta\sqrt{\delta_1 \delta_f}} - 1 \tag{33}$$

and the coefficients can be correspondingly simplified to

$$C_3 = -C_1 = \frac{Pa}{4\beta^2 EI}, \quad C_2 = \frac{1}{2}\left[\frac{-\sqrt{2}\beta \cdot P}{bk_2} - \frac{\theta_0}{\sqrt{2}\beta}\right],$$

$$C_4 = \frac{1}{2}\left[\frac{\sqrt{2}\beta \cdot P}{bk_2} - \frac{\theta_0}{\sqrt{2}\beta}\right] \tag{34}$$

Note that θ_0 is a function of P; therefore, the coefficients C_1, C_2, C_3, and C_4 are also a function of P for the given cohesive law. From Eqs. (21)–(24), we can obtain

$$\cos(\sqrt{2}\beta d_1) = \frac{C_1 \cdot Y_2 - C_2 \cdot Y_1}{C_1^2 + C_2^2}, \quad \sin(\sqrt{2}\beta d_1) = \frac{C_2 \cdot Y_2 + C_1 \cdot Y_1}{C_1^2 + C_2^2} \tag{35}$$

$$\sinh(\sqrt{2}\beta d_1) = \frac{C_3 \cdot Y_3 - C_4 \cdot Y_4}{C_3^2 - C_4^2}, \quad \cosh(\sqrt{2}\beta d_1) = \frac{C_3 \cdot Y_4 - C_4 \cdot Y_3}{C_3^2 - C_4^2} \tag{36}$$

where

$$Y_1 = \frac{-\delta_1 \eta^3[\cot(\alpha d_0) - 1]}{2\sqrt{2}} + \frac{\delta_1 \eta[1 + \cot(\alpha d_0)]}{2\sqrt{2}},$$

$$Y_2 = -\frac{\delta_1}{2}\left[\left(\frac{\delta_f - \delta_1}{\delta_1}\right) + \eta^2 \cot(\alpha d_0)\right]$$

$$Y_3 = \frac{-\delta_1 \eta^3[\cot(\alpha d_0) - 1]}{2\sqrt{2}} - \frac{\delta_1 \eta[1 + \cot(\alpha d_0)]}{2\sqrt{2}},$$

$$Y_4 = -\frac{\delta_1}{2}\left[\left(\frac{\delta_f - \delta_1}{\delta_1}\right) - \eta^2 \cot(\alpha d_0)\right] \tag{37}$$

From Eqs. (35) and (36), respectively, we can further obtain

$$\cot(\sqrt{2}\beta d_1) = \frac{C_1 \cdot Y_2 - C_2 \cdot Y_1}{C_1 \cdot Y_1 + C_2 \cdot Y_2} = f_1(P) \tag{38}$$

$$\sinh(\sqrt{2}\beta d_1) + \cosh(\sqrt{2}\beta d_1) = \exp(\sqrt{2}\beta d_1) = \frac{Y_3 + Y_4}{C_3 + C_4} = f_2(P) \tag{39}$$

Note that all parameters in Eqs. (38) and (39) are explicit functions of the peel load P with the given bilinear cohesive law, specimen geometry, and material properties. However, it is also noted that with different values of d_1, Eqs. (38) and (39) can be satisfied for the coefficient set C_1, C_2, Y_1, and Y_2 and the coefficient set C_3, C_4, Y_3, and Y_4, respectively. Obviously, a physically meaningful d_1 should satisfy both Eqs. (38) and (39) simultaneously. Therefore, we have the intrinsic geometry constraint condition for solving the remote peel load P as follows:

$$\operatorname{arccot}\left[\frac{C_1 \cdot Y_2 - C_2 \cdot Y_1}{C_1 \cdot Y_1 + C_2 \cdot Y_2}\right] = \ln\left[\frac{Y_3 + Y_4}{C_3 + C_4}\right] = \sqrt{2}\beta d_1 \tag{40}$$

The remote peel force P can be obtained by solving the constraint equation (40). The real remote peel load P is given by the first positive solution of Eq. (40). The solution can be obtained by iterative method or numerical method. With the determined peel load P, the softening zone size d_1 can be expressed as follows:

$$d_1 = \frac{1}{\sqrt{2}\beta} \cdot \ln\left[\frac{Y_3 + Y_4}{C_3 + C_4}\right] \tag{41}$$

From Eq. (32), the elastic zone size d_0 can be readily determined as follows:

$$d_0 = \frac{1}{\alpha}\operatorname{arccot}\left[\frac{2\sqrt{C_1^2 + C_2^2 - C_3^2 + C_4^2}}{\eta\sqrt{\delta_1 \delta_f}} - 1\right] \tag{42}$$

The relative opening at the load line for the DCB specimen can be written as

$$\Delta = 2\left[\delta + \frac{Pa^3}{3EI} + \theta_0 a\right] \tag{43}$$

where δ is the crack tip opening in the crack initiation process. When $\delta = \delta_f$, crack starts to propagate. The origin of the coordinate x_1 is set at the crack tip, and it moves forward with the propagated crack tip. Therefore, once the crack tip starts growing after its initiation, $\delta \equiv \delta_f$, and $J(\delta) \equiv \Gamma$, if the value of toughness Γ is treated as a material constant.

In principle, the method developed in this study can be applied to any multilinear model using the continuous boundary conditions. However, as an example, only the simplest multilinear model: Bilinear cohesive law is presented in the current study. It is noted that the local deformation and stress distribution are determined in a simple form when the softening zone size d_1 and elastic zone size d_0 are completely explicit as a function of P for a given cohesive law. Once d_1 and d_0 are obtained, the local displacement field beyond the crack tip can be obtained with Eqs. (10) and (12). With the obtained local displacement field and by applying the bilinear constitutive law as described by Eq. (8), the local interfacial stress distribution beyond the crack tip can be finally determined.

When the crack tip separation δ is smaller than δ_1, based on the linear elastic model [14] and with the origin of the coordinate x at the crack tip, the local displacement field can be simply rewritten by

$$w(x) = e^{-\alpha x}\left[-\frac{Pa}{2EI\alpha^2}\sin(\alpha x) + \frac{P(a + 1/\alpha)}{2EI\alpha^2}\cos(\alpha x)\right] \tag{44}$$

With Eq. (44), the elastic zone size d_0, which is the distance between the crack tip and the first zero-deflection cross section, can be found for linear elastic stage as follows:

$$\tan(\alpha d_0) = \frac{a + 1/\alpha}{a} \tag{45}$$

Equation (45) indicates that when the crack tip separation δ is smaller than δ_1 (linear elastic loading stage), the elastic zone size d_0 is a material and geometry constant during the crack initiation process (crack length a is a constant) and is independent of the peel load P. This shows an important difference between the linear elastic model and the nonlinear model. One can also see that for a linear elastic model, the value of d_0 can only vary in the range between $\pi/(4\alpha)$ and $\pi/(2\alpha)$ during the crack propagation process when the crack length a changes from 0 to infinity.

For a bilinear cohesive zone model, when any three parameters are specified, the entire model can be completely determined. The three parameters are chosen as the interfacial fracture energy (toughness) Γ, the maximum interfacial stress σ_f, and the interfacial stiffness ratio $K = k_1/k_2$. Once these three parameters are specified, all other parameters can be obtained as below:

$$\delta_f = \frac{2\Gamma}{\sigma_f}, \quad \delta_1 = \frac{\delta_f}{1 + k_1/k_2}, \quad k_1 = \frac{\sigma_f}{\delta_1}, \quad k_2 = \frac{\sigma_f}{\delta_f - \delta_1},$$

$$\alpha = \sqrt[4]{\frac{bk_1}{4EI}}, \quad \beta = \sqrt[4]{\frac{bk_2}{4EI}} \tag{46}$$

Table 1 Geometry and material properties of FEA and test DCB specimen

	Initial crack a_0 (mm)	Width b (mm)	Height h (mm)	Modulus E (GPa)	σ_f (MPa)	Toughness Γ (N/mm)
Test	50	5	4.5	210	19	0.65
FEA	20	5	1.5	210	19	0.65

4 Validations and Parametric Studies

In order to validate the derivation in the current study, the analytical result is compared with numerical and experimental results. The parameters for finite element analysis (FEA) and experimental data are listed in Table 1, and they are exactly followed by the present analytical study. The experimental data were reported by Andersson and Biel [21]. The interfacial stiffness ratio K is set as 8 for these two comparisons, and its effect will be evaluated in the parametric study. The FEA and analytical results for steel-steel bonded joints are shown in Fig. 5. From Fig. 5, it can be seen that both crack initiation and propagation process are accurately predicted by the current model. The nonlinear response in the ascending branch of loading is well captured. Note that when $\delta = 4\delta_1$ (the energy release rate is approximately 65% of the toughness Γ), the peel load P has reached about 85% of the maximum peel load. When $\delta = \delta_1$ (the energy release rate is approximately 11% of the toughness Γ), the peel load P has reached about 35% of the maximum peel load. When the crack tip opening $\delta \leq \delta_1$ (elastic range), the loading and unloading process may be treated as completely recoverable. This load might be useful for fatigue design of bonded joints. Figure 5 also indicates that the maximum peel load does not correspond to the final crack tip opening δ_f, but slightly less than that value, which is about 88% of the final separation δ_f. However, the critical peel load P_{cr} (crack starts to propagate, $\delta = \delta_f$) is very close to the maximum peel load P_{max} (less than 1%). Therefore, it may be reasonable to approximate the maximum peel load by the critical peel load for the sake of simplicity. Figure 6 shows the comparison between the analytical results and experimental data adopted from the study [21]. The excellent agreement further validates the model developed in the current study.

The parameters from the experimental data of Andersson and Biel [21] are used for the calculation of the local deformation and stress beyond the crack tip. Based on the derivations in the current study, Figs. 7 and 8 give the local deformation and stress beyond the crack tip at different crack tip opening δ (up to δ_f) by using bilinear CZM with the interfacial stiffness ratio $K=8$ and initial crack length $a=50$ mm. For comparison purposes, the local deformation and interfacial stress distribution with an initial crack length of $a=100$ mm at crack tip opening $\delta = \delta_f$ are also included. Generally, with the increase in crack tip opening δ, the softening zone d_1 increases, while the elastic zone d_0 decreases. However, once the crack is propagated, the local deformation and stress distribution remain stable. As seen in Figs. 7 and 8, the local deformation and stress distribution at crack length $a=50$ mm and 100 mm are almost overlapped. It is emphasized that this result is based on the assumption that the toughness and cohesive law remain unchanged regardless of the crack length a. If the plastic dissipation is involved, the toughness will be contributed by the intrinsic work of separation Γ_0 and the plastic work of the adhesive layer or even the adherends, and the softening zone may grow with the increase in the crack length a [22].

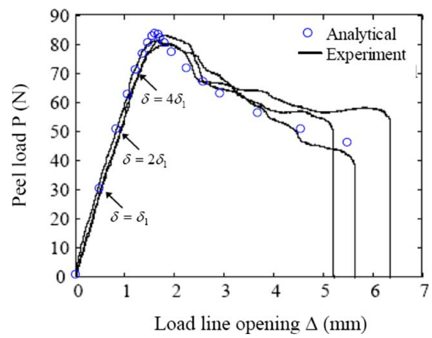

Fig. 6 Comparison of analytical and experimental results

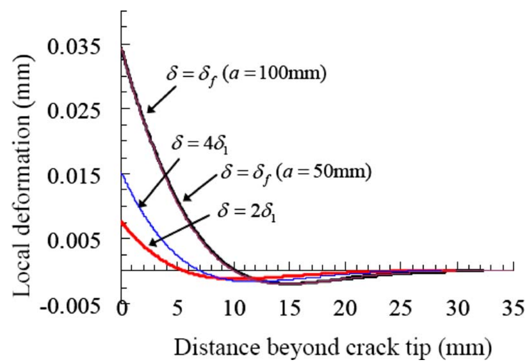

Fig. 7 Local deformation of beam's neutral axis beyond crack tip with various crack tip openings and initial crack lengths

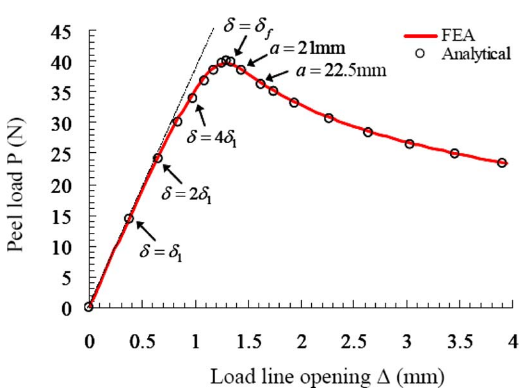

Fig. 5 Comparison of analytical and FEA results

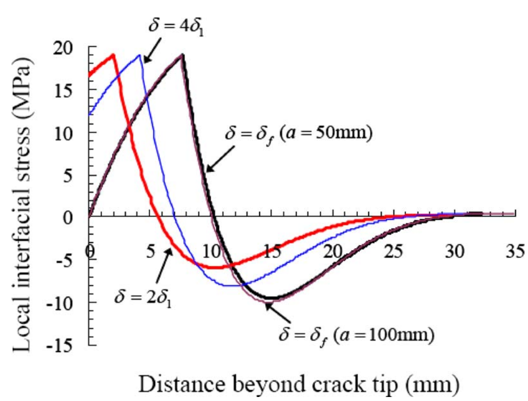

Fig. 8 Local interfacial stress beyond crack tip with various crack tip openings and initial crack lengths

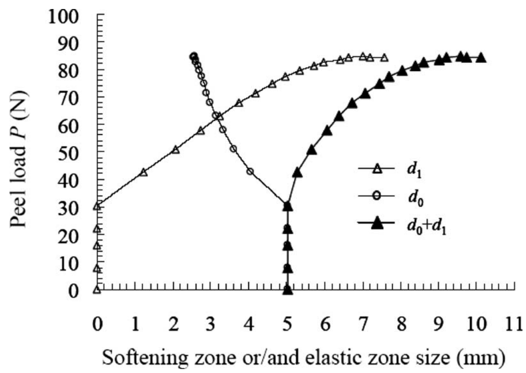

Fig. 9 Evolution of softening and elastic zone as a function of the remote peel load P

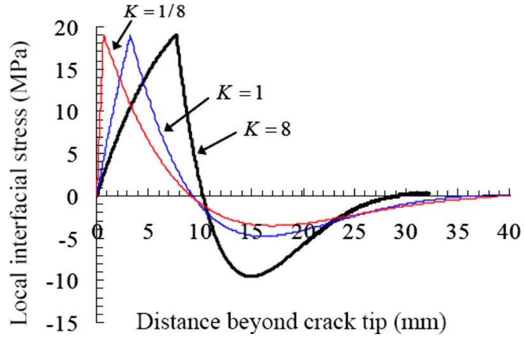

Fig. 11 Effect of interfacial stiffness ratio K on local interfacial stress beyond crack tip when crack tip separation $\delta = \delta_f$ at the initial crack length $a=50$ mm

Figure 9 provides the relationship between the remote peel load P and the size of the softening zone and elastic zone. From Fig. 9, it can be seen that the damage zone (d_1) grows nonlinearly as the remote peel load increases. On the other hand, the elastic zone (d_0) descends nonlinearly as the remote peel load increases. However, it is interesting to note that the total process zone (d_1+d_0) grows nonlinearly with the increase in the remote peel load. Obviously, this is in agreement with common knowledge. It is also noted that, when the crack tip separation δ is smaller than δ_1, the elastic zone size d_0 is a constant during the crack initiation process as discussed before.

In order to investigate the effect of the interfacial stiffness ratio K in the bilinear CZM on the peel load and local deformation beyond the crack tip, a parametric study is conducted. Figures 10 and 11, respectively, show the local deformation and interfacial stress beyond the crack tip with different K when the crack tip separation $\delta = \delta_f$ at the initial crack length $a=50$ mm. The difference between the peel load P for different $K=1/8$, 1, and 8 is less than 0.5%. However, the local deformation and stress distribution are significantly different for different K values, as seen in Figs. 10 and 11. The distinction of local deformation might become very important when one considers a cyclic loading process since the distribution of the local damage can be dominant for a cyclic loading process. However, for a monotonic loading process, the insensitivity of the remote peel load to the interfacial stiffness ratio K is a very useful feature for the simplification of the debonding problem as concluded by previous study [17]. As seen in Fig. 10, the crack tip rotation θ_0 for different K is almost identical, although the overall local deformations beyond the crack tip are very different.

To further evaluate the effect of another parameter—the maximum interfacial stress σ_f on the remote peel load P and remote loadline deflection Δ—a parametric study is also conducted. The critical peel load P_{cr} and corresponding loadline deflection Δ_{cr} are plotted in Fig. 12 as a function of σ_f (σ_f varies from 0.5 MPa up to 100 MPa) with constant interfacial stiffness ratio $K=8$. From Fig. 12, the effect of the maximum interfacial stress σ_f on P_{cr} and Δ_{cr} is different. When the maximum interfacial stress σ_f is larger than a certain value, its effect is insignificant. However, for a relatively lower value, such as 5 MPa, than that found from experiment (19 MPa) [22], the experimental P_{cr} is significantly underestimated and Δ_{cr} is considerably overestimated. Therefore, it is suggested that one should be careful in choosing a proper value of σ_f for a cohesive law.

5 Discussions and Conclusions

The current work develops a new analytical approach that can consider both crack initiation and propagation process for bilinear cohesive laws. In the current model, the concept of extended crack length (characteristic length l) is no longer required. The local deformation beyond crack tip is modeled by a more natural approach, which does not require that all deformations should be simultaneously equal to zero at the location of the characteristic length l beyond the crack tip. This is the first natural boundary condition based solution for bilinear cohesive laws under peel load, instead of the enforced boundary conditions. One of the features of the current solution is that the local deformation and interfacial stress distribution can be simply and explicitly obtained with the determined remote peel load P. Another attractive feature of the present solution is that the crack initiation process can be obtained. The crack initiation process as well as its actual stress and damage distribution beyond the crack tip may be very impor-

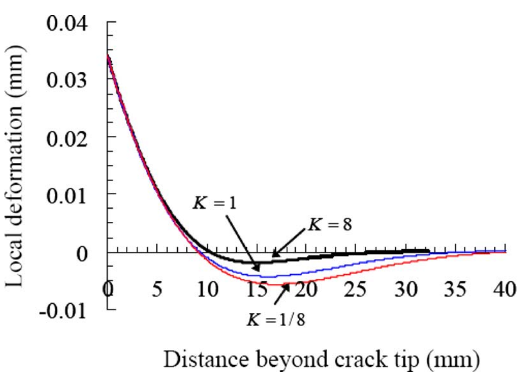

Fig. 10 Effect of interfacial stiffness ratio K on local deformation beyond crack tip when crack tip separation $\delta = \delta_f$ at the initial crack length $a=50$ mm

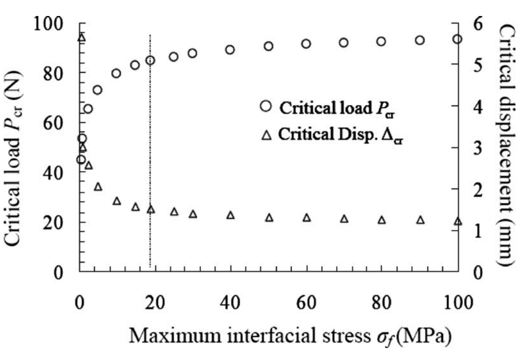

Fig. 12 Effect of maximum interfacial stress σ_f on the critical load and loadline displacement at initial crack length $a=50$ mm

tant for the cyclic loading conditions and for understanding fracture of materials and debonding of adhesively bonded joints. From the comparison with numerical results, it can be seen that the nonlinear response during the ascending branch of loading is accurately captured. Although the local deformation and stress distribution with different interfacial stiffness ratio K vary significantly, the rotation θ_0 at the crack tip seems very close. This might be helpful in explaining the high insensitivity of the remote peel load P to the details of the shape of the cohesive law, as concluded by previous studies. This is because for identical crack tip rotation θ_0 and toughness Γ, the remote peel load must be the same [23].

The parametric study also indicates that after the crack initiation process, the local deformation and stress distribution remain relatively stable during the crack propagation stage if one assumes that the cohesive law and toughness keep unchanged during the entire process. However, the parametric study indicates that the effect of σ_f on the peel load P and loadline deflection is different. When the maximum interfacial stress σ_f is smaller than a certain level, the effect of σ_f on the peel load P and loadline deflection Δ can be very significant.

Acknowledgment

This study is based on the work supported by the NSF under Grant No. NSF 0734845 and by the NASA/EPSCoR under Grant No. NASA/LEQSF (2007-10)-Phase3-01.

References

[1] Atkinson, C., 1979, "Stress Singularities and Fracture Mechanics," Appl. Mech. Rev., **32**(2), pp. 123–135.
[2] Barenblatt, G. I., 1959, "The Formation of Equilibrium Cracks During Brittle Fracture. General Ideas and Hypothesis. Axisymmetrical Cracks," J. Appl. Math. Mech. (PMM), **23**, pp. 622–636.
[3] Dugdale, D. S., 1960, "Yielding of Steel Sheets Containing Slits," J. Mech. Phys. Solids, **8**, pp. 100–104.
[4] Rose, J. H., Smith, J. R., and Ferrante, J., 1983, "Universal Features of Bonding in Metals," Phys. Rev. B, **28**, pp. 1835–1845.
[5] Needleman, A., 1987, "A Continuum Model for Void Nucleation by Inclusion Debonding," ASME J. Appl. Mech., **54**, pp. 525–531.
[6] Needleman, A., 1990, "An Analysis of Tensile Decohesion Along an Interface," J. Mech. Phys. Solids, **38**, pp. 289–324.
[7] Tvergaard, V., 1990, "Effect of Fibre Debonding in a Whisker-Reinforced Metal," Mater. Sci. Eng., A, **125**, pp. 203–213.
[8] Tvergaard, V., and Hutchinson, J. W., 1992, "The Relation Between Crack Growth Resistance and Fracture Process Parameters in Elastic-Plastic Solids," J. Mech. Phys. Solids, **40**, pp. 1377–1397.
[9] Xu, X. P., and Needleman, A., 1993, "Void Nucleation by Inclusion Debonding in a Crystal Matrix," Modell. Simul. Mater. Sci. Eng., **1**, pp. 111–132.
[10] Camacho, G. T., and Ortiz, M., 1996, "Computational Modeling of Impact Damage in Brittle Materials," Int. J. Solids Struct., **33**, pp. 2899–2938.
[11] Hillerborg, A., Modeer, M., and Petersson, P. E., 1976, "Analysis of Crack Formation and Crack Growth in Concrete by Means of Fracture Mechanics and Finite Elements," Cem. Concr. Res., **6**, pp. 773–782.
[12] Geubelle, P. H., and Baylor, J., 1998, "The Impact-Induced Delamination of Laminated Composites: A 2D Simulation," Composites, Part B, **29**, pp. 589–602.
[13] Hutchinson, J. W., and Evans, A. G., 2000, "Mechanics of Materials: Topdown Approaches to Fracture," Acta Mater., **48**, pp. 125–135.
[14] Kanninen, M. F., 1973, "An Augmented Double Cantilever Beam Model for Studying Crack Propagated and Arrest," Int. J. Fract., **9**, pp. 83–92.
[15] Williams, J. G., 1989, "End Correction for Orthotropic DCB Specimen," Compos. Sci. Technol., **35**, pp. 367–376.
[16] Kinloch, A. J., Lau, C. C., and Williams, J. G., 1994, "The Peeling of Flexible Laminates," Int. J. Fract., **66**, pp. 45–70.
[17] Williams, J. G., and Hadavinia, H., 2002, "Analytical Solutions for Cohesive Zone Models," J. Mech. Phys. Solids, **50**, pp. 809–825.
[18] Olsson, P., and Stigh, U., 1989, "On the Determination of the Constitutive Properties of Thin Interphase Layers-An Exact Inverse Solution," Int. J. Fract., **41**, pp. R71–R76.
[19] Andersson, T., and Stigh, U., 2004, "The Stress-Elongation Relation for an Adhesive Layer Loaded in Peel Using Equilibrium of Energetic Forces," Int. J. Solids Struct., **41**, pp. 413–434.
[20] Rice, J. R., 1968, "Stresses Due to a Sharp Notch in a Work-Hardening Elastic-Plastic Material Loaded by Longitudinal Shear," ASME J. Appl. Mech., **35**, pp. 379–386.
[21] Andersson, T., and Biel, A., 2006, "On the Effective Constitutive Properties of a Thin Adhesive Layer Loaded in Peel," Int. J. Fract., **141**, pp. 227–246.
[22] Blackman, B. R. K., Hadavinia, H., Kinloch, A. J., and Williams, J. G., 2003, "The Use of a Cohesive Zone Model to Study the Fracture of Fibre Composites and Adhesively-Bonded Joints," Int. J. Fract., **119**, pp. 25–46.
[23] Eshelby, J. D., 1951, "The Force on an Elastic Singularity," Philos. Trans. R. Soc. London, Ser. A, **244**, pp. 87–112.

On a Screw Dislocation Interacting With Two Viscous Interfaces

X. Wang[1]
e-mail: xuwang_sun@hotmail.com

E. Pan
e-mail: pan2@uakron.edu

Department of Civil Engineering,
and Department of Applied Mathematics,
University of Akron,
Akron, OH 44325-3905

We investigate a screw dislocation interacting with two concentric circular linear viscous interfaces. The inner viscous interface is formed by the circular inhomogeneity and the interphase layer, and the outer viscous interface by the interphase layer and the unbounded matrix. The time-dependent stresses in the inhomogeneity, interphase layer, and unbounded matrix induced by the screw dislocation located within the interphase layer are derived. Also obtained is the time-dependent image force on the screw dislocation due to its interaction with the two viscous interfaces. It is found that when the interphase layer is more compliant than both the inhomogeneity and the matrix, three transient equilibrium positions (two are unstable and one is stable) for the dislocation can coexist at a certain early time moment. If the inhomogeneity and matrix possess the same shear modulus, and the characteristic times for the two viscous interfaces are also the same, a fixed equilibrium position always exists for the dislocation. In addition, when the interphase layer is stiffer than the inhomogeneity and matrix, the fixed equilibrium position is always an unstable one; on the other hand, when the interface layer is more compliant than the inhomogeneity and matrix, the nature of the fixed equilibrium position depends on the time: the fixed equilibrium position is a stable one if the time is below a critical value, and it is an unstable one if the time is above the critical value. In addition, a saddle point transient equilibrium position for the dislocation can also be observed under certain conditions. [DOI: 10.1115/1.3112743]

Keywords: three-phase fibrous composite, viscous interface, screw dislocation, image force, transient equilibrium position

1 Introduction

It is well known that the interphase layer between the fiber and the surrounding matrix exerts a significant influence on the local and overall mechanical behaviors of fibrous composites [1–3]. In earlier modeling attempts [1–3], the interphase layer was assumed to be perfectly bonded to the fiber and the surrounding matrix, i.e., all the tractions and the displacements are continuous across the interfaces between two different bonded phases. However, at the microscopic level, the interface between two different bonded phases is generally not a perfect one but is with waviness or steps. At elevated temperatures, diffusional transport becomes important on these rough interfaces due to the differences in the normal tractions that are present along the rough interfaces [4,5]. It was suggested [4–8] that the microscopically mass diffusion-controlled mechanism can be macroscopically described by the linear law for a viscous interface: $\dot{\delta}=\tau/\eta$, where $\dot{\delta}$ is the sliding velocity (i.e., the differentiation of the relative sliding with respect to time t), τ is the interfacial shear stress, and η is the interfacial viscosity. Recently, the influence of the interfacial viscosity on the mechanical behaviors of composite has been addressed (see, for example, Refs. [9–12]). In addition, it was recently verified that the heterostructures in which composition/doping are modulated at the *nanometer scale* can be realized in core-shell nanowires [13]. If these core-shell nanowires are then reinforced in a metal matrix, then the three-phase cylindrical model, which will be studied in this research, becomes more relevant.

The objective of this research is to incorporate the Newtonian viscosity into the inner interface between the fiber and interphase layer and the outer interface between the interphase layer and the matrix. More specifically, we investigate in this work a screw dislocation in an annular interphase layer of uniform thickness bonded through Newtonian viscous interfaces to a circular inhomogeneity and to the surrounding unbounded matrix. It was recently observed that it is possible to find a transient equilibrium position for a screw dislocation interacting with a circular viscous interface [11]. Then it is expected that some more complex and more interesting phenomena may exist when a screw dislocation interacts with not one but two nearby viscous interfaces. Due to the fact that we consider two viscous interfaces, then it is only possible to arrive at series form solutions for this interaction problem. This paper is structured as follows. In Sec. 2, we derive the time-dependent stress field induced by the screw dislocation by means of the complex variable method. It is observed that the unknowns are determined by solving a decoupled set of state-space equations. In Sec. 3, we first obtain an expression for the time-dependent image force on the dislocation due to its interaction with the two nearby viscous interfaces; then we calculate and discuss in detail the time-dependent image force, with the focus on finding the possible transient equilibrium positions for the dislocation on which the image force is zero at a certain moment.

2 Formulation

In this section, we will analyze the time-dependent stress field associated with a three-phase circular inhomogeneity with two concentric circular linear viscous interfaces, as shown in Fig. 1. The linearly elastic materials occupying the inhomogeneity, the interphase layer, and the matrix are assumed to be homogeneous and isotropic with the associated shear moduli μ_1, μ_2, and μ_3, respectively. We represent the matrix by the domain $S_3: x^2+y^2 \geq b^2$ and assume that the circular inhomogeneity occupies the

[1]Corresponding author.

Contributed by the Applied Mechanics Division of ASME for publication in the Journal of Applied Mechanism. Manuscript received May 2, 2008; final manuscript received October 3, 2008; published online June 17, 2009. Review conducted by Anthony Wass.

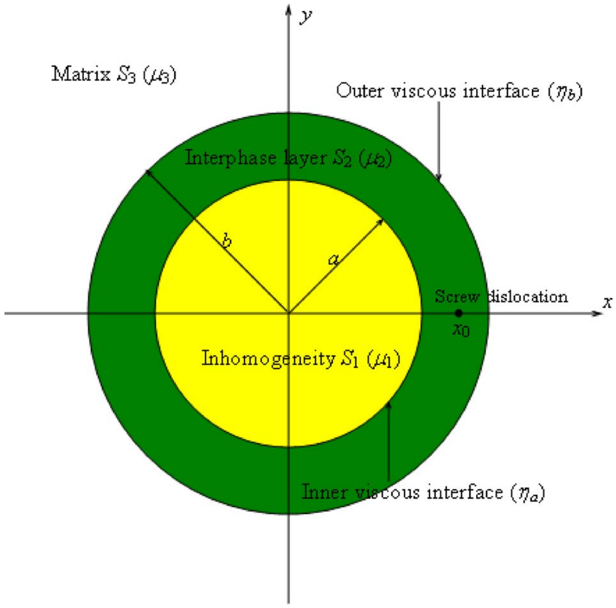

Fig. 1 A screw dislocation in a three-phase circular inhomogeneity with two concentric circular linear viscous interfaces

circular region $S_1: x^2+y^2 \le a^2$, and the interphase layer occupies the annulus $S_2: a^2 \le x^2+y^2 \le b^2$. Furthermore at time $t=0$, a screw dislocation with Burgers vector b_z is introduced into the interphase layer S_2 and fixed at $[x_0, 0]$, $(a < x_0 < b)$ on the positive real axis. Throughout this paper, the subscripts 1, 2, and 3 (or the superscripts (1), (2), and (3)) are used to identify the quantities in S_1, S_2, and S_3, respectively. In this research, the inertia force in the inhomogeneity, the interphase layer, and the matrix is ignored in order to simplify the analysis involved. As such, the out-of-plane displacement w, the stress components σ_{zx} and σ_{zy} in the Cartesian coordinate system, and the stress components σ_{zr} and $\sigma_{z\theta}$ in the polar coordinate system can be expressed in terms of a single analytic function $f(z,t)$ as [14]

$$w = \mathrm{Im}\{f(z,t)\}$$

$$\sigma_{zy} + i\sigma_{zx} = \mu f'(z,t)$$

$$\sigma_{z\theta} + i\sigma_{zr} = \mu e^{i\theta} f'(z,t) \tag{1}$$

where μ is the shear modulus, t is the real time variable while $z = x+iy = re^{i\theta}$ is the complex variable, and $f'(z,t) = \partial f(z,t)/\partial z$. The appearance of the real time variable t in the analytic function f is due to the influence of the two viscous interfaces at $r=a$ and $r=b$.

The boundary conditions on the two linear viscous interfaces $r=a$ and $r=b$ can be described by

$$\sigma_{zr}^{(1)} = \sigma_{zr}^{(2)} = \eta_a(\dot{w}^{(2)} - \dot{w}^{(1)}), \quad r=a, \quad t>0$$

$$\sigma_{zr}^{(3)} = \sigma_{zr}^{(2)} = \eta_b(\dot{w}^{(3)} - \dot{w}^{(2)}), \quad r=b, \quad t>0 \tag{2}$$

where an overdot denotes the derivative with respect to the time t, and η_a and η_b are the non-negative viscosity coefficients for the two interfaces, respectively.

In view of Eq. (1), the above set of boundary conditions on the two viscous interfaces can also be expressed in terms of three analytic functions—$f_1(z,t)$ defined in the circular inhomogeneity, $f_2(z,t)$ defined in the interphase layer, and $f_3(z,t)$ defined in the unbounded matrix as

$$\mu_1 f_1^+(z,t) + \mu_1 \bar{f}_1^-\left(\frac{a^2}{z},t\right) = \mu_2 f_2^-(z,t) + \mu_2 \bar{f}_2^+\left(\frac{a^2}{z},t\right) \tag{3a}$$

$$\dot{f}_2^-(z,t) - \dot{\bar{f}}_2^+\left(\frac{a^2}{z},t\right) - \dot{f}_1^+(z,t) + \dot{\bar{f}}_1^-\left(\frac{a^2}{z},t\right)$$
$$= \frac{\mu_1}{a\eta_a}\left[z f_1'^+(z,t) - \frac{a^2}{z}\bar{f}_1'^-\left(\frac{a^2}{z},t\right)\right], \quad |z|=a \tag{3b}$$

and

$$\mu_2 f_2^+(z,t) + \mu_2 \bar{f}_2^-\left(\frac{b^2}{z},t\right) = \mu_3 f_3^-(z,t) + \mu_3 \bar{f}_3^+\left(\frac{b^2}{z},t\right) \tag{4a}$$

$$\dot{f}_3^-(z,t) - \dot{\bar{f}}_3^+\left(\frac{b^2}{z},t\right) - \dot{f}_2^+(z,t) + \dot{\bar{f}}_2^-\left(\frac{b^2}{z},t\right)$$
$$= \frac{\mu_3}{b\eta_b}\left[z f_3'^-(z,t) - \frac{b^2}{z}\bar{f}_3'^+\left(\frac{b^2}{z},t\right)\right], \quad |z|=b \tag{4b}$$

where the superscript "+" denotes approaching the interface from inside, while the superscript "−" denotes approaching the interface from outside.

We first consider the inner viscous interface. It follows from Eq. (3a) for the continuity condition of traction across the inner viscous interface $|z|=a$ that

$$f_2(z,t) = \frac{\mu_1}{\mu_2}\bar{f}_1\left(\frac{a^2}{z},t\right) + \frac{1}{\mu_2}\sum_{n=1}^{+\infty}[A_n(t)z^n - a^{2n}A_n(t)z^{-n}]$$
$$+ \frac{b_z}{2\pi}\ln(z-x_0) - \frac{b_z}{2\pi}\ln\left(\frac{z-a^2/x_0}{z}\right), \quad a<|z|<b$$

$$\bar{f}_2\left(\frac{a^2}{z},t\right) = \frac{\mu_1}{\mu_2}f_1(z,t) - \frac{1}{\mu_2}\sum_{n=1}^{+\infty}[A_n(t)z^n - a^{2n}A_n(t)z^{-n}]$$
$$- \frac{b_z}{2\pi}\ln(z-x_0) + \frac{b_z}{2\pi}\ln\left(\frac{z-a^2/x_0}{z}\right), \quad \frac{a^2}{b}<|z|<a \tag{5}$$

where $A_n(t)$ $(n=1,2,\ldots,+\infty)$ are real but time-dependent coefficients to be determined.

Substituting Eq. (5) into Eq. (3b), we obtain the following:

$$\frac{\mu_1}{a\eta_1}z f_1'^+(z,t) + \frac{\mu_1+\mu_2}{\mu_2}\dot{f}_1^+(z,t) - \frac{2}{\mu_2}\sum_{n=1}^{+\infty}\dot{A}_n(t)z^n = \frac{\mu_1}{a\eta_1}\frac{a^2}{z}\bar{f}_1'^-\left(\frac{a^2}{z},t\right)$$
$$+ \frac{\mu_1+\mu_2}{\mu_2}\dot{\bar{f}}_1\left(\frac{a^2}{z},t\right) - \frac{2}{\mu_2}\sum_{n=1}^{+\infty}a^{2n}\dot{A}_n(t)z^{-n}, \quad |z|=a \tag{6}$$

Apparently the left-hand side of Eq. (6) is analytic and single valued within the circle $|z|=a$, while the right-hand side of Eq. (6) is analytic and single-valued outside the circle including the point at infinity. By employing Liouville's theorem, the left- and right-hand sides should be identically zero. Consequently, we arrive at the following inhomogeneous first-order partial differential equation for $f_1(z,t)$:

$$z f_1'(z,t) + t_1\dot{f}_1(z,t) = \frac{2a\eta_a}{\mu_1\mu_2}\sum_{n=1}^{+\infty}\dot{A}_n(t)z^n, \quad |z|<a \tag{7}$$

where $t_1 = a\eta_a(\mu_1+\mu_2)/\mu_1\mu_2 > 0$ is the characteristic time for the inner viscous interface $|z|=a$.

Equation (7) can be easily solved by using power series expansion as

$$f_1(z,t) = \frac{1}{\mu_1}\sum_{n=1}^{+\infty}B_n(t)z^n, \quad |z|<a \tag{8}$$

where $B_n(t)$ is related to $A_n(t)$ through the following:

$$nB_n(t) + t_1\dot{B}_n(t) = t_1\Gamma_1\dot{A}_n(t) \quad (n = 1,2, \ldots, +\infty) \tag{9}$$

with $\Gamma_1 = 2\mu_1/(\mu_1+\mu_2)$ $(0 \leq \Gamma_1 \leq 2)$ being a measure of the relative stiffness of the inhomogeneity with respect to the interphase layer.

Once we obtain $f_1(z,t)$, it is not difficult to arrive at the expression of $f_2(z,t)$ as

$$f_2(z,t) = \frac{1}{\mu_2}\sum_{n=1}^{+\infty} a^{2n}B_n(t)z^{-n} + \frac{1}{\mu_2}\sum_{n=1}^{+\infty}[A_n(t)z^n - a^{2n}A_n(t)z^{-n}] - \frac{b_z}{2\pi}\ln\left(\frac{z-a^2/x_0}{z}\right) + \frac{b_z}{2\pi}\ln(z-x_0), \quad a<|z|<b \tag{10}$$

Next we address the outer viscous interface. It follows from Eq. (4*a*) for the continuity condition of traction across the outer viscous interface $|z|=b$ that

$$f_2(z,t) = \frac{\mu_3}{\mu_2}\bar{f}_3\left(\frac{b^2}{z},t\right) + \frac{1}{\mu_2}\sum_{n=1}^{+\infty}[C_n(t)z^n - b^{2n}C_n(t)z^{-n}] + \frac{b_z}{2\pi}\ln(z-x_0) - \frac{b_z}{2\pi}\ln(z-b^2/x_0) + \frac{b_z}{2\pi}\frac{\mu_3}{\mu_2}\ln z, \quad a<|z|<b$$

$$\bar{f}_2\left(\frac{b^2}{z},t\right) = \frac{\mu_3}{\mu_2}f_3(z,t) - \frac{1}{\mu_2}\sum_{n=1}^{+\infty}[C_n(t)z^n - b^{2n}C_n(t)z^{-n}] - \frac{b_z}{2\pi}\ln(z-x_0) + \frac{b_z}{2\pi}\ln(z-b^2/x_0) - \frac{b_z}{2\pi}\frac{\mu_3}{\mu_2}\ln z, \quad b<|z|<\frac{b^2}{a} \tag{11}$$

where $C_n(t)$ $(n=1,2,\ldots,+\infty)$ are real but time-dependent coefficients to be determined.

Substituting Eq. (11) into Eq. (4*b*), we obtain the following:

$$\frac{\mu_2+\mu_3}{\mu_2}\dot{\bar{f}}_3^{+}\left(\frac{b^2}{z},t\right) - \frac{\mu_3}{b\eta_b}\frac{b^2}{z}\bar{f}_3'^{+}\left(\frac{b^2}{z},t\right) + \frac{2}{\mu_2}\sum_{n=1}^{+\infty}\dot{C}_n(t)z^n = \frac{\mu_2+\mu_3}{\mu_2}\dot{f}_3^{-}(z,t) - \frac{\mu_3}{b\eta_b}zf_3'^{-}(z,t) + \frac{2}{\mu_2}\sum_{n=1}^{+\infty}b^{2n}\dot{C}_n(t)z^{-n}, \quad |z|=b \tag{12}$$

Apparently the left-hand side of Eq. (12) is analytic and single valued within the circle $|z|=b$, while the right-hand side of Eq. (19) is analytic and single-valued outside the circle including the point at infinity. Again, by employing Liouville's theorem, the left- and right-hand sides should be identically zero. Consequently, we arrive at the following inhomogeneous first-order partial differential equation for $f_3(z,t)$:

$$zf_3'(z,t) - t_2\dot{f}_3(z,t) = \frac{2b\eta_b}{\mu_2\mu_3}\sum_{n=1}^{+\infty}b^{2n}\dot{C}_n(t)z^{-n}, \quad |z|>b \tag{13}$$

where $t_2 = b\eta_b(\mu_2+\mu_3)/\mu_2\mu_3 > 0$ is the characteristic time for the outer viscous interface $|z|=b$.

Equation (13) can also be solved by using power series expansion as

$$f_3(z,t) = \frac{b_z}{2\pi}\ln z + \frac{1}{\mu_3}\sum_{n=1}^{+\infty}D_n(t)z^{-n}, \quad |z|>b \tag{14}$$

where $D_n(t)$ is related to $C_n(t)$ through

$$-nD_n(t) - t_2\dot{D}_n(t) = t_2\Gamma_2 b^{2n}\dot{C}_n(t) \quad (n=1,2,\ldots,+\infty) \tag{15}$$

with $\Gamma_2 = 2\mu_3/(\mu_3+\mu_2)$ $(0 \leq \Gamma_2 \leq 2)$ being a measure of the relative stiffness of the matrix with respect to the interphase layer. It is of interest to observe from the above expression that as $t\to\infty$ $D_n(\infty)=0$. Consequently, $f_3(z,\infty) = (b_z/2\pi)\ln z$, which is the complex potential for a screw dislocation with Burgers vector b_z lodged within a circular hole of radius b.

Once we obtain $f_3(z,t)$, it is not difficult to arrive at another expression of $f_2(z,t)$ as

$$f_2(z,t) = \frac{1}{\mu_2}\sum_{n=1}^{+\infty}b^{-2n}D_n(t)z^n + \frac{1}{\mu_2}\sum_{n=1}^{+\infty}[C_n(t)z^n - b^{2n}C_n(t)z^{-n}] - \frac{b_z}{2\pi}\ln(z-b^2/x_0) + \frac{b_z}{2\pi}\ln(z-x_0), \quad a<|z|<b \tag{16}$$

Apparently the two expressions (10) and (16) for $f_2(z,t)$ should be exactly the same, from which we arrive at the following relations:

$$\sum_{n=1}^{+\infty}a^{2n}B_n(t)z^{-n} - \sum_{n=1}^{+\infty}a^{2n}A_n(t)z^{-n} + \sum_{n=1}^{+\infty}b^{2n}C_n(t)z^{-n} = \frac{\mu_2 b_z}{2\pi}\ln\left(\frac{z-a^2/x_0}{z}\right)$$

$$\sum_{n=1}^{+\infty}b^{-2n}D_n(t)z^n - \sum_{n=1}^{+\infty}A_n(t)z^n + \sum_{n=1}^{+\infty}C_n(t)z^n = \frac{\mu_2 b_z}{2\pi}\ln(z-b^2/x_0), \quad a<|z|<b \tag{17}$$

Therefore, from Eq. (17) the following set of algebraic equations for the unknowns can be obtained:

$$B_n(t) = A_n(t) - \left(\frac{b}{a}\right)^{2n}C_n(t) - \frac{\mu_2 b_z}{2\pi}\frac{x_0^{-n}}{n} \quad (n=1,2,\ldots,+\infty)$$

$$D_n(t) = b^{2n}A_n(t) - b^{2n}C_n(t) - \frac{\mu_2 b_z}{2\pi}\frac{x_0^{n}}{n} \quad (n=1,2,\ldots,+\infty) \tag{18}$$

Furthermore, using the relationships in Eq. (18), Eqs. (9) and (15) can be expressed, in terms of $A_n(t)$ and $C_n(t)$, into the following standard state-space equations:

$$\begin{bmatrix} t_1(\Gamma_1-1) & t_1\left(\frac{b}{a}\right)^{2n} \\ t_2 & t_2(\Gamma_2-1)\end{bmatrix}\begin{bmatrix}\dot{A}_n(t) \\ \dot{C}_n(t)\end{bmatrix} = n\begin{bmatrix} 1 & -\left(\frac{b}{a}\right)^{2n} \\ -1 & 1\end{bmatrix}\begin{bmatrix}A_n(t) \\ C_n(t)\end{bmatrix} + \frac{\mu_2 b_z}{2\pi}\begin{bmatrix}-x_0^{-n} \\ x_0^n b^{-2n}\end{bmatrix} \quad (n=1,2,\ldots,+\infty) \tag{19}$$

The general solutions to $A_n(t)$ and $C_n(t)$ can be obtained from the above equation as

$$A_n(t) = k_1^{(n)}\delta_{11}^{(n)}e^{-\lambda_1^{(n)}t} + k_2^{(n)}\delta_{12}^{(n)}e^{-\lambda_2^{(n)}t} + \rho_1^{(n)}$$

$$C_n(t) = k_1^{(n)}\delta_{21}^{(n)}e^{-\lambda_1^{(n)}t} + k_2^{(n)}\delta_{22}^{(n)}e^{-\lambda_2^{(n)}t} + \rho_2^{(n)} \quad (n=1,2,\ldots,+\infty) \tag{20}$$

where $\lambda_1^{(n)}, \lambda_2^{(n)}, \delta_{11}^{(n)}, \delta_{12}^{(n)}, \delta_{21}^{(n)}, \delta_{22}^{(n)}, \rho_1^{(n)}, \rho_2^{(n)}$ are given by

$$\frac{\lambda_1^{(n)}}{n} = \frac{c_2^{(n)} + \sqrt{c_2^{(n)2} - 4c_1^{(n)}c_3^{(n)}}}{2c_1^{(n)}} > 0,$$

$$\frac{\lambda_2^{(n)}}{n} = \frac{c_2^{(n)} - \sqrt{c_2^{(n)2} - 4c_1^{(n)}c_3^{(n)}}}{2c_1^{(n)}} > 0 \tag{21a}$$

$$\delta_{11}^{(n)} = \lambda_1^{(n)} t_2(\Gamma_2 - 1) + n, \quad \delta_{21}^{(n)} = n - \lambda_1^{(n)} t_2$$

$$\delta_{12}^{(n)} = \lambda_2^{(n)} t_2(\Gamma_2 - 1) + n, \quad \delta_{22}^{(n)} = n - \lambda_2^{(n)} t_2 \tag{21b}$$

$$\rho_1^{(n)} = \frac{\mu_2 b_z (x_0^n a^{-2n} - x_0^{-n})}{2\pi n c_3^{(n)}}, \quad \rho_2^{(n)} = \frac{\mu_2 b_z (x_0^n b^{-2n} - x_0^{-n})}{2\pi n c_3^{(n)}} \tag{21c}$$

with

$$c_1^{(n)} = t_1 t_2 (c_3^{(n)} - \Gamma_1\Gamma_2 + \Gamma_1 + \Gamma_2),$$

$$c_2^{(n)} = t_1\Gamma_1 + t_2\Gamma_2 + c_3^{(n)}(t_1 + t_2),$$

$$c_3^{(n)} = \left(\frac{b}{a}\right)^{2n} - 1 \tag{22}$$

and $k_1^{(n)}$ and $k_2^{(n)}$ are related to the initial conditions of $A_n(t)$ and $C_n(t)$ through the following:

$$k_1^{(n)} = \frac{\delta_{22}^{(n)} A_n(0) - \delta_{12}^{(n)} C_n(0) + \delta_{12}^{(n)} \rho_2^{(n)} - \delta_{22}^{(n)} \rho_1^{(n)}}{\delta_{11}^{(n)}\delta_{22}^{(n)} - \delta_{12}^{(n)}\delta_{21}^{(n)}} \quad (n = 1,2,\ldots,+\infty)$$

$$k_2^{(n)} = \frac{\delta_{11}^{(n)} C_n(0) - \delta_{21}^{(n)} A_n(0) + \delta_{21}^{(n)} \rho_1^{(n)} - \delta_{11}^{(n)} \rho_2^{(n)}}{\delta_{11}^{(n)}\delta_{22}^{(n)} - \delta_{12}^{(n)}\delta_{21}^{(n)}} \quad (n = 1,2,\ldots,+\infty) \tag{23}$$

At the initial moment $t=0$ when the screw dislocation is just introduced into the interphase layer, the displacement across the viscous interface has no time to experience any jump [15]. Consequently, both the inner interface $r=a$ and the outer interface $r=b$ are perfect at $t=0$, i.e., the traction and displacement are both continuous across the two interfaces at the initial moment $t=0$. Then we can easily obtain the initial values of $A_n(t)$ and $C_n(t)$ as

$$A_n(0) = \frac{\mu_2 b_z (1-\Gamma_2)[x_0^n a^{-2n} - (1-\Gamma_1)x_0^{-n}]}{2\pi n(c_3^{(n)} + \Gamma_1 + \Gamma_2 - \Gamma_1\Gamma_2)},$$

$$C_n(0) = \frac{\mu_2 b_z (1-\Gamma_1)[(1-\Gamma_2)x_0^n b^{-2n} - x_0^{-n}]}{2\pi n(c_3^{(n)} + \Gamma_1 + \Gamma_2 - \Gamma_1\Gamma_2)} \quad (n = 1,2,\ldots,+\infty) \tag{24}$$

It is observed that, when $\Gamma_1=\Gamma_2=0$, we have $\rho_1^{(n)}=A_n(0)$ and $\rho_2^{(n)}=C_n(0)$. This fact is easy to understand. It follows from Eq. (20) that $A_n(\infty)=\rho_1^{(n)}$ and $C_n(\infty)=\rho_2^{(n)}$. When $t\to\infty$ the two viscous interfaces become traction-free surfaces, while traction-free surfaces can also be obtained by assuming the shear moduli of the inhomogeneity and the matrix to be zero ($\Gamma_1=\Gamma_2=0$). Now the unknowns $A_n(t)$ and $C_n(t)$ have been uniquely determined. The other unknowns $B_n(t)$ and $D_n(t)$ can then be uniquely obtained from Eq. (18).

The time-dependent stresses in the composite induced by the screw dislocation can then be given by

$$\sigma_{zy}^{(1)} + i\sigma_{zx}^{(1)} = \sum_{n=1}^{+\infty} nB_n(t)z^{n-1}, \quad |z| < a \tag{25}$$

$$\sigma_{zy}^{(2)} + i\sigma_{zx}^{(2)} = \sum_{n=1}^{+\infty} n[A_n(t)(z^{n-1} + a^{2n}z^{-n-1}) - a^{2n}B_n(t)z^{-n-1}] - \frac{\mu_2 b_z}{2\pi}\frac{a^2}{z(x_0 z - a^2)} + \frac{\mu_2 b_z}{2\pi}\frac{1}{z - x_0}, \quad a < |z| < b \tag{26}$$

$$\sigma_{zy}^{(3)} + i\sigma_{zx}^{(3)} = -\sum_{n=1}^{+\infty} nD_n(t)z^{-n-1} + \frac{\mu_3 b_z}{2\pi z}, \quad |z| > b \tag{27}$$

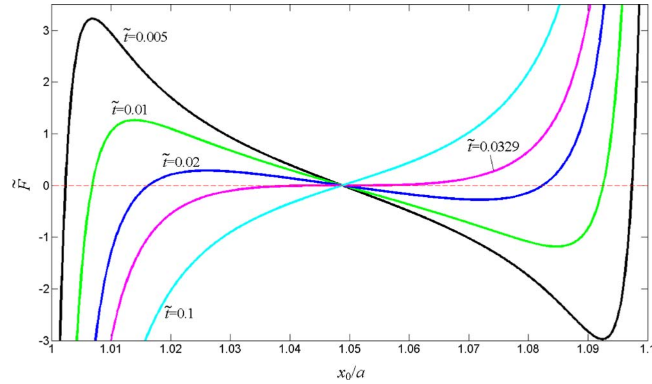

Fig. 2 The normalized time-dependent image force $\tilde{F} = aF_x/\mu_2 b_z^2$ on the screw dislocation at five different times $\tilde{t} = t/t_0 = 0.005,\ 0.01,\ 0.02,\ 0.0329,\ 0.1$ with $t_1=t_2=t_0$, $\Gamma_1=\Gamma_2=\Gamma=1.8$, and $b=1.1a$

It is obvious that the stresses are singular at the location of the screw dislocation $z=x_0$.

3 Time-Dependent Image Force on the Screw Dislocation

By employing the Peach–Koehler formula (see, for example, Refs. [16,17]), the time-dependent image force on the screw dislocation due to its interaction with the two viscous interfaces can be finally obtained as

$$F_x(t) = b_z\sum_{n=1}^{+\infty} n[k_1^{(n)}(\delta_{11}^{(n)}x_0^{n-1} + \delta_{21}^{(n)}b^{2n}x_0^{-n-1})\exp(-\lambda_1^{(n)}t) + k_2^{(n)} \times(\delta_{12}^{(n)}x_0^{n-1} + \delta_{22}^{(n)}b^{2n}x_0^{-n-1})\exp(-\lambda_2^{(n)}t) + x_0^{n-1}\rho_1^{(n)} + b^{2n}x_0^{-n-1}\rho_2^{(n)}] \quad (a < x_0 < b) \tag{28}$$

where F_x is the x component of the image force while $F_y=0$. During calculation the infinite series in Eq. (28) is truncated at a large integer $n=N$ to get sufficiently accurate result.

Apparently it follows from Eq. (28) that

$$F_x(0) = b_z\sum_{n=1}^{+\infty} n[x_0^{n-1}A_n(0) + b^{2n}x_0^{-n-1}C_n(0)] \tag{29}$$

is the image force on the screw dislocation interacting with two perfect interfaces, while

$$F_x(\infty) = b_z\sum_{n=1}^{+\infty} n[x_0^{n-1}\rho_1^{(n)} + b^{2n}x_0^{-n-1}\rho_2^{(n)}] = b_z\sum_{n=1}^{+\infty} n[x_0^{n-1}A_n(\infty) + b^{2n}x_0^{-n-1}C_n(\infty)] \tag{30}$$

is the image force on the screw dislocation interacting with two traction-free surfaces. In addition, it can be strictly proved from Eq. (28) that when the inhomogeneity and the matrix possess the same shear modulus, i.e., $\Gamma_1=\Gamma_2=\Gamma$, and the characteristic times for the two viscous interfaces are exactly the same, i.e., $t_1=t_2=t_0$, then the fixed location $x_0=\sqrt{ab}$ is always an equilibrium position for the dislocation at any time, i.e., $F_x(t)\equiv 0$ when $x_0=\sqrt{ab}$. Apparently when the interphase layer is stiffer than both the inhomogeneity and the matrix, i.e., $\Gamma\leq 1$, the fixed equilibrium position is always an unstable one. On the other hand, when the interphase layer is more compliant than both the inhomogeneity and the matrix, i.e., $\Gamma>1$, the nature of the fixed equilibrium position is dependent on time. In the following calculations, we truncate the series in Eq. (28) at $n=360$ to obtain a result with a relative truncation error less than 0.01%. We illustrate in Fig. 2 the

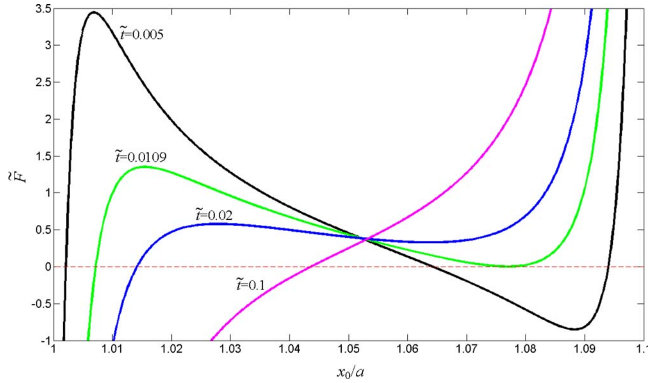

Fig. 3 The normalized time-dependent image force $\tilde{F}=aF_x/\mu_2 b_z^2$ on the screw dislocation at four different times $\tilde{t}=t/t_0=0.005$, 0.0109, 0.02, 0.1 with $t_1=t_2=t_0$, $\Gamma_1=1.8$, $\Gamma_2=1.5$, and $b=1.1a$

normalized image force $\tilde{F}=aF_x/\mu_2 b_z^2$ at five different times $\tilde{t}=t/t_0=0.005$, 0.01, 0.02, 0.0329, 0.1 with $\Gamma=1.8>1$ and $b=1.1a$. It is clearly observed from Fig. 2 that (i) $x_0=\sqrt{ab}=1.0488a$ is always an equilibrium position, and this fixed equilibrium position is a stable one when $\tilde{t}<0.0329$ and it is an unstable one when $\tilde{t}>0.0329$; (ii) two unstable and one stable transient equilibrium positions for the dislocation coexist when $\tilde{t}<0.0329$, while only one fixed equilibrium position exists when $\tilde{t}>0.0329$. Next we consider the more general case in which $\Gamma_1\neq\Gamma_2$ (for simplification we still assume that $t_1=t_2=t_0$). Figure 3 demonstrates the normalized image force $\tilde{F}=aF_x/\mu_2 b_z^2$ at four different times $\tilde{t}=t/t_0=0.005$, 0.0109, 0.02, 0.1 with $\Gamma_1=1.8$, $\Gamma_2=1.5$, and $b=1.1a$. It is observed from Fig. 3 that (i) two unstable and one stable transient equilibrium positions for the dislocation coexist when $\tilde{t}<0.0109$, (ii) a saddle point (neither stable nor unstable) transient equilibrium position at $x_0\approx 1.078a$ and another unstable transient equilibrium position coexist when $\tilde{t}=0.0109$, and (iii) only one single unstable transient equilibrium position exists when $\tilde{t}>0.0109$ and the single unstable transient equilibrium position moves toward $x_0=\sqrt{ab}=1.0488a$ as the time evolves. As a comparison to Fig. 3, Fig. 4 demonstrates the normalized image force $\tilde{F}=aF_x/\mu_2 b_z^2$ at four different times $\tilde{t}=t/t_0=0.005$, 0.0109, 0.02, 0.1 with $\Gamma_1=1.5$, $\Gamma_2=1.8$, and $b=1.1a$. It is observed that Fig. 4 has very similar features as Fig. 3. For instance, when $\tilde{t}=0.0109$ we also observe from Fig. 4 a saddle point transient equilibrium position at $x_0\approx 1.021a$. The above results indicate that the situations for the transient equilibrium positions are rather complex and are dependent on Γ_1 and Γ_2 and the chosen time. We show in Fig. 5 the different situations for the transient equilibrium positions of the dislocation at a certain fixed normalized time $\tilde{t}=t/t_0$ with the assumption that $t_1=t_2=t_0$ and $b=1.1a$. It is observed from Fig. 5 that (i) when $[\Gamma_1,\Gamma_2]$ is just located on the curve for a certain normalized time $\tilde{t}$, a saddle point and another unstable transient equilibrium positions coexist at this normalized time; (ii) when $[\Gamma_1,\Gamma_2]$ is located within the region formed by the curve for a certain fixed normalized time $\tilde{t}$ and the two straight lines $\Gamma_1=2$ and $\Gamma_2=2$, two unstable and one stable transient equilibrium positions for the dislocation coexist at this normalized time; (iii) otherwise, for other combinations of $[\Gamma_1,\Gamma_2]$ only one unstable transient equilibrium position exists at this normalized time; (iv) if $[\Gamma_1,\Gamma_2]$ is on the curve for a certain normalized time $\tilde{t}$, then $[\Gamma_2,\Gamma_1]$ is also on this curve; and (v) it is only possible to find a single unstable transient equilibrium position if $\tilde{t}>\tilde{t}_c=0.03983$. The results in Fig. 5 imply that there exist simultaneously three transient equilibrium positions if the interphase layer is more compliant than both the inhomogeneity and the matrix and the time chosen is fast enough. Figure 5 also indicates that there exists only one unstable transient equilibrium position if the time chosen is above a critical value no matter how stiff the inhomogeneity and the matrix are. Here it is of interest to look into the dependence of $\tilde{t}_c$ on the thickness of the interphase layer in more detail with the assumption that $t_1=t_2=t_0$. We present in Fig. 6 the variation in $\tilde{t}_c$ as a function of the relative thickness $(b-a)/a$ of the interphase layer. It is observed from Fig. 6 that (i) $\tilde{t}_c$ is an increasing function of $(b-a)/a$ and (ii) $\tilde{t}_c$ approaches zero as the interphase layer is infinitely thin (i.e., $b\to a$), and it approaches $\ln 2=0.6931$ as the interphase layer is infinitely thick (i.e., $(b-a)/a\to\infty$). It is of interest to notice that the asymptotic behavior of $\tilde{t}_c\to\ln 2$ as $(b-a)/a\to\infty$ is in agreement with our previous exact result for a single viscous interface [11]. The results in Fig. 6 imply that it is only possible to find a single unstable transient equilibrium position if $\tilde{t}>\ln 2$ no matter how thick the interphase layer is.

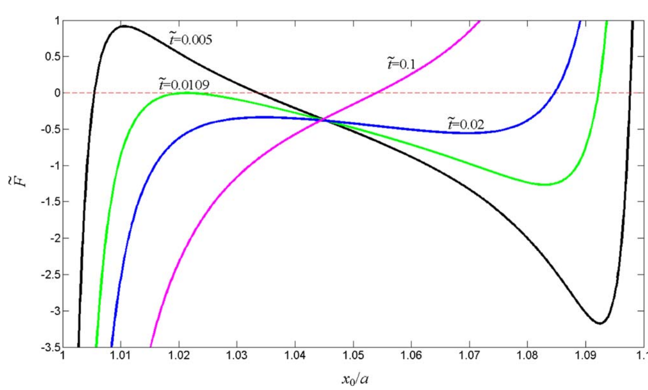

Fig. 4 The normalized time-dependent image force $\tilde{F}=aF_x/\mu_2 b_z^2$ on the screw dislocation at four different times $\tilde{t}=t/t_0=0.005$, 0.0109, 0.02, 0.1 with $t_1=t_2=t_0$, $\Gamma_1=1.5$, $\Gamma_2=1.8$, and $b=1.1a$

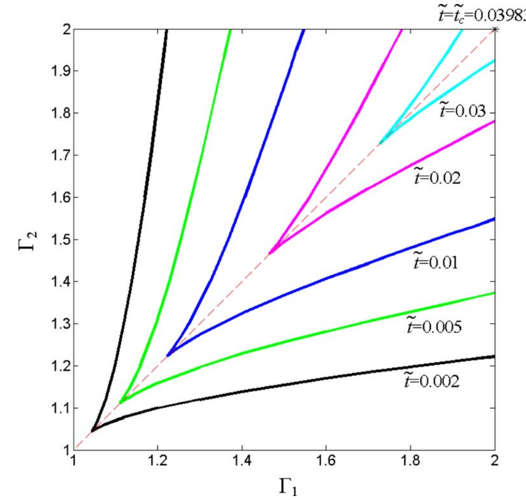

Fig. 5 The different situations for the transient equilibrium positions of the dislocation at a certain fixed normalized time $\tilde{t}=t/t_0$ with $t_1=t_2=t_0$ and $b=1.1a$

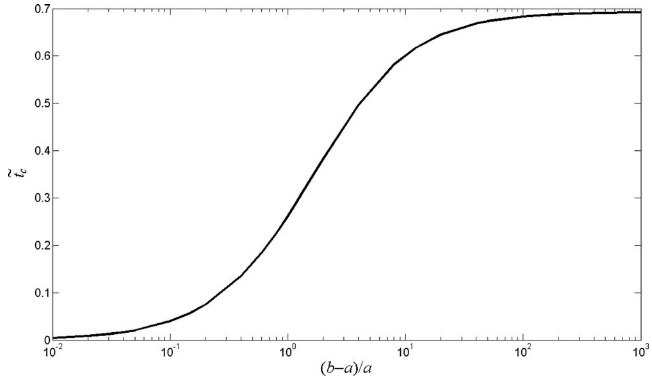

Fig. 6 The variation in $\tilde{t}_c$ as a function of the relative thickness $(b-a)/a$ of the interphase layer with the assumption that $t_1 = t_2 = t_0$

4 Conclusions

We investigated the problem associated with a screw dislocation interacting with two concentric linear viscous interfaces by means of the complex variable method. The time-dependent stress field and image force acting on the dislocation due to its interaction with the two viscous interfaces were derived. Our results demonstrated that three situations are possible for the transient equilibrium positions depending on the relative stiffness among the three material phases and the time chosen: (i) two unstable and one stable transient equilibrium positions coexist, (ii) a saddle point and an unstable transient equilibrium positions coexist, and (iii) only one single unstable transient equilibrium position exists. The image force as a function of these parameters was presented numerically to illustrate these features, along with the criterion diagrams for determining the specific situation for the transient equilibrium positions.

Acknowledgment

This work was partially supported by AFRL and ARL grants. The authors would like to thank the reviewers for their constructive comments.

References

[1] Ru, C. Q., 1999, "Three-Phase Elliptical Inclusions With Internal Uniform Hydrostatic Stresses," J. Mech. Phys. Solids, **47**, pp. 259–273.
[2] Liu, Y. J., Xu, N., and Luo, J. F., 2000, "Modeling of Interphases in Fiber-Reinforced Composites Under Transverse Loading Using the Boundary Element Method," ASME J. Appl. Mech., **67**, pp. 41–49.
[3] Xiao, Z. M., and Chen, B. J., 2000, "A Screw Dislocation Interacting With a Coated Fiber," Mech. Mater., **32**, pp. 485–494.
[4] Raj, R., and Ashby, M. F., 1971, "On Grain Boundary Sliding and Diffusional Creep," Metall. Trans., **2**, pp. 1113–1127.
[5] Ke, T. S., 1999, "Fifty-Year Study of Grain-Boundary Relaxation," Metall. Mater. Trans. A, **30**, pp. 2267–2295.
[6] Ashby, M. F., 1972, "Boundary Defects and Atomistic Aspects of Boundary Sliding and Diffusional Creep," Surf. Sci., **31**, pp. 498–542.
[7] Suo, Z., 1997, "Motion of Microscopic Surface in Materials," Adv. Appl. Mech., **33**, pp. 193–294.
[8] Nagarajan, R., Dutta, I., Funn, J. V., and Esmele, M., 1999, "Role of Interfacial Sliding on the Longitudinal Creep Response of Continuous Fiber Reinforced Metal-Matrix Composite," Mater. Sci. Eng., A, **259**, pp. 237–252.
[9] He, L. H., and Lim, C. W., 2001, "Time-Dependent Interfacial Sliding in Fiber Composites Under Longitudinal Shear," Compos. Sci. Technol., **61**, pp. 579–584.
[10] He, L. H., and Lim, C. W., 2003, "Electromechanical Responses of Piezoelectric Fiber Composites With Sliding Interface Under Anti-Plane Deformations," Composites, Part B, **34**, pp. 373–381.
[11] Wang, X., Pan, E., and Roy, A. K., 2008, "Interaction Between a Screw Dislocation and a Piezoelectric Circular Inclusion With Viscous Interface," J. Mech. Mater. Struct., **3**(4), pp. 761–773.
[12] Wang, X., Pan, E., and Albrecht, J. D., 2008, "Two-Dimensional Green's Functions in Anisotropic Multiferroic Bimaterials With Viscous Interface," J. Mech. Phys. Solids, **56**, pp. 2863–2875.
[13] Lauhon, L. J., Gudiksen, M. S., Wang, D. L., and Lieber, C. M., 2002, "Epitaxial Core-Shell and Core Multishell Nanowire Heterostructures," Nature (London), **420**, pp. 57–61.
[14] Muskhelishvili, N. I., 1953, *Some Basic Problems of the Mathematical Theory of Elasticity*, Noordhoff, Groningen.
[15] Fan, H., and Wang, G. F., 2003, "Interaction Between a Screw Dislocation and Viscoelastic Interfaces," Int. J. Solids Struct., **40**, pp. 763–776.
[16] Ohr, S. M., Chang, S. J., and Thomson, R., 1985, "Elastic Interaction of a Wedge Crack With a Screw Dislocation," J. Appl. Phys., **57**, pp. 1839–1843.
[17] Lee, K. Y., Lee, W. G., and Pak, Y. E., 2000, "Interaction Between a Semi-Infinite Crack and a Screw Dislocation in a Piezoelectric Material," ASME J. Appl. Mech., **67**, pp. 165–170.

Confined Thin Film Delamination in the Presence of Intersurface Forces With Finite Range and Magnitude

Kai-tak Wan
Associate Professor

Scott E. Julien
Graduate Student

Department of Mechanical and Industrial Engineering,
Northeastern University,
Boston, MA 02115

A circular membrane clamped at the periphery is allowed to adhere to or to delaminate from a planar surface of a cylindrical punch in the presence of intersurface forces with finite range and magnitude. Assuming a uniform disjoining pressure within the cohesive zone at the delamination front, the adhesion-delamination mechanics is obtained by a thermodynamic energy balance. Interrelations between the instantaneous applied load, punch displacement, and contact circle, and the resulting critical thresholds of "pinch-off," "pull-off," and "pull-in" are derived from the first principles. Two limiting cases are obtained: (i) intersurface force with long range and small magnitude in reminiscence of the classical Derjaguin–Muller–Toporov (DMT) model and (ii) short range and large magnitude alluding to the Johnson–Kendall–Roberts (JKR) model. The DMT-JKR transitional behavior has significant impacts on adhesion measurements, microelectromechanical systems, and life-sciences. [DOI: 10.1115/1.3112745]

Keywords: thin film adhesion, delamination, surface force, disjoining pressure, cohesive zone

1 Introduction

In the presence of intersurface interactions, such as electrostatics and van der Waals, a solid surface might compel or repel a freestanding membrane depending on the sign, magnitude, and range of the intersurface forces. Once the adherends are in contact, an external force is necessary to separate them and to retain mechanical equilibrium throughout. A thorough understanding of the coupled action of surface forces and applied load associated with deformation of the elastic bodies is thus the key to characterize a membrane-substrate interface. The mechanical behavior and adhesion-delamination mechanics of thin membranes has significant impacts on many branches of life-sciences, microelectromechanical systems (MEMSs) and nanotechnology. For instance, (i) two or more apposing biological cells adhere to form multicell aggregates and ultimately tissues [1–3], (ii) nanostructures of trusses and membranes collapse in the presence of high humidity and strong surface forces [4,5], (iii) micro- and nanoelectromechanical systems (MEMS/NEMS) involving electrostatic driven bridges and diaphragms fail in the presence of strong stiction [6,7], and (iv) diminished adhesion of the protective encapsulating membranes limits the reliability and life span of electronic packages [8].

Adhesion between two solid spheres or asperities has been under intensive investigations in the last few decades ever since the now-celebrated Johnson–Kendall–Roberts (JKR) and Derjaguin–Muller–Toporov (DMT) models were formulated in the 1970s [9–11]. The two ostensibly contradictory models represent the two extreme limits of a universal adhesion model. While JKR is applicable to surface forces with a large magnitude and virtually zero range, DMT is valid for small magnitude and long range. The idea of cohesive zone with intermediate surface force magnitude and range was first developed conceptually by Dugdale, furnished by the mathematically rigorous model by Barenblatt, and shown to fit the JKR-DMT transition by Maugis [12]. The equivalence of fracture in brittle materials was demonstrated by a number of elegant papers [13–15]. Voluminous experimental verifications of the models can be found in the literature. It is important to note that these celebrated theories in solid-solid adhesion are not quite applicable to thin membranes.

We have lately introduced a "punch" test to investigate thin film adhesion. Figure 1(*a*) shows a film clamped by two identical rings forming a freestanding diaphragm. A flat-ended cylindrical punch with a diameter fitting to the rings is brought to adhesive contact with the membrane. When a tensile force is applied to the punch in a displacement-controlled manner, a circular delamination is driven radially inward into the punch-film interface until pull-off occurs when the film spontaneously detaches from the substrate. The method is especially useful in probing local adhesion, since the delamination is confined to the diaphragm dimension. We have earlier derived the adhesion-delamination mechanics for the JKR-limit, including mixed membrane deformation mode of plate-bending and membrane-stretching [16], coupled tensile/compressive residual stresses and interfacial adhesion [17], and progressively increasing residual membrane stress [18]. Experimental results in a variety of membranes of different materials and thicknesses are shown to be consistent with the model [5,19].

In this paper, we investigate the situation for surface forces with intermediate and fixed magnitude and range, and demonstrate how the universal model approaches the limits of JKR and DMT. The quasistatic delamination mechanics is chosen to be based on a thermodynamic energy minimization, though other methods, such as balance of stress intensity factors, are available in the literature [20].

2 Theory

Figures 1(*b*) and 1(*b*) show the schematic of an isotropic membrane clamped at the periphery and in adhesion contact with the planar surface of a cylindrical punch. All dimensional and dimensionless variables are listed and defined in Table 1. In essence, all horizontal dimensions are scaled by the membrane radius, and vertical dimensions by the membrane thickness. As the punch

Contributed by the Applied Mechanics Division of ASME for publication in the Journal of Applied Mechanics. Manuscript received July 1, 2008; final manuscript received February 2, 2009; published online June 18, 2009. Review conducted by Matthew R. Begley.

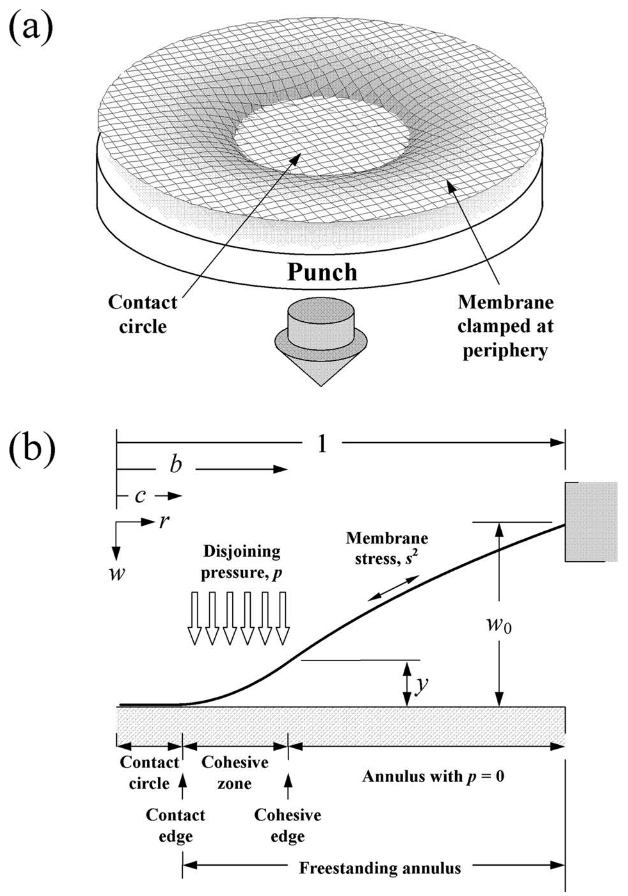

Fig. 1 (*a*) Schematic of a clamped membrane adhered to planar punch surface. (*b*) Drawing in normalized coordinates and variables.

moves away from the plane of the nondeformed membrane, the resulting tensile stress causes the membrane to delaminate from the substrate and the contact circle shrinks. The long-range surface force acting across the membrane-substrate gap gives rise to a cohesive zone at the delamination front. The cohesive edge divides the freestanding annulus into an inner region, where the disjoining pressure acts ($c < r \leq b$ and $0 < (w_0 - w) \leq y$), and an outer region, where the intersurface force is beyond reach ($b < r \leq 1$ and $y < (w_0 - w) \leq w_0$). A few assumptions are taken as follows: (i) the thin membrane has negligible flexural rigidity and thus only membrane-stretching prevails, (ii) an average strain with equal radial and tangential stresses, $\sigma_r = \sigma_t$, is assumed, (iii) the deformed annulus subtends a small angle to the nondeformed plane ($\theta \approx 0$), and (iv) residual stress is ignored.

2.1 The Attractive Surface Force Law. The Lennard-Jones potential is the most common intersurface force law adopted in the adhesion literature. To solve for the membrane profile, however, requires a mathematically involved self-consistent method or an appropriate Green's function. Figure 2(*a*) shows the classical force law, which in this paper is replaced by a uniform attractive disjoining pressure with a finite range [21]. The approximation is expressed as a Heaviside step function, similar to the classical work by Dugdale–Barenblatt–Maugis [12,22]

$$\Phi(w) = p \quad \text{within the cohesive zone,} \quad 0 < (w_0 - w) \leq y$$

$$= 0 \quad \text{without the cohesive zone,} \quad y < (w_0 - w) \leq w_0 \qquad (1)$$

The area under the curve is known as the adhesion energy, i.e., $\gamma = py$, which is a constant for a specific interface under consideration. Without loss of generality, $\gamma = 1$ hereafter. The JKR-limit ($p \to \infty$ and $y \to 0$) is shown against the DMT-limit ($p \to 0$ and $y \to \infty$), whereas the product of p and y remains identical in both cases. Equation (1) describes the surface interactions as function of intersurface separation, though it can also be translated to the horizontal membrane-punch interface as shown in Fig. 2(*b*). Within the contact circle ($r < c$), the membrane is stress free. Immediately behind the delamination front is the cohesive zone ($c < r \leq b$). The external load, $F = p(b^2 - c^2)$, maintains mechanical

Table 1 Normalized coordinates and variables

	Physical parameters (bold)	Normalized parameters
Geometrical parameters	$\boldsymbol{r}$=radial distance (m) $\boldsymbol{w}$=deformation profile (m) $\boldsymbol{w_0}$=vertical displacement of punch (m) $\boldsymbol{a}$=radius of sample membrane (m) $\boldsymbol{c}$=radius of contact circle (m) $\boldsymbol{b}$=radius of cohesive edge (m) $\boldsymbol{h}$=membrane thickness (m)	$r = \frac{\boldsymbol{r}}{\boldsymbol{a}}$, $w = \frac{\boldsymbol{w}}{\boldsymbol{h}}, \quad w_0 = \frac{\boldsymbol{w_0}}{\boldsymbol{h}}$ $c = \frac{\boldsymbol{c}}{\boldsymbol{a}}, \quad b = \frac{\boldsymbol{b}}{\boldsymbol{a}}$
Material parameters	$\boldsymbol{\nu}$=Poisson's ratio $\boldsymbol{E}$=elastic modulus (N m^{-2}) $\boldsymbol{\sigma}$=tensile membrane stress (N m^{-2}) $\boldsymbol{\gamma}$=interfacial adhesion energy (J m^{-2}) $\boldsymbol{p}$=disjoining pressure (N m^{-2}) $\boldsymbol{y}$=surface force range (m)	$s = \boldsymbol{\sigma}^{1/2}\left[\frac{12(1-\boldsymbol{\nu})\boldsymbol{a}^2}{\boldsymbol{E}\boldsymbol{h}^2}\right]^{1/2}$, $\gamma = \boldsymbol{\gamma}\left[\frac{6(1-\boldsymbol{\nu})\boldsymbol{a}^4}{\boldsymbol{E}\boldsymbol{h}^5}\right]$, $p = \boldsymbol{p}\left[\frac{6(1-\boldsymbol{\nu})\boldsymbol{a}^4}{\boldsymbol{E}\boldsymbol{h}^4}\right]$, $y = \frac{\boldsymbol{y}}{\boldsymbol{h}}$
Mechanical loading	$\boldsymbol{F}$=applied external force (N) $\boldsymbol{U}$=energy terms (J)	$F = \boldsymbol{F}\left[\frac{6(1-\boldsymbol{\nu})\boldsymbol{a}^2}{\pi\boldsymbol{E}\boldsymbol{h}^4}\right]$ $U = \boldsymbol{U}\left[\frac{6(1-\boldsymbol{\nu})\boldsymbol{a}^2}{\pi\boldsymbol{E}\boldsymbol{h}^5}\right]$

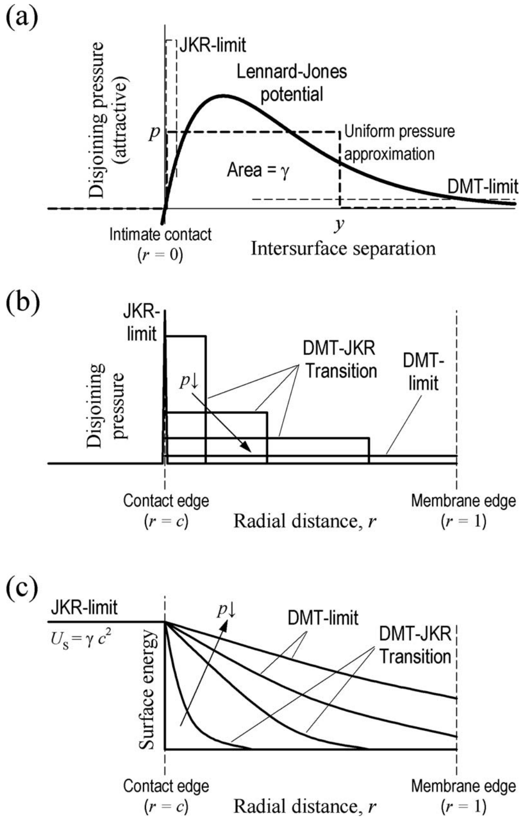

Fig. 2 (*a*) Lennard-Jones potential and the uniform disjoining pressure approximation as function of intersurface separation (w_0-w). (*b*) Disjoining pressure distribution and (*c*) surface energy density as function of radial distance in the membrane-punch interface for a range of decreasing disjoining pressure.

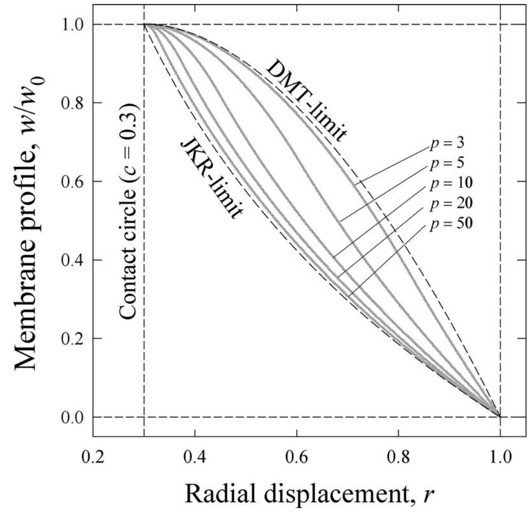

Fig. 3 Membrane profile for fixed contact radius $c=0.3$ and a range of disjoining pressure. The delamination front is shaped as a cusp in all the curves and in the DMT-limit, besides the JKR-limit.

equilibrium. Beyond the cohesive edge ($b<r\leq 1$) the outer annulus is under the influence of membrane stress only. Classical linear elastic fracture mechanics in the JKR context requires the vanishingly small cohesive zone to maintain its dimension and to translate with the delamination front upon loading [23]. In this paper, the cohesive zone is allowed to vary its width along the membrane-substrate interface. The DMT-limit is loosely defined here to be the situation when the entire freestanding annulus is under the influence of the disjoining pressure. The cohesive edge extends to the membrane periphery, and the cohesive zone is underdeveloped (see Sec. 2.5).

A schematic of the corresponding surface energy density is shown in Fig. 2(*c*). The JKR-limit is shown as a step function dropping to zero at the contact edge. As the force range increases, the energy drops to zero gradually over a finite range. The cohesive zone is "fully developed." In the DMT-limit, the cohesive zone extends to the membrane edge ($r=1$), the corresponding energy does not drop to zero, as shown, and the cohesive zone is underdeveloped.

2.2 Elastic Equation Governing the Membrane Profile.

The external load applied to the punch is balanced by the disjoining pressure that acts on the membrane. The elastic equation can be written as

$$-\boldsymbol{\sigma h}\cdot\nabla^2\boldsymbol{w}=\boldsymbol{p}\Rightarrow -s^2 r\frac{\partial w}{\partial r}=p(r^2-c^2)\quad\text{for }\ c<r\leq b$$

$$-\boldsymbol{\sigma h}\cdot\nabla^2\boldsymbol{w}=\boldsymbol{F}\cdot\delta(\boldsymbol{r})\Rightarrow -s^2 r\frac{\partial w}{\partial r}=p(b^2-c^2)\quad\text{for }\ b<r\leq 1 \tag{2}$$

where ∇^2 is the Laplacian operator in cylindrical coordinates and $\delta(\boldsymbol{r})$ is a delta function denoting the applied load. The ostensible singularity at $r=0$ never occurs since the contact circle never approaches zero, as will be shown later. Equation (2) can be solved exactly

$$w=\begin{cases}\dfrac{p}{2s^2}\left[(b^2-r^2)+b^2\log\left(\dfrac{1}{b^2}\right)-c^2\log\left(\dfrac{1}{r^2}\right)\right] & \text{for }\ c<r\leq b\\[2ex] \dfrac{F}{2s^2}\log\left(\dfrac{1}{r^2}\right) & \text{for }\ b<r\leq 1\end{cases} \tag{3}$$

Figure 3 shows a typical normalized membrane profile, $w(r)$, for $c=0.3$ and a range of p. The cohesive edge at $r=b$ is continuous and differentiable in all cases, and the cohesive zone always possesses a "cusp" geometry at the delamination front, $(\partial w/\partial r)_{r=c}=0$. Beyond the cohesive zone, the membrane profile is governed by the classical $\log(1/r^2)$ term typical of membranes. The punch displacement is given by

$$w_0=w(r=c)=\frac{p}{2s^2}\left[(b^2-c^2)+b^2\log\left(\frac{1}{b^2}\right)-c^2\log\left(\frac{1}{c^2}\right)\right] \tag{4}$$

It is easy to show that the surface force range is

$$y=w_0-w(r=b)=\frac{p}{2s^2}\left[(b^2-c^2)+c^2\log\left(\frac{c^2}{b^2}\right)\right] \tag{5}$$

2.3 Thermodynamic Energy Balance.

There are two possible ways to drive delamination. The load-controlled configuration requires the punch to be loaded by a fixed force ($F=\text{constant}$), while the displacement-controlled configuration requires a fixed punch displacement ($w_0=\text{constant}$). The two modes are equivalent in deriving the thermodynamic energy balance and thus the delamination trajectory. We choose the latter. Total energy of the membrane-substrate system is given by $U_T=U_E-U_S$, with U_E as the elastic energy stored in the membrane and U_S as the surface energy to create new surfaces. For delamination to occur, $(\partial U_T/\partial c)_{w_0=\text{constant}}=0$.

The elastic energy can be found as follows. Since the mechanical response of a thin flexible membrane is always cubic with $F\propto w_0{}^3$, $U_E=\int F\cdot dw_0=\frac{1}{4}F\cdot w_0$. Alternatively, U_E can be expressed in terms of the membrane stress, U_E=energy density×area, where the energy density is $s^4/24$. The membrane stress is a complicated function of radial distance from the membrane center. To circumvent the involved mathematics, we assume an average membrane strain, $\varepsilon=(1/2)(\partial w/\partial r)^2$, as in our previous work [16]. There are two equivalent alternatives to proceed. The first is to average elastic strain over the entire overhanging annulus, and the second is to take two separate average strains within and without the cohesive edge. We choose the latter

$$s^2=\begin{cases}\dfrac{6}{b^2-c^2}\displaystyle\int_c^b \frac{1}{2}\left(\frac{\partial w}{\partial r}\right)^2 2rdr & \text{for } c<r\le b\\ \dfrac{6}{1-b^2}\displaystyle\int_b^1 \frac{1}{2}\left(\frac{\partial w}{\partial r}\right)^2 2rdr & \text{for } b<r\le 1\end{cases} \tag{6a}$$

Substituting w in Eq. (3) into Eq. (6a)

$$s=\begin{cases}\left\{\dfrac{3p^2}{2(b^2-c^2)}\left[3c^4-4b^2c^2+b^4+2c^4\log\left(\dfrac{b^2}{c^2}\right)\right]\right\}^{1/6} & \text{for } c<r\le b\\ \left[\dfrac{3p^2(b^2-c^2)^2}{1-b^2}\log\left(\dfrac{1}{b^2}\right)\right]^{1/6} & \text{for } b<r\le 1\end{cases} \tag{6b}$$

The corresponding elastic energy is therefore given by

$$U_E=\underbrace{\frac{s^4}{24}(b^2-c^2)}_{\text{for } c<r\le b}+\underbrace{\frac{s^4}{24}(1-b^2)}_{\text{for } b<r\le 1} \tag{7}$$

Substituting s in Eq. (6b) into Eq. (7)

$$U_E=\frac{3[3c^4-4b^2c^2+b^4+2c^4\log(b^2/c^2)]^2}{2(b^2-c^2)[b^2-c^2-c^2\log(b^2/c^2)]^4}y^4+\frac{6}{(1-c^2)\log(1/b^2)\log(1/b^2)}(y-w_0)^4 \tag{8}$$

Derivation of the surface energy is quite different from the classical fracture mechanics approach because of the presence of long-range surface forces. Here U_S comprises three parts: (i) within the contact circle ($r\le c$), where $U_S=\gamma c^2$ is a maximum, (ii) within the cohesive zone ($c<r\le b$), where U_S decreases to zero at the cohesive edge, and (iii) beyond the cohesive edge ($b<r\le 1$) where $U_S=0$. Mathematically,

$$U_S=\underbrace{\gamma c^2}_{\text{contact circle}}+\underbrace{\int_c^b p[y-(w_0-w)]2rdr}_{\text{cohesive zone}}=\gamma c^2+\left\{\gamma(b^2-c^2)-\left[c^2+\frac{(b^2-c^2)(b^2-c^2-2c^2\log(1/c^2))}{2(b^2-c^2+b^2\log(1/b^2)-c^2\log(1/c^2))}\right]pw_0\right\} \tag{9}$$

A distinct characteristic here is that U_S is a function of w_0 (c.f. Fig. 2(c)). The total energy of the system and thus the delamination trajectory can now be determined by Eqs. (8) and (9). The DMT and JKR limits will be analyzed next, followed by the DMT-JKR transition.

2.4 The JKR-Limit. The JKR-limit requires a zero force range and infinite magnitude, i.e., the disjoining pressure is a delta function around the contact edge, $\Phi(w)=p\cdot\delta(r-c)$. The cohesive zone width is zero ($b=c$). The membrane profile (c.f. Eq. (3)) requires a sharp angle at the contact edge with $(\partial w/\partial r)_{r=c^-}=0$ and $(\partial w/\partial r)_{r=c^+}=-F/s^2c$, which is no longer differentiable. The cusp geometry is lost (Fig. 3). The upper and lower limits of the first integral in Eq. (6a) merge, and the membrane stress is reduced to the second integral only. The governing equations are summarized as follows:

$$w=\frac{F}{2s^2}\log\left(\frac{1}{r^2}\right) \tag{10}$$

$$w_0=\frac{F}{2s^2}\log\left(\frac{1}{c^2}\right) \tag{11}$$

$$s=\left[\frac{3F^2}{1-c^2}\log\left(\frac{1}{c^2}\right)\right]^{1/6} \tag{12}$$

$$U_E=\frac{6}{(1-c^2)\log(1/c^2)\log(1/c^2)}w_0^4 \tag{13}$$

$$U_S=\gamma c^2 \tag{14}$$

The constitutive relation without delamination is found by eliminating s from Eqs. (11) and (12)

$$F=\frac{24}{(1-c^2)[\log(1/c^2)]^2}{w_0}^3 \tag{15}$$

The energy balance yields

$$w_0=\left\{\frac{c^2(1-c^2)^2[\log(1/c^2)]^3}{6[2-2c^2+c^2\log(1/c^2)]}\right\}^{1/4}\gamma^{1/4} \tag{16}$$

consistent with our earlier derivation [16]. Figure 4 shows the mechanical response, $F(w_0)$. In a load-controlled measurement, delamination does not occur until F reaches a maximum at S with $F_{\max}=2.74636$. An incremental increase in F then leads to spontaneous separation of membrane from substrate and the membrane snaps. Since the instantaneous contact radius is nonzero with $c=1$; the phenomenon is known as pull-off in the literature. Alternatively, in a displacement-controlled measurement, delamination begins at S and continues along the path SRQP with a stable monotonic decreasing contact radius. At P ($F^*=0.413994$, $w_0^*=0.562441$, and $c^*=0.194545$), $(\partial F/\partial w_0)\to\infty$. Incremental increase beyond w_0^* leads to a displacement-controlled pull-off, denoted by an asterisk hereafter. The branch OP is physically inaccessible. The nonzero pull-off radius is in reminiscence of the classical JKR solid-solid adhesion theory [9].

2.5 The DMT-Limit. In the DMT-limit, the entire freestanding annulus is under the influence of the surface force ($b=1$). The underdeveloped cohesive zone only becomes full-fledged when $c=0$ and $w_0=y$. The cusp delamination front is preserved (Fig. 3). The upper and lower limits of the second integral in Eq. (6a) merge, and the membrane stress is reduced to the first integral only. In summary

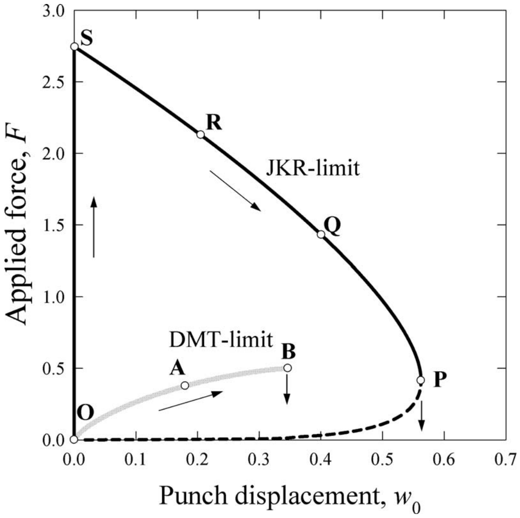

Fig. 4 The JKR-limit follows path OSRQP with contact radii, $c_O=c_S=1.00$, $c_R=0.7792$, $c_Q=0.5395$, and $c_P=c^*=0.1945$. Load-controlled pull-off occurs at S, and displacement-controlled pull-off at P. The branch OP (dashed) is physically inaccessible. The DMT-limit follows path OAB with $c_A=0.49649$ and $c_B=0$.

$$w=\frac{p}{2s^2}\left[1-r^2-c^2\log\left(\frac{1}{r^2}\right)\right] \tag{17}$$

$$w_0=\frac{p}{2s^2}\left[1-c^2-c^2\log\left(\frac{1}{c^2}\right)\right] \tag{18}$$

$$s=\left\{\frac{3p^2}{2(1-c^2)}\left[3c^4-4c^2+1+2c^4\log\left(\frac{1}{c^2}\right)\right]\right\}^{1/6} \tag{19}$$

$$U_E=\frac{3[3c^4-4c^2+1+2c^4\log(1/c^2)]^2}{2(1-c^2)[1-c^2-c^2\log(1/c^2)]^4}{w_0}^4 \tag{20}$$

$$U_S=\gamma c^2+\left\{\gamma(1-c^2)-\left[1-\frac{(1-c^2)^2}{2(1-c^2-c^2\log(1/c^2))}\right]pw_0\right\} \tag{21}$$

For a fixed w_0, $(\partial U_T/\partial c)=0$ can be solved exactly to yield analytical expressions for $w_0(c)$, $F(c)$, and thus $F(w_0)$ using MATHEMATICA, though the lengthy expressions are not given here. Figure 4 shows $F(w_0)$ for $p=0.5$. At $F=0$, $w_0=0$ and the membrane is in full contact with the punch. As delamination proceeds along path OAB, F monotonically increases while the contact circle shrinks. At B, the contact is reduced to a central point with $c=0$. Further increase in w_0 causes the membrane to pinch-off (contrasting the pull-off with $c>0$). Either load-controlled or displacement-controlled measurement leads to identical stable delamination. Regardless of the surface force range, the initial loading ($w_0=0$) always begins with the DMT-limit.

The pinch-off loci can be obtained by putting $c\to 0$ into Eqs. (18)–(21), yielding $w_0^*=(p/12)^{1/3}$, $s^*=(3p^2/2)^{1/6}$, $U_E^*=(3/2)\times(w_0^*)^4$, and $U_S^*=\gamma-(pw_0^*/2)$, respectively. It can be easily shown that $F^*=12(w_0^*)^3$. The condition $w_0^*\le y$ implies that the punch displacement does not reach the surface force range when the membrane completely separates from the punch. The special case of $w_0=y$ requires $b=1$ and $p=12y^3$. But since $\gamma=py$, so the elimination of y yields $p=p^\dagger=12^{1/4}=1.86121$. This is the maximum disjoining pressure where the DMT-limit alone is sufficient to describe the entire delamination process.

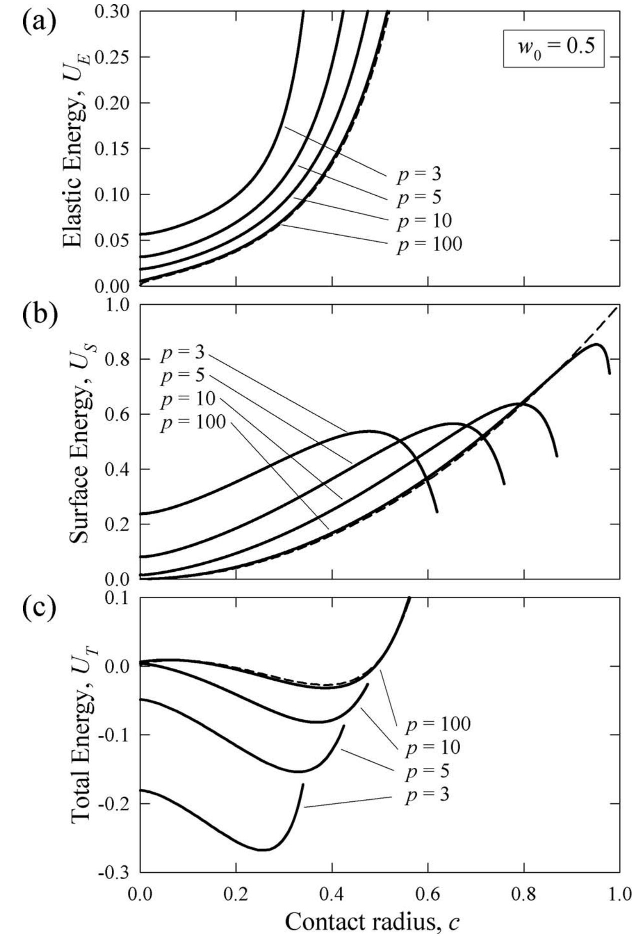

Fig. 5 Energy as a function of contact radius for punch displacement $w_0=0.5$ and a range of disjoining pressure: (*a*) elastic energy stored in the membrane, (*b*) surface energy, and (*c*) total energy of the membrane-punch system.

From Fig. 4, it is remarkable that the JKR- and DMT-limits are distinctly different from each other, even though the same adhesion energy γ is assumed. The JKR-DMT transition relating the two limits is therefore of much interest.

2.6 The DMT-JKR Transition. To determine the delamination behavior for a surface force with finite range and finite magnitude, a computational routine is coded using MATHEMATICA. The first step is to determine the cohesive edge by numerically solving Eq. (5). Next, U_E, U_S, and U_T are obtained as functions of c for fixed w_0. Figures 5(*a*)–5(*c*) show the positively defined energy terms for $w_0=0.5$ and a range of p. At large p (>100), all energy terms approach the JKR-limit (dashed curves). In Fig. 5(*b*), U_S can only be obtained for c below a certain limit because the cohesive edge is bounded by $c\le b\le 1$. In Fig. 5(*c*), the local minimum of U_T represents the stable equilibrium value of c. The computation is repeated for a range of w_0 with fixed p, and the resulting U_T is shown in Figs. 6(*a*)–6(*c*). Delamination proceeds from right ($c=1$) to left and terminates at either $c=0$ or $c=c^*$. In Fig. 6(*a*), $p=0.5$ and DMT-limit applies. As the punch moves from $w_0=0$ to 0.1, the minimum shifts to the left, indicating a reduced contact radius. The process continues until pinch-off occurs at w_0^*. The delamination trajectory is shown as a dashed line joining the minimum of each curve. In Fig. 6(*b*), $p=5$ and DMT-JKR transition is expected at $w_0=0.2$. DMT-limit is valid for $w_0=0$ to 0.2, but fails thereafter because the cohesive zone is fully developed and the punch displacement exceeds the force range. The DMT-JKR transition prevails. Pinch-off eventually occurs at

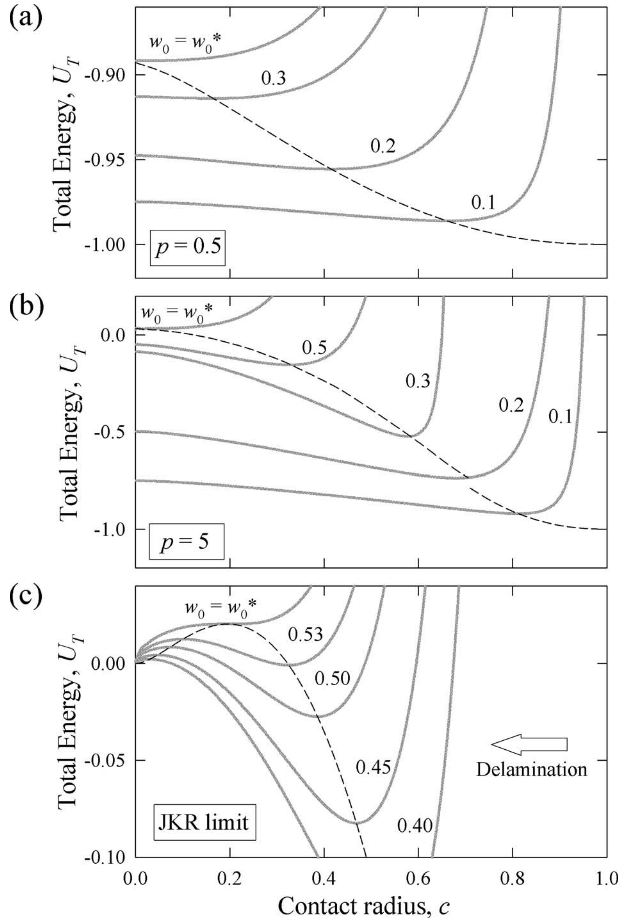

Fig. 6 Total energy of the membrane-punch system for disjoining pressure (*a*) p=0.5, (*b*) p=5, and (*c*) $p \rightarrow \infty$ (JKR-limit). Dashed curves joining the minima of individual curves indicate mechanical equilibrium and delamination process.

w_0^*. The small break of the dashed curve at w_0=0.2 is the result of the mismatch of the *average* membrane stresses at the cohesive edge and round-up errors in computing b, but it is ignored here. Figure 6(c) shows the delamination process at a much larger p that approaches the JKR-limit. All U_T curves show a local minimum at a larger value of c (stable equilibrium) and a maximum at a smaller value (unstable equilibrium). As w_0 increases, the two extrema approach each other. At $w_0 = w_0^*$, the two extrema merge into an inflexion with $(\partial^2 U_T / \partial c^2) = 0$ (neutral equilibrium). Further punch movement leads to pull-off. The equilibrium dashed curve shows a maximum that corresponds to the inflexion of $U_T(w_0^*)$. Portion of the dashed curve joining the maxima is physically inaccessible (c.f. path OP in Fig. 4). For $p > 7$, an inflexion point always exists in U_T and c^* is always nonzero.

The last step is to generate the mechanical response, $F(w_0)$, for a range of p (Fig. 7). For $p \le p^\dagger$, the DMT-limit is expected. All such curves (p=0.5 and p=1) terminate at the locus along OAB with $F^* = 12(w_0^*)^3$. For $p > p^\dagger$, the DMT-JKR transition occurs at $w_0 = y$. For instance, for p=5, DMT is valid until $w_0 = \gamma / p = 0.20$ at J. In a load-controlled measurement, pull-off occurs at J. In a displacement-controlled configuration, further increase in w_0 reduces both external load and contact circle along JC. The energy balance allows one to obtain the last loading point at C, where c=0 and the membrane pinches off the substrate. Pinch-off occurs along OABCD. For p exceeds approximately 7, pull-off with a nonzero radius is expected, and the locus is shown as curve DH. At p=100, the loading curve resembles the JKR-limit (c.f. Fig. 4)

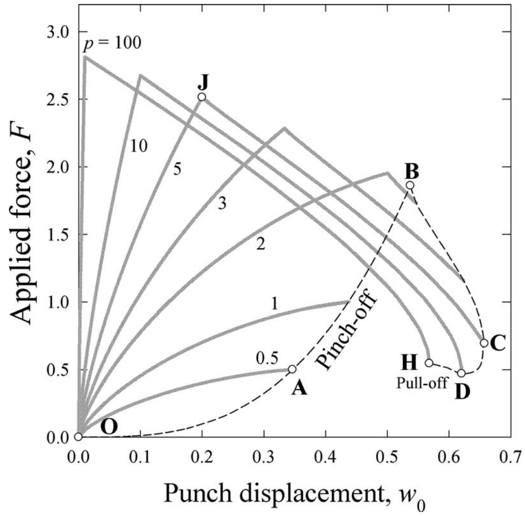

Fig. 7 Mechanical response for a range of disjoining pressure. The dashed curve OABCD corresponds to pinch-off with zero contact radius, and curve DH is pull-off with nonzero contact radius.

with a sharp increase in F in the initial loading, and pull-off occurs at H. Alternative expressions linking the measurable quantities, $F(c)$ and $w_0(c)$, are shown in Figs. 8 and 9, respectively. In Fig. 8, delamination proceeds from bottom right (c=1 and F=0) to the left (c=0 or $c = c^*$). Load-controlled pull-off occurs at the maximum load F_{max}, followed by the subsequent displacement-controlled delamination. The curves terminate either at c=0 or $c = c^*$. In Fig. 9, the dashed line labeled "DMT-JKR" denotes the transition and the load-controlled pull-off load F_{max}. At displacement-controlled pull-off, $(\partial w_0 / \partial c) = 0$. Figure 10 shows the pull-off radius as a function of disjoining pressure. As p increases, c^* approaches the JKR-limit of 0.194545.

Figure 11 shows the varying cohesive edge as a function of contact radius. For $p \le p^\dagger$, DMT-limit is valid and the cohesive edge extends to the membrane periphery (b=1). Delamination proceeds from the right top corner (b=1) to left top corner (c=0 and b=1). For $p^\dagger < p < 7$, the trajectory deviates from the DMT-limit at F_{max} and continues to decrease until pinch-off. For $p > 7$, the curves terminate at the pull-off locus. Behavior of very large p

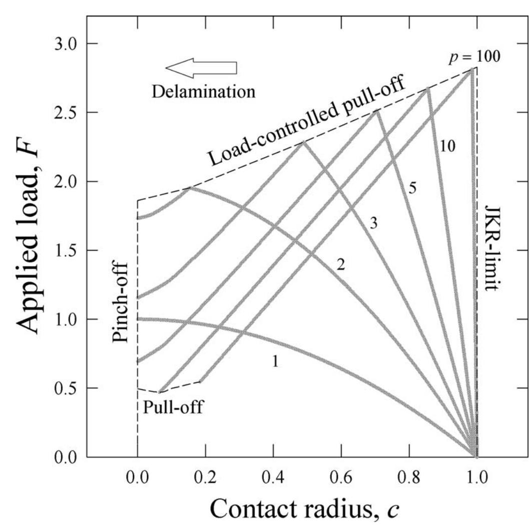

Fig. 8 Mechanical response for a range of disjoining pressures

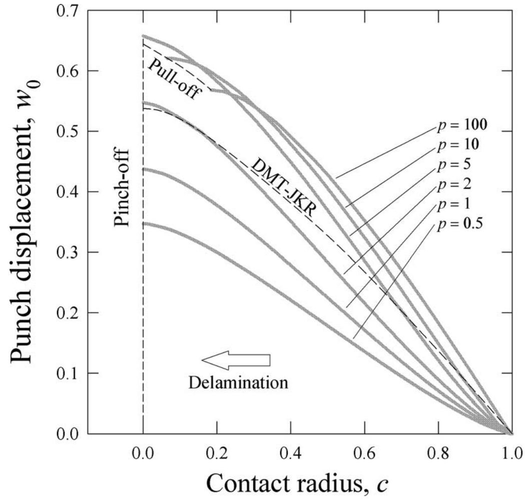

Fig. 9 Mechanical response for a range of disjoining pressures. The dashed curve DMT-JKR indicates the transitional behavior.

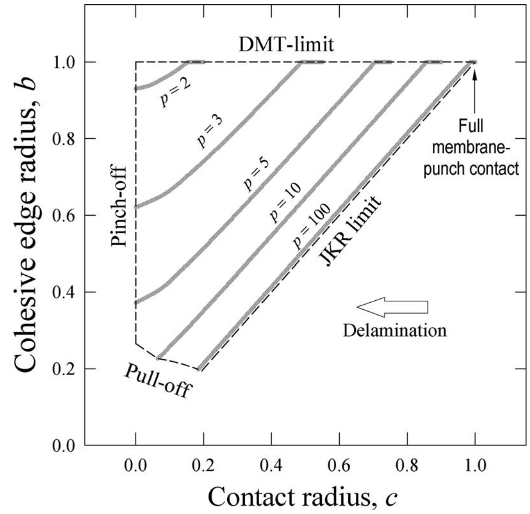

Fig. 11 Cohesive edge as a function of contact radius for a range of disjoining pressures. Delamination proceeds from right to left. All curves initiate at $c=1$ and $b=1$ until deviation occurs at critical contact radii.

approaches the JKR-limit of $b=c$. Figure 12 shows the cohesive zone width (b-c) as a function of contact radius. In the DMT-limit, delamination proceeds from the right bottom corner ($b=c=1$) to the left top corner ($b=1$ and $c=0$) to maintain $b=1$. Deviation from the DMT-limit occurs once the disjoining pressure exceeds $p^{\dagger}$. The JKR-limit requires the cohesive zone width to be always zero. Note that the cohesive zone width is roughly constant in the initial loading, while deviation aggravates when the contact circle contracts to a central point at the membrane-substrate interface. At large p (>100), the cohesive zone is constant and virtually zero throughout the delamination process, consistent with the classical linear elastic fracture mechanics.

3 Discussion

The new model is useful in extracting materials parameters from adhesion measurements. The punch can be treated as a probe similar to the standard nano-indenter or atomic force microscope (AFM) tip moving toward a clamped membrane. The punch displacement, w_0, is treated as the probe position from the nondeformed sample surface. The experiment is expected to yield the results shown in Figs. 13(a)–13(c). In Fig. 13(a), $p=1.25$ and $y=\gamma/p=0.8$, the probe does not sense the existence of the membrane until the probe moves into the force range, $w_0=y=0.8$, at A. The membrane deforms into a spherical cap at B, but there is no intimate probe-membrane contact until C. The applied load remains constant along BC. At C, the membrane makes a one point contact with the probe. Further probe motion expands the contact circle along the reversible curve CO. Unloading retraces the path OCBA. No hysteresis is expected for the loading-unloading process. Figure 13(b) shows the limiting case of $p=p^{\dagger}$. When the probe falls within the surface force range at B, pull-in occurs and the membrane jumps into a single point contact with the probe at C. Figure 13(c) shows a more fascinating situation when $p=5(>p^{\dagger})$ and DMT-JKR transition is expected. Since $y=0.2$, the probe only senses the surface force when it reaches B. At B, pull-in occurs with a nonzero contact radius reaching C, and the probe senses a sharp attractive force. If the probe now recedes, the contact circle shrinks following a different path CD until pull-off occurs at D and then returns to A. The area ABCD thus represents

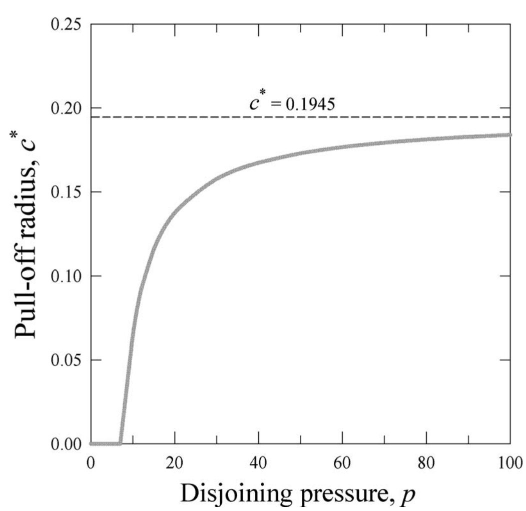

Fig. 10 Pull-off radius as a function of disjoining pressure. The critical radius approaches the JKR-limit at large p.

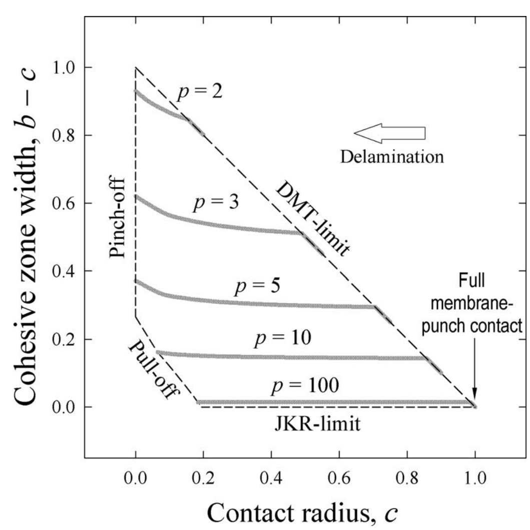

Fig. 12 Cohesive zone width as a function of contact radius for a range of disjoining pressure. Delamination proceeds from right to left. All curves initiate at $c=1$ and $b-c=0$ until deviation occurs at critical contact radii.

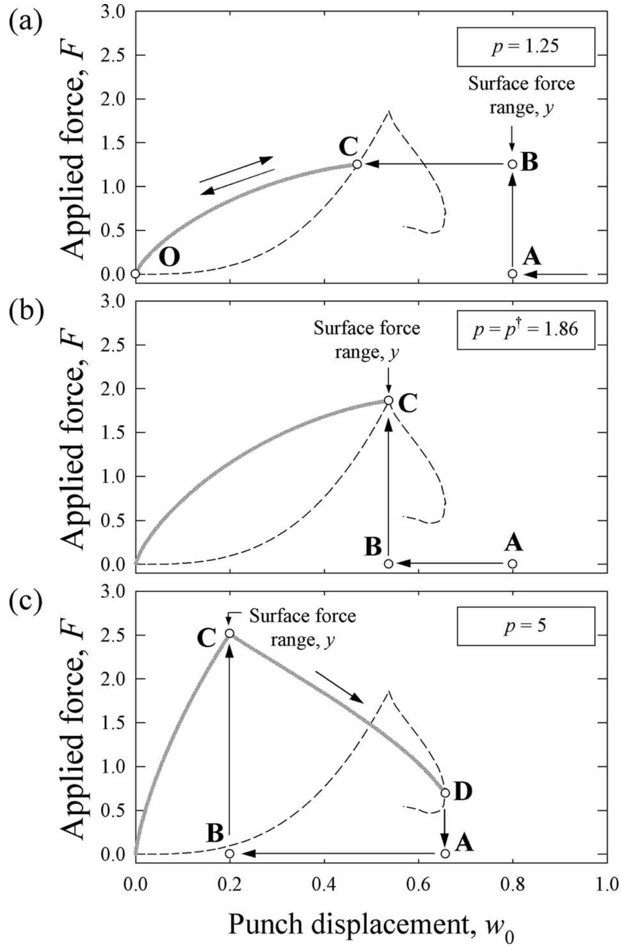

Fig. 13 Mechanical force measured by a punch probe as it moves toward a clamped membrane. The dashed curve is a reference to the pinch-off-pull-off locus. (*a*) For *p*=1.25 and range *y*=0.8, probe senses the membrane at A. Loading-unloading follows ABCO-OCBA. No hysteresis is expected. (*b*) For *p*=1.86 and *y*=0.5373, loading-unloading follows ABC-CBA. No hysteresis is expected. (*c*) For *p*=5 and *y*=0.2, loading-unloading follows ABC-CDA. Hysteresis is expected.

a loading-unloading hysteresis loop. Another possible scenario is that since the total energy at D is lower than that at A, a small instability or vibration of the measuring device might cause pull-in at AD, then the loading-unloading follows ADC-CDA and the hysteresis is lost. The abrupt increase in attractive forces on the probe in Figs. 13(*a*)–13(*c*) is the artifact of the Heaviside function of disjoining pressure (c.f. Fig. 1). In reality, the Lennard-Jones-like potential leads to a more gradual change.

A significant implication of the above analysis is the necessity to measure instantaneous contact dimension in addition to the conventional mechanical response $F(w_0)$. Most published AFM data reported in the literature are by and large force measurement, and the adhesion energy is deduced using the classical JKR model of solid adhesion, such as $F^* = (3/2)\pi R\gamma$ with R the sphere radius. The fact that most biomimetic microcapsules or biological cells are not solid spheres but membrane encapsulated vesicles implies that new membrane-substrate model similar to the present work is needed. Moreover, force measurement alone is not sufficient to determine the interfacial adhesion because the mechanical response depends predominantly on (i) the magnitude and range of the surface forces and (ii) whether measurement is done in load-controlled or displacement-controlled mode. The missing information in most reported experiments is the instantaneous contact radius along with the applied load and probe displacement.

The new model has significant impacts on the design of a number of MEMS with moveable membranes [24]. A micropump comprises a diaphragm directly controlled by an external potential applied to an electrostatic pad underneath. At a threshold voltage, pull-in occurs and the membrane comes into intimate contact with the pad. Our previous model used the cohesive zone approximation similar to the present one to derive the critical pull-in voltage. The current model addresses the contact problem when the applied voltage is removed and the diaphragm is expected to return to its nondeformed plane. In the presence of surface forces, energy is dissipated as a result of the hysteresis loop depicted in Fig. 13(*c*). The device operation is obstructed accordingly, and the resonance frequency is deliberately shifted. In the worst situation, should the surface force be sufficiently large and the diaphragm-pad gap is narrow down to the order of the surface force range, a full elastic recovery is not possible and the diaphragm remains in contact with the pad even at the removal of applied voltage. The device thus fails. Our model provides indispensable design guidelines to MEMS especially when the dimensions shrink from microscale to nanoscale.

The model is also applicable to cell adhesion and tissue engineering. Adhesion at local spots on a tissue sample or even a single cell can be measured provided a fixed circular boundary can be defined. A map of propensity to adhesion can be experimentally determined for a small sample. The present 2D planar problem can also be extended to 3D cell adhesion. In the presence of long-range surface forces, biomimetic microcapsules or cells adhere or repel depending on attractive/repulsive nature of the disjoining pressure. We have earlier shown how a spherical thin-walled vesicle adheres to and detaches from a planar substrate via a zero-range disjoining pressure [25], though most intersurface interactions are long-range in nature. It is beyond the scope of this paper to discuss the 3D deformation here, but some generalization is possible. For instances, (a) the membrane radius in our model is of the same order of magnitude as radius of a cell, and (b) the ratio of cell radius to surface force range is a gauge to determine whether the disjoining pressure is effectively long- or short-ranged. Cell detachment from a substrate or an apposing cell either by an internal osmotic pressure or mechanical force essentially follow the processes depicted in Fig. 13.

As a last remark, it is worth mentioning that the "constrained blister test," developed by Chang et al. [26] and extensively studied by Plaut at al. [27] in terms of long-range surface forces, is similar to the present setup despite a number of major differences. A membrane clamped at the periphery is deformed by a uniform hydrostatic pressure, rather than a mechanical force on the punch, before the bulging membrane is brought into contact with the punch surface. Moreover, the separation between the plane of the nondeformed membrane and the flat substrate is *fixed*, rather than being a controlled variable, so that the blister membrane does not undergo an unstable growth at a critical hydrostatic pressure.

4 Conclusion

The adhesion-delamination mechanics of a thin membrane clamped at the periphery is obtained. The model provides the interrelationship between the measureable quantities of applied load, punch displacement, and contact radius, and how the experimental data can be analyzed to yield the materials parameters, such as adhesion energy, range and magnitude of the disjoining pressure, and elastic modulus. Critical thresholds of pinch-off, pull-off, and pull-in in both force-controlled and displacement-controlled configurations, which can be empirically measured, are also identified. The model is consistent with the now-celebrated models of JKR and DMT solid adhesion.

Acknowledgment

This work is supported by the National Science Foundation CMMI Nos. 0757140 and 0757138. We are grateful to Mr. Guangxu Li for discussions and proofreading the manuscript.

References

[1] Wan, K.-T., 2007, "Solid-Mechanics of Soft Biological Tissues," Key Eng. Mater., **334–335**, pp. 633–636.

[2] Lim, J. Y., Shaughnessy, M. C., Zhou, Z., Noh, H., Vogler, E. A., and Donahue, H. J., 2008, "Surface Energy Effects on Osteoblast Spatial Growth and Mineralization," Biomaterials, **29**, pp. 1776–1784.

[3] Huang, W., Bahman, A., Torres, A., LeBaron, R. G., and Athanasiou, K. A., 2003, "Temporal Effects of Cell Adhesion on Mechanical Characteristics of the Single Chondrocyte," J. Orthop. Res., **21**, pp. 88–95.

[4] Wong, M.-F., Duan, G., and Wan, K.-T., 2007, "Adhesion-Delamination Mechanics of a Pre-Stressed Rectangular Film Adhered Onto a Rigid Substrate," J. Appl. Phys., **101**(2), pp. 024903.

[5] Raegen, A. N., Dalnoki-Veress, K., Wan, K.-T., and Jones, R. A. L., 2006, "Measurement of Adhesion Energies and Young's Modulus in Thin Polymer Films Using a Novel Axi-Symmetric Peel Test Geometry," Eur. Phys. J. E, **19**, pp. 453–459.

[6] Maboudian, R., Ashurst, W. R., and Carraro, C., 2002, "Tribological Challenges in Micromechanical Systems," Tribol. Lett., **12**, pp. 95–100.

[7] Maboudian, R., and Howe, R. T., 1997, "Critical Review: Adhesion in Surface Micromechanical Structures," J. Vac. Sci. Technol. B, **15**, pp. 1–20.

[8] Lau, J. H., Wong, C. P., Prince, J. L., and Nakayama, W., 1998, *Electronic Packaging: Design, Materials, Process, and Reliability*, McGraw-Hill, New York.

[9] Johnson, K. L., Kendall, K., and Roberts, A. D., 1971, "Surface Energy and the Contact of Elastic Solids," Proc. R. Soc. London, Ser. A, **324**, pp. 301–313.

[10] Derjaguin, B. V., Muller, V. M., and Toporov, Y. P., 1975, "Effect of Contact Deformations on the Adhesion of Particles," J. Colloid Interface Sci., **53**(2), pp. 314–326.

[11] Maugis, D., 2000, *Contact, Adhesion and Rupture of Elastic Solids*, Springer, New York.

[12] Maugis, D., 1992, "The JKR-DMT Transition Using a Dugdale Model," J. Colloid Interface Sci., **150**, pp. 243–269.

[13] Chan, D. Y. C., Hughes, B. D., and White, L. R., 1987, "A Physically Consistent Theory of Fracture in a Brittle Solid," J. Colloid Interface Sci., **115**(1), pp. 240–259.

[14] Klein, P. A., Foulk, J. W., Chen, E. P., Wimmer, S. A., and Gao, H. J., 2001, "Physics-Based Modeling of Brittle Fracture: Cohesive Formulations and the Application of Meshfree Methods," Theor. Appl. Fract. Mech., **37**, pp. 99–166.

[15] Williams, J. G., and Hadavinia, H., 2002, "Analytical Solutions for Cohesive Zone Models," J. Mech. Phys. Solids, **50**, pp. 809–825.

[16] Wan, K.-T., 2002, "Adherence of an Axisymmetric Flat Punch Onto a Clamped Circular Plate—Transition From a Rigid Plate to a Flexible Membrane," ASME J. Appl. Mech., **69**, pp. 110–116.

[17] Wong, M.-F., Duan, G., and Wan, K.-T., 2007, "Adhesion-Delamination Mechanics of a Pre-Stressed Circular Film Adhered Onto a Rigid Substrate," J. Adhes., **83**, pp. 67–83.

[18] Wan, K.-T., and Kogut, L., 2005, "The Coupling Effect of Interfacial Adhesion and Tensile Residual Stress on a Thin Membrane Adhered to a Flat Punch," J. Micromech. Microeng., **15**, pp. 778–784.

[19] Ju, B.-F., Liu, K.-K., Wong, M.-f., and Wan, K.-T., 2007, "A Novel Punch Method to Characterize Interfacial Adhesion and Residual Stress of a Thin Polymer Film," Eng. Fract. Mech., **74**, pp. 1101–1106.

[20] Barthel, E., and Perriot, A., 2007, "Adhesive Contact to a Coated Elastic Substrate," J. Phys. D: Appl. Phys., **40**, pp. 1059–1067.

[21] Derjaguin, B. V., 1989, *Theory of Stability of Colloids and Thin Films*, Consultants Bureau, New York.

[22] Wan, K.-T., and Lawn, B. R., 1992, "Effect of Chemical Interaction on Barenblatt Crack Profiles in Brittle Solids," Acta Metall. Mater., **40**(2), pp. 3331–3337.

[23] Lawn, B. R., 1993, *Fracture of Brittle Solids* (Cambridge Solid State Science Series), E. A. Davis and I. M. Ward, eds., Cambridge University Press, Cambridge, UK.

[24] Duan, G., and Wan, K.-T., 2007, "Analysis of 1-D and 2-D Thin Film "Pull-In" Phenomena Under the Influence of an Electrostatic Potential," ASME J. Appl. Mech., **74**, pp. 927–934.

[25] Liu, K. K., Wang, H. G., Wan, K.-T., Liu, T., and Zhang, Z., 2002, "Characterizing Capsule-Substrate Adhesion in Presence of Osmosis," Colloids Surf., B, **25**(4), pp. 293–298.

[26] Chang, Y. S., Lai, Y. H., and Dillard, D. A., 1989, "The Constrained Blister—A Nearly Constant Strain Energy Release Rate Test for Adhesives," J. Adhes., **27**, pp. 197–211.

[27] Plaut, R. H., White, S. A., and Dillard, D. A., 2003, "Effect of Work of Adhesion on Contact of a Pressurized Blister With a Flat Surface," Int. J. Adhes. Adhes., **23**, pp. 207–214.

Ananth Kumar
Department of Aerospace Engineering,
Indian Institute of Technology Madras,
Chennai 600036, India
e-mail: ae05b004@iitm.ac.in

Ranjan Ganguli[1]
Associate Professor
Mem. ASME
Department of Aerospace Engineering,
Indian Institute of Science,
Bangalore 560012, India
e-mail: ganguli@aero.iisc.ernet.in

Rotating Beams and Nonrotating Beams With Shared Eigenpair

In this paper, we look for rotating beams whose eigenpair (frequency and mode-shape) is the same as that of uniform nonrotating beams for a particular mode. It is found that, for any given mode, there exist flexural stiffness functions (FSFs) for which the jth mode eigenpair of a rotating beam, with uniform mass distribution, is identical to that of a corresponding nonrotating uniform beam with the same length and mass distribution. By putting the derived FSF in the finite element analysis of a rotating cantilever beam, the frequencies and mode-shapes of a nonrotating cantilever beam are obtained. For the first mode, a physically feasible equivalent rotating beam exists, but for higher modes, the flexural stiffness has internal singularities. Strategies for addressing the singularities in the FSF for finite element analysis are provided. The proposed functions can be used as test-functions for rotating beam codes and for targeted destiffening of rotating beams.
[DOI: 10.1115/1.3112741]

1 Introduction

Rotating beams serve as useful mathematical models of helicopter rotor blades, wind turbine blades, propeller blades, gas turbine blades, and other important mechanical structures. Such beams can suffer from vibration problems if their rotating natural frequencies coincide with multiples of the rotation speed. Therefore, the accurate determination of natural frequencies and mode-shapes of a rotating beam is an important problem [1]. The dynamics of a rotating beam is governed by a fourth-order partial-differential equation, which cannot be solved exactly for natural frequencies and mode-shapes, even for a uniform rotating beam [2]. Therefore, the frequencies of a rotating beam are usually predicted by approximate methods like the Rayleigh–Ritz method [3,4], Galerkin method [5,6], etc., or by the finite element method (FEM) [7–14].

However, in the absence of an exact solution to the governing equation, the approximate methods are checked by comparing with other numerical methods or with series solutions obtained using the Frobenius method of solving differential equations [15]. The series solution approach is also called a semi-analytical approach and is the closest we can get to the exact solution of the rotating beam equation. Another semi-analytical approach is the dynamic stiffness method [16,17]. The dynamic stiffness method uses frequency dependent shape functions obtained from the solution of the governing equations of the structure. One advantage of the dynamic stiffness method is that one element can give all the natural frequencies and mode-shapes to any desired level of accuracy [18]. Banerjee et al. [18] recommended the dynamic stiffness method for checking the results of finite element analysis of rotating beams.

The finite element method, in its various forms, has emerged as a popular approach to the vibration analysis of rotating beams. While most early works on finite element analysis of rotating beams concentrated on the h-version, recent works advocate the use of a single element using p-version, Fourier-p, dynamic finite element, and spectral approaches [12,13,19]. In the h-version FEM, the number of elements is increased until convergence is achieved. Typically, the stiffness and mass distribution are assumed to be uniform within the element. Therefore, a large number of elements are needed for nonuniform beams. In other approaches based on a single element, the order of the basis functions is increased for convergence. Practical structures have highly nonuniform variations in mass and stiffness properties. Use of a single element allows easy inclusion of the nonuniformity as functions $EI(x)$ and $m(x)$ for flexural stiffness and mass per unit length, respectively. Also, the model order using spectral and Fourier-p FEM approaches is typically less than that with h-version, which is useful for control applications [7].

As new single element methods for rotating beam analysis are created, it would be useful if they could be validated without requiring a different analysis. Similarly, the h-version codes need to be validated. The main problem lies in the absence of an exact solution for vibration analysis of rotating beams. However, a uniform nonrotating beam has exact solutions to its frequencies and mode-shapes, obtained by solving a transcendental equation [20]. In this paper, we seek to find out an equivalent rotating beam with the same frequency and mode-shape of a uniform nonrotating beam for a particular mode. Such beams, if they exist, would be of interest from a fundamental science perspective and also yield test-functions, which could be used to check approximate methods for rotating beams and for the design of such beams to match the frequencies and mode-shapes of nonrotating beams.

2 Formulation

Consider a beam rotating about the vertical axis with uniform angular velocity Ω and with dimensions, as shown in Fig. 1. The governing equation for the out-of-plane vibrations of the rotating beam is given by [1]

$$(EI_1(x)w'')'' + m(x)\ddot{w} - (T(x)w')' = 0 \tag{1}$$

where $T(x)=\int_x^L m(x)\Omega^2(R+x)dx+F$, $EI_1(x)$ is the flexural stiffness, $m(x)$ is the mass per unit length of the beam, $w(x,t)$ is the out-of-plane bending displacement, R is the hub radius, L is the beam length, and F is the axial force applied at the free end of the beam.

Now, consider a nonrotating beam of the same length, L, mass per unit length, $m(x)$, and boundary conditions as the rotating beam in Eq. (1). This beam is governed by the equation [20]

$$(EI_2(x)w'')'' + m(x)\ddot{w} = 0 \tag{2}$$

where $EI_2(x)$ is the flexural stiffness of this beam.

Let the jth mode-shape and the frequency of these beams be the same and equal to ϕ_j and ω_j, respectively. The bending displacement w_j for the jth mode is given by

[1]Corresponding author.

Contributed by the Applied Mechanics Division of ASME for publication in the Journal of Applied Mechanics. Manuscript received July 11, 2008; final manuscript received February 5, 2009; published online June 18, 2009. Review conducted by Sanjay Govindjee.

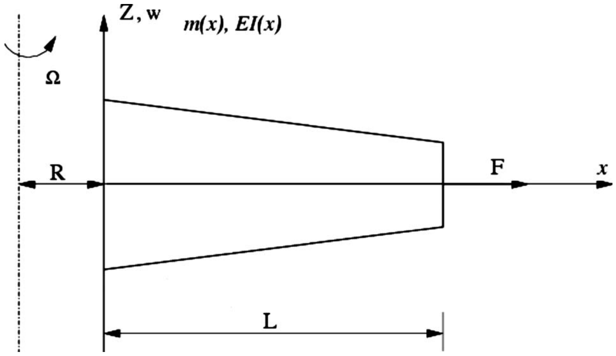

Fig. 1 Schematic of a rotating beam

$$w_j = \phi_j e^{i\omega_j t} \tag{3}$$

Obviously, the mode-shape ϕ_j must satisfy the governing differential equation. Substituting Eq. (3) into Eqs. (1) and (2), we obtain

$$(EI_1(x)\phi_j'')'' - m(x)\omega_j^2\phi_j - (T(x)\phi_j')' = 0 \tag{4}$$

$$(EI_2(x)\phi_j'')'' - m(x)\omega_j^2\phi_j = 0 \tag{5}$$

Subtracting Eq. (5) from Eq. (4) yields

$$(EI_1(x)\phi_j'')'' - (EI_2(x)\phi_j'')'' - (T(x)\phi_j')' = 0 \tag{6}$$

Equation (6) gives the relation between the flexural stiffness of a rotating beam and that of a nonrotating beam with the same eigenpair. Note that the expression ϕ_j is different for different modes, and thus different expressions for $EI_1(x)$ are obtained for different modes. Explicitly, $EI_1(x)$ in terms of $EI_2(x)$ is

$$EI_1(x) = \frac{\int \left(\int ((EI_2(x)\phi_j'')'' + (T(x)\phi_j')')dx \right) dx}{\phi_j''} \tag{7}$$

If we consider a nonrotating beam of uniform flexural stiffness, then $m(x)=m$, $EI_2(x)=EI_2$, and Eq. (7) becomes

$$EI_1(x) = \frac{\int \left(\int (EI_2\phi_j^{(4)} + (T(x)\phi_j')')dx \right) dx}{\phi_j''} \tag{8}$$

The mode-shapes of a uniform cantilever beam can be solved exactly and are given by the beam function [21]

$$\phi_j(x) = C_j(\cos(\alpha_j x) - \cosh(\alpha_j x)) + C_j\left(\frac{\sin(\alpha_j L) - \sinh(\alpha_j L)}{\cos(\alpha_j L) + \cosh(\alpha_j L)}(\sin(\alpha_j x) - \sinh(\alpha_j x)) \right) \tag{9}$$

where $\alpha_j's$ are solutions to the characteristic equation $\cos(\alpha_j L)\cosh(\alpha_j L)=-1$ and $C_j's$ are arbitrary constants. The frequencies ω_j are given by [20]

$$\omega_j = (\alpha_j L)^2\sqrt{\frac{EI_2}{mL^4}} \tag{10}$$

where $(\alpha_1 L)^2=3.5160$, $(\alpha_2 L)^2=22.0345$, $(\alpha_3 L)^2=61.6972$, and $(\alpha_4 L)^2=120.902$ are the exact values up to four decimal places for the first four modes.

3 Flexural Stiffness Functions

We seek to find flexural stiffness variations $EI_1(x)$ for each mode such that the frequency and mode-shape for the corresponding mode of the rotating beam are the same as that of a nonrotating beam. Equations (9) and (10) can be substituted in Eq. (8) to obtain the corresponding $EI_1(x)$ of a rotating beam. We consider a nonrotating beam with uniform properties and dimensions, as shown in Table 1 [22]. The first four natural frequencies of this beam, up to four decimal places, are 142.4015 rad/s, 892.4150 rad/s, 2498.7879 rad/s, and 4896.6271 rad/s, respectively. The corresponding nondimensional frequencies ($\mu=\sqrt{m\omega^2L^4/EI}$) are 3.5160, 22.0345, 61.6972, and 120.902, respectively. The functions $EI_1(x)$ obtained from Eq. (8) are given in Eq. (11) for the first four mode-shapes. Here $(EI_1)_i$ corresponds to the ith mode.

Table 1 Properties of uniform nonrotating beam

Property	Value
Length (L)	0.6 m
Elasticity modulus (E)	2×10^{11} Pa
Moment of inertia (I)	2×10^{-9} m^4
Mass density (ρ)	7840 kg/m^3
Cross-section area (A)	2.4×10^{-6} m^2
Linear mass density (m)	1.8816 kg/m

$$(EI_1)_i = \frac{N_i}{D_i} \tag{11}$$

where

$$\begin{aligned} N_1 = {} & \left(\frac{-3.5160EI_2}{L^2} + 0.78441m\Omega^2L^2 \right)\cos(z_1) \\ & - \frac{3.5160EI_2}{L^2}\cosh(z_1) + \frac{2.5811EI_2}{L^2}\sinh(z_1) \\ & + \left(\frac{2.5811EI_2}{L^2} - 0.57583m\Omega^2L^2 \right)\sin(z_1) \\ & + 0.53330m\Omega^2Lx\sin(z_1) + 0.3915m\Omega^2Lx\cos(z_1) \\ & - 0.02866m\Omega^2L^2e^{z_1} + 0.36705m\Omega^2x^2\sin(z_1) \\ & - 0.5m\Omega^2x^2\cos(z_1) - 0.18692m\Omega^2L^2e^{-z_1} \\ & - 0.07094m\Omega^2Lxe^{z_1} + 0.46240m\Omega^2Lxe^{-z_1} \\ & + 0.06647m\Omega^2x^2e^{z_1} + 0.43352m\Omega^2x^2e^{-z_1} + c_1x + c_2 \end{aligned} \tag{12}$$

$$\begin{aligned} D_1 = {} & \frac{-3.5160}{L^2}\cos(z_1) + \frac{-3.5160}{L^2}\cosh(z_1) + \frac{2.5811}{L^2}\sin(z_1) \\ & + \frac{2.5811}{L^2}\sinh(z_1) \end{aligned} \tag{13}$$

$$\begin{aligned} N_2 = {} & \left(\frac{-22.034EI_2}{L^2} + 0.54538m\Omega^2L^2 \right)\cos(z_2) \\ & - \frac{-22.034EI_2}{L^2}\cosh(z_2) + \frac{22.441EI_2}{L^2}\sinh(z_2) \\ & + \left(\frac{22.441EI_2}{L^2} - 0.55546m\Omega^2L^2 \right)\sin(z_2) \\ & + 0.21303m\Omega^2Lx\sin(z_2) + 0.21697m\Omega^2Lx\cos(z_2) \\ & + 0.00420m\Omega^2L^2e^{z_2} + 0.50923m\Omega^2x^2\sin(z_2) \\ & - 0.5m\Omega^2x^2\cos(z_2) - 0.45881m\Omega^2L^2e^{-z_2} \\ & + 0.00197m\Omega^2Lxe^{z_2} + 0.21500m\Omega^2Lxe^{-z_2} \\ & + 0.00462m\Omega^2x^2e^{z_2} + 0.50462m\Omega^2x^2e^{-z_2} + c_1x + c_2 \end{aligned} \tag{14}$$

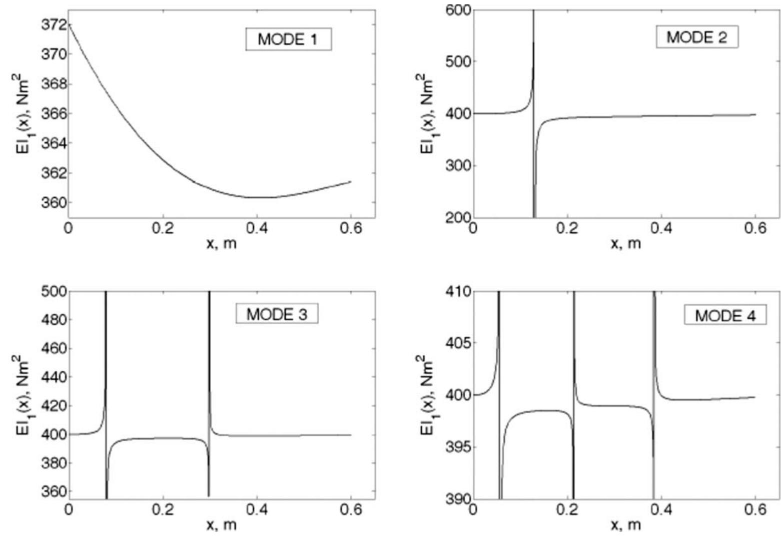

Fig. 2 ***EI*₁(*x*) variation for first four modes for a beam with properties given in Table 1**

$$D_2 = \frac{-22.034}{L^2}\cos(z_2) + \frac{-22.034}{L^2}\cosh(z_2) + \frac{22.441}{L^2}\sin(z_2) + \frac{22.441}{L^2}\sinh(z_2) \quad (15)$$

$$N_3 = \left(\frac{-61.697EI_2}{L^2} + 0.51621m\Omega^2L^2\right)\cos(z_3) - \frac{61.697EI_2}{L^2}\cosh(z_3) + \frac{61.649EI_2}{L^2}\sinh(z_3) + \left(\frac{61.649EI_2}{L^2} - 0.51581m\Omega^2L^2\right)\sin(z_3) + 0.12731m\Omega^2Lx\sin(z_3) + 0.12721m\Omega^2Lx\cos(z_3) - 0.00018m\Omega^2L^2e^{z_3} + 0.49961m\Omega^2x^2\sin(z_3) - 0.5m\Omega^2x^2\cos(z_3) - 0.48360m\Omega^2L^2e^{-z_3} - 0.49365 \times 10^{-4}m\Omega^2Lxe^{z_3} + 0.12726m\Omega^2Lxe^{-z_3} + 0.49981m\Omega^2x^2e^{-z_3} + 0.19388\times 10^{-3}m\Omega^2x^2e^{z_3} + c_1x + c_2 \quad (16)$$

$$D_3 = \frac{-61.697}{L^2}\cos(z_3) + \frac{-61.697}{L^2}\cosh(z_3) + \frac{61.649}{L^2}\sin(z_3) + \frac{61.649}{L^2}\sinh(z_3) \quad (17)$$

$$N_4 = \left(\frac{-120.90EI_2}{L^2} + 0.50827m\Omega^2L^2\right)\cos(z_4) - \frac{120.90EI_2}{L^2}\cosh(z_4) + \frac{120.91EI_2}{L^2}\sinh(z_4) + \left(\frac{120.91EI_2}{L^2} - 0.50829m\Omega^2L^2\right)\sin(z_4) + 0.09095m\Omega^2Lx\sin(z_4) + 0.09095m\Omega^2Lx\cos(z_4) - 0.49174m\Omega^2L^2e^{z_4} + 0.50001m\Omega^2x^2\sin(z_4) - 0.5m\Omega^2x^2\cos(z_4) - 0.49174m\Omega^2L^2e^{-z_4} - 0.15258 \times 10^{-5}m\Omega^2Lxe^{z_4} + 0.09095m\Omega^2Lxe^{-z_4} + 0.50002m\Omega^2x^2e^{-z_4} + 0.83883\times 10^{-5}m\Omega^2x^2e^{z_4} + c_1x + c_2 \quad (18)$$

$$D_4 = \frac{-120.90}{L^2}\cos(z_4) + \frac{-120.90}{L^2}\cosh(z_4) + \frac{120.91}{L^2}\sin(z_4) + \frac{120.91}{L^2}\sinh(z_4) \quad (19)$$

Here $z_1=1.875x/L$, $z_2=4.694x/L$, $z_3=7.855x/L$, $z_4=10.996x/L$, and c_1 and c_2 are arbitrary constants resulting from integration. We see that these functions contain trigonometric, hyperbolic, polynomial, and exponential functions. It can be observed that as $\Omega \to 0$, $EI_1 \to EI_2$.

The variation in $EI_1(x)$ versus x with constants c_1 and c_2 equal to 0 is shown in Fig. 2 for a beam with properties listed in Table 1 and $\Omega=360$ rpm ($R=F=0$) for the first four modes. The corresponding nonrotating beam has a uniform flexural stiffness, $EI_2=400$ N m^2. Note that the $EI_1(x)$ variation for the jth mode has $j-1$ internal singularities. The singularities are explained as follows. If the nodal coordinates of the jth mode of a uniform nonrotating beam are $x_1, x_2, \ldots, x_{j-1}$, then the second derivative of the corresponding mode-shape, ϕ_j'', vanishes at $x=L-x_1$, $L-x_2, \ldots, L-x_{j-1}$. The proof is given in Appendix A. Also, at $x=L$, the second derivative must vanish because of the boundary condition $M=EIw''=0$ at the free end of the beam. Since Eqs. (7) and (8) have ϕ_j'' in the denominator, the singularities occur at each of these points. The tip singularities are not shown in Fig. 2. We show later in this paper that the tip singularities can be ignored for numerical results.

4 Numerical Simulations: p-Version FEM

The derived variation $EI_1(x)$ in a rotating beam should give the same frequencies and mode-shapes as that of a nonrotating beam. For a uniform nonrotating beam, these frequencies and mode-shapes can be solved exactly to any desired level of accuracy. If the functions $EI_1(x)$ obtained above are inserted into a rotating beam finite element code, then we should obtain the frequencies and mode-shapes of a nonrotating beam [23]. This can be used to test the exactness of the solutions obtained from the rotating beam code.

For the FEM modeling, we use the p-version formulation, where only one element is used for the entire beam [1]. As mentioned in the Introduction, such approaches are popular in rotating beam analysis for handling nonuniformity and obtaining reduced order. The displacement w is expanded in terms of an n degree polynomial function as

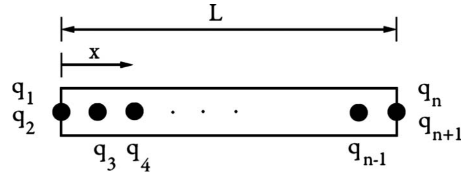

Fig. 3 Beam element used for p-version FEM

$$w=\sum_{i=0}^{n} p_i x^i \tag{20}$$

Let the vector of generalized coordinates be $\mathbf{P}=\{p_i\}$. A set of $n-3$ nodes $\{\alpha_1,\alpha_2,\ldots,\alpha_{n-3}\}$ is identified in the interior of the beam at equidistant points as in Fig. 3. Define variables q_i as $q_1=w(0)$, $q_2=w'(0)$, $q_3=w(\alpha_1)$, $q_4=w(\alpha_2),\ldots$, $q_{n-1}=w(\alpha_{n-3})$, $q_n=w(L)$, and $q_{n+1}=w'(L)$.

Let $\mathbf{Q}=\{q_i\}$. Substituting Eq. (20) in these gives a relation between the $\mathbf{P}$ and $\mathbf{Q}$. The interpolation functions ψ_i are derived for the $(n-1)$-node element by satisfying the conditions $Q_j=\delta_{ij}$, where δ is the Kronecker delta function, and obtaining the corresponding constants, p_{ij}. The interpolation polynomials are then given by

$$\psi_i=\sum_{j=0}^{n} p_{ij} x^j \tag{21}$$

The expressions for kinetic and potential/strain energy of the rotating beam are given by

$$T=\frac{1}{2}\int_0^L m(x)\dot{w}^2 dx \tag{22}$$

$$U=\frac{1}{2}\int_0^L EI_1(x)(w'')^2 dx+\frac{1}{2}\int_0^L T(x)(w')^2 dx \tag{23}$$

After putting the displacement expressions into Eqs. (22) and (23) and applying Lagrange's equations of motion, the natural frequencies of the rotating beam are found out from the familiar eigenvalue problem given by

$$[\mathbf{K}]\{x\}=\omega^2[\mathbf{M}]\{x\} \tag{24}$$

The (global) mass and stiffness matrices are given by

$$(M_{ij})_n=\int_0^L m(x)\psi_i\psi_j dx \tag{25}$$

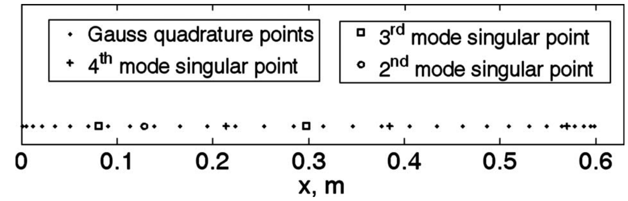

Fig. 4 Gauss-quadrature points of order 30 for the domain (0,0.6) and the singularity points of the flexural stiffness functions

$$(K_{ij})_n=\int_0^L EI_1(x)\psi_i''\psi_j'' dx+\int_0^L T(x)\psi_i'\psi_j' dx \tag{26}$$

Here $(M_{ij})_n$ and $(K_{ij})_n$ represent the global mass and stiffness matrices obtained by using an nth order expansion for w. Note that the integration limits in Eqs. (25) and (26) are 0 and L because only one element is used for the entire beam.

We first check the validity of the p-version FEM code, for different nondimensional rotating speeds ($\lambda=\sqrt{m\Omega^2L^4/EI}=0$ and 12), by comparing obtained results with published literature [1,2,7,11]. The comparison is shown in Tables 2 and 3. For the beam with properties in Table 1 and with $\Omega=360$ rpm, the first four nondimensional rotating frequencies are 3.6600, 22.1615, 61.8225, and 121.0311, respectively.

The functions $EI_1(x)$ obtained from Eqs. (11)–(19) may now be substituted in Eqs. (25) and (26) to test the exactness of the numerical code for a rotating beam. Since $EI_1(x)$ obtained from Eqs. (11)–(19) is a complicated function of x, the first term in Eq. (26) cannot be exactly calculated. Therefore, this integral has to be evaluated using numerical methods. We use the Gauss quadrature to evaluate the integral. Since the functions $EI_1(x)$ are not simple polynomial functions, we use a large number of Gauss–Legendre points for the quadrature. We have used 30 points in our analysis. We ensure that the Gauss-quadrature nodes do not fall on the singularity points for correct estimate of the integral. Such an approach is typically used to address singularities using numerical methods [24–27]. With 30 Gauss–Legendre nodes in the domain (0 m, 0.6 m), it is observed that none of the nodes fall within a range of ± 0.01 m of any singular points of the first four modes. This is illustrated in Fig. 4. However, they provide sufficient sampling for an accurate evaluation of the integral as we shall see from numerical results. The same number of points can be used for any length of the beam as the property is maintained for all

Table 2 Comparison of nondimensional frequencies of a uniform cantilever beam ($\lambda=0$)

Mode	Present FEM	Gunda and Ganguli [11]	Wang and Wereley [7]	Wright et al. [2]	Hodges and Rutkowsky [1]
1	3.5160	3.5160	3.5160	3.5160	3.5160
2	22.0345	22.0345	22.0345	22.0345	22.0345
3	61.6972	61.6972	61.6972	61.6972	61.6972
4	120.902	120.902	120.902	120.902	N/A

Table 3 Comparison of nondimensional frequencies of a uniform cantilever beam ($\lambda=12$)

Mode	Present FEM	Gunda and Ganguli [11]	Wang and Wereley [7]	Wright et al. [2]	Hodges and Rutkowsky [1]
1	13.1702	13.1702	13.1702	13.1702	13.1702
2	37.6031	37.6032	37.6031	37.6031	37.6031
3	79.6145	79.6146	79.6145	79.6145	79.6145
4	140.534	140.535	140.534	140.534	N/A

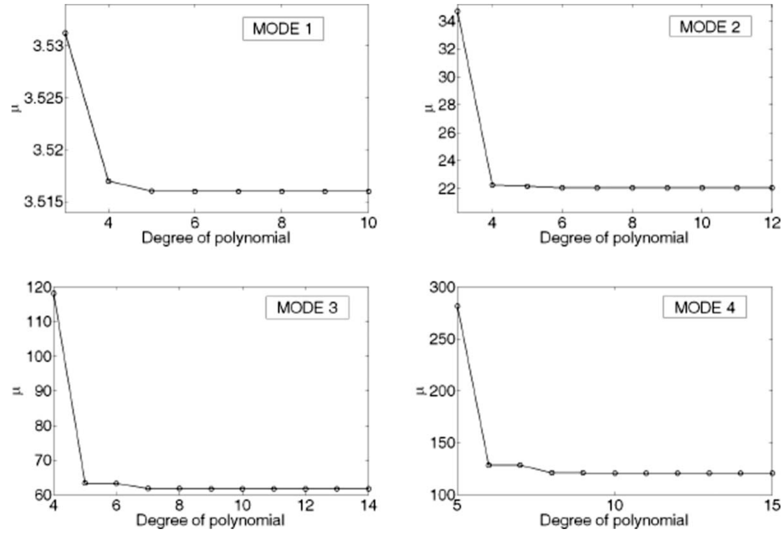

Fig. 5 Convergence of the p-version finite element code for first four modes using derived flexural stiffness functions

beam lengths. The algorithm for calculating the points and weights of Gauss quadrature for a general domain is given in Appendix B.

Convergence of the code to the exact value of frequency, in rad/s, within four decimal places of accuracy was achieved using polynomial order $n=6$, 8, 11, and 14 for the first four modes, respectively. The beauty of the derived functions is that they give the exact value of the nondimensional frequencies ($\mu = \sqrt{m\omega^2 L^4/EI}$) of a nonrotating beam, which are 3.5160, 22.0345, 61.6972, and 120.902, respectively, for the first four modes. The convergence is very fast and is illustrated in Fig. 5. The nodal displacements are obtained as eigenvectors $\{x\}$ from Eq. (26). The mode-shapes are obtained by using the interpolation polynomials to interpolate the displacements between nodal values. The normalized mode-shapes (with a value of 1 at $x=L$) obtained at convergence compare very well with the exact mode-shapes from Eq. (9). The residue of mode-shapes obtained is of order of 10^{-7} or less and is shown in Fig. 6. We have thus numerically shown that the derived flexural stiffness functions give rotating beams with the same eigenpair of the corresponding uniform nonrotating beam for a given mode. For the first mode, there are no internal singularities, and a physically feasible equivalent rotating beam exists. Moreover, the functions for modes higher than the first are integrable using Gauss quadrature despite the presence of singularities.

5 Numerical Simulations: h-Version FEM

Though many rotating beam codes use p-version type single element formulations, there exist h-version codes, where a smeared value for the stiffness and mass per unit length is used for each element.

In the h-version FEM, the beam is discretized into many finite elements, and relevant interpolation functions are used to set up equations in each element. We use Hermite cubic interpolation functions and 4DOF finite elements with displacement and slope DOF at each node [22]. The natural frequencies of the rotating beam are obtained from the eigenvalue problem of Eq. (24).

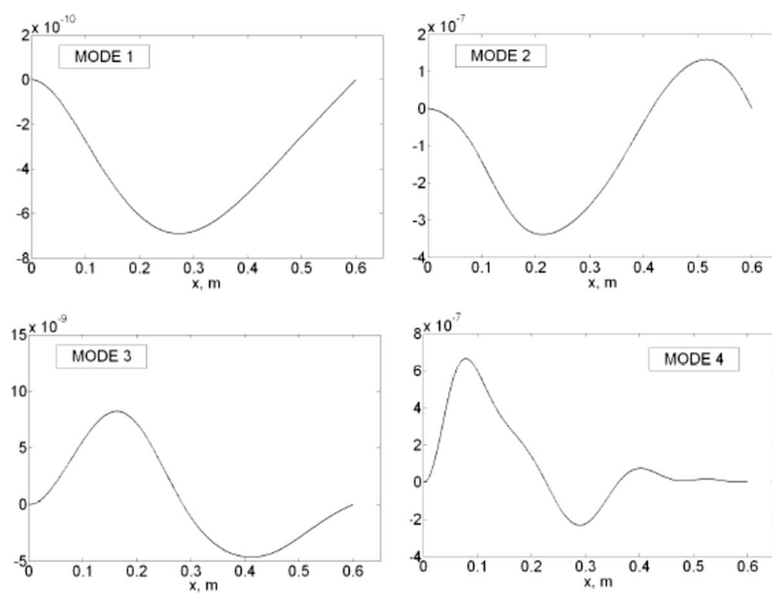

Fig. 6 Residue of mode-shapes obtained from p-version FEM

Table 4 Hermite interpolation polynomials

ψ_1	$2\left(\frac{\bar{x}}{e}\right)^3-3\left(\frac{\bar{x}}{e}\right)^2+1$
ψ_2	$\left(\left(\frac{\bar{x}}{e}\right)^3-2\left(\frac{\bar{x}}{e}\right)^2+\left(\frac{\bar{x}}{e}\right)\right)e$
ψ_3	$-2\left(\frac{\bar{x}}{e}\right)^3+3\left(\frac{\bar{x}}{e}\right)^2$
ψ_4	$\left(\left(\frac{\bar{x}}{e}\right)^3-\left(\frac{\bar{x}}{e}\right)^2\right)e$

Here, the global mass matrix $[\mathbf{M}]$ and the global stiffness matrix $[\mathbf{K}]$ of the beam are obtained by assembling the elemental mass and stiffness matrices. These matrices for the nth finite element are given by

$$(M_{ij})_n=\int_{x_n}^{x_{n+1}} m(\widetilde{x_n})\psi_i\psi_j dx \tag{27}$$

$$(K_{ij})_n=\int_{x_n}^{x_{n+1}} EI_1(\widetilde{x_n})\psi_i''\psi_j''dx+\int_{x_n}^{x_{n+1}} T(\widetilde{x_n})\psi_i'\psi_j'dx \tag{28}$$

where x_n, x_{n+1}, and $\widetilde{x_n}$ are the coordinates of the left node, the right node, and the midpoint of the nth finite element and $\psi_{1,2,3,4}$ are the Hermite cubic interpolation polynomials defined in the interval (x_n,x_{n+1}). These are given in Table 4, where $\bar{x}=x-x_n$ refers to the local coordinate and $e=x_{n+1}-x_n$ refers to the element length.

The code is validated first by comparing the results with different rotation speeds with published literature [1,2,7,11]. Next, we substitute the functions $EI_1(x)$ from Eqs. (11)–(19) in Eqs. (27) and (28). Since $EI_1(\widetilde{x_n})$, $m(\widetilde{x_n})$, and $T(\widetilde{x_n})$ are constants and $\psi_{1,2,3,4}$ are simple polynomial functions, the integrals in Eqs. (25) and (26) can be calculated in a closed form. The convergence characteristics for different modes are studied next.

5.1 First Mode. For the first mode, we discretize the domain into a uniform mesh and gradually refine the mesh by increasing the number of elements. Since the function $EI_1(x)$ for mode 1 is a benign function with a gradual variation and no internal singularities (see Fig. 2), the h-version code converges very rapidly. With 16 uniform elements, the first-mode nondimensional frequency converges to the exact value up to four decimal places, which equals 3.5160. The convergence is illustrated in Fig. 7. The mode-shapes also converge to that of the corresponding uniform nonrotating beam. The residue of the nodal displacements obtained from the eigenvalue problem, with 16 uniform elements in the domain, is shown in Fig. 7. We see that for the fundamental mode, a physically feasible equivalent rotating beam exists as internal singularities are absent.

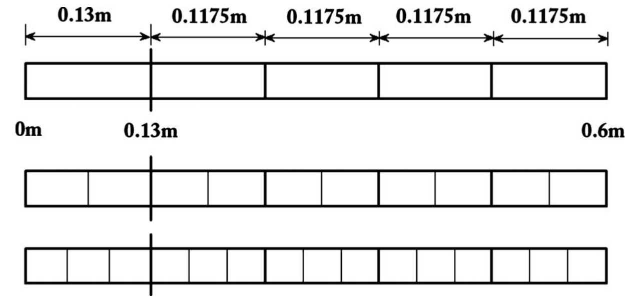

Fig. 8 Fundamental mesh for the second mode h-version FEM, and the first two refinements

5.2 Second Mode. The flexural stiffness function corresponding to the second mode has one internal singularity and unfortunately, the regular h-version FEM does not converge uniformly. There is a blow up in the value of frequency when a certain number of elements are used in the domain. This happens when the midpoint of an element coincides with or falls very close to the point of singularity. In particular, the code blows up for 30 uniform elements in the domain where the midpoint of the seventh element ($x=0.13$ m) coincides with the singularity point. To address this problem, we place a node at the singularity point, which ensures that the midpoint of no element coincides with the singularity point. This method is typical of finite element analysis in fracture mechanics, where a node is placed at the crack for the analysis [28]. Here, we create a fundamental mesh with a node at the singularity point and a fixed number of elements in the domain. Then we keep refining the mesh by dividing each of these elements into m equal parts ($m=1,2,3,\ldots$). As the number of elements increases, the h-version code approaches the exact value of the frequency.

For mode 2, the nodes are identified by setting $\phi(x)=0$. The nodes are found to exist at a nondimensional coordinate of $\eta=x/L=0.783$, which for a beam of length, 0.6 m, occurs at $x=0.470$ m. Hence, the singularity occurs at $x=0.6$ m-0.470 m $=0.130$ m. We develop an initial discretization for this mode with a mesh, as shown in Fig. 8. The refined mesh for $m=2$ and $m=3$ is also shown in Fig. 8. Note that the fundamental mesh has elements of more or less equal lengths. Elements of equal lengths are created for faster and uniform convergence. With gradual refining of the mesh, the total number of elements in the domain, n, increases as multiples of 5, i.e., $n=5$ m. The number of elements needed for the nondimensional frequency to converge to an accuracy of four decimal places ($\mu=22.0345$) is $n=55$. The convergence rate and the residue of the nodal displacements obtained with $n=55$ ($m=11$) are shown in Fig. 9.

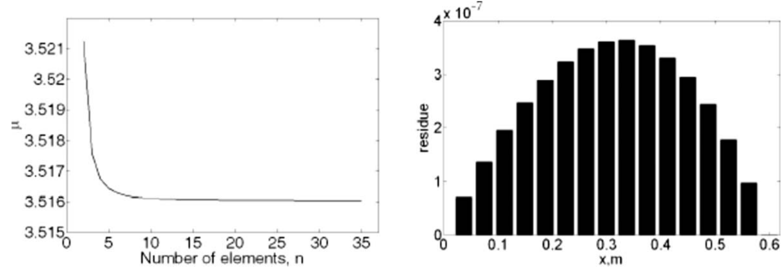

Fig. 7 Convergence characteristics and residue of nodal displacements for first mode with h-version finite element code

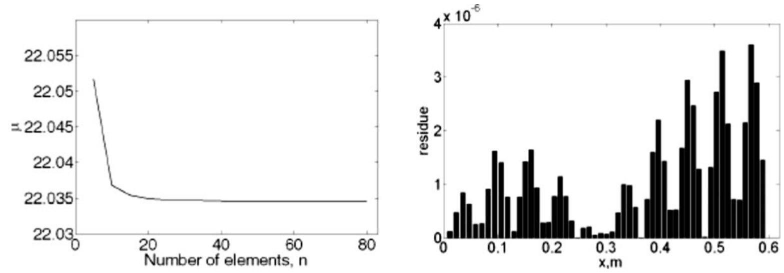

Fig. 9 Convergence characteristics and residue of nodal displacements for second mode with h-version finite element code

5.3 Third Mode. The nodal positions for the third mode of a uniform rotating beam are found to exist at $\eta=0.503$ and $\eta=0.868$. For the h-version finite element analysis, we place a node at each of the singularity points, $x=0.079$ m and $x=0.298$ m. The fundamental mesh for this mode is formed by dividing the region between the singularities into elements of nearly equal size. The fundamental mesh and the refined mesh for $m=2$ and $m=3$ are given in Fig. 10. The total number of elements in the domain after m refinements is given by $n=8$ m. The code converges to the exact value of nondimensional frequency up to four decimal places ($\mu=61.6972$) for $n=96$. The convergence rate and the residue of the nodal displacements are shown in Fig. 11.

5.4 Fourth Mode. The nodal positions for the fourth mode are identified at $\eta=0.358$, 0.644, and 0.906, respectively. The singularities occur at $x=0.057$ m, 0.213 m, and 0.385 m. By placing a node at each of these points, we form the fundamental mesh for mode 4, as given in Fig. 12. For this case, $n=11$ m. Convergence of nondimensional frequency μ to four decimal places of accuracy ($\mu=120.9019$) happens for $n=121$. The convergence of frequency and residue of nodal displacements is given in Fig. 13.

It is clear that by placing the element nodes at the singularity locations, any h-version FEM code can be checked using the flexural stiffness $EI_1(x)$ derived in this paper. For all cases, monotonic convergence is obtained to the frequencies and mode-shapes of a nonrotating beam.

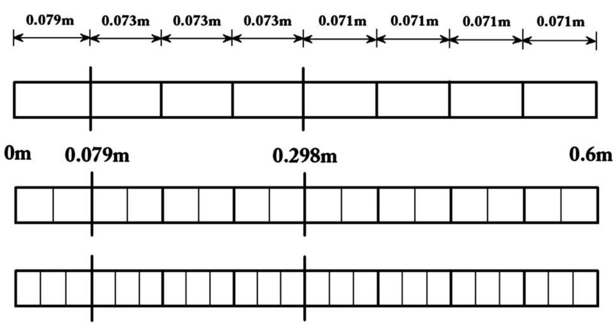

Fig. 10 Fundamental mesh for the third mode h-version FEM, and the first two refinements

6 Realistic Beams

It may be of interest to manufacture rotating beams with the spectra jth mode eigenpair of nonrotating beams. In Secs. 2–5, we showed that there exists a rotating beam with the same jth frequency and mode-shape of a uniform nonrotating beam whose length and mass variation is also the same. Mathematically speaking, the centrifugal stiffening effects of the rotating beam have been nullified by appropriate tailoring of the flexural stiffness variation. Such beams may be useful in structural design if we want to counter the effects of centrifugal stiffening by stiffness variation. We study the beams corresponding to the first four modes in this section.

6.1 First Mode. It can be seen from Fig. 2 that only the first mode gives a physically reasonable $EI_1(x)$ profile, if we ignore the tip singularity. The tip singularity does not cause any problem in the numerical integration or finite element analysis. Thus, there may exist realistic rotating beams whose fundamental eigenpair matches that of a uniform nonrotating beam. As an example, consider a rectangular cross-sectional beam defined by breadth b and height h. Then we have mass per unit length of the beam as $m=\rho bh$ and the flexural stiffness as $EI_1=E(bh^3/12)$. Assuming that $b=b(x)$, $h=h(x)$, $m=1.8816$ kg/m^3, $E=2\times 10^{11}$ Pa, and $\rho=7840$ kg/m^3, we obtain the required beam with the following cross section dimensions:

$$h(x)=\sqrt{\frac{12\rho EI_1(x)}{Em}} \tag{29}$$

$$b(x)=\sqrt{\frac{Em^3}{12\rho^3 EI_1(x)}} \tag{30}$$

Substituting for $EI_1(x)$, the flexural stiffness function for the first mode, from Eqs. (11)–(13), we obtain a variation for $b(x)$ and

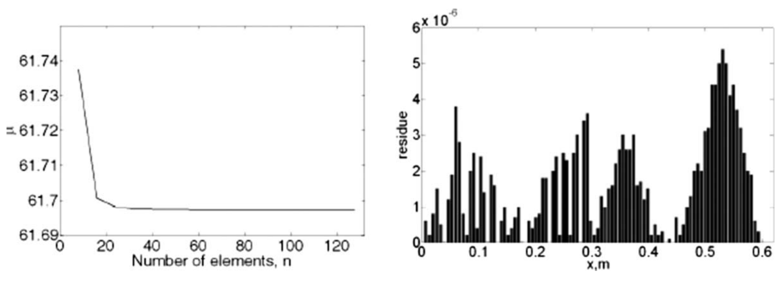

Fig. 11 Convergence characteristics and residue of nodal displacements for third mode with h-version finite element code

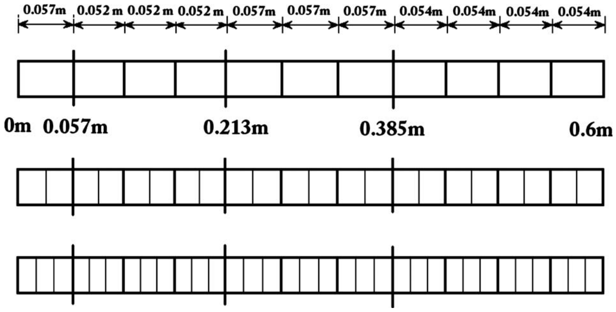

Fig. 12 Fundamental mesh for the fourth mode h-version FEM, and the first two refinements

$h(x)$, as shown in Fig. 14. The top and the front views of a symmetric beam with these dimensions are shown in Fig. 15. Note that the height and the breadth of this beam do not differ significantly from the values of the corresponding nonrotating beam. For the corresponding nonrotating beam, $b=24$ mm and $h=10$ mm. Therefore, the rotating beam with the same first-mode eigenpair is physically possible.

6.2 Second Mode. The expressions $EI_1(x)$ obtained from Eqs. (11)–(19), for modes higher than the first, are very complicated and have a very high degree of nonlinearity in their variation. Rotating beams with the $EI_1(x)$ variation corresponding to the higher modes will be difficult to manufacture. Moreover, as is evident from Fig. 2, the value of $EI_1(x)$ blows up near the singularities. The value of $EI_1(x)$ tends to $\pm\infty$ on either side of these singularities. Hence it is physically impossible to make such beams, though the flexural stiffness can be used as test-functions by avoiding the singularities via numerical integration or nodal placement. However, approximations for $EI_1(x)$ can be constructed by selecting a finite number of points in the domain of the beam and satisfying the value of $EI_1(x)$ at these points. Then we can develop a function for $EI_1(x)$ passing through these points by constructing interpolation functions between these points. Cubic Hermite interpolating polynomials are used because they preserve the shape and the monotonicity of the curve. Figure 16 shows three different approximations to the function $EI_1(x)$ for the second mode. Beams A and B are continuous beams based on cubic interpolation polynomials. Beam A has a sharp variation near the point of singularity and beam B has a mild variation. Beam C is modeled as a step beam, where the value of EI_1 changes abruptly at the point of singularity. For this beam, the function $EI_1(x)$ is replaced by its average values on either sides of the singularity. The second-mode frequencies of these beams are calculated using the p-version FEM. The calculated frequencies are shown in Table 5. The percentage deviation of these frequencies from the exact value is less than 0.1%.

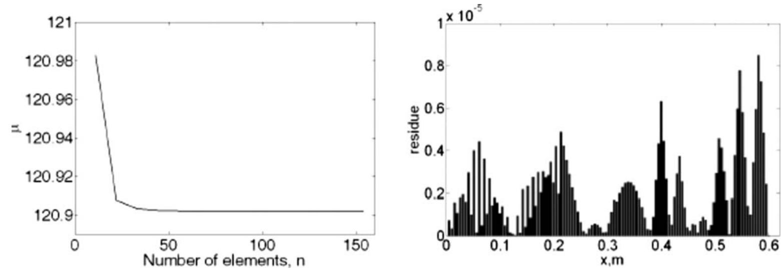

Fig. 13 Convergence characteristics and residue of nodal displacements for fourth mode with h-version finite element code

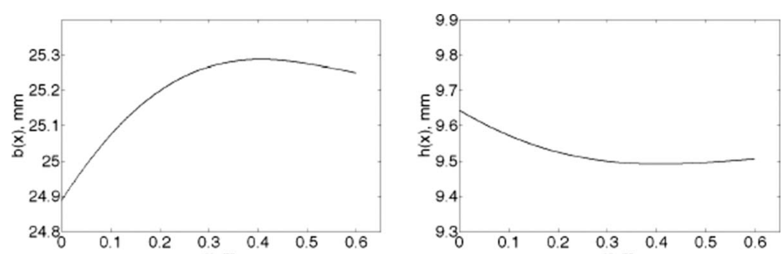

Fig. 14 Variation in height and breadth of a rotating beam equivalent to a uniform nonrotating beam for the first mode

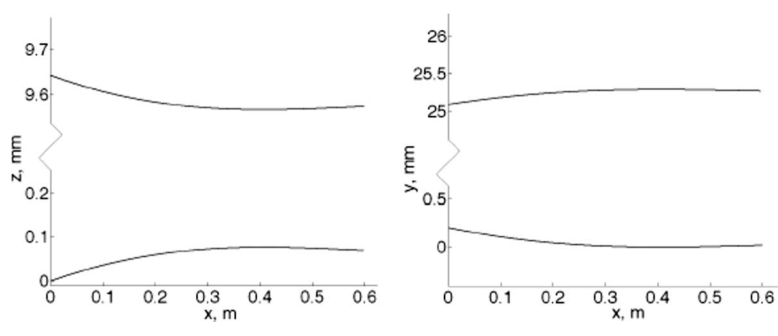

Fig. 15 Top and side views of a rotating beam equivalent to a uniform rotating beam for the first mode

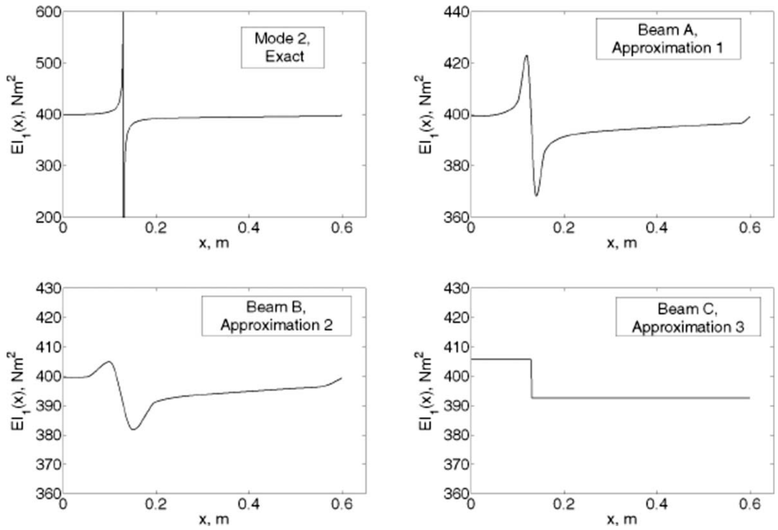

Fig. 16 Realistic beams: approximations to the exact function for the second mode

The corresponding mode-shapes, ϕ, of these beams are normalized with $\phi(L)=1$ and compared with the exact mode-shapes of Fig. 6. The difference in the value of ϕ and the exact mode-shape is calculated as a vector of residues, $\{R\}$, at 600 equidistant points in the domain. The norm of the vector, $\{R\}$, calculated by $\sqrt{\Sigma_i R(i)^2}$ is found to be very small and is shown in Table 5. Beam B gives the best match for frequency and Beam A gives the best match for the mode-shape. However, the stepped Beam C also gives reasonable results and shows the possibility of countering the centrifugal force effects in a simple manner. Therefore, we see that by approximating the flexural stiffness functions derived in this paper, we can obtain realistic rotating beams whose mode-shapes and frequencies match with that of second mode of the uniform nonrotating beam.

Next, we look at the dimensions of these beams if they have rectangular cross sections. The height and breadth variations, $h(x)$ and $b(x)$, calculated from Eqs. (29) and (30) are shown in Fig. 17. We can see that the variation in the dimensions is reasonable and Beam C, and to some extent Beam B, is physically feasible. Higher thickness at the root and higher breadth in the outboard region are required for Beam C. Note that the nonrotating beam has dimensions $b=24$ mm and $h=10$ mm. By giving a small level of nonuniformity, the centrifugal effects for the second mode are countered.

6.3 Third Mode. The flexural stiffness function for the third mode has two internal singularities, thus making it impossible to construct a physical beam with this flexural stiffness variation. Approximations to the function as above may be constructed, resulting in Beams A–C (Fig. 18). Beam A is closer to the exact flexural stiffness function but has steeper variation at the singular points. Beam B varies mildly at the singular points. Beam C is a step beam with three different flexural stiffness constants along its length. The estimated frequencies and the norm of the residues of the third mode-shape, with 600 equidistant points in the domain, are shown in Table 6. Here, Beam A gives the best match for both frequency and mode-shape, followed closely by Beam B. Beam C gives an acceptable match. All the frequency deviations are less than or equal to 0.1%.

The height and breadth variation in these beams with square cross sections is shown in Fig. 19. Again, we see that by adding a

Table 5 Frequencies and mode-shapes of the approximate beams for mode 2

Approximation	Estimated frequency (rad/s)	% deviation from exact	Norm of residues of mode-shape
Beam A	892.4341	0.0021	8.45×10^{-4}
Beam B	892.4176	0.0003	1.73×10^{-3}
Beam C	893.2886	0.0979	3.89×10^{-1}

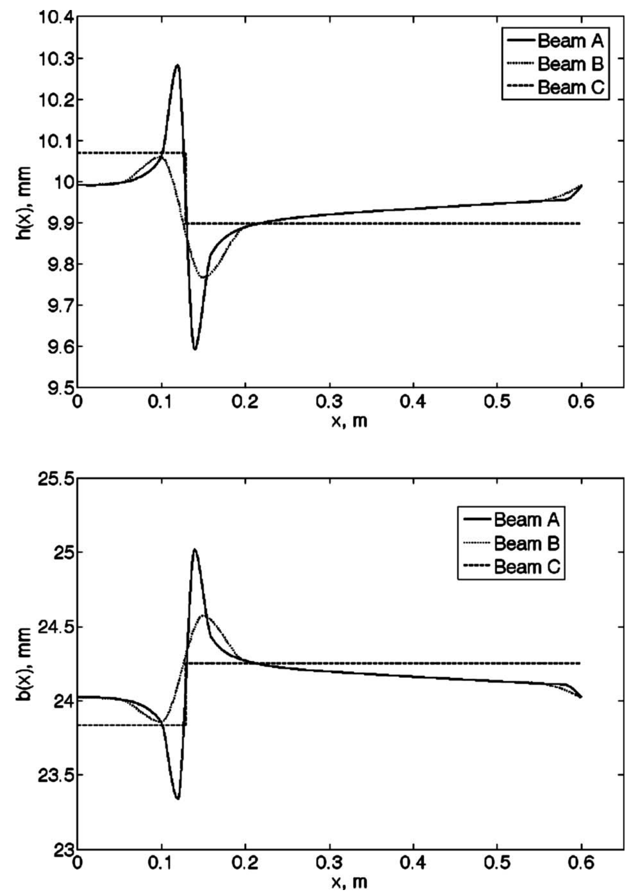

Fig. 17 Variation in height and breadth of a rotating beam equivalent to a uniform nonrotating beam for the second mode

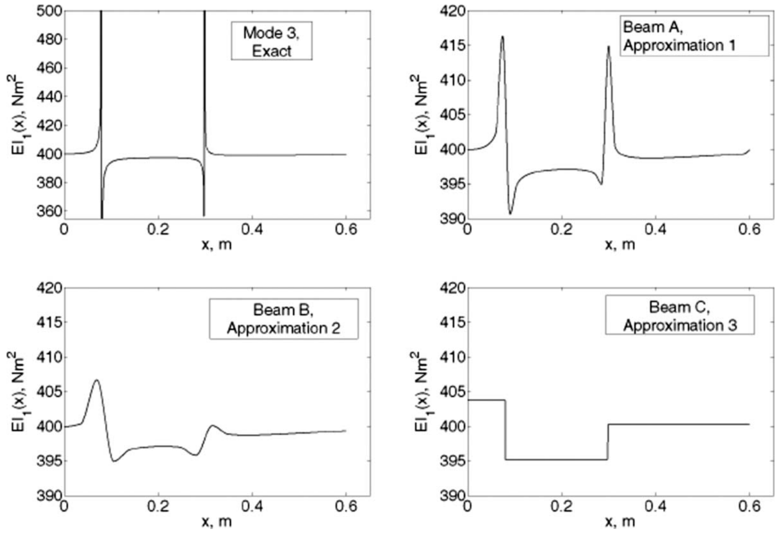

Fig. 18 Realistic beams: approximations to the exact function for the third mode

small level of nonuniformity in the dimensions of the rotating beam, the effect of centrifugal stiffening for the third mode can be countered.

6.4 Fourth Mode. The fourth mode flexural stiffness function is approximated in three ways, as in Fig. 20. The corresponding frequencies and the residue of the mode-shapes estimated for these beams are given in Table 7. Beam A is closer in frequency and mode-shape to the exact values. Beams B and C give reasonable approximations too. The frequency deviations are less than 0.025% for all the beams.

The height and breadth variation in the beams is illustrated in Fig. 21. We see that Beam C gives a physically feasible cross section. We also see that in each case, there are $N-1$ discontinuities corresponding to the singularities for mode N. Also, the dimensions of the stepped beam are close to the nonrotating uniform beam.

6.5 Destiffening Effects. We have shown that physically realizable rotating beams with the same eigenpair of nonrotating beams exist for the first four modes. Similar beams can be found for higher modes. By using the cross sections obtained in this work, any mode can be destiffened to alleviate the effect of centrifugal stiffening. This can be useful in design where it is sometimes necessary to move one mode away from a particular value of frequency being a multiple of the rotation speed. To study this possibility, we find the stiffness reduction required for a uniform rotating beam to match the frequencies of the nonuniform beam for the first four modes. We reduce the uniform beam stiffness from a value of $EI_2=400\ \text{N m}^2$ to $EI_1^{(r)}$ so that for a given mode, the frequency reduction is identical to that obtained using the derived flexural stiffness of the stepped beam, $EI_1^{(C)}$ for modes 2–4, and the exact beam, $EI_1^{(\text{exact})}$, for mode 1.

Table 6 Frequencies and mode-shapes of the approximate beams for mode 3

Approximation	Estimated frequency (rad/s)	% deviation from exact	Norm of residues of mode-shape
Beam A	2498.8163	0.0011	1.10×10^{-3}
Beam B	2498.9089	0.0048	1.48×10^{-3}
Beam C	2501.3019	0.1006	1.06×10^{-2}

Table 8 compares the first four frequencies of the two beams. Note that the uniform rotating beam with a stiffness constant of $400\ \text{N m}^2$ has first four natural frequencies as 148.2320 rad/s, 897.5588 rad/s, 2503.8612 rad/s, and 4901.8567 rad/s, respectively. We can see from Table 8 that the frequencies of higher modes such as mode 4 can be reduced with less effect on the

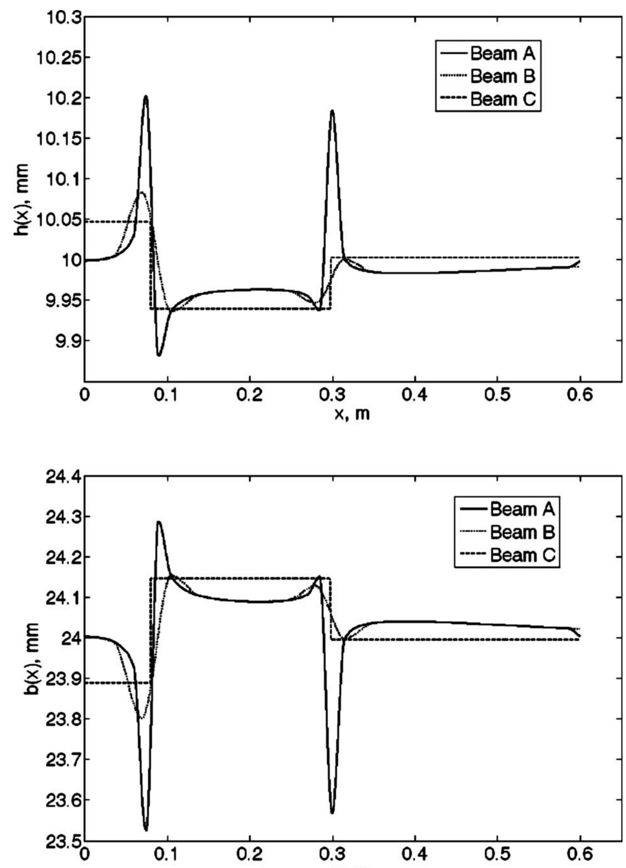

Fig. 19 Variation in height and breadth of a rotating beam equivalent to a uniform nonrotating beam for the third mode

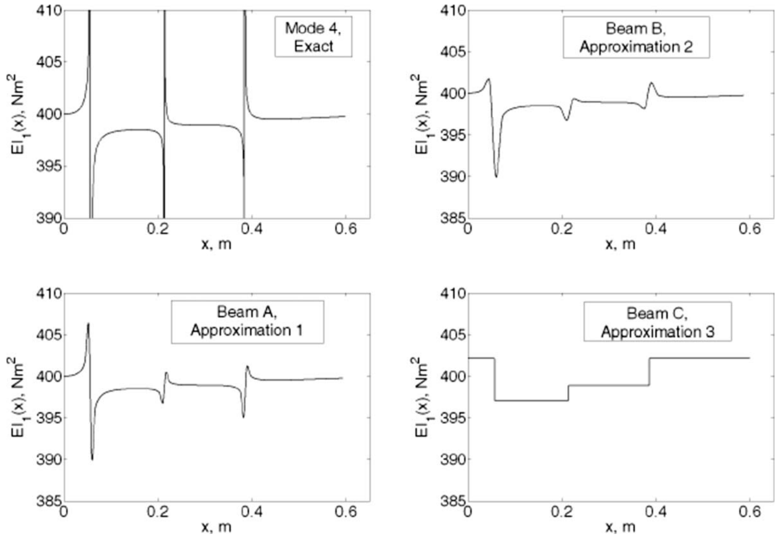

Fig. 20 Realistic beams: approximations to the exact function for the fourth mode

lower mode frequencies (1–3) compared with the uniform beam. For the lower modes such as mode 1, the exact beam yields larger reduction in the frequencies for the higher modes (2–4). In general, if we target mode j for matching with the nonrotating frequency, the modes below j will show less reduction than the uniform beam and for modes greater than j, the reduction will be greater. Thus the beam profiles can be used in tailoring beams to achieve targeted frequencies.

The stiffness constant of the uniform beam, labeled $EI_1^{(r)}$, is compared with the stiffness variation in the nonuniform beams in Fig. 22. It is observed from Fig. 22 that the derived flexural stiffness functions provide a means to destiffen the rotating beams without compromising for the stiffness of the beam at the root. In fact, for modes 2–4, the root stiffness is higher than that of the baseline rotating beam (400 N m^2). Since the root stiffness is critical for handling stresses in cantilever beams, being able to reduce frequencies while not having to reduce root stiffness is a desirable feature.

7 Conclusions

In the present paper, we have shown that there exist rotating beams with the same eigenpair as corresponding uniform nonrotating beams for a given mode. The flexural stiffness, $EI_1(x)$, in this rotating beam varies differently for different mode-shapes and the beams have the same length and mass per unit length as the uniform nonrotating beam. The flexural stiffness function, $EI_1(x)$, of the equivalent rotating beams can be used to test numerical codes written for rotating beams. For the fundamental mode, a physically feasible equivalent rotating beam exists, but for higher modes, the flexural stiffness has internal singularities. We have verified the p-version and h-version FEMs for the first four modes. For p-version FEM, the singularities present in the higher

Table 7 Frequencies and mode-shapes of the approximate beams for mode 4

Approximation	Estimated frequency (rad/s)	% deviation from exact	Norm of residues of mode-shape
Beam A	4896.6340	0.0015	6.13×10^{-4}
Beam B	4896.5547	0.0001	9.63×10^{-4}
Beam C	4897.8586	0.0251	9.21×10^{-3}

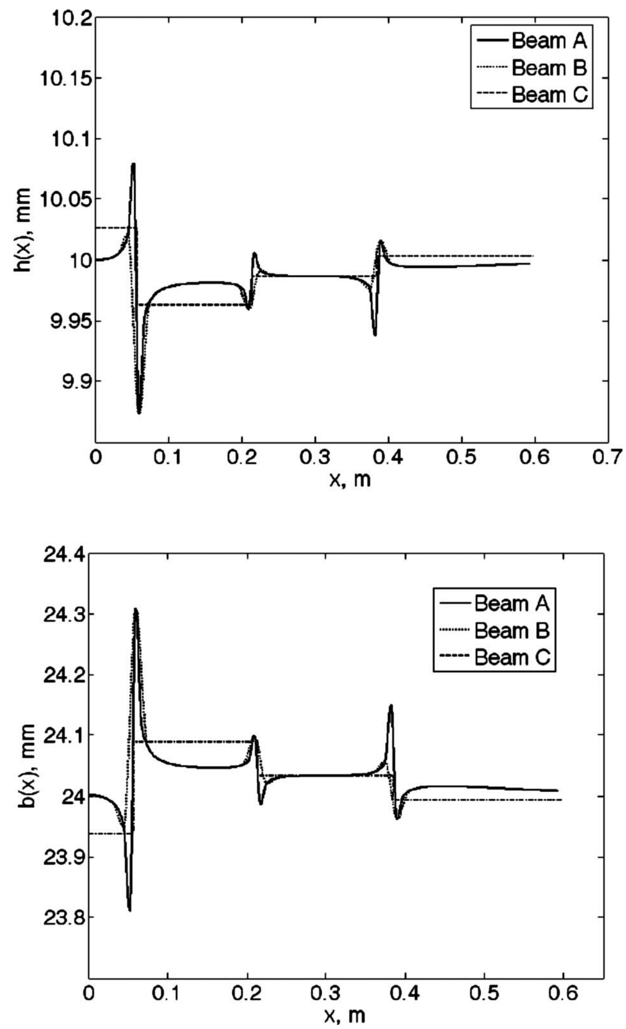

Fig. 21 Variation in height and breadth of a rotating beam equivalent to a uniform nonrotating beam for the fourth mode

Table 8 Frequencies and mode-shapes of the approximate beams for mode 4

Mode	$EI_1(x)$	ω_1 (rad/s)	ω_2 (rad/s)	ω_3 (rad/s)	ω_4 (rad/s)
	$EI_1^{(\text{exact})}(x)$	142.4015	856.1476	2386.1690	4670.2321
Mode 1	$EI_1^{(r)}(x)$	142.4015	859.6891	2397.4121	4693.0495
	$EI_1^{(C)}(x)$	148.3470	893.2886	2488.1736	4873.0676
Mode 2	$EI_1^{(r)}(x)$	147.5737	893.2886	2491.8591	4878.3147
	$EI_1^{(C)}(x)$	148.0982	897.1842	2501.3019	4894.2987
Mode 3	$EI_1^{(r)}(x)$	148.0813	896.6487	2501.3019	4896.8352
	$EI_1^{(C)}(x)$	148.0853	897.2456	2502.4406	4897.8586
Mode 4	$EI_1^{(r)}(x)$	148.0827	896.8270	2501.8171	4897.8586

modes can be avoided by appropriate placement of Gauss-quadrature points for numerical integration. For h-version FEM, the singularities can be avoided by placing the nodes at the singularity locations and taking the element flexural stiffness at its midpoint. The codes converge to the expected value of the first four natural frequencies of the nonrotating beam for which the exact solution is available. When the exact nonrotating beam solutions are obtained, we can be assured that the governing differential equation of the rotating beam has been accurately solved by the numerical method. This is because the beam deflections can be expressed in terms of mode-shapes as the basis functions. It is also found that approximate profiles of the flexural stiffness distributions can be obtained, which yield physically feasible beams. Such beams could be useful for destiffening rotating beams without requiring considerable stiffness loss at the root, which is otherwise needed by uniform beams.

Appendix A

The equation for the jth mode-shape of a uniform nonrotating cantilever beam from Eq. (9) can be written as

$$\phi_j(x) = C_j[\cos(\alpha_j x) - \cosh(\alpha_j x) + K(\sin(\alpha_j x) - \sinh(\alpha_j x))] \tag{A1}$$

where

$$K = \frac{\sin(\alpha_j L) - \sinh(\alpha_j L)}{\cos(\alpha_j L) + \cosh(\alpha_j L)} \tag{A2}$$

Differentiating Eq. (A1) twice with respect to x gives

$$\phi_j''(x) = -C_j\alpha_j^2[\cos(\alpha_j x) + \cosh(\alpha_j x) + K(\sin(\alpha_j x) + \sinh(\alpha_j x))] \tag{A3}$$

Substituting for x, $L-y$, in Eq. (A2) and expanding the resultant expression, we obtain

$$\phi_j''(x) = -C_j\alpha_j^2[a_1 \cos(\alpha_j y) + a_2 K \sin(\alpha_j y) + a_3 \cosh(\alpha_j y) + a_4 K \sinh(\alpha_j y)] \tag{A4}$$

where

$$a_1 = \cos(\alpha_j L) + K \sin(\alpha_j L) \tag{A5}$$

$$a_2 = \frac{\sin(\alpha_j L)}{K} - \cos(\alpha_j L) \tag{A6}$$

$$a_3 = \cosh(\alpha_j L) + K \sinh(\alpha_j L) \tag{A7}$$

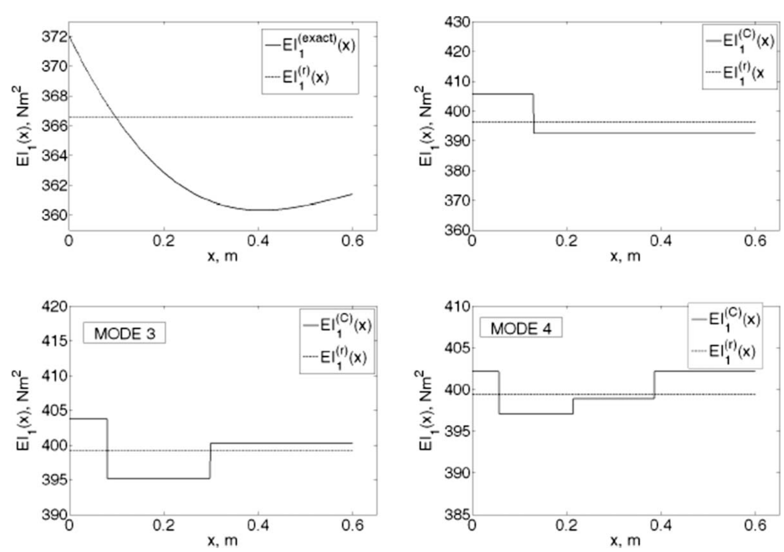

Fig. 22 Destiffening effects of flexural stiffness variations for various modes compared with uniform rotating beam ($EI_1^{(r)}$)

$$a_4 = -\frac{\sinh(\alpha_j L)}{K} - \cosh(\alpha_j L) \tag{A8}$$

Squaring the characteristic equation, $\cos(\alpha_j L)\cosh(\alpha_j L) = -1$, and using basic trigonometric identities, we obtain

$$(1 - \sin^2(\alpha_j L))(\cosh^2(\alpha_j L)) = 1 \tag{A9}$$

$$\Rightarrow \sin^2(\alpha_j L)\cosh^2(\alpha_j L) = \sinh^2(\alpha_j L) \tag{A10}$$

$$\Rightarrow \frac{\sin^2(\alpha_j L)}{\cos^2(\alpha_j L)} = \sinh^2(\alpha_j L) \tag{A11}$$

$$\Rightarrow \sin^2(\alpha_j L) = \cos^2(\alpha_j L)\sinh^2(\alpha_j L) \tag{A12}$$

Since $(\alpha_j L)$ is positive for all modes, we have $\sinh(\alpha_j L) > 0$ and $\cosh(\alpha_j L) > 0$. This with $\cos(\alpha_j L)\cosh(\alpha_j L) = -1$ yields $\cos(\alpha_j L) < 0$. From Eqs. (A10) and (A12), we obtain $\sin(\alpha_j L)\cosh(\alpha_j L) = \pm \sinh(\alpha_j L)$ and $\sin(\alpha_j L) = \mp \cos(\alpha_j L)\sinh(\alpha_j L)$. The algebraic sign on the right-hand side of these equations is decided by the sign of $\sin(\alpha_j L)$.

Substituting K from Eq. (A2) in Eq. (A5), we obtain

$$\begin{aligned} a_1 &= \cos(\alpha_j L) + \frac{\sin(\alpha_j L) - \sinh(\alpha_j L)}{\cos(\alpha_j L) + \cosh(\alpha_j L)}\sin(\alpha_j L) \\ &= \frac{\cos^2(\alpha_j L) - 1 + \sin^2(\alpha_j L) - \sin(\alpha_j L)\sinh(\alpha_j L)}{\cos(\alpha_j L) + \cosh \alpha_j L} \\ &= \frac{-\sin(\alpha_j L)\sinh(\alpha_j L)}{\cos(\alpha_j L) + \cosh(\alpha_j L)} = \frac{-\sin(\alpha_j L)\sinh(\alpha_j L)}{\cos(\alpha_j L) - \frac{1}{\cos(\alpha_j L)}} \\ &= \frac{\sinh(\alpha_j L)\cos(\alpha_j L)}{\sin(\alpha_j L)} = \mp 1 \end{aligned} \tag{A13}$$

Expanding other coefficients in a similar manner yields $a_2 = \mp 1$, $a_3 = \pm 1$, and $a_4 = \pm 1$. Hence Eq. (A4) simplifies as

$$\phi_j''(x) = \pm C_j \alpha_j^2 [\cos(\alpha_j y) + K \sin(\alpha_j y) - \cosh(\alpha_j y) - K \sinh(\alpha_j y)] \tag{A14}$$

Therefore,

$$\phi_j''(x) = \pm \alpha_j^2 \phi(y) \tag{A15}$$

Hence, $\phi(y) = 0 \Leftrightarrow \phi_j''(x) = 0$. The assumption $y = L - x$ completes the proof.

Appendix B

The n point Gauss-quadrature rule for numerical integration over the interval $(-1,1)$ is given by

$$\int_{-1}^{1} f(x)dx \approx \sum_{i=0}^{n} w_i f(t_i) \tag{B1}$$

The points t_i are the eigenvalues of the matrix $\mathbf{J}$ [29], where matrix $\mathbf{J}$ is defined by

$$\mathbf{J} = \begin{pmatrix} 0 & a_1 & 0 & \dots & 0 & 0 \\ a_1 & 0 & a_2 & \dots & 0 & 0 \\ 0 & a_2 & 0 & \dots & 0 & 0 \\ \vdots & \vdots & \vdots & \ddots & \vdots & \vdots \\ 0 & 0 & 0 & \dots & 0 & a_n \\ 0 & 0 & 0 & \dots & a_n & 0 \end{pmatrix}_{(n+1)\times(n+1)} \tag{B2}$$

and the constants a_i are defined by $a_i = i/\sqrt{4i^2 - 1}$. The weights w_i are then given by

$$w_i = 2(V_{1,i})^2 \tag{B3}$$

where $\mathbf{V}$ is the matrix of the normalized eigenvectors of $\mathbf{J}$.

Table 9 Gauss-quadrature points and weights of order 30 for the domain (0,1)

i	t_i	w_i
1	0.0016	0.0040
2	0.0082	0.0092
3	0.0200	0.0144
4	0.0369	0.0194
5	0.0587	0.0242
6	0.0852	0.0287
7	0.1161	0.0330
8	0.1511	0.0369
9	0.1897	0.0404
10	0.2317	0.0434
11	0.2765	0.0461
12	0.3236	0.0482
13	0.3727	0.0498
14	0.4231	0.0509
15	0.4743	0.0514
16	0.5257	0.0514
17	0.5769	0.0509
18	0.6273	0.0498
19	0.6764	0.0482
20	0.7235	0.0461
21	0.7683	0.0434
22	0.8103	0.0404
23	0.8489	0.0369
24	0.8839	0.0330
25	0.9148	0.0287
26	0.9413	0.0242
27	0.9631	0.0194
28	0.9800	0.0144
29	0.9918	0.0092
30	0.9984	0.0040

The transformation rules for the Gaussian quadrature points and weights for an integral over (a,b) are given by

$$w_i|_{(a,b)} = w_i|_{(-1,1)} \times \frac{b-a}{2} \tag{B4}$$

$$t_i|_{a,b} = t_i|_{(-1,1)} \times \frac{b-a}{2} + \frac{a+b}{2} \tag{B5}$$

For the domain (0,1), these formulas become

$$w_i|_{(0,1)} = w_i|_{(-1,1)} \times \tfrac{1}{2} \tag{B6}$$

$$t_i|_{0,1} = t_i|_{(-1,1)} \times \tfrac{1}{2} + \tfrac{1}{2} \tag{B7}$$

The Gauss-quadrature points, sorted in an increasing order, and the corresponding weights with $n = 30$ for the domain (0,1) are given in Table 9.

References

[1] Hodges, D. J., and Rutkowsky, M. J., 1981, "Free Vibration Analysis of Rotating Beams by a Variable Order Finite Element Method," AIAA J., **19**(11), pp. 1459–1466.
[2] Wright, A. D., Smith, C. E., Thresher, R. W., and Wang, J. L. C., 1982, "Vibration Modes of Centrifugally Stiffened Beams," ASME J. Appl. Mech., **49**(2), pp. 197–202.
[3] Yoo, H. H., and Shin, S. H., 1998, "Vibration Analysis of Rotating Cantilever Beams," J. Sound Vib., **212**(5), pp. 807–828.
[4] Sinha, S. K., 2007, "Combined Torsional-Bending-Axial Dynamics of a Twisted Rotating Cantilever Timoshenko Beam With Contact-Impact Loads at the Free End," ASME J. Appl. Mech., **74**(3), pp. 505–522.
[5] Avramov, K. V., Pierre, C., and Shyriaieva, N., 2007, "Flexural-Flexural-Torsional Non-Linear Vibrations of Pre-Twisted Rotating Beams With Asymmetric Cross-Sections," J. Vib. Control, **13**(4), pp. 329–364.
[6] Lauzon, D. M., and Murthy, V. R., 1993, "Determination of Vibration Characteristics of Multiple-Load-Path Blades by a Modified Galerkin Method," Comput. Struct., **46**(6), pp. 1007–1020.
[7] Wang, G., and Wereley, N. M., 2004, "Free Vibration Analysis of Rotating Blades With Uniform Tapers," AIAA J., **42**(12), pp. 2429–2437.

[8] Banerjee, J. R., 2000, "Free Vibration of Centrifugally Stiffened Uniform and Tapered Beams Using the Dynamic Stiffness Method," J. Sound Vib., **233**(5), pp. 857–875.
[9] Udupa, K. M., and Varadan, T. K., 1990, "Hierarchical Finite Element Method for Rotating Beams," J. Sound Vib., **138**(3), pp. 447–456.
[10] Gunda, J. B., and Ganguli, R., 2008, "New Rational Interpolation Functions for Finite Element Analysis of Rotating Beams," Int. J. Mech. Sci., **50**(3), pp. 578–588.
[11] Gunda, J. B., and Ganguli, R., 2008, "Stiff String Basis Functions for Vibration Analysis of High Speed Rotating Beams," ASME J. Appl. Mech., **75**(2), p. 024502.
[12] Gunda, J. B., Singh, A. P., Chabbra, P. P. S., and Ganguli, R., 2007, "Free Vibration Analysis of Rotating Tapered Blades Using Fourier-p Superelement," Struct. Eng. Mech., **27**(2), pp. 243–257.
[13] Vinod, K. G., Gopalakrishnan, S., and Ganguli, R., 2007, "Free Vibration and Wave Propagation Analysis of Uniform and Tapered Rotating Beams Using Spectrally Formulated Finite Elements," Int. J. Solids Struct., **44**(18–19), pp. 5875–5893.
[14] Naguleswaran, S., 1994, "Lateral Vibration of a Centrifugally Tensioned Uniform Euler-Bernouli Beam," J. Sound Vib., **176**(5), pp. 613–624.
[15] Lee, S. Y., and Sheu, J. J., 2007, "Free Vibrations of Rotating Inclined Beam," ASME J. Appl. Mech., **74**(3), pp. 406–414.
[16] Banerjee, J. R., 2001, "Dynamic Stiffness Formulation and Free Vibration Analysis of Centrifugally Stiffened Timoshenko Beams," J. Sound Vib., **247**(1), pp. 97–115.
[17] Banerjee, J. R., 2003, "Free Vibration of Sandwich Beams Using the Dynamic Stiffness Method," Comput. Struct., **81**(18–19), pp. 1915–1922.
[18] Banerjee, J. R., Su, H., and Jackson, D. R., 2006, "Free Vibration of Rotating Tapered Beams Using the Dynamic Stiffness Method," J. Sound Vib., **298**(4–5), pp. 1034–1054.
[19] Hashemi, S. M., and Richard, M. J., 2001, "Natural Frequencies of Rotating Uniform Beams With Coriolis Effects," ASME J. Vibr. Acoust., **123**(4), pp. 444–455.
[20] Mierovitch, L., 1986, *Elements of Vibration Analysis*, 2nd ed., McGraw-Hill, New York.
[21] Drexel, M. V., and Ginsberg, J. H., 2001, "Modal Overlap and Dissipation Effects of a Cantilever Beam With Multiple Attached Oscillators," ASME J. Vibr. Acoust., **123**(2), pp. 181–187.
[22] Pawar, P. P., and Ganguli, R., 2003, "Genetic Fuzzy System for Damage Detection in Beams and Helicopter Rotor Blades," Comput. Methods Appl. Mech. Eng., **192**(16–18), pp. 2031–2057.
[23] Reddy, J. N., 1993, *An Introduction to the Finite Element Method*, 3rd ed., McGraw-Hill, New York.
[24] Biondi, B., and Caddemni, S., 2005, "Closed Form Solutions of Euler-Bernouli Beams With Singularities," Int. J. Solids Struct., **42**(9–10), pp. 3027–3044.
[25] Biondi, B., and Caddemni, S., 2007, "Euler-Bernouli Beams With Multiple Singularities in the Flexural Stiffness," Eur. J. Mech. A/Solids, **26**(5), pp. 789–809.
[26] Jin, X., Leon, M., and Wang, Q., 2008, "A Practical Method for Singular Integral Equations of the Second Kind," Eng. Fract. Mech., **75**(5), pp. 1005–1014.
[27] Miller, R. K., 1971, "On Ignoring the Singularity in Numerical Quadrature," Math. Comput., **25**(115), pp. 521–532.
[28] Liu, D. S., and Chiou, D. Y., 2003, "A Coupled IEM/FEM Approach for Solving Elastic Problems With Multiple Cracks," Int. J. Solids Struct., **40**(8), pp. 1973–1993.
[29] Schwarz, H. R., 1989, *Numerical Analysis: A Comprehensive Introduction*, Wiley, New York.

Fully Lagrangian Modeling of Dynamics of MEMS With Thin Beams—Part I: Undamped Vibrations

Ranajay Ghosh
Graduate Student
Department of Theoretical and Applied Mechanics,
Cornell University,
Thurston Hall,
Ithaca, NY 14853

Subrata Mukherjee
Professor
Fellow ASME
Department of Theoretical and Applied Mechanics and Sibley School of Mechanical and Aerospace Engineering,
Cornell University,
Kimball Hall,
Ithaca, NY 14853

Micro-electro-mechanical systems (MEMSs) often use beam or plate shaped conductors that can be very thin—with $h/L \approx \mathcal{O}(10^{-2}-10^{-3})$ (in terms of the thickness h and length L of the beam or side of a square plate). Such MEMS devices find applications in microsensors, micro-actuators, microjets, microspeakers, and other systems where the conducting beams or plates oscillate at very high frequencies. Conventional boundary element method analysis of the electric field in a region exterior to such thin conductors can become difficult to carry out accurately and efficiently—especially since MEMS analysis requires computation of charge densities (and then surface traction) separately on the top and bottom surfaces of such beams. A new boundary integral equation has been proposed to handle the computation of charge densities for such high aspect ratio geometries. In the current work, this has been coupled with the finite element method to obtain the response behavior of devices made of such high aspect ratio structural members. This coupling of electrical and mechanical problems is carried out using a Newton scheme based on a Lagrangian description of the electrical and mechanical domains. The numerical results are presented in this paper for the dynamic behavior of the coupled MEMS without damping. The effect of gap between a beam and the ground, on mechanical response of a beam subjected to increasing electric potential, is studied carefully. Damping is considered in the companion paper (Ghosh and Mukherjee, 2009, "Fully Lagrangian Modeling of Dynamics of MEMS With Thin Beams—Part II: Damped Vibrations," ASME J. Appl. Mech. **76***, p. 051008).* [DOI: 10.1115/1.3086785]

Keywords: boundary integral equations, boundary element method, singular integrals, micro-electro-mechanical systems, aspect ratio, thin beam, Newton scheme

1 Introduction

The field of micro-electro-mechanical system (MEMS) is a very broad one that includes fixed or moving microstructures, encompassing micro-electro-mechanical, microfluidic, micro-electro-fluidic-mechanical, micro-opto-electro-mechanical, and micro-thermo-mechanical devices and systems. MEMS usually consists of released microstructures that are suspended and anchored, or captured by a hub-cap structure and set into motion by mechanical, electrical, thermal, acoustical or photonic energy source(s).

Typical MEMS structures consist of arrays of thin plates with cross sections in the order of microns and lengths in the order of ten to hundreds of microns (see, for example, Fig. 1). Sometimes, MEMS structural elements are beams. An example is a small rectangular silicon beam with length in the order of millimeters and thickness of the order of microns, which deforms when subjected to electric fields. Owing to its small size, significant forces and/or deformations can be obtained with the application of low voltages ($\approx$10 V). Examples of devices that utilize vibrations of such beams are comb drives (see Fig. 1), synthetic microjets [2] (for chemical mixing, cooling of electronic components, micropropulsion, turbulence control, and other macroflow properties), microspeakers [3], etc.

Numerical simulation of electrically actuated MEMS devices have been carried out for nearly two decades using the boundary element method (BEM) (see, e.g., Refs. [4–8]) to model the exterior electric field and the finite element method (FEM) (see, e.g., Refs. [9–11]) to model deformation of the structure. The commercial software package MEMCAD [12], for example, uses the commercial FEM software package ABAQUS for mechanical analysis, together with a BEM code FASTCAP [13] for electric field analysis. Other examples of such work are Refs. [14–16], as well as Refs. [12,17], for the dynamic analysis of MEMS.

The focus of this paper is the study of dynamic response of MEMS devices made up of very thin conducting beams. This requires BEM analysis of the electric field exterior to these thin conducting beams. A convenient way to model such a problem is to assume beams with vanishing thickness and solve for the sum of the charges on the upper and lower surfaces of each beam [18]. The standard boundary integral equation (BIE) with a weakly singular kernel is used here and this approach works well for determining, for example, the capacitance of a parallel plate capacitor. For MEMS calculations, however, one must obtain the charge densities separately on the upper and lower surfaces of a beam since the traction at a surface point on a beam depends on the square of the charge density at that point. The gradient BIE is employed in Ref. [19] to obtain these charge densities separately. The formulation given in Ref. [19] is a BEM scheme that is particularly well suited for MEMS analysis of very thin plates—for $h/L \approx 0.001$—in terms of the length L (of a side of a square plate) and its thickness h. A similar approach has also been developed for MEMS and nano-electro-mechanical system (NEMS) with very thin beams [20]. Similar work has also been reported by

Contributed by the Applied Mechanics Division of ASME for publication in the JOURNAL OF APPLIED MECHANICS. Manuscript received July 18, 2008; final manuscript received January 5, 2009; published online June 18, 2009. Review conducted by Robert M. McMeeking.

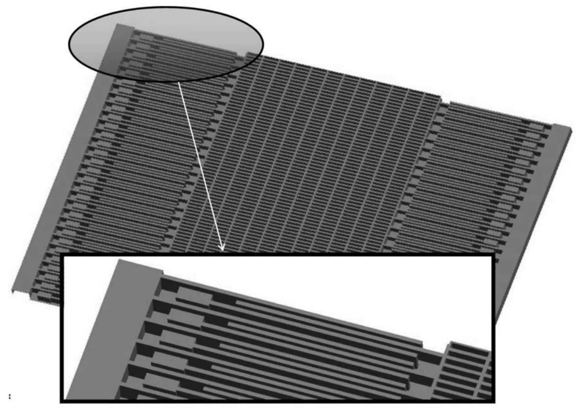

Fig. 1 Parallel plate resonator: geometry and detail of the parallel plate fingers from Ref. [1]

Chen et al. [21] in the context of determining fringing fields and levitating forces for two-dimensional (2D) beam shaped conductors in MEMS combdrives.

The coupled BEM/FEM methods employed in many of the references cited above perform a mechanical analysis on the undeformed configuration of a structure (Lagrangian approach) and an electrical analysis on the deformed configuration (Eulerian approach). A relaxation method is then used for self-consistency between the two domains. Therefore, the geometry of the structure must be updated before an electrical analysis is performed during each relaxation iteration. This procedure increases computational effort and introduces additional numerical errors since the deformed geometry must be computed at every stage. Li and Aluru [22] first proposed a Lagrangian approach for the electrical analysis as well, thus obviating the need to carry out calculations based on the deformed shapes of a structure. Two and three-dimensional (3D) quasistatic Lagrangian exterior BEM analysis was addressed in Refs. [23,24], while a fully coupled 2D quasistatic MEMS analysis has been carried out in Ref. [22]. A fully coupled 2D dynamic Lagrangian MEMS analysis has been carried out by De and Aluru [25]. Additional advantages of the fully Lagrangian approach, for dynamic analysis of MEMS, are described in Ref. [25], in which a Newton method has been developed and compared with the relaxation scheme. It must be noted that Refs. [23–26] employ a standard (not thin feature) BEM. Finally, quasistatic deformation of thin plates, using the thin plate BEM is addressed in Ref. [27].

This paper is an attempt to analyze and simulate vibrations of a practical MEM system involving a coupling of the electrical and mechanical problem. Additional coupling with fluid fields exterior to the system is considered in Ref. [28]. The external electric field is modeled using the Lagrangian version of the thin beam BEM approach [20] together with a hypersingular postprocessing gradient BIE to find the individual charges. The mechanical problem is tackled using a moderately large deflection FEM analysis. Finally, a Newton scheme developed analogous to Ref. [25] is used to solve the entire coupled nonlinear problem.

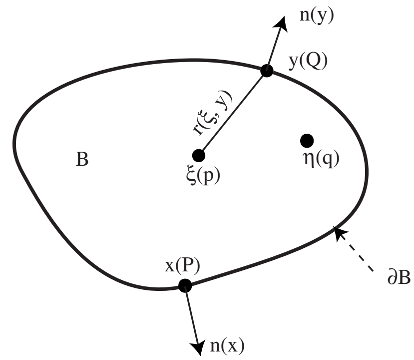

Fig. 3 Notation used in boundary integral equations

This paper starts with regularization of the conventional and hypersingular BIEs for potential theory in an infinite region outside the thin conducting beams. The equations are then reformulated in a total Lagrangian framework. A finite element scheme is then presented for the mechanical deformation of the structure. The paper then proceeds to explain the Newton scheme for coupling the electrical and mechanical domains. The numerical results are then presented and discussed. This paper concludes with a section on discussions of the results and scope for future research.

2 Electrical Problem in the Exterior Domain

Figure 2 shows (as an example of a MEMS device) a deformable clamped beam over a fixed ground plane. The undeformed configuration is B with boundary ∂B. The beam deforms when a potential V is applied between the two conductors, and the deformed configuration is called b with boundary ∂b. The charge redistributes on the surface of the deformed beam, thereby changing the electrical force on it and this causes the beam to deform further. The system then undergoes vibrations and the complete analysis of the system is done using the Newton scheme.

2.1 Electric Field BIE in a Simply Connected Body. The boundary element formulation of the electric problem can be derived from the Laplace equation, which governs the potential in the region outside a conductor.

2.1.1 Conventional BIE: Indirect Formulation. Referring to Fig. 3, for a source point $\xi \in B$ (with bounding surface ∂B), one has the indirect BIE:

$$\phi(\xi) = \int_{\partial B} -\frac{\ln(r(\xi,\mathbf{y}))}{2\pi\epsilon}\nu(\mathbf{y})ds(\mathbf{y}) \tag{1}$$

where $\mathbf{y}$ is a field point, ϕ is the potential, $r(\xi,\mathbf{y})=\mathbf{y}-\xi$, $r=|\mathbf{r}|$, ϵ is the permittivity of the medium, ds is the area of an infinitesimal surface element on ∂B, and ν is the (unknown) surface density function on ∂B.

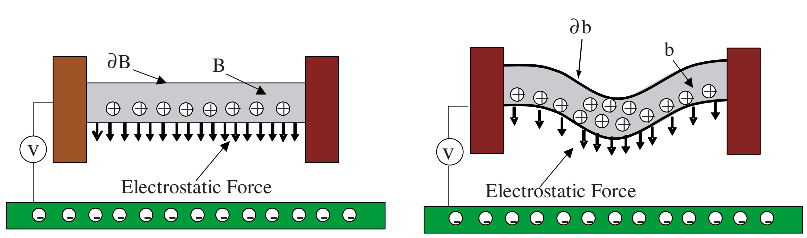

Fig. 2 Deformable clamped beam over a fixed ground plate

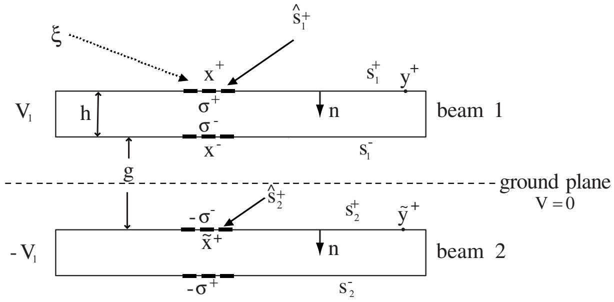

Fig. 4 Two parallel conducting beams

2.1.2 Gradient BIE: Indirect Formulation. Taking the derivative of the potential ϕ at the source point leads to an auxiliary hypersingular equation:

$$\nabla_\xi \phi(\xi) = \int_{\partial B} -\frac{\nu(\mathbf{y})}{2\pi\epsilon}\nabla_\xi \ln(r(\xi,\mathbf{y}))ds(\mathbf{y}) = \int_{\partial B} \frac{\nu(\mathbf{y})\mathbf{r}(\xi,\mathbf{y})}{2\pi r^2(\xi,\mathbf{y})\epsilon}ds(\mathbf{y}) \tag{2}$$

Note that, in general, the function $\nu(\mathbf{y})$ is not the charge density. It becomes equal to the charge density when B is the infinite region exterior to the conductors. This is discussed in Sec. 2.2.

2.2 BIEs in Infinite Region Containing Two Thin Conducting Beams. Now consider the situation shown in Fig. 4. Of interest is the solution of the following Dirichlet problem for Laplace's equation:

$$\nabla^2\phi(\mathbf{x}) = 0, \quad \mathbf{x} \in B, \quad \phi(\mathbf{x})\text{prescribed for } \mathbf{x} \in \partial\mathbf{B} \tag{3}$$

where B is now the region *exterior* to the two beams. The unit normal $\mathbf{n}$ to B is defined to point away from B (i.e., into the beam).

2.2.1 Regular BIE: Source Point Approaching a Beam Surface s_1^+. It has been shown by Bao and Mukherjee [20] that for this case,

$$\phi(\mathbf{x}^+) = -\int_{s_1^+-\hat{s}_1^+} \frac{\ln r(\mathbf{x}^+,\mathbf{y})\beta(\mathbf{y})}{2\pi\epsilon}ds(\mathbf{y}) - \int_{\hat{s}_1^+} \frac{\ln r(\mathbf{x}^+,\mathbf{y})\beta(\mathbf{y})}{2\pi\epsilon}ds(\mathbf{y}) - \int_{s_2^+} \frac{\ln r(\mathbf{x}^+,\mathbf{y})\beta(\mathbf{y})}{2\pi\epsilon}ds(\mathbf{y}) \tag{4}$$

Here $\beta(\mathbf{y}) = \sigma(\mathbf{y}^+) + \sigma(\mathbf{y}^-)$, where σ is now the charge density at a point on the beam surface. The second integral in Eq. (4) is logarithmically singular and the rest are regular except when the beam thickness and the gap become very small.

A similar equation can be written for $\mathbf{x}^+ \in s_2^+$. For the case shown in Fig. 4, however, it is not necessary since $\beta(\mathbf{y})$ is equal and opposite on the two beams. Therefore, for this case, Eq. (4) is sufficient to solve for β on both the beams.

2.2.2 Hypersingular BIE: Source Point Approaching a Beam Surface s_1^+. It is first noted that for $\mathbf{x}^+ \in s_k^+ \cup s_k^-$, $k=1,2$,

$$\sigma(\mathbf{x}) = \epsilon\frac{\partial\phi}{\partial n}(\mathbf{x}) = \epsilon\mathbf{n}(x)\cdot[\nabla_\xi\phi(\xi)]_{\xi=x} \tag{5}$$

Consider the limit $\xi \to \mathbf{x}^+ \in \hat{s}_1^+ \in s_1^+$. It is important to realize that this limit is meaningless for point $\mathbf{x}$ on the edge of a beam, since the charge density is singular on its edges. One obtains the following HBIE:

$$\begin{aligned}\sigma(\mathbf{x}^+) &= \int_{s_1^+-\hat{s}_1^+} \frac{\beta(\mathbf{y})\mathbf{r}(\mathbf{x}^+,\mathbf{y})\cdot\mathbf{n}(\mathbf{x}^+)}{2\pi r^2(\mathbf{x}^+,\mathbf{y})}ds(\mathbf{y}) \\ &+ \int_{\hat{s}_1^+} \frac{\mathbf{r}(\mathbf{x}^+,\mathbf{y})[\beta(\mathbf{y})\cdot\mathbf{n}(\mathbf{x}^+) - \beta(\mathbf{x})\cdot\mathbf{n}(\mathbf{y})]}{2\pi r^2(\mathbf{x}^+,\mathbf{y})}ds(\mathbf{y}) \\ &+ \frac{\beta(\mathbf{x})}{2\pi}\Psi(\hat{s}_1^+,\mathbf{x}^+) + \int_{s_2^+} \frac{\beta(\mathbf{y})\mathbf{r}(\mathbf{x}^+,\mathbf{y})\cdot\mathbf{n}(\mathbf{x}^+)}{2\pi r^2(\mathbf{x}^+,\mathbf{y})}ds(\mathbf{y})\end{aligned} \tag{6}$$

In the above, the angle subtended by the line element s_1^+ at the point $\mathbf{x}^+$ (see [19] and [20] and Fig. 5) is

$$\Psi(\hat{s}_1^+,\mathbf{x}^+) = \fint_{\hat{s}_1^+} \frac{\mathbf{r}(\mathbf{x}^+,\mathbf{y})\cdot\mathbf{n}(\mathbf{y})}{r^2(\mathbf{x}^+,\mathbf{y})}ds(\mathbf{y}) = \psi_A + \psi_B \tag{7}$$

Here, the symbol $\fint$ denotes the finite part of the integral in the sense of Mukherjee [29]. Also (see Fig. 5), a unit vector $\mathbf{u}$, through the point $\mathbf{x}^+$, is chosen such that it intersects $\hat{s}_1^+$. Now, ψ is the angle between the positive $\mathbf{u}$ vector and $\mathbf{r}(\mathbf{x}^+,\mathbf{y})$ with $\mathbf{y} \in \hat{s}_1^+$. This angle can be obtained from the equation

$$\cos(\psi(\mathbf{y})) = \frac{\mathbf{r}(\mathbf{x}^+,\mathbf{y})\cdot\mathbf{u}}{r(\mathbf{x}^+,\mathbf{y})} \tag{8}$$

Writing Eq. (6) at $\mathbf{x}^-$ together with some algebraic manipulation gives

$$\begin{aligned}\frac{1}{2}[\sigma(\mathbf{x}^+) - \sigma(\mathbf{x}^-)] &= \int_{s_1^+-\hat{s}_1^+} \frac{\beta(\mathbf{y})\mathbf{r}(\mathbf{x}^+,\mathbf{y})\cdot\mathbf{n}(\mathbf{x}^+)}{2\pi r^2(\mathbf{x}^+,\mathbf{y})}ds(\mathbf{y}) \\ &+ \int_{\hat{s}_1^+} \frac{\mathbf{r}(\mathbf{x}^+,\mathbf{y})[\beta(\mathbf{y})\cdot\mathbf{n}(\mathbf{x}^+) - \beta(\mathbf{x})\cdot\mathbf{n}(\mathbf{y})]}{2\pi r^2(\mathbf{x}^+,\mathbf{y})}ds(\mathbf{y}) \\ &- \frac{\beta(\mathbf{x})}{2\pi}[\pi - \Psi(\hat{s}_1^+,\mathbf{x}^+)]\end{aligned}$$

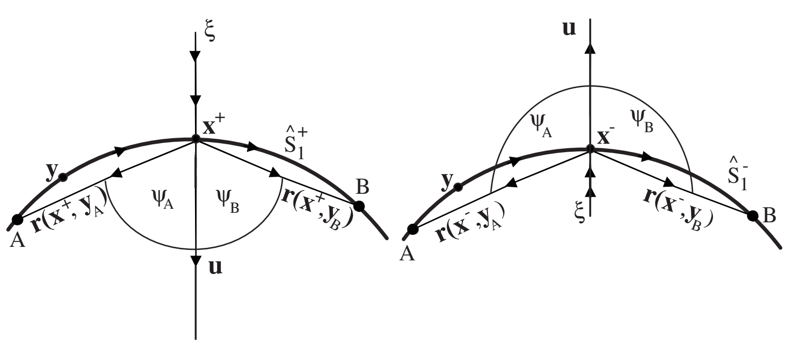

Fig. 5 Evaluations of angles

$$+\int_{s_2^+}\frac{\beta(\mathbf{y})\mathbf{r}(\mathbf{x}^+,\mathbf{y})\cdot\mathbf{n}(\mathbf{x}^+)}{2\pi r^2(\mathbf{x}^+,\mathbf{y})}ds(\mathbf{y}) \tag{9}$$

Equation (4) gives the sum of the charge densities and the HBIE equation (9) can be used as a postprocessing step to compute the values of individual charge densities on each of the beams.

2.3 Electrostatic Boundary Integral Equation in the Lagrangian Framework. Converting Eqs. (4) and (9) in the Lagrangian framework can be started by using Nanson's law [30]

$$\mathbf{n}ds = J\mathbf{N}\cdot\mathbf{F}^{-1}dS \tag{10}$$

Here $\mathbf{n}$ and $\mathbf{N}$ are the unit normal vectors to ∂b and ∂B, at the generic points $\mathbf{x}$ and $\mathbf{X}$, respectively, $\mathbf{F}=\partial\mathbf{x}/\partial\mathbf{X}$ is the deformation gradient, $J=\det(\mathbf{F})$, and dS is an area element on ∂B. Also, $\mathbf{X}$ and $\mathbf{x}$ denote the coordinates in the undeformed and deformed configurations, respectively. From Eq. (10), it follows that

$$ds = J|\mathbf{N}\cdot\mathbf{F}^{-1}|dS \tag{11}$$

Next, define Σ, the charge density per unit undeformed surface area. Since $\Sigma dS=\sigma ds$, one has

$$\Sigma = J\sigma|\mathbf{N}\cdot\mathbf{F}^{-1}| \tag{12}$$

Also define

$$B = \Sigma^+ + \Sigma^- \tag{13}$$

2.3.1 Lagrangian Version of the Regular BIE. Using the relations developed in Sec. 2.2, one arrives at the Lagrangian version of Eq. (4),

$$\phi(\mathbf{X}^+) = -\int_{S_1^+-\hat{S}_1^+}\frac{\ln R(\mathbf{X}^+,\mathbf{Y})B(\mathbf{Y})}{2\pi\epsilon}dS(\mathbf{Y}) - \int_{\hat{S}_1^+}\frac{\ln R(\mathbf{X}^+,\mathbf{Y})B(\mathbf{Y})}{2\pi\epsilon}dS(\mathbf{Y}) - \int_{S_2^+}\frac{\ln R(\mathbf{X}^+,\mathbf{Y})B(\mathbf{Y})}{2\pi\epsilon}dS(\mathbf{Y}) \tag{14}$$

where

$$\mathbf{r}(\mathbf{x}(\mathbf{X}),\mathbf{y}(\mathbf{Y})) \equiv \mathbf{R}(\mathbf{X},\mathbf{Y}) = \mathbf{y}(\mathbf{Y}) - \mathbf{x}(\mathbf{X}) = \mathbf{Y}+\mathbf{u}(\mathbf{Y}) - \mathbf{X} - \mathbf{u}(\mathbf{X}) = \mathbf{R}_0(\mathbf{X},\mathbf{Y}) + \mathbf{u}(\mathbf{Y}) - \mathbf{u}(\mathbf{X}) \tag{15}$$

$$\mathbf{R_0}(\mathbf{X},\mathbf{Y}) = \mathbf{Y} - \mathbf{X} \tag{16}$$

$$r(\mathbf{x}(\mathbf{X}),\mathbf{y}(\mathbf{Y})) \equiv R(\mathbf{X},\mathbf{Y}) = |\mathbf{R}(\mathbf{X},\mathbf{Y})| \tag{17}$$

with $\mathbf{u}$ denoting the displacement at a point in B.

Also,

$$\mathbf{h}(\mathbf{y}) = -\frac{\sigma^2(\mathbf{y})}{2\epsilon}\mathbf{n} \tag{18}$$

$$\int_{\partial B}\mathbf{H}dS = \int_{\partial b}\mathbf{h}ds \tag{19}$$

where $\mathbf{h}$ and $\mathbf{H}$ are the tractions per unit deformed and undeformed surface areas, respectively. Using Eqs. (10), (11), (18), and (19), one gets

$$\mathbf{H} = -\frac{J\sigma^2\mathbf{N}\cdot\mathbf{F}^{-1}}{2\epsilon} = -\frac{\Sigma^2}{2J\epsilon}\frac{\mathbf{N}\cdot\mathbf{F}^{-1}}{|\mathbf{N}\cdot\mathbf{F}^{-1}|} \tag{20}$$

2.3.2 Lagrangian Version of the Gradient BIE. The Lagrangian version of the Eq. (9) is derived as follows:

$$\text{First term} = \int_{S_1^+-\hat{S}_1^+}\frac{B(\mathbf{Y})\mathbf{R}(\mathbf{X}^+,\mathbf{Y})\cdot\left(\frac{\mathbf{N}\cdot\mathbf{F}^{-1}}{|\mathbf{N}\cdot\mathbf{F}^{-1}|}\right)(\mathbf{X}^+)}{2\pi R^2(\mathbf{X}^+,\mathbf{Y})}dS(\mathbf{Y}) \tag{21}$$

$$\text{Second term} = \int_{\hat{S}_1^+}\frac{\mathbf{R}(\mathbf{X}^+,\mathbf{Y})B(\mathbf{Y})}{2\pi R^2(\mathbf{X}^+,\mathbf{Y})}\cdot\left(\frac{\mathbf{N}\cdot\mathbf{F}^{-1}}{|\mathbf{N}\cdot\mathbf{F}^{-1}|}\right)(\mathbf{X}^+)dS(\mathbf{Y}) - \int_{\hat{S}_1^+}\frac{\mathbf{R}(\mathbf{X}^+,\mathbf{Y})}{2\pi R^2(\mathbf{X}^+,\mathbf{Y})}\cdot\frac{B(\mathbf{X})}{J(\mathbf{X}^+)|\mathbf{N}\cdot\mathbf{F}^{-1}(\mathbf{X}^+)|}\cdot J(\mathbf{Y})(\mathbf{N}\cdot\mathbf{F}^{-1})(\mathbf{Y})dS(\mathbf{Y}) \tag{22}$$

$$\text{Third term} = -\frac{B(\mathbf{X})}{2\pi J(\mathbf{X}^+)|\mathbf{N}\cdot\mathbf{F}^{-1}|(\mathbf{X}^+)}\Psi(\hat{S}_1^+,\mathbf{X}^+) \tag{23}$$

The fourth term can be treated in the same way as the first. Now, multiply the entire equation by $J(\mathbf{X}^+)|\mathbf{N}\cdot\mathbf{F}^{-1}|(\mathbf{X}^+)$, use the midplane values[1] for $\mathbf{F}(\mathbf{X}^+)=\mathbf{F}(\mathbf{X}^-)$, and use the fact that $\mathbf{N}(\mathbf{X}^+)=-\mathbf{N}(\mathbf{X}^-)$ to simplify the equation further. The resulting equation has the form

$$\begin{aligned}\frac{1}{2}[\Sigma(\mathbf{X}^+)-\Sigma(\mathbf{X}^-)] &= \int_{S_1^+-\hat{S}_1^+}\frac{B(\mathbf{Y})\mathbf{R}(\mathbf{X}^+,\mathbf{Y})\cdot J(\mathbf{X}^+)(\mathbf{N}\cdot\mathbf{F}^{-1}(\mathbf{X}^+))}{2\pi R^2(\mathbf{X}^+,\mathbf{Y})}dS(\mathbf{Y})\\ &+ \int_{\hat{S}_1^+}\frac{B(\mathbf{Y})\mathbf{R}(\mathbf{X}^+,\mathbf{Y})\cdot J(\mathbf{X}^+)(\mathbf{N}\cdot\mathbf{F}^{-1}(\mathbf{X}^+))}{2\pi R^2(\mathbf{X}^+,\mathbf{Y})}dS(\mathbf{Y})\\ &- \int_{\hat{S}_1^+}\frac{B(\mathbf{X})\mathbf{R}(\mathbf{X}^+,\mathbf{Y})\cdot J(\mathbf{Y})(\mathbf{N}\cdot\mathbf{F}^{-1}(\mathbf{Y}))}{2\pi R^2(\mathbf{X}^+,\mathbf{Y})}dS(\mathbf{Y})\\ &- \frac{B(\mathbf{X})}{2\pi}[\pi-\Psi(\hat{S}_1^+,\mathbf{X}^+)]\\ &+ \int_{S_2^+}\frac{B(\mathbf{Y})\mathbf{R}(\mathbf{X}^+,\mathbf{Y})\cdot J(\mathbf{X}^+)(\mathbf{N}\cdot\mathbf{F}^{-1}(\mathbf{X}^+))}{2\pi R^2(\mathbf{X}^+,\mathbf{Y})}dS(\mathbf{Y})\end{aligned} \tag{24}$$

It must be noted that the second and third terms must be evaluated together for numerical purposes. The angle can be easily computed from taking dot products of the position vectors of the required points on the surface of the body.

3 Mechanical Problem for the Elastic Beam

Nonlinear deformation of a beam with no initial axial force is discussed in this section. The beam is linearly elastic, has immovable ends, and is of uniform cross section. The cross section is symmetric such that there is no twisting of the beam under applied bending moments. Also, $u(x)$ is the axial deformation and $w(x)$ is the transverse displacement of the midline of the beam.

3.1 The Model. The kinematic equations can be derived starting from the following nonlinear strain-displacement equation [31]:

$$\epsilon_{ij} = \frac{1}{2}\left(\frac{\partial u_i}{\partial x_j}+\frac{\partial u_j}{\partial x_i}\right) + \frac{1}{2}\left(\frac{\partial u_m}{\partial x_i}\cdot\frac{\partial u_m}{\partial x_j}\right) \tag{25}$$

This leads to the kinematic equations:

$$\epsilon_{xx} = u_{,x} + 1/2\cdot(w_{,x})^2 \tag{26}$$

[1] Also called the membrane assumption.

$$\kappa_x = -w_{,xx} \tag{27}$$

Here, ϵ_{xx} is the midline axial strain and κ_x is the curvature. Also subscript $,x$ denotes the derivative with respect to the axial coordinate x. The strain energy $\mathcal{E}^{(s)}$ and the kinetic energy $\mathcal{E}^{(k)}$ of an uniform beam of length L are

$$\mathcal{E}^{(s)} = \frac{ES}{2}\int_0^L [(u_{,x})^2 + u_{,x}(w_{,x})^2 + (1/4)(w_{,x})^4]dx + \frac{EI}{2}\int_0^L (w_{,xx})^2 dx \tag{28}$$

$$\mathcal{E}^{(k)} = \frac{\rho S}{2}\int_0^L [(\dot{u})^2 + (\dot{w})^2]dx \tag{29}$$

Here, E, ρ, L, S, and I are Young's modulus, density (mass per unit volume), length, area of cross section, and area moment of inertia of the cross section of the beam, respectively, and a superposed dot denotes differentiation with respect to time t. Similarly the work expression can be written as

$$\mathcal{W} = \int_0^L (H_x du + H_y dw + M dw_{,x})dx \tag{30}$$

Here H_x, H_y, and M are the axial force, transverse force, and bending moment, respectively.

3.2 Finite Element Model for Beams With Immovable Ends. The procedure followed here, for FEM discretization of vibrating beams, is similar to standard methods (see, e.g., Ref. [10]). However, in this particular problem, the standard beam element needs a slight modification. This modification is necessitated because the usual linear interpolation for the axial deformation results in discontinuities during residual computation in Newton's scheme. Hence, a quadratic interpolation is taken for the axial deformation. A standard Hermitian interpolation is used for bending. Hence, the beam element used in this present problem has a total of seven degrees of freedom: three axial at three axial nodes and two transverse and two rotational degrees of freedom at the end nodes. These degrees of freedom can be written as

$$\mathbf{u} = [u_1 \quad u_2 \quad u_3]$$

$$\mathbf{w} = [w_1 \quad w_2]$$

$$\theta = [w_{,x1} \quad w_{,x2}]$$

Now, the values of the primary deformations $\mathbf{u}$ and $\mathbf{w}$ inside the elements can be interpolated from the above nodal values using

$$\begin{bmatrix} u(x,t) \\ w(x,t) \end{bmatrix} = \begin{bmatrix} N^{(I)}(x) & 0 \\ 0 & N^{(0)}(x) \end{bmatrix} \cdot \begin{bmatrix} q^{(I)}(t) \\ q^{(O)}(t) \end{bmatrix} \tag{31}$$

wherein

$$[N^{(I)}(x)] = [N_1 \quad N_2 \quad N_3], \quad [N^{(O)}] = [P_1 \quad P_2 \quad P_3 \quad P_4] \tag{32}$$

$$[q^{(I)}(t)] = [u_1 \quad u_2 \quad u_3]^T, \quad [q^{(O)}(t)] = [w_1 \quad \theta_1 \quad w_2 \quad \theta_2] \tag{33}$$

Here N_k and P_k are the quadratic Lagrange and cubic (Hermite polynomials) interpolation functions, respectively, and $q^{(I)}$ and $q^{(O)}$ contain the appropriate nodal degrees of freedom. Now, define

$$D = w_{,x}, \quad [G] = [N^{(O)}_{,x}], \quad [B^{(I)}] = [N^{(I)}_{,x}], \quad [B^{(O)}] = -[N^{(O)}_{,xx}] \tag{34}$$

Substitution of the interpolations from Eq. (31) into the work energy expressions from Eqs. (28)–(30) and use of Hamilton's principle lead to the following element level equations [32]:

$$\begin{bmatrix} M^{(I)} & 0 \\ 0 & M^{(0)} \end{bmatrix} \cdot \begin{bmatrix} \ddot{q}^{(I)}(t) \\ \ddot{q}^{(O)}(t) \end{bmatrix} + \begin{bmatrix} K^{(I)} & 0 \\ 0 & K^{(0)} \end{bmatrix} \cdot \begin{bmatrix} q^{(I)}(t) \\ q^{(O)}(t) \end{bmatrix} + \begin{bmatrix} 0 & K^{IO} \\ 2K^{(IO)T} & K^{(NI)} \end{bmatrix} \cdot \begin{bmatrix} q^{(I)}(t) \\ q^{(O)}(t) \end{bmatrix} = \begin{bmatrix} P^{(I)}(t) \\ P^{(O)}(t) \end{bmatrix} \tag{35}$$

In the above:

$$[M^{(I)}] = \frac{\rho S}{2}\int_0^L [N^{(I)}]^T[N^{(I)}]dx$$

$$[M^{(O)}] = \frac{\rho S}{2}\int_0^L [N^{(O)}]^T[N^{(O)}]dx \tag{36}$$

$$[K^{(I)}] = ES\int_0^L [B^{(I)}]^T[B^{(I)}]dx$$

$$[K^{(O)}] = EI\int_0^L [B^{(O)}]^T[B^{(O)}]dx \tag{37}$$

$$[K^{(IO)}] = \frac{ES}{2}\int_0^L [B^{(I)}]^T[DG]dx$$

$$[K^{(NI)}] = \frac{ES}{2}\int_0^L [DG]^T[DG]dx \tag{38}$$

$$[P] = \int_0^L \begin{pmatrix} N^{(I)} & 0 \\ 0 & N^{(O)} \end{pmatrix}^T \begin{pmatrix} \bar{H}_x \\ \bar{H}_y \\ \bar{M} \end{pmatrix} dx \tag{39}$$

where L is the length of the finite element and $[\bar{H}]$ is the resultant traction on the midline of the beam. If one denotes $\xi = (I/S)^{1/2}$ as the radius of gyration of the beam cross section, one can observe a few interesting points about the relations just derived. The in-plane (axial) and out-of-plane (bending) matrices $[K^{(I)}]$ and $[K^{(O)}]$ are $\propto$ to S and $S\xi^2$, respectively; the matrix $[K^{(IO)}] \propto AS$, where A is the beam deflection, represents coupling between the axial and bending displacements; and the matrix $[K^{(NI)}] \propto A^2 S$ arises purely from the nonlinear axial strains. It is well known that for the linear theory $K^{(O)} \ll K^{(I)}$ as $\xi \to 0$. It is very interesting, however, to note that if A/ξ remains $\mathcal{O}(1)$ (moderately large deformation), the bending matrix $K^{(O)}$, which arises from the linear theory, and the matrix $K^{(NI)}$ from the nonlinear theory, remain of the same order as $\xi \to 0$ [32].

4 Newton's Scheme for Solving the Coupled Problem

Newton's method is an iterative root-finding algorithm that uses the first few terms of the Taylor series of a function $f: \mathbb{R} \to \mathbb{R}$ in the vicinity of a suspected root. The algorithm can be written for a one dimensional case as

$$x_{n+1} = x_n - \frac{f(x_n)}{f'(x_n)}, \quad n \geq 0$$

For the multivariate case, $\boldsymbol{f}: \mathbb{R}^p \to \mathbb{R}^p$,

$$\boldsymbol{x} \in \mathbb{R}^p : \boldsymbol{f}(\boldsymbol{x}) = \boldsymbol{0} \in \mathbb{R}^p$$
$$\boldsymbol{x}_{n+1} = \boldsymbol{x}_n - \boldsymbol{Jf}(\boldsymbol{x}_n)^{-1}\boldsymbol{f}(\boldsymbol{x}_n), \quad n \geq 0 \tag{40}$$

where $\boldsymbol{Jf}(\boldsymbol{x})$ denotes the Jacobian of the function $\boldsymbol{f}(\boldsymbol{x})$. It is straightforward to recast Eq. (40) in the context of the current problem by replacing the vector function $\boldsymbol{f}(\boldsymbol{x})$ by the relevant vector function for the present problem.

4.1 Residuals and Their Gradients. Newton's scheme is used to solve the entire system of equations of the coupled electro-mechanical problem together. The relevant vector functions used in the present case are called residuals. Equation (14) gives the electrical residual and Eq. (35) gives the mechanical residual. In addition, the auxiliary equation (24) is used in conjunction with Eq. (20) as an interdomain coupling equation. It must be noted that the primary variables are B and $\mathbf{U}=[\mathbf{u}\ \ \mathbf{w}\ \ \theta]$, respectively, the electrical and mechanical variables.

4.1.1 The Electrical Residual and Its Derivatives. The electrical residual can be formed from Eq. (14) as

$$R_E(\mathbf{U},B) = \phi(\mathbf{X}^+) + \int_{S_1^+-\hat{S}_1^+} \frac{\ln R(\mathbf{X}^+,\mathbf{Y})B(\mathbf{Y})}{2\pi\epsilon} dS(\mathbf{Y}) + \int_{\hat{S}_1^+} \frac{\ln R(\mathbf{X}^+,\mathbf{Y})B(\mathbf{Y})}{2\pi\epsilon} dS(\mathbf{Y}) + \int_{S_2^+} \frac{\ln R(\mathbf{X}^+,\mathbf{Y})B(\mathbf{Y})}{2\pi\epsilon} dS(\mathbf{Y}) \tag{41}$$

To compute the gradient of the electrical residual, one can rewrite Eq. (41) in standard BEM form using suitable interpolation functions:

$$\begin{pmatrix} \mathbf{R}_E(\mathbf{U}(\mathbf{X_1^+}),B(\mathbf{X_1})) \\ \vdots \\ \mathbf{R}_E(\mathbf{U}(\mathbf{X_N^+}),B(\mathbf{X_N})) \end{pmatrix} = \begin{pmatrix} \phi(\mathbf{X_1^+}) \\ \vdots \\ \phi\mathbf{X_N^+} \end{pmatrix} + \begin{pmatrix} \Upsilon_{11} & & \Upsilon_{1N} \\ \vdots & \ddots & \vdots \\ \Upsilon_{N1} & & \Upsilon_{NN} \end{pmatrix} \begin{pmatrix} B(\mathbf{X_1}) \\ \vdots \\ B(\mathbf{X_N}) \end{pmatrix} \tag{42}$$

where subscripts $1,\ldots,N$ denote the value of the variable at the corresponding node positions and $[\Upsilon]$ is the matrix of BEM integration constants, which depends on both the geometry and interpolation functions used in the problem. One can differentiate Eq. (42) with respect to $B(\mathbf{X})$ and arrive at the following expression:

$$\frac{\partial R_E}{\partial \mathbf{B}}(\mathbf{U},B) = [\Upsilon] \tag{43}$$

The other residual can be computed by differentiating Eq. (41) with respect to the mechanical variable $\mathbf{U}$. Now using

$$\frac{\partial R}{\partial \mathbf{U}(\mathbf{X})} = -\frac{\mathbf{R}}{R} \tag{44a}$$

$$\frac{\partial R}{\partial \mathbf{U}(\mathbf{Y})} = \frac{\mathbf{R}}{R} \tag{44b}$$

one gets

$$\frac{\partial R_E}{\partial \mathbf{U}(\mathbf{X}^+)}(\mathbf{U},B) = -\int_{S_1^+-\hat{S}_1^+} \frac{\mathbf{R}(\mathbf{X}^+,\mathbf{Y})B(\mathbf{Y})}{2\pi\epsilon R^2} dS(\mathbf{Y}) - \fint_{\hat{S}_1^+} \frac{\mathbf{R}(\mathbf{X}^+,\mathbf{Y})B(\mathbf{Y})}{2\pi\epsilon R^2} dS(\mathbf{Y}) - \int_{S_2^+} \frac{\mathbf{R}(\mathbf{X}^+,\mathbf{Y})B(\mathbf{Y})}{2\pi\epsilon R^2} dS(\mathbf{Y}) + \fint_{\hat{S}_1^+} \frac{\mathbf{R}(\mathbf{X}^+,\mathbf{Y})B(\mathbf{X})}{2\pi\epsilon R^2} dS(\mathbf{Y}). \tag{45}$$

The first three terms on the right hand side of Eq. (45) are obtained by applying Eq. (44*a*) to Eq. (41), while the last one is obtained by applying Eq. (44*b*) and using $\partial R_E/\partial \mathbf{U}|_{\mathbf{Y}=\mathbf{X}^+}$. The second and the fourth term on the right hand side of Eq. (45) can be combined into a single term:

$$-\int_{\hat{S}_1} \frac{\mathbf{R}(\mathbf{X}^+,\mathbf{Y})(B(\mathbf{Y})-B(\mathbf{X}))}{2\pi\epsilon R^2} dS(\mathbf{Y}) \tag{46}$$

which is only weakly singular.

4.1.2 The Mechanical Residuals and Their Gradients. The mechanical residual can be written as

$$R_M(\mathbf{U},B) = \begin{bmatrix} M^{(I)} & 0 \\ 0 & M^{(0)} \end{bmatrix} \cdot \begin{bmatrix} \ddot{q}^{(I)}(t) \\ \ddot{q}^{(O)}(t) \end{bmatrix} + \begin{bmatrix} K^{(I)} & 0 \\ 0 & K^{(0)} \end{bmatrix} \cdot \begin{bmatrix} q^{(I)}(t) \\ q^{(O)}(t) \end{bmatrix} + \begin{bmatrix} 0 & K^{IO} \\ 2K^{(IO)T} & K^{(NI)} \end{bmatrix} \cdot \begin{bmatrix} q^{(I)}(t) \\ q^{(O)}(t) \end{bmatrix} - [P] \tag{47}$$

The last term of the above equation is the load term and contains information of the electrical influence. Using Eq. (20) as well as the relations,

$$\overline{\mathbf{H}} = \mathbf{H}^+ + \mathbf{H}^-, \quad \mathbf{N} = \mathbf{N}^+ = -\mathbf{N}^-, \quad \mathbf{F} = \mathbf{F}^+ = \mathbf{F}^- \tag{48}$$

one gets

$$\overline{\mathbf{H}} = -\frac{AB}{2J\epsilon}\frac{\mathbf{N}\cdot\mathbf{F}^{-1}}{|\mathbf{N}\cdot\mathbf{F}^{-1}|^2} \tag{49}$$

where $A=\Sigma^+-\Sigma^-$.

From Eq. (47),

$$\frac{\partial R_M}{\partial B}(\mathbf{U},B) = -\frac{\partial[P]}{\partial B} \tag{50}$$

The gradient $\partial R_M/\partial \mathbf{U}$ has two parts. The first part comes from the first two terms of the right side of Eq. (47) (It must be noted from Eq. (33) that $[q^{(I)}]$ and $[q^{(O)}]$ involve the displacement components as well as twists. Also, the stiffness matrices $[K^{(IO)}]$ and $[K^{(NI)}]$ involve slopes.) The second part of the gradient requires evaluation of the derivative of the load vector, which in turn involves computation of $\partial \mathbf{F}/\partial \mathbf{U}$ and $\partial J/\partial \mathbf{U}$, together with the application of the chain rule. For these computations, it is useful, in general, to use the formulas

$$\frac{\partial F_{ij}}{\partial U_k} = \frac{\partial F_{ij}}{\partial X_m}F_{mk}^{-1}, \quad \frac{\partial J}{\partial U_k} = J\frac{\partial F_{ij}}{\partial U_k}F_{ji}^{-1}, \quad \frac{\partial \mathbf{F}^{-1}}{\partial \mathbf{U}} = -\mathbf{F}^{-1}\cdot\frac{\partial \mathbf{F}}{\partial \mathbf{U}}\cdot\mathbf{F}^{-1} \tag{51}$$

It is noted that, in the present case, the deformation gradient can be written down as

$$\mathbf{F} = \begin{bmatrix} 1+u_{,x} & 0 \\ w_{,x} & 1 \end{bmatrix} \tag{52}$$

Now, with $w_{,x}=\theta$, one has

$$\mathbf{F} = \begin{bmatrix} 1+u_{,x} & 0 \\ \theta & 1 \end{bmatrix} \tag{53}$$

Also, $J=\det(\mathbf{F})=1+u_{,x}$.

Finally, the auxiliary equation, Eq. (24), is viewed as

$$\frac{1}{2}A = f(\mathbf{U},B) \tag{54}$$

and is used within each Newton iteration.

5 Dynamic Analysis of MEMS

The computational procedures for dynamic analysis of MEMS are considered next. The governing equation for the dynamic response of MEMS is

$$\mathbf{M}\ddot{\mathbf{U}}(t) + \mathbf{K}\mathbf{U}(t) = \mathbf{F}(\mathbf{U}(t),\Sigma(t)) \tag{55}$$

Here, $\mathbf{U}(t)$ is the displacement vector, $\Sigma(t)$ is the charge density, and the dots indicate the time derivatives. $\mathbf{M}$ and $\mathbf{K}$ are, respectively, the consistent mass matrix and stiffness matrix. $\mathbf{F}(\mathbf{U}(t),\Sigma(t))$ represents the electrostatic force, which depends on the charge distribution $\Sigma(t)$. Equation (55) can be solved using several direct integration methods when the forces are linear in displacement [9]. However, many of these methods are not directly applicable to MEMS. Two methods applicable to MEMS analysis are the central difference method and the Newmark method. Equation (55) is solved for $\mathbf{U}(t)$ with the initial conditions

$$\mathbf{U}(0) = \mathbf{0}$$
$$\dot{\mathbf{U}}(0) = \mathbf{0} \tag{56}$$

Now one can define $\dot{\mathbf{U}}=\mathbf{v}$ and $\ddot{\mathbf{U}}=\mathbf{a}$ and discretize the time period $[0\ \ T]$ into $[t_1, t_2, \ldots, t_n, t_{n+1}, \ldots, t_N]$ with $t_1=0$ and $t_N=0$. Consider a typical time interval $[t_n\ \ t_{n+1}]$. Assume that the solution is known at time t_n, i.e., $[\mathbf{U_n}, \mathbf{v_n}, \mathbf{a_n}]$ are known, and the unknown quantities at t_{n+1} are $[\mathbf{U_{n+1}}, \mathbf{v_{n+1}}, \mathbf{a_{n+1}}]$. In the present work, the Newmark method has been employed to update the variables.

5.1 The Newmark Method. The Newmark method [33] is a widely used time integration scheme for dynamic analysis in finite element modeling. There are various ways of implementing the Newmark scheme. The version, which is used in the present work, is called the *a*-form [11]. Define *predictors*:

$$\widetilde{\mathbf{U}}_{\mathbf{n+1}} = \mathbf{U_n} + \Delta t \mathbf{v_n} + \frac{\Delta t^2}{2}(1-2\beta)\mathbf{a_n}$$
$$\widetilde{\mathbf{v}}_{\mathbf{n+1}} = \mathbf{v_n} + (1-\gamma)\Delta t \mathbf{a_n} \tag{57}$$

The next step is to use the predictors to obtain the actual quantities

$$\mathbf{U_{n+1}} = \widetilde{\mathbf{U}}_{\mathbf{n+1}} + \beta \Delta t^2 \mathbf{a_n}$$
$$\mathbf{v_{n+1}} = \widetilde{\mathbf{v}}_{\mathbf{n+1}} + \gamma \Delta t \mathbf{a_{n+1}} \tag{58}$$

Here β and γ are the algorithmic parameters that are fine-tuned for integration accuracy and numerical stability. For a discussion on the effect of these parameters on the performance on the algorithm, see Ref. [11].

To start the process, $\mathbf{a_0}$ can be calculated from

$$\mathbf{Ma_0} = -\mathbf{KU}(0) + \mathbf{F}(\mathbf{U}(0), \Sigma(0)) \tag{59}$$

To march forward in time for acceleration, one needs to solve the time discrete version of the dynamic equation (55):

$$\mathbf{Ma}_{n+1} + \mathbf{KU}_{n+1} = \mathbf{F}(\mathbf{U}_{n+1}, \Sigma_{n+1}) \tag{60}$$

This equation set is nonlinear and would be solved using the Newton scheme.

5.2 Implicit Time Integration. Finally, time integration for the problem is implemented using the Newmark scheme utilizing Newton's scheme. The method follows closely from Belytschko et al. [34]. Using the version of BEM derived in the current work, one can recast Eq. (55) as

$$\mathbf{M}\ddot{\mathbf{U}}(t) + \mathbf{KU}(t) = \mathbf{f}^{\text{elec}}(\mathbf{U}(t), B(t)) \tag{61}$$

Here $\mathbf{f}^{\text{elec}}(\mathbf{U}(t), B(t))$ denotes the entire force loading term obtained through BEM analysis of the electrostatic problem.

Now define

$$\mathbf{R}(\mathbf{U}, B) = \begin{pmatrix} R_E \\ R_M \end{pmatrix} \tag{62}$$

Here, $\mathbf{R}$ is the grand residual for the problem. The Newton iterative scheme is essentially

$$\begin{pmatrix} \frac{\partial R_E}{\partial B} & \frac{\partial R_E}{\partial \mathbf{U}} \\ \frac{\partial R_M}{\partial B} & \frac{\partial R_M}{\partial \mathbf{U}} \end{pmatrix}^{(k)} \cdot \begin{pmatrix} \Delta B \\ \Delta \mathbf{U} \end{pmatrix}^{(k)} = -\begin{pmatrix} R_E \\ R_M \end{pmatrix}^{(k)} \tag{63}$$

$$\mathbf{U}^{(k+1)} = \mathbf{U}^{(k)} + \Delta \mathbf{U}^{(k)}, \quad B^{(k+1)} = B^{(k)} + \Delta B^{(k)} \tag{64}$$

Superscripts are used to denote the iteration step and subscripts for the Newmark integrator. Starting with $k=0$, Eq. (63) is iterated until convergence. At convergence, $\mathbf{R}^{(k)} \equiv R(\mathbf{U}^{(\mathbf{k})}, B^{(k)}) \to \mathbf{0}$. This iteration helps one find the value of $\mathbf{a_n}$ needed at each step of time integration through an update of $\mathbf{U}_{\mathbf{n}}^{(\mathbf{k})}$. The algorithm for the coupled scheme is described as:

1. Solve BEM on ∂B for applied voltage and compute the traction $\mathbf{H}_0$ from Eq. (20).
2. Set initial values of displacement $\mathbf{U_0}$ and velocity $\mathbf{v_0}$ to $\mathbf{0}$ and compute initial acceleration using $\mathbf{a_0}=\mathbf{M^{-1}H_0}$.
3. Set $\mathbf{a}_{n+1}^{(0)}=\mathbf{a}_n$, $\mathbf{v}_{n+1}^{(0)}=\mathbf{v}_n$ and $\mathbf{U}_{n+1}^{(0)}=\mathbf{U}_n$.
4. Estimate $\widetilde{\mathbf{U}}_{n+1}$ and $\widetilde{\mathbf{v}}_{n+1}$ from $\mathbf{U}_n$ and $\mathbf{v}_n$ using Eq. (57).
5. $B_{n+1}^{(0)}=B_n$.
6. Set $k=1$.
7. Newton iteration for time step $n+1$.

(a) Use Eqs. (41) and (47) to compute the value of requisite residuals $B=B_{n+1}^{(k)}$ and $\mathbf{U}=\mathbf{U}_{n+1}^{(k)}$.
(b) Use Eqs. (43) and (45) to get residual gradient for the electrical part, where $B=B_{n+1}^{(k)}$ and $\mathbf{U}=\mathbf{U}_{n+1}^{(k)}$.
(c) Similarly proceed to compute the other four gradients from the relevant equations.
(d) Update acceleration as $\mathbf{a}_{n+1}^{(k)}=1/\beta\Delta t^2(\mathbf{U}_{n+1}^{(k)}-\widetilde{\mathbf{U}}_{n+1})$ and $\mathbf{v}_{n+1}^{(k)}=\widetilde{\mathbf{v}}_{n+1}+\gamma\Delta t\mathbf{a}_{n+1}^{(k)}$.
(e) $R_M^{(k)}=R_M^{(k)}+\mathbf{Ma}_{n+1}^{(k)}$ and $\partial R_M/\partial \mathbf{U}|^{(k)}=\partial R_M/\partial \mathbf{U}|^{(k)}+1/(\beta\Delta t^2)\mathbf{M}$.
(f) Plug the above residuals into Eq. (63) and solve for the increments.
(g) Use Eq. (64), to update the primary variables.
(h) Compute the tolerance, $\text{Tol}=\|\mathbf{U}_{n+1}^{(k)}-\mathbf{U}_{n+1}^{(k-1)}\|/\|\mathbf{U}_{n+1}^{(k-1)}\| \times 100\%$.
(i) Update $k=k+1$.
(j) If tolerance is high, repeat from step (7).

8. $\mathbf{a}_{n+1}=\mathbf{a}_{n+1}^{(k)}$, $\mathbf{v}_{n+1}=\mathbf{v}_{n+1}^{(k)}$, $\mathbf{U}_{n+1}=\mathbf{U}_{n+1}^{(k)}$.
9. $B_{n+1}=B_{n+1}^{(k)}$.
10. $n=n+1$ and repeat from step (3) until required time limit is reached.

6 Numerical Verification

6.1 Code Verification. The computer code for the thin beam Lagrangian BEM has been carefully verified at several stages.

6.1.1 BEM for Region Exterior to a Thin Flat Beam. The BEM code has been carefully verified by comparing the charge densities obtained with the values reported by Liu and Shen [35]. The charge density obtained at the midpoint of the thin beam has been found to agree within 1% of that reported by Liu and Shen [35] in the thin beam limit.

6.1.2 FEM for Thin Beam. The FEM formulation for deformable von Karman plates, presented earlier in Ref. [26], has been carefully verified and the code has also been independently verified for classical problems like bending deformation of beams and plates under uniform pressure.

6.1.3 FEM-BEM Coupling. FEM-BEM coupling has been carried out using Newton's method on the Lagrangian version and the results are discussed in Sec. 6.2.

6.2 Thin Beam Dynamics

6.2.1 Material Properties. Material properties used for silicon conductors are [36,37]

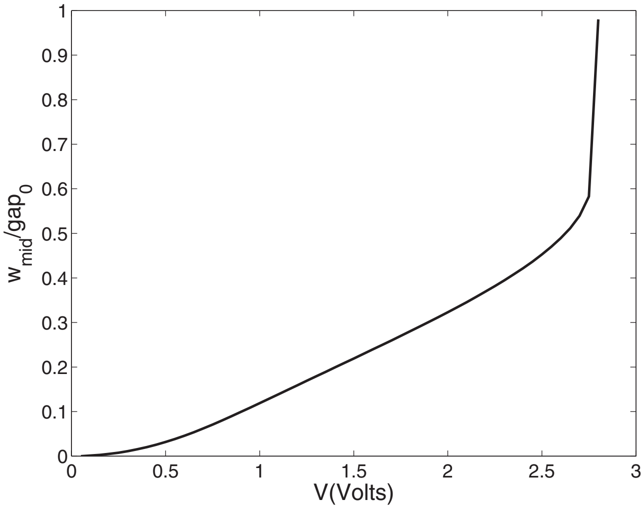

Fig. 6 Response behavior of MEMS beam. Pull in behavior.

$$E = 169 \text{ GPa}, \quad \nu = 0.22, \quad \rho = 2231 \text{ kg/m}^3, \quad \epsilon = 8.85 \times 10^{-12} \text{ F/m} \qquad (65)$$

Here, E, ν, and ρ refer to Young's modulus, Poisson's ratio, and the density of silicon, respectively, whereas ϵ is the permittivity of free space. It is assumed that the anisotropy is negligible and the beam is made up of polysilicon for this system.

6.2.2 The Problem. Dynamics of a MEMS beam (the silicon is doped so that it is a conductor), subjected to both dc and ac biases (electric field) is simulated using the BEM-FEM coupled approach described earlier in the paper. Each beam is in clamped-clamped configuration and two beams are used in order to have a zero voltage ground plane (plane of symmetry) midway between them. The MEMS beam is 1000 μm long, 40 μm wide, and 0.5 μm in height. The initial gap (gap_0) is 5 μm. The transverse midpoint deflection is denoted by w_{mid} and the amplitude of vibration of the midpoint of the beam, corresponding to ac excitation frequency ω, is denoted by $\text{Amp}(\omega)$.

6.2.3 Results. Figure 6 shows the normalized deflection as a function of voltage for a quasistatic version with dc bias. The beam suffers instability when the gap reduces by approximately 57% of the initial value. This result agrees very well with the results obtained using reduced order modeling [38].

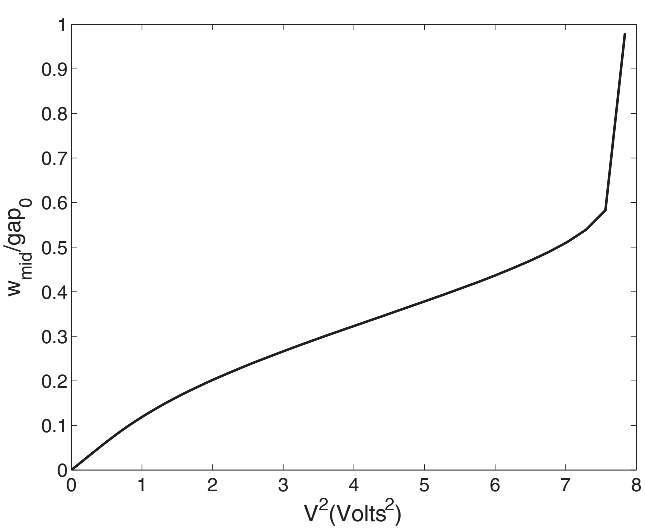

Fig. 7 Response behavior of MEMS beam. Competing nonlinearities.

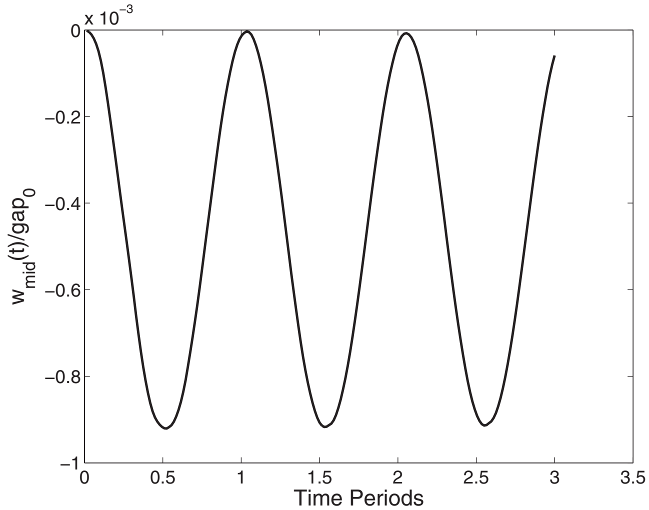

Fig. 8 Vibration under a dc bias

Figure 7 is a plot of normalized deflection as a function of voltage squared. Since electric force is proportional to the square of the voltage, the slope of this curve can be used to deduce the stiffness of the system. The presence of competing electrical and mechanical nonlinearities and their influence on the stiffness has been explained in Ref. [27]. The curve obtained here closely agrees with the results of the quasistatic 3D plate version of the problem [27].

The dynamic behavior of the beam under dc bias can be seen in Fig. 8. The time period in the plot refers to $T_p = 2\pi/\Omega_{\text{Nat}}$, where $\Omega_{\text{Nat}} = (4.73)^2 (EI/\rho S L^4)^{1/2}$ from the classical linear beam theory [39]. For the current beam geometry, $T_p \approx 226.75$ μs. The frequency of vibration agrees within 1% with this value for a relatively low excitation voltage, which limits the nonlinear effect.

The MEMS beam can also be excited using ac excitation and its response is also studied. When excited close to the beam's natural frequency, the beat phenomenon can be clearly observed from Fig. 9. A more informative picture can be obtained by plotting the amplitude for various frequencies of the ac excitation. Figure 10 shows the frequency response of the MEMS structure under a sinusoidal ac loading of constant amplitude and different frequencies. The curve has the characteristic flip-over profile with the

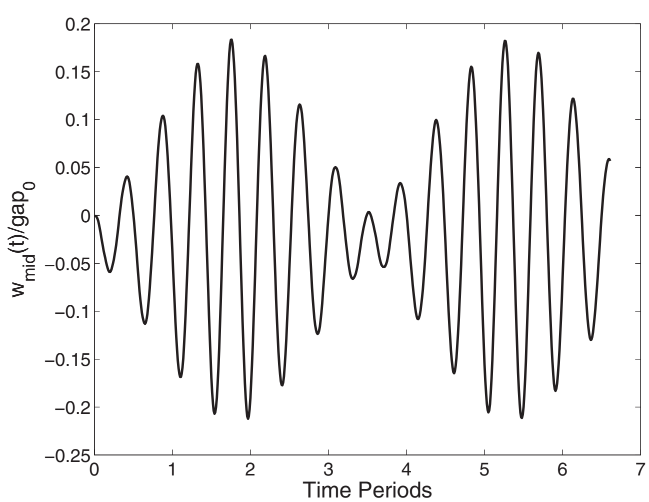

Fig. 9 Beat phenomenon for near natural frequency excitation

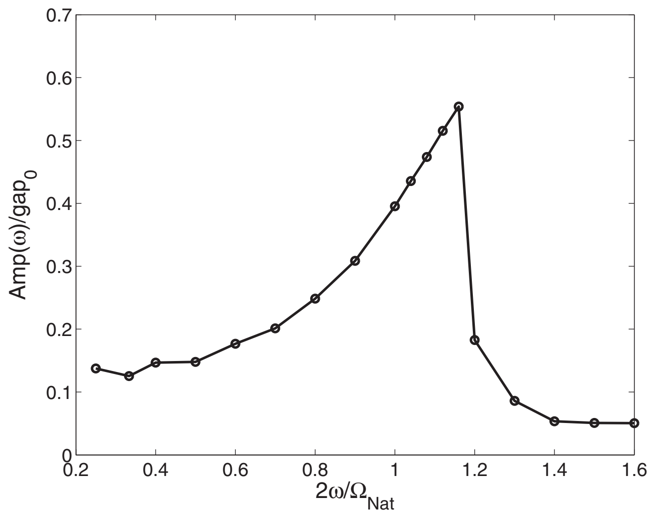

Fig. 10 Amplitude-frequency response of a MEM beam

peak. Since the electric force is proportional to the square of the applied voltage, the resonance peak occurs near half the natural frequency, as shown in Fig. 10.

7 Conclusions

Free and forced vibrations of thin MEMS beams caused by applied dc and ac excitations have been studied in this work. The BEM (a special version suitable for thin features) is used to model the exterior electrostatic charge distribution and forces, while the FEM is used to model moderately large deflections of thin beams. A fully Lagrangian description is employed for both the electrical and mechanical equations. Coupling of the BEM and FEM is carried out by the Newton scheme with time integration carried out by the Newmark method. Derivatives of the residuals necessary for the Newton method are carefully obtained by analytical differentiation of the relevant integral and FEM equations. Nonlinearities arise in this problem from the moderately large deflections of the beams, from the fact that the deformed shape of a beam affects the electrical forces on it, and the quadratic relationship between the charge density and the corresponding traction. Damping caused by the presence of fluid exterior to the beams is included in a companion paper [28] in which a Stokes flow model is employed for the fluid flow.

The code developed to simulate the coupled electro-mechanical problem is carefully verified by comparison with other solutions reported in the literature. The numerical results for the beam vibrations both free (under dc bias) and forced by ac excitation are presented here for selected problems. The approach presented in this paper can be extended to study vibrations of MEMS with plates or NEMS with nanowires and nanotubes in a straightforward manner. A static deformation analysis of plates is presented in Ref. [27], while charge distribution on conducting carbon nanotubes and semiconducting silicon nanowires have been studied in recent work [40,41].

Acknowledgment

This research has been supported by the National Science Foundation Grant No. CMS-0508466 to Cornell University.

References

[1] Frangi, A., and di Gioa, A., 2005, "Multipole BEM for Evaluating Damping Forces on MEMS," Comput. Mech., **37**(1), pp. 24–31.
[2] Roman, M., and Aubry, N., 2003, "Design and Fabrication of Electrostatically Actuated Synthetic Microjets," ASME, New York, **AMD-259**, pp. 517–524.
[3] Ko, S. C., Kim, Y. C., Lee, S. S., Choi, S. S., and Kim, S. R., 2003, "Micromachined Piezoelectric Membrane Acoustic Device," Sens. Actuators, A, **103**, pp. 130–134.
[4] Mukherjee, S., 1982, *Boundary Element Methods in Creep and Fracture*, Applied Science, London.
[5] Banerjee, P. K., 1994, *Boundary Element Methods in Engineering*, McGraw-Hill, Europe.
[6] Chandra, A., and Mukherjee, S., 1997, *Boundary Element Methods in Manufacturing*, Oxford University Press, New York.
[7] Bonnet, A., 1999, *Boundary Element Equation Methods for Solids and Fluids*, Wiley, Chichester, UK.
[8] Mukherjee, S., and Mukherjee, Y. X., 2005, *Boundary Methods: Elements, Contours and Nodes*, Taylor & Francis, London/CRC, Boca Raton, FL.
[9] Yang, T. Y., 1986, *Finite Element Structural Analysis*, Prentice-Hall, Englewood Cliffs, NJ.
[10] Zienkiewicz, O. C., and Taylor, R. L., 2005, *The Finite Element Method*, Vols. 1 and 2, 4th ed., McGraw-Hill, Berkshire, UK.
[11] Hughes, T. J. R., 2000, *The Finite Element Method: Linear Static and Dynamic Finite Element Analysis*, Dover, Mineola, NY.
[12] Senturia, S. D., Harris, R. M., Johnson, B. P., Kim, S., Nabors, K., Shulman, M. A., and White, J. K., 1992, "A Computer Aided Design System for Microelectromechanical Systems (MEMCAD)," J. Microelectromech. Syst., **1**, pp. 3–13.
[13] Nabors, K., and White, J., 1991, "FastCap: A Multi-Pole Accelerated 3-D Capcacitance Extraction Program," IEEE Trans. Comput.-Aided Des., **10**, pp. 1447–1459.
[14] Gilbert, J. R., Legtenberg, R., and Senturia, S. D., 1995, "3D Coupled Electromechanics for MEMS: Applications of CoSolve-EM," *Proceedings of the IEEE MEMS*, pp. 122–127.
[15] Shi, F., Ramesh, P., and Mukherjee, S., 1995, "Simulation Methods for Micro-Electro-Mechanical Structures (MEMS) With Applications to Microtweezer," Compos. Struct., **56**, pp. 769–783.
[16] Aluru, N. R., and White, J., 1997, "An Efficient Numerical Technique for Electromechanical Simulation of Complicated Microelectromechancial Structures," Sens. Actuators, A, **58**, pp. 1–11.
[17] Shi, F., Ramesh, P., and Mukherjee, S., 1996, "Dynamic Analysis of Micro-Electro-Mechanical Systems," Int. J. Numer. Methods Eng., **39**, pp. 4119–4139.
[18] Harrington, R. F., 1993, *Field Computation by Moment Methods*, IEEE, Piscataway, NJ.
[19] Bao, Z., and Mukherjee, S., 2004, "Electrostatic BEM for MEMS With Thin Conducting Plates and Shells," Eng. Anal. Boundary Elem., **28**, pp. 1427–1435.
[20] Bao, Z., and Mukherjee, S., 2005, "Electrostatic BEM for MEMS With Thin Beams," Commun. Numer. Methods Eng., **21**, pp. 297–312.
[21] Chuyan, S.-W., Liao, Y.-S., and Chen, J.-T., 2005, "Computational Study of the Effect of Finger Width and Aspect Ratios for the Electrostatic Levitating Force of MEMS Comb Drive," J. Microelectromech. Syst., **14**, pp. 305–312.
[22] Li, G., and Aluru, N. R., 2003, "Efficient Mixed-Domain Analysis of Electrostatic MEMS," IEEE Trans. Comput.-Aided Des., **22**, pp. 1228–1242.
[23] Li, G., and Aluru, N. R., 2002, "A Lagrangian Approach for Electrostatic Analysis of Deformable Conductors," J. Microelectromech. Syst., **11**, pp. 245–254.
[24] Shrivastava, V., Aluru, N. R., and Mukherjee, S., 2004, "Numerical Analysis of 3D Electrostatics of Deformable Conductors Using a Lagrangian Approach," Eng. Anal. Boundary Elem., **28**, pp. 583–591.
[25] De S. K., and Aluru N. R., 2004, "Full-Lagrangian Schemes for Dynamic Analysis of Electrostatic MEMS," IEEE J. Microelectromech. Syst., **13**, pp. 737–758.
[26] Mukherjee, S., Bao, Z., Roman, M., and Aubry, N., 2005, "Nonlinear Mechanics of MEMS Plates With a Total Lagrangian Approach," Compos. Struct., **13**, pp. 758–768.
[27] Telukunta, S., and Mukherjee, S., 2006, "Fully Lagrangian Modeling of MEMS With Thin Plates," J. Microelectromech. Syst., **15**(4), pp. 795–810.
[28] Ghosh, R., and Mukherjee, S., 2009, "Fully Lagrangian Modeling of Dynamics of MEMS With Thin Beams—Part II: Damped Vibrations," ASME J. Appl. Mech., **76**, p. 051008.
[29] Mukherjee, S., 2000, "Finite Parts of Singular and Hypersingular Integrals With Irregular Boundary Source Points," Eng. Anal. Boundary Elem., **24**, pp. 767–776.
[30] Nanson, E. J., 1877, "Note on Hydrodynamics," The Messenger of Mathematics, **7**, pp. 182–183.
[31] Reddy, J. N., 2004, *Introduction to Nonlinear Finite Element Analysis*, Oxford University Press, New York.
[32] Bao, Z., Mukherjee, S., Roman, M., and Aubry, N., 2004, "Nonlinear Vibrations of Beams, Strings, Plates and Membranes Without Initial Tension," ASME J. Appl. Mech., **71**(4), pp. 551–559.
[33] Newmark, N. M., 1959, "A Method of Computation for Structural Dynamics," J. Engrg. Mech. Div., **85**, pp. 67–94.
[34] Belytschko, T., Liu, W. K., and Moran, B., 2000, *Nonlinear Finite Element for Continua and Structures*, Wiley, Chichester, West Sussex, England.
[35] Liu, Y. J., and Shen, L., 2007, "A Dual BIE Approach for Large-Scale Modelling of 3-D Electrostatic Problems With the Fast Multipole Boundary Element Method," Int. J. Numer. Methods Eng., **71**(7), pp. 837–855.
[36] Petersen, K. E., 1982, "Silicon as a Mechanical Material," Proc. IEEE, **70**, pp. 420–455.
[37] Sharpe, W. N., Jr., 2001, "Mechanical Properties of MEMS Materials," *The*

MEMS Handbook, CRC, Boca Raton, FL.
[38] Younis, M. I., Abdel-Rahman, E. M., and Nayfeh, A. H., 2003, "A Reduced-Order Model for Electrically Actuated Microbeam-Based MEMS," J. Microelectromech. Syst., **12**(5), pp. 672–680.
[39] Hurty, W. C., and Rubinstein, M. F., 1964, *Dynamics of Structures*, Prentice-Hall, Englewood Cliffs, NJ.
[40] Chen, H., and Mukherjee, S., 2006, "Charge Distribution on Thin Conducting Nanotubes—Reduced 3-D Model," Int. J. Numer. Methods Eng., **68**(5), pp. 503–524.
[41] Chen, H., Mukherjee, S., and Aluru, N., 2008, "Charge Distribution on Thin Semiconducting Silicon Nanowire," Comput. Methods Appl. Mech. Eng., **197**, pp. 3366–3377.

Fully Lagrangian Modeling of Dynamics of MEMS With Thin Beams—Part II: Damped Vibrations

Ranajay Ghosh
Graduate Student
Department of Theoretical and Applied Mechanics,
Cornell University,
Thurston Hall,
Ithaca, NY 14853

Subrata Mukherjee
Professor
Fellow ASME
Department of Theoretical and Applied Mechanics and Sibley School of Mechanical and Aerospace Engineering,
Cornell University, Kimball Hall,
Ithaca, NY 14853

*Micro-electro-mechanical systems (MEMS) often use beam or plate shaped conductors that are very thin with $h/L \approx \mathcal{O}(10^{-2}-10^{-3})$ (in terms of the thickness h and length L of a beam or side of a square plate). A companion paper (Ghosh and Mukherjee, 2009, "Fully Lagrangian Modeling of Dynamics of MEMS With Thin Beams—Part I: Undamped Vibrations," ASME J. Appl. Mech., **76**, p. 051007) addresses the coupled electromechanical problem of MEMS devices composed of thin beams. A new boundary element method (BEM) is coupled with the finite element method (FEM) by Ghosh and Mukherjee, and undamped vibrations are addressed there. The effect of damping due to the surrounding fluid modeled as Stokes flow is included in the present paper. Here, the elastic field modeled by the FEM is coupled with the applied electric field and the fluid field, both modeled by the BEM. As for the electric field, the BEM is adapted to efficiently handle narrow gaps between thin beams for the Stokes flow problem. The coupling of the various fields is carried out using a Newton scheme based on a Lagrangian description of the various domains. Numerical results are presented for damped vibrations of MEMS beams.* [DOI: 10.1115/1.3086786]

Keywords: boundary integral equations, boundary element method, singular integrals, micro-electro-mechanical systems, damping, Stokes flow, aspect ratio, thin beam, Newton scheme

1 Introduction

The field of micro-electro-mechanical systems (MEMSs) is a very broad one that includes fixed or moving microstructures, encompassing micro-electro-mechanical, microfluidic, micro-electro-fluidic-mechanical, micro-opto-electro-mechanical, and micro-thermal-mechanical devices and systems. MEMS usually consists of released microstructures that are suspended and anchored or captured by a hub-cap structure and set into motion by mechanical, electrical, thermal, acoustical, or photonic energy source(s).

Typical MEMS structures consist of arrays of thin plates with cross sections in the order of microns and lengths in the order of tens to hundreds of microns. Sometimes, MEMS structural elements are beams. An example is a small rectangular silicon beam with length in the order of millimeters and thickness in the order of microns that deforms when subjected to electric fields. Owing to its small size, significant forces and/or deformations can be obtained with the application of low voltages (≈ 10 V). Examples of devices that utilize vibrations of such beams are comb drives, synthetic micro-jets ([1] – for chemical mixing, cooling of electronic components, micropropulsion, turbulence control, and other macroflow properties), microspeakers [2], etc. Numerical simulation of electrically actuated MEMS devices has been carried out for approximately a decade by using the boundary element method (BEM) (see, e.g., Refs. [3–7]) to model the exterior electric field and the finite element method (FEM) (see, e.g., Refs. [8–10]) to model deformation of the structure. The commercial software package MEMCAD [11], for example, uses the commercial FEM software package ABAQUS for mechanical analysis, together with a BEM code FASTCAP [12] for the electric field analysis. Other examples of such work are Refs. [13–15] as well as Refs. [1,16] for dynamic analysis of MEMS.

The present paper focuses on the influence of fluidic damping on the dynamic behavior of MEMS devices made up of very thin conducting beams. Analysis of the electromechanical problem has already been carried out in the companion paper [17]. Ye et al. [18] showed Stokes flow to be adequate for modeling the fluidic effects in MEMS systems. This model is used in the current paper. A convenient way to model such a problem is to assume beams with vanishing thickness and recast the boundary integral equations (BIEs) in terms of sum of tractions and difference of velocities between the upper and lower surfaces, respectively [19]. Further simplification can be obtained by noting that the difference of velocities between the upper and lower surfaces, for very thin beams, is negligible, and the sum of tractions between upper and lower surfaces is equal to the net traction on the beam.

The BEM developed in Refs. [11,13–16,18] performs the electrical analysis on the deformed configuration (Eulerian approach). Therefore, the geometry of the structure must be updated before an electrical analysis is performed during each relaxation iteration. This procedure increases computational effort and introduces additional numerical errors since the deformed geometry must be computed at every stage. Hence, a Lagrangian approach, which obviates the need to carry out calculations based on the deformed shapes of a structure [20], has been used in the current work. The fluid equations are then coupled with the electric and mechanical equations developed in Ref. [17] to form a total Lagrangian version of the entire problem. Finally, a Newton scheme developed analogous to Ref. [21] is used to solve the entire coupled nonlinear problem.

This paper starts with modeling the fluid. The fluid is assumed to be Stokes. A conventional BIE representing the fluid is first

Contributed by the Applied Mechanics Division of ASME for publication in the JOURNAL OF APPLIED MECHANICS. Manuscript received July 18, 2008; final manuscript received January 5, 2009; published online June 18, 2009. Review conducted by Robert M. McMeeking.

presented and a thin beam approximation follows. The equations are then reformulated in a total Lagrangian framework. Weak fluid compressibility to reduce high stresses generated in very small gaps is discussed next. This paper then proceeds to explain the Newton scheme for coupling the fluid domain with the electrical and mechanical domains. Numerical results are then presented and discussed. This paper concludes with a section on discussions of the results and scope for future research.

2 Damping Problem in a Stokes Fluid

An extensive literature exists on the subject of damping forces in MEMS. The key issue, of course, is the choice of a particular mathematical model in order to calculate the damping forces correctly. Various options exist, such as a squeeze film model (e.g., Ref. [22]), an incompressible steady Stokes flow model (e.g., Ref. [23]), an incompressible oscillatory Stokes flow model (e.g., Refs. [18,24]), inclusion [24] or exclusion of slip at the solid/fluid interface, and molecular dynamics (MD) simulation (e.g., Ref. [25]). The last option must be employed if continuum theory breaks down, as often happens at the nanoscale or due to extreme rarefaction of the surrounding air at very low pressures. Sometimes, even if continuum theory does apply, a quasisteady Stokes model may not be due to very high resonant frequencies (around 100 MHz [26]).

MEMS plates and beams, however, are typically tens to hundreds of micrometers long and with thickness in the order of micrometers [27]. There exists a regime where due to the micrometer-scales involved, the Reynolds numbers of the surrounding flow are generally small enough, and natural frequencies are low enough (in the range of 100 s of kilohertz) to allow the use of a steady-state Stokes flow (sometimes called creeping flow) model. Moreover, if the MEMS operate at pressures where the air can be treated as a continuum, the usual operating frequencies very often require an incompressible fluid model [23]. Further, in synthetic microjet applications, the medium surrounding the beam is typically a liquid for which an incompressible model is, of course, the appropriate one. Problems in which an incompressible steady-state Stokes model applies are of interest in this work. It is important to point out that numerical and experimental study of typical MEMS structures [18] demonstrates that a 3D, incompressible, no slip, oscillatory Stokes model can predict measured quality factors within 10%. Although only the steady Stokes model is employed in the present work, it is important to note that the forms of the integral equations used here remain unchanged for the oscillatory case, provided that the appropriate kernels for oscillatory flow are used in these integral equations [18,24].

2.1 Governing Equations. As discussed above, the Reynolds numbers of the surrounding flow are generally small enough to allow for the use of a steady-state Stokes flow (sometimes called creeping flow) model. The governing equations for the Stokes flow are as follows:

$$\nabla p(\mathbf{x}) - \mu \nabla^2 \mathbf{v}(\mathbf{x}) = \mathbf{0}, \quad \mathbf{x} \in B \tag{1}$$

$$\nabla \cdot \mathbf{v}(\mathbf{x}) = 0, \quad \mathbf{x} \in B \tag{2}$$

$$\mathbf{v}(\mathbf{x}) = \mathbf{g}(\mathbf{x}), \quad \mathbf{x} \in \partial B \tag{3}$$

In the above, $\mathbf{v}$ is the velocity, p is the pressure, and μ is the dynamic viscosity of the fluid. Also, B is the region *exterior* to the structure and ∂B is its boundary. The stress tensor σ inside the fluid and the fluid surface traction τ on the solid surface are defined by equations

$$\boldsymbol{\sigma}(\mathbf{x}) = -p(\mathbf{x})\mathbb{I} + \mu[\nabla \mathbf{v}(\mathbf{x}) + \nabla^T \mathbf{v}(\mathbf{x})], \quad \mathbf{x} \in B \tag{4}$$

$$\boldsymbol{\tau}(\mathbf{x}) = \boldsymbol{\sigma}(\mathbf{x}) \cdot \mathbf{n}(\mathbf{x}), \quad \mathbf{x} \in \partial B \tag{5}$$

where $\mathbf{n}$ is the unit outward normal to the fluid domain at a point on its boundary.

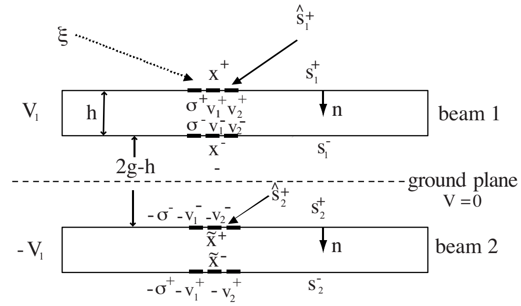

Fig. 1 Two parallel beams in a surrounding Stokes fluid

2.2 Interface Conditions. In addition to the governing equations, interface conditions on the velocity $\mathbf{v}$ and traction $\boldsymbol{\tau}$ are required to simulate the coupled dynamics of MEMS devices. The interface conditions for the fluid-solid interface can be written as

$$\begin{aligned} \mathbf{v}^f &= \mathbf{v}^s \\ \boldsymbol{\tau}^e - \boldsymbol{\tau}^f &= \boldsymbol{\tau}^s \end{aligned} \tag{6}$$

where superscripts f and s denote the fluid and solid sides of the interface, respectively, $\boldsymbol{\tau}^s$ is the total traction on the solid side, and $\boldsymbol{\tau}^e$ and $\boldsymbol{\tau}^f$ are the electric and fluid parts of the traction.

2.3 Stokes Flow: Standard BIE Formulation. The general BIE formulation of the governing differential equations of Sec. 2.2 can be written as [28]

$$v_i(\mathbf{x}) = g_i(\mathbf{x}) = \neq\!\!\!\!\!\int_{\partial B} T_{ij}(\mathbf{x},\mathbf{y}) v_j(\mathbf{y}) ds(\mathbf{y}) + \int_{\partial B} G_{ij}(\mathbf{x},\mathbf{y}) \tau_j(\mathbf{y}) ds(\mathbf{y}), \quad \mathbf{x} \in \partial B \tag{7}$$

where the Green's function G is

$$G_{ij}(\mathbf{x},\mathbf{y}) = \frac{1}{4\pi\mu}[-\delta_{ij} \ln r + r_{,i} r_{,j}] \tag{8}$$

and the traction kernel is

$$T_{ij}(\mathbf{x},\mathbf{y}) = T_{ijk}(\mathbf{x},\mathbf{y}) n_k(\mathbf{y}) \tag{9}$$

with

$$T_{ijk}(\mathbf{x},\mathbf{y}) = \frac{1}{\pi r} r_{,i} r_{,j} r_{,k} \tag{10}$$

In the above, $\mathbf{x}$ is a source point, $\mathbf{y}$ is a field point, r is the Euclidean distance between the source and field points, $r_{,i} = \partial r / \partial y_i = (y_i - x_i)/r$, and δ_{ij} are the components of the Kronecker delta. Also, the symbol $\neq\!\!\!\!\!\int$ denotes the finite part of the integral in the sense of Mukherjee [29,30].

2.4 BIE in Stokes Flow in Infinite Region Around Very Thin Beams. Analogous to the BIE for the electrostatic problem [31,32], consider the flow in a region outside of, in this case, a single thin beam. (One beam is considered for simplicity of explanation—flow around many beams can also be easily modeled.) It has been shown by Mukherjee et al. [19] that for a thin beam, with $\mathbf{x}^+ \in s^+$ (see Fig. 1),

$$v_i(\mathbf{x}^+) = g_i(\mathbf{x}^+) = \neq\!\!\!\!\!\int_{s^+} T_{ij}(\mathbf{x}^+,\mathbf{y}) w_j(\mathbf{y}) ds(\mathbf{y}) + \int_{s^+} G_{ij}(\mathbf{x}^+,\mathbf{y}) q_j(\mathbf{y}) ds(\mathbf{y}), \quad \mathbf{x}^+ \in s^+ \tag{11}$$

where $q_j = \tau_j^+ + \tau_j^-$, $w_j = v_j^+ - v_j^-$, and $s^+ = s_1^+ \cup s_2^+$.

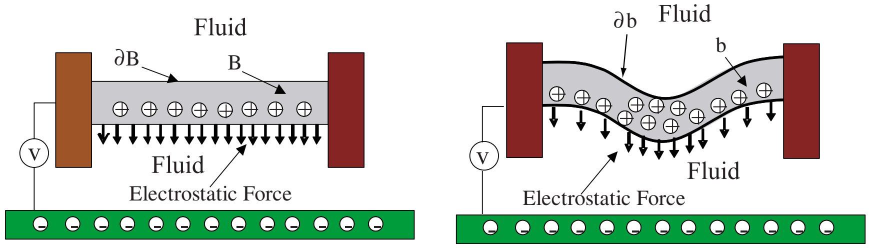

Fig. 2 Deformable clamped beam over a fixed ground plate

For a thin beam $v_j^+ \approx v_j^-$, causing the first integral on the right hand side to disappear in Eq. (11). The above equation then simplifies to

$$v_i(\mathbf{x}^+) = g_i(\mathbf{x}^+) = \int_{s^+} G_{ij}(\mathbf{x}^+,\mathbf{y}) q_j(\mathbf{y}) ds(\mathbf{y}), \quad \mathbf{x}^+ \in s^+ \tag{12}$$

It has been shown by Mukherjee et al. [19] that the null space of the kernel $\mathbf{G}$ in Eq. (12) is empty and this equation has a unique solution for any prescribed velocity $\mathbf{g}(\mathbf{x})$ on $\partial B = s^+ \cup s^-$. Thus Eq. (12) has the double advantage of avoiding ill behaved matrices resulting from thin structures and gaps as well as singularities present in $\mathbf{G}$ in Eq. (7) [19,28].

2.5 Lagrangian Version of the Stokes BIE. Using the same line of reasoning as for the electrical problem [17], one can derive the Lagrangian formulation of the Stokes flow BIE:

$$V_i(\mathbf{X}^+) = \int_{S^+} \frac{1}{4\pi\mu}\left(-\delta_{ij} \ln R(\mathbf{X}^+,\mathbf{Y}) + \frac{R(\mathbf{X}^+,\mathbf{Y})_i R(\mathbf{X}^+,\mathbf{Y})_j}{R(\mathbf{X}^+,\mathbf{Y})^2} \right) \bar{H}_j^{\text{flu}}(\mathbf{Y}) dS(\mathbf{Y}), \quad \mathbf{X}^+ \in S^+ \tag{13}$$

Here $R = R(\mathbf{X}^+,\mathbf{Y})$, $V_i(\mathbf{X}^+)$, and $\bar{H}_j^{\text{flu}}(\mathbf{Y})$ are, respectively, the Lagrangian description of the position, velocity, and the resultant fluidic surface traction. Please note that the resultant fluidic surface traction acting on the beam is $\mathbf{H}^{\text{flu}} = -\bar{\mathbf{H}}^{\text{flu}}$.

3 Compressible Stokes Flow

In view of the fact that real fluids are at least somewhat compressible (especially some gases), inclusion of compressibility in the Stokes flow model is investigated in this section. (A similar model is used in Ref. [33] for a different reason.) It is noted that inclusion of a small amount of compressibility in the model can help in convergence of the solutions by avoiding high stresses generated when the gap between two beams is very small (gap $\approx \mathcal{O}(0.005L)$).

It is first noted that the constitutive model for Stokes flow (Eq. (4)) is analogous to that for incompressible linear elasticity. This equation is now replaced by one analogous to that for compressible elasticity, i.e.,

$$\sigma(\mathbf{x}) = \lambda(\nabla \cdot \mathbf{v})\mathbb{I} + \mu[\nabla \mathbf{v}(\mathbf{x}) + \nabla^T \mathbf{v}(\mathbf{x})], \quad \mathbf{x} \in B \tag{14}$$

where

$$\lambda = \frac{2\mu\nu}{1-2\nu} \tag{15}$$

in terms of dynamic viscosity μ and a new material constant ν, which is analogous to Poisson's ratio for linear elasticity. Also, K, analogous to bulk modulus, is

$$K = \frac{2\mu(1+\nu)}{3(1-2\nu)} \tag{16}$$

and this is a measure of the compressibility of the fluid. It is well known that at the incompressibility limit $\nu \to \frac{1}{2}$ and both λ and $K \to \infty$.

Please note that Eq. (14) is identical to Eq. (1) in Ref. [33] where it is written in a different way by adding and subtracting the pressure term to the right hand side of Eq. (14).

The previous BIE formulation (Eq. (12)) remains the same except that instead of (Eq. (8)) one has

$$G_{ij}(\mathbf{x},\mathbf{y}) = \frac{1}{8\pi(1-\nu)\mu}[-(3-4\nu)\ln(r)\delta_{ij} + r_{,i}r_{,j}] \tag{17}$$

One can note that Eq. (17) reduces to Eq. (8) when $\nu \to \frac{1}{2}$.

4 Newton's Scheme for Solving the Coupled Problem

Newton's method is an iterative root-finding algorithm that uses the first few terms of the Taylor series of a function $f:\mathbb{R} \to \mathbb{R}$ in the vicinity of a suspected root. The algorithm can be written for a one dimensional case as

$$x_{n+1} = x_n - \frac{f(x_n)}{f'(x_n)}, \quad n \geq 0$$

For the multivariate case, $\boldsymbol{f}:\mathbb{R}^p \to \mathbb{R}^p$,

$$\begin{gathered} \boldsymbol{x} \in \mathbb{R}^p : \boldsymbol{f}(\boldsymbol{x}) = \boldsymbol{0} \in \mathbb{R}^p \\ \boldsymbol{x}_{n+1} = \boldsymbol{x}_n - \boldsymbol{J}\boldsymbol{f}(\boldsymbol{x}_n)^{-1}\boldsymbol{f}(\boldsymbol{x}_n), \quad n \geq 0 \end{gathered} \tag{18}$$

where $\boldsymbol{J}\boldsymbol{f}(\boldsymbol{x})$ denotes the Jacobian of the function $\boldsymbol{f}(\boldsymbol{x})$. It is straightforward to recast Eq. (18) in the context of the current problem by replacing the vector function $\boldsymbol{f}(\boldsymbol{x})$ by the relevant vector function for the present problem.

4.1 Coupled MEMS System. The system of interest in the present paper is a thin MEMS beam electrically actuated and vibrating in a fluid medium. The electromechanics of a typical system has been analyzed in Ref. [17], and the introduction of fluidic effects in this paper completes the full analysis of such a system. Figure 2 shows (as an example of such a MEMS device) a deformable, clamped beam over a fixed ground plane. The undeformed configuration is B with boundary ∂B. The beam deforms when a potential V is applied between the two conductors, and the deformed configuration is called b with boundary ∂b. The charge redistributes on the surface of the deformed beam, thereby changing the electrical force on it and this causes the beam to deform further. As the deformation starts, the damping effects due to fluids come into play. The system then undergoes vibrations, and the complete analysis of the system is carried out using the Newton scheme. The coupling of the mechanical and fluid equations involves continuity of velocity and equilibrium of traction. The fluid traction at the interface contributes as an additional external fluid force on the beam (see Eq. (6)).

4.2 Residuals and Their Gradients. The Newton scheme is used to solve equations for the entire system of the coupled electro-mechanical-fluid problem together. The relevant vector functions used in the present case are called residuals, which can be formed using the relevant governing equations, as shown in the companion paper [17]. For the sake of brevity the electrical, mechanical, and fluidic variables are denoted as E, M, and F respectively. Hence, the residuals are denoted, respectively, as R_E, R_M, and R_F. The gradient notation follows as $\partial R_E/\partial B = R_{EE}$, $\partial R_E/\partial \mathbf{U} = R_{EM}$, $\partial R_E/\partial \mathbf{H}^{\text{flu}} = R_{EF}$, and so on.

4.2.1 The Electrical Residual and Its Derivatives. One can recall from Ref. [17] that

$$R_E(\mathbf{U},B) = \phi(\mathbf{X}^+) + \int_{S_1^+ - \hat{S}_1^+} \frac{\ln R(\mathbf{X}^+,\mathbf{Y})B(\mathbf{Y})}{2\pi\epsilon} dS(\mathbf{Y}) + \int_{\hat{S}_1^+} \frac{\ln R(\mathbf{X}^+,\mathbf{Y})B(\mathbf{Y})}{2\pi\epsilon} dS(\mathbf{Y}) + \int_{S_2^+} \frac{\ln R(\mathbf{X}^+,\mathbf{Y})B(\mathbf{Y})}{2\pi\epsilon} dS(\mathbf{Y}) \tag{19}$$

where B is the sum of charges of the upper and lower surfaces of a thin beam, ϵ is the permittivity of the medium, and ϕ is the electric potential (voltage) on the surface. From the physics of the problem, it is clear that there is no direct influence of fluidic variables on the electric field and hence one can at once deduce that R_{EE} and R_{EM} remain the same as in Ref. [17] and

$$R_{EF} = \frac{\partial R_E}{\partial \mathbf{H}^{\text{flu}}} = [0] \tag{20}$$

4.2.2 The Mechanical Residuals and Their Gradients. The mechanical residual can be formed along the lines of Ref. [17] except that the force due to the fluid is added to the forcing term. One can recall from Ref. [17] that the mechanical residual can be written as

$$R_M(\mathbf{U},B,\mathbf{H}^{\text{flu}}) = \begin{bmatrix} M^{(I)} & 0 \\ 0 & M^{(0)} \end{bmatrix} \cdot \begin{bmatrix} \ddot{q}^{(I)}(t) \\ \ddot{q}^{(O)}(t) \end{bmatrix} + \begin{bmatrix} K^{(I)} & 0 \\ 0 & K^{(0)} \end{bmatrix} \cdot \begin{bmatrix} q^{(I)}(t) \\ q^{(O)}(t) \end{bmatrix} + \begin{bmatrix} 0 & K^{IO} \\ 2K^{(IO)T} & K^{(NI)} \end{bmatrix} \cdot \begin{bmatrix} q^{(I)}(t) \\ q^{(O)}(t) \end{bmatrix} - [P] \tag{21}$$

The last term of the above equation is the load term and contains electrical and fluidic forces:

$$[P] = [P]^{\text{elec}} + [P]^{\text{flu}} = \int_0^L \begin{pmatrix} N^{(I)} & 0 \\ 0 & N^{(O)} \end{pmatrix}^T \begin{pmatrix} \bar{H}_x^{\text{elec}} \\ \bar{H}_y^{\text{elec}} \\ \bar{M}_x^{\text{elec}} \end{pmatrix} - \int_0^L \begin{pmatrix} N^{(I)} & 0 \\ 0 & N^{(O)} \end{pmatrix}^T \begin{pmatrix} \bar{H}_x^{\text{flu}} \\ \bar{H}_y^{\text{flu}} \\ \bar{M}_x^{\text{flu}} \end{pmatrix} \tag{22}$$

where "elec" and "flu" superscripts denote, respectively, the electrical and fluidic components of tractions and forces.

It can be deduced that R_{ME} remains the same as in Ref. [17]. R_{MM} also remains the same assuming that $\overline{\mathbf{H}}^{\text{flu}}$ does not depend on $\mathbf{U}$. The remaining gradient R_{MF} would entail the computation of $\partial R_M/\partial \mathbf{H}^{\text{flu}} = -\partial [P]/\partial \mathbf{H}^{\text{flu}}$. The load has two parts, electrostatic and the fluidic. The fluidic part alone contributes to the gradient. One can note using a suitable finite element interpolation

$$\mathbf{P}^{\text{flu}}(\mathbf{x}) = bL[N(\mathbf{x})]\{\mathbf{H}^{\text{flu}}\} \tag{23}$$

where b and L are beam depth and length, $\mathbf{P}^{\text{flu}}$ is the fluid force, $[N(\mathbf{x})]$ is a suitable interpolation matrix, and $\{\mathbf{H}^{\text{flu}}\}$ is the nodal fluid traction. Using Eq. (23), one can compute R_{MF}:

$$R_{MF} = \partial R_M/\partial \mathbf{H}^{\text{flu}} = -\partial [P]/\partial \mathbf{H}^{\text{flu}} = -\partial \mathbf{P}^{\text{flu}}/\partial \mathbf{H}^{\text{flu}} = -bL[N(\mathbf{x})]\mathbb{1} \tag{24}$$

4.2.3 The Fluidic Residuals and Their Gradients. The fluidic residual can be written as

$$R_{Fi}(\mathbf{U},\mathbf{H}^{\text{flu}}) = V_i(\mathbf{X}^+) + \int_{S^+} \frac{1}{4\pi\mu}\left(-\delta_{ij}\ln R(\mathbf{X}^+,\mathbf{Y}) + \frac{R(\mathbf{X}^+,\mathbf{Y})_i R(\mathbf{X}^+,\mathbf{Y})_j}{R(\mathbf{X}^+,\mathbf{Y})^2}\right) H_j^{\text{flu}}(\mathbf{Y}) dS(\mathbf{Y}), \quad \mathbf{X}^+ \in S^+ \tag{25}$$

where the index i denotes the component of the residual (axial or transverse). The above equation confirms the lack of coupling between the fluid and electric fields and hence $R_{FE}=0$. Computing R_{FF} requires the computation of the gradient of Eq. (25) with respect to H_k^{flu}:

$$\frac{\partial R_{Fi}}{\partial H_j^{\text{flu}}}(\mathbf{X}^+) = \int_{S^+} \frac{1}{4\pi\mu}\left(-\delta_{ij}\ln R(\mathbf{X}^+,\mathbf{Y}) + \frac{R(\mathbf{X}^+,\mathbf{Y})_i R(\mathbf{X}^+,\mathbf{Y})_j}{R(\mathbf{X}^+,\mathbf{Y})^2}\right) dS(\mathbf{Y}) \tag{26}$$

Finally, finding the residual with respect to the mechanical domain, R_{FM} needs computing gradient with respect to the displacement $\mathbf{U}$ variable. One can rewrite Eq. (25) as

$$R_{Fi}(\mathbf{U},\mathbf{H}^{\text{flu}}) = V_i(\mathbf{X}^+) + \int_{S^+} \frac{1}{4\pi\mu} K_{ij}(\mathbf{X}^+,\mathbf{Y}) H_j^{\text{flu}}(\mathbf{Y}) dS(\mathbf{Y}) \tag{27}$$

where

$$K_{ij}(\mathbf{X}^+,\mathbf{Y}) = -\delta_{ij}\ln R(\mathbf{X}^+,\mathbf{Y}) + \frac{R(\mathbf{X}^+,\mathbf{Y})_i R(\mathbf{X}^+,\mathbf{Y})_j}{R(\mathbf{X}^+,\mathbf{Y})^2} \tag{28}$$

Now one can write

$$\frac{\partial K_{ij}(\mathbf{X}^+,\mathbf{Y})}{\partial U_k(\mathbf{X}^+)} = D_{ijk}(\mathbf{X}^+,\mathbf{Y}) \tag{29}$$

where

$$D_{ijk} = \frac{\delta_{ij}R_k}{R^2} - \frac{\delta_{ik}R_j}{R^2} - \frac{\delta_{jk}R_i}{R^2} + 2\frac{R_iR_jR_k}{R^4} \tag{30}$$

Following the derivation of Eq. (46) in Ref. [17],

$$\frac{\partial R_{Fi}(\mathbf{U},\mathbf{H}^{\text{flu}})}{\partial U_k(\mathbf{X}^+)} = \int_{S_1^+ - \hat{S}_1^+} \frac{1}{4\pi\mu} D_{ijk}(\mathbf{X}^+,\mathbf{Y}) H_j^{\text{flu}}(\mathbf{Y}) dS(\mathbf{Y}) + \int_{S_2^+} \frac{1}{4\pi\mu} D_{ijk}(\mathbf{X}^+,\mathbf{Y}) H_j^{\text{flu}}(\mathbf{Y}) dS(\mathbf{Y}) + \int_{\hat{S}_1^+} \frac{1}{4\pi\mu} D_{ijk}(\mathbf{X}^+,\mathbf{Y})(H_j^{\text{flu}}(\mathbf{Y}) - H_j^{\text{flu}}(\mathbf{X})) dS(\mathbf{Y}) \tag{31}$$

5 Dynamic Analysis of MEMS

We are now in a position to consider the computational procedures for dynamic analysis of MEMS. The governing equation for the dynamic response of the MEMS system is

$$\mathbf{M}\ddot{\mathbf{U}}(t) + \mathbf{K}\mathbf{U}(t) = \mathbf{F}^{\mathrm{elec}}(B(t),\mathbf{U}(t)) + \mathbf{F}^{\mathrm{flu}}(\mathbf{H}^{\mathrm{flu}}(\dot{\mathbf{U}}(t))) \tag{32}$$

Here, $\mathbf{U}$ is the displacement vector and dots indicate time derivatives. $\mathbf{M}$ and $\mathbf{K}$ are, respectively, the consistent mass matrix and stiffness matrix. $\mathbf{F}^{\mathrm{elec}}(B(t))$ represents the electrostatic force, which depends on the charge distribution $B(t)$, and $\mathbf{F}^{\mathrm{flu}}$ represents the fluidic force vector, which depends on the traction distribution $\mathbf{H}^{\mathrm{flu}}=\mathbf{H}^{\mathrm{flu}}(\dot{\mathbf{U}})$, where $\dot{\mathbf{U}}$ is the velocity vector. Equation (32) can be solved using several direct integration methods when the forces are linear in displacement [8]. However, many of these methods are not directly applicable to MEMS. Two methods applicable to MEMS analysis are the central difference method and the Newmark method. Equation (32) is solved for $\mathbf{U}(t)$ with the initial conditions

$$\begin{aligned}\mathbf{U}(0) &= \mathbf{0}\\ \dot{\mathbf{U}}(0) &= \mathbf{0}\end{aligned} \tag{33}$$

Now one can define $\dot{\mathbf{U}}=\mathbf{v}$ and $\ddot{\mathbf{U}}=\mathbf{a}$ and discretize the time period $[0\ \ T]$ into $[t_1,t_2,\ldots,t_n,t_{n+1},\ldots,t_N]$ with $t_1=0$ and $t_N=T$. Consider a typical time interval $[t_n\ \ t_{n+1}]$. Assuming that the solution is known at time t_n, i.e., $[\mathbf{U_n},\mathbf{v_n},\mathbf{a_n}]$ are known, the unknown quantities at t_{n+1} are $[\mathbf{U_{n+1}},\mathbf{v_{n+1}},\mathbf{a_{n+1}}]$. In the present work, the Newmark method has been employed to update the variables.

5.1 The Newmark Method. The Newmark method [34] is a widely used time integration scheme for dynamic analysis in finite element modeling. There are various ways of implementing the Newmark scheme, one which is used in the present work is called the a-form [10]. Define *predictors*

$$\begin{aligned}\tilde{\mathbf{U}}_{\mathbf{n+1}} &= \mathbf{U_n} + \Delta t\mathbf{v_n} + \frac{\Delta t^2}{2}(1-2\beta)\mathbf{a_n}\\ \tilde{\mathbf{v}}_{\mathbf{n+1}} &= \mathbf{v_n} + (1-\gamma)\Delta t\mathbf{a_n}\end{aligned} \tag{34}$$

The next step is to use the predictors to obtain the actual quantities

$$\begin{aligned}\mathbf{U_{n+1}} &= \tilde{\mathbf{U}}_{\mathbf{n+1}} + \beta\Delta t^2\mathbf{a_n}\\ \mathbf{v_{n+1}} &= \tilde{\mathbf{v}}_{\mathbf{n+1}} + \gamma\Delta t\mathbf{a_{n+1}}\end{aligned} \tag{35}$$

Here β and γ are algorithmic parameters that are fine tuned for integration accuracy and numerical stability. For a discussion on the effect of these parameters on the performance on the algorithm, see Ref. [10].

To start the process, $\mathbf{a_0}$ can be calculated from

$$\mathbf{M}\ddot{\mathbf{a}}(0) = -\mathbf{K}\mathbf{U}(0) + \mathbf{F}^{\mathrm{elec}}(B(0),\mathbf{U}(\mathbf{0})) + \mathbf{F}^{\mathrm{flu}}(\mathbf{H}^{\mathrm{flu}}(0)) \tag{36}$$

To march forward in time for acceleration, one needs to solve the time discrete version of the dynamic equation (32),

$$\mathbf{M}\mathbf{a}_{n+1} + \mathbf{K}\mathbf{U}_{n+1} = \mathbf{F}^{\mathrm{elec}}(B_{n+1},\mathbf{U}_{n+1}) + \mathbf{F}^{\mathrm{flu}}(\mathbf{H}^{\mathrm{flu}}_{n+1}) \tag{37}$$

This equation set is nonlinear and is solved using the Newton scheme.

5.2 Implicit Time Integration. Finally, time integration for the problem is implemented using the Newmark scheme utilizing Newton's scheme. The method follows closely from Belytschko et al. [35].

Write Eq. (32) as

$$\mathbf{M}\ddot{\mathbf{U}}(t) + \mathbf{K}\mathbf{U}(t) = \mathbf{f}(B(t),\mathbf{U}(t),\mathbf{H}^{\mathrm{flu}}(t)) \tag{38}$$

Here $\mathbf{f}(B(t),\mathbf{U}(t),\mathbf{H}^{\mathrm{flu}}(t))$ denotes the entire force loading term obtained through BEM analysis. One can define

$$\mathbf{R}(\mathbf{U},B,\mathbf{H}^{\mathrm{flu}}) = \begin{pmatrix} R_E \\ R_M \\ R_F \end{pmatrix} \tag{39}$$

Here, $\mathbf{R}$ is the grand residual for the problem. The Newton iterative scheme is essentially

$$\begin{pmatrix} R_{EB} & R_{EM} & R_{EF} \\ R_{ME} & R_{MM} & R_{MF} \\ R_{FE} & R_{FM} & R_{FF} \end{pmatrix}^{(k)} \cdot \begin{pmatrix} \Delta B \\ \Delta\mathbf{U} \\ \Delta\mathbf{H}^{\mathrm{flu}} \end{pmatrix}^{(k)} = -\begin{pmatrix} R_E \\ R_M \\ R_F \end{pmatrix}^{(k)} \tag{40}$$

$$\mathbf{U}^{(k+1)} = \mathbf{U}^{(k)} + \Delta\mathbf{U}^{(k)},\quad B^{(k+1)} = B^{(k)} + \Delta B^{(k)},\quad \mathbf{H}^{\mathrm{flu}(k+1)} = \mathbf{H}^{\mathrm{flu}(k)} + \Delta\mathbf{H}^{\mathrm{flu}(k)} \tag{41}$$

Superscripts denote a Newton iteration step and subscripts a Newmark integrator step. Starting with $k=0$, Eq. (40) is iterated until convergence. At convergence, $\mathbf{R}^{(k)}\equiv R(\mathbf{U}^{(\mathbf{k})},B^{(k)},\mathbf{V}^{(\mathbf{k})})\rightarrow\mathbf{0}$. This iteration helps one to find the value of $\mathbf{a_n}$ needed at each step of time integration through an update of $\mathbf{U}^{(\mathbf{k})}_{\mathbf{n}}$. The algorithm for the coupled scheme is described below.

1. Solve BEM on ∂B for applied voltage and compute the traction $\mathbf{H_0}$ from Ref. [17].
2. Set initial values of displacement $\mathbf{U_0}$ and velocity $\mathbf{v_0}$ to $\mathbf{0}$ and compute initial acceleration using $\mathbf{a_0}=\mathbf{M^{-1}H_0}$.
3. Set $\mathbf{a}^{(0)}_{n+1}=\mathbf{a}_n$, $\mathbf{v}^{(0)}_{n+1}=\mathbf{v}_n$, and $\mathbf{U}^{(0)}_{n+1}=\mathbf{U}_n$.
4. Estimate $\tilde{\mathbf{U}}_{n+1}$ and $\tilde{\mathbf{v}}_{n+1}$ from $\mathbf{U}_n$ and $\mathbf{v}_n$ using Eq. (34).
5. $B^{(0)}_{n+1}=B_n$ and $\mathbf{H}^{\mathrm{flu}(0)}_{n+1}=\mathbf{H}^{\mathrm{flu}}_n$.
6. Set $k=1$.
7. Newton iteration for time step $n+1$:
   (a) Use Eqs. (19), (21), and (25) to compute the value of requisite residuals. $B=B^{(k)}_{n+1}$, $\mathbf{U}=\mathbf{U}^{(k)}_{n+1}$, and $\mathbf{H}^{\mathrm{flu}}=\mathbf{H}^{\mathrm{flu}(k)}_{n+1}$.
   (b) Use Ref. [17] and Eq. (20) to get residual gradient for the electrical part, where $B=B^{(k)}_{n+1}$, $\mathbf{U}=\mathbf{U}^{(k)}_{n+1}$, and $\mathbf{H}^{\mathrm{flu}}=\mathbf{H}^{\mathrm{flu}(k)}_{n+1}$.
   (c) Similarly proceed to compute the other six gradients from the relevant equations.
   (d) Update acceleration as $\mathbf{a}^{(k)}_{n+1}=1/\beta\Delta t^2(\mathbf{U}^{(k)}_{n+1}-\tilde{\mathbf{U}}_{n+1})$ and $\mathbf{v}^{(k)}_{n+1}=\tilde{\mathbf{v}}_{n+1}+\gamma\Delta t\mathbf{a}^{(k)}_{n+1}$.
   (e) $R^{(k)}_M=R^{(k)}_M+\mathbf{M}\mathbf{a}^{(k)}_{n+1}$ and $\partial R_M/\partial\mathbf{U}|^{(k)}=\partial R_M/\partial\mathbf{U}|^{(k)}+1/(\beta\Delta t^2)\mathbf{M}$.
   (f) Plug the above residuals to Eq. (40) and solve for the increments.
   (g) Use Eq. (40) to compute the increments.
   (h) Use Eq. (41) to update the primary variables.
   (i) Compute the tolerance, $\mathrm{tol}=(\|\mathbf{U}^{(k)}_{n+1}-\mathbf{U}^{(k-1)}_{n+1}\|)/\|\mathbf{U}^{(k-1)}_{n+1}\|\times 100\%$.
   (j) Update $k=k+1$.
   (k) If tolerance is high, repeat from step (7).
8. $\mathbf{a}_{n+1}=\mathbf{a}^{(k)}_{n+1}$, $\mathbf{v}_{n+1}=\mathbf{v}^{(k)}_{n+1}$, and $\mathbf{U}_{n+1}=\mathbf{U}^{(k)}_{n+1}$.
9. $B_{n+1}=B^{(k)}_{n+1}$ and $\mathbf{H}^{\mathrm{flu}}_{n+1}=\mathbf{H}^{\mathrm{flu}(k)}_{n+1}$.
10. $n=n+1$ and repeat from step (3) until required time limit is reached.

6 Numerical Verification

6.1 Code Verification. The computer code with thin beam Lagrangian Stokes BEM has been carefully verified at several stages. The beam dimensions have been taken to be 1000×40

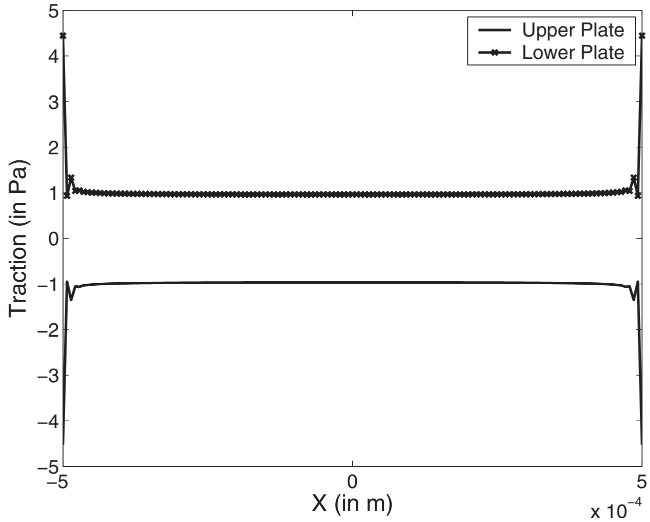

Fig. 3 Horizontal traction on plates for plane Couette flow

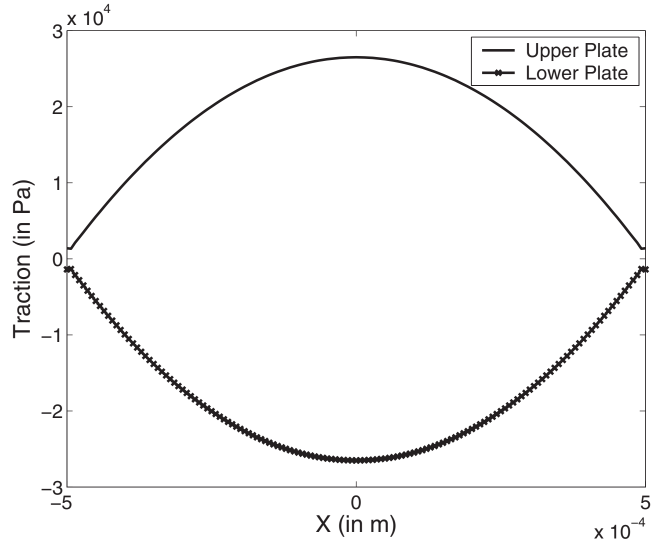

Fig. 4 Vertical traction on plates moving vertically toward each other

$\times 0.5\ \mu m^3$ and the dynamic viscosity is assumed to be 1×10^{-5} Pa s for the numerical results. The incompressible Stokes equations are employed in Secs. 6.1.1 and 6.1.2.

6.1.1 Plane Couette Flow. Couette flow refers to the flow between two parallel plates, one of which is moving with respect to the other. The analytical solution for this kind of flow is known. If the bottom plate is fixed and the top plate is moving with speed v_0 at a distance D from the latter and the fluid has dynamic viscosity μ, then the horizontal traction τ on the top surface can be written as

$$\tau = \mu \frac{v_0}{D} \tag{42}$$

It must be noted that the value of the traction at the bottom surface would be equal and opposite to the above.

For numerical verification the gap D between the plates has been taken to be 10 μm and the velocity of the top plate is 1 m/s. The analytical value of the horizontal traction in this case would be (from Eq. (42)) 1 Pa. The numerical results are shown in Fig. 3 and agree to within 3% of the analytical result.

6.1.2 Vertically Moving Plate. When the plates are moving vertically toward each other, to the best of the author's knowledge, there is no closed form solution. However, certain inferences can be drawn for this kind of flow.

For numerical verification, the initial gap D between the plates has been taken to be 10 μm and the velocity of the top plate is 1 m/s downward and that of the bottom plate is 1 m/s upward. Figure 4 shows the vertical traction generated by such motion. It can be deduced from the physics that the vertical traction would be equal and opposite on the two plates and will have maximum value at the center and decrease toward the sides as the fluid escapes. This trend can be clearly observed in the plot. Figure 5 shows a plot of the horizontal traction for this motion. One can deduce that as the plates move toward each other, they displace fluid from the central part of the plates to the periphery in opposite directions. Hence the horizontal traction should be antisymmetric with respect to the centerline on either side of the top plate. The exact same effect would be visible for the bottom plate via symmetry of the problem. This effect is clearly observed in the plot of horizontal traction.

6.1.3 Compressibility and Convergence. When the initial gap between the plates is reduced to $\mathcal{O}(0.005L)$ unrealistically large stresses result and convergence takes disproportionately larger time. The effect of incompressibility on convergence can be clearly seen in the plot presented here for such small gaps (see Fig. 6). The computing requirement increases very sharply as one approaches the incompressibility limit of $\nu \to \frac{1}{2}$.

It is noted, however, that the values of ν for air and water are approximately 0.499999999999 and 0.49999999999999, respectively, at room temperature. Hence, $\nu = \frac{1}{2}$ should be used for practical calculations involving these fluids.

6.2 Thin Beam Dynamics

6.2.1 Material Properties. Material properties used for silicon conductors are [36,37] as follows:

$$E = 169\ \text{GPa}, \quad \nu^s = 0.22, \quad \rho = 2231\ \text{kg/m}^3 \tag{43}$$

whereas properties of the surrounding medium are as follows:

$$\epsilon = 8.85 \times 10^{-12}\ \text{F/m}, \quad \mu = 1.0 \times 10^{-5}\ \text{Pa s}$$
$$\nu^f = 0.50 \quad (\text{except for Figs. 6 and 8}) \tag{44}$$

Here, E, ν^s, and ρ refer to Young's modulus, Poisson's ratio, and density of silicon, respectively, whereas ϵ, μ, and ν^f are the permittivity of free space, dynamic viscosity, and Poisson param-

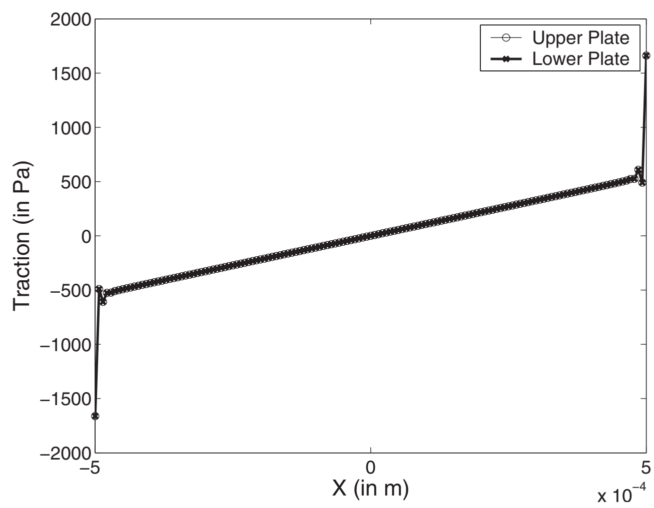

Fig. 5 Horizontal traction on plates moving vertically toward each other

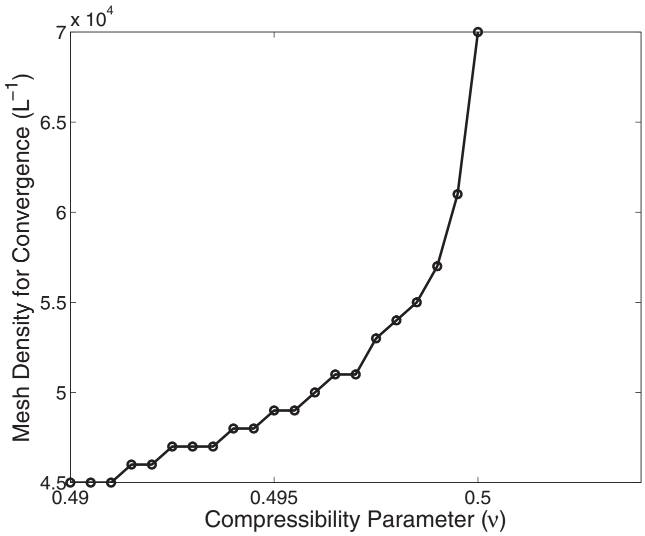

Fig. 6 Compressibility influence on convergence

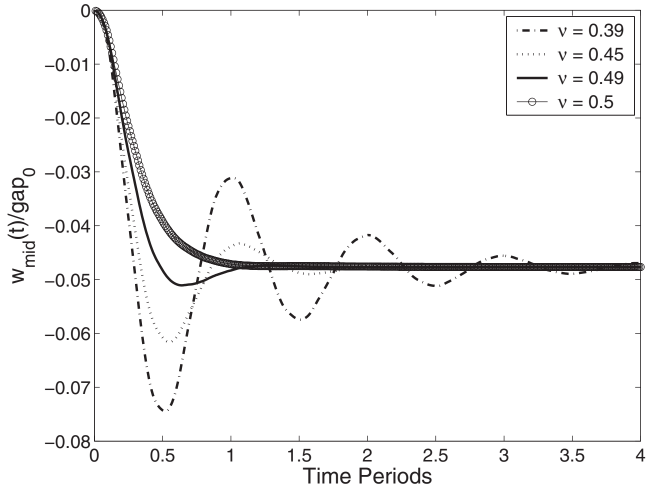

Fig. 8 Damped vibrations for various Poisson parameters (dc bias=0.5 V)

eter of air, respectively. It is assumed that the anisotropy is negligible, and the beam is made up of polysilicon for this system.

6.2.2 The Problem. Dynamics of a MEMS beam (the silicon is doped so that it is a conductor), subjected to both dc and ac biases (electric field) inside a fluid medium, is simulated using a BEM-FEM coupled approach described earlier in this paper. Each beam is clamped-clamped configuration, and two beams are used in order to have a zero voltage and velocity at the ground plane (plane of symmetry) midway between them (see Fig. 1). The MEMS beam is 1000 μm long, 40 μm wide, and 0.5 μm tall. The initial gap (gap_0) is 5 μm. The transverse midpoint deflection is denoted by w_{mid}.

6.2.3 Results. The dynamic behavior of the beam under a dc bias of 0.5 V can be seen in Fig. 7. The time period in the plot refers to $T_p=2\pi/\Omega_{Nat}$, where $\Omega_{Nat}=(4.73)^2(EI/\rho SL^4)^{1/2}$ from the classical linear beam theory [38]. For the current beam geometry, $T_p\approx 226.75$ μs.

It should be noted that incompressible Stokes flow in the current configuration causes overdamped motion, as shown in Fig. 7. The equilibrium position of the beam in Fig. 7 agrees to within 1% of the quasistatic value obtained in Ref. [17].

The effect of compressibility of the fluid medium is indicated in Fig. 8. It is clear that damping resistance offered by the fluid greatly increases as the Poisson parameter $\nu\rightarrow\frac{1}{2}$ (incompressible limit).

Figure 9 shows the response of the beam under an ac bias of $0.5\cos(0.5\Omega_{Nat}t)$. As the forcing is proportional to the square of the voltage, the response frequency is twice the applied frequency.

Figure 10 shows the response of the beam under a combined ac and dc bias. The dc component of the bias is 0.5 V and the ac component is $0.05\cos(0.5\Omega_{Nat}t)$. The beam vibrates about the quasistatic value corresponding approximately to the dc bias and with a frequency almost equal to $0.5\Omega_{Nat}$. This is expected since

$$\begin{aligned}F_{\text{elec}}(t) \propto V_{\text{app}}^2 &= (0.5+0.05\cos(0.5\Omega_{Nat}t))^2 = 0.25\\ &+ 0.05\cos(0.5\Omega_{Nat}t) + 0.0025\cos^2(0.5\Omega_{Nat}t) = 0.2513\\ &+ 0.05\cos(0.5\Omega_{Nat}t) + 0.0013\cos(\Omega_{Nat}t)\end{aligned} \tag{45}$$

From Eq. (45), the dominant ac term has frequency $0.5\Omega_{Nat}$, and the oscillations occur about the quasistatic response of 0.2513 V≈0.25 V (see Figs. 7 and 10).

7 Conclusions

Damped free and forced vibrations of thin MEMS beams surrounded by a fluid medium caused by applied dc and ac excita-

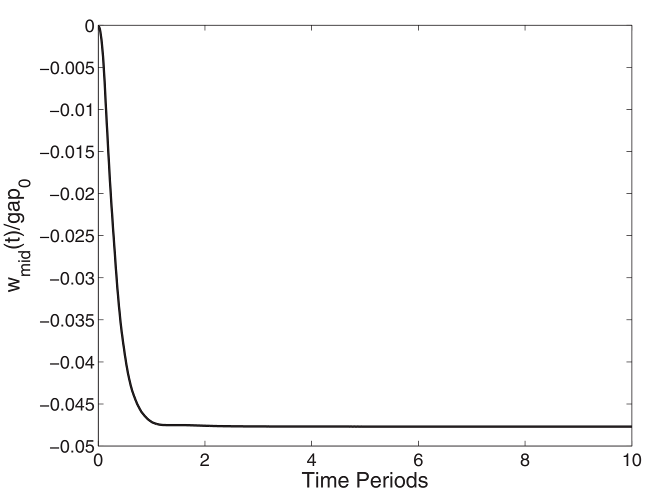

Fig. 7 Damped response for a dc bias of 0.5 V

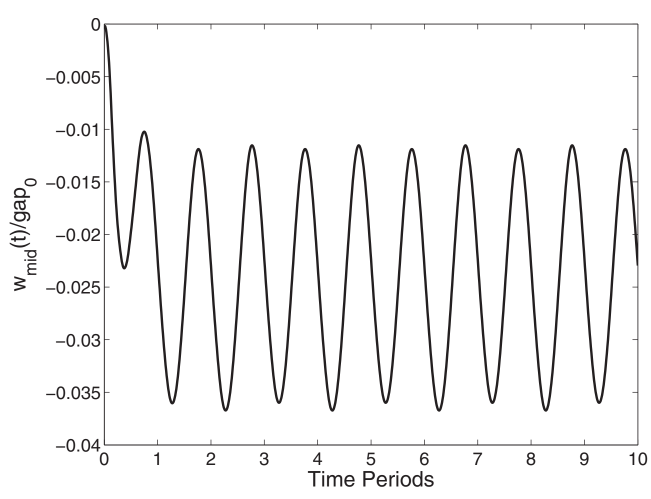

Fig. 9 Damped vibration for ac 0.5 cos(0.5$\Omega_{Nat}t$) V

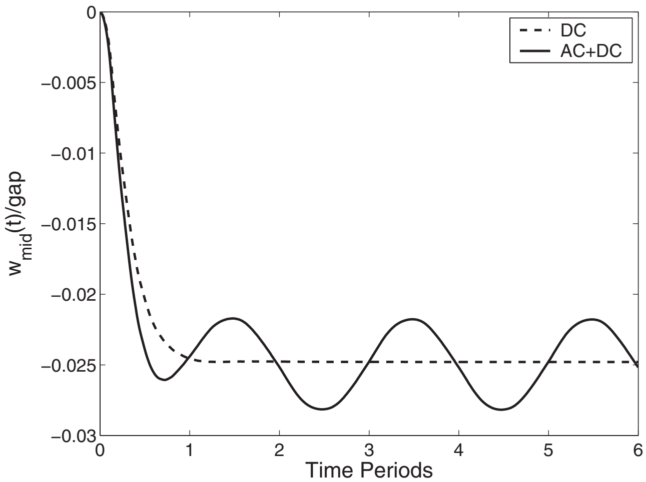

Fig. 10 Damped vibration for ac+dc bias of 0.5 +0.05 cos(0.5$\Omega_{Nat}t$) V

tions have been studied in this work. The BEM (a special version suitable for thin features) is used to model the exterior electric field as well as the fluid fields assuming Stokes flow. A fully Lagrangian version of the fluid flow equations is employed and integrated with the Lagrangian versions of the electrical and mechanical equations developed in the companion paper [17]. The fluidic domain is coupled with the mechanical domain through continuity of velocity and equilibrium of traction, and the entire Lagrangian coupled problem is solved using a Newton scheme with time integration carried out by the Newmark method. The derivatives of the residuals necessary for the Newton method (which now incorporate the fluid variables as well) are carefully obtained by analytic differentiation of the relevant integral and FEM equations.

An a posteriori check confirms that the typical Reynolds number for the examples given in this paper is $\mathcal{O}(10^{-3})$. This justifies the Stokes flow model employed here.

The code developed to simulate the coupled electro-mechanical-fluidic problem is carefully verified by comparison with other solutions reported in the literature. Numerical results for the beam vibrations both free (under dc bias) and forced by ac excitation are presented here for selected problems. The approach presented in this paper can be extended to study vibrations of MEMS with plates or nano-electro-mechanical-systems (NEMS) with nanowires and nanotubes in a straightforward manner.

It is noted that the method developed here can be extended to handle more detailed numerical calculations needed for complex configurations like variable thickness beams and plates with holes, etc., as compared with analytical or semi-analytical methods, which are usually restricted to problems with simple geometry. (A static deformation analysis of plates without a surrounding fluid has been presented in Ref. [39].)

A genuine numerical difficulty is encountered (requiring very small time steps and tighter tolerances for the Newton iteration) when the surrounding fluid is incompressible Stokes and the initial gap between the two beams is very small. A similar observation has also been made in Ref. [23]. Unfortunately, the common fluids such as air and water are very nearly incompressible with $\nu^f \approx 0.5$. It has also been found that the most important residual gradients needed for successful Newton's iteration are the ones with respect to their own domain variables, i.e., R_{EE}, R_{MM}, and R_{FF}.

Acknowledgment

This research was supported by National Science Foundation Grant No. CMS-0508466 to Cornell University.

References

[1] Roman, M., and Aubry, N., 2003, "Design and Fabrication of Electrostatically Actuated Synthetic Microjets," ASME, New York, **AMD-259**, pp. 517–524.
[2] Ko, S. C., Kim, Y. C., Lee, S. S., Choi, S. S., and Kim, S. R., 2003, "Micromachined Piezoelectric Membrane Acoustic Device," Sens. Actuators, A, **103**, pp. 130–134.
[3] Mukherjee, S., 1982, *Boundary Element Methods in Creep and Fracture*, Applied Science, London.
[4] Banerjee, P. K., 1994, *Boundary Element Methods in Engineering*, McGraw-Hill, Europe.
[5] Chandra, A., and Mukherjee, S., 1997, *Boundary Element Methods in Manufacturing*, Oxford University Press, New York.
[6] Bonnet, A., 1999, *Boundary Element Equation Methods for Solids and Fluids*, Wiley, Chichester, UK.
[7] Mukherjee, S., and Mukherjee, Y. X., 2005, *Boundary Methods: Elements, Contours and Nodes*, CRC, Boca Raton, FL.
[8] Yang, T. Y., 1986, *Finite Element Structural Analysis*, Prentice-Hall, Englewood Cliffs, NJ.
[9] Zienkiewicz, O. C., and Taylor, R. L., 2005, *The Finite Element Method*, Vols. 1 and 2, 4th ed., McGraw-Hill, Berkshire, UK.
[10] Hughes, T. J. R., 2000, *The Finite Element Method: Linear Static and Dynamic Finite Element Analysis*, Dover, Mineola, NY.
[11] Senturia, S. D., Harris, R. M., Johnson, B. P., Kim, S., Nabors, K., Shulman, M. A., and White, J. K., 1992, "A Computer Aided Design System for Microelectromechanical Systems (MEMCAD)," J. Microelectromech. Syst., **1**, pp. 3–13.
[12] Nabors, K., and White, J., 1991, "FastCap: A Multi-Pole Accelerated 3-D Capacitance Extraction Program," IEEE Trans. Comput.-Aided Des., **10**, pp. 1447–1459.
[13] Gilbert, J. R., Legtenberg, R., and Senturia, S. D., 1995, "3D Coupled Electromechanics for MEMS: Applications of CoSolve-EM," *Proceedings of the IEEE MEMS*, pp. 122–127.
[14] Shi, F., Ramesh, P., and Mukherjee, S., 1995, "Simulation Methods for Micro-Electro-Mechanical Structures (MEMS) With Applications to Microtweezer," Comput. Struct., **56**, pp. 769–783.
[15] Aluru, N. R., and White, J., 1997, "An Efficient Numerical Technique for Electromechanical Simulation of Complicated Microelectromechanical Structures," Sens. Actuators, A, **58**, pp. 1–11.
[16] Shi, F., Ramesh, P., and Mukherjee, S., 1996, "Dynamic Analysis of Micro-Electro-Mechanical Systems," Int. J. Numer. Methods Eng., **39**, pp. 4119–4139.
[17] Ghosh, R., and Mukherjee, S., 2009, "Fully Lagrangian Modeling of Dynamics of MEMS With Thin Beams—Part I: Undamped Vibrations," ASME J. Appl. Mech., **76**, p. 051007.
[18] Ye, W., Wang, X., Hemmert, W., Freeman, D., and White, J., 2003, "Air Damping Forces in Laterally Oscillatory Microresonators: A Numerical and Experimental Study," J. Microelectromech. Syst., **12**, pp. 557–566.
[19] Mukherjee, S., Telukunta, S., and Mukherjee, Y. X., 2005, "BEM Modeling of Damping Forces on MEMS With Thin Plates," Eng. Anal. Boundary Elem., **29**, pp. 1000–1007.
[20] Li, G., and Aluru, N. R., 2003, "Efficient Mixed-Domain Analysis of Electrostatic MEMS," IEEE Trans. Comput.-Aided Des., **22**, pp. 1228–1242.
[21] De, S. K., and Aluru, N. R., 2004, "Full-Lagrangian Schemes for Dynamic Analysis of Electrostatic MEMS," J. Microelectromech. Syst., **13**, pp. 737–758.
[22] Pan, F., Kubby, J., Peeters, E., Tran, A. T., and Mukherjee, S., 1998, "Squeeze Film Damping Effect on the Dynamic Response of a MEMS Torsion Mirror," J. Micromech. Microeng., **8**, pp. 200–208.
[23] Frangi, A., and di Gioa, A., 2005, "Multipole BEM for Evaluating Damping Forces on MEMS," Comput. Mech., **37**(1), pp. 24–31.
[24] Ding, J., and Ye, W., 2004, "A Fast Integral Approach for Drag Force Calculation Due to Oscillatory Slip Stokes Flows," Int. J. Numer. Methods Eng., **60**, pp. 1535–1567.
[25] Hutcherson, S., and Ye, W., 2004, "On the Squeeze Film Damping of Micro-Resonators in the Free-Molecule Regime," J. Micromech. Microeng., **14**, pp. 1726–1733.
[26] Bhiladvala, R. B., and Wang, Z. J., 2004, "Effect of Fluids on the *Q* Factor and Resonance Frequency of Oscillating Micrometer and Nanometer Scale Beams," Phys. Rev. E, **69**, p. 036307.
[27] Bao, Z., Mukherjee, S., Roman, M., and Aubry, N., 2004, "Nonlinear Vibrations of Beams, Strings, Plates and Membranes Without Initial Tension," ASME J. Appl. Mech., **71**(4), pp. 551–559.
[28] Pozrikidis, C., 1992, *Boundary Integral and Singularity Methods for Linearized Viscous Flow*, Cambridge University Press, Cambridge, UK.
[29] Mukherjee, S., 2000, "CPV and HFP Integrals and Their Applications in the Boundary Element Method," Int. J. Solids Struct., **37**, pp. 6623–6634.
[30] Mukherjee, S., 2000, "Finite Parts of Singular and Hypersingular Integrals With Irregular Boundary Source Points," Eng. Anal. Boundary Elem., **24**, pp. 767–776.
[31] Bao, Z., and Mukherjee, S., 2004, "Electrostatic BEM for MEMS With Thin Conducting Plates and Shells," Eng. Anal. Boundary Elem., **28**, pp. 1427–1435.
[32] Liao, Y. S., Chyuan, S. W., and Chen, J. T., 2004, "Efficaciously Modeling Exterior Electrostatic Problems With Singularity for Electron Devices," IEEE Circuits Devices Mag., Sept./Oct., pp. 25–34.
[33] Cunha, F. C., De Sousa, A. J., and Loewenberg, M., 2003, "A Mathematical

Formulation of the Boundary Integral Equations for the Compressible Stokes Flow," Comput. Appl. Math., **22**(1), pp. 53–73.
[34] Newmark, N. M., 1959, "A Method of Computation for Structural Dynamics," J. Engrg. Mech. Div., **85**, pp. 67–94.
[35] Belytschko, T., Liu, W. K., and Moran, B., 2000, *Nonlinear Finite Element for Continua and Structures*, Wiley, New York.
[36] Petersen, K. E., 1982, "Silicon as a Mechanical Material," Proc. IEEE, **70**, pp. 420–455.
[37] Sharpe, W. N., Jr., 2001, "Mechanical Properties of MEMS Materials," *The MEMS Handbook*, CRC, Boca Raton, FL.
[38] Hurty, W. C., and Rubinstein, M. F., 1964, *Dynamics of Structures*, Prentice-Hall, Englewood Cliffs, NJ.
[39] Telukunta, S., and Mukherjee, S., 2006, "Fully Lagrangian Modeling of MEMS With Thin Plates," J. Microelectromech. Syst., **15**(4), pp. 795–810.

Jeong-Hoon Song[1]
Postdoctoral Fellow
e-mail: j-song2@northwestern.edu

Ted Belytschko
Walter P. Murphy Professor
McCormick Professor

Theoretical and Applied Mechanics,
Northwestern University,
Evanston, IL 60208-3111

Dynamic Fracture of Shells Subjected to Impulsive Loads

A finite element method for the simulation of dynamic cracks in thin shells and its applications to quasibrittle fracture problem are presented. Discontinuities in the translational and angular velocity fields are introduced to model cracks by the extended finite element method. The proposed method is implemented for the Belytschko–Lin–Tsay shell element, which has high computational efficiency because of its use of a one-point integration scheme. Comparisons with elastoplastic crack propagation experiments involving quasibrittle fracture show that the method is able to reproduce experimental fracture patterns quite well. [DOI: 10.1115/1.3129711]

1 Introduction

Simulation of fracture of shell structures is engendering considerable interest in the industrial and defense communities. Many components where fracture is of concern, such as windshields, ship hulls, fuel tanks, and car bodies, are not amenable to three dimensional solid modeling, for the expense would be enormous. Furthermore, fracture is often an important criterion in determining their performance envelopes.

Here, we describe a finite element method based on the extended finite element method (XFEM) [1,2] for modeling shell structures in explicit finite element programs and illustrate their performance in nonlinear problems involving dynamic fracture. The methodology is based on the Hansbo and Hansbo [3] approach, which has previously been applied by Mergheim et al. [4], Song et al. [5], and Areias et al. [6,7]. The equivalence of the Hansbo and Hansbo [3] basis functions to XFEM [1,2] is shown in Ref. [8]. The method employs an elementwise progression of the crack, i.e., the crack tip is always on an element edge. The elementwise crack propagation scheme may cause some noise during the crack propagation with coarse meshes. However, in Ref. [5], it is shown that such noise diminishes with mesh refinements and the crack propagation speeds converge to the progressive crack propagation results [9]. Réthoré et al. [10] reported that this is usually adequate for dynamic crack propagation. We do not use any near-tip enrichment, although Elguedj et al. [11] achieved good success with near-tip enrichments for static problems.

The literature in dynamic crack propagation in shells is quite limited. Cirak et al. [12] developed an interelement crack method, where the crack is limited to propagation along the element edges. The method is based on the Kirchhoff shell theory. Penalty functions were used to enforce continuity on all interelement edges. Areias and Belytschko [13] and Areias et al. [6,7] developed a method for shell fracture based on the extended finite element method for static and implicit time integrations.

The formulation described here also employs a cohesive law, but it requires a fracture criterion. As pointed out by Belytschko et al. [9], in models that inject a discontinuity in finite elements and in the governing partial differential equations, this appears to be a necessity, for a cohesive law is not sufficient to determine a direction or a speed of crack propagation. In the interelement crack methods, such as Cirak et al. [12], a fracture criterion is avoided by injecting cohesive laws either from the beginning of the simulation or in the vicinity of the crack tip [14]. In related work, Armero and Ehrlich [15] used embedded discontinuity elements to model hinge lines in plates.

The development of a fracture criterion that is computationally efficient and is easily applied in terms of available data poses a significant difficulty. Fracture criteria for quasibrittle materials, such as aluminum, are usually expressed in terms of the critical maximum principal tensile strain. However, in low order finite element models solved by explicit time integration, the maximum principal tensile strain tends to be quite noisy, so that crack paths computed by direct application of such a criterion tend to be erratic and do not conform to experimentally observed crack paths.

Here, we propose a nonlocal form of a strain-based fracture criterion. The nonlocal form is obtained by a kernel-weighted average over a sector in front of the crack tip. In addition, we describe a combination of this kernel-weighted average with an angular component that can be used to indicate crack branching.

The methodology is applied to the fracture of shell experiments performed by Chao and Shepherd [16]. Although these experiments are very interesting, they do not provide enough experimental data for a validation of the methodology. Nevertheless, we show that the method is able to reproduce the change in failure mode that occurs for longer notches as compared with shorter notches and that the overall final configuration agrees reasonably well with that observed in the experiments.

2 Shell Formulation With Fracture

The discontinuous shell formulation is based on the degenerated shell concept [17–19], which is almost equivalent to the Mindlin–Reissner formulation when the edges connecting the top and bottom surfaces are normal to the midsurface. We will use a kinematic theory based on the corotational rate-of-deformation and corotational Cauchy stress rate. These features are briefly summarized in Sec. 3, but are well known, so we will focus on the modifications needed for the XFEM treatment of fracture.

The velocity field is given by

$$\mathbf{v}(\boldsymbol{\xi},t) = \mathbf{v}^{\mathrm{mid}}(\boldsymbol{\xi},t) - \zeta \mathbf{e}_3 \times \boldsymbol{\theta}^{\mathrm{mid}}(\boldsymbol{\xi},t) \tag{1}$$

where $\mathbf{v}^{\mathrm{mid}} \in \mathcal{R}^3$ are the velocities of the shell midsurface, $\boldsymbol{\theta}^{\mathrm{mid}} \in \mathcal{R}^3$ are angular velocities of the normals to the midsurface, ζ varies linearly from $-h/2$ to $h/2$ along the thickness, and $\boldsymbol{\xi} = (\xi_1, \xi_2)$ are material coordinates of the manifold that describes the midsurface of the shell; at any point of the shell, we construct tangent unit vectors $\mathbf{e}_1$ and $\mathbf{e}_2$ so that

$$\mathbf{e}_3 = \mathbf{e}_1 \times \mathbf{e}_2 \tag{2}$$

The nomenclature is illustrated in Fig. 1.

For the further development of the discontinuous shell formulation, we will limit ourselves to cracks with surfaces normal to

[1]Corresponding author.

Contributed by the Applied Mechanics Division of ASME for publication in the Journal of Applied Mechanics. Manuscript received November 30, 2007; final manuscript received September 16, 2008; published online June 12, 2009. Review conducted by Ashkan Vaziri.

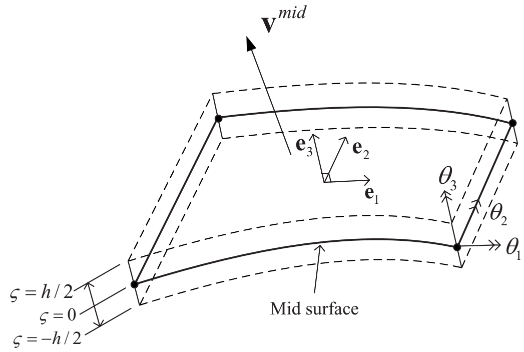

Fig. 1 The nomenclature of a continuum shell description

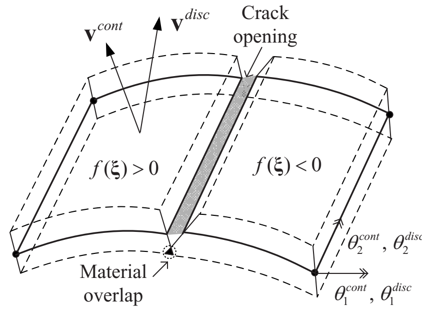

Fig. 3 Nomenclature of a fractured shell descriptions: incompatible material overlaps occurred at the bottom surface due to crack opening

the shell midsurfaces as shown in Fig. 2. Although this is not an intrinsic limitation of the method, it simplifies several aspects of the formulation.

The discontinuous velocity fields due to a crack in any Mindlin–Reissner theory can be described by

$$\mathbf{v}^{\mathrm{mid}}(\boldsymbol{\xi},t) = \mathbf{v}^{\mathrm{cont}}(\boldsymbol{\xi},t) + H(f(\boldsymbol{\xi}))\mathbf{v}^{\mathrm{disc}}(\boldsymbol{\xi},t) \tag{3}$$

$$\boldsymbol{\theta}^{\mathrm{mid}}(\boldsymbol{\xi},t) = \boldsymbol{\theta}^{\mathrm{cont}}(\boldsymbol{\xi},t) + H(f(\boldsymbol{\xi}))\boldsymbol{\theta}^{\mathrm{disc}}(\boldsymbol{\xi},t) \tag{4}$$

where $f(\boldsymbol{\xi})=0$ gives the intersection of the crack surface with the midsurface of the shell and $H(\cdot)$ is the Heaviside function given by

$$H(x) = \begin{cases} 1, & x > 0 \\ 0, & x \le 0 \end{cases} \tag{5}$$

In the above, $\mathbf{v}^{\mathrm{cont}}$ and $\mathbf{v}^{\mathrm{disc}}$ are continuous functions that are used to model the continuous and the discontinuous parts of the velocity fields, respectively; similarly, $\boldsymbol{\theta}^{\mathrm{cont}}$ and $\boldsymbol{\theta}^{\mathrm{disc}}$ are continuous functions. The discontinuities that model the cracks arise from the step function that precedes $\mathbf{v}^{\mathrm{disc}}$ and $\boldsymbol{\theta}^{\mathrm{disc}}$. It can be seen from Eqs. (3) and (4) with Eq. (1) that these velocity fields can result in a loss of compatibility and, in particular, material overlaps in the displacements, as indicated in Fig. 3, when there are significant discontinuities in the angular motion but the crack opening is small. We will deal this incompatibility with a penalty component in the cohesive law; see Sec. 4.

3 Element Formulation

The shell element used here is a four-node shell element originally described in Ref. [20] with improvements in Refs. [5,21]. The shell element employs a one-point quadrature rule with stabilization [22,23] for computational efficiency.

When the velocity fields given in Eqs. (3) and (4) are specialized to shell finite elements, the continuous part of the corotational velocity components is given by

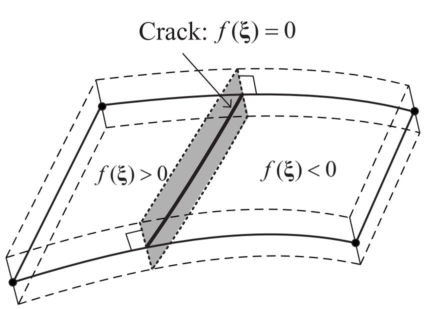

Fig. 2 Representation of discontinuity in the reference configuration by a level set implicit function $f(\xi)$ in the shell midsurface

$$\hat{v}_x(\boldsymbol{\xi},t) = N_I(\boldsymbol{\xi})\hat{\mathbf{v}}_{xI}(t) + \zeta N_I(\boldsymbol{\xi})\hat{\boldsymbol{\theta}}_{yI}(t) \tag{6}$$

$$\hat{v}_y(\boldsymbol{\xi},t) = N_I(\boldsymbol{\xi})\hat{\mathbf{v}}_{xI}(t) - \zeta N_I(\boldsymbol{\xi})\hat{\boldsymbol{\theta}}_{xI}(t) \tag{7}$$

where N_I are the conventional four-node finite element bilinear shape functions and the repeated subscripts I denote summation over all nodes. The corotational components of the rate-of-deformation tensor are given by

$$\hat{D}_{ij} = \frac{1}{2}\left(\frac{\partial \hat{v}_i}{\partial \hat{x}_j} + \frac{\partial \hat{v}_j}{\partial \hat{x}_i}\right) \tag{8}$$

Substituting Eqs. (6) and (7) into Eq. (8) yields an expression for the rate-of-deformation components

$$\hat{D}_x = \mathbf{b}_{\hat{x}I}\hat{\mathbf{v}}_{\hat{x}I} + \zeta(\mathbf{b}^c_{\hat{x}I}\mathbf{v}_{\hat{x}I} + \mathbf{b}_{\hat{x}I}\boldsymbol{\theta}_{yI}) \tag{9}$$

$$\hat{D}_y = \mathbf{b}_{\hat{y}I}\hat{\mathbf{v}}_{\hat{y}I} + \zeta(\mathbf{b}^c_{\hat{y}I}\mathbf{v}_{\hat{y}I} - \mathbf{b}_{\hat{y}I}\boldsymbol{\theta}_{xI}) \tag{10}$$

$$2\hat{D}_{xy} = \mathbf{b}_{\hat{x}I}\hat{\mathbf{v}}_{\hat{x}I} + \mathbf{b}_{\hat{y}I}\hat{\mathbf{v}}_{\hat{y}I} + \zeta(\mathbf{b}^c_{\hat{x}I}\mathbf{v}_{\hat{x}I} + \mathbf{b}^c_{\hat{y}I}\mathbf{v}_{\hat{y}I} + \mathbf{b}_{\hat{x}I}\boldsymbol{\theta}_{yI} - \mathbf{b}_{\hat{y}I}\boldsymbol{\theta}_{xI}) \tag{11}$$

where

$$\begin{Bmatrix} \mathbf{b}_{\hat{x}I} \\ \mathbf{b}_{\hat{y}I} \end{Bmatrix} = \frac{1}{2A}\begin{bmatrix} \hat{y}_{24} & \hat{y}_{31} & \hat{y}_{42} & \hat{y}_{13} \\ \hat{x}_{42} & \hat{x}_{13} & \hat{x}_{24} & \hat{x}_{31} \end{bmatrix} \tag{12}$$

$$\begin{Bmatrix} \mathbf{b}^c_{\hat{x}I} \\ \mathbf{b}^c_{\hat{y}I} \end{Bmatrix} = \frac{2\hat{\gamma}_K \hat{z}_K}{A^2}\begin{bmatrix} \hat{x}_{13} & \hat{x}_{42} & \hat{x}_{31} & \hat{x}_{24} \\ \hat{y}_{13} & \hat{y}_{42} & \hat{y}_{31} & \hat{y}_{24} \end{bmatrix} \tag{13}$$

along with $\hat{x}_{IJ}=\hat{x}_I-\hat{x}_J$, A is the area of the element, and $\hat{\gamma}_K$ is a projection operator: See Ref. [22]. A state of plane stress is assumed. In Ref. [21], two methods are proposed for the evaluation of $\mathbf{b}^c$. Here in Eq. (13), we adopted the $\hat{z}$ method. In this case, curvature is only coupled with the translations for *a warped element*.

We also used the shear projection scheme introduced in Ref. [21]. This shear projection scheme gives the transverse shear strain components by

$$\hat{D}_{xz} = \mathbf{b}^s_{x1I}\hat{\mathbf{v}}_{zI} + \mathbf{b}^s_{x2I}\hat{\boldsymbol{\theta}}_{xI} + \mathbf{b}^s_{x3I}\hat{\boldsymbol{\theta}}_{yI} \tag{14}$$

$$\hat{D}_{yz} = \mathbf{b}^s_{y1I}\hat{\mathbf{v}}_{zI} + \mathbf{b}^s_{y2I}\hat{\boldsymbol{\theta}}_{xI} + \mathbf{b}^s_{y3I}\hat{\boldsymbol{\theta}}_{yI} \tag{15}$$

where

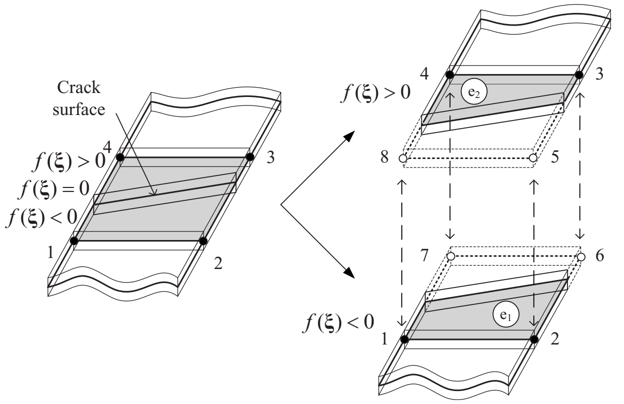

Fig. 4 The decomposition of a cracked element with generic nodes 1–4 into two elements e_1 and e_2; solid and hollow circles denote the original nodes and the added phantom nodes, respectively

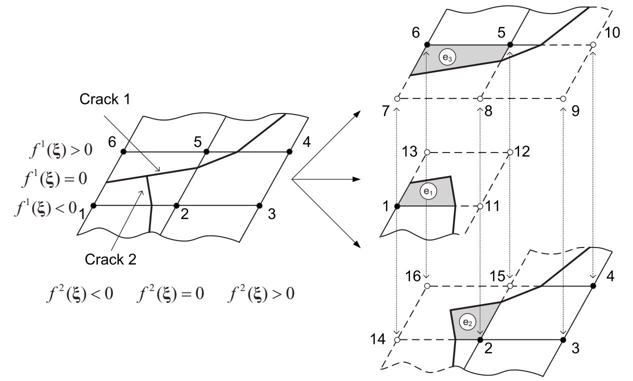

Fig. 5 The decomposition of an element into three elements e_1, e_2, and e_3 to model crack branching; solid and hollow circles denote the original nodes and the added phantom nodes, respectively

$$\begin{Bmatrix} \mathbf{b}^s_{x1I} & \mathbf{b}^s_{x2I} & \mathbf{b}^s_{x3I} \\ \mathbf{b}^s_{y1I} & \mathbf{b}^s_{y2I} & \mathbf{b}^s_{y3I} \end{Bmatrix} = \frac{1}{4}\begin{bmatrix} 2(\bar{x}_{JI}-\bar{x}_{IK}) & (\hat{x}_{JI}\bar{y}_{JI}+\hat{x}_{IK}\bar{y}_{IK}) & -(\hat{x}_{JI}\bar{y}_{JI}+\hat{x}_{IK}\bar{y}_{IK}) \\ 2(\bar{y}_{JI}-\bar{y}_{IK}) & (\hat{y}_{JI}\bar{y}_{JI}+\hat{y}_{IK}\bar{y}_{IK}) & -(\hat{y}_{JI}\bar{y}_{JI}+\hat{y}_{IK}\bar{y}_{IK}) \end{bmatrix} \tag{16}$$

along with $(I,J,K)=\{(I,J,K)\,|\,(1,2,4),(2,3,1),(3,4,1),(4,1,3)\}$ and $\bar{x}_{IJ}=\hat{x}_{IJ}/\|\hat{x}_{IJ}\|$.

3.1 Representation of the Discontinuity. The velocity field of the fractured shell element, which is given by Eqs. (3) and (4), can be approximated in the XFEM by

$$\hat{\mathbf{v}}^{\text{mid}}(\boldsymbol{\xi},t)=N_I(\boldsymbol{\xi})\hat{\mathbf{v}}_I^{\text{cont}}(t)+H(f(\boldsymbol{\xi}))N_I(\boldsymbol{\xi})\hat{\mathbf{v}}_I^{\text{disc}}(t) \tag{17}$$

$$\hat{\boldsymbol{\theta}}^{\text{mid}}(\boldsymbol{\xi},t)=N_I(\boldsymbol{\xi})\hat{\boldsymbol{\theta}}^{\text{cont}}(t)+H(f(\boldsymbol{\xi}))N_I(\boldsymbol{\xi})\hat{\boldsymbol{\theta}}_I^{\text{disc}}(t) \tag{18}$$

However, when elementwise crack propagation is employed, we have found that it is simpler to program the implementation in the Hansbo and Hansbo [3] form, as developed by Song et al. [5]. The element completely cut by a crack is represented by a set of overlapping elements with added phantom nodes as shown in Fig. 4.

The discontinuous velocity field is then constructed by two superimposed velocity fields

$$\hat{\mathbf{v}}(\boldsymbol{\xi},t)=\hat{\mathbf{v}}^{e_1}(\boldsymbol{\xi},t)+\hat{\mathbf{v}}^{e_2}(\boldsymbol{\xi},t)=\sum_{I\in S_1}N_I(\boldsymbol{\xi})H(-f(\boldsymbol{\xi}))\hat{\mathbf{v}}_I^{e_1}(t) + \sum_{I\in S_2}N_I(\boldsymbol{\xi})H(f(\boldsymbol{\xi}))\hat{\mathbf{v}}_I^{e_2}(t) \tag{19}$$

$$\hat{\boldsymbol{\theta}}(\boldsymbol{\xi},t)=\hat{\boldsymbol{\theta}}^{e_1}(\boldsymbol{\xi},t)+\hat{\boldsymbol{\theta}}^{e_2}(\boldsymbol{\xi},t)=\sum_{I\in S_1}N_I(\boldsymbol{\xi})H(-f(\boldsymbol{\xi}))\hat{\theta}_I^{e_1}(t) + \sum_{I\in S_2}N_I(\boldsymbol{\xi})H(f(\boldsymbol{\xi}))\hat{\theta}_I^{e_2}(t) \tag{20}$$

where S_1 and S_2 are the sets of the nodes of the overlapping elements e_1 and e_2, respectively. Note that velocity fields $\hat{\mathbf{v}}^{e_1}(\boldsymbol{\xi},t)$ and $\hat{\mathbf{v}}^{e_2}(\boldsymbol{\xi},t)$ (or $\hat{\boldsymbol{\theta}}^{e_1}(\boldsymbol{\xi},t)$ and $\hat{\boldsymbol{\theta}}^{e_2}(\boldsymbol{\xi},t)$) are nonzero only for $f(\boldsymbol{\xi})<0$ and $f(\boldsymbol{\xi})>0$, respectively, due to the Heaviside step function $H(x)$ that appears in the above equations. The phantom nodes are integrated in time by the same central difference explicit method as the remaining nodes.

3.2 Representation of Multiple Discontinuities: Crack Branching. The concept of the overlapping element method can be easily extended to crack branch modeling. When the original crack, crack 1, branches into crack 1 and crack 2, as shown in Fig. 5, the element in which the crack branches is replaced with three overlapping elements. Let $f^1(\boldsymbol{\xi})=0$ describe the original crack and one branch, and let $f^2(\boldsymbol{\xi})=0$ describe the second branch. The discontinuous velocity field is then given by

$$\begin{aligned}\hat{\mathbf{v}}(\boldsymbol{\xi},t)&=\hat{\mathbf{v}}^{e_1}(\boldsymbol{\xi},t)+\hat{\mathbf{v}}^{e_2}(\boldsymbol{\xi},t)+\hat{\mathbf{v}}^{e_3}(\boldsymbol{\xi},t)\\&=\sum_{I\in S_1}N_I(\boldsymbol{\xi})H(-f^1(\boldsymbol{\xi}))H(-f^2(\boldsymbol{\xi}))\hat{\mathbf{v}}_I^{e_1}(t)\\&\quad+\sum_{I\in S_2}N_I(\boldsymbol{\xi})H(-f^1(\boldsymbol{\xi}))H(f^2(\boldsymbol{\xi}))\hat{\mathbf{v}}_I^{e_2}(t)\\&\quad+\sum_{I\in S_3}N_I(\boldsymbol{\xi})H(f^1(\boldsymbol{\xi}))H(-f^2(\boldsymbol{\xi}))\hat{\mathbf{v}}_I^{e_3}(t)\end{aligned} \tag{21}$$

The element nodal forces are developed as in Ref. [20]. In addition, curvature-translation coupling terms are added and a shear projection operator replaces the previous transverse shear terms. The principle of virtual power is used to derive the relationship for the internal nodal forces. The principle states that

$$\delta\mathcal{P}^{\text{int}}=\underbrace{A(\mathbf{B}_m\delta\mathbf{v})^T\begin{Bmatrix}\hat{f}^r_x\\\hat{f}^r_y\\\hat{f}^r_{xy}\end{Bmatrix}}_{\text{virtual membrane power}}+\underbrace{A(\mathbf{B}_b\delta\mathbf{v})^T\begin{Bmatrix}\hat{m}^r_x\\\hat{m}^r_y\\\hat{m}^r_{xy}\end{Bmatrix}}_{\text{virtual bending power}}+\underbrace{\bar{\kappa}A(\mathbf{B}_s\delta\mathbf{v})^T\begin{Bmatrix}\hat{f}^r_{xz}\\\hat{f}^r_{yz}\end{Bmatrix}}_{\text{virtual transverse shear power}} \tag{22}$$

where $\bar{\kappa}$ is the shear reduction factor from the Mindlin shell theory, and $\hat{f}^r_{ij}$ and $\hat{m}^r_{ij}$ are the resultant forces and moments, which are integrated through the element thickness.

$$\hat{f}^r_{ij}=\int\hat{\sigma}_{ij}d\hat{z} \tag{23}$$

$$\hat{m}^r_{ij}=\int\hat{z}\hat{\sigma}_{ij}d\hat{z} \tag{24}$$

where $\hat{z}=\zeta(h/2)$.

We substitute Eqs. (9)–(16) into Eq. (22), and evoking the arbitrariness of $\delta\mathbf{v}$ yields the discretized element nodal forces

$$\hat{f}_{xI}^{\text{int}} = A_e(b_{xI}\hat{f}_x^r + b_{yI}\hat{f}_{xy}^r + b_{xI}^c\hat{m}_x^r + b_{yI}^c\hat{m}_{xy}^r \tag{25}$$

$$\hat{f}_{yI}^{\text{int}} = A_e(b_{yI}\hat{f}_y^r + b_{xI}\hat{f}_{xy}^r + b_{yI}^c\hat{m}_y^r + b_{xI}^c\hat{m}_{xy}^r) \tag{26}$$

$$\hat{f}_{zI}^{\text{int}} = A_e\bar{\kappa}(b_{x1I}^s\hat{f}_{xz}^r + b_{y1I}^s\hat{f}_{yz}^r) \tag{27}$$

$$\hat{m}_{xI}^{\text{int}} = A_e[\bar{\kappa}(b_{x2I}^s\hat{f}_{xz}^r + b_{y2I}^s\hat{f}_{yz}^r) - (b_{yI}\hat{m}_y^r + b_{xI}\hat{m}_{xy}^r)] \tag{28}$$

$$\hat{m}_{yI}^{\text{int}} = A_e[\bar{\kappa}(b_{x3I}^s\hat{f}_{xz}^r + b_{y3I}^s\hat{f}_{yz}^r) + (b_{xI}\hat{m}_x^r + b_{yI}\hat{m}_{xy}^r)] \tag{29}$$

$$\hat{m}_{zI}^{\text{int}} = 0 \tag{30}$$

The final form of the element internal forces in the global coordinates can be determined by performing the transformation between the corotational and global coordinates as follows:

$$\mathbf{f}_e^{\text{int}} = \mathbf{T}_e^T(\hat{\mathbf{f}}_e^{\text{int}} + \hat{\mathbf{f}}_e^{\text{stab}}) \tag{31}$$

where $\mathbf{T}$ is the transformation matrix between global and corotational components and $\hat{\mathbf{f}}_e^{\text{int}}$ is the nodal internal force vector in the corotational coordinate systems. In Eq. (31), to circumvent the rank deficiency due to one-point integration, an hourglass control force, $\hat{\mathbf{f}}_e^{\text{stab}}$, is added to the internal force vector. For a description of the hourglass control scheme, see Refs. [21,22].

For each of the overlapped elements on a crack, the nodal forces are given by

$$\mathbf{f}_e^{\text{int}} = \left(\sum_{k=1}^{N_{\text{ele}}^{\text{ovr}}} \frac{A_{e_k}}{A_e} \mathbf{T}_{e_k}^T \hat{\mathbf{f}}_{e_k}^{\text{int}} \right) + \mathbf{T}_e^T \hat{\mathbf{f}}_e^{\text{stab}} \tag{32}$$

where $N_{\text{ele}}^{\text{ovr}}$ is the total number of overlapped elements, A_{e_k} is the activated area of the corresponding overlapping elements in the corotational coordinates, $\mathbf{f}_e$ is the nodal force vector of a cracked element, and $\hat{\mathbf{f}}_{e_k}$ is the corotational nodal force vector of the overlapped element e_k. Note that the internal nodal forces of elements e_k can be calculated by multiplying Eqs. (25)–(30) by the area fraction, A_{e_k}/A_e. A more detailed discussion of the concept of the modification of cracked element nodal forces by area fractions can be found in Ref. [5].

4 Material Model and Fracture

4.1 Hardening Plasticity for Quasibrittle Material. We employed a von Mises type hardening J_2-plasticity model. For the integration of the constitutive model we used a first-order forward Euler explicit integration scheme. In the simulation of fracture within the explicit simulation framework, the integration time step is limited to a small fraction of the critical time step and is usually smaller than a critical time step for the integration of the constitutive equation.

The rate form of the constitutive equation in the corotational system is given by

$$\frac{D\hat{\boldsymbol{\sigma}}}{Dt} = \hat{\mathbf{C}}^{\text{elas}}:(\hat{\mathbf{D}} - \hat{\mathbf{D}}^p) \tag{33}$$

where $\hat{\boldsymbol{\sigma}}$ is the corotational Cauchy stress rate, $\hat{\mathbf{C}}^{\text{elas}}$ is the corotational elastic moduli tensor, and $\hat{\mathbf{D}}^p$ is the corotational rate of plastic deformation tensor. For the von Mises material with isotropic hardening, the plastic corotational rate-of-deformation tensor is given by

$$\hat{\mathbf{D}}^p = \mathbf{r}\dot{\lambda} = \mathbf{r}\frac{\mathbf{r}:\hat{\mathbf{C}}^{\text{elas}}:\hat{\mathbf{D}}}{\mathbf{r}:\hat{\mathbf{C}}^{\text{elas}}:\mathbf{r} + h_p} \tag{34}$$

where $\mathbf{r}$ is J_2-plasticity flow direction, $\dot{\lambda}$ is plastic flow rate parameter, and h_p is the plastic hardening modulus.

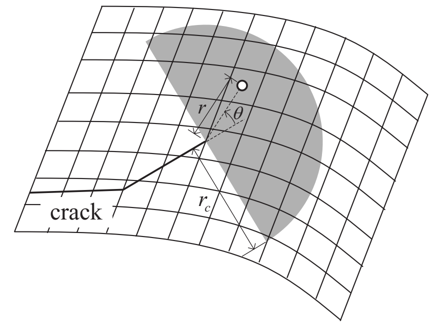

Fig. 6 Schematic of averaging domain: averaging domain, which has averaging size of r_c

4.2 Fracture Criterion and Cohesive Model. A strain-based fracture criterion was used to determine the onset point of a post-strain localization behavior of a material, i.e., fracture. When the strain at a crack tip material point reaches a fracture threshold, we inject a strong discontinuity at the previous crack tip according to maximum principal tensile strain direction of an averaged strain, ϵ^{avg}. For the computation of an averaged strain, ϵ^{avg}, we used a nonlocal (i.e., surface weighted average) scheme, which is given by

$$\epsilon^{\text{avg}} = \frac{4}{\pi}\int_{-\pi/2}^{\pi/2}\int_0^{r_c} w(r)\epsilon \, dr \, d\theta \tag{35}$$

where r and θ are the distance from the crack tip and the angle with the tangent to the crack path, respectively, and $w(r)$ is weight function; for the latter, we use a cubic spline function given by

$$w(r) = \begin{cases} 4\left(\frac{r}{r_c} - 1\right)\left(\frac{r}{r_c}\right)^2 + \frac{2}{3}, & 0 < r < 0.5r_c \\ \frac{4}{3}\left(1 - \frac{r}{r_c}\right)^3, & 0.5r_c \le r \le r_c \\ 0 & \text{otherwise} \end{cases} \tag{36}$$

where $r_c(\simeq 3h_e)$ is the size of the averaging domain, and h_e is the size of the crack tip element. A typical averaging domain is shown in Fig. 6.

A cohesive crack model is prescribed along the newly injected strong discontinuity surfaces until the crack opening is fully developed, i.e., cohesive traction has vanished. In this study, we prescribed only the normal traction of the linear cohesive model, as shown in Fig. 7. We have found that mode II and mode III

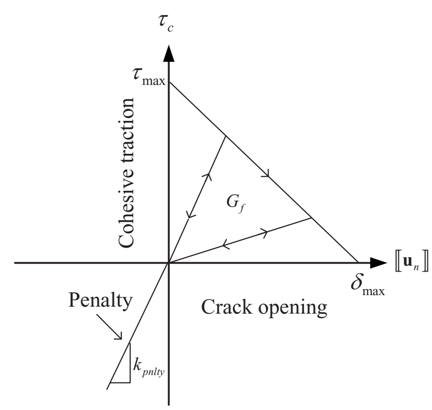

Fig. 7 Schematic showing of a linear cohesive law: the area under curve is the fracture energy, G_f

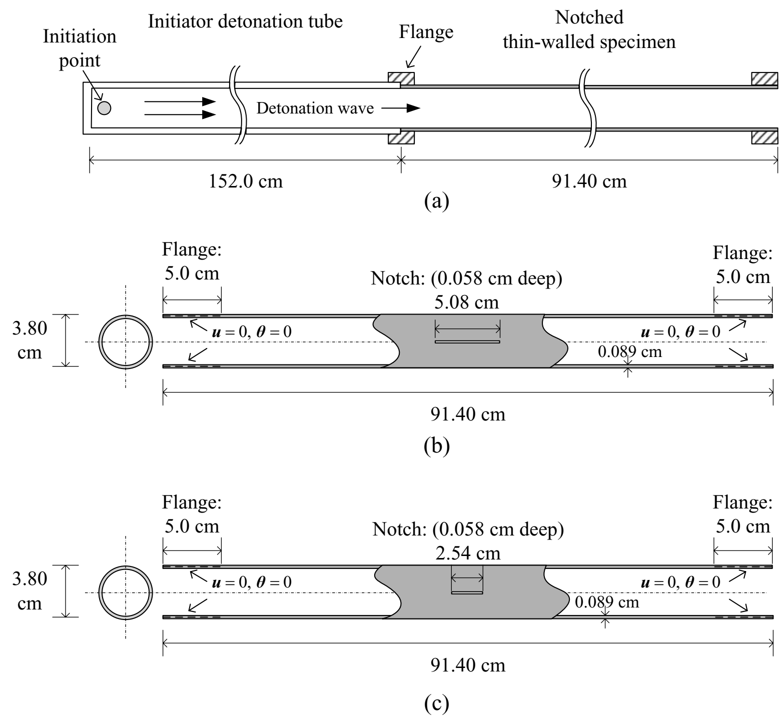

Fig. 8 Setup for the notched cylinder fracture under internal detonation pressure [16]: (*a*) total experiment assembly, (*b*) notched thin-walled specimen for shot 7, and (*c*) notched thin-walled specimen for shot 4

behavior is minimal in these problems, perhaps because fracture occurs in a tearing mode.

The cohesive model is constructed so that the dissipated energy due to the crack propagation is equivalent to the fracture energy

$$G_f = \int_0^{\delta_{\max}} \tau_c(\delta_n)\,d\delta = \frac{1}{2}\tau_{\max}\delta_{\max} \tag{37}$$

where $\delta_{\max}$ is the maximum crack opening displacement, G_f is the fracture energy, and δ_n is the jump in the displacement normal to the crack surface, Γ_d, which is given by

$$\delta_n = \mathbf{n}\cdot[\![\mathbf{u}(\boldsymbol{\xi},t)]\!]_{\boldsymbol{\xi}\in\Gamma_d} \tag{38}$$

$$= \mathbf{n}\cdot[N_I(\boldsymbol{\xi})\mathbf{u}_I^{e_2}(t) - N_J(\boldsymbol{\xi})\mathbf{u}_J^{e_1}(t)]_{\boldsymbol{\xi}\in\Gamma_d} \tag{39}$$

where $\mathbf{n}$ is the normal to the crack surface. Note that the cohesive strength $\tau_{\max}$ is not a constant parameter in this method. Unless $\tau_{\max}$ takes on the current value of the traction when a crack segment is injected into a continuum finite element, the cohesive traction does not satisfy time continuity and may lead to severe noise; see Ref. [24].

As shown in Fig. 7, a penalty force was added in compression. This penalty force depends only on δ_n and is given by $\tau_c = \delta_n k_{\text{pnlty}}$ when $\delta_n < 0$. We used a value of two to three orders of magnitudes of the normalized Young's modulus by the element size, i.e., E/h_e, for k_{pnlty}.

The discretized form of the cohesive nodal forces is computed by

$$\mathbf{f}_e^{\text{coh}} = \sum_{k=1}^{2} \mathbf{T}_{e_k}^T \hat{\mathbf{f}}_{e_k}^{\text{coh}} \tag{40}$$

$$= \sum_{k=1}^{2} \mathbf{T}_{e_k}^T (-1)^k \int_{\Gamma_d} \mathbf{N}^T \tau_c(\delta_n)\hat{\mathbf{n}}\,d\Gamma_d \tag{41}$$

where k represents the overlaid element layer number.

5 Numerical Examples

5.1 Notched Cylinder Fracture Under Internal Detonation Pressure. An interesting series of experiments concerned with the quasibrittle fracture of shells has been reported by Chao and Shepherd [16], and Chao [25]. These experiments involve notched thin-wall pipes filled with gaseous explosives through which a detonation wave is passed. This is accomplished in the experiment by filling the pipe with an explosive gas and initiating a detonation wave at the left end as shown in Fig. 8(*a*).

In this study, we focused on numerical simulations of two experimental results, shot 7 (L=5.08 cm) and shot 4 (L=2.54 cm) [16,25], since these two experimental results exhibit strikingly different growths of the fracture, which is ascribed to the length of the notch. Chao and Shepherd [16], and Chao [25] reported that with a notch size of L=5.08 cm, the *backward* crack tip, which is closer to the detonation initiation point, showed a curving crack path, whereas the *forward* crack tip propagates only a short distance in a straight line and then bifurcated into two cracks. However, with a notch size of L=2.54 cm, the backward crack tip curved, whereas the forward crack tip propagates only a short distance in a straight line and then is arrested.

For the numerical simulation, we discretized the right segment of the cylinder length of the 91.40 cm with 54,382 four-node quadrilateral shell elements ($h_e \simeq 0.90$ mm); see Figs. 8(*b*) and 8(*c*). The shell material is aluminum 6061-T6 and we modeled it with J_2-plasticity, density ρ=2780.0 kg/m^3, Young's modulus E =69.0 GPa, Poisson's ratio ν=0.30, and yield stress σ_y =275.0 MPa. We used linear hardening with constant slope h_p =640.0 MPa. The cohesive fracture energy G_f=19.0 kJ/m^2 is treated in terms of a cohesive law (the assigned fracture energy is based on Refs. [26–28]).

In order to induce unsymmetrical crack propagation with an axisymmetric shell structure and loading, we introduced a small scatter in the yield strength of bulk material. The yield strength at every material point is perturbed by factors ranging from −5.0% to 5.0%: The perturbation factor is obtained from a log-normal

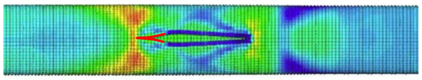

(a)

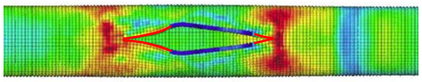

(b)

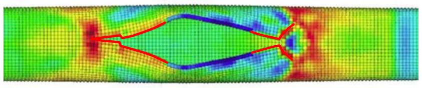

(c)

Fig. 9 Evolution of crack paths and distributions of effective plastic stress at different time steps: (*a*) t=213.55 μs, (*b*) t=228.61 μs, and (*c*) t=238.01 μs. Note that finite element nodes are plotted and crack paths are explicitly marked.

distribution around the mean value of 1.0 and a standard deviation of 2.0%. We also considered bulk materials in which the yield strength is perturbed by $\pm 10.0\%$; the results are almost identical.

For the fracture criterion, we used 6% maximum tensile strain as the fracture strain. This strain value was used to nucleate any new cracks and to propagate cracks, but in these simulations no new crack were nucleated as the notches and subsequent cracks served as the only nucleation mechanism. The cracks were propagated in the direction normal to the direction of maximum principal strain.

For the applied pressure, we used a pressure time history function, $p(x,t)$, which is provided by Beltman and Shepherd [29] as follows:

$$p(x,t) = \begin{cases} 0, & t < x/v^{cj} \\ p^{cj} \exp(-(t - x/v^{cj})/T_0), & t > x/v^{cj} \end{cases} \tag{42}$$

where x is the axial distance from the detonation initiation source to the material point, t is the simulation time, $T_0(\simeq 3.0x/v^{cj})$ is pressure decay time, and p^{cj} and v^{cj} are the Chapmand–Jouguet pressure and detonation wave propagation velocity, respectively. For the simulation, we used p^{cj}=6.2 MPa and v^{cj}=2390 m/s to model the internal detonation wave as in Ref. [29] and applied this pressure normal to all surfaces of the shell model throughout the entire simulation, even after extensive fracture and large deformation. Fluid-structure interaction effects were not modeled.

Here, we need to make a remark on the way we modeled the initial notch. The notches in the experiment were not machined through the entire depth of the shell. In this study, we modeled the notch by using the XFEM methodology, so we immediately allowed the translational and angular velocity fields across the notch to be discontinuous. The penalty part of the cohesive law in the compressive regime was activated to prevent incompatibilities in the compressive part (below the notch), but the tensile part of the cohesive law is not activated in the notch since the fracture in the notch is assumed to be completed. The penalty constants for these constraints did not affect the final results very much.

5.1.1 Cylinder With Notch Size of L=5.08 cm *(Shot 7)*. Figure 9 shows deformed configurations and contour plots of the effective plastic stress at the beginning of the backward crack propagation and just before and after the forward crack branches into two cracks. As we can see Fig. 9(*c*), the forward crack tip branches with an angle of 45 deg and forms stress concentrations ahead of two branched tips. In contrast to the forward moving branched tips, the backward tip retains its straight path.

Figure 10 shows the different perspective views of the computed deformed configurations at an intermediate stage at time t=256.86 μs. Subsequently, the forward branches turn to propagate along the circumferential direction. The computed final configuration is shown in Fig. 11(*a*) along with the final experimental configuration, which is shown at Fig. 11(*b*). The computation reproduces some of the key features of the experiment quite well. In the computations, the crack propagates from the notch to the backward and the forward tips. The forward propagating crack then branches initially at 45 deg, but then turns to propagate along the axis of the cylinder. The experimental specimen shows evidence of similar crack branching and turning. As can be seen from Fig. 11(*b*), in the part of the pipe that has opened up, the crack progresses initially at an angle, but then the final crack path is circumferential, i.e., normal to the axis of the pipe. The computed crack paths are quite similar. In the center of the fracture, a little wedge shaped pipe is apparent. This is absent in the computation.

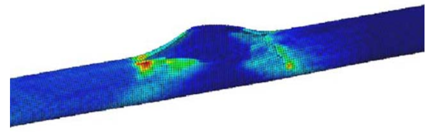

(a)

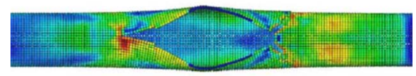

(b)

Fig. 10 Evolution of crack opening at time t=256.86 μs along with distribution of effective plastic stress: (*a*) side view and (*b*) top view

There are some discrepancies in the final configurations as can be seen from Fig. 11. The lower flap, as computed, opens up more than in the experiments. In the experiment, both the lower and the upper flaps show significant bends, but these are not apparent in the computation. This can be due to (1) absence of fluid-structure interaction effects in the computation, (2) errors in detonation wave loading function, particularly in the later stages, and (3) lack of fidelity in fracture criterion or material model.

Figure 12 shows time histories of the forward and backward crack propagation speeds. The forward crack tip starts to propagate around t=210.0 μs and then linearly speeds up and shows a peak speed around t=229.0 μs; at this point the crack branches into two cracks. After branching, the crack tip loses speed, but then the speed recovers and reaches a plateau.

5.1.2 Cylinder With Notch Size of L=2.54 cm *(Shot 4)*. Experiments with the shorter notch showed substantially different crack evolution, and this is also evident in the computations. Figure 13 shows the distribution of effective plastic stress in the

(a)

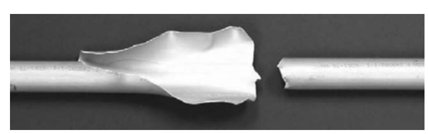

(b)

Fig. 11 Comparison of the final deformed shape between (*a*) the simulation result and (*b*) the experimental result (shot 7) [16,25]

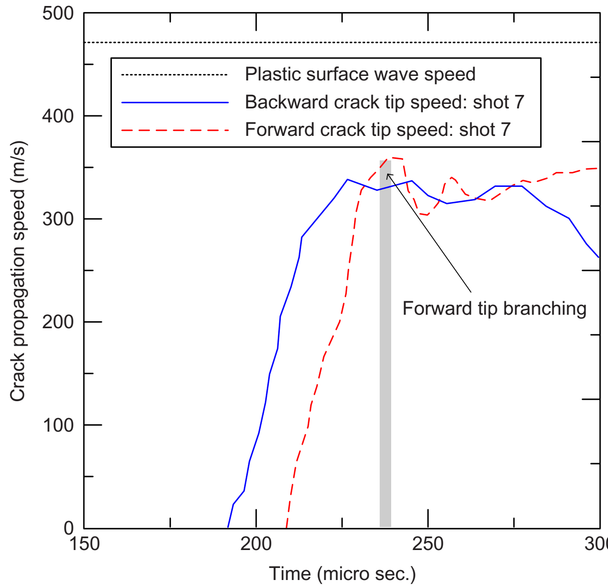

Fig. 12 Comparison propagation speeds of two crack tips for the cylinder with the notch size of $L=5.08$ cm (shot 7)

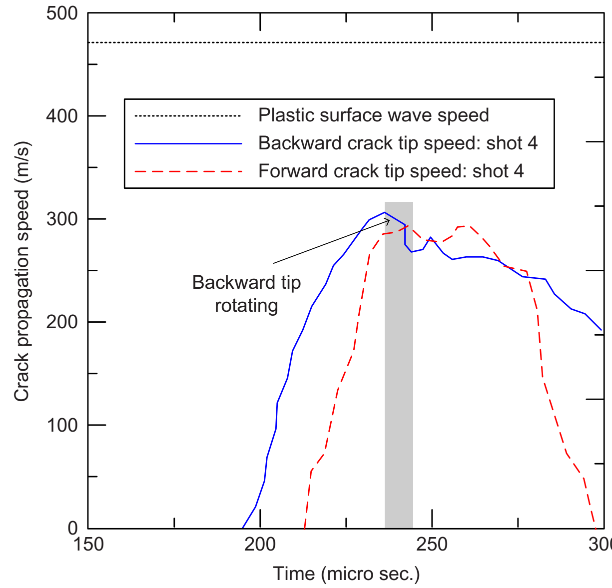

Fig. 14 Comparison propagation speeds of two crack tips for the cylinder with the notch size of $L=2.54$ cm (shot 4)

computed deformed configuration before the backward crack starts to rotate. As can be seen from Fig. 13(*a*), the axisymmetry of the stress field ahead of a backward crack tip is broken and then the crack tip path exhibits a change in direction as shown in Fig. 13(*b*). Note that this sudden direction change in crack path causes a concentration of plastic strain at the kinked points and it slows the crack speed as indicated in Fig. 14.

Figure 15 shows the different perspective views of the computed deformed configuration at time $t=261.98$ μs. As we can see from the figure, the backward crack turns to a circumferential path but the forward crack tip remains in a straight path. Shortly after this point, the strain concentration ahead of a forward crack tip is diffused and the crack tip is arrested.

A comparison between computational and experimental results of the final configuration is shown in Fig. 16. Again, the computed size of the crack opening in the pipe agrees reasonably well with the experiment and so do the crack paths, except that the transition from the axial path to a circumferential path is quite smooth in the experiment, but rather rough in the computation. The shapes of the flaps are not predicted well. Evidently, fluid-structure interaction effects play a substantial role in their shapes.

The computed crack propagation speeds for shot 7 and shot 4, which are shown in Figs. 12 and 14, respectively, are somewhat faster than the reported experimental crack speeds (maximum 250 m/s) [25]. This may be due to the shortcomings in the numerical representation of the crack, i.e., lack of crack tip blunting and tunneling phenomena in the numerical simulations.

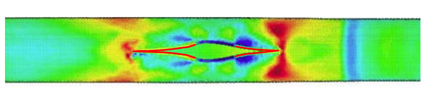

(a)

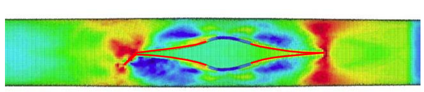

(b)

Fig. 13 Evolution of crack and distributions of effective plastic stress at time times (*a*) $t=231.41$ μs and (*b*) $t=239.05$ μs. Note that finite element nodes are plotted and crack paths are explicitly marked.

5.2 Cylinder Fracture With an Initial Weak Spot. We examine fracture patterns of the cylinder shown in Fig. 17(*a*). The cylinder is initially pressurized to 6.9 MPa ($\simeq 1000$ psi) and then the pressure at the center of the cylinder on a domain of radius $r=2.50$ cm is increased until a fracture nucleates. We set an initial weak spot at two different locations as shown in Figs. 17(*b*) and 17(*c*), i.e., at the center of cylinder or close to the end cap.

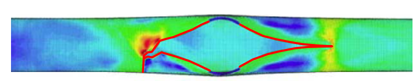

(a)

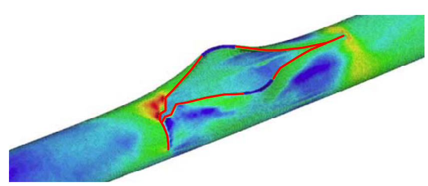

(b)

Fig. 15 Evolution of crack and distributions of effective plastic stress at time $t=261.98$ μs: (*a*) top view and (*b*) side view

(a)

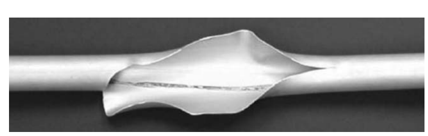

(b)

Fig. 16 Comparison of the final deformed shape between (*a*) the simulation result and (*b*) the experimental result (shot 4) [16,25]

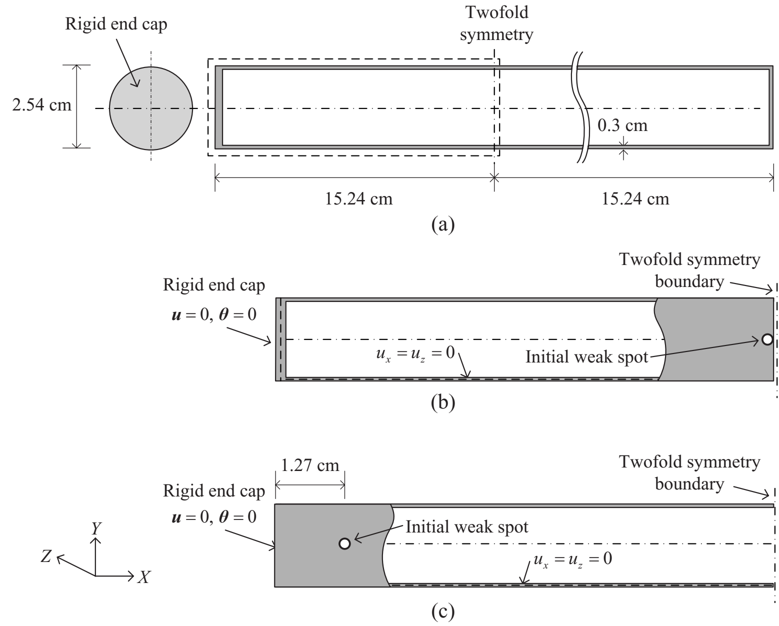

Fig. 17 Setup for cylinder fracture with an initial weak spot: (*a*) only half of the cylinder is modeled due to the twofold symmetry, (*b*) cylinder with an initial weak spot at the center of the cylinder, and (*c*) cylinder with an initial weak spot close to the end cap

Since the original cylinder, which has a length of 30.48 cm, has twofold symmetry, we modeled only half of the cylinder as shown in Figs. 17(*b*) and 17(*c*); $u_x=0$ and $\theta_x=\theta_y=\theta_z=0$ along the plane of twofold symmetry. This is somewhat unrealistic, but we just wish to demonstrate the ability to follow complicated crack paths. The model is discretized with a structured mesh of 8056 four-node quadrilateral shell elements. The rigid end cap is modeled by constraining all degrees of freedoms at the end cap. The material is aluminum 5086-H32, which has material properties: density $\rho=2660.0\ \mathrm{kg/m^3}$, Young's modulus $E=71.0$ GPa, Poisson's ratio $\nu=0.30$, and yield stress $\sigma_y=207.0$ MPa. We used J_2-plasticity with a constant hardening slope $h_p=634.0$ MPa. The fracture parameters are the same as in the previous example. The yield strength is reduced by 10% at the weak spots.

As we can see from Fig. 18, the crack initially forms at the weak spot and then propagates toward the end cap parallel to the axis of the cylinder. However, as the crack tip approaches the rigid end cap, the crack tip stress develops a strong shear component, which causes a sudden rotation of the crack trajectory.

The rigid end cap has a significant effect on the crack path. This can be observed by locating an initial weak spot near the rigid end cap as shown in Fig. 17(*c*). Under this setting, we originally anticipated development of three crack paths: two of them propagating toward the end cap after branching, and the other propagating toward the opposite end. However, only two crack tips are developed and propagate toward the end cap. This is due to the fact that the stored energy was only sufficient for two cracks, but it is not sufficient to develop a third crack toward the opposite side end. The deformed shape with crack opening is shown in Fig. 19. As we can see from Fig. 19, two cracks have propagated toward the end cap with the angle of 45 deg to the center line.

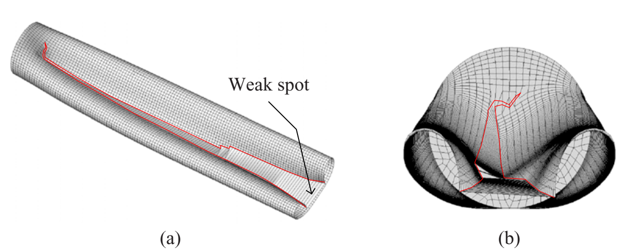

Fig. 18 The computed final deformed shape along with marked opened crack surfaces: (*a*) perspective view and (*b*) axial view

6 Conclusions

A method has been developed for the prediction of dynamic crack propagation in shells with explicit finite element methods. The methodology is based on the XFEM [1,2], but uses the Hansbo and Hansbo [3] implementation where the cracked element is treated by two superimposed elements with phantom nodes on the cracked portions [5,7].

A nonlocal fracture criterion based on the maximum tensile principal strain has been developed for a quasibrittle fracture where significant plastic deformation precedes fracture. In order to mitigate spurious predictions of fracture, the method uses a

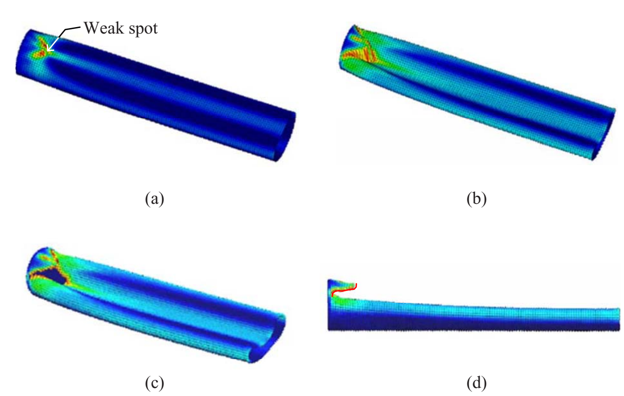

Fig. 19 Evolution of crack opening and effective plastic strain distributions at different times: (*a*) $t=187.0\ \mu$s and (*b*) $t=252.0\ \mu$s. For a clear representation of crack opening, finite element nodes are plotted: (*c*) top view and (*d*) side view.

weighted average of the strain ahead of the crack tip, i.e., a nonlocal strain. For the weighting function, a cubic spline that extends to approximately the edge of the near-tip plastic field was used.

In addition, a cohesive law was used across the crack surface. The cohesive law serves to represent plastic work and other fracture processes that are not resolved by the model.

Computations were made for two of the Chao and Shepherd [16] experiments of explosively loaded pipes. The finite element model was simply loaded by the pressure time history of the detonation traveling wave; fluid-structure interaction effects were not considered. Nevertheless, the computations reproduce many of the salient features of each experiment and differences in crack paths between two experiments.

For the pipe with the longer prenotch, the computations correctly predict crack branching at one end and the subsequent wrap-around of the crack path that severs the pipe at the other end. In the computation, the crack is arrested before the tube is completely severed, but there is some evidence (the notched piece in Fig. 11) that the complete breakage involved in the experiment a different loading. For the pipe with a shorter prenotch, a twisting of the crack path is correctly predicted. However, the deformed configurations observed experimentally show some deformations of the flaps of the pipe that are not replicated in the computation. These are probably due to fluid-structure effects that were not modeled.

Overall, these computational results show substantial promise for predicting the dynamic fracture behavior of explosively loaded shell structures. They furthermore indicate that in quasibrittle dynamic fracture, fracture criteria based on nonlocal strains are quite effective. It should be stressed that this observation probably only holds for relatively thin structure in quasibrittle materials such as aluminum, which exhibit fracture in tearinglike modes.

Acknowledgment

The support of the Office of Naval Research under Grant Nos. N00014-06-1-0380 and N00014-06-1-0266 are gratefully acknowledged.

References

[1] Belytschko, T., and Black, T., 1999, "Elastic Crack Growth in Finite Elements With Minimal Remeshing," Int. J. Numer. Methods Eng., **45**(5), pp. 601–620.
[2] Moës, N., Dolbow, J., and Belytschko, T., 1999, "A Finite Element Method for Crack Growth Without Remeshing," Int. J. Numer. Methods Eng., **46**(1), pp. 131–150.
[3] Hansbo, A., and Hansbo, P., 2004, "A Finite Element Method for the Simulation of Strong and Weak Discontinuities in Solid Mechanics," Comput. Methods Appl. Mech. Eng., **193**, pp. 3523–3540.
[4] Mergheim, J., Kuhl, E., and Steinmann, P., 2005, "A Finite Element Method for the Computational Modelling of Cohesive Cracks," Int. J. Numer. Methods Eng., **63**, pp. 276–289.
[5] Song, J. H., Areias, P. M. A., and Belytschko, T., 2006, "A Method for Dynamic Crack and Shear Band Propagation With Phantom Nodes," Int. J. Numer. Methods Eng., **67**, pp. 868–893.
[6] Areias, P. M. A., Song, J. H., and Belytschko, T., 2005, "A Finite-Strain Quadrilateral Shell Element Based on Discrete Kirchhoff-Love Constraints," Int. J. Numer. Methods Eng., **64**, pp. 1166–1206.
[7] Areias, P. M. A., Song, J. H., and Belytschko, T., 2006, "Analysis of Fracture in Thin Shells by Overlapping Paired Elements," Comput. Methods Appl. Mech. Eng., **195**, pp. 5343–5360.
[8] Areias, P. M. A., and Belytschko, T., 2006, "A Comment on the Article: A Finite Element Method for Simulation of Strong and Weak Discontinuities in Solid Mechanics," Comput. Methods Appl. Mech. Eng., **195**, pp. 275–1276.
[9] Belytschko, T., Chen, H., Xu, J., and Zi, G., 2003, "Dynamic Crack Propagation Based on Loss of Hyperbolicity With a New Discontinuous Enrichment," Int. J. Numer. Methods Eng., **58**, pp. 1873–1905.
[10] Réthoré, J., Gravouil, A., and Combescure, A., 2005, "An Energy-Conserving Scheme for Dynamic Crack Growth Using the Extended Finite Element Method," Int. J. Numer. Methods Eng., **63**, pp. 631–659.
[11] Elguedj, T., Gravouil, A., and Combescure, A., 2006, "Appropriate Extended Functions for X-Fem Simulation of Plastic Fracture Mechanics," Comput. Methods Appl. Mech. Eng., **195**, pp. 501–515.
[12] Cirak, F., Ortiz, M., and Pandolfi, A., 2005, "A Cohesive Approach to Thin-Shell Fracture and Fragmentation," Comput. Methods Appl. Mech. Eng., **194**, pp. 2604–2618.
[13] Areias, P. M. A., and Belytschko, T., 2005, "Nonlinear Analysis of Shells With Arbitrary Evolving Cracks Using XFEM," Int. J. Numer. Methods Eng., **62**, pp. 384–415.
[14] Ortiz, M., and Pandolfi, A., 1999, "Finite-Deformation Irreversible Cohesive Elements for Three–Dimensional Crack-Propagation Analysis," Int. J. Numer. Methods Eng., **44**, pp. 1267–1282.
[15] Armero, F., and Ehrlich, D., 2006, "Finite Element Methods for the Multi-Scale Modeling of Softening Hinge Lines in Plates at Failure," Comput. Methods Appl. Mech. Eng., **195**, pp. 1283–1324.
[16] Chao, T. W., and Shepherd, J. E., 2002, "Fracture Response of Externally-Flawed Cylindrical Shells to Internal Gaseous Detonation Loading," *Emerging Technologies in Fluids, Structures, and Fluid/Structure Interactions*, ASME Pressure Vessels and Piping Conference, Vancouver, BC, pp. 85–98.
[17] Ahmad, S., Irons, B. B., and Zienkiewicz, O. C., 1970, "Analysis of Thick and Thin Shell Structures by Curved Finite Elements," Int. J. Numer. Methods Eng., **2**, pp. 419–451.
[18] Hughes, T. J. R., and Liu, W. K., 1981, "Nonlinear Finite Element Analysis of Shells: Part 2, Two dimensional Shells," Comput. Methods Appl. Mech. Eng., **27**, pp. 167–181.
[19] Hughes, T. J. R., and Liu, W. K., 1981, "Nonlinear Finite Element Analysis of Shells: Part 1, Three Dimensional Shells," Comput. Methods Appl. Mech. Eng., **26**, pp. 331–362.
[20] Belytschko, T., Lin, J. I., and Tsay, C. S., 1984, "Explicit Algorithms for the Nonlinear Dynamics of Shells," Comput. Methods Appl. Mech. Eng., **42**, pp. 225–251.
[21] Belytschko, T., Wong, B. L., and Chiang, H. Y., 1992, "Advances in One-Point Quadrature Shell Elements," Comput. Methods Appl. Mech. Eng., **96**, pp. 93–107.
[22] Belytschko, T., and Bachrach, W. E., 1986, "Efficient Implementation of Quadrilaterals With High Coarse-Mesh Accuracy," Comput. Methods Appl. Mech. Eng., **54**, pp. 279–301.
[23] Belytschko, T., and Leviathan, I., 1994, "Physical Stabilization of the 4-Node Shell Element With One Point Quadrature," Comput. Methods Appl. Mech. Eng., **113**, pp. 321–350.
[24] Papoulia, K. D., Sam, C. H., and Vavasis, S. A., 2003, "Time Continuity in Cohesive Finite Element Modeling," Int. J. Numer. Methods Eng., **58**, pp. 679–701.
[25] Chao, T. W., 2004, "Gaseous Detonation-Driven Fracture of Tubes," Ph.D. thesis, California Institute of Technology, Pasadena, CA.
[26] Johnson, F. A., and Radon, J. C., 1975, "Evaluation of Fracture Energy of Aluminum Alloys," J. Test. Eval., **3**, pp. 364–367.
[27] Johnson, F. A., and Radon, J. C., 1976, "Fracture Energy and Crack Tunnelling," J. Test. Eval., **4**, pp. 209–217.
[28] Roychowdhury, S., Roy, Y. D. A., and Dodds, R. H., Jr., 2002, "Ductile Tearing in Thin Aluminum Panels: Experiments and Analyses Using Large-Displacement, 3-D Surface Cohesive Elements," Eng. Fract. Mech., **69**, pp. 983–1002.
[29] Beltman, W. M., and Shepherd, J. E., 2002, "Linear Elastic Response of Tubes to Internal Detonation Loading," J. Sound Vib., **252**, pp. 617–655.

Finite Element Analysis of Plugging Failure in Steel Plates Struck by Blunt Projectiles

A. Kane
Department of Structural Engineering,
Structural Impact Laboratory (SIMLab),
Centre of Research-Based Innovation,
Norwegian University of Science and Technology,
NO-7491 Trondheim, Norway

T. Børvik[1]
Department of Structural Engineering,
Structural Impact Laboratory (SIMLab),
Centre of Research-Based Innovation,
Norwegian University of Science and Technology,
NO-7491 Trondheim, Norway;
Department of Research and Development,
Norwegian Defence Estates Agency,
NO-0015 Oslo, Norway
e-mail: tore.borvik@ntnu.no

O. S. Hopperstad

M. Langseth

Department of Structural Engineering,
Structural Impact Laboratory (SIMLab),
Centre of Research-Based Innovation,
Norwegian University of Science and Technology,
NO-7491 Trondheim, Norway

In this paper, the influence of mesh sensitivity on the fracture predictions during penetration and perforation of hardened blunt-nose cylindrical steel projectiles in plates of Weldox 460E, Weldox 700E, and Weldox 900E steel has been studied. The main objective is to try to describe the experimentally obtained trend of a decrease in ballistic limit velocity with increased target strength when the plates are impacted by blunt projectiles. This behavior is due to the occurrence of highly localized shear bands as the target strength increases. The impact tests are analyzed using the explicit solver of a nonlinear finite element code. A thermoelastic-thermoviscoplastic constitutive model with coupled or uncoupled ductile damage was used in the simulations. It was found that the residual velocity continuously increases when the element size is decreased from 125 μm to 15 μm in the shear zone, and that this increase is significantly stronger for impact velocities close to the ballistic limit. The ballistic limit decreases by up to 25% when the size of the element is decreased from 125 μm to 30 μm; the decrease being somewhat greater for the two steels with the highest strength. Even with the finest mesh, the experimental trend of a decreasing ballistic limit with increasing target strength was not predicted in the simulations, neither with coupled nor uncoupled damage. Nonlocal simulations based on smoothing of the damage and temperature fields, which are the two variables causing the softening, were carried out for the Weldox steels and a mesh size of 30 μm. These simulations indicate a reduction in the mesh sensitivity for both the coupled and uncoupled damage approaches when nonlocal averaging is employed.
[DOI: 10.1115/1.3129722]

Keywords: projectile perforation, Weldox steel, target strength, thermoelastic-thermoviscoplastic damage model, numerical simulations, softening

1 Introduction

Structural impact problems are of interest to many engineering disciplines, such as civil, automotive, offshore, military, and aeronautics, and have been studied in the literature for a long time (see, e.g., the review articles given in Refs. [1–3]). Earlier these types of problems were mainly studied experimentally. However, the development of numerical tools such as the finite element method (FEM) has offered new possibilities for attaining further and more generally applicable knowledge to these complex problems, and today FEM-based computer codes play an increasingly important role in engineering design.

One long-lasting numerical uncertainty in many impact related problems is the influence of mesh size when the structure deforms into strongly localized shear bands under adiabatic conditions. Such deformation modes often appear when blunt-nose projectiles strike metal plates at high velocities.

In presence of strain softening, related to strain localization in the material, mesh size effects and the associated mathematical background have been widely investigated in the literature (see, e.g., Ref. [4] for dynamic problems, Ref. [5] for brittle materials, and Ref. [6] where an extension is proposed to include thermal effects and thermomechanical couplings). It has also been shown [7,8] that the incorporation of rate-dependent constitutive relations introduces an implicit length scale through the viscous parameter that may limit the localization. However, the mesh size effect in the case of crack development due to localized adiabatic shear banding (ASB) is still an open question and requires more investigation. Zukas and Scheffler [9] discussed various factors related to the effects of meshing, which can lead to a disagreement between computations and experience of dynamic events. Voyiadjis and Abu Al-Rub [10] developed a nonlocal rate-dependent and gradient-dependent theory of plasticity and damage in order to reduce the mesh size dependence and showed a possible application in some particular cases of perforation of Weldox 460E steel by a blunt projectile. An improved multiphysics modeling approach was proposed by Zhou et al. [11] and Li and co-workers [12,13] for structural impact problems where finite element simulations consider different constitutive relations for the material inside and outside the ASB to take into account a possible phase transformation in the material. Crack propagation due to ASB was also captured using a simple strain-rate and temperature sensitive model (i.e., the Johnson–Cook model [14,15]) to predict shear bands combined with a recently developed ductile fracture criterion by Teng et al. [16].

In this paper, the influence of the mesh size on fracture predictions during impact and perforation by blunt-nose projectiles will be considered for plates of Weldox 460E, Weldox 700E, and Weldox 900E steels. Particular attention is given to describing the experimental trend of a decrease in ballistic limit with an increase in target strength, which was obtained by Dey et al. [17]. Since no proofs of a phase transformation were found in scanning electron microscope (SEM) and transmission electron microscope (TEM) investigations of the steel plates considered in this study [18], modified versions of the Johnson–Cook constitutive relation and fracture criterion [19] seem reasonable for perforation predictions and will be adopted in our simulations.

[1]Corresponding author.
Contributed by the Applied Mechanics Division of ASME for publication in the Journal of Applied Mechanism. Manuscript received February 1, 2008; final manuscript received October 2, 2008; published online June 12, 2009. Review conducted by Ashkan Vaziri.

2 Perforation of Steel Plates

Dey et al. [17] studied the effect of target strength on the perforation resistance of steel plates. Three different steels, namely, Weldox 460E, Weldox 700E, and Weldox 900E (where the numbers indicate nominal yield stress), were considered. Weldox is the brand name of a series of high-strength steels, produced and delivered by SSAB in Sweden, which combines high strength with high ductility and good weldability. The main difference between the steels is caused by tempering after hot rolling. Weldox 460E is a thermomechanical (TM) steel, and has obtained its high strength by rolling at a particular temperature followed by controlled cooling. Compared with normalized steel, TM steels have a microstructure containing less pearlite. Weldox 700E and Weldox 900E are materials in a group that goes through a significant quenching and tempering process and is termed as QT. As understood, the microstructure of the three steels varies considerably.

To study the material behavior under impact-generated loading conditions, the effects of strain hardening, strain-rate hardening, temperature softening, and stress triaxiality on the strength and ductility of the various steels have been determined. This was done by conducting three types of tensile tests: quasistatic tests with smooth and notched specimens, quasistatic tests at elevated temperatures, and dynamic tests over a wide range of strain rates (see Ref. [17] for details regarding the material tests). Some main results from the experimental material tests are given in Fig. 1. The data were then used to determine the material constants given in Table 1 for the steels using modified versions [19] of the well-known Johnson–Cook constitutive equation [14] and fracture criterion [15] (the applied models will be presented in detail in Sec. 3). Model results are compared with the experimental data in Fig. 1. Even though some deviations are seen, the agreement between experimental data and model predictions is satisfactory within the given experimental range.

Perforation tests were then carried out on 12 mm thick plates with blunt-, conical- and ogival-nose hardened steel projectiles. Nominal diameter, mass, and Rockwell C hardness value of the projectiles were 20 mm, 197 g, and 53, respectively, in all tests. A compressed gas gun (see, e.g., Ref. [20]) was used to launch projectiles at impact velocities between 150 m/s and 350 m/s. The initial and residual velocities of the projectile were measured, while the perforation process was captured using a digital high-speed camera system. Based on the measured data, the ballistic limit velocities plotted in Fig. 2 were obtained. Note that the tip of the conical-nose projectile shattered in tests with Weldox 700E and Weldox 900E targets. The experimental results further showed that for perforations with blunt projectiles the ballistic limit velocity (or perforation resistance) decreased for increasing strength, while the opposite trend was found in tests with conical and ogival projectiles. The reason for this was thoroughly discussed in a recent paper by Solberg et al. [18] based on a metallurgical investigation. It was found that the variation in failure mode caused by the various nose shapes was the primary reason for the contradictory trends. Both conical and ogival projectiles perforated the target by ductile hole enlargement, i.e., the material in front of the moving projectile is pushed aside by plastic flow, and it seems reasonable to assume that projectiles giving such a failure mode require more work to perforate a material when the strength increases. Thus, the ballistic limit velocity will increase for increasing material strength when using conical and ogival projectiles. For blunt projectiles, on the other hand, the targets fail by shear plugging. Here, strongly localized adiabatic shear bands were observed throughout the target plates after impact (see Fig. 3). It was found that the width of the shear band decreased significantly with increasing material strength (from more than 100 μm for Weldox 460E to less than 10 μm for Weldox 900E), which is a reasonable explanation for the decreasing ballistic limit. Even though white bands of intense shear were seen in the strongest targets after penetration, no proofs of a phase transformation were found in the consecutive SEM and TEM studies. Thus, it was concluded that the temperature inside the bands had never reached the temperature necessary for a phase transformation to austenite (at about 730 °C) in the 12 mm thick target plates (but proofs of such a phase transformation were found in 20 mm thick Weldox 460E steel plates impacted by blunt projectiles).

Finally, numerical simulations of the experimental tests were carried out using the nonlinear finite element code LS-DYNA [21]. It was found that the numerical simulations were able to describe the physical mechanisms in the perforation events with good accuracy. However, the experimental trend of a decrease in ballistic limit with an increase in target strength for blunt projectiles was not obtained with the numerical models used in the study by Dey et al. [17]. The obvious reason for this seems to be the change in strain localization, going from deformed to localized shear bands when the target strength increases (see Fig. 3). Since the width of the localized shear bands was much smaller than the smallest element size used in the numerical models, it is not surprising that the simulations failed to capture the drop in ballistics limit velocity with increasing target strength. For conical- and ogival-nose projectiles, on the other hand, where the strong shear localization with increasing target strength was not seen, a good agreement between the experimental data and numerical results was found.

3 Constitutive Equations and Regularization Techniques

The numerical simulations are carried out based on a phenomenological material model proposed by Børvik et al. [19]. The thermoelastic-thermoviscoplastic constitutive model with coupled or uncoupled ductile damage relies on modified versions of the constitutive relation [14] and fracture criterion [15] by Johnson and Cook. The model allows for large plastic strains, high strain rates, and adiabatic heating. The reader is referred to Ref. [19] for the detailed formulation of the modified model (see also Ref. [22]), while the main relations are recalled below for completeness.

The coupling between damage and plasticity is expressed using the effective stress concept [23]. Then, with the assumption of isotropic strain and strain-rate hardening and isotropic ductile damage, the equivalent stress σ_{eq} is defined by

$$\sigma_{eq} = (1 - \beta D)(A + Br^n)(1 + \dot{r}^*)^C(1 - T^{*m}) \tag{1}$$

where β is the coupling parameter (i.e., when β=1, damage is coupled with the constitutive equation; when β=0, no coupling is considered). The five material constants A, B, n, C, and m are determined from material tests. The internal variable r governs isotropic hardening and $\dot{r}^* = \dot{r}/\dot{\varepsilon}_0$ is a dimensionless strain-rate, where $\dot{r}$ is the rate of r and $\dot{\varepsilon}_0$ is a user-defined reference strain-rate. The homologous temperature T^* is given as $T^* = (T - T_0)/(T_m - T_0)$, where T, T_0, and T_m are the current temperature, the room temperature, and the melting temperature, respectively.

The associated flow rule is adopted, and r is then identified as the damage accumulated plastic strain

$$\dot{r} = (1 - \beta D)\dot{p} \tag{2}$$

where

$$\dot{p} = \sqrt{\frac{2}{3}\dot{\boldsymbol{\varepsilon}}^p : \dot{\boldsymbol{\varepsilon}}^p} \tag{3}$$

Here, $\dot{\boldsymbol{\varepsilon}}^p$ is the plastic rate-of-deformation tensor. The evolution of temperature is computed from the energy balance by assuming adiabatic conditions

$$\dot{T} = \chi \frac{\sigma_{eq}\dot{p}}{\rho C_p} \tag{4}$$

where ρ is the density, C_p is the specific heat at constant pressure, and the Taylor–Quinney empirical constant χ is the fraction of plastic work converted to heat (generally χ=0.9).

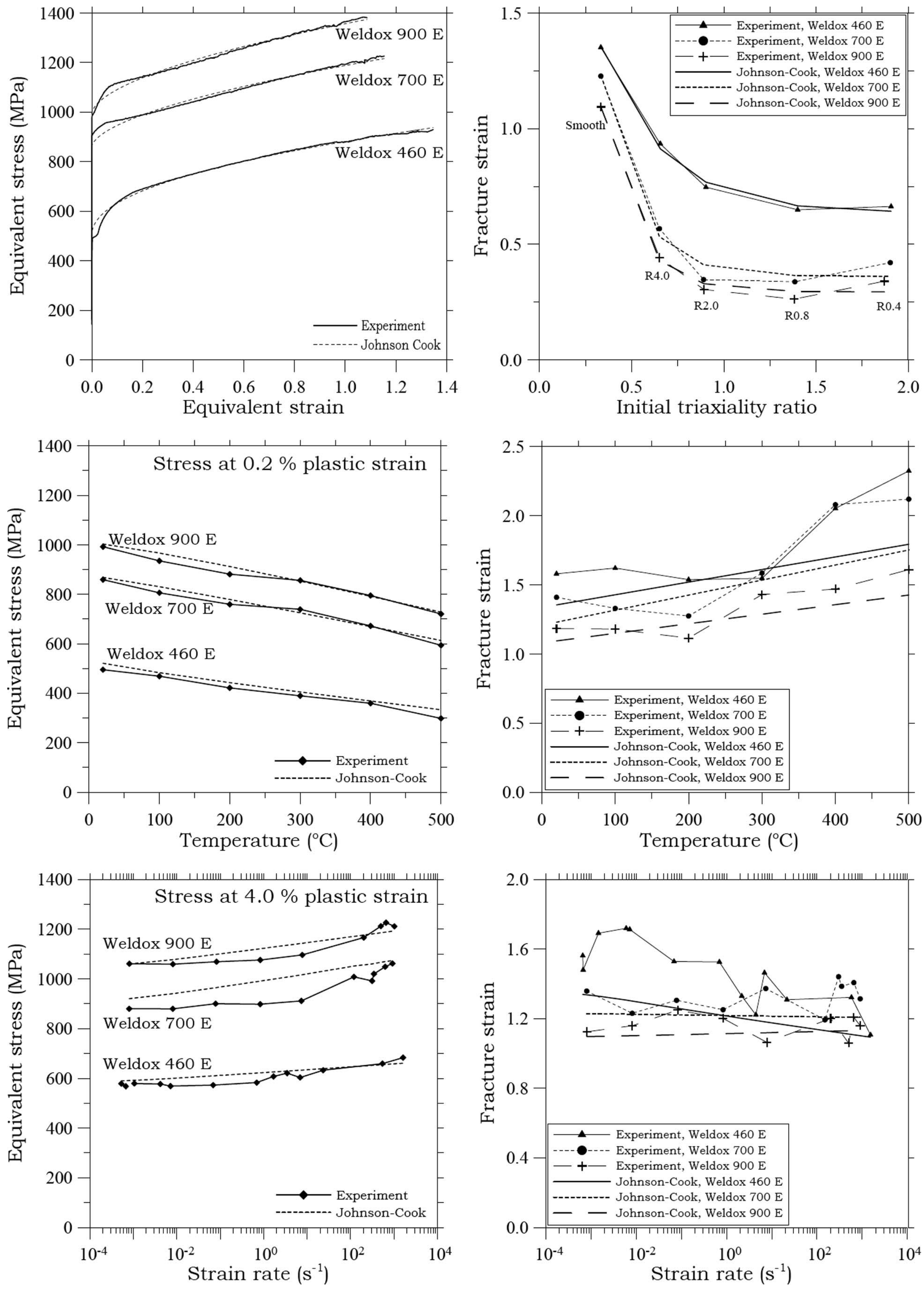

Fig. 1 Comparison between experimental data and model results for Weldox 460E, Weldox 700E, and Weldox 900E [17]

Table 1 Uncoupled and coupled (in brackets) modified JC-constants for the steels

Material		Weldox 460 E	Weldox 700 E	Weldox 900 E
Yield stress	A (MPa)	490	859	992
Strain hardening	B (MPa)	383 (656)	329 (785)	364 (988)
	n	0.45 (0.77)	0.58 (0.97)	0.57 (0.99)
Strain rate hardening	C	0.0079	0.0115	0.0087
Temperature softening	m	0.893	1.071	1.131
Fracture strain	D_1	0.636	0.361	0.294
	D_2	1.936	4.768	5.149
	D_3	−2.969	−5.107	−5.583
	D_4	−0.014	−0.0013	0.0023
	D_5	1.014	1.333	0.951
	D_c	1 (0.3)	1 (0.3)	1 (0.3)

Based on the Johnson and Cook failure strain model [15], the evolution of the damage variable is defined as [19]

$$\dot{D} = \begin{cases} 0 & \text{for} \quad p \leq p_d \\ D_c \dfrac{\dot{p}}{p_f - p_d} & \text{for} \quad p > p_d \end{cases} \tag{5}$$

where D_c is the critical damage, p_d is a damage threshold, and p_f is the fracture strain for dynamic loading, depending on the values of stress triaxiality, strain rates, and temperature

$$p_f = [D_1 + D_2 \exp(D_3 \sigma^*)][1 + \dot{p}^*]^{D_4}[1 + D_5 T^*] \tag{6}$$

where $D_1, D_2, \ldots, D_5$ are five additional material constants, $\sigma^* = \sigma_H / \sigma_{\text{eq}}$ is the stress triaxiality ratio, where σ_H is the hydrostatic stress, and $\dot{p}^* = \dot{p} / \dot{\varepsilon}_0$. It is assumed that $D_c \leq 1$ is a material constant and further that $p_d = 0$. Note that for each material, one set of material constants is identified when the constitutive relation is uncoupled from damage softening ($\beta = 0$), and another set of material constants is used when damage softening is taken into account in the constitutive relation ($\beta = 1$).

For an uncoupled damage model, material constants for the three different steels are presented in Table 1 [17]. For the coupled damage model, the critical damage D_c is assumed equal to 0.3 (see Refs. [19,23]). When damage is coupled to the constitutive relation, the damage softening is taken into account through the hardening parameters. The strain hardening constants B and n at $\sigma^* = 1/3$ are then determined by minimizing the residual between the stress-strain curves obtained with, respectively, the uncoupled and coupled models at quasistatic strain-rate and room temperature, using the method of least-squares. The agreement between the stress-strain curves under such conditions for the uncoupled and coupled models is shown in Fig. 4. Model constants for the three different steels affected by damage coupling are listed in the brackets in Table 1. Additional material constants for the steels required in the numerical simulations are listed in Table 2. The hardened steel projectile was modeled using a bilinear elastic-plastic von Mises material with isotropic hardening (i.e., Material Type 3 in LS-DYNA) and the material constants are given in Table 3 (see Ref. [19] for details and material tests).

Sufficiently small finite elements have to be used to discretize the target in simulation of projectile impact to take into account

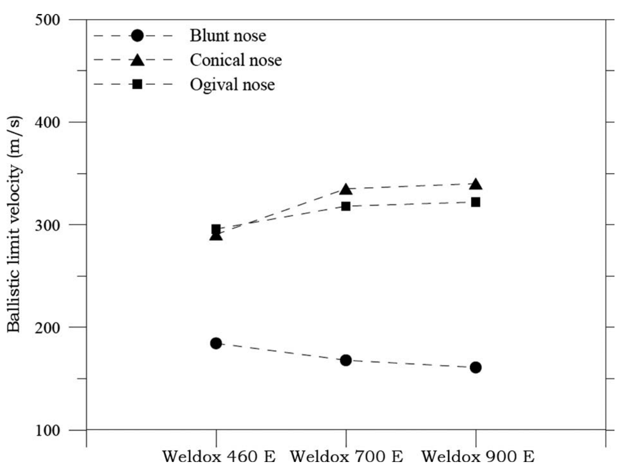

Fig. 2 Experimentally obtained ballistic limit velocities for the three steels for blunt-, conical-, and ogival-nose steel projectiles [17]

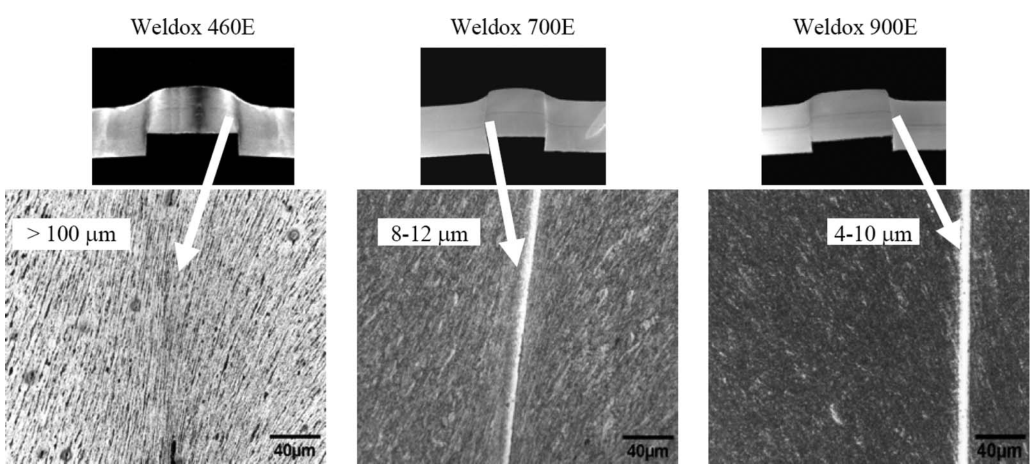

Fig. 3 Pictures of shear bands in the various steels after penetration by a blunt projectile [18]

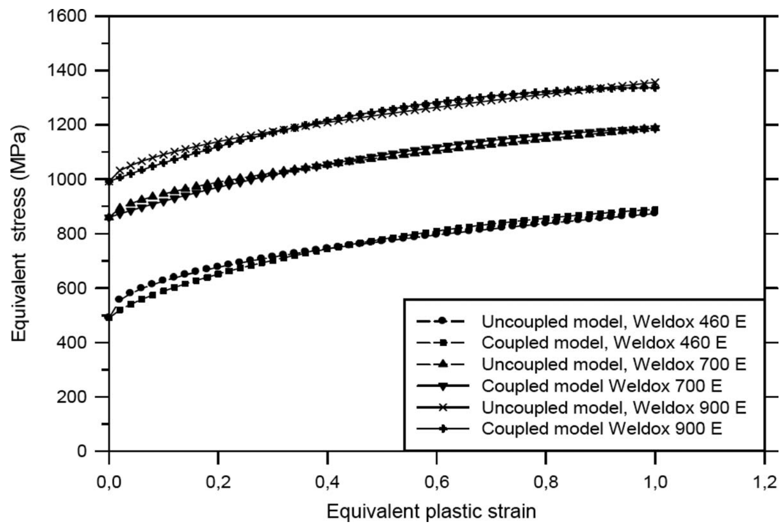

Fig. 4 Stress-strain curves obtained with the uncoupled and coupled model at quasistatic strain-rate and room temperature

high stress and strain gradients. But pathological mesh size dependency may also appear, since material softening is considered in the model [24]. According to Needleman [7], an implicit length scale appears for a rate-dependent model that may limit this pathological effect when the internal length scale is dominant over the size of the elements. However, for ballistic impacts a numerical study performed by Teng et al. [16] has shown that this viscous length scale (of the order of 1 μm) is too small to control the development of adiabatic shear bands. Therefore, in an attempt to reduce the influence of mesh sensitivity on the fracture predictions, simulations could be performed by introducing an explicit length scale into the constitutive equation using the nonlocal method of Pijaudier-Cabot and Bãzant [24].

In nonlocal simulations carried out with the explicit solver of LS-DYNA [21], the local history variable f is replaced by an "average" $\bar{f}$ of the variable within the neighborhood Ω_r of radius L using the material card *MAT_NONLOCAL described as follows

$$\bar{f}(\mathbf{x}) = \frac{1}{W_r}\int_{\Omega_r} w(\mathbf{x}-\mathbf{y})f(\mathbf{y})d\Omega \tag{7}$$

where

$$W_r = \int_{\Omega_r} w(\mathbf{x}-\mathbf{y})d\Omega \tag{8}$$

and

$$w(\mathbf{x}-\mathbf{y}) = \frac{1}{\left[1+\left(\frac{\|\mathbf{x}-\mathbf{y}\|}{L}\right)^p\right]^q} \tag{9}$$

Here, w is the nonlocal weight function, $\mathbf{x}$ and $\mathbf{y}$ are position vectors, and the parameters p and q determine the bell-shape of the weighting function.

Two variables in the constitutive relation, namely, the damage D and the temperature T, cause softening in the material during straining, and must thus be smoothed. At each time increment, the nonlocal damage D^{nloc} and the nonlocal temperature T^{nloc} can be computed applying the nonlocal integral operator on the plastic strain rate. Similar effects may be obtained by applying the nonlocal operator directly on each internal variable causing softening, but this increases the cost of computation. The increments of the nonlocal variables are defined as

$$\Delta D^{\mathrm{nloc}} = D_c\frac{\overline{\Delta p}}{p_f - p_d} \tag{10}$$

and

$$\Delta T^{\mathrm{nloc}} = \chi\frac{\sigma_{\mathrm{eq}}\overline{\Delta p}}{\rho C_p} \tag{11}$$

During simulations using nonlocal averaging, the flow stress is computed simply by using nonlocal values of damage and/or temperature while the plastic strain and strain rate are always determined locally.

Voyiadjis and Abu Al-Rub [10] proposed to include several length scales and a possible variation of length scales with the state of loading, as a function of different mechanisms associated with softening. However, in our simulations these possible effects will be neglected, and the same length scale is introduced in order to compute the two nonlocal internal variables (i.e., D^{nloc} and T^{nloc}) associated to material softening. This length scale is further associated with the element size used in the finest mesh that is applied in the simulations, which again was limited by the computational resources available. Based on this, simulations were performed with a length scale of 30 μm, which is about three times the measured average grain size of the steels [18]. In the nonlocal averaging algorithm, the elements included in the nonlocal volume of interaction are obtained by computing the distance

Table 2 Additional material constants for the steels

Elastic constants and density			Strain rate hardening	Temperature softening and adiabatic heating				
E (GPa)	ν	ρ (kg/m^3)	$\dot{\varepsilon}_0$ (s^{-1})	T_r (K)	T_m (K)	C_p (J/kg/K)	χ	α (K^{-1})
210	0.33	7850	5×10^{-4}	293	1800	452	0.9	1.2×10^{-5}

Table 3 Material constants used for the hardened steel projectile [19]

E (GPa)	ν	ρ (kg/m^3)	σ_0 (MPa)	E_t (MPa)
204	0.33	7850	1900	15,000

between the integration points (at the center of each element). The coefficients p and q of the bell-shaped weighting function in Eq. (9) are chosen constant and equal to $p=8$ and $q=2$ in all simulations to have a strong nonlocal effect in all the region of interaction determined by the length scale.

4 Numerical Simulations

Following the work of Dey et al. [17], a mesh sensitivity study is performed where various refined meshes are used in the attempt to describe the experimental trend of a decrease in ballistic limit with an increase in target strength when struck by blunt projectiles. All impact tests are analyzed using the explicit solver of the nonlinear FE code LS-DYNA [21], using the material model and the procedures described above.

Four-node axisymmetric elements with one integration point and stiffness-based hourglass control are used. Considering identical initial conditions to those used in a corresponding experimental test (regarding geometry, initial projectile velocity, boundary conditions, etc.), simulations are repeated using an initial element size in the impact region of 125 μm, 60 μm, 30 μm, and 15 μm (see Fig. 5). This gave from 96 to 800 elements over the thickness of the 12 mm thick steel plates. In order to satisfy the stability criteria, time increments of the order $10^{-9}-10^{-11}$ s are used for the coarsest and finest meshes, respectively.

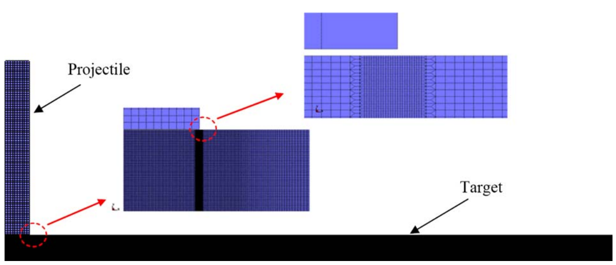

Fig. 5 Axisymmetric finite element model used in the penetration analysis for a 12 mm thick plate with a diameter of 500 mm and initial element size of 30 μm in the impact region

Element erosion by an element-kill algorithm available in LS-DYNA is used in the simulations to remove elements that have reached various fracture criteria. In addition to the damage criterion, giving element erosion when D equals D_c, two other erosion criteria were adopted. First, a temperature-based fracture criterion, causing element erosion when the temperature T within an element reaches a critical value given as $T_c=0.9T_m$, was used to remove elements that had practically lost all their shear strength. Second, a shape-based fracture criterion was adopted, which erodes the element when the aspect ratio, identified as the ratio between the diagonals in the case of rectangular elements, reaches a critical value equal to 0.05. The two latter fracture criteria were included to avoid numerical problems in severely distorted elements. Note that the last failure criterion only acted on pathological elements, which were prejudicial to the simulation (causing premature termination) and the value was fixed in order not to disturb the crack prediction too much, which is mainly conducted by the damage failure criterion. The result of including these failure criteria in the simulations will be discussed in more details below.

Figure 5 shows how the projectile and target plate are meshed. The mesh is much finer in the target than in the projectile. Furthermore, the plate is divided into different regions with different fineness of the mesh, and a very fine mesh is applied in the region where the adiabatic shear band is expected. An example of the adiabatic shear banding process is given in Fig. 6 for the Weldox 700E plate, as fringes of accumulated plastic strain. It is seen that a zone of intense shear develops in the plate below the periphery of the projectile, leading to crack propagation through the plate from the top side to the bottom side. The projectile then perforates the plate by pushing out a nearly cylindrical plug. The experiments showed that the shear zone became more localized and intense as the strength of the material increased. Figure 7 compares the accumulated plastic strain field for the Weldox 460E (left) and Weldox 700E (right) plates. It is clearly seen that the shear zone is more localized also in the simulation when the target strength increases, and thus this experimental trend is captured. We further notice that the crack propagates in front of the projectile, which was also seen in the experiments [17,19].

The effect of mesh size on the velocity-time curve is shown in Fig. 8 for simulations of a Weldox 700E plate struck by the projectile at an initial velocity of 300 m/s, using uncoupled damage without nonlocal averaging. By reducing the element size from 125 μm to 15 μm, the computational time increased from about

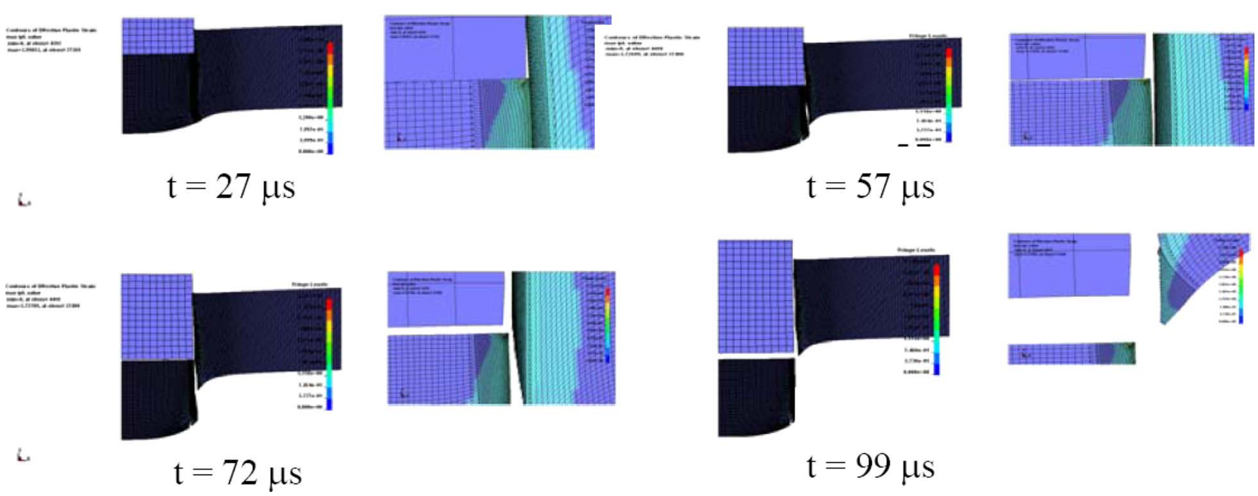

Fig. 6 Effective plastic strain field development during perforation of a Weldox 700E plate, obtained with the coupled ductile damage model for an initial projectiles velocity $v_i=265$ m/s

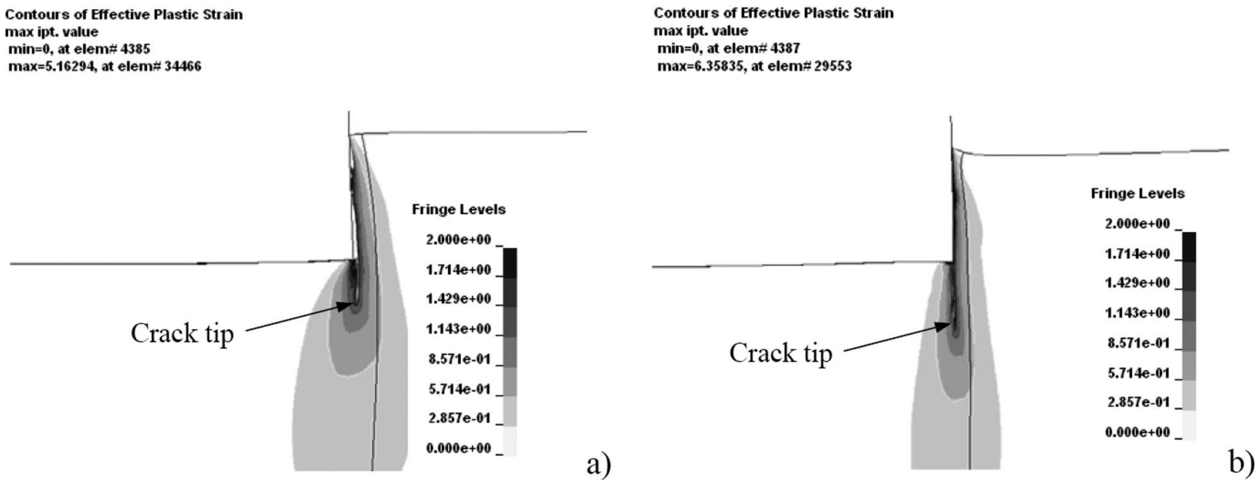

Fig. 7 Effective plastic strain field during penetration at $t=21$ μs (initial velocity $v_i=300$ m/s, initial element size of 15 μm in the impact region): (*a*) Weldox 460E and (*b*) Weldox 700E

2 CPU hours to more than 150 CPU hours when running on a HP dual quadcore 2.66 GHz (16 Gbyte RAM) workstation. The residual velocity continuously increases as the element size becomes smaller, and the solution has not converged even for the smallest element size. The reason for the steady increase in the residual velocity is intensified strain localization as the elements in the shear zone get smaller.

Due to the severe increase in CPU-time and added numerical difficulties when using an element size of 15 μm, it was decided to use a minimum element size of 30 μm in the remaining simulations. The residual velocities obtained by the uncoupled damage model and the local approach for Weldox 460E with respect to mesh density are plotted for various initial velocities in Fig. 9. The results show that the residual velocity increases (indicating a decrease in ballistic limit velocity or capacity) when the mesh is refined, and the effect becomes stronger for simulations close to the ballistic limit velocity. Similar results were observed for the Weldox 700 E and Weldox 900 E steels. From this it may be concluded that the effect of mesh size in ballistic problems should always be studied at impact velocities close to the numerical ballistic limit of the target in order to ensure reliable results.

The analytical model by Recht and Ipson [25] was then used to compute the ballistic limit velocity v_{bl} based on a number of runs. The Recht–Ipson model may be generalized as

$$v_r = \begin{cases} 0 & for \quad 0 \le v_i \le v_{\text{bl}} \\ a(v_i^p - v_{\text{bl}}^p)^{1/p} & for \quad v_i > v_{\text{bl}} \end{cases} \tag{12}$$

where v_i and v_r are the initial and residual velocities of the projectile, respectively. For impact velocities higher than the ballistic limit, i.e., $v_i > v_{\text{bl}}$, the Recht–Ipson model can be rewritten as

$$v_{\text{bl}} = (v_i^p - (v_r/a)^p)^{1/p} \tag{13}$$

Considering projectile residual velocities from simulations for at least three distinct initial velocities, estimates of v_{bl} can be obtained using the method of least-squares when values for the model constants a and p are taken from the experimental study by Dey et al. [17].

Based on Eq. (13), the ballistic limit velocities for the various steels were computed as a function of element size using uncoupled and coupled damage without nonlocal averaging. The results are shown in Fig. 10 and confirm in all cases the same type of mesh dependence as observed in Fig. 9 (where only the uncoupled model for Weldox 460E was considered). From these plots it is seen that the ballistic limit velocity decreases with up to 25% when the mesh size is decreased from 125 μm to 30 μm.

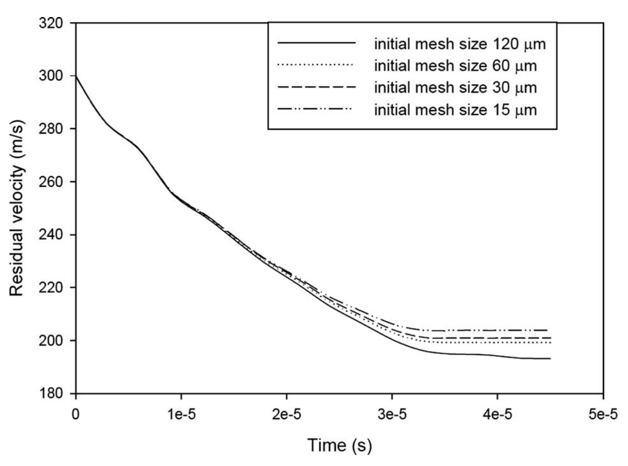

Fig. 8 Effect of mesh-size on the velocity-time curve from simulations using an uncoupled approach during perforation of a Weldox 700E plate at an initial velocity of 300 m/s

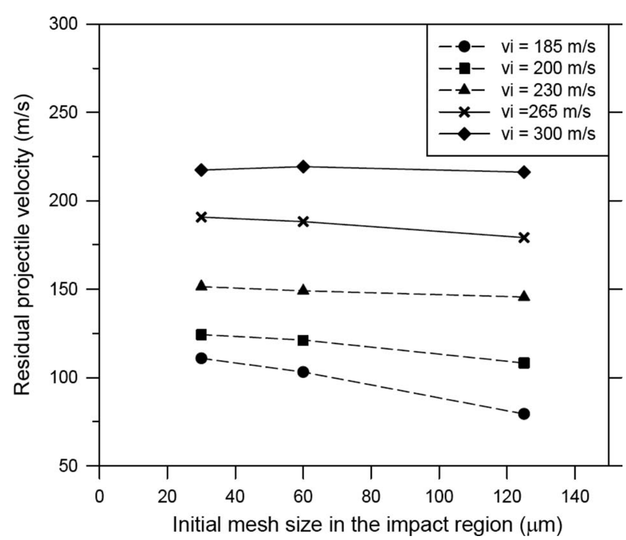

Fig. 9 Mesh-size sensitivity on the residual velocity of Weldox 460E for different initial impact velocities using an uncoupled model and a local approach

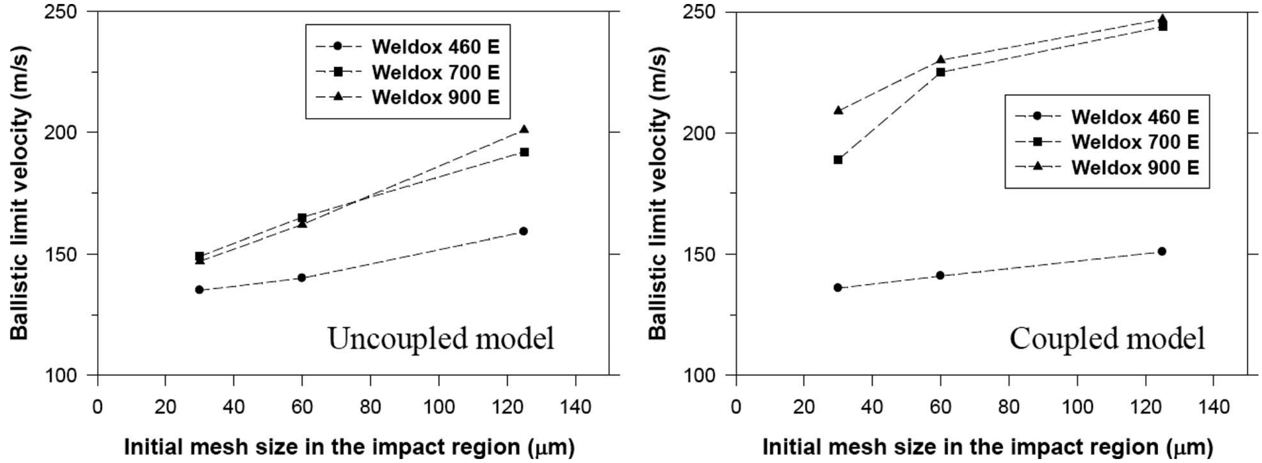

Fig. 10 Mesh-size sensitivity on the ballistic limit velocity for the three steels using a local approach in the simulations

The decrease seems to be somewhat stronger for Weldox 700E and 900E than for Weldox 460E, which is consistent with the metallurgical study showing more intense shear bands for the two steels of highest strength.

Ballistic limit velocities obtained using uncoupled and coupled damage and the local approach (i.e., without nonlocal averaging) are compared with the experimental data in Fig. 11. The experimentally obtained trend of a decreasing ballistic limit velocity with increasing target strength is not reproduced in the simulations even with an element size of 30 μm. Weldox 460E consistently obtains the lowest capacity for both uncoupled and coupled simulations. The uncoupled simulations give slightly higher capacity for Weldox 700E than for Weldox 900E, in agreement with the experimental observations. The predicted ballistic limit shows a steady increase with plate hardness for the simulations with coupled damage and is significantly higher than in the uncoupled simulations for Weldox 700E and Weldox 900E. The coupled and uncoupled damage formulations were calibrated to give about the same stress-strain behavior in uniaxial tension, i.e., for stress triaxiality equal to $\frac{1}{3}$. For higher stress triaxiality (or more tension), damage will grow faster and the coupled damage model will give lower strength than the uncoupled one due to softening. On the contrary, for lower stress triaxiality (or higher pressures), the evolution of damage will be slowed down (as compared with uniaxial tension), and accordingly the coupled damage model will give the highest strength. In the first phase of the plugging problem, the stress state is dominated by high pressures, in particular for the high-strength steels Weldox 700E and 900E, and this is believed to be the cause for the higher ballistic limit velocity obtained with the coupled damage model for these materials. Although time consuming, a mesh size finer than 30 μm should be used in the shear zone to capture the strain localization properly for the two steels with the highest strength. However, this is not practical with today's personal computers, and supercomputing using massive parallel processing (MPP) may be required.

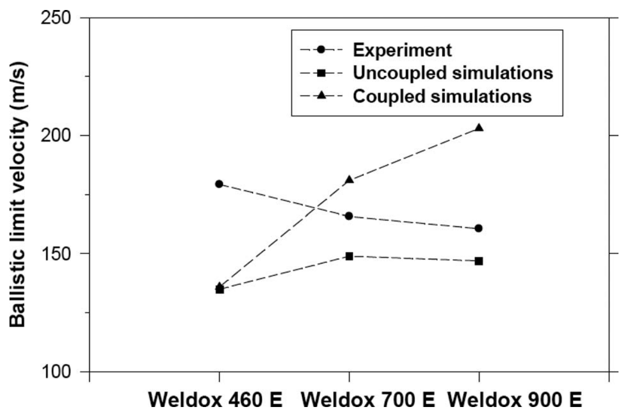

Fig. 11 Ballistic limit velocities for the three steels with an initial element size of 30 μm in the impact region: comparison between uncoupled and coupled models

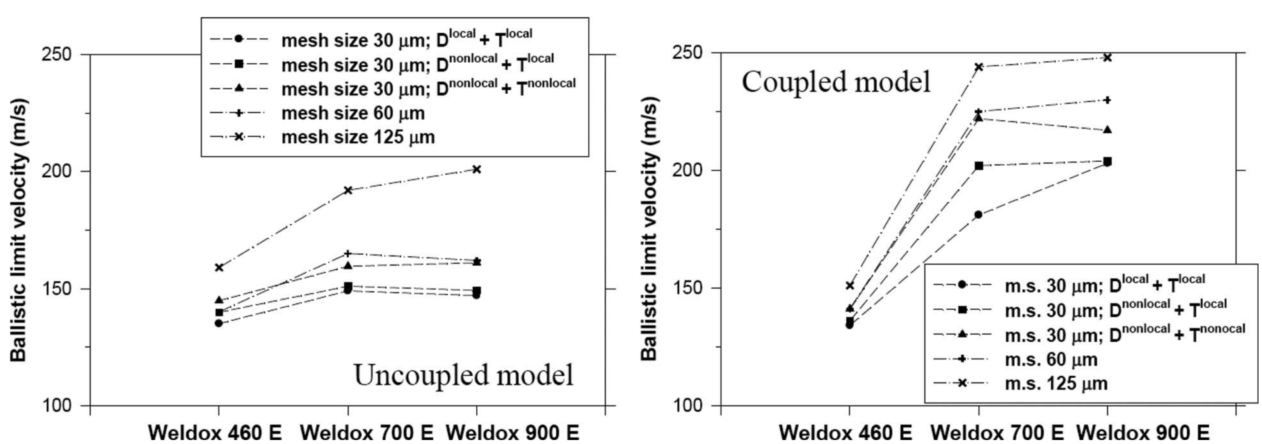

Fig. 12 Ballistic limit velocity for the three steels showing the influence of mesh size and nonlocal averaging: uncoupled simulations to the left and coupled simulations to the right

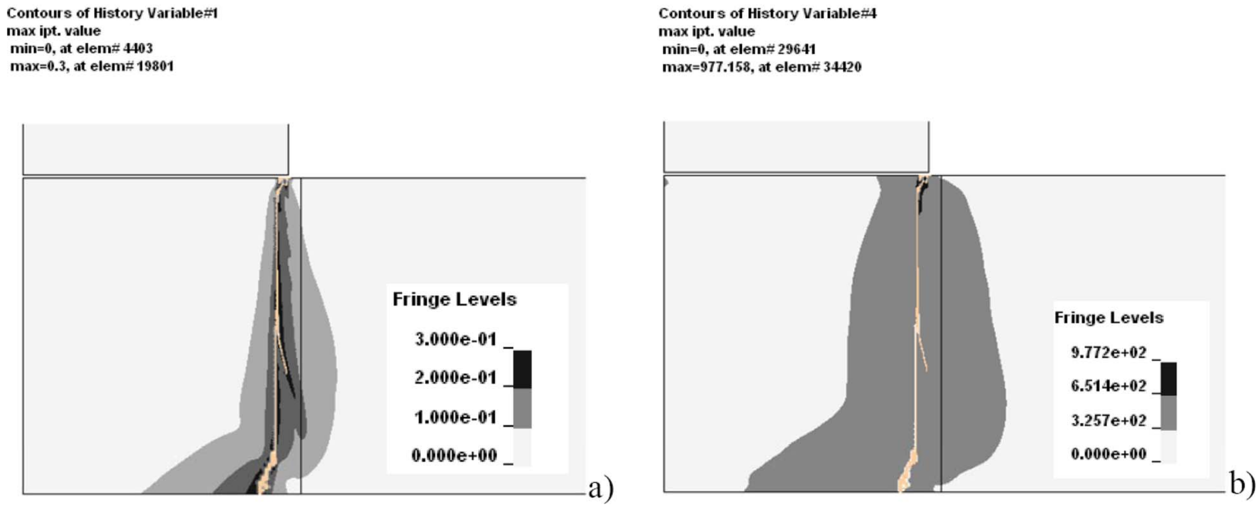

Fig. 13 Perforation of Weldox 460E (coupled simulations with initial velocity $v_i = 265$ m/s and initial element size of 15 μm in the impact region): (*a*) damage field and (*b*) temperature field

Nonlocal simulations were performed for the Weldox steels using 30 μm element size and a nonlocal radius L equal to 30 μm. It should be noticed that the length scale introduced in the nonlocal simulations is still too high to take properly into account the inelastic process in the strongly localized adiabatic shear bands of Weldox 700E and Weldox 900E. Element sizes less than 10 μm would be necessary to run more appropriate nonlocal simulations for these materials, which was not feasible with the available computer facilities (without using MPP).

The effect of nonlocal regularization on the predicted ballistic limit for Weldox 460E steel is shown in Fig. 12. Since a nonlocal radius $L = 30$ μm was adopted in the simulations, nonlocal simulations were only performed with the finest mesh having an element size equal to 30 μm. In the uncoupled simulations, nonlocal averaging leads to an increase in the ballistic limits compared with the local approach; the increase is being about the same for all steels. The effect is higher when both the variables causing softening are made nonlocal. The picture is somewhat less clear for the coupled simulations, even though nodal averaging consistently leads to higher capacity compared with the local approach. It transpires that the effect of nodal averaging is much stronger for Weldox 700E than for the other two steels. In general, it seems like the simulations with nodal averaging of both temperature and damage give about the same capacities as the simulations with 60 μm element size.

Simulations can also be envisaged by introducing two distinct material length scales to take into account the variations of temperature and damage distribution in the impact region, but once again such simulations are limited by computer capacity. Another possible route is to include thermocoupling in the simulation to get a better prediction of the temperature distribution in the narrow shear zone, especially since the high temperatures seen in the FE simulations could not be proven in metallurgical investigations of the impacted plates [18].

As described above, three different erosion criteria were used in the simulations, based on damage, temperature, and the aspect ratio of the element. For the softest steel (Weldox 460E), the elements were eroded by reaching the critical damage and temperature, with only some few exceptions. Figure 13 shows the damage and temperature fields for one simulation for a Weldox 460E target plate. It is seen that there is a concentration of highly damaged elements along the crack path, while the temperature field is more diffused except for a small region in the first part of the crack path. In this region, the pressure is high (low stress triaxiality) and thus the damage evolution is slow – implying that high temperatures may be important for the initiation of crack propagation. Similar plots are shown for Weldox 700E in Fig. 14. In this case, we see almost no damage evolution along the first part of the crack path, while the temperature is high and more localized. The reason is the very high pressure in this zone, allowing for large plastic strains without damage (see also top right in Fig. 1). However, in the final part of the crack path, the damage is high and is governing the crack propagation, because here the stress triaxiality becomes positive. Thus, the plastic strain at fracture is lower, leading to less mechanical dissipation and less temperature increase. Owing to the large plastic strain and low damage in the upper part of the crack path, fracture was initiated either by the temperature criterion or the aspect-ratio criterion for the two steels of highest strength. The temperature fields due to plastic work displayed in Figs. 13 and 14 correspond quite well with the micrographs of diffuse versus localized shear bands revealed in the plates after impact (see Fig. 3). It should also be commented that the crack propagation seems somewhat limited by the size of the refined region, and that the crack seems to branch into two cracks close to the rear side of the Weldox 700E plate (Fig. 14). This is consistent to the jagged surface of the plug observed experimentally for the highest strength steels, while the surface of the plug was smooth for the Weldox 460E steel [17].

The aspect-ratio criterion is a purely numerical criterion used to get rid of troublesome elements that would lead to premature termination, and it was set to 0.05 in all simulations. Since the initial aspect ratio of the elements was unity, this represents a highly deformed element. To investigate the effect of the value of this criterion on the predicted residual velocity a limited sensitivity study was undertaken for a Weldox 700E plate. The results are shown in Fig. 15. It transpires that there is no effect on the residual velocity, provided that the critical aspect ratio is set equal to or less than the chosen value of 0.05. On the other side, if this value is taken too high, it will certainly affect the residual velocity. In general, a higher residual velocity is expected when the value of the critical aspect ratio increases, but for the chosen example the residual velocity actually decreases. The reason for this is that additional elements outside the primary crack path were deleted, disturbing the complete perforation process and leading to unphysical results. We further found that when the critical aspect ratio was less than or equal to 0.05, only some few elements were deleted due to this criterion, mainly in the initial stage of impact, while the bulk of elements was eroded by damage or high temperature.

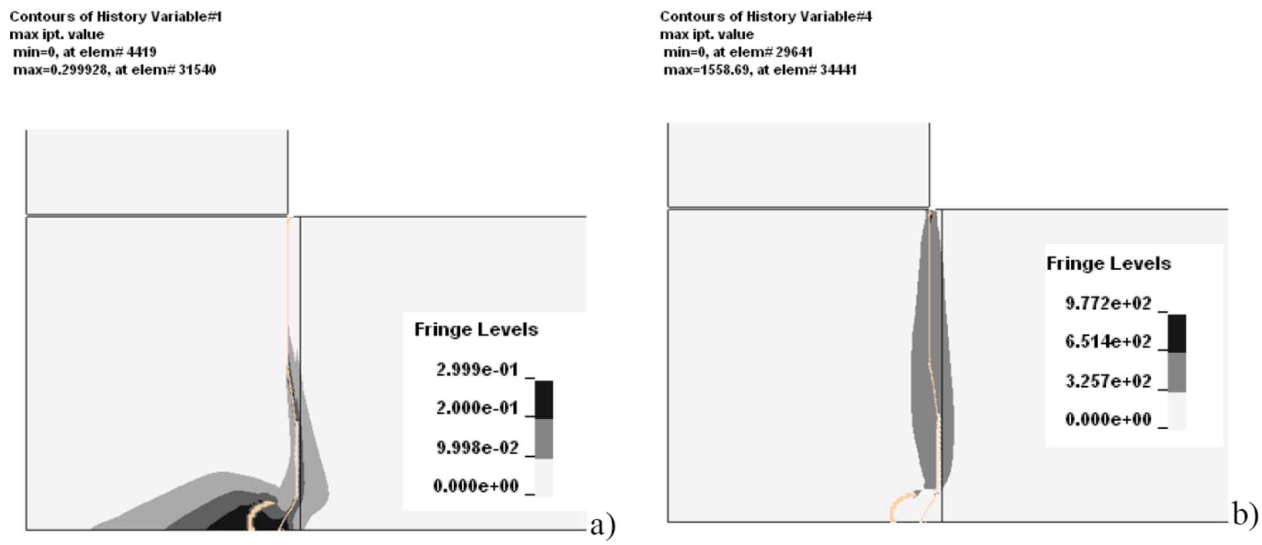

Fig. 14 Perforation of Weldox 700E (coupled simulations with initial velocity v_i=265 m/s and initial element size of 15 μm in the impact region): (*a*) damage field and (*b*) temperature field

5 Concluding Remarks

In this paper we have studied the influence of mesh size on fracture predictions during ballistic impact of hardened blunt-nose cylindrical steel projectiles in target plates of Weldox 460E, Weldox 700E, and Weldox 900E steels. Such impact problems cause failure by shear plugging, where the deformation localizes into narrow adiabatic shear bands.

A thermoelastic-thermoviscoplastic constitutive model with coupled or uncoupled ductile damage was used to carry out the numerical simulations. The effect on the ballistic limit velocity by introducing a length scale into the constitutive equations using a nonlocal approach was also investigated. In this approach, nonlocal averaging of the damage and temperature fields, which are the two variables causing the softening in the material during plastic straining, were considered. Mesh refinement was used in an attempt to describe the experimental trend of a decrease in ballistic limit velocity with an increase in target strength for blunt projectiles due to the occurrence of highly localized shear bands.

Considering the various steels, mesh size dependence was observed for both uncoupled and coupled models, leading to increased residual projectile velocities and reduced ballistic limit velocities as the element size was refined. Even with an initial element size of 30 μm in the impact region, the experimental trend of a decrease in ballistic limit velocity with increasing material strength for blunt projectiles was not predicted. The minimum size mesh used in the impact region in this study still appears high compared with the width of the localized shear bands measured in impacted plates of Weldox 700E and Weldox 900E.

Nonlocal simulations were performed for the Weldox steels with 30 μm mesh size and nonlocal radius 30 μm. When nonlocal averaging of both the damage and temperature fields is applied, the mesh sensitivity of the ballistic limit velocity is reduced for both the coupled and uncoupled models.

The simulation of ductile fracture during projectile perforation is conditioned by the ability of the constitutive model to take into account the complex processes of material degradation. The as-

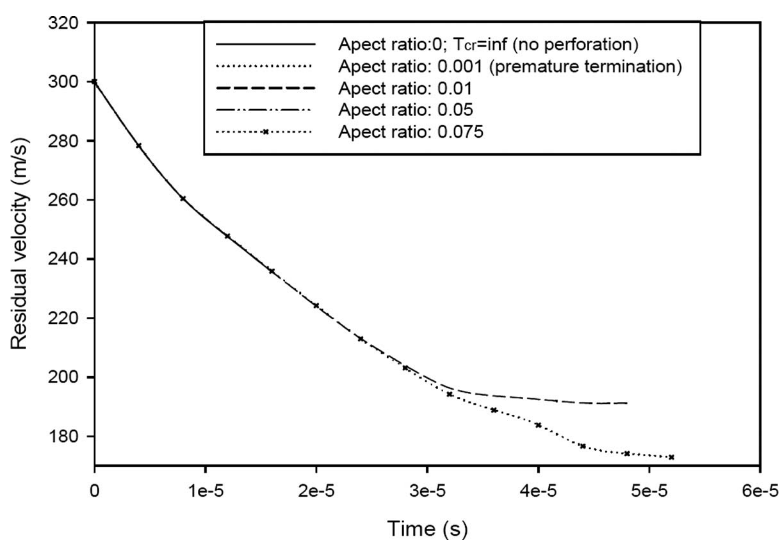

Fig. 15 Influence of the value of the critical element aspect ratio (from 0.001 to 0.075) on the residual velocity versus time curve in penetration for Weldox 700E (coupled simulations with element size 30 μm)

sumptions made in the simple isotropic damage law adopted in the current study should therefore be considered, and further investigations will be performed to improve the damage formulation and to evaluate its consequences on the prediction of the ballistic limit velocity.

The influence of mesh size in simulations of plugging has, in this paper, been investigated in a rather heuristic manner, and the current conclusions are based on the comparison of a limited number of experimental data with complex numerical simulations at a structural level. To gain a better understanding of the mesh size effect in simulations of dynamic fracture, a more rigorous approach should be taken and discussed in a concise mathematical way.

Acknowledgment

The financial support of this work from the Structural Impact Laboratory (SIMLab), Centre for Research-based Innovation (CRI) at the Norwegian University of Science and Technology (NTNU), is gratefully acknowledged. Furthermore, the authors would like to express their gratitude to Dr. Torodd Berstad for help in obtaining the numerical results.

References

[1] Backman, M. E., and Goldsmith, W., 1978, "The Mechanics of Penetration of Projectiles Into Targets," Int. J. Eng. Sci., **16**, pp. 1–99.
[2] Corbett, G. G., Reid, S. R., and Johnson, W., 1996, "Impact Loading of Plates and Shells by Free-Flying Projectiles," Int. J. Impact Eng., **18**(2), pp. 141–230.
[3] Goldsmith, W., 1999, "Review: Non-Ideal Projectile Impact on Targets," Int. J. Impact Eng., **22**, pp. 95–395.
[4] Hadamard, J., 1903, *Leçons sur la propagation des ondes et les équations de l'hydrodynamique*, Hermann, Paris, Chap. 6.
[5] Bãzant, Z. P., 1986, "Mechanics of Distributed Cracking," Appl. Mech. Rev., **39**(5), pp. 675–705.
[6] Benallal, A., and Bigoni, D., 2004, "Effects of Temperature and Thermo-Mechanical Couplings on Material Instabilities and Strain Localization of Inelastic Materials," J. Mech. Phys. Solids, **52**, pp. 725–753.
[7] Needleman, A., 1988, "Material Rate Dependent and Mesh Sensitivity in Localization Problems," Comput. Methods Appl. Mech. Eng., **67**, pp. 69–85.
[8] Perzyna, P., 1963, "The Constitutive Equations for Rate-Sensitive Materials," Q. Appl. Math., **20**, pp. 321–332.
[9] Zukas, J. A., and Scheffler, D. R., 2000, "Practical Aspects of Numerical Simulations of Dynamic Events: Effects of Meshing," Int. J. Impact Eng., **24**, pp. 925–945.
[10] Voyiadjis, G. Z., Abu Al-Rub, R. K., and Palazotto, A. N., 2008. "Constitutive Modeling and Simulation of Perforation of Targets by Projectiles," AIAA J., **46**, pp. 304–316.
[11] Zhou, M., Ravichandran, G., and Rosakis, A. J., 1996b, "Dynamically Propagating Shear Bands in Impact-Loaded Prenotched Plates—II. Numerical simulations," J. Mech. Phys. Solids, **44**(6), pp. 1007–1032.
[12] Li, S., Liu, W. K., Qian, D., Guduru, P. R., and Rosakis, A. J., 2001, "Dynamic Shear Band Propagation and Microstructure of Adiabatic Shear Band," Comput. Methods Appl. Mech. Eng., **191**(1–2), pp. 73–92.
[13] Li, S., Liu, W. K., Rosakis, A. J., Belytschko, T., and Hao, W., 2002, "Mesh-Free Galerkin Simulations of Dynamic Shear Band Propagation and Failure Mode Transition," Int. J. Solids Struct., **39**(5), pp. 1213–1240.
[14] Johnson, G. R., and Cook, W. H., 1983, "A Constitutive Model and Data for Metals Subjected to Large Strains, High Strain Rates and High Temperatures," Proceedings of the Seventh International Symposium on Ballistics, Hague, pp. 541–547.
[15] Johnson, G. R., and Cook, W. H., 1985, "Fracture Characteristics of Three Metals Subjected to Various Strains, Strain Rates, Temperatures and Pressures," Eng. Fract. Mech., **21**, pp. 31–48.
[16] Teng, X., Wierzbicki, T., and Couque, H., 2007, "On the Transition From Adiabatic Shear Banding to Fracture," Mech. Mater., **39**, pp. 107–125.
[17] Dey, S., Børvik, T., Hopperstad, O. S., Leinum, J. R., and Langseth, M., 2004, "The Effect of Target Strength on the Perforation of Steel Plates Using Three Different Projectile Nose Shapes," Int. J. Impact Eng., **30**(8–9), pp. 1005–1038.
[18] Solberg, J. K., Leinum, J. R., Embury, J. D., Dey, S., Børvik, T., and Hopperstad, O. S., 2007, "Localised Shear Banding in Weldox Steel Plates Impacted by Projectiles," Mech. Mater., **39**, pp. 865–880.
[19] Børvik, T, Hopperstad, OS, Berstad, T, and Langseth, M., 2001, "A Computational Model of Viscoplasticity and Ductile Damage for Impact and Penetration," Eur. J. Mech. A/Solids, **20**, pp. 685–712.
[20] Børvik, T., Hopperstad, O. S., Langseth, M., and Malo, K. A., 2003, "Effect of Target Thickness in Blunt Projectile Penetration of Weldox 460 E Steel Plates," Int. J. Impact Eng., **28**(4), pp. 413–464.
[21] Hallquist, J. O., 2003, *LS-DYNA Keyword User's Manual, Version 970*, Livermore Software Technology Corporation, California.
[22] Camacho, G. T., and Ortiz, M., 1997, "Adaptive Lagrangian Modelling of Ballistic Penetration of Metallic Targets," Comput. Methods Appl. Mech. Eng., **142**, pp. 269–301.
[23] Lemaitre, J., 1992, *A Course on Damage Mechanics*, Springer, Berlin.
[24] Pijaudier-Cabot, G., and Bãzant, Z. P., 1987, "Nonlocal Damage Theory," J. Eng. Mech., **113**, pp. 1512–33.
[25] Recht, R. F., and Ipson, T. W., 1963, "Ballistic Perforation Dynamics," ASME J. Appl. Mech., **30**(3), pp. 384–390.

Fluid-Structure and Shock-Bubble Interaction Effects During Underwater Explosions Near Composite Structures

Yin L. Young
e-mail: yyoung@princeton.edu

Zhanke Liu
e-mail: zhankel@princeton.edu

Wenfeng Xie
e-mail: wxie@princeton.edu

Department of Civil and Environmental Engineering,
Princeton University,
Princeton, NJ 08544

*There is an increasing interest in the use of composites for marine/naval structures to reduce weight and maintenance cost, and to improve hydrodynamic and/or structural performance. In particular, recent works suggest that the use of a lightweight, soft core layer can significantly reduce the load transfer to the back layer of a sandwich structure when subjected to shock or impulse loads. The objective of this work is to investigate the role of fluid-structure interaction (FSI) and shock-bubble interaction in the transient response of composite structures during underwater explosions (UNDEX). The spatial distribution of UNDEX loads is different from uniform planar shocks due to the spherically propagating pressure front, and the temporal characteristics are also different due to the importance of shock-bubble interactions. Both effects influence the FSI response of the composite structure. A previously validated 2D Eulerian–Lagrangian numerical method is used to investigate fluid-structure and shock-bubble interaction effects during UNDEX near composite structures. Via a series of numerical experiments, the relative importance of different effects, namely, the Taylor's FSI effect (1963, "The Pressure and Impulse of Submarine Explosion Waves on Plates" Scientific Papers of G. I. Taylor, **3**, pp. 287–303), the bending/stretching effect, the core compression effect, and the boundary effect, are quantitatively and qualitatively evaluated. Insights for practical modeling, analysis, and design of blast-resistant sandwich structures are also drawn from the analysis.* [DOI: 10.1115/1.3129718]

1 Introduction

Since the pioneering analytical works of Taylor [1], it has been recognized that fluid-structure interaction (FSI) can be exploited to reduce the momentum transmitted to a free-standing air-backed plate against underwater shock or impulse loads. Recently, Taylor's 1D analytical model was extended by Kambouchev and coworkers [2,3] to account for the effects of nonlinear fluid compressibility for air-backed plates of arbitrary mass and shock intensity. They found that the beneficial reduction in momentum transmitted to the structure due to FSI is more significant when nonlinear fluid compressibility is considered, which further encourages the use of thin lightweight structures for blast resistance. More recently, Taylor's analytical model was extended by Liu and Young [4] to study the influence of backing conditions (i.e., air-backed versus water-backed) on the fluid response and structural dynamics of a rigid free-standing plate. They showed that a water-backed plate experiences higher interface pressure, but lower net pressure loading between the face and the back of the plate. The added resistance provided by the water on the back face reduces the structural response, shortens the time to reach peak momentum, and lengthens the time to reach cavitation inception.

In addition to the above analytical models of rigid free-standing plates, recent theoretical and experimental works (e.g., Refs. [5–14]) have significantly expanded the knowledge on the dynamic response of metallic sandwich beams and plates subject to underwater shock and blast loads. In Ref. [7], an analytical three-stage model was introduced to temporally decouple the mechanical responses of metallic sandwich plates with soft cores into a sequence of distinct phases with different time scales. According to their model, the first stage concerns the response of the front face to the primary shock, which can be simplified as a free-standing rigid plate subject to an acoustic impulse load. The plate motion and the rarefaction wave reduce the pressure to zero, which initiates cavitation. In the second stage, the front face decelerates while compressing the soft core, and the transmitted momentum accelerates the back face until all three layers reach a common velocity. In the final stage, the sandwich structure behaves as a homogeneous monolithic beam, and the mechanics is dominated by beam bending and stretching until the structure is brought to rest. This three-stage model introduced by Fleck and Deshpande [7] was later extended by Deshpande and Fleck [8] and Hutchinson and Xue [9] to consider the sandwich structures with varying core strengths. The effects of cross-coupling between the three stages were discussed in Refs. [10,13,15,16] by comparing decoupled and coupled solutions via numerical simulations. They found that the coupling between the FSI and core compression stages can significantly increase the momentum transmission and back face deflection, while the coupling between the core compression and beam bending/stretching stages can reduce the back face deflection. In Ref. [10], they defined the process as decoupled and coupled, respectively, depending if the front and back face velocities equalize while or after the back face attain its maximum velocity. In both cases, partial or complete densification of the core can occur. For high intensity shocks or very low strength cores, slapping may occur where the front face slams into the back face due to full densification of the core, leading to loss of bending strength and high support reactions [10].

In all of the above mentioned theoretical and experimental studies, the focus was on the mechanical behavior of sandwich composite structures subject to water blast loads, where the incoming pressure pulse is idealized as a uniform shock over the entire length of the plate. Hence, the first FSI stage and the second core compression stage can be idealized as 1D, while a 2D model is

Contributed by the Applied Mechanics Division for publication in the JOURNAL OF APPLIED MECHANICS. Manuscript received January 1, 2008; final manuscript received July 11, 2008; published online June 15, 2009. Review conducted by Ashkan Vaziri.

used to solve for the third beam bending/stretching stage. The effect of cavitation reloads due to subsequent cavitation collapses is assumed to be negligible. In an underwater explosion (UNDEX), however, these assumptions may not be valid because the mechanics are dominated by spherically propagating pressure font and shock-bubble interactions. The conversion of solid explosives to a gaseous state releases a large amount of energy at a very high rate, creating a high intensity shock wave followed by an expanding gas front that propagate spherically outward from the point of detonation [17]. Hence, the initial shock impact and momentum transmission to the front face is also nonuniform, and the resulting structural deformation leads to a semispherical wave with a localized rarefaction component propagating back toward the expanding gas bubble. Depending on the strength of the initial shock and the rate of structural deformation, cavitation may be created at the low-pressure region. The interaction of the reflected wave with the expanding gas bubble creates another rarefaction wave reflecting back toward the structure. The collision of the two low-pressure regions between the expanding gas bubble and the structure creates a minimum pressure region that further encourages cavitation. The cavitation that forms under either scenarios will quickly collapse due to the surrounding high pressure, creating a very localized secondary reload to the already weakened structure. As shown in Ref. [18], the pressure oscillations at the wet face due to bubble-shock interaction during a close-in UNDEX can be significant in magnitude and duration even in the absence of a cavitation for both rigid and deformable targets. Hence, the spatial and temporal variations of the pressure pulses exerted on the wet face, and the transient interactions with the sandwich structure due to UNDEX can lead to very different fluid and structural responses from a uniform planar shock impact.

1.1 Objective. The objective of this work is to investigate the role of FSI on the transient response of composite structures subject to UNDEX. The response of marine structures subject to UNDEX has been studied intensely since [17]. However, most of them focused on isotropic and homogeneous structures that are relatively stiff. An excellent compilation of analytical, numerical, and experimental UNDEX benchmarks can be found in Ref. [19]. Recent works such as Refs. [20–22] have also examined the transient response of composite structures subject to UNDEX, but the structures examined are typically made of high strength and high stiffness material such as glass fiber-reinforced polymer (GRP) laminates, and thus the structural deformation and FSI effects are limited. Hence, the mechanical responses of thin lightweight composite structures that can undergo significant deformations during UNDEX should be investigated. The objective of this paper is to use a previously validated 2D Eulerian–Lagrangian numerical method to investigate the transient response of sandwich structures during UNDEX. The focus is to investigate the different coupling effects and their relative significance during UNDEX near sandwich structures. Insights for practical modeling, analysis, and design of blast-resistant sandwich structures are discussed.

2 Methodology

In this work, the strongly coupled 2D Euelerian–Lagrangian FSI solver presented in Refs. [23,24] is used to study the fluid and structural responses of composite structures and shock-bubble interactions during UNDEX. Notice that 3D effects, which are essentially important for more complex configurations such as marine propellers, rudders, and ship hulls, are neglected in the current work. However, the extension of the current methodology to 3D is straightforward. For the sake of completeness, the numerical methodology is summarized below.

The UNDEX event is assumed to take place in a cold water environment, where the dominant driving force is the fluid pressure. The thermal, viscous, and surface tension effects are assumed to be negligible for the fluid. The resulting governing equations for the compressible fluid (Eq. (1)) and equations of state (EOSs) (Eqs. (2)–(4)) are

$$\frac{\partial \mathbf{U}}{\partial t} + \frac{\partial \mathbf{F}(\mathbf{U})}{\partial x} + \frac{\partial \mathbf{G}(\mathbf{U})}{\partial y} = 0 \tag{1}$$

$$p = (\gamma_g - 1)\rho e \quad \text{for the gas} \tag{2}$$

$$p = B(\rho/\rho_o)^{\gamma_l} - B + A \quad \text{for the water} \tag{3}$$

$$\rho = \frac{K\rho_g^{\text{cav}} + \rho_l^{\text{cav}}}{\left(\dfrac{\bar{p}}{\bar{p}_{\text{cav}}}\right)^{-1/\gamma_l} + K\left(\dfrac{p}{p_{\text{cav}}}\right)^{-1/\gamma_g}} \quad \text{for the cavitation mixture} \tag{4}$$

where

$$\mathbf{U} = [\rho, \rho u, \rho v, E]^T \tag{5}$$

$$\mathbf{F}(\mathbf{U}) = [\rho u, \rho u^2 + p, \rho u v, (E+\rho)u]^T \tag{6}$$

$$\mathbf{G}(\mathbf{U}) = [\rho v, \rho u v, \rho v^2 + p, (E+\rho)v]^T \tag{7}$$

where, p, ρ, u, and v are the flow pressure, density, and velocity in the horizontal (x) and vertical (y) directions, respectively. The fluid density is calculated using $\rho=\alpha\rho_g+(1-\alpha)\rho_l$, where ρ_l and ρ_g are the densities of the liquid and vapor components, respectively, and α is the void fraction. $\alpha=0$ and $\alpha=1$ indicate a pure liquid and a pure gas (vapor), respectively. $E=\rho e+0.5\rho(u^2+v^2)$ is the total energy, where e is the internal energy per unit mass.

Equations (2)–(4) are the perfect gas law, barotropic Tait's EOS for water, and the isentropic one-fluid cavitation model [25], respectively. $\gamma_g=1.4$ is the ratio of specific heat for the gas, and $\rho_o=1000\ \text{kg/m}^3$ is the reference density. B, A, and γ_l are set equal to 3.31×10^8 Pa, 10^5 Pa, and 7.0, respectively. $K=\alpha_o/(1-\alpha_o)$ is a parameter for the isentropic one-fluid cavitation model [25], where α_o is the known void fraction of the mixture density at P_{cav}. The value of K or α_o indicates the pressure jump across the cavitation interface, and K is adjusted dynamically using the method presented in Ref. [25]. ρ_g^{cav} and ρ_l^{cav} are the associated gas and liquid densities, respectively, at the cavitation pressure p_{cav}. Finally, $\bar{p}=p+\bar{B}$, $\bar{p}_{\text{cav}}=p_{\text{cav}}+\bar{B}$, and $\bar{B}=B-A$. It should be noted that the nonlinear compressibility effects in water only become important under extremely high pressure (higher than 10 GPa in general according to Ref. [26]). For the problem solved in the current work, the gas bubble has an initial pressure of 500 bars, which falls out of the range where nonlinear compressibility effects are significant. Hence, the bilinear EOS [27] can also be used instead of the Tait's EOS. Nevertheless, Tait's EOS is valid within the considered pressure range. It also has the advantage of being applicable for cases involving higher pressure where nonlinear compressibility effects come into play.

The compressible Euler equations for the multiphase fluid are solved using a finite difference method on a Eulerian framework using a fixed Cartesian grid. The isentropic one-fluid cavitation model [25] and the level set method [28] are used to track the phase changes within the fluid and the location of the fluid-fluid interfaces, respectively. A modified ghost fluid method [29] is used to determine the fluid status of the fluid-fluid interface by solving two nonlinear fluid characteristic equations using a double shock approximate Riemann problem solver (ARPS).

For a solid structure with negligible structural damping, the governing equation of motion in matrix form can be written as

$$\mathbf{M}\ddot{\delta} + \mathbf{K}\delta = \mathbf{F} \tag{8}$$

where $\mathbf{M}=\int \mathbf{N}^T\rho_s\mathbf{N}dV$ and $\mathbf{K}=\int \mathbf{B}^T\mathbf{C}\mathbf{B}dV$ are the solid mass and stiffness matrices, respectively, with ρ_s as the solid density, $\mathbf{N}$ as the displacement interpolation matrix, and $\mathbf{B}$ as the strain-

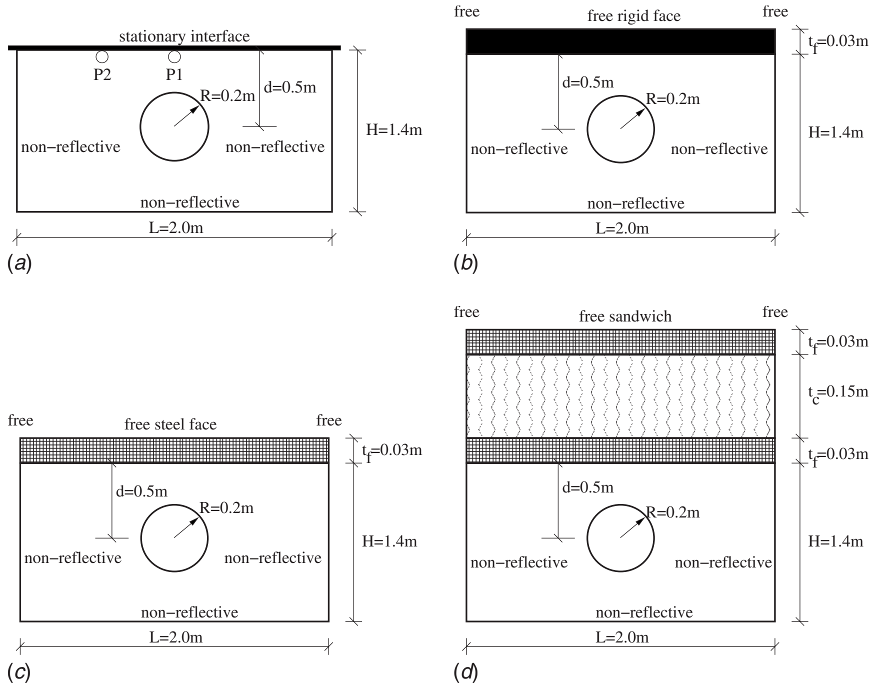

Fig. 1 Computational diagrams for the four different configurations (left top: stationary interface; right top: freely sliding rigid panel; left bottom: freely sliding steel panel; right bottom: freely sliding steel-foam-steel panel)

displacement matrix. $\ddot{\delta}$ and δ are the Lagrangian solid acceleration and displacement vectors, respectively. $\mathbf{C}$ is the elastic stiffness matrix, which satisfies the stress-strain relationship $\sigma=\mathbf{C}\epsilon^{\mathrm{el}}=\mathbf{C}(\epsilon-\epsilon^{\mathrm{pl}})$. σ is the Cauchy stress tensor. ϵ, ϵ^{el}, and ϵ^{pl} are the total logarithmic strain tensor, elastic logarithmic strain tensor, and plastic logarithmic strain tensor, respectively. $\mathbf{F}=\int\mathbf{N}\mathbf{f}dV+\int\mathbf{N}\mathbf{h}dA$ is the equivalent force vector. $\mathbf{f}$ and $\mathbf{h}$ are the body force vector and boundary traction vector, respectively. In addition to the elastic-viscoplastic material model used for the foam core layer, the geometric nonlinearity option available in ABAQUS [30] was also employed during the structural simulation to consider finite deformation. It should be noted that the stiffness matrix $\mathbf{K}$ is a function of the structural response due to geometric and material nonlinearities. Hence, Eq. (8) also represents the generic nonlinear form of the discrete finite element method (FEM) formulation.

The solid equation of motion and constitutive equations are solved using the commercial finite element software, ABAQUS/EXPLICIT [30] on a Lagrangian framework using a moving structured mesh. The one-way fluid characteristics equation is utilized:

$$\frac{dp_I}{dt}+\rho_{IL}c_{IL}\frac{du_I}{dt}=0 \qquad (9)$$

p_I is the interface pressure. u_I and v_I are the horizontal and vertical components of the interface velocity. ρ_{IL} and c_{IL} are the density and speed of sound, respectively, of the shock wave on the fluid side of the fluid-solid interface. A modified ghost fluid method (MGFM) is used to treat the fluid-solid interface by solving the fluid characteristic equation (Eq. (9)) and the solid equation of motion (Eq. (8)) together to satisfy the pressure equilibrium ($\sigma\cdot\mathbf{n}=p_I$, where $\mathbf{n}$ is the unit outward normal vector) and kinematic compatibility conditions ($\dot{\delta}\cdot\mathbf{n}_y=v_I$, where $\mathbf{n}_y$ is the vertical component of the normal vector). The interface pressure obtained from the characteristics equation (applied as normal surface traction to the solid medium) is kept synchronous with the fluid field leading to a strongly coupled Eulerian–Lagrangian scheme. It is achieved by writing the multiphase compressible fluid solver and the interface coupling algorithm as a user subroutine for ABAQUS [30], which adjusts the right hand side of the FEM formulation at every computational step. Details of the fluid-solid interface treatment are given in Refs. [23,24].

The resulting strongly coupled Eulerian–Lagrangian solver is able to capture nonlinear FSI involving strong shocks, gas bubble dynamics, cavitation inception and collapse, and complex stress and deformation fields of deformable composite structures. The Eulerian–Lagrangian FSI solver has been validated using analytical, numerical, and experimental results for planar shock impact on rigid and composite structures, as well as close-in underwater explosion inside a deformable aluminum cylinder. The readers are referred to Refs. [23,24] for details of the numerical model and validation studies. For more details about ghost-fluid type method, the readers are referred to Refs. [31–36].

3 Results and Discussions

3.1 Simulated Cases. Five distinct configurations, four of which are illustrated in Fig. 1, are simulated in the current work:

- Case 1: UNDEX near a stationary interface
- Case 2: UNDEX near a freely sliding rigid panel
- Case 3: UNDEX near a freely sliding steel panel
- Case 4: UNDEX near a freely sliding steel-foam-steel sandwich panel
- Case 5: UNDEX near a clamped-clamped steel-foam-steel sandwich panel

The freely sliding rigid panel (case 2) has the same mass per unit area as the freely sliding steel panel (case 3). However, it undergoes rigid body motion without any bending/stretching subject to UNDEX. Notice that case 5 is not shown in Fig. 1. Its configuration is otherwise the same as case 4 with clamped ends.

As proposed in Ref. [7], there exist three major effects or stages that govern the mechanical response of sandwich structures subject to planar shock, namely, the one-dimensional momentum transfer effect, the core compression effect, and the bending-stretching effect. These effects are physically distinct but are tem-

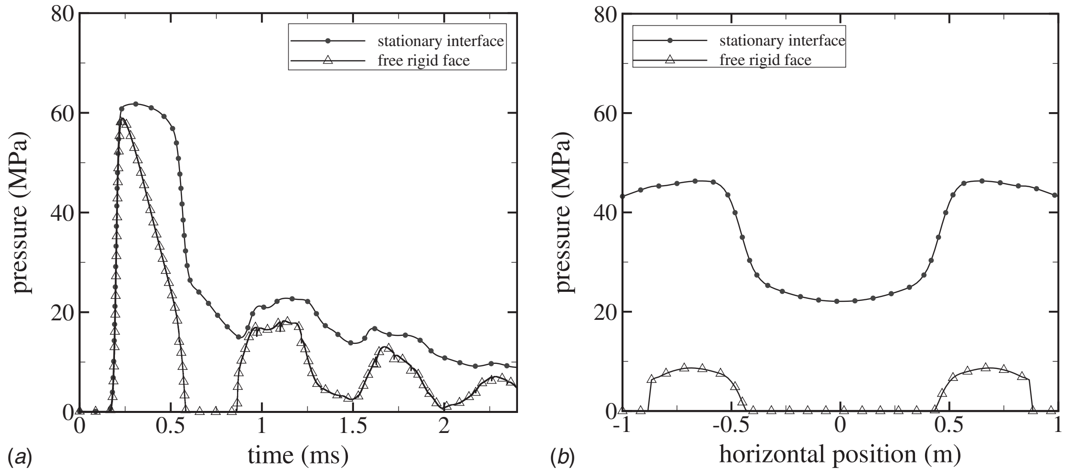

Fig. 2 Taylor's FSI effect: comparison of the interface pressure between case 1 (stationary interface) and case 2 (free rigid face) (left: pressure histories at P1; right: pressure profiles along the wet face at t=0.7 ms)

porally staggered. Order of magnitude difference in time scales between these effects allows partially coupled treatment, such as presented in Refs. [8–10,13,15,16].

For UNDEX near sandwich structures, couplings between the different effects become more complex. The bending/stretching effect immediately initiates when UNDEX shock impinges on the structure due to spatially nonuniform pressure distribution on the wet surface; for the case of planar shock, the bending/stretching effect initiates due to boundary constraints, which comes much later. Formally, there exist four distinct effects which are governing the FSI during UNDEX near sandwich structures. The word "effect" is chosen over "stage" because these effects are temporarily coupled due to 2D loading and response. These four different effects can be calibrated as follows:

- difference between cases 1 and 2 → Taylor's FSI effect
- difference between cases 2 and 3 → bending/stretching effect
- difference between cases 3 and 4 → core compression effect
- difference between cases 4 and 5 → boundary effect

Though it is difficult to find a clear-cut distinction between the different effects, a formal division will provide metrics to assess the relative importance of the different effects during UNDEX near sandwich structures. The current work aims to identify to what time and what degree various simplified partially decoupled models are valid. Insights from the computational experiments will shed light on the realistic design and analytical modeling based on physical assumptions and simplifications.

For all the simulated configurations, the horizontal and vertical dimensions of the fluid domain are taken to be 2.0 m and 1.3 m, respectively. The initial high-pressure gas bubble is located at 0.5 m below the initial fluid-solid interface, with an initial radius of 0.2 m and a pressure of 500 bars. The panel length is taken to be 2.0 m. A thickness of 0.03 m is assumed for both the wet- and dry-face steel panels. The thickness of the foam core layer is assumed to be 0.15 m. The steel face panels have a density of $\rho_f=8000\ \mathrm{kg/m^3}$, Young's modulus of $E_f=210$ GPa, Poisson's ratio of $\nu_f=0.27$, and yield strength of $\sigma_f=900$ MPa. No strain hardening is considered for the steel panels. The core structure is assumed to be made of the Alporas aluminum foam material [37]. The quasistatic compressive stress-strain relation is calibrated based on experimental data presented in Ref. [37]. It has a density of $\rho_c=236\ \mathrm{kg/m^3}$, Young's modulus of $E_c=10$ GPa, Poisson's ratio of $\nu_c=0.0$, plateau yield strength of $\sigma_c=1.5$ MPa, and densification strain of $\epsilon_c=0.8$. An overstress viscoplastic model as in Ref. [37] is adopted to account for the rate dependence of the core material. The logarithmic plastic strain rate is calculated as $\dot{\epsilon}^p=\max(0,[\sigma-\sigma_c(\epsilon^p)]/\eta)$, where the viscosity coefficient is taken to be $\eta=1000$ Pa s. Via extensive convergence study, a fluid grid with 480×240 cells, a solid grid with 120×42 elements, and a time step size of 0.5 μs for both the fluid and solid computations are determined and consistently used in the following simulation. Notice that $C3D8R$ elements in ABAQUS [30] are adopted for the solid simulation.

3.2 Taylor's FSI Effect. Taylor's FSI effect is illustrated in Figs. 2 and 3. The pressure histories at the midspan of the wet face (point P1 as in the left top drawing of Fig. 1) are compared in the left drawing of Fig. 2 between case 1 (stationary interface) and case 2 (free rigid face). It can be seen that the Taylor's FSI effect leads to significant and consistent pressure drop at point P1. Four pressure peaks can be identified for both cases. The first peak corresponds to the incident primary shock impact. The following peaks correspond to secondary shock impacts due to cavitation collapse (at around t=0.8 ms) and shock-bubble interactions. The peaks' magnitude decreases with time due to energy dissipation. The fluid starts to cavitate at point P1 around t=0.6 ms for the case of free rigid face. The cavitation is formed due to the rarefaction wave generated by the rigid body motion. The cavitation collapses at around t=0.8 ms due to the high ambient pressure and decrease in wet face velocity. The pressure profiles along the fluid-solid interface at t=0.7 ms are plotted in the right drawing of Fig. 2. Significant pressure drop due to Taylor's FSI effect can be clearly seen along the interface. The cavitation is not relevant for the case of stationary interface since its reflected shocks does not contain a rarefaction component. A large cavitation region near the midspan can be found for the case of free rigid face. Two additional small cavitation regions are formed at the interface edges. The wet face pressure profiles are not uniform for both cases due to the spherical pressure front from the UNDEX. The fluid fields (pressure contours, velocity vectors, and bubble and interface positions) at t=0.7 ms are presented in Fig. 3. Notice that the original and expanded bubbles are denoted by dashed and solid lines, respectively. Due to symmetry, only half of the domain is shown. On the left is the case of the stationary interface and on the right is the case of the free rigid face. A high-pressure front in the shape of semicircle reflected back from the fluid-solid interface can be identified for both cases. The case with the stationary interface features a much higher pressure level and no cavitation is observed. Consistent with the pressure plots in Fig. 2, two cavi-

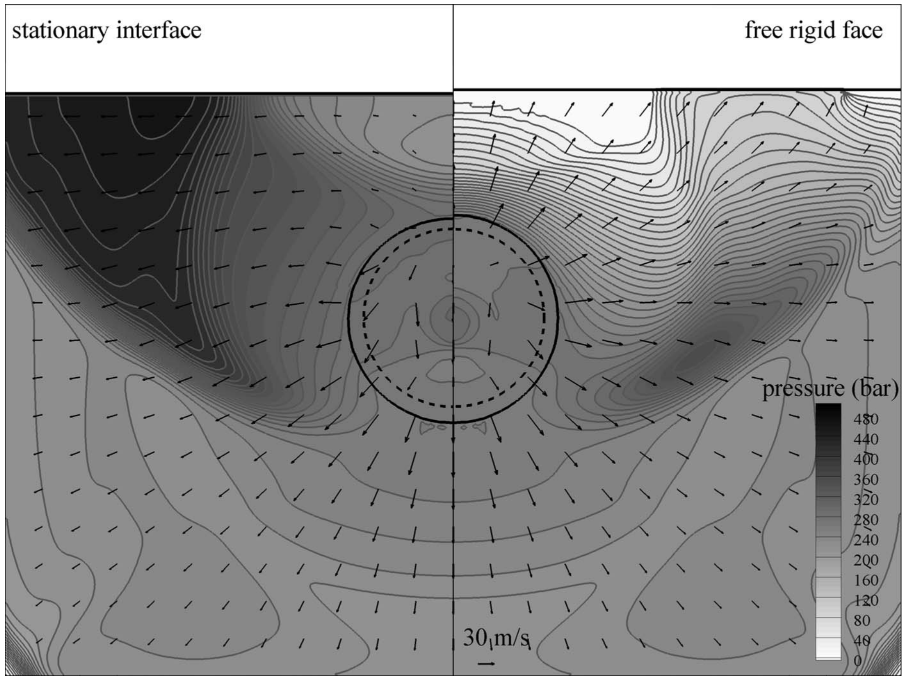

Fig. 3 Taylor's FSI effect: comparison of the fluid field at t=0.7 ms between case 1 (stationary interface) and case 2 (free rigid face)

tation regions can be found for the case of free rigid face, with one near the center and the other on the edge. For the case of stationary interface, the bubble is slightly compressed and is being driven away. On the other hand, the bubble almost expands symmetrically for the case of free rigid face. Fluid is diverted away from the central region near the interface for the case of stationary interface, while fluid is rushing toward the structure to fill the void created by the cavitation regions. For both cases, the field outside the semicircle pressure front (reflected) remains identical since the interface influence has not yet reached that region.

3.3 Bending/Stretching Effect. Bending/stretching effect is illustrated in Figs. 4 and 5. The pressure histories at point P1 are compared in the left drawing of Fig. 4 between case 2 (free rigid face) and case 3 (free steel face). It can be seen that the bending/stretching effect leads to pressure decreasing at the initial stage before cavitation inception. After cavitation collapse, the average pressures are similar between these two cases, though the case with the free rigid face features a larger pressure oscillation. For both cases, the fluid starts to cavitate at around t=0.6 ms. The cavitation collapses earlier for the case of free steel face arising from shock focusing effect caused by larger deformation near the midspan. The pressure profiles along the fluid-solid interface at t=0.7 ms are plotted in the right drawing of Fig. 4. Three cavitation regions (one large+two small) can be found for the case of free rigid face as described before. There is only one cavitation region for the case of free steel face (slightly larger than the case of free rigid face). For the case with the free steel face, pressure is lower adjacent to the central cavitation region but higher at the edges compared with the case of free rigid face. This is because the central portion of the free steel face moves faster and the edge portions move slower due to bending/stretching effect. The fluid fields at t=0.7 ms are presented in the left and right drawings of

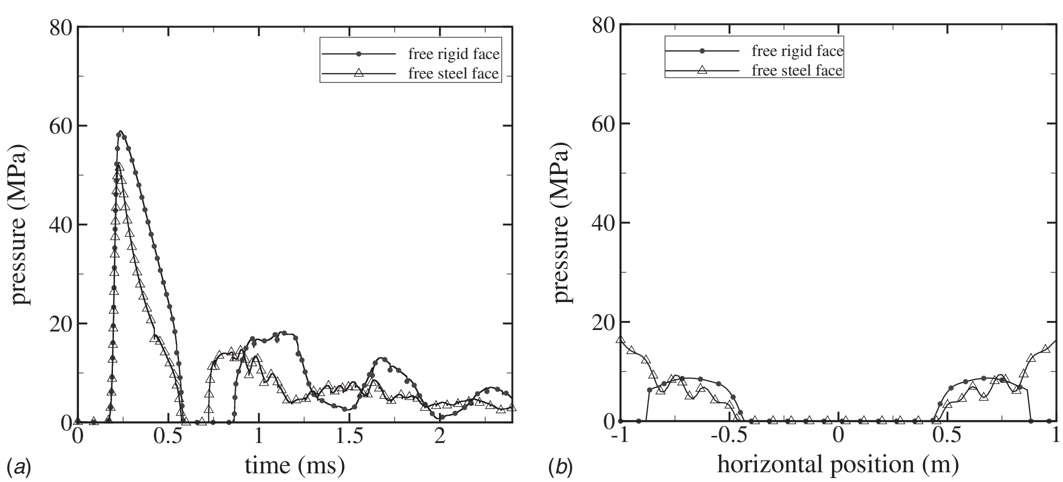

Fig. 4 Bending/stretching effect: comparison of the interface pressure between case 2 (free rigid face) and case 3 (free steel face) (left: pressure histories at P1; right: pressure profiles along the wet face at t=0.7 ms)

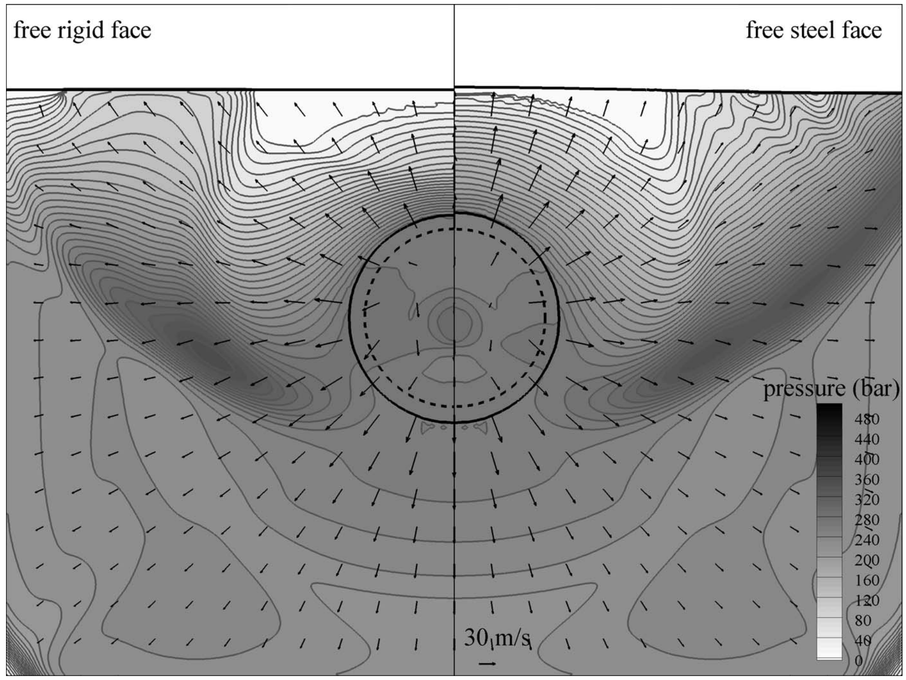

Fig. 5 Bending/stretching effect: comparison of the fluid field at $t=0.7$ ms between case 2 (free rigid face) and case 3 (free steel face)

Fig. 5, respectively, for the case with the free rigid face and the free steel face. The bubble size is slightly larger for the case with the free steel face due to higher wet face flexibility in the central region. The cavitation region is contracting near the center for the case of free steel face, which will eventually lead to earlier collapse, as can be seen from the pressure history in the left of Fig. 4.

3.4 Core Compression Effect. Core compression effect is illustrated in Figs. 6 and 7. As shown in the left drawing of Fig. 6, the core compression effect leads to consistent pressure rise at point P1 due to the increase in resistance provided by the core. Pressure peaks from shock-bubble interactions are no longer distinguishable except for the first peak after cavitation collapse. The fluid starts to cavitate for both cases at around $t=0.6$ ms. The cavitation duration is even shorter for the case of free sandwich. The pressure profiles along the fluid-solid interface at $t=1.5$ ms are plotted in the right drawing of Fig. 6. Due to core compression effect, the pressure is consistently higher for the case of free sandwich along the interface. The fluid fields at $t=1.5$ ms are presented in Fig. 7. The interface retreats less significantly for the case of free sandwich due to extra resistance provided by the core structure, which leads to smaller bubble size and higher pressure compared with the case of free steel face. The influence of interface conditions has swept through the whole computational domain at $t=1.5$ ms. The symmetry between the left and right parts of Fig. 7 has completely disappeared because the first reflected shock from the fluid-solid interface has moved outside of the computational domain.

3.5 Boundary Effect. Boundary effect is illustrated from Figs. 8–10. Comparison of pressure histories is shown in Fig. 8. For point P1 (midspan), the pressure response is very similar for

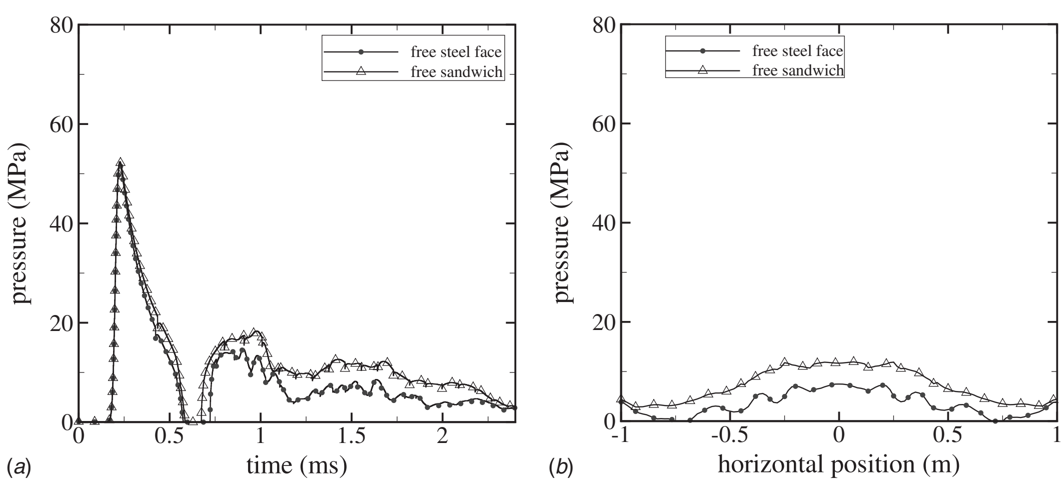

Fig. 6 Core compression effect: comparison of the interface pressure between case 3 (free steel face) and case 4 (free sandwich) (left: pressure histories at P1; right: pressure profiles along the wet face at $t=1.5$ ms)

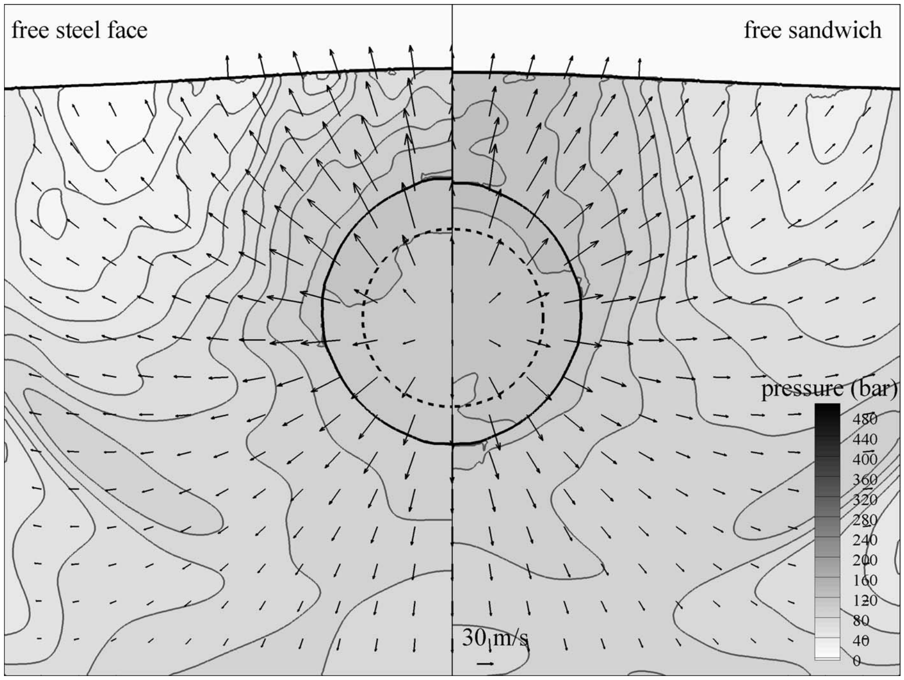

Fig. 7 Core compression effect: comparison of the fluid field at t=1.5 ms between case 3 (free steel face) and case 4 (free sandwich)

both cases. However, for point P2 (quarter-span), the case with the clamped sandwich leads to higher pressure in general because the fixed ends restrain the nearby structure from moving. This indicates that the boundary effect is dominating over the peripheral regions but not over the central region. To investigate structural response characteristics, the maximum principle plastic strain fields are plotted in Fig. 9. On the left is the case of free sandwich and on the right is the case of clamped sandwich. Notice that the vertical dimensions (the structure and its deformation) have been magnified by four times to elucidate the relatively thin steel face layers. The initiation and propagation of core yielding can be clearly observed by examining different time frames from the top to the bottom. Except near the boundaries, the plastic strain contours are very similar between these two cases up to the time t =1.5 ms. This indicates that before t=1.5 ms, the boundary effects are mainly restricted to regions close to the ends. At the later stage (t=2.4 ms), the influence of boundary effect has reached the central portion. For the clamped sandwich, plastic regions start to form near the ends of the wet steel face at t=1.5 ms and they expand in the later stage (t=2.4 ms), which lead to rotation near the supports. The case of free sandwich is free of plastic regions due to free boundary conditions. Benefited from shock absorption and isolation of the foam core, the dry steel face consistently remains elastic. Also plotted are the face velocity and core compressive strain histories in Fig. 10 for point P1. As shown in the left of Fig. 10, the wet and dry faces have reached a common velocity at time t=2.4 ms for both cases. The wet face velocity history is more stable for the free sandwich while more oscillating for the clamped sandwich due to boundary effect. Velocity oscillation originates from competition between the fluid pressure loading and the structure restoration force. It indicates that the FSI process is more violent for the clamped sandwich. As shown in the right of Fig. 10, the compressive strain has reached a plateau

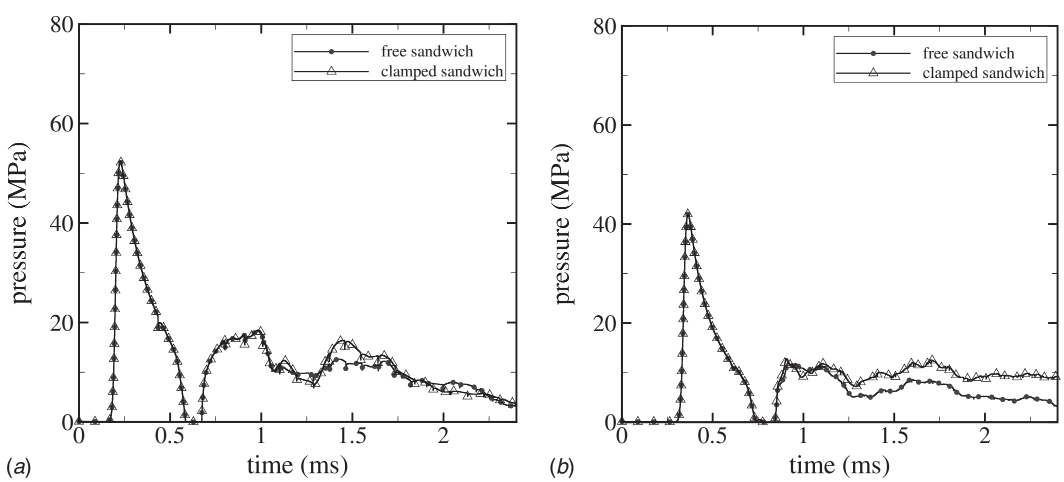

Fig. 8 Boundary effect: comparison of the interface pressure between case 4 (free sandwich) and case 5 (clamped sandwich) (left: pressure histories at P1; right: pressure histories at P2)

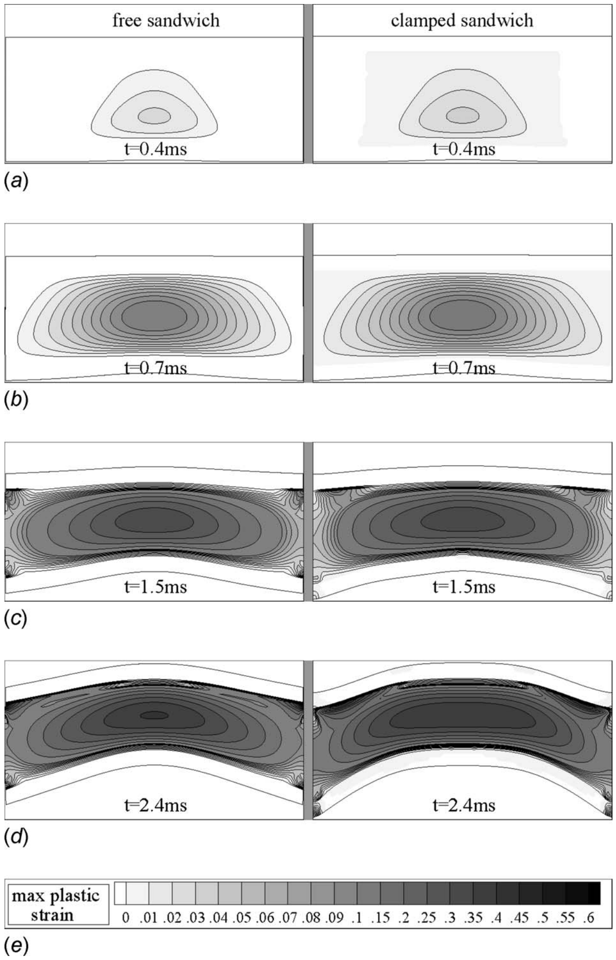

Fig. 9 Boundary effect: comparison of the maximum principle plastic strain field between case 4 (free sandwich) and case 5 (clamped sandwich). Notice that the vertical dimensions (the structure and its deformation) have been magnified by four times.

due to face velocity equalization. A lower compressive strain value has been reached for the clamped sandwich due to boundary effect. Basically, the clamped boundary restrains the wet face steel from running into the foam core structure.

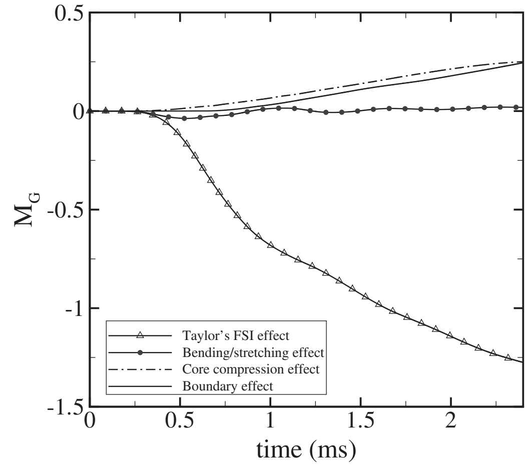

Fig. 11 Comparison of the different effects in terms of dimensionless change in momentum transfer (ΔM_T) at the fluid-solid interface

3.6 Summary of Various Effects. Various effects have been discussed previously in terms of pressure histories, pressure profiles, fluid field (pressure contours, velocity vectors, and bubble and interface positions), plastic regions, face velocities, and core compressive strains. Qualitative trends have been identified. A more global parameter is used in this section to summarize the influence of various effects. The global parameter is chosen to be the momentum transfer at the fluid-solid interface denoted by T_M. It is defined as $T_M \equiv \int_t \int_A p(A,t) dA dt$, where A is the fluid-solid interface area, t is the physical time, and $p(A,t)$ is the spatially and temporarily nonuniform pressure loading. The momentum transfer difference between different simulated configurations provides a metric to evaluate the relative importance of different effects. For example, the momentum transfer due to Taylor's FSI effect can be estimated as $\Delta T_M = T_M^2 - T_M^1$, where the superscripts 1 and 2 denote case 1 (stationary interface) and case 2 (free rigid face), respectively. The momentum gauge (normalized momentum transfer difference) can be defined as $T_G \equiv \Delta T_M / \max(T_M^5)$, where $\max(T_M^5)$ denotes the value of momentum transfer for case 5 (clamped sandwich) at the end of computation, which is set at $t = 2.4$ ms.

The history of momentum gauges for various effects are shown in Fig. 11. It can be seen that Taylor's FSI effect is dominating

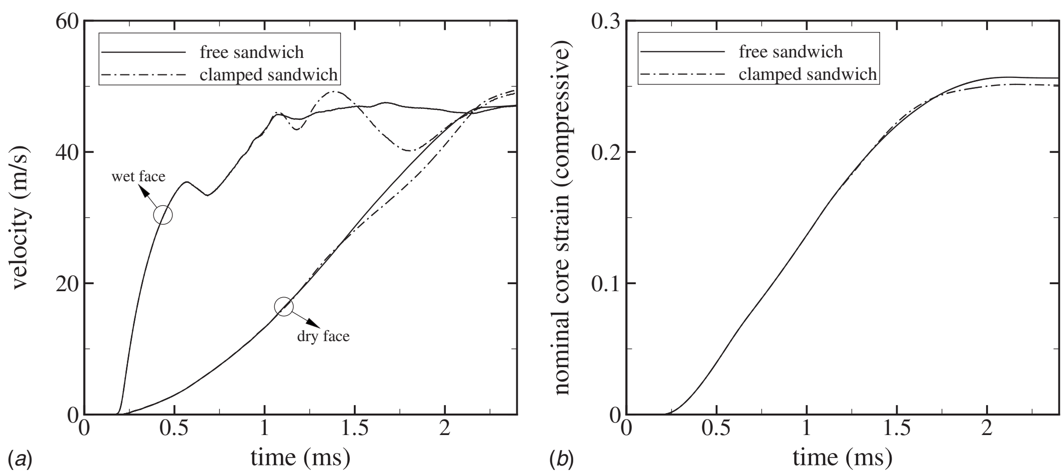

Fig. 10 Comparison of face velocities and nominal core compressive strains between case 4 (free sandwich) and case 5 (clamped sandwich) left: P1 (midspan); right: P2 (quarter-span)

over all other effects. It leads to significant reduction in shock momentum transfer, which is the major source of shock mitigation via light-weight sandwich structures. Its magnitude can be even higher than the total momentum transfer to the clamped sandwich structure in later stage ($t > 1.5$ ms). The bending/stretching effect is small and oscillating. It can be neglected for all practical purpose, for long slender panels. The core compression effect increases the momentum transfer by providing extra resistance to the wet face steel panel. It initiates later than the Taylor's FSI effect because it takes time for the core structure to deform and then influence the momentum transfer at the wet face. Its magnitude can be as high as one-quarter of the total momentum transfer to the clamped sandwich structure in the later stage. The boundary effect also increases the momentum transfer by restraining the structure motion near the end supports. It initiates much later than the other effects since the structure motion starts from the central portion and it takes time for the boundary conditions to take effect. Its magnitude is close to that of the core compression stage.

4 Conclusions

A previously developed 2D Eulerian-Lagrangian numerical method is used to investigate the transient response of lightweight, sandwich structures subject to UNDEX loading. The fluid is assumed to be a multiphase compressible mixture where the effects of thermal conductivity, viscosity, and surface tension are negligible. It is solved using a finite difference method on an Eulerian framework using a fixed Cartesian grid. An isentropic one-fluid cavitation model and a level set method are used to track the phase changes and the fluid-fluid boundaries, respectively, within the fluid. A modified ghost fluid method is used to solve for the fluid status at the fluid-fluid interfaces. The solid structure is assumed to be a multilayer sandwich structure with steel faces and a soft foam core. Perfect bonding is assumed between the layers. It is solved using a finite element method on a Lagrangian framework using a moving structured mesh. A modified ghost fluid method is used to ensure satisfaction of the kinematic and dynamic boundary conditions at the fluid-solid interfaces.

The 2D Eulerian–Lagrangian method is used to analyze the transient response of UNDEX near a stationary interface (case 1), freely sliding rigid face sheet (case 2), freely sliding steel face sheet (case 3), freely sliding sandwich structure (case 4), and clamped sandwich structure (case 5). Via carefully designed and well controlled numerical experiments, the significance of different coupling effects during underwater explosions near sandwich panels are delineated. The difference between the five simulated cases is used as a metric to evaluate the relative importance of four different coupling effects, namely the Taylor's FSI effect (difference between case 1 and case 2), the bending/stretching effect (difference between case 2 and case 3), the core compression effect (difference between case 3 and case 4), and the boundary effect (difference between case 4 and case 5). Results show that simulations based on stationary interface significantly overestimate the fluid pressure loading. The fluid-structure interaction effects can be utilized to reduce the shock momentum transfer to sandwich structures during underwater explosions. Among all these effects, the Taylor's FSI effect is the most significant. The bending/stretching effect oscillates with time, but it can be safely neglected for long slender beams/panels. The core compression effect and boundary effect increase the momentum transfer significantly in the later stage. For the initial stage response of sandwich structures subject to UNDEX, inclusion of Taylor's FSI effect will yield satisfactory results; for the later stage response, a fully coupled modeling is required to accurately predict the momentum transfer and structure response.

The results demonstrated the importance of multidimensional effects, fluid-structure interaction, shock-bubble interaction, and nonlinear material behavior for UNDEX near a sandwich structure. In addition, the following insights can be drawn.

- The results can also be interpreted in another way. Basically, the difference between case 1 and case 2 is due to FSI effects for a freely sliding rigid plate, between case 1 and case 3 is due to FSI effects for a freely sliding steel (deformable) plate, between case 1 and case 4 is due to FSI effects for a freely sliding sandwich plate, and between case 1 and case 5 is due to FSI effects for a clamped sandwich plate. In all cases, neglecting FSI effects leads to significant overestimation of the structural response by approximately a factor of two or more.
- The fluid loading on the structure is different for a close-in UNDEX compared to a planar shock due to the continual loading caused by the shock-bubble interaction after the end of the first Taylor's FSI stage. Although the peak pressure caused by the shock-bubble interaction is small compared to the initial peak pressure, the duration is much longer, and thus momentum transfer to the structure interface due to shock-bubble interaction can be equal to or great than the first FSI stage.
- 2D effects due to spherical wave propagations and the continual momentum transfer due to the shock-bubble interaction cause the Taylor's FSI effect, the bending/stretching effect, the core compression effect, and boundary effect to be tightly coupled, and cause the front and back faces to continue to accelerate after all the layers near the midspan portion reach a common velocity. The results also suggest that for very high intensity UNDEX or very low strength cores, slapping can occur in the midspan portion of the panel, which can significantly change the dynamics due to shock focusing effects caused by the large localized interface deformation and subsequent shock-bubble interactions.
- The influence of cavitation collapse appears to be small compared to shock-bubble interaction for the case considered.
- The results confirm previous findings [1,7] that lightweight deformable composite structures are good candidates to resist blast loads due to their ability to reduce the momentum transfer via FSI.
- The immobile regions of a member, e.g., end supports, can be subjected to very high stresses, which may in turn transfer significant amount of the load to the supports and cause failure of the structural system. Allowing the ends to develop plastic hinges help to limit the maximum load transfer to the supports and increases energy dissipation via plastic deformation and FSI.

It should be noted that only the momentum gauge has been used in the current work as a metric, which is directly related to FSI effects at the fluid-solid interface. In the future work, other metrics should be investigated, such as the histories of maximum stresses (von Mises stress for instance) and energy gaining (including total work, plastic dissipation, and net energy). Moreover, parametric study warrants further investigation. It is worth conducting similar analysis to determine the influence of varying mass, thickness, and stiffness ratios between the steel plates and the plastic core, on the various FSI effects.

Acknowledgment

The authors are grateful to the Office of Naval Research (ONR) and Dr. Ki-Han Kim (program manager) for their financial support through Grant Nos. N00014-05-1-0694, N00014-07-1-0491, and N00014-08-1-0475.

References

[1] Taylor, G. I., 1963, "The Pressure and Impulse of Submarine Explosion Waves on Plates," *The Scientific Papers of G. I. Taylor*, Vol. 3, Cambridge University Press, Cambridge, pp. 287–303.

[2] Kambouchev, N., Noels, L., and Radovitzky, R., 2006, "Nonlinear Compressibility Effects in Fluid-Structure Interaction and Their Implications on the Air-Blast Loading of Structures," J. Appl. Phys., **100**, p. 063519.

[3] Kambouchev, N., Radovitzky, R., and Noels, L., 2007, "Fluid-Structure Interaction Effects in the Dynamic Response of Free-Standing Plates to Uniform Shock Loading," ASME J. Appl. Mech., **74**, pp. 1042–1045.
[4] Liu, Z., and Young, Y. L., 2008, "Transient Response of Submerged Plates Subject to Underwater Shock Loading: An Analytical Perspective," ASME J. Appl. Mech., **75**, p. 044504.
[5] Xue, Z., and Hutchinson, J. W., 2003, "Preliminary Assessment of Sandwich Plates Subject to Blast Loads," Int. J. Mech. Sci., **45**, pp. 687–705.
[6] Xue, Z., and Hutchinson, J. W., 2004, "A Comparative Study of Impulse-Resistant Metal Sandwich Plates," Int. J. Impact Eng., **30**, pp. 1283–1305.
[7] Fleck, N. A., and Deshpande, V. S., 2004, "The Resistance of Clamped Sandwich Beams to Shock Loading," ASME J. Appl. Mech., **71**, pp. 386–401.
[8] Deshpande, V. S., and Fleck, N. A., 2005, "One-Dimensional Response of Sandwich Plates to Underwater Shock Loading," J. Mech. Phys. Solids, **53**, pp. 2347–2383.
[9] Hutchinson, J. W., and Xue, Z., 2005, "Metal Sandwich Plates Optimized for Pressure Impulses," Int. J. Mech. Sci., **47**, pp. 545–569.
[10] Tilbrook, M. T., Deshpande, V. S., and Fleck, N. A., 2006, "The Impulsive Response of Sandwich Beams: Analytical and Numerical Investigation of Regimes of Behaviour," J. Mech. Phys. Solids, **54**, pp. 2242–2280.
[11] Espinosa, H. D., Lee, S., and Moldovan, N., 2006, "A Novel Fluid Structure Interaction Experiment to Investigate Deformation of Structural Elements Subjected to Impulsive Loading," Exp. Mech., **46**, pp. 805–824.
[12] Librescu, L., Oh, S. Y., and Hohe, J., 2006, "Dynamic Response of Anisotropic Sandwich Flat Panels to Underwater and In-Air Explosions," Int. J. Solids Struct., **43**, pp. 3794–3816.
[13] Liang, Y., Spuskanyuk, A. V., Flores, S. E., Hayhurst, D. R., Hutchinson, J. W., McMeeking, R. M., and Evans, A. G., 2007, "The Response of Metallic Sandwich Panels to Water Blast," ASME J. Appl. Mech., **74**, pp. 81–99.
[14] Rabczuk, T., Samaniego, E., and Belytschko, T., 2007, "Simplified Model for Predicting Impulsive Loads on Submerged Structures to Account for Fluid-Structure Interaction," Int. J. Impact Eng., **34**, pp. 163–177.
[15] McShane, G. J., Deshpande, V. S., and Fleck, N. A., 2007, "The Underwater Blast Resistance of Metallic Sandwich Beams With Prismatic Lattice Cores," ASME J. Appl. Mech., **74**, pp. 352–364.
[16] McMeeking, R. M., Spuskanyuk, A. V., He, M. Y., Deshpande, V. S., Fleck, N. A., and Evans, A. G., 2008, "An Analytic Model for the Response to Water Blast of Unsupported Metallic Sandwich Panels," Int. J. Solids Struct., **45**, pp. 478–496.
[17] Cole, R. H., 1965, *Underwater Explosions*, Dover, New York.
[18] Wardlaw, J. A. B., and Luton, J. A., 2000, "Fluid-Structure Interaction Mechanisms for Close-In Explosions," Shock Vib., **7**, pp. 265–275.
[19] Mair, H. U., 1999, "Benchmarks for Submerged Structure Response to Underwater Explosions," Shock Vib., **6**, pp. 169–181.
[20] Mouritz, A. P., Saunders, D. S., and Buckley, S., 1993, *Fifth Australian Aeronautical Conference*, Regent Hotel, Melbourne, Australia.
[21] Mourltz, A. P., 1996, "The Effect of Underwater Explosion Shock Loading on the Flexural Properties of GRP Laminates," Int. J. Impact Eng., **18**, pp. 129–139.
[22] McCoy, R. W., and Sun, C. T., 1997, "Fluid-Structure Interaction Analysis of a Thick-Section Composite Cylinder Subjected to Underwater Blast Loading," Compos. Struct., **37**, pp. 45–55.
[23] Liu, Z., Xie, W., and Young, Y. L., 2009, "Numerical Modeling of Complex Interactions Between Underwater Shocks and Composite Structures," Comput. Mech., **43**, pp. 239–251.
[24] Xie, W., Liu, Z., and Young, Y. L., 2009, "Application of a Coupled Eulerian-Lagrangian Method to Simulate Interactions Between Deformable Composite Structures and Compressible Multiphase Flow," Int. J. Numer. Methods Eng., under review.
[25] Liu, T. G., Khoo, B. C., and Xie, W., 2004, "Isentropic One-Fluid Modelling of Unsteady Cavitating Flow," J. Comput. Phys., **201**, pp. 80–108.
[26] Kambouchev, N., Noels, L., and Radovitzky, R., 2007, "Numerical Simulation of the Fluid-Structure Interaction Between Air Blast Waves and Free-Standing Plates," Comput. Struct., **85**, pp. 923–931.
[27] Xie, W., Young, Y. L., Liu, T. G., and Khoo, B. C., 2007, "A Smoothed Finite Element Method for Mechanics Problems," Compos. Mech., **40**, pp. 667–681.
[28] Osher, S., and Sethian, J. A., 1988, "Fronts Propagating With Curvature-Dependent Speed: Algorithms Based on Hamilton-Jacobi Formulations," J. Comput. Phys., **79**, pp. 12–49.
[29] Liu, T. G., Khoo, B. C., and Yeo, K. S., 2003, "Ghost Fluid Method for Strong Shock Impacting on Material Interface," J. Comput. Phys., **190**, pp. 651–681.
[30] ABAQUS, 2005, Version 6.6 Documentation, ABAQUS, Inc., Pawtucket, RI.
[31] Cummings, J., Aivazis, M., Samtaney, R., Radovitzky, R., Mauch, S., and Meiron, D., 2001, "A Virtual Test Facility for the Simulation of Dynamic Response in Materials," J. Supercomput., **23**, pp. 39–50.
[32] Arienti, M., Hung, P., Morano, E., and Shepherd, J. E., 2003, "A Level Set Approach to Eulerian-Lagrangian Coupling," J. Comput. Phys., **185**, pp. 213–251.
[33] Tam, D., Radovitzky, R., and Samtaney, R., 2005, "An Algorithm for Modelling the Interaction of a Flexible Rod With a Two-dimensional High-Speed Flow," Int. J. Numer. Methods Eng., **64**, pp. 1057–1077.
[34] Cirak, F., and Radovitzky, R., 2005, "A Lagrangian-Eulerian Shell-Fluid Coupling Algorithm Based on Level Sets," Comput. Struct., **88**, pp. 491–498.
[35] Deiterding, R., Radovitzky, R., Mauch, S. P., Noels, L., Cummings, J. C., and Meiron, D. I., 2006, "A Virtual Test Facility for the Efficient Simulation of Solid Material Response Under Strong Shock and Detonation Wave Loading," Eng. Comput., **22**, pp. 325–347.
[36] Cirak, F., Deiterding, R., and Mauch, S. P., 2007, "Large-Scale Fluid-Structure Interaction Simulation of Viscoplastic and Fracturing Thin-Shells Subjected to Shocks and Detonations," Comput. Struct., **85**, pp. 1049–1065.
[37] Deshpande, V. S., Heaver, A., and Fleck, N. A., 2006, "An Underwater Shock Simulator," Proc. R. Soc. London, Ser. A, **462**, pp. 1021–1041.

Computational Modeling of Damage Development in Composite Laminates Subjected to Transverse Dynamic Loading

Alireza Forghani

Reza Vaziri[1]
e-mail: reza.vaziri@ubc.ca

Department of Civil Engineering,
and Department of Materials Engineering,
Composites Group,
University of British Columbia,
6250 Applied Science Lane,
Vancouver, BC, V6T 1Z4, Canada

This paper presents a robust computational model for the response of composite laminates to high intensity transverse dynamic loading emanating from local impact by a projectile and distributed pressure pulse due to a blast. Delaminations are modeled using a cohesive type tie-break interface introduced between sublaminates while intralaminar damage mechanisms within the sublaminates are captured in a smeared manner using a strain-softening plastic-damage model. In the latter case, a nonlocal regularization scheme is used to address the spurious mesh dependency and mesh-orientation problems that occur with all local strain-softening type constitutive models. The results for the predicted damage patterns using the nonlocal approach are encouraging and qualitatively agree with the experimental observations. The predictive performance of the proposed numerical model is assessed through comparisons with available instrumented impact test results on a class of carbon-fiber reinforced polymer (CFRP) composite laminates. Force-time histories and other derived cross-plots such as the force versus projectile displacement and progression of projectile energy loss as a function of time are compared with available experimental results to demonstrate the efficacy of the model in capturing the details of the dynamic response. Another case study involving the blast loading of CFRP composite laminates is used to further highlight the capability of the proposed model in simulating the global structural response of composite laminates subjected to distributed pressure pulses. [DOI: 10.1115/1.3129705]

Keywords: laminated composites, impact loading, damage and fracture, delamination, nonlocal damage model, cohesive crack model, explicit finite element analysis

1 Introduction

Large scale components made of advanced fiber reinforced composite materials are increasingly being used as primary structural components in applications where weight saving and portability are of critical concern. In many situations, these structures are likely to be impacted by foreign object projectiles or blast-type loading resulting in severe degradation of structural strength and stiffness. Through development of various damage mechanisms polymeric composite laminates offer desirable properties as protective type structures used to absorb energies released from blast and impact type loadings. In order to design composite structures that will survive such threats it is crucial to develop efficient and reliable techniques to predict their response under a wide variety of dynamic loading conditions.

Modeling the impact behavior of laminated composites has been a subject of considerable interest to researchers in aerospace and military applications for many years. As a result, a relatively large body of literature has been accumulated. Many significant research contributions, far too extensive to be mentioned here, have been made to both analytical and numerical approaches to impact modeling. However, despite the wealth of knowledge generated in computational techniques and constitutive modeling of materials in general, the computer simulation of the impact behavior of composite materials remains an elusive goal. The reason for this is the relative inexperience in prediction of the damage behavior of composite materials as compared with the basically isotropic and homogeneous metallic structures as well as a general lack of detailed experimental data on the evolution of damage during the course of impact loading.

From the failure mechanics standpoint, laminated composite materials fall under the category of quasibrittle materials that exhibit a strain-softening behavior marked by a progressive growth of damage. Predicting the initiation and evolution of damage in such structures is crucial and poses considerable challenges to the structural analyst. In general, computational modeling of composite structures faces a number of obstacles because of their highly anisotropic material behavior and multitude of damage mechanisms. The complexity of the problem escalates when the applied loads are of a dynamic nature such as those that occur during impact and blast.

In this study, a computationally oriented structural model is proposed, which is capable of simulating the two major modes of failure in composite panels: The interlaminar damage (delamination) is modeled using the discrete cohesive crack concept [1] while the intralaminar damage modes (matrix cracking and fiber breakage) are treated in a smeared manner [2] using a strain-softening plastic-damage model. The mesh size and orientation sensitivity issues that plague all strain-softening based constitutive models are addressed using a nonlocal regularization scheme. The predictive capability of the proposed model in capturing the nonlinear dynamic response of composite structures will be demonstrated by considering two case studies involving transverse dynamic loading of CFRPs plates. In the first case study, the responses of CFRP laminates subjected to nonpenetrating impact by projectiles with high mass (low velocity) or low mass (high velocity) resulting in various levels of incident energies are con-

[1]Corresponding author.

Contributed by the Applied Mechanics Division of ASME for publication in the Journal of Applied Mechanics. Manuscript received February 27, 2008; final manuscript received May 13, 2008; published online June 15, 2009. Review conducted by Ashkan Vaziri.

sidered. The present numerical predictions are compared favorably with previously measured experimental data in terms of the impact force-time and force-displacement signatures as well as energy dissipations decomposed into delamination and intralaminar mechanisms. The second case study deals with the simulation of CFRP panels subjected to a blast-type pressure pulse for which experimental data on the instantaneous back-face velocity of the plate and postmortem damage patterns are available for model validation.

2 Damage Modeling Framework

In quasibrittle materials such as many of today's structural composites, the size of the nonlinear process zone near the crack tip is not negligible. To simulate the fracture and damage in such materials at the macroscopic scale two distinct computational approaches, namely, discrete and continuum representations, have been generally proposed. The cohesive crack method, which is among the discrete techniques, has been used to model the interlaminar damage mode, i.e., delamination, and the generalized smeared crack method, which falls under the realm of continuum approaches, has been adopted to model intralaminar damage modes, i.e., fiber breakage and matrix cracking. In some of the modern computational analyses, e.g., Ref. [3], both these approaches have been employed in tandem to model the degradation of the ply interfaces due to delamination as well as the propagation of damage within the plies.

2.1 Cohesive Crack Method for Modeling Delamination. The cohesive crack model is widely being used for modeling progressive crack growth in quasibrittle materials. This method is based on the premise that damage is localized along a line (plane) known as the fictitious crack [1] and the cohesive (closing) traction is applied on the crack surfaces to simulate the subsequent resistance of the crack after its initiation. In the works of Camacho and Ortiz [4] and Yu et al. [5] the cohesive crack is employed at the interfaces of all elements to provide the possibility of crack initiation and growth everywhere in the structure. Although in these studies the cohesive crack model is used to simulate arbitrary cracks in the structure, this technique is typically adopted when the position and direction of crack growth are known in advance. In such cases, the cohesive interfaces can be placed where the potential for crack initiation and growth exists.

Delamination is an inherently discrete mode of damage that can be modeled effectively using the cohesive crack approach. Various forms of the cohesive crack concept have been used in modeling delamination, e.g., cohesive interface elements (Refs. [6], [7], [3], [8], and [9] among others), discrete cohesive failure models (e.g., Ref. [10]), and advanced partition of unity-based methods (e.g., Refs. [11,12]).

In dynamic problems, where the closure of delamination cracks is likely during the event, the interface should be able to transfer compressive loads, and thus in order to inhibit interpenetration of adjacent layers, the cohesive crack model can be implemented within the framework of penalty contact interfaces in finite element codes.

2.2 Continuum Damage Mechanics Approach for Modeling Intralaminar Damage. Rather than modeling the fracture as a discrete entity, a formidable computational task when there are a multitude of fracture planes, one can represent fracture in a smeared manner using continuum damage mechanics (CDM) models. In this manner fracture can be assumed to be damage propagating within a specific zone of a representative volume element (RVE) of the material resulting in a reduction in its stiffness and an overall strain-softening constitutive behavior (i.e., stress reduction with increasing strain). Perhaps the best advantage of this method is its ease of implementation in commercial finite element codes.

The CDM technique attempts to predict the effect of micro-/mesoscale defects and damage at the macrolevel. This effect is usually modeled by reducing the material's modulus.

$$\boldsymbol{\sigma} = \mathbf{C}^d \boldsymbol{\varepsilon} \tag{1}$$

where $\mathbf{C}^d$ is the degraded material stiffness tensor given by

$$\mathbf{C}^d = \mathbf{R}(d)\mathbf{C}^0 \tag{2}$$

In Eq. (2), $\mathbf{R}$ is the reduction tensor that is a function of the damage state and $\mathbf{C}^0$ is the undamaged material stiffness tensor. d is the damage parameter that represents degradation of the material and is usually defined as a function of the state of strain, stress, or energy potential. The value of the damage parameter varies between 0 for a virgin, undamaged material and 1 for a fully damaged material.

The challenge here is to define the damage state and the reduction tensor so that it can appropriately simulate the initiation and growth of damage under different loading scenarios. The highly anisotropic nature of composite materials combined with their complex modes and sequence of failure processes makes it difficult to formulate a criterion that can signal the initiation of damage and its progression under multi-axial stress (strain) states.

A popular approach in modeling intralaminar damage is the so-called ply-based model, where a damage model is applied to each individual ply of the laminate. In the work of Ladeveze et al. [3], a 2D damage model is proposed to simulate intralaminar damage, where three damage parameters are defined to describe the damage state within each ply. Maimi et al. [13,14] defined a damage model based on the generalized crack band approach [1] where the softening part of the constitutive relation is adjusted according to the size (height) of the elements to maintain mesh-insensitivity (or objectivity) of the numerical results.

The advantage of the ply-based approach is that it leads to a convenient formulation of the damage model and since it uses ply properties as its basis, the parameters can be measured using standard ply-based tests and in principle do not require recalibration when the laminate lay-up is altered [13]. However, this approach has two shortcomings: First, since each and every ply of the composite laminate is simulated, the method is computationally inefficient. Second, and perhaps more importantly, the ply-based method is unable to represent the interactions that exist between the plies in the nonlinear regime where initiation and evolution of damage in a given ply are strongly influenced by its neighboring plies. In other words, damage in each ply cannot be treated independently of the laminate lay-up.

In the recent work by Williams et al. [2], a composite damage model (CODAM) has been proposed to capture the effect of matrix cracking and fiber breakage on the macroscale. CODAM is a phenomenological model that smears the material response (stress-strain behavior) over a finite RVE of the laminate made up of a repeating unit or a sublaminate through the thickness and a characteristic size, h_c, in the plane of the laminate. The construction of the model at this scale ensures that (1) by considering a sublaminate the lamina interactions in terms of damage initiation and evolution are implicitly taken into account, and (2) the characteristic planar length provides a measure of the inherent toughness (or brittleness) of the material (the larger the h_c, the tougher the material). The latter introduces an inherent length scale that is related to the size of the fully developed fracture process zone (i.e., the height of the damage zone ahead of a crack in a test configuration that leads to a stable crack growth). In formulating CODAM two sets of curves are defined: one relating the damage variables to an effective strain, and the other relating the modulus reduction to the damage variables. This results in a strain-softening type stress-strain curve for the characteristic RVE. Damage variables are defined for each of the principal orthotropic directions as well as in shear loading, and the damage growth and modulus reduction curves are unique in each case and sensitive to differences in tension and compression. The CODAM approach has been designed to be computationally oriented, conceptually simple, and easy to characterize.

Implementation of continuum damage models in finite element codes takes the form of generalized smeared crack methods. This approach encounters some numerical difficulties known as localization, which is discussed in Sec. 3.

3 Nonlocal Approach

3.1 Localization Problem. It is widely acknowledged that the finite element modeling of materials with strain-softening behavior exhibits spurious mesh dependency problems due to the ill-posedness of the governing equations. In such cases damage/crack pattern tends to localize to the smallest length scale of the model, which is the height of one element. Therefore, with successive mesh refinement, damage localizes into a zone of zero volume and the numerical results fail to converge to a unique solution. Consequently, the global response of the system shows dependency on the spatial discretization [15,16].

To remedy this problem in a simple and computationally effective way, Bažant and co-workers [1,17] proposed the crack band theory according to which the product of the area under the stress-strain curve (in the softening regime) and the characteristic size of the RVE represents the fracture energy (energy per unit area), G_f. This fracture energy is assumed to be a material constant. Therefore, regardless of the choice of the mesh, which is a subjective aspect of numerical analyses, the overall energy dissipation due to damage and hence G_f must remain constant.

According to the crack band approach, damage localizes into a zone that is one element in height. This requires one to know the crack path a priori and design a conforming mesh. Also the crack band method is applicable to cases where there is a distinct localization of damage/crack into one row of elements, e.g., in quasistatic loading of notched specimens. In very fast dynamic events such as blast and impact where the damage takes a more spatially distributed (diffuse) form and thus a well-defined path for the crack propagation does not exist, the applicability of the crack band concept becomes questionable [18].

Other approaches have been proposed to regularize the numerical simulation of boundary-value problems with strain-softening materials. These so-called localization limiter [19] methods introduce a length scale to the equations on which the height of the damage in the numerical simulation will depend. Nonlocal averaging method (Refs. [20,21] among others), explicit and implicit gradient formulations (e.g., Ref. [22]), Cosserat continuum (e.g., Ref. [23]), and regularizations based on rate dependent and visco-plastic models (e.g., Refs. [24,25]) are among the techniques that render the numerical simulation results objective.

The averaging concept was first proposed as nonlocal continuum in elasticity (e.g., Ref. [26]). Since the mid-1980s this idea has been implemented for strain-softening materials and used to model damage and crack growth in quasibrittle materials [1,15,18,20,27,28].

3.2 Nonlocal Averaging Formulation. In the nonlocal approach, in contrast with the local methods, the state of stress at a material point not only depends on the state of strain and history parameters at that point but also on the state of neighboring points. This approach is based on averaging of an appropriate state parameter over a finite region using a weighting function.

According to the work of Jirasek [28], the inelastic strain component is an appropriate parameter for nonlocal averaging that leads to realistic results and prevents stress locking. One can write the averaging on the equivalent strain in the form

$$\tilde{\varepsilon}_{\text{eff}}(X) = \frac{1}{W}\int_V \varepsilon_{\text{eff}}(\xi) w(|X-\xi|) d\xi \tag{3}$$

where w is the weight function that depends on the distance between the original point and the target point. The integration is carried out over a finite neighborhood, V, and W is the summation of the weight function over the integral domain as follows:

$$W = \int_V w(r) dr \tag{4}$$

Different weight functions are proposed for the averaging scheme such as Gauss distribution function

$$w(r) = \exp\left(-\frac{r^2}{2l^2}\right) \tag{5}$$

or bell-shaped power functions

$$w(r) = \left[1 + \left(\frac{r}{l}\right)^p\right]^{-q} \tag{6}$$

In Eq. (6), the shape of the weight function can be altered by adjusting the parameters p and q. In both Eqs. (5) and (6), the parameter l is a length scale that is incorporated in the formulation. It should be noted that the height of damage depends on the definition of the weight function as well as on the length parameter. Therefore the weight functions defined by Eqs. (5) and (6) may lead to different solutions even with the same length parameter.

The damage state is defined as a function of the nonlocal effective strain as follows:

$$d(X) = d(\tilde{\varepsilon}_{\text{eff}}(X)) \tag{7}$$

Another shortcoming of numerical simulations based on local damage models is that they result in damage/crack patterns that are dependent on the orientation of the mesh. This so-called mesh-orientation bias of local models has been demonstrated and reported elsewhere (e.g., Refs. [18,29]) in simulation of quasistatic problems. Nonlocal methods have been shown to have the added benefit of being effective in avoiding the unrealistic mesh-orientation dependency of the damage propagation.

It is worth mentioning that computational implementation of the nonlocal approaches is usually more complicated, and numerical analyses based on them are computationally more intensive than local models. Furthermore, the nonlocal averaging method is not a feature that is generally available in commercial finite element codes. The notable exception is the explicit finite element code LS-DYNA, in which this scheme has been implemented [30] and can be applied to a selected number of its built-in material models.

3.3 Calibration of Nonlocal Parameters. In addition to parameters that are required in local damage models, the key parameter in the nonlocal averaging method is the determination of an appropriate length parameter (l in Eqs. (5) and (6)). This parameter plays an important role in nonlocal models since it influences the height of the damaged area and consequently the energy absorbed in the damage process.

The overheight compact tension (OCT) test proposed by Kongshavn and Poursartip [31] is an effective experimental technique that can be used to determine the nonlocal damage parameters. This test is based on a modification of the standard compact tension (CT) test and generally leads to a stable growth of damage in composite specimens. When combined with an image processing technique that can track the local displacement and strain fields on the surface of the OCT specimen, one can extract the height of the damage zone, h_c, and the energy release rate (fracture energy, G_f) associated with the intralaminar damage mechanisms [29].

Numerical simulation of the OCT test using a nonlocal model can be carried out to determine the appropriate length parameter, l, that results in accurate prediction of the height of the damage zone, h_c. The relation between the length scale and the height of damage in the nonlocal model is governed by the form of the

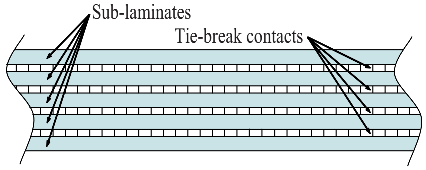

Fig. 1 Schematic showing a stack of shell elements each representing a sublaminate of the composite panel and connected together using tie-break contact interfaces

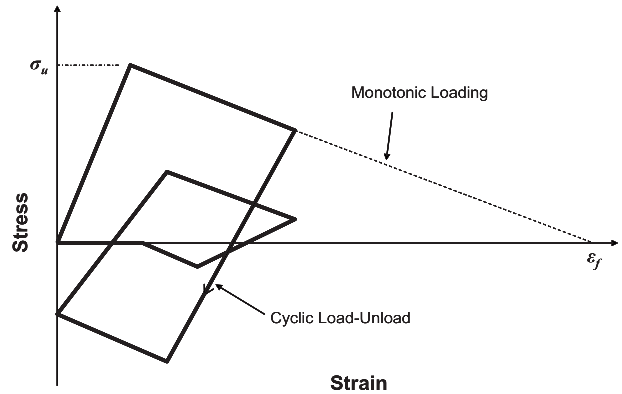

Fig. 2 Typical stress-strain curves produced by the material model MAT_81 in LS-DYNA under both monotonic loading and a complete load-unload cycle resulting in damage saturation

weight function, w. The length parameter should be adjusted so that the height of damage predicted by the nonlocal model closely matches the actual height of damage observed in the tests.

The energy dissipated in the damage process is another important parameter that should be captured by the nonlocal model. The energy release rate in a nonlocal model is a function of the length parameter, l, as well as the energy release rate density, g_f, that is essentially the area under the stress-strain curve. Since l is adjusted according to the height of damage h_c, the energy release rate density g_f should also be calibrated (scaled) to result in a predicted global load-displacement curve that is consistent with the experimental measurements.

It is worth noting that nonlocal regularization cannot be applied appropriately to the ply-based damage models since the length parameter employed in the nonlocal averaging scheme is a measure of the toughness (or brittleness) of the composite laminate. The latter not only depends on the ply properties, but also on the laminate lay-up. For the same reasoning, the nonlocal parameters cannot be calibrated using ply-based tests. Therefore, for the purposes of extracting the material damage parameters, the laminate must be treated as a material in its own right and the test specimen should be representative of the actual laminate configuration (lay-up) that is going to be numerically simulated.

The test specimen used to extract the material parameters should properly represent the damage/fracture behavior of the laminate that is going to be numerically simulated.

4 Numerical Model

Owing to its proven computational capabilities and efficiencies in handling contact/impact problems involving extremely nonlinear material behavior, the numerical test-bed selected for this study is the explicit finite element code LS-DYNA. In the structural model proposed here, the laminated plate is divided into a number of layers of shell elements each representing a sublaminate (or repeating unit) that are then tied together by cohesive type interfaces as shown in Fig. 1. The shell elements used are the fully integrated element (type 16 in LS-DYNA) with multiple through-thickness integration points.

4.1 Intralaminar Damage Model. The intralaminar damage is modeled by assigning strain-softening material models to the shell elements. For comparative purposes two different constitutive models are employed: one is based on the classical local damage model and the other is a nonlocal damage model.

The CODAM [2] is a user-defined material model that has been implemented in LS-DYNA. This model is based on the generalized crack band concept and is essentially a local damage model that is designed to predict the initiation and progressive growth of damage in composite materials.

Nonlocal enhancement is provided in LS-DYNA software for a limited number of its built-in material models. The nonlocal parameter can be chosen to be either the effective plastic (inelastic) strain (in the form of von Mises effective strain) or damage parameter or both. As discussed in Sec. 3.2, the inelastic strain is a more suitable parameter for nonlocal averaging compared with the damage parameter, which suffers from stress locking problems.

The current nonlocal capability in LS-DYNA only supports scalar damage models and therefore cannot be used for general anisotropic damage models. Since the laminates of interest in this study have quasi-isotropic lay-ups, this limitation is deemed to be insignificant.

Among the built-in material models, the MAT_PLASTICITY-_WITH_DAMAGE (MAT_81) model is considered to be a suitable choice as it allows for progressive damage modeling and the use of effective strain as the nonlocal parameter. This material model provides a combination of damage and plasticity. In a monotonic loading scenario, as shown in Fig. 2, the model exhibits a strain-softening behavior.

The damage formulation is written based on strain equivalence between the undamaged and damaged materials [32] according to

$$A_{\text{eff}} = A^0(1-d) \tag{8}$$

$$\boldsymbol{\sigma} = \boldsymbol{\sigma}_{\text{eff}}(1-d) \tag{9}$$

$$\mathbf{C}^d = \mathbf{C}^0(1-d) \tag{10}$$

where A_{eff} is the effective undamaged area of the material and σ_{eff} is the associated effective stress. The reduction multiplier $(1-d)$ is applied to both the ultimate stress (strength) and material stiffness. The damage parameter d is defined by the user as a function of the equivalent inelastic strain.

The behavior of this material model in a typical cyclic loading under uniaxial stress conditions is shown in Fig. 2 where the modulus degradation in unloading is evident but in contrast to the classical elastic-damage models, the unloading does not follow a secant path to the origin. As will be discussed in Sec. 5.1, the combination of plasticity and damage proves to be a useful feature of the model to help capture the residual deformation of composite plates under transverse impact loading. Note that in its local form, and provided that similar input parameters are used, the above material model results in a strain-softening curve that is similar to that produced by CODAM. The notable exception is that in CODAM, being an elastic damaging model, unloading results in stiffness degradation only while in MAT_81 it leads to a combination of permanent strain and modulus reduction.

The LS-DYNA software uses the bell-shaped weight function (Eq. (6)) for nonlocal averaging [33]. The recommended values of p and q parameters in LS-DYNA are 8.0 and 2.0, respectively. This averaging scheme is performed on the integration points lying on the same plane.

4.2 Tie-Break Interface. The tie-break interface, which is one of the built-in contact options available in LS-DYNA, is employed here to model delamination in composite plates. The interface layers are initially tied together and then released after satisfying a certain mixed-mode traction-based criterion defined by

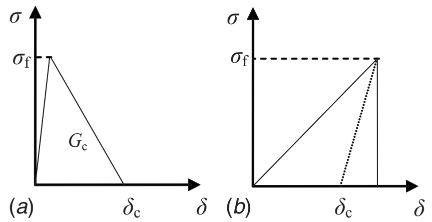

Fig. 3 Typical traction-separation curves with (*a*) high initial stiffness and (*b*) low initial stiffness causing a local snap-back behavior

Eq. (11) [33]. The postpeak behavior of the cohesive contact is governed by a bilinear softening traction-separation law as shown in Fig. 3(*a*). In situations where the closure of the delamination crack compresses the interface, the interface behaves as a penalty-based contact that prevents penetration of the contacting layers.

$$\left(\frac{\sigma_n}{\sigma_{fn}}\right)^2 + \left(\frac{\sigma_s}{\sigma_{fs}}\right)^2 \geq 1 \tag{11}$$

The behavior of the tie-break interface as a cohesive crack model under quasistatic loading conditions was validated in Ref. [34] where simulations of a double cantilever beam (DCB) were compared with the benchmark problem studied by Alfano and Crisfield [6].

The tie-break interface is a penalty-based contact model, the stiffness of which affects the behavior of the structure. This interface is responsible for tying the layers of shell elements together so that the stack of elements acts as an integrated plate. Using a compliant penalty stiffness leads to sliding of the contacting layers and hence a more compliant bending response of the structure. Overly compliant penalty stiffness can also result in a so-called snap-back in the cohesive model as shown in Fig. 3. The snap-back leads to a sudden release of the tie, which introduces an undesirable jittery (noisy) response in the explicit finite element simulation. Snap-back also causes convergence problems in implicit finite element simulations that can be avoided by appropriate incorporation of fictitious viscosity in the interface model (see Ref. [35], for example). From the fracture mechanics viewpoint, when snap-back occurs, the absorbed energy in the crack opening process deviates from the prescribed energy release rate G_c. This is shown schematically in Fig. 3(*b*), where the solid line corresponds to the actual traction-separation behavior, and as shown, the area under this curve, which is the energy absorbed in the opening process per unit area, exceeds the prescribed energy release rate G_c.

A very stiff contact on the other hand leads to stress concentration and formation of premature delamination sites. It also introduces high frequency modes in the structural response that lead to a reduction in the time step size (for numerical stability of explicit solvers) and hence an increase in the computational run-time. Therefore, the contact interface stiffness needs to be optimized in order to obtain a realistic structural response while avoiding computational difficulties.

5 Simulations of Dynamic Response of Composite Plates

5.1 Case Study 1: Transverse Impact by Projectiles. The case study used here to validate the predictive capability of the proposed computational model involves the analysis of the non-penetrating impact response of T800/3900-2 CFRP laminates with quasi-isotropic stacking sequence of $[45/90/-45/0]_{3S}$. The standard Boeing compression after impact (CAI) test geometry that was used in the impact tests is shown in Fig. 4. The impact tests

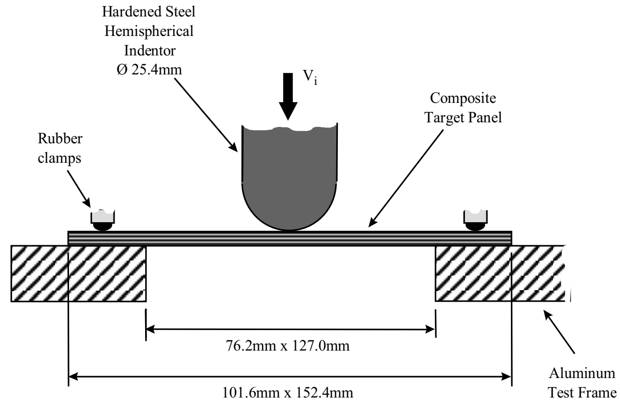

Fig. 4 Setup of the impact tests [36]

were conducted by Delfosse et al. [36] and covered a wide range of incident energies consisting of both high-mass (drop-weight) and low-mass (gas gun) tests.

5.1.1 Description of the Tests. The target geometry was a plate with dimensions $152.4 \times 101.6 \times 2.69$ mm^3 clamped onto an aluminum backing plate with a 76.2×127.0 mm^2 rectangular opening. The indenter (projectile) was a 25.4 mm diameter hemispherical shaped hardened steel as shown in Fig. 4. The low velocity impact tests, with velocities ranging from 1.76 m/s to 4.29 m/s, were performed using the drop-weight tower, which had a mass of 6.33 kg. A gas gun, which launched a 0.314 kg projectile, was employed to perform the high velocity tests with striking velocities ranging from 7.74 m/s to 23.19 m/s.

5.1.2 Material Characterization. The lamina elastic properties of the T800H/3900-2 CFRP and the effective sublaminate properties are listed in Table 1. Damage and failure-related properties of the quasi-isotropic sublaminate are listed in Table 2.

In keeping with the crack band scaling law for maintaining a constant fracture energy release rate G, the strain-to-failure (damage saturation strain ε_f) in the local damage model is scaled depending on the size of the element used in the mesh.

The length scale l in the nonlocal model is chosen to be equal to 2 mm. This results in a damage height $h_c \approx 4-5$ mm (in a quasi-static test like OCT), which is reasonable for this class of material [2,31]. The strain-to-failure in the nonlocal material model was adjusted to attain reasonable values of the global energy absorption in the damage process. This can be achieved by obtaining a good correlation between the predicted and measured load-

Table 1 Physical and in-plane elastic properties for the T800/3900-2 CFRP [2]

Parameter	Value	Units
Lamina		
Density (ρ)	1543	kg/m^3
Longitudinal modulus (E_1)	129.1	GPa
Transverse modulus (E_2)	7.45	GPa
Shear modulus (G_{12})	3.25	GPa
Major Poisson's ratio (υ_{12})	0.33	
Thickness of the ply (t_{ply})	0.194	mm
Sublaminate [45/90/−45/0]		
Density (ρ)	1543	kg/m^3
Effective principal modulus (E_x)	48.37	GPa
Effective principal modulus (E_y)	48.37	GPa
Effective shear modulus (G_{xy})	18.36	GPa
Effective Poisson's ratio (υ_{xy})	0.32	
Thickness of the sublaminate (t_{sublam})	0.775	mm

Table 2 Damage-related material properties for [45/90/−45/0] sublaminate of T800/3900-2 CFRP

Parameter	Value	Units
Intralaminar energy release rate (G_f) [a]	55.6	kJ/m^2
Mode I interlaminar fracture toughness (G_{Ic}) [b]	0.8	kJ/m^2
Mode II interlaminar fracture toughness (G_{IIc}) [b]	2.0	kJ/m^2

[a]Reference [2].
[b]Reference [37].

displacement curves in an OCT test. The parameters used in intralaminar and interlaminar damage models are listed in Table 3.

5.1.3 Structural Model. From a computational efficiency viewpoint, it is practically impossible to introduce delamination interfaces between all the layers. A prior knowledge about the behavior of the structure would help to identify potential delamination sites where cohesive interfaces can be planted. In the current case study, where the plate is subjected to an out-of-plane local impact loading, the transverse shear stresses are the major cause of delamination with the critical values of these stresses occurring at the midplane. Therefore, in the structural model used in this study, the laminate is modeled as two identical layers of shell elements tied together using the tie-break interface.

The boundary conditions are simplified with roller supports on the edges of the panel as shown schematically in Fig. 5.

To study the effect of spatial discretization on the predictions, two different mesh sizes have been used in the numerical simulations. The coarse and fine meshes consist of square elements of sizes 2 mm and 1 mm, respectively. The metal indenter is simulated as a spherical rigid object with a prescribed initial velocity.

Table 3 Material model parameters used in numerical simulations of T800/3900-2 CFRP laminate

Parameter	Value	Units
Intralaminar peak stress (σ_u) [a]	760	MPa
Saturation strain of local model—coarse mesh (ε_f)	0.074	
Saturation strain of local model—fine mesh (ε_f)	0.148	
Saturation strain of the nonlocal model (ε_f)	0.037	
Mode I delamination initiation stress (σ_{fn}) [a]	80	MPa
Mode II delamination initiation stress (σ_{fs})	150[b]	MPa
Delamination critical opening displacement (δ_c)	0.025[b]	mm

[a]Reference [2].
[b]The material parameters that are available from tests are the energy release rates for modes I and II of delamination (G_{Ic} and G_{IIc}) and the transverse tensile strength of the matrix material used as the initiation stress for mode I delamination, σ_{fn}. The parameters δ_c and σ_{fs} are computed such that the effective energy release rates for modes I and II used in the simulations are consistent with the measured values of G_{Ic} and G_{IIc}.

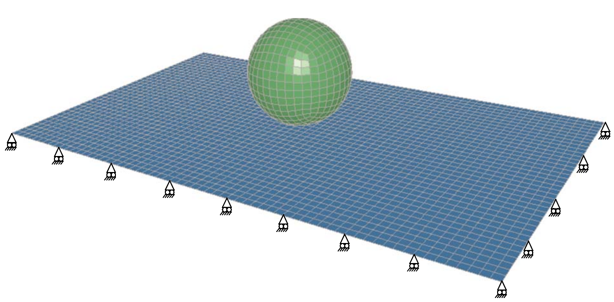

Fig. 5 Schematic showing the structural model consisting of the spherical indenter and the target panel constrained at its edges by frictionless simple supports

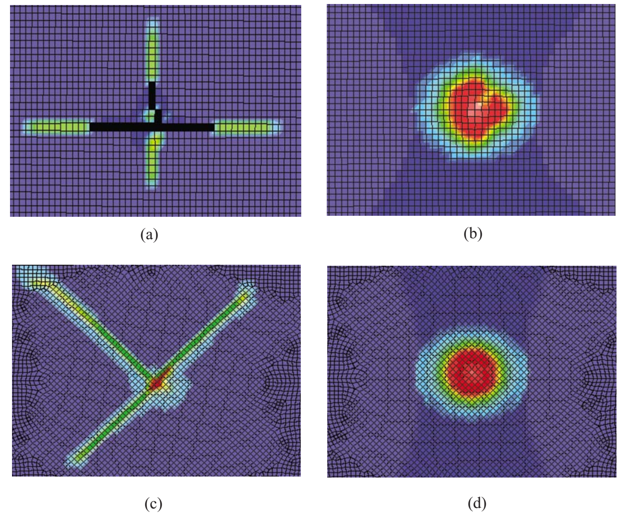

Fig. 6 The predicted damage pattern at the center of the impacted composite panel using (*a*) local and (*b*) nonlocal damage models on a regular structured mesh; and (*c*) local and (*d*) nonlocal damage models on an inclined mesh

5.1.4 Results

5.1.4.1 Damage pattern: Local versus nonlocal. To examine the sensitivity of the finite elements (FE) predictions to the orientation of the elements, a skewed mesh with 45 deg inclination of elements has been generated. The regular structured mesh and the skewed mesh have been used to study mesh-orientation dependency of the damage pattern. Figures 6(*a*) and 6(*b*) show the intralaminar damage patterns predicted with the regular mesh using the local and nonlocal damage models, respectively, while Figs. 6(*c*) and 6(*d*) show the corresponding damage patterns obtained with the inclined mesh.

It can be clearly seen from these figures that in the FE simulations based on the local version of the damage model the damage/crack tends to grow parallel to the orientation of the elements. This is due to the fact that the predicted local stresses/strains are not accurate enough and a criterion based on these parameters leads to mesh-dependent results. Since the damage is localized in one row of elements, the size of damage zone depends on the size of elements.

On the other hand, the nonlocal averaging reduces the effect of inaccurate local distributions of strain/stress and leads to a more reasonable prediction of damage propagation while alleviating the mesh size and orientation dependency problems.

Having demonstrated the benefits of a nonlocal approach to modeling damage development from a qualitative standpoint, in the following we will explore the validity of the nonlocal damage model predictions quantitatively by comparing the numerical results with the measured experimental data.

5.1.4.2 Time history of the contact force. Figure 7 shows two examples of the predicted impact force-time history in (a) low velocity–high-mass and (b) high velocity–low-mass dynamic events, both of which correspond to fairly high incident energies that impart significant damage to the CFRP panel. In these figures the predicted response based on both coarse and fine meshes has been compared with the experimental measurements by Delfosse et al. [36]. It can be seen that the predictions agree with the experiments in terms of peak force and duration of the event, which serves as a measure of the model performance in capturing the global response to impact. The agreement at the early stages of loading shows that the elastic behavior of the system is well captured by the numerical model while the agreement during the unloading stage is indicative of how well the response of the damaged system has been simulated.

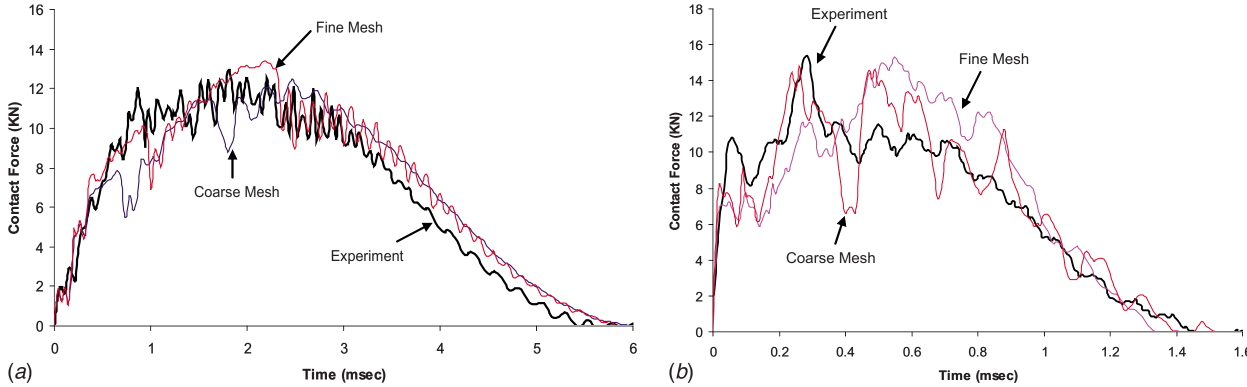

Fig. 7 Comparison between the measured and predicted impact forces versus time relationships in a (*a*) low velocity–high-mass ($v=4.29$ m/s, $E=58.2$ J) and a (*b*) high velocity–low-mass ($v=23.19$ m/s, $E=84.4$ J) impact event

5.1.4.3 Load-displacement curves. The impact load-deformation plots corresponding to the two cases considered above are shown in Fig. 8. It can be seen that the numerical simulations reasonably predict the trend of the behavior as well as the peak force and the maximum displacement.

The nonlinear unloading curve, as well as the residual deformation, is seen to be well predicted with the combination of the intralaminar plastic-damage model and the interlaminar cohesive tie-break interface model. This is an improvement over the previous elastic-damage model by Williams et al. [2], which led to a linear unloading path back to the origin with no residual deformation.

5.1.4.4 Energy absorbed by the plate. Figures 9(*a*) and 9(*b*) show the loss of the kinetic energy by the projectile during the course of the two impact events considered above. Since the energy dissipated in damping is negligible in this structural model, the residual energy loss of the projectile (the plateau value in each graph) is a measure of the energy absorbed by the structure due to the damage development (both interlaminar and intralaminar). Results obtained with fine and coarse meshes are shown in these graphs and both show reasonable agreement with the experimental data.

5.1.4.5 Partitioning of energy. The predicted partitioning of the absorbed energy of the target versus the incident impact energy are shown in Figs. 10(*a*) and 10(*b*) for a range of high-mass–low velocity and low-mass–high velocity impact events, respectively. The experimentally measured values of the projectile energy loss [38] are also shown on these plots to facilitate com-

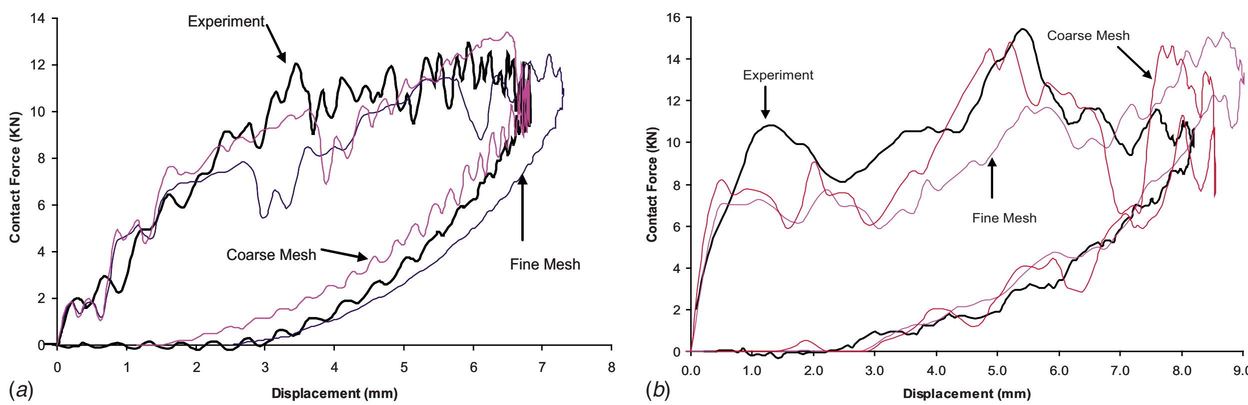

Fig. 8 Comparison between the measured and predicted impact forces versus plate deflection in a (*a*) low velocity–high-mass ($v=4.29$ m/s, $E=58.2$ J) and a (*b*) high velocity–low-mass ($v=23.19$ m/s, $E=84.4$ J) impact event

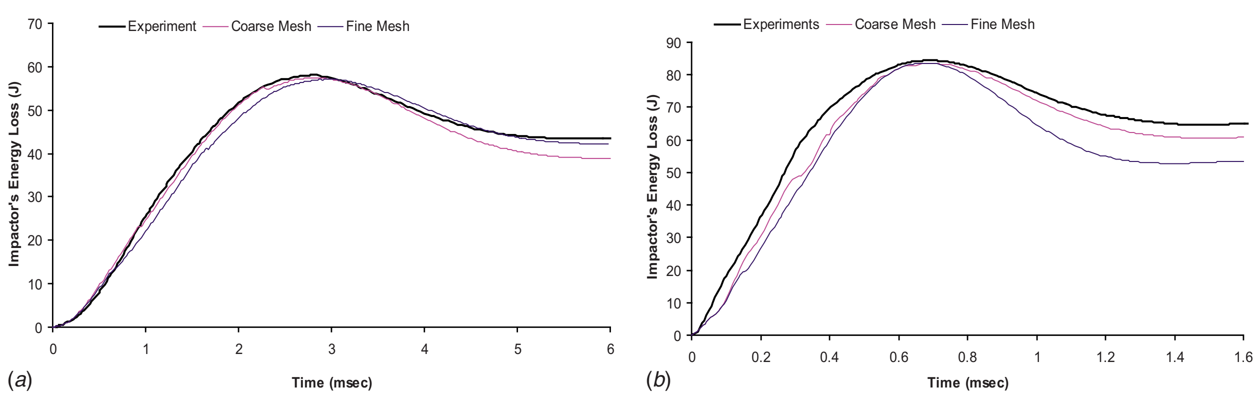

Fig. 9 Comparison between the measured and predicted histories of the projectile energy loss for a (*a*) low velocity–high-mass ($v=4.29$ m/s, $E=58.2$ J) and a (*b*) high velocity–low-mass ($v=23.19$ m/s, $E=84.4$ J) impact event

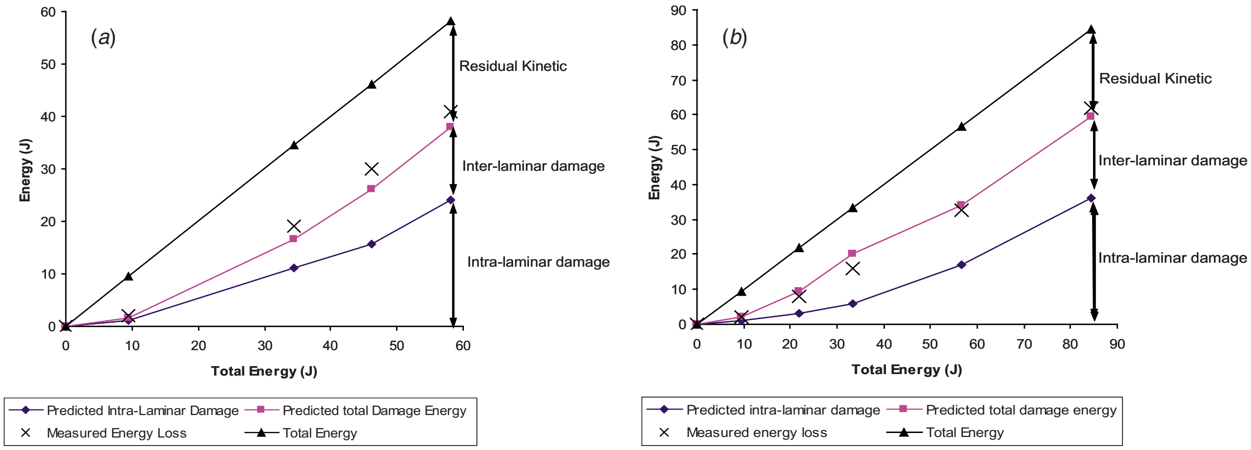

Fig. 10 Predicted energy absorbed in the damage process and measured energy loss in various (*a*) low velocity–high-mass and (*b*) high velocity–low-mass impact events

Table 4 Predicted dissipated damage energy and its breakdown into interlaminar and intralaminar components for the low velocity–high-mass impact cases. The values in parentheses are energies in joules.

Velocity (m/s)	Measured projectile energy loss (J)	Predicted energy loss in damage (J)	Predicted energy loss (% of impact energy)		
			Total damage	Intralaminar damage	Interlaminar damage
1.76(9.5)	2.1	1.6	16	12	4
3.3(34.5)	19	16.5	47	32	16
3.82(46.2)	30	26.2	56	34	23
4.29(58.2)	41	38	65	42	22

Table 5 Predicted dissipated damage energy and its breakdown into interlaminar and intralaminar components for the high velocity–low-mass impact cases. The values in parentheses are energies in joules.

Velocity (m/s)	Measured projectile energy loss (J)	Predicted energy loss in damage (J)	Predicted energy loss (% of impact energy)		
			Total damage	Intralaminar damage	Interlaminar damage
7.74(9.4)	2.1	2.0	21	10	11
11.84(22.0)	7.9	9.5	43	34	9
14.59(33.4)	16.2	20.2	59	30	29
18.97(56.5)	32.5	33.9	60	30	30
23.19(84.4)	62.3	59.4	70	43	28

parison with the numerically predicted values of the total energy absorbed by the CFRP plates. The latter can be decomposed into the energy absorbed in intralaminar and interlaminar damage processes, the values of which are listed in Tables 4 and 5 for the low and high velocity cases, respectively.

5.2 Case Study 2: Blast Loading.[2] The objective of this case study is to validate the performance of the proposed structural model in an intense dynamic event resulting from a blast load. The focus in this section is on delamination and the transient structural response.

5.2.1 Description of the Test. Explosive loading trials were conducted at the Canadian Department of National Defense (DRDC-Valcartier) [34] on IM7/8552 CFRP composite plates with quasi-isotropic lay-ups: $[90/45/-45/0/0/-45/45/90]_8$ (thin plates) and $[90/45/-45/0/0/-45/45/90]_{12}$ (thick plates). The dimensions of the panels were approximately $610\times305\ \text{mm}^2$ with thicknesses of 12 mm and 18 mm for thin and thick plates, respectively. The test setup is shown schematically in Fig. 11. The composite test plate was held loosely between removable steel cylinders, allowing it to slide freely as the plate bends due to the blast impulse. The trials consisted of explosively loading the plates with a 50 g C4 explosive at a stand-off distance of 140 mm.

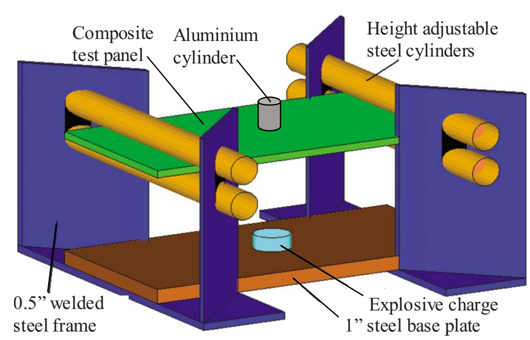

Fig. 11 Schematic of the test setup used for blast loading

[2]The results of this case study were presented at the 16th International Conference on Composite Materials in Kyoto, Japan (ICCM 16), 2007.

Table 6 Material properties of [90/45/−45/0/0/−45/45/90] IM7/8552 CFRP sublaminate [34]

Parameter	Value	Units
In-plane elastic modulus (E_x and E_y)	61.6	GPa
Shear modulus (G_{xy})	23.0	GPa
Poisson's ratio (υ_{xy})	0.32	
In-plane failure stress (σ_u)	550	MPa
Initiation stress for delamination (σ_{fn})	50	MPa
Delamination's critical opening displacement (δ_c)	0.012	mm

The back-face velocity of the plate was recorded by measuring the velocity of an aluminum cylinder that was placed on top of the composite plate as shown.

5.2.2 Material Characterization. The effective material properties for the quasi-isotropic [90/45/−45/0/0/−45/45/90] sublaminate are listed in Table 6.

5.2.3 Numerical Model. The structural model in this case is similar to the one used in the previous impact simulations. In order to address the effect of through-thickness discretization on the predicted response of the structure, the plate is modeled by stacking different numbers of shell elements (one, four, and eight layers) connected by the tie-break interface. The pressure-time pulse generated by the blast load is simulated using the conventional weapons effects (CONWEP) model [33]. The histories of blast pressure generated by CONWEP at different locations of the plate are shown in Fig. 12. The delay in the pressure-time graphs reflects the time taken for the blast wave to arrive at the plate surface after the explosive is set off.

5.2.4 Results

5.2.4.1 Dependency of the response on number of tie-break interface layers. As discussed previously, the tie-break contact is based on the penalty method and its stiffness may affect the dynamic characteristics of the structure. The goal here is to adjust the properties of the contact to render the structural response independent of the number of sublaminates and position of the tie-break contacts. The LS-DYNA software automatically calculates the penalty stiffness based on dynamic characteristics of the structure. This parameter can be scaled by the user; however, the default value of the penalty scale factor is 0.1 [33].

In this section the response of the thick plate using three different through-thickness discretizations, namely, one, four, and eight layers of shell elements, is studied. The analysis is performed both using the default value of the contact stiffness scale factor, i.e., 0.1, and a modified scale factor equal to 2.0. To conform to the experiments, a virtual aluminum cylinder is placed on the distal face of the plate to monitor its back-face velocity.

Table 7 shows the values of the back-face velocity of the plate (υ_b) and the velocity of the aluminum cylinder (υ_a) while using the default and modified contact stiffnesses. It can be seen that with the default contact stiffness, the results are not objective. In this case the values of υ_b and υ_a both depend on the number of layers used in the structural model. This is due to the fact that the interfacial tie is not stiff enough to ensure that the layers move together as a unit. Thus, the momentum transferred from the blast load is not carried by the whole laminate; rather it is carried by one or some of the layers at any given time. Given that each layer or sublaminate is thinner (and hence lighter) than the entire laminate, the back-face velocities are generally overpredicted and strongly depend on the number of shell layers (sublaminates).

The above can be addressed by appropriate scaling of the initial contact stiffness as shown in the right hand columns of Table 7. It

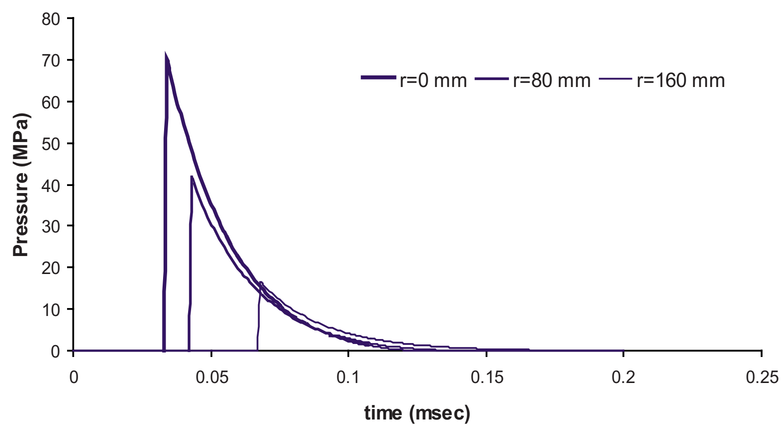

Fig. 12 Pressure-time pulse generated by the CONWEP model at different locations on the plate (radial distances *r* from the center) corresponding to a charge of 50 g C4 at a stand-off distance of 140 mm

Table 7 Predicted back-face velocity and velocity of the aluminum cylinder using default values of contact stiffness and modified contact stiffness

	Contact properties			Default contact stiffness		Modified contact stiffness	
No. of layers	σ_f (MPa)	δ_c (mm)	G_c (kJ/m^2)	υ_b (m/s)	υ_a (m/s)	υ_b (m/s)	υ_a (m/s)
1	-------	-------	-------	45	45	45	45
4	50	0.1	2.5	65	60	50	46
4	50	0.01	0.25	65	60	49	46
8	50	0.1	2.5	90	72	52	47
8	50	0.01	0.25	92	72	52	47

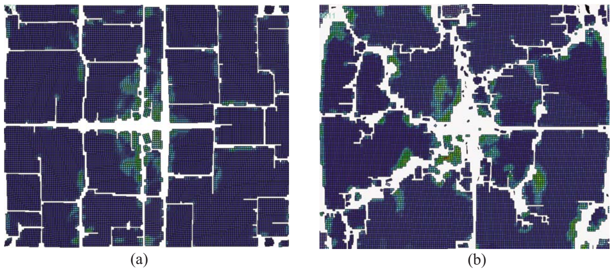

Fig. 13 Predicted damage pattern in the composite plate under blast load using a (*a*) local and a (*b*) nonlocal material model

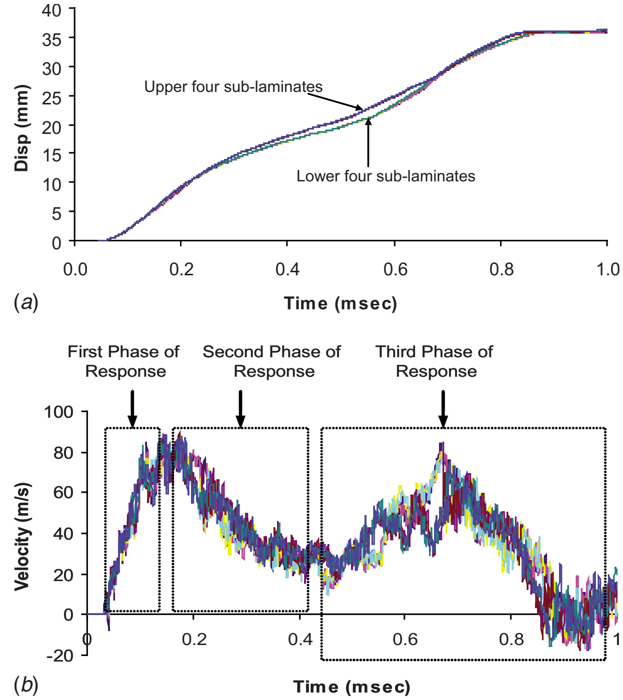

Fig. 14 Predicted time histories of the out-of-plane (*a*) displacement and (*b*) velocity of the various layers at the center of the plate

can be seen that with this modification the results have improved significantly and the velocities are almost invariant with the number of layers. Also it can be seen from the table that the maximum back-face velocity and velocity of the aluminum cylinder are independent of the strength of the cohesive model (in terms of energy release rate G_c). This is because the maximum velocity occurs during the first phase of the response when none of the interfacial ties are loaded in tension.

It is worth noting that the average measured velocity was about 62 m/s [34] while the predicted velocity of the aluminum cylinder is about 46 m/s as shown in Table 7. Therefore, the numerical simulation underestimates the back-face velocity. The accuracy of the CONWEP blast model in this case where the stand-off distance is only 140 mm is questionable, and this underestimation of the blast load may be the main reason for the predicted velocities being less than the measured data.

5.2.4.2 Damage pattern. The images in Fig. 13 show the predicted pattern of damage/crack on the one-layer model using the local damage model (Fig. 13(*a*)) and the nonlocal enhancement (Fig. 13(*b*)). It can be seen that the damage pattern and crack path in the classical smeared crack method are biased with respect to orientation of the mesh whereas the nonlocal regularization results in a much more realistic damage pattern.

5.2.4.3 Evaluation of the response of the structure. The eight-layer structural model is employed here to evaluate the response of the thin composite plate to the blast load. Figure 14(*a*) shows the time history of the transverse displacement at the center of each layer (sublaminate) underneath the aluminum cylinder. Layer 1 is the first sublaminate located at the bottom of the plate (impact face) and layer 8 is the last sublaminate at the top of the plate (distal face). The lack of overlap between the displacements of the sublaminates above and below the midplane is indicative of a major delamination occurring at the midplane of the plate. This agrees well with the experimental observations [34].

The structural response can be decomposed into three phases, as shown in Fig. 14(*b*). The first phase starts when the blast load strikes the plate and loading continues for about 40 μs. In this phase, the response of the structure is governed by the balance of momentum induced by the blast load. Therefore, the velocity of the system depends mainly on the blast impulse as well as on the thickness and density of the plate. At the end of this first phase and at the maximum velocity of the plate, the aluminum cylinder detaches from the back-face of the plate. Thus, the velocity of the aluminum cylinder and maximum back-face velocity of the plate are mainly driven by the impulse content of the blast load and the plate thickness and density.

The second phase starts about 50 μs after the blast hits the plate. In this phase, due to the deformation of the plate, strains and consequently stresses develop and the structure starts to resist the load. According to Fig. 14(*b*), the velocity reduces and therefore during this phase the acceleration at the center of the plate is negative. To resist the blast load, a significant punching shear develops, which leads to delamination of the layers. Since the maximum transverse shear stress occurs at the midplane of the plate, that is the site where a major delamination occurs.

The third phase starts about 300 μs after the blast initiation at which point in time the blast load duration has terminated and the structure responds in a free vibration mode. Due to the delaminations that had developed earlier, the layers are no longer constrained by their neighbors and the response is generally more compliant with lower frequencies than the intact plate. In this phase, delaminations may grow further due to local tensile or shear tractions between the layers.

6 Conclusions

A computational model for predicting the response of composite laminates subjected to out-of-plane dynamic loading has been presented. The explicit commercial finite element code LS-DYNA has been used as the numerical test-bed.

The intralaminar damage mechanisms consisting of fiber breakage and matrix cracking are captured using a continuum-based plastic-damage model applied at the sublaminate level. This level of resolution, which considers a stack of layers representing a repeating unit of the laminate, is deemed to be a physically realistic RVE at the macroscopic scale that can implicitly account for the damage interactions among the various layers. The sublaminate level for damage modeling introduces an inherent length scale that is unique to the particular laminate being considered. This length scale affects the size of the fracture process zone in a loading geometry of the laminate that results in a stable crack growth. A nonlocal regularization scheme is used to address the spurious mesh dependency and mesh-orientation problems associated with local strain-softening models. In dynamic loading events where the damage takes on a dispersed and random pattern, rather than being localized in a well-defined band, the nonlocal approach becomes a more effective method for smeared damage modeling.

Delaminations are modeled using a cohesive type tie-break interface introduced between the shell layers that represent the sublaminates. The tie-break interface uses the penalty stiffness method, which introduces an inherent finite stiffness between the tied layers. The value of this stiffness can significantly affect the dynamic structural response of the laminate and has to be judiciously selected to allow the laminate to act as an integral plate while maintaining a reasonable computational time step size. Overly compliant tie-break stiffnesses can lead to potential snap-back problems (depending on the value of the interlaminar energy release rate) while overly stiff values can be computationally taxing.

Both the interlaminar and intralaminar damage models used in this study draw on physically realistic and justifiable parameters for their calibration. These parameters are free from empiricism and have been gathered from the available literature data for the material systems used in the current study.

The predictive performance of the proposed methodology is validated using two numerical case studies carried out on CFRP plates: one involving the transverse impact loading by low- and high-mass projectiles covering a range of impact energies and the other involving dynamic pressure loading applied to the plates as a result of an explosive charge being set off. The predicted damage patterns using the nonlocal smearing approach are shown to be numerically objective and representative of the observed damage propagations. The combination of the cohesive interface model (for interlaminar behavior) and nonlocal plastic-damage model (for intralaminar behavior) is found to be quite effective in simulating the details of the force-time histories and force-displacement signatures of the projectile during the impact events. The real test of the capability of a model lies in its ability to predict the unloading response of the plates as it reveals the residual structural stiffness and displacement. The former is affected by the material stiffness degradations due to damage evolution as well as the global structural stiffness reduction due to delaminations, while the latter is the result of permanent deformations in the fracture processes. Through comparisons with the available experimental measurements, it is shown that the current structural model captures such intricate details of the dynamic response reasonably well.

The methodology presented in this paper is a promising step forward in the quest for a robust computational tool that can be used to analyze and design composite structures that can be either damage tolerant in service or expected to survive the intense dynamic loading conditions due to blast and impact.

Acknowledgment

Financial support for this work was provided by the Natural Sciences and Engineering Research Council of Canada through a discovery grant to R.V. and the Canadian Department of National Defense under a contract with the DRDC-Valcartier (Scientific Authority: Dr. Amal Bouamoul). The authors would like to thank many of the present and past members of the Composites Group at UBC who have made significant contributions to the work reported in this paper. In particular, they are grateful to Mr. Scott McClennan for designing and performing the blast load experiments and also Dr. Fernand Ellyin and Dr. Anoush Poursartip for many insightful discussions.

References

[1] Bažant, Z. P., and Planas, J., 1998, *Fracture and Size Effect in Concrete and Other Quasibrittle Materials*, 1st ed., CRC, Boca Raton, FL.
[2] Williams, K. V., Vaziri, R., and Poursartip, A., 2003, "A Physically Based Continuum Damage Mechanics Model for Thin Laminated Composite Structures," Int. J. Solids Struct., **40**, pp. 2267–2300.
[3] Ladeveze, P., Allix, O., Deu, J., and Leveque, D., 2000, "Mesomodel for Localisation and Damage Computation in Laminates," Comput. Methods Appl. Mech. Eng., **183**, pp. 105–122.
[4] Camacho, G. T., and Ortiz, M., 1996, "Computational Modelling of Impact Damage in Brittle Materials," Int. J. Solids Struct., **33**, pp. 2899–2938.
[5] Yu, C., Ortiz, M., and Rosakis, A. J., 2002, "Three-Dimensional Modeling of Intersonic Shear-Crack Growth in Asymmetrically Loaded Unidirectional Composite Plates," Int. J. Solids Struct., **39**, pp. 6135–6157.
[6] Alfano, G., and Crisfield, M. A., 2001, "Finite Element Interface Models for the Delamination Analysis of Laminated Composites: Mechanical and Computational Issues," Int. J. Numer. Methods Eng., **50**, pp. 1701–1736.
[7] El-Sayed, S., and Sridharan, S., 2001, "Predicting and Tracking Interlaminar Crack Growth in Composites Using a Cohesive Layer Model," Composites, Part B, **32**, pp. 545–553.
[8] Yang, Q., and Cox, B., 2005, "Cohesive Models for Damage Evolution in Laminated Composites," Int. J. Fract., **133**, pp. 107–137.
[9] Camanho, P. P., Davila, C. G., and de Moura, M. F., 2003, "Numerical Simulation of Mixed-Mode Progressive Delamination in Composite Materials," J. Compos. Mater., **37**, pp. 1415–1438.
[10] Borg, R., Nilsson, L., and Simonsson, K., 2001, "Simulation of Delamination in Fiber Composites With a Discrete Cohesive Failure Model," Compos. Sci. Technol., **61**, pp. 667–677.
[11] Wells, G. N., de Borst, R., and Sluys, L. J., 2002, "A Consistent Geometrically Non-Linear Approach for Delamination," Int. J. Numer. Methods Eng., **54**, pp. 1333–1355.
[12] de Borst, R., 2003, "Numerical Aspects of Cohesive-Zone Models," Eng. Fract. Mech., **70**, pp. 1743–1757.
[13] Maimi, P., Camanho, P. P., Mayugo, J. A., and Davila, C. G., 2007, "A Continuum Damage Model for Composite Laminates: Part I—Constitutive Model," Mech. Mater., **39**, pp. 897–908.
[14] Maimi, P., Camanho, P. P., Mayugo, J. A., and Davila, C. G., 2007, "A Continuum Damage Model for Composite Laminates: Part II—Computational Implementation and Validation," Mech. Mater., **39**, pp. 909–919.
[15] Bažant, Z. P., Belytschko, T. B., and Chang, T., 1984, "Continuum Theory for Strain-Softening," J. Eng. Mech., **110**, pp. 1666–1692.
[16] De Borst, R., Sluys, L. J., Muhlhaus, H., and Pamin, J., 1993, "Fundamental Issues in Finite Element Analyses of Localization of Deformation," Eng. Comput., **10**, pp. 99–121.
[17] Bažant, Z. P., and Oh, B. H., 1983, "Crack Band Theory for Fracture of Concrete," Mater. Constr., **16**, pp. 155–177.
[18] Bažant, Z. P., and Jirásek, M., 2002, "Nonlocal Integral Formulations of Plasticity and Damage: Survey of Progress," J. Eng. Mech., **128**, pp. 1119–1149.
[19] Bažant, Z. P., and Belytschko, T. B., 1985, "Wave Propagation in a Strain-Softening Bar: Exact Solution," J. Eng. Mech., **111**, pp. 381–389.
[20] Pijaudier-Cabot, G., and Bažant, Z. P., 1987, "Nonlocal Damage Theory," J. Eng. Mech., **113**, pp. 1512–1533.
[21] Bažant, Z. P., and Lin, F. B., 1988, "Nonlocal Smeared Cracking Model for Concrete Fracture," J. Struct. Eng., **114**, pp. 2493–2510.
[22] Peerlings, R. H. J., de Borst, R., Brekelmans, W. A. M., and Geers, M. G. D., 2002, "Localisation Issues in Local and Nonlocal Continuum Approaches to Fracture," Eur. J. Mech. A/Solids, **21**, pp. 175–189.
[23] De Borst, R., 1991, "Simulation of Strain Localisation: A Reappraisal of the Cosserat Continuum," Eng. Comput., **8**, pp. 317–332.
[24] Needleman, A., 1989, "Dynamic Shear Band Development in Plane Strain," ASME J. Appl. Mech., **56**, pp. 1–9.
[25] Georgin, J. F., Sluys, L. J., and Reynouard, J. M., 2004, "A Coupled Damage-Viscoplasticity Model for the Analysis of Localisation and Size Effects," Comput. Concr., **1**, pp. 169–199.
[26] Kroener, E., 1968, "Interrelations Between Various Branches of Continuum Mechanics," *Mechanics of Generalized Continua*, E. Kroener, ed., Springer-Verlag, Berlin, Germany, pp. 330–340.
[27] Bažant, Z. P., and Ozbolt, J., 1990, "Nonlocal Microplane Model for Fracture, Damage, and Size Effect in Structures," J. Eng. Mech., **116**, pp. 2485–2505.
[28] Jirasek, M., 1998, "Nonlocal Models for Damage and Fracture: Comparison of Approaches," Int. J. Solids Struct., **35**, pp. 4133–4145.
[29] Zobeiry, N., Forghani, A., McGregor, C., Vaziri, R., and Poursartip, A., 2007, "Progressive Damage Modeling of Composite Materials Under Both Tensile and Compressive Loading Regimes," ECCOMAS Thematic Conference on Mechanical Response of Composites.
[30] Kamel, A. K., Worswick, M. J., and Nandall, D., 1998, "Effect of Non-Local Damage Treatment on Dynamic Fracture Predictions," ASME PVP Congress.
[31] Kongshavn, I., and Poursartip, A., 1999, "Experimental Investigation of a Strain-Softening Approach to Predicting Failure in Notched Fibre-Reinforced Composite Laminates," Compos. Sci. Technol., **59**, pp. 29–40.
[32] Du Bois, P., Feucht, M., Haufe, A., and Kolling, S., 2006, "A Generalized Damage and Failure Formulation for SAMP," Presented at the Fifth German LS-DYNA Forum.
[33] Livermore Software Technology Company, 2007, LS-DYNA Keyword User's Manual-Version 971, Vols. I and II, p. 2206.
[34] Forghani, A., McGregor, C., Zobeiry, N., Vaziri, R., Ellyin, F., and Poursartip, A., 2007, "Modeling of Effect of Blast Load on Composite Panels," UBC-DRDC, Technical Report No. W7701-062619/001/QCL.
[35] Gao, Y. F., and Bower, A. F., 2004, "A Simple Technique for Avoiding Convergence Problems in Finite Element Simulations of Crack Nucleation and Growth on Cohesive Interfaces," Modell. Simul. Mater. Sci. Eng., **12**, pp. 453–463.
[36] Delfosse, D., Poursartip, A., Coxon, B. R., and Dost, E. F., 1995, "Non-Penetrating Impact Behavior of CFRP at Low and Intermediate Velocities," Proceedings of the Fifth Symposium on Composite Materials: Fatigue and Fracture, pp. 333–350.
[37] Davidson, B. D., Bialaszewski, R. D., and Sainath, S. S., 2006 "A Non-Classical, Energy Release Rate Based Approach for Predicting Delamination Growth in Graphite Reinforced Laminated Polymeric Composites," Compos. Sci. Technol., **66**, pp. 1479–1496.
[38] Delfosse, D., and Poursartip, A., 1997, "Energy-Based Approach to Impact Damage in CFRP Laminates," Composites, Part A, **28**, pp. 647–655.

The Influence of Material Properties and Confinement on the Dynamic Penetration of Alumina by Hard Spheres

Z. Wei
Department of Materials,
University of California,
Santa Barbara, CA 93106

A. G. Evans
Department of Materials,
and Department of Mechanical Engineering,
University of California,
Santa Barbara, CA 93106

V. S. Deshpande
Department of Mechanical Engineering,
University of California,
Santa Barbara, CA 93106

The ability of a ceramic to resist penetration by projectiles depends, in a coupled manner, on its confinement and its mechanical properties. In order to explore the fundamental inter-relationships, a simulation protocol is required that permits the microstructure and normative properties (hardness and toughness) to be used as input parameters. Potential for attaining this goal has been provided by a recent constitutive model, devised by Deshpande and Evans (DE) [2008, "Inelastic Deformation and Energy Dissipation in Ceramics: A Mechanics-Based Dynamic Constitutive Model," J. Mech. Phys. Solids, ***56****, pp. 3077–3100] that incorporates the contributions to the inelastic strain from both plasticity and microcracking. Before implementing the DE model, various comparisons with experimental measurements are required. Previously, the model has been successfully used to predict the quasistatic penetration of alumina by hard spheres. In the present assessment, simulations of the dynamic penetration of confined alumina cylinders are presented as a function of microstructure and properties and compared with literature measurements of the ballistic mass efficiency. It is shown that the model replicates the measured trends with hardness and grain size. Motivated by this comparison, further simulations are used to gain a basic understanding of the respective roles of plasticity and microcracking on penetration and to elucidate the phenomena governing projectile defeat.* [DOI: 10.1115/1.3129765]

Keywords: alumina, sphere impact, grain size, microcracks, plastic deformation, constraint, hardness

1 Introduction

When confined within a metallic medium, ceramics have sufficient dynamic strength in compression to deform and erode impacting projectiles [1–6]. Without the confinement, the induced tensile stresses cause extensive cracking that eliminates the benefit. The practical challenge is to conceive designs and to choose material properties that maintain the confinement for the longest duration. This challenge occupies a sufficiently large design space that simulations are required to seek optimal solutions. Moreover, the dynamic constitutive law used for the ceramic must be capable of incorporating the microstructure and normative material properties (toughness and hardness) as input parameters.

The most complete dynamic model is that devised by Johnson–Holmquist (JH) [5], which embodies a Drucker–Prager yield surface [7] that evolves damage through the effective plastic strain, analogous to the Johnson–Cook model [8] devised for metals. Once calibrated, this model is capable of predicting the penetration of projectiles into ceramic targets [9]. The limitation for present purposes is that, since the coefficients and exponents in the model are not connected to basic microstructure/property relationships, they must be recalibrated for each candidate ceramic. The Deshpande and Evans [10] (DE) model addresses this deficiency by specifically incorporating the inelastic deformation phenomena: microcracking and plastic slip (Appendix). Because the model explicitly incorporates the mechanisms, most of the properties required for simulations can be obtained from a few straightforward quasistatic tests [10]. The capabilities of the model have been illustrated by predicting the response of alumina to quasistatic impression by hard spheres [11]. It reproduces the observation that the proportion of the inelastic strain contributed by plasticity increases as the grain size decreases [12] and successfully predicts the grain size dependence of both the inelastic zone dimensions and the penetration pressure. To be comparably credible under dynamic circumstances, the model must (at least) be capable of predicting the influence of material properties on the depth-of-penetration under highly confined conditions, characterized by the ballistic mass efficiency, E_m (Fig. 1). For alumina, a large body of experimental measurements has revealed that E_m increases with increasing hardness [13] (Fig. 1(*b*)) but is unaffected by the grain size [14] (Fig. 1(*a*)).

The present article addresses the suitability of the DE model for dynamic simulations by replicating the foregoing experimentally obtained penetration trends (Fig. 1). For this purpose, simulations are conducted by using a rigid sphere that impacts an alumina cylinder subject to various levels of confinement (Fig. 2). The results are presented in the following sequence. In a first step, the basic inelastic responses to impact predicted by the DE model are established. In a second step, simulations of the penetration depth as functions of hardness and grain size are conducted and used to compare with the trends in ballistic mass efficiency. Motivated by this comparison, the trends in inelastic deformation with hardness (yield strength) are established as well as the consequences for the projectile defeat mechanism. Thereafter, the coupled effects of grain size and confinement are analyzed.

Contributed by the Applied Mechanics Division of ASME for publication in the Journal of Applied Mechanics. Manuscript received April 30, 2008; final manuscript received January 26, 2009; published online June 15, 2009. Review conducted by Ashkan Vaziri.

2 Dynamic Penetration of Confined Alumina Targets

To illustrate the capabilities of the DE constitutive model, a prototypical dynamic problem is analyzed. It involves a rigid

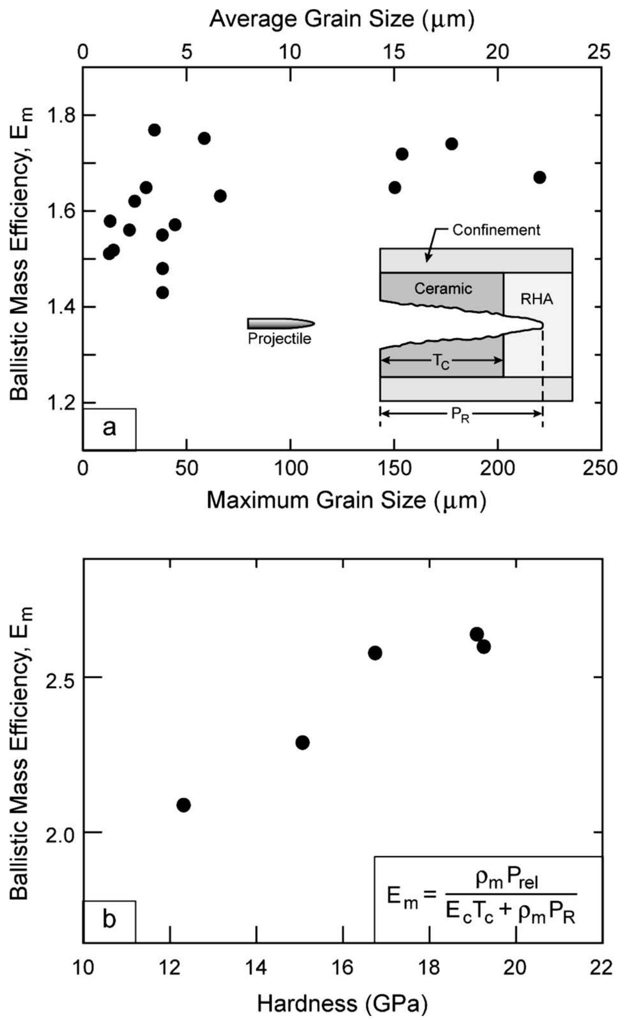

Fig. 1 Measured values of the ballistic mass efficiency E_m of alumina as a function of (*a*) the grain size d [13] and (*b*) Vickers hardness [15]. E_m is defined in the insets with T_c the thickness of the ceramic layer, P_R the residual penetration into RHA, and P_{ref} the penetration of the projectile into a reference RHA block without the ceramic front plate. Here ρ_c and ρ_m are the densities of the ceramic and RHA, respectively. $\sigma_Y = 4$ GPa.

sphere (diameter D_p) impacting an alumina cylinder (diameter $D_c > D_p$ and height H) at velocity v_o subject to various levels of confinement (Fig. 2). In representative experiments [13,14], the cylinder is confined by a steel sleeve. This situation is simulated by constraining the displacement of the outer surface, as sketched in Fig. 2(*a*). The DE model, along with the various material parameters and their reference values, are summarized in the Appendix.

For specified ceramic strain-rate sensitivity and strain hardening (fixed values of $\dot{l}_o$, m, M, ε_Y, n, $\dot{\varepsilon}_o$, and $\dot{\varepsilon}_t$), the general dimensionless form of the stress in the ceramic cylinder at time t after the impact is

$$\frac{\sigma_{ij}(t)}{\sigma_f} = F_{ij}\left[\frac{t\sqrt{\sigma_f/\rho}}{D_p}, \frac{\rho_p}{\rho}, \Omega, \frac{\sigma_f}{\sigma_Y}, \frac{d}{D_p}, \frac{\sigma_f}{G}, \nu, \mu\right] \quad (1)$$

where $\sigma_f \equiv K_{IC}/\sqrt{\pi D_p}$, $\bar{t} \equiv t\sqrt{\sigma_f/\rho}/D_p$, and Ω is the nondimensional kinetic energy of the impacting sphere, $\Omega \equiv \pi\rho_p v_o^2/12\sigma_f$, with ρ_p its density. The time-dependent histories of the crater depth $u(\bar{t})/D_p$ and width $w(\bar{t})/D_p$ depend on the same set of variables. Implicit are weak dependencies on the friction between the projectile and the alumina, as well as the ratio, D_c/D_p.

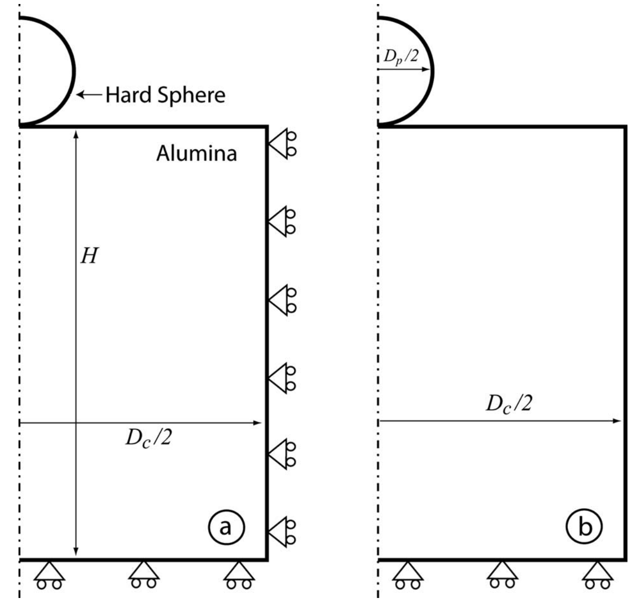

Fig. 2 Schematic of the alumina cylinder impacted by a hard sphere. The dashed line represents the symmetry axis. (*a*) The confined target and (*b*) the unconfined target.

Simulation setup. The constitutive model has been implemented in the finite element (FE) code ABAQUS/EXPLICIT through a user-defined material subroutine. The simulations were performed using four-noded, axisymmetric elements with reduced integration (CAX4R). A uniform mesh size was employed in order to accurately capture the propagation of damage away from the impact site. All calculations employ a mesh size of 64 μm (further refinement did not change the results). Mesh insensitivity and stability are inherent features of the DE model, not present in other damage models. This desirable feature is imparted by the dilatation that occurs as the alumina microcracks. The consequence is that, during penetration, the dilatation is resisted by the constraint, thereby increasing the stress triaxiality and elevating the shear strength of the damaged alumina. Thus, unlike tension-dominated loading situations, catastrophic softening does not occur and the simulation results are largely mesh-size insensitive.

Specific calculations have been conducted using alumina cylinders, with diameter $D_c = 25.4$ mm and height $H = 25.4$ mm, impacted by a sphere having diameter $D_p = 6.35$ mm and density $\rho_p = 15.6$ mg m^{-3} (representative of Tungsten Carbide). Sticking friction was assumed between the sphere and the alumina over the contact area. To avoid numerical artifacts, damping associated with volumetric straining in ABAQUS/EXPLICIT was switched off (using the default viscosity results in substantial artificial viscous dissipation upon bulking).

Basic features. The fundamentals entailed in high velocity penetration emerge from calculations conducted at $v_0 = 1000$ m s^{-1} on fine-grained material ($d = 3$ μm) with the reference yield strength, $\sigma_Y = 4$ GPa. The ensuing damage D and plastic strain ε_e^{pl} contours at selected times t after the impact event are plotted in Fig. 3. The damage plots are shaded so as to illustrate only the fully comminuted zone ($D = 1$) and undamaged zones ($D = D_0$), while the plastic deformation plots reveal strains up to $\varepsilon_e^{pl} \sim 0.6$. Along the axis, the damage only initiates after the impacting sphere begins to rebound (at $t \geq 3$ μs), whereas plastic strains evolve only during penetration (at $t \leq 3$ μs). The interpretation of these features is motivated by the spherical cavity expansion calculation described elsewhere [10]. As the spherical elastic wave emanates from the contact, the associated triaxiality, λ, is large enough to inhibit the growth of microcracks. Later, at lower impact velocities < 1000 m s^{-1}, the decrease in λ with distance into

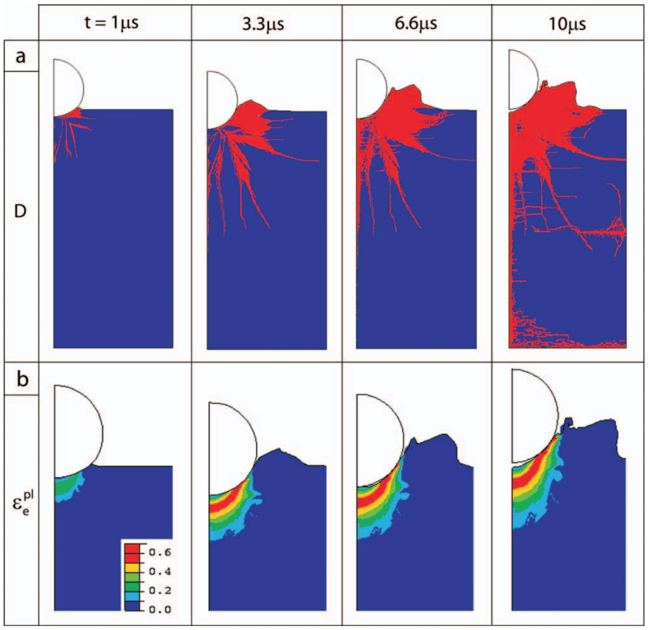

Fig. 3 The distribution of (*a*) damage *D* and (*b*) plastic strain ε_e^{pl} in the confined ceramic target with reference properties at selected times *t* after the impact of the sphere traveling at v_o =1000 m s^{-1}. The contours in (*a*) are shaded so as to only illustrate the fully damaged (D=1) and undamaged (D=D_0) regions.

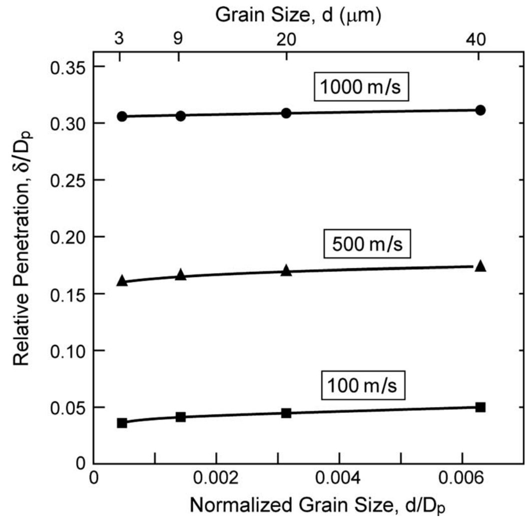

Fig. 5 Predictions of the normalized maximum penetration of the projectile (δ/D_p) as a function of the normalized grain size d/D_p for three selected values of the normalized kinetic energy Ω corresponding to impact velocities v_o=1000, 500, and 100 m s^{-1}. The results pertain to the confined ceramic target with σ_Y=4 GPa.

the elastic wake is sufficient to allow a microcrack zone to form and propagate behind the elastic front [10]. At higher impact velocity ($>$1000 m s^{-1}), the response changes because the stresses generated become large enough to induce plastic slip (in preference to a microcrack zone), causing a plastic zone to form and expand in the wake of the elastic wave, as the projectile penetrates. Moreover, behind the plastic wave, λ increases significantly, continuing to suppress microcracking. Subsequently, as the impacting sphere begins to rebound (at about t=3 μs), the tensile elastic waves generated from the contact increase λ, causing damage to permeate the cylinder.

This simple view of the impact process is not applicable near the periphery of the contact where the free surface disrupts spherical symmetry. The free surface reduces the triaxiality relative to that along the symmetry line, resulting in extensive damage, with-

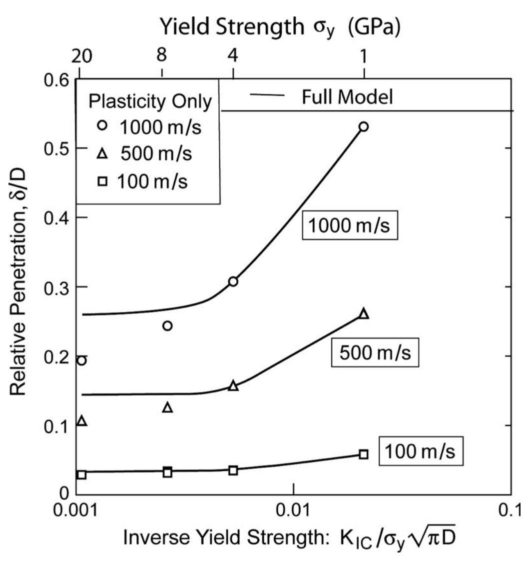

Fig. 4 The variation of the normalized maximum penetration δ/D_p of the d=3 μm confined ceramic target as a function of the normalized inverse yield strength σ_f/σ_Y. Results are shown for three selected values of the normalized kinetic energy Ω corresponding to impact velocities v_o=1000, 500, and 100 m s^{-1}. For comparison purposes, the corresponding results with damage inhibited are also included and labeled "plasticity-only."

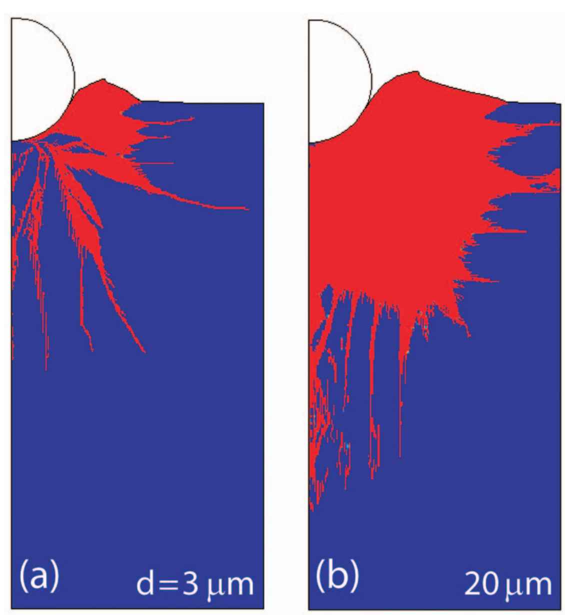

Fig. 6 Distributions of damage at maximum penetration in the confined ceramic targets with grain sizes (*a*) d=3 μm and (*b*) d=20 μm impacted at v_o=1000 m s^{-1}. The ceramic yield strength is taken as σ_Y=4 GPa. The contours are shaded so as to only illustrate the fully damaged (D=1) and undamaged (D=D_0) regions.

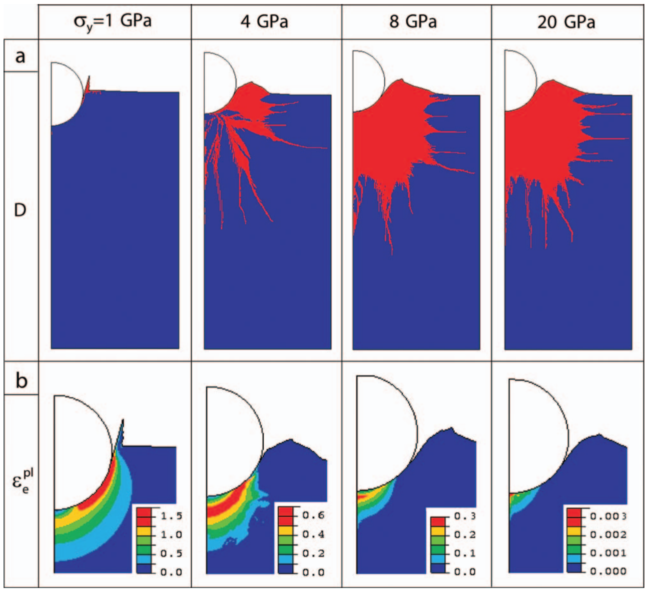

Fig. 7 The distribution of (*a*) damage *D* and (*b*) plastic strain ε_e^{pl} in the confined ceramic targets impacted by a hard sphere traveling at v_o=1000 m s^{-1}. The distributions are shown at the instant of maximum penetration, t_p, for the d=3 μm ceramic with yield strengths in the range 1 GPa$\le \sigma_Y \le$20 GPa. The contours in (*a*) are shaded so as to only illustrate the fully damaged (D=1) and undamaged (D=D_0) regions.

out detectable plastic deformation. Moreover, the material that comminutes in this zone is ejected from the periphery, resulting in a crater.

3 Comparison Between Simulations and Experiments

To examine the influence of yield strength (hardness) on the penetration resistance of the confined fine-grained (d=3 μm) alumina, the maximum penetration δ is calculated (for 1 GPa$\le \sigma_Y \le$20 GPa) and plotted as a function of the inverse yield strength σ_f/σ_Y (Fig. 4) for the three selected values of the initial kinetic energy Ω (projectile velocities, v_o=1000, 500, and 100 m s^{-1}). In all cases, the penetration decreases with increasing σ_Y, before saturating, consistent with the trend in the ballistic mass efficiency (Fig. 1(*b*)). Corresponding predictions of the maximum penetration at fixed yield strength (Fig. 5) reveal that, at all velocities, the penetration is grain size invariant, again consistent with the trend in the ballistic mass efficiency (Fig. 1(*a*)) [14]. This invariance arises despite the grain size sensitivity of the stress/strain response (Fig. 13) and even though significantly more damage is observed in the coarser-grained alumina (Fig. 6). The rationalization is that the bulking upon microcracking sufficiently increases the triaxiality (due to the confinement) that the damaged material maintains a pressure comparable to that of the undamaged material [10].

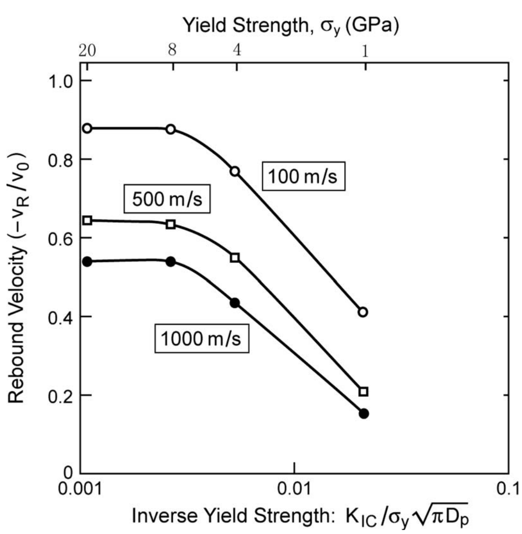

Fig. 8 The variation of the normalized final velocity of the impacting sphere $-v_r/v_o$ with the normalized inverse yield strength σ_f/σ_Y. The numerical results are for the d=3 μm confined ceramic target and three selected values of the normalized kinetic energy Ω corresponding to impact velocities v_o =1000, 500, and 100 m s^{-1}. By convention a positive velocity is in the direction of the impact velocity of the projectile.

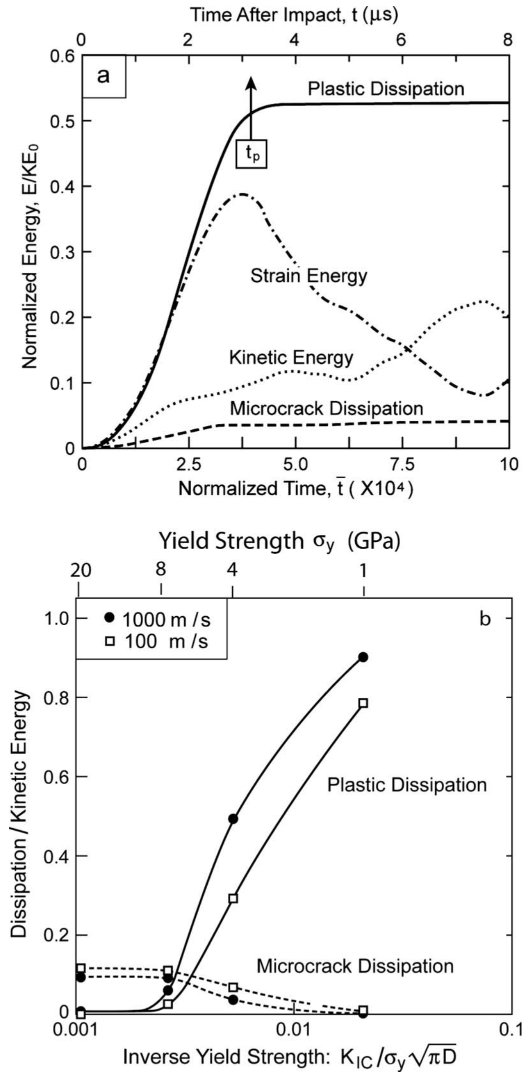

Fig. 9 (*a*) The temporal variations of the energy dissipations, strain energy, and kinetic energy of the alumina cylinder impacted by a sphere traveling at v_o=1000 m s^{-1}. The alumina has a grain size d=3 μm and yield strength σ_Y=4 GPa. (*b*) The normalized final plastic and fracture dissipations in the d =3 μm confined ceramic target as a function of the normalized inverse yield strength σ_f/σ_Y. The dissipations are normalized by the initial kinetic energy of the projectile and the results are shown for two selected values of the normalized kinetic energy Ω corresponding to impact velocities v_o=1000 and 100 m s^{-1}.

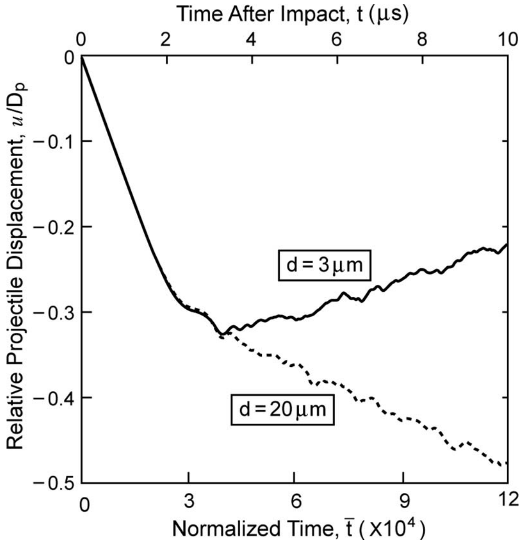

Fig. 10 The temporal variation of the normalized displacement u/D_p of the hard sphere impacting the unconfined ceramic target at v_o=1000 m s^{-1}. The ceramic has a yield strength σ_Y =4 GPa and results are shown for grain sizes d=3 and 20 μm.

The correspondence between these two simulations and the ballistic experiments provides sufficient credibility in the mechanistic basis of the DE model to use it to examine some of the fundamentals affecting penetration.

4 Influence of Yield Strength

The distribution of damage and plastic strain at the instant of maximum penetration[1] is shown in Fig. 7. The extent of the plastic zone and the strains within the zone both decrease with increasing σ_Y. The damage also increases with increasing σ_Y but saturates at about σ_Y=8 GPa. That is, the damage is nearly identical when σ_Y=8 and 20 GPa. This feature emerges because plasticity suppresses microcracks by increasing triaxiality (discussed above). Namely, increasing σ_Y diminishes plasticity, thereby decreasing λ in the elastic wake, allowing larger levels of damage. Moreover, at a critical σ_Y the alumina becomes an elastic-brittle solid.

To clarify the transition from a plasticity- to damage-dominated response we suppressed the growth of the microcracks by employing an artificially high toughness. The results are included in Fig. 4. Note that the penetration now decreases monotonically with an increase in σ_Y. Moreover, at low σ_Y, the predicted penetrations are unaffected by the inclusion of microcracking, indicating that plasticity dominates the response. The switch from plasticity to damage domination alters the armor defeat mechanism from kinetic energy absorbing to "reflecting," as illustrated in Fig. 8, where the ratio of the rebound-to-initial projectile velocity $-v_r/v_o$ is plotted as function of σ_f/σ_Y. Upon increasing the yield strength, the projectile loses a smaller fraction of its initial kinetic energy as it penetrates, causing it to rebound with increasing velocity.

The change in the defeat mechanism is also evident in the temporal variations of the dissipations (plastic and fracture) (Fig. 9(*a*)) as well as the dependence of the final dissipations on σ_Y (Fig. 9(*b*)). While the plastic dissipation decreases with increasing σ_Y, and the microcrack dissipation increases, the latter is always a small fraction of the initial kinetic energy of the projectile. Thus,

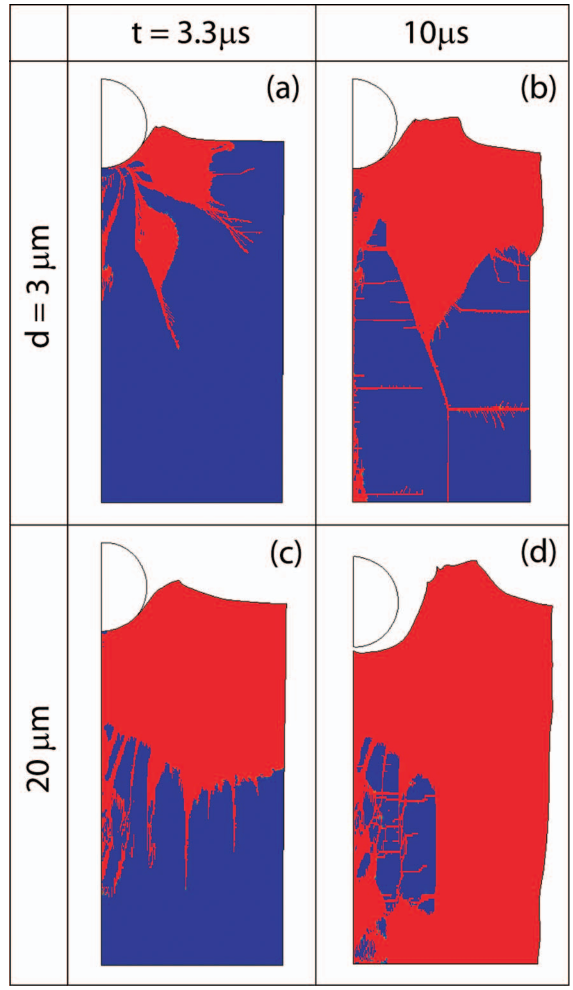

Fig. 11 Distributions of damage at two selected times in the unconfined ceramic targets with grain sizes ((*a*) and (*b*)) d =3 μm and ((*c*) and (*b*)) d=20 μm impacted at v_o =1000 m s^{-1}. The ceramic yield strength is taken as σ_Y =4 GPa. The contours are shaded so as to only illustrate the fully damaged (D=1) and undamaged (D=D_0) regions.

when microcracking dominates, the ceramic reflects the projectile rather than absorbing its kinetic energy and vice versa, when plasticity dominates.

5 Effect of Grain Size

The calculations are repeated upon removing the confinement on the cylindrical surface, as indicated in Fig. 2(*b*). The temporal variation of the normalized displacement u/D_p is plotted in Fig. 10 for two choices of the grain size (d=3 μm and 20 μm) and the corresponding states of damage are presented in Fig. 11. The d=3 μm alumina defeats the incoming projectile, causing it to rebound. However, for the d=20 μm alumina the projectile continues to travel into the target, albeit at a reduced velocity. This happens because the loss of constraint causes the damage zone to extend to the outer surface of the cylinder (Fig. 11), resulting in collapse.

The coupled roles of confinement and grain size can be understood as follows. In the unconfined state, the elastic wave that impinges on the side surfaces of the cylinder reflects as a tensile wave. This wave creates damage in its wake for the d=20 μm material, but its amplitude is too small to microcrack the d =3 μm material (Fig. 13 illustrates the differences of the strengths of the coarse and fine-grained materials). For the coarse-

[1]The time at which maximum penetration occurs is $t=t_p\approx 3$ μs, except for the σ_Y=1 GPa case, when $t_p\approx 5$ μs.

grained material, the tensile (spallation) zone converges with the compressive damage zone emanating from the impact site, resulting in fully comminuted material that ejects from the sides. Consequently, the projectile continues to penetrate. With confinement, the wave reflected from the sides is compressive and does not contribute to damage progression.

6 Concluding Remarks

The inelastic constitutive law for polycrystalline ceramics recently devised by Deshpande and Evans [10] has been implemented in ABAQUS/EXPLICIT and used to generate mechanistic insights into the dynamic response of polycrystalline alumina impacted at high velocity. The emphasis has been on the heretofore unexplained influences of grain size and yield strength on the penetration. An elucidation of the subtle effects of the triaxiality, λ, induced during impact has provided the requisite insight. The following effects have emerged: (i) the strong influence of λ on the incidence of damage, (ii) the onset of plasticity further increases triaxiality and suppresses damage, and (iii) in the presence of constraint, the damage creates its own triaxiality elevation. The consequence is a major influence of constraint on the temporal and spatial evolution of damage. This, in turn, causes the grain size to be unimportant for test scenarios with substantial constraint, but extremely important when the constraint is diminished, in accordance with findings reported in the literature. Moreover, the model predicts that, within a certain range, alumina becomes more penetration resistant upon increasing hardness, consistent with measurements.

Acknowledgment

Support from the Office of Naval Research through a Multidisciplinary University Research Initiative Program on "Cellular Materials Concepts for Force Protection," Prime Award No. N00014-07-1-0764 is gratefully acknowledged.

Nomenclature

a = radius of initial flaw
c_1, c_2, c_3 = functions defined in the Appendix
d = grain size
f = microcracks per unit area
g_1 = $a \equiv g_1 d$
g_2 = $1/f^{1/3} \equiv g_2 d$
l = length of wing crack
$\dot{l}_0$ = reference crack growth rate
m = crack growth rate exponent
n = plasticity strain-rate exponent
t = time after impact
t_p = time at maximum penetration
$\bar{t}$ = normalized time $t\sqrt{\sigma_f/\rho}/D_p$
u = crater depth
v_o = impact velocity
v_r = rebound velocity of projectile
w = crater width
A, B, C, E = functions that govern the stress intensity
A_1, A_3 = functions defined in the Appendix
E_m = ballistic mass efficiency
D = current damage level
D_0 = initial damage level
D_c = diameter of ceramic cylinder
D_p = diameter of projectile
H = height of ceramic cylinder
G = shear modulus of the uncracked ceramic
K_{I} = mode I stress intensity factor at periphery of wing crack
K_{IC} = mode I fracture toughness
M = strain hardening exponent
S_{ij} = components of deviatoric stresses
W = strain energy density of the ceramic
W_0 = strain energy density of the uncracked ceramic
β, γ = constants defined in the Appendix
δ = maximum penetration
$\varepsilon_e^{\mathrm{pl}}$ = von Mises effective plastic strain
ε_{ij} = components of total strain
ε_{ij}^e = elastic strain components
ε_{ij}^p = plastic strain components
$\dot{\varepsilon}_0$ = reference strain rate
$\dot{\varepsilon}_t$ = transition strain rate to linear viscous behavior
ε_Y = ceramic yield strain
λ = stress triaxiality σ_m/σ_e
μ = friction coefficient along faces of initial flaws
ν = Poisson's ratio of the uncracked ceramic
Ω = $\equiv \pi\rho_p v_o^2/12\sigma_f$
ρ = density of the uncracked ceramic
ρ_p = density of projectile material
σ_e = von Mises effective stress
σ_f = $\equiv K_{\mathrm{IC}}/\sqrt{\pi D_p}$
σ_m = hydrostatic stress
σ_0 = flow stress of ceramic
σ_{ij} = stress components
σ_Y = yield strength of ceramic

Appendix: Synopsis of the DE Constitutive Model

1 Microcracking. Following Ashby and Sammis [15], the DE [10] model envisages an array of f microcracks per unit volume, growing in an otherwise elastic medium (Fig. 12) subject to principal stresses, σ_1 and σ_3. Each microcrack develops from an initial flaw, radius a, by means of two wings, length l, extending parallel to X_1 (Fig. 12). The inclined flaws are subject to Coulomb friction (coefficient, μ). The flaw radius and separation scale with the grain size as $a=g_1 d$ and $1/f^{1/3}=g_2 d$, respectively. The initial and current levels of damage are expressed as $D_0=(\sqrt{2}/3)\pi a^3 f$ and $D=(4/3)\pi(l+a/\sqrt{2})^3 f$. The mode I stress intensity, K_{I}, at the periphery of the wing cracks depends on the stress triaxialility, $\lambda \equiv \sigma_m/\sigma_e$ (where σ_m is the hydrostatic stress and σ_e is the von Mises effective stress) in accordance with three regimes (I, II, and III) and four nonlinear functions of the damage and friction. Functions A, B, C, and E are detailed below. In regime I ($\lambda \le -B/A$), the cracks are shut, with $K_{\mathrm{I}}=0$. In regime II, frictional slip occurs along the initial flaw with

$$K_{\mathrm{I}}/\sqrt{\pi a} = A\sigma_m + B\sigma_e \tag{A1}$$

In regime III, $\lambda \ge AB/[C^2-A^2]$, loss of contact along the faces of the initial flaw occurs, whereupon

$$K_{\mathrm{I}}/\sqrt{\pi a} = (C^2\sigma_m^2 + E^2\sigma_e^2)^{1/2} \tag{A2}$$

The crack growth rate, $\dot{l}$, is related to the stress intensity factor by

$$\dot{l} = \min[\dot{l}_0(K_{\mathrm{I}}/K_{\mathrm{IC}})^m, \sqrt{G/\rho}] \tag{A3}$$

where K_{IC} is the mode I (short-crack) fracture toughness, $10 \le m \le 20$ is the rate exponent, and $\dot{l}_0$ is the reference crack growth rate at $K_{\mathrm{I}}=K_{\mathrm{IC}}$, with G and ρ the shear modulus and density of the uncracked ceramic, respectively. The drop in effective modulus as the microcracks extend is governed by the stress intensities in accordance with the following strain energy densities. In Regime I,

$$W = W_0 = \frac{1}{4G}\left[\frac{2}{3}\sigma_e^2 + \frac{3(1-2\nu)}{1+\nu}\sigma_m^2\right] \tag{A4a}$$

In Regime II,

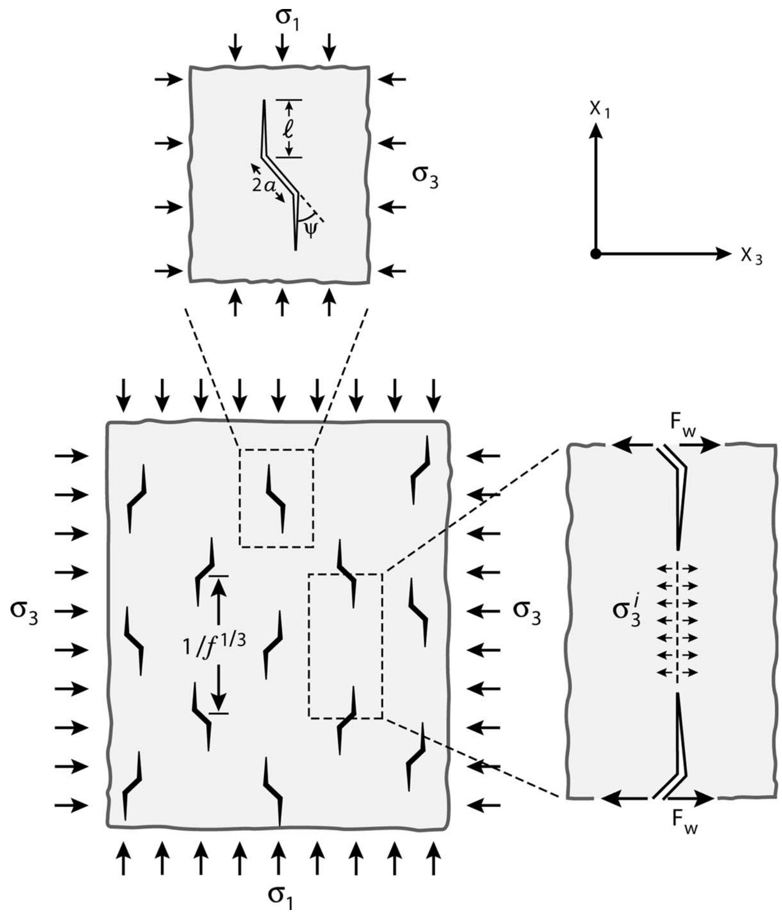

Fig. 12 A sketch of a microcracked solid containing a distribution of wing cracks. The insets show an isolated crack with the wedging force F_w acting at the midpoint and the matrix stress σ_3^i that determines the interaction of adjacent cracks.

$$W = W_0 + \frac{\pi D_0}{\sqrt{2}G(1+\nu)}(A\sigma_m + B\sigma_e)^2 \tag{A4b}$$

In Regime III,

$$W = W_0 + \frac{\pi D_0}{\sqrt{2}G(1+\nu)}(C^2\sigma_m^2 + E^2\sigma_e^2) \tag{A4c}$$

where W_0 and ν are the strain energy density and Poisson ratio of the uncracked ceramic, respectively. The elastic strains ε_{ij}^e follow directly from $\varepsilon_{ij}^e = \partial W/\partial\sigma_{ij}$.

2 Plasticity. When the confining pressure $(-\sigma_m)$ increases, microcracking becomes increasingly difficult and is supplanted by plasticity. In oxides (such as α-Al_2O_3) plasticity is limited by the lattice resistance at low strain rates and by phonon drag at high rates [16], and we can relate the plastic strain rate $\dot{\varepsilon}_{ij}^{pl}$ to the deviatoric stress S_{ij} by

$$\frac{\dot{\varepsilon}_{ij}^{pl}}{\dot{\varepsilon}_0} = \begin{cases} \dfrac{3}{2}\dfrac{S_{ij}}{\sigma_0}\left(\dfrac{\sigma_e}{\sigma_0}\right)^{n-1} & \text{if } \dot{\varepsilon}_e^{pl} < \dot{\varepsilon}_t \\ \dfrac{3}{2}\left(\dfrac{\dot{\varepsilon}_0}{\dot{\varepsilon}_t}\right)^{(1-n)/n}\dfrac{S_{ij}}{\sigma_0} & \text{otherwise} \end{cases} \tag{A5}$$

where $\sigma_0(\varepsilon_e^{pl})$ is the flow stress at an equivalent plastic strain ε_e^{pl}, $\dot{\varepsilon}_0$ and $\dot{\varepsilon}_t$ are the reference and transition strain rates, respectively, and $10 \le n \le 20$ is the rate-sensitivity exponent. Strain hardening due to the blocking of slip by grain boundaries is expressed in the power law form

$$\sigma_0 = (\sigma_Y/2)[1 + (\varepsilon_e^{pl}/\varepsilon_Y)^M] \tag{A6}$$

where σ_Y is the uniaxial yield strength, ε_Y is the yield strain, and M is the strain hardening exponent. The total strain rate is

$$\dot{\varepsilon}_{ij} = \dot{\varepsilon}_{ij}^e + \dot{\varepsilon}_{ij}^{pl} \tag{A7}$$

Recall that strain-rate effects are included in the model through two phenomena: (i) a rate dependent damage or crack growth law (Eq. (A3)) and (ii) rate dependent plasticity (Eq. (A5)).

3 Material Parameters. The following properties, taken from Ref. [10], are used for alumina: $G=146$ GPa, $\nu=0.2$, $\rho=3700$ kg m^{-3}, $K_{IC}=3$ MPa m$^{1/2}$, $\varepsilon_Y=0.002$, $\dot{l}_0=100$ μm s^{-1}, $\dot{\varepsilon}_0=1$ s^{-1}, $\dot{\varepsilon}_t=10^6$ s^{-1}, $\mu=0.75$, $\beta=0.1$, $\gamma=2$, $m=n=10$, and $M=0.1$. Since the flaws have dimensions restricted to the grain facet length, $g_1=0.25$ [17]. The spacing of the flaws is largely dictated by the separation of the grains at the large extreme. Calibrations conducted by comparing predictions and measurements of the dimensions of the inelastic zone size upon impressing with a hard sphere [11] have revealed that $g_2=2$ is an appropriate choice.

4 Stress/Strain Responses. The foregoing constitutive representation predicts high strain-rate ($\dot{\varepsilon}_e=100$ s^{-1}) trends in the von Mises effective stress σ_e as a function of the effective strain ε_e (ε_e is the work conjugate to σ_e) depicted in Fig. 13 for alumina with $\sigma_Y=4$ GPa and grain sizes, $d=3$ μm and 20 μm. Predictions are included for triaxialities ranging from uniaxial tension ($\lambda=1/3$) to a high confining pressure ($\lambda<-0.4$). At lower triaxialities ($\lambda\ge$

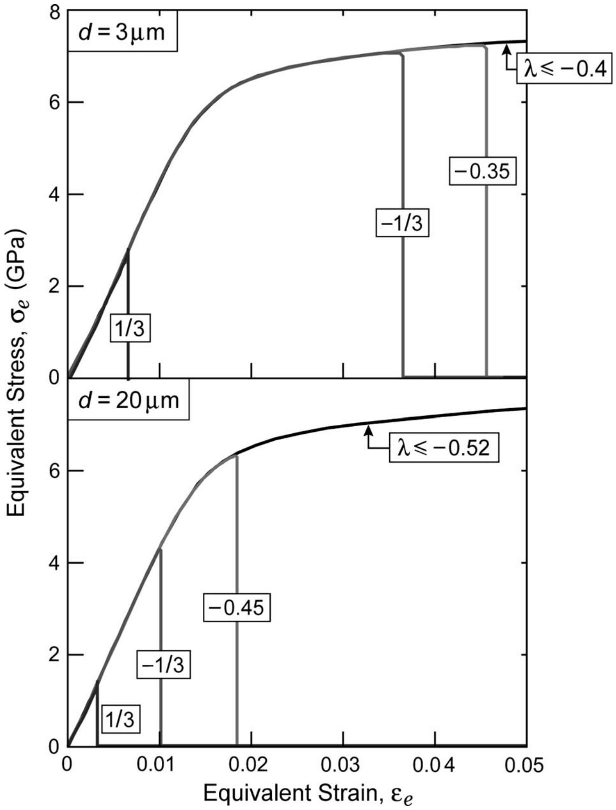

Fig. 13 Predictions of the trend in von Mises stress with effective strain for the (*a*) $d=3$ μm and (*b*) $d=20$ μm alumina. Results are shown for selected stress triaxialities λ for an applied strain rate $\dot{\varepsilon}_e=100$ s^{-1} and yield strength.

$-1/3$), the strengths are microcrack governed. In such cases, the material with the finer grains is stronger and some plasticity precedes failure, even under uniaxial compression. The occurrence of plastic strain has not been reported experimentally because of the extreme difficulty in the conduct of uniaxial compression experiments [18,19]. The closest experimental affirmation is that associated with indentation, as elaborated in Ref. [11]. At high triaxialities ($\lambda \leq -0.45$ and $-1/3$, respectively), plasticity is the dominant mechanism at both grain sizes, rendering identical responses.

5 Details of the Coefficients. Functions A, B, C, and E in the DE model are strongly dependent on the damage and friction coefficient μ, as detailed below. Readers are referred to Ref. [10] for detailed derivations. Here we list the formulas for the sake of completeness. Functions A and B are given as

$$A \equiv c_1(c_2A_3 - c_2A_1 + c_3) \tag{A8a}$$

and

$$B \equiv \frac{c_1}{\sqrt{3}}(c_2A_3 + c_2A_1 + c_3) \tag{A8b}$$

respectively, where

$$c_1 = \frac{2^{3/4}}{\pi^2\left[\left(\frac{D}{D_0}\right)^{1/3} - 1 + \beta\sqrt{2}\right]^{3/2}} \tag{A9a}$$

$$c_2 = 1 + 2\left[\left(\frac{D}{D_0}\right)^{1/3} - 1\right]^2\left(\frac{D_0^{2/3}}{1 - D^{2/3}}\right) \tag{A9b}$$

and

$$c_3 = \pi^2\left[\left(\frac{D}{D_0}\right)^{1/3} - 1\right]^2 \tag{A9c}$$

while

$$A_1 = \pi\sqrt{\frac{\beta}{3}}[(1+\mu^2)^{1/2} - \mu] \tag{A10a}$$

$$A_3 = A_1\left\{\frac{(1+\mu^2)^{1/2} + \mu}{(1+\mu^2)^{1/2} - \mu}\right\} \tag{A10b}$$

The functions C and E are obtained by matching the elastic strains across the boundaries of regimes II and III and dictate that

$$C \equiv A + \gamma\sqrt{2^{1/2}\left(\frac{D}{D_0}\right)^{1/3}} \tag{A11}$$

while

$$E^2 = \frac{B^2C^2}{C^2 - A^2} \tag{A12}$$

References

[1] Rajendran, A. M., and Grove, D. J., 1996, "Modeling the Shock Response of Silicon Carbide, Boron Carbide and Titanium Diboride," Int. J. Impact Eng., **18**, pp. 611–631.
[2] Camacho, G. T., and Ortiz, M., 1996, "Computational Modeling of Impact Damage in Brittle Materials," Int. J. Solids Struct., **33**, pp. 2899–2938.
[3] Hazell, P. J., and Iremonger, M. J., 1997, "Crack Softening Damage Model for Ceramic Impact and Its Application Within a Hydrocode," J. Appl. Phys., **82**, pp. 1088–1092.
[4] Espinosa, H. D., Zavattieri, P. D., and Dwivedi, S. K., 1998, "A Finite Deformation Continuum/Discrete Model for the Description of Fragmentation and Damage in Brittle Materials," J. Mech. Phys. Solids, **46**, pp. 1909–1942.
[5] Johnson, G. R., and Holmquist, T. J., 1999, "Response of Boron Carbide Subjected to Large Strains, High Strain Rates, and High Pressures," J. Appl. Phys., **85**, pp. 8060–8073.
[6] Simha, C. H. M., Bless, S. J., and Bedford, A., 2002, "Computational Modeling of the Penetration Response of a High-Purity Ceramic," Int. J. Impact Eng., **27**, pp. 65–861.
[7] Drucker, D. C., and Prager, W., 1952, "Soil Mechanics and Plastic Analysis or Limit Design," Q. Appl. Math., **10**, pp. 157–165.
[8] Johnson, G. R., and Cook, W. H., 1985, "Fracture Characteristics of Three Metals Subjected to Various Strains, Strain Rates Temperatures and Pressures," Eng. Fract. Mech., **21**, pp. 31–48.
[9] Templeton, D. W., Holmquist, T. J., Meyer, H. W., Grove, D. J., and Leavy, B., 2001, "A Comparison of Ceramic Material Models," *Proceedings of the Ceramic Armor by Design Symposium*, Pacific Rim IV International Conference on Advanced Glass and Ceramics, Wailea, Maui, HI, pp. 299–308.
[10] Deshpande, V. S., and Evans, A. G., 2008, "Inelastic Deformation and Energy Dissipation in Ceramics: A Mechanics-Based Dynamic Constitutive Model," J. Mech. Phys. Solids, **56**, pp. 3077–3100.
[11] Wei, Z., Deshpande, V. S., and Evans, A. G., 2008, "Mechanisms and Mechanics Governing the Indentation of Polycrystalline Alumina," J. Am. Ceram. Soc., **91**, pp. 2987–2996.
[12] Guiberteau, F., Padture, N. P., and Lawn, B. R., 1994, "Effect of Grain Size on Hertzian Contact Damage in Alumina," J. Am. Ceram. Soc., **77**, pp. 1825–1831.
[13] Krell, A., and Strassburger, E., 2001, "High Purity Sub-Micron α-Al_2O_3 Armor Ceramics: Design, Manufacture and Ballistic Performance," *Proceedings of the Ceramic Armor by Design Symposium*, Pacific Rim IV International Conference on Advanced Glass and Ceramics, Wailea, Maui, HI, pp. 403–412.
[14] James, B., 1995 "The Influence of the Material Properties of Alumina on Ballistic Performance," 15th International Symposium on Ballistics, Jerusalem, Israel, pp. 3–10,.
[15] Ashby, M. F., and Sammis, C. F., 1990, "The Damage Mechanics of Brittle Solids in Compression," PAGEOPH, **133**, pp. 489–521.
[16] Frost, H. J., and Ashby, M. F., 1982, *Deformation-Mechanism Maps*, Pergamon, Oxford, UK.
[17] Evans, A. G., 1978, "Microfracture From Thermal Expansion Anisotropy," Acta Metall., **26**, pp. 1845–1853.
[18] Adams, M., and Sines, G., 1976, "Determination of Biaxial Compressive Strength of a Sintered Alumina Ceramic," J. Am. Ceram. Soc., **59**, pp. 300–304.
[19] Lagerlof, K. P. D., Heuer, A. H., Castaing, J., Riviere, J. P., and Mitchell, T. E., 1994, "Slip and Twining in Sapphire," J. Am. Ceram. Soc., **77**, pp. 385–397.

Integrated Experimental, Atomistic, and Microstructurally Based Finite Element Investigation of the Dynamic Compressive Behavior of 2139 Aluminum

K. Elkhodary
Department of Mechanical and Aerospace Engineering,
North Carolina State University,
2412 Broughton Hall,
Box 7910,
Raleigh, NC 27695-7910

Lipeng Sun

Douglas L. Irving

Donald W. Brenner

Department of Materials Science and Engineering,
North Carolina State University,
Raleigh,
NC 27587-7907

G. Ravichandran
Graduate Aeronautical Laboratories,
California Institute of Technology, Aeronautics and Mechanical Engineering,
Mail Stop 105-50,
Pasadena, CA 91125

M. A. Zikry
Department of Mechanical and Aerospace Engineering,
North Carolina State University,
2412 Broughton Hall,
Box 7910,
Raleigh, NC 27695-7910

The objective of this study was to identify the microstructural mechanisms related to the high strength and ductile behavior of 2139-Al, and how dynamic conditions would affect the overall behavior of this alloy. Three interrelated approaches, which span a spectrum of spatial and temporal scales, were used: (i) The mechanical response was obtained using the split Hopkinson pressure bar, for strain-rates ranging from 1.0×10^{-3} *s to* 1.0×10^{4} s^{-1}*. (ii) First principles density functional theory calculations were undertaken to characterize the structure of the interface and to better understand the role played by Ag in promoting the formation of the* Ω *phase for several* Ω*-Al interface structures. (iii) A specialized microstructurally based finite element analysis and a dislocation-density based multiple-slip formulation that accounts for an explicit crystallographic and morphological representation of* Ω *and* θ' *precipitates and their rational orientation relations were conducted. The predictions from the microstructural finite element model indicated that the precipitates continue to harden and also act as physical barriers that impede the matrix from forming large connected zones of intense plastic strain. As the microstructural FE predictions indicated, and consistent with the experimental observations, the combined effects of* θ' *and* Ω*, acting on different crystallographic orientations, enhance the strength and ductility, and reduce the susceptibility of 2139-Al to shear strain localization due to dynamic compressive loads.* [DOI: 10.1115/1.3129769]

1 Introduction

High strength Al–Cu–Mg alloys, such as 2024-Al and 2048-Al, were widely used in applications that require high fracture toughness and crack propagation resistance, such as aircraft structures, automotive applications, armored vehicles, and electronic packaging devices. These alloys do not generally perform well at high temperatures. Therefore, heat resistant alloys, such as 2219-Al and 2618-Al, were used in applications that require high specific strength and high temperature capability. These heat resistant Al–Cu–Mg alloys, however, have limited fracture strength and damage tolerance [1].

The addition of small amounts of Ag to Al–Cu–Mg alloys with high Cu to Mg ratios can significantly improve the age hardening response by the nucleation of thermally stable, platelike Ω precipitates on {111} planes in the aluminum matrix [2]. Moreover, Al–Cu–Mg–Ag alloys have less grain boundary (GB) precipitation, and therefore retain most of their toughness after age hardening, and were less susceptible to intergranular fracture [3,4].

Therefore, Al–Cu–Mg–Ag alloys can potentially have relatively high strength, temperature resistance, toughness, and damage tolerance. Specifically, the Al–Cu–Mg–Ag alloy 2139-T8 developed by Cho and Bes [5] showed, after the addition of Mn for dispersoid formation, significantly improved fatigue life and fracture toughness in comparison to currently used alloys in the aerospace industry. Moreover, the ballistic performance of 2139-Al was also shown to be potentially superior to that of Al-2519, which is used in armored vehicles [5].

The potential use of Al–Cu–Mg–Ag alloys for different applications was therefore predicated on understanding, identifying, and optimizing the material mechanisms and behavior related to increased strength and toughness. If these alloys were to be tailored for a desired application, optimal trade-offs between the competing requirements of strength and toughness have to be identified and controlled. Hence, a detailed understanding of the microstructural constituents in 2139-Al and their influence on the mechanical behavior is needed. Specifically, it has to be understood why the addition of Ag was favorable to the formation of Ω precipitates, how Ω and θ' precipitates affect toughening and strengthening behavior at different scales in terms of microstructural characteristics, such as crystal orientation and dislocation-density interactions at matrix-precipitate interfaces. A comprehensive experimental-cum-modeling overview of these issues was lacking, especially for high strain-rate modes and regimes.

Hence, the objective of this study was to identify the microstructural mechanisms related to the high strength and ductile behavior of 2139-Al, and how dynamic conditions would affect the overall response of this alloy. Hence, three interrelated approaches were used: (i) The mechanical response (stress-strain) behavior was obtained using the split Hopkinson (Kolsky) pressure bar, for

Contributed by the Applied Mechanics Division of ASME for publication in the Journal of Applied Mechanism. Manuscript received June 5, 2008; final manuscript received December 29, 2008; published online June 15, 2009. Review conducted by Ashkan Vaziri.

strain-rates ranging from 1.0×10^{-3} s to 1.0×10^{4} s^{-1}. (ii) First principles density functional theory calculations were conducted to characterize the structure of the interface and to better understand the role played by Ag in promoting the formation of the Ω phase for several Ω-Al interface structures. (iii) A specialized microstructurally based finite element (FE) analysis and dislocation-density based multiple-slip formulation that accounts for an explicit representation of precipitates and their rational orientation relations was conducted. This microstructural formulation accounted for precipitate shape, aspect ratio, volume fraction, crystal structure, and the different slip systems and orientations associated with the alloy matrix and precipitates. The effects of stress and plastic slip accumulation at precipitate interfaces, GBs, grain interiors, and dislocation-density evolution at the matrix-precipitate interfaces were investigated. This integrated approach provided insights that are difficult, if not impossible to obtain, if only an experimental or a computational approach was used.

This paper is organized as follows: An overview of the experimental method was presented in Sec. 1, the first principles results are given in Sec. 2, an outline of the microstructural approach and specialized FE approach are given in Sec. 3, the results are discussed in Sec. 4, and a summary of the salient conclusions are given in Sec. 5.

2 High Strain-Rate Experiments

The high strain-rate behavior of metals and alloys was widely recognized to play an important role in several technologies including manufacturing processes, such as rolling, forming, and high-speed machining, as well as in ballistic failure, dynamic crack growth, and shear banding. Accurate computational modeling of these processes requires the knowledge of material behavior at large strains over a wide range of strain rates. Relevant constitutive data were also essential for validating and developing multiscale material models [6,7]. The validation of such models requires robust experimental measurements that can be used to aid in the refinement of these models aimed at bridging length scales in high strain-rate deformation of metals. The dynamic nature of the above mentioned processes motivated the study of high-strain rate deformations.

In this section a description of the large strain mechanical response of 2139-Al over strain rates ranging from $\dot{\varepsilon}\approx 10^{-3}-10^{4}$ s^{-1} is presented. The material of this study was supplied as rolled plates from Alcan Rolled Products (Ravenswood, WV) and then machined as cylinders.

Quasistatic testing was carried out on a computer controlled MTS servohydraulic machine, operated under displacement control. The machine's stiffness was taken into account when producing stress-strain data. High-rate constitutive behavior was investigated using a 19 mm diameter Kolsky (split Hopkinson) pressure bar [8], made of C300 maraging steel. The signal processing accounted for wave dispersion according to the algorithm of Lifshitz and Leber [9]. Strain-rate jump tests were carried out using specially designed 30 cm long cylindrical projectiles. Two cylindrical impactors were used. The geometry of the first had a length of 15 cm where the diameter is constant at 19 mm, and for the remainder of the 30 cm length, the diameter was stepwise reduced from 19 mm to 12.7 mm. The second impactor also had a constant diameter of 19 mm along the first 15 cm of length, and for the remainder of the impactor length, the diameter was also stepwise reduced from 19 mm to 9.61 mm. The specimens were cylindrical, with 6 mm in diameter and 6 mm in length.

Typical stress-strain curves obtained over a wide range of strain rates are shown in Fig. 1. At quasistatic strain rates ($\sim 10^{-3}$ s^{-1}), the material exhibited considerable hardening; it deformed to large equivalent strains of up to 10% and had a strength of approximately 800 MPa, which is significantly higher than most aluminum alloys. As the strain rate was increased to 8100/s, the material exhibited significant ductility of up to 80%. There was slight stress softening, but as seen from Fig. 1, the strengths were only slightly lower than those observed in the quasistatic regime. The strain-hardening behavior did not seem to be highly rate dependent. The stress-strain response softened in the dynamic regime at true strains below 10%. The flow stress at $\varepsilon_{\text{true}}=0.06$ is plotted as a function of strain rate in Fig. 2. The material exhibited considerable rate sensitivity, particularly at strain rates beyond 10^3 s^{-1}. The highest strain rate achieved was approximately 10^4 s^{-1}, a strain rate that was generally not achievable in a split Hopkinson (Kolsky) pressure bar using cylindrical specimens. These results were an indication of 2139-Al's high strength and significant ductility over a span of different strain rates. Atomistic and microstructurally based FEM modelings were used to further understand the underlying mechanisms that affect this response.

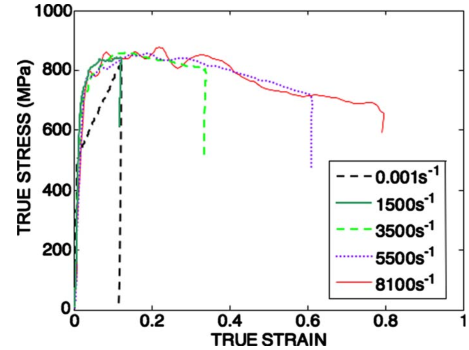

Fig. 1 True-stress true-strain curves for 2139-Al under varied loading rates. The quasistatic stress-strain curve, obtained from the MTS servohydraulic machine under displacement control, shows considerable hardening. The high strain-rate curves, obtained from the split Hopkinson pressure bar, show extensive ductility (up to 80%) and slight stress softening of the 2139-Al alloy.

3 Atomistic Modeling of Omega Precipitates

To characterize the structure of the interface and to better understand the role played by Ag in promoting the formation of the Ω phase, which could be one of the main microstructural characteristics affecting the desirable behavior of 2139-Al, first principles density functional theory calculations were carried out on several Ω-Al interface structures both with and without Ag and Mg. The calculations used the Vienna ab initio simulation package (VASP) [10,11], and were carried out within the generalized gradient approximation using the PW91 parameterization [12,13]. Valence-core electron interactions were treated using ultrasoft pseudopotentials [14], and the valence electron wave functions were expanded in plane wave basis sets with a 300 eV energy cutoff using the Monkhorst–Pack method for special k-point sam-

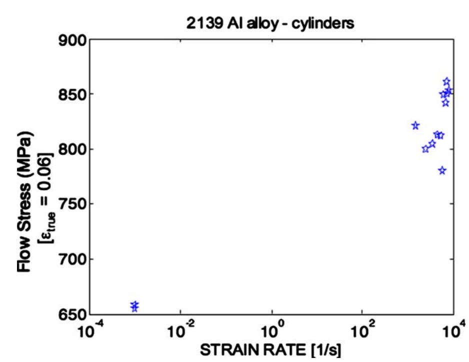

Fig. 2 Strain-rate sensitivity of flow stress in 2139-Al at an equivalent strain of 0.06 exhibiting considerable material rate sensitivity, particularly at strain rates beyond 10^3 s^{-1}

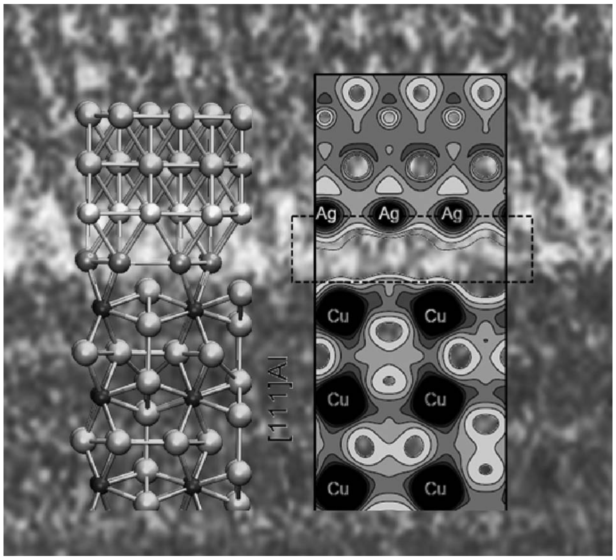

Fig. 3 Superposition of the atomic arrangement (left) and the electron density (right) from the first principles calculations over the experimental *Z* contrast HRTEM image from Ref. [1] of the Al-Ω interface

pling for the Brillouin zone integration [15]. Three-dimensional periodic boundary conditions were applied, and both the cell volume and atomic positions within the cell were relaxed.

A small supercell of 76 atoms was used to characterize the pure α-Al/Ω interfacial structure. Three different types of chemical bonds, Al–Al, Al–Cu, or Al–Cu plus Al–Al may be formed across the α-Al/Ω interface depending on the termination of the (001) Ω planes. Several relative displacements of the Ω structure, with respect to the Al lattice, were used as initial structures within these three termination types followed by energy minimization. The most stable structure of the α-Al/Ω interface was found to be connected by Al–Al bonds with a hexagonal Al lattice on the surface of the Ω phase, sitting on the vacant hollow sites of the Al {111} matrix plane.

Starting with this interface structure, heats of formation were calculated for an extensive set of trial structures in which Mg and/or Ag atoms were substituted for the interfacial Al. A larger 152 atom supercell was used for these calculations to reduce size effects and supercell image interactions. The results of these calculations indicate that when only Mg is introduced, the tendency for segregation to the interface was minimal and the strength of the interface was not enhanced. In contrast, Ag has a strong tendency to segregate to a dense substitutional layer that was one layer away from the interface into the Al lattice. This occurs because Ag and Al form relatively strong bonds, and there was a reduced planar density of Al atoms in the Ω phase to which the Ag can bond. However, the strongest bonding, and hence the greatest stabilization of the interface, occurs when the Mg substitutes for the Al layer closest to Ω phase and the Ag substitutes for the Al in the next layer into the Al, hence forming an interfacial bilayer like that observed experimentally. To illustrate the relationship of structure to experiment, shown in Fig. 3 is a superposition of the atomic arrangement (left) and the electron density (right) from the first principle calculations over the experimental *Z* contrast high resolution transmission electron microscopy (HRTEM) image from Ref. [16] of the Al-Ω interface. Our theoretically determined structure allows strong Ag–Al, Mg–Cu, and Ag–Mg bonding while excluding the weaker Ag–Cu bonds. The analysis of the charge density at the interface shows a net transfer of electrons to the Ω and Al matrix from the interface region that contributes to interface stabilization. Hence, the first principle modeling provides both a viable atom-resolved structure consistent with experiment and provides insight into the driving force for the stability of this interface in terms of bonding strengths and electron charge transfer.

4 Microstructural Finite Element Model

4.1 Crystal Plasticity Formulation. Constitutive formulations for the rate-dependent multiple-slip crystal plasticity, which are coupled to the evolutionary equations for the dislocation densities, were used. For a detailed presentation, see Refs. [17–19].

The velocity gradient was decomposed into a symmetric deformation rate tensor D_{ij} and an antisymmetric spin tensor W_{ij}. D_{ij} and W_{ij} were then additively decomposed into elastic and plastic components as

$$D_{ij} = D_{ij}^{*} + D_{ij}^{p} \tag{1a}$$

$$W_{ij} = W_{ij}^{*} + W_{ij}^{p} \tag{1b}$$

The inelastic parts are defined in terms of the crystallographic slip rates as

$$D_{ij}^{p} = P_{ij}^{(\alpha)} \dot{\gamma}^{(\alpha)} \tag{2a}$$

$$W_{ij}^{p} = \omega_{ij}^{(\alpha)} \dot{\gamma}^{(\alpha)} \tag{2b}$$

where α is summed over all slip systems, and $P_{ij}^{(\alpha)}$ and $\omega_{ij}^{(\alpha)}$ are the symmetric and antisymmetric parts of the Schmid tensor in the current configuration, respectively.

The rate-dependent constitutive description on each slip system can be characterized by a power law relation, for strain rates below a critical value of $\dot{\gamma}_{\mathrm{critical}}$ as

$$\dot{\gamma}^{(\alpha)} = \dot{\gamma}_{\mathrm{ref}}^{(\alpha)} \left[\frac{\tau^{(\alpha)}}{\tau_{\mathrm{ref}}^{(\alpha)}} \right] \left[\frac{|\tau^{(\alpha)}|}{\tau_{\mathrm{ref}}^{(\alpha)}} \right]^{1/m-1} \tag{3}$$

where $\dot{\gamma}_{\mathrm{ref}}^{(\alpha)}$ is the reference shear strain rate, which corresponds to a reference shear stress $\tau_{\mathrm{ref}}^{(\alpha)}$, and m is the rate sensitivity parameter. Above the critical strain rate $\dot{\gamma}_{\mathrm{critical}}$, where the phonon drag is assumed to dominate, m is taken as 1 and $\dot{\gamma}_{\mathrm{ref}}^{(\alpha)} = \dot{\gamma}_{\mathrm{critical}}$. Mughrabi [20] stressed that what was used here was a modification of widely used classical forms that relate the reference stress to a square-root dependence on the dislocation density (ρ_{im}) as

$$\tau_{\mathrm{ref}}^{(\alpha)} = \left(\tau_{y}^{(\alpha)} + G \sum_{\rho=1}^{\mathrm{nss}} a_{\rho} B^{(\rho)} \sqrt{\rho_{im}^{(\rho)}} \right) \left(\frac{T}{T_0} \right)^{-\xi} \tag{4}$$

where $\tau_{y}^{(\alpha)}$ is the static yield stress on slip system (α), G is the shear modulus, nss is the number of slip systems, $B^{(\rho)}$ is the magnitude of the Burgers vector, and the coefficients a_{ρ} are the slip-system interaction coefficients. T is the temperature, T_0 is the reference temperature, and ξ is the thermal softening exponent.

For a given deformed state of the material, the dislocation structure of total dislocation density $\rho^{(\alpha)}$ is additively decomposed into a mobile and an immobile dislocation density $\rho_{m}^{(\alpha)}$ and $\rho_{im}^{(\alpha)}$, respectively, as

$$\rho^{(\alpha)} = \rho_{m}^{(\alpha)} + \rho_{im}^{(\alpha)} \tag{5}$$

It is assumed that during an increment of strain, there ensues a change in the dislocation structure. The balance between generation and annihilation of dislocation densities as a function of strain is thus taken as a basis for the following equations that describe the evolution of mobile and immobile dislocation densities:

$$\frac{d\rho_{m}^{(\alpha)}}{dt} = |\dot{\gamma}^{(\alpha)}| \left[\frac{g_{\mathrm{sour}}}{B^{(\alpha)} B^{(\alpha)}} \left(\frac{\rho_{im}^{(\alpha)}}{\rho_{m}^{(\alpha)}} \right) - \frac{g_{\mathrm{minter}}}{B^{(\alpha)} B^{(\alpha)}} \exp\left(- \frac{\Delta H}{kT} \right) - \frac{g_{\mathrm{immob}}}{B^{(\alpha)}} \sqrt{\rho_{im}^{(\alpha)}} \right] \tag{6}$$

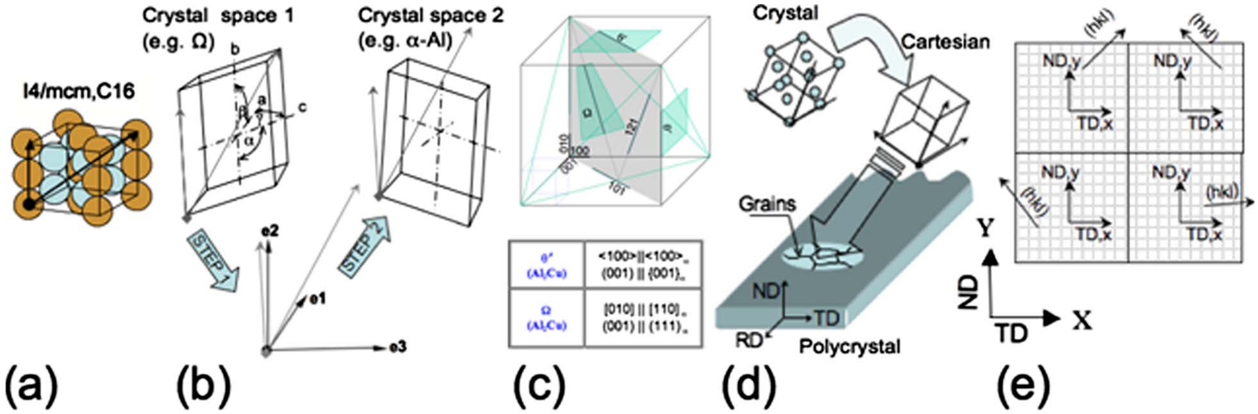

$$V_j^{elem} = T_{Poly}^{elem} T_{cart}^{Poly} M_{\alpha}^{cart} T_{\alpha*}^{\alpha} M_{cart}^{\alpha*} M_{\Omega}^{cart} V_j^{\Omega} \quad \text{(transforming } V_j^{\Omega} \text{ from the } \Omega \text{ crystal to element axes)}$$

$$V_j^{elem} = T_{Poly}^{elem} T_{cart}^{Poly} M_{\alpha}^{cart} V_j^{\alpha} \quad \text{(transforming } V_j^{\alpha} \text{ from the matrix crystal to element axes)}$$

Fig. 4 Illustration of slip vector (V_j) transformation sequence ((*a*)–(*e*)) to the element axes. (*a*) The slip system is identified in fractional coordinates. (*b*) The slip system vectors are transformed from precipitate space to matrix space. (*c*) The precipitate vectors are aligned with the matrix vectors in accordance with the orientation relationships. (*d*) The oriented slip vectors are mapped to the axes of the polycrystalline aggregate. (*e*) The vectors are mapped from the polycrystalline aggregate to the element axes.

$$\frac{d\rho_{im}^{(\alpha)}}{dt} = |\dot{\gamma}^{(\alpha)}| \left[\frac{g_{\text{minter}}}{B^{(\alpha)}B^{(\alpha)}} \exp\left(-\frac{\Delta H}{kT}\right) + \frac{g_{\text{immob}}}{B^{(\alpha)}} \sqrt{\rho_{im}^{(\alpha)}} - g_{\text{recov}} \exp\left(\frac{\Delta H}{kT}\right) \rho_{im}^{(\alpha)} \right] \quad (7)$$

where g_{sour}, g_{minter}, g_{recov}, and g_{immob} are coefficients corresponding to the generation of mobile dislocation densities, trapping of mobile dislocations by dislocation-dislocation interactions, rearrangement and annihilation of immobile dislocations by recovery, and immobilization of mobile dislocations, respectively. For a determination of these coefficients, see Ref. [21]. ΔH is the enthalpy of activation of plastic deformation, and k is the Boltzmann constant.

4.2 Precipitate-Crystal Representation. As seen from the Sec. 4.1, the crystal plasticity constitutive formulation requires the identification of the specific crystal structures, slip systems, and material properties. In Al–Cu alloys, the θ phase (Al_2Cu) has an $I4/mcm$ structure with $a=0.607$ nm and $c=0.487$ nm [22]. The θ' phase has a tetragonal structure $I\bar{4}m2$, with $a=0.404$ nm and $c=0.58$ nm [23]. The Ω phase (Al_2Cu) was proposed as monoclinic [24,25], hexagonal [26], and tetragonal distorted θ phases [27]. The accepted structure for the Ω phase was the orthorhombic structure ($Fmmm$) proposed by Knowles and Stobbs [28], with $a=0.496$ nm, $b=0.858$ nm, and $c=0.848$ nm. In this study, the Ω and θ' phases were modeled as $I4/mcm$ [27,29], using 12 slip systems corresponding to the shortest two Burgers vectors in the θ crystals ($C16$ structure) [30,31], and with the concomitant rational orientation relations to the matrix [22].

4.3 Orientation of Crystal Lattice With Respect to Element Axes. First, the Miller indices of planes and directions that define orientation relations between precipitates and matrix were defined. The following procedure was then used to crystallographically orient slip normals and directions within precipitates and the matrix with respect to the global axes, while observing matrix-precipitate orientation relations. A schematic representation of this procedure is shown in Fig. 4 along with the entire sequence of transformation matrices.

The slip directions and planes for the matrix and precipitates are defined in fractional coordinates. Since the precipitates are noncubic, the vectors defining slip-plane normals are not equivalent to their miller indices, and normals may be obtained by a reciprocal lattice construct. The vectors are then mapped from the precipitate space to the matrix space. This is achieved by the transformation sequence $[M_{\text{Cart}}^{\alpha*}][M_{\Omega}^{\text{Cart}}]$, where $[M_{\Omega}^{\text{Cart}}]$ transforms a vector in the precipitate (e.g., Ω) to a vector in a Cartesian frame, and $[M_{\text{Cart}}^{\alpha*}]$ takes the transformed vector from the Cartesian frame to the matrix crystal. The form of $[\boldsymbol{M}]$ is adapted from Ref. [32]. The vectors are then aligned according to the orientation relations by matrix $[T_{\alpha*}^{\alpha}]$, followed by another transformation $[M_{\alpha}^{\text{Cart}}]$, taking vectors from the matrix space to a Cartesian space if necessary (i.e., matrix crystal is noncubic). Random Euler angles are then assigned to every grain to align crystal lattices, with respect to the polycrystalline aggregate axes. This transformation, defined as $[T_{\text{Cart}}^{\text{poly}}]$, is adapted from Ref. [33]. The polycrystalline aggregate axes are then aligned with the corotational frame of the element (initially identical to the drawing plane) using $[T_{\text{poly}}^{\text{elem}}]$.

4.4 Geometry of the Precipitate Crystals. A large aspect ratio ($L/t=24$) was chosen to be consistent with observed values in quaternary alloys [34]. Further, to capture a microstructural length scale consistent with precipitates, a thickness of 500 nm was used. Finally, a total volume fraction of 3% was assumed for the precipitates.

4.5 2D Finite Element Model. The multiple-slip dislocation-density based crystal plasticity formulation was implemented within the framework of the explicit dynamic FE program ABAQUS/EXPLICIT to investigate the behavior of a polycrystalline aggregate representative of 2139-Al under large compressive inelastic strains and strain rates. An 18 grain aggregate with dimensions of 100×100 μm^2 (Fig. 5) was used, where the grain size was of a maximum of 1000 μm^2. Random Euler angles were assigned for relative grain misorientations that did not exceed 10 deg. The Ω and θ' precipitates were placed near the centroid of each grain based on the crystallographic formulations as outlined earlier (i.e., having aligned their thickness and long directions in accordance with their rational orientation relationships, with re-

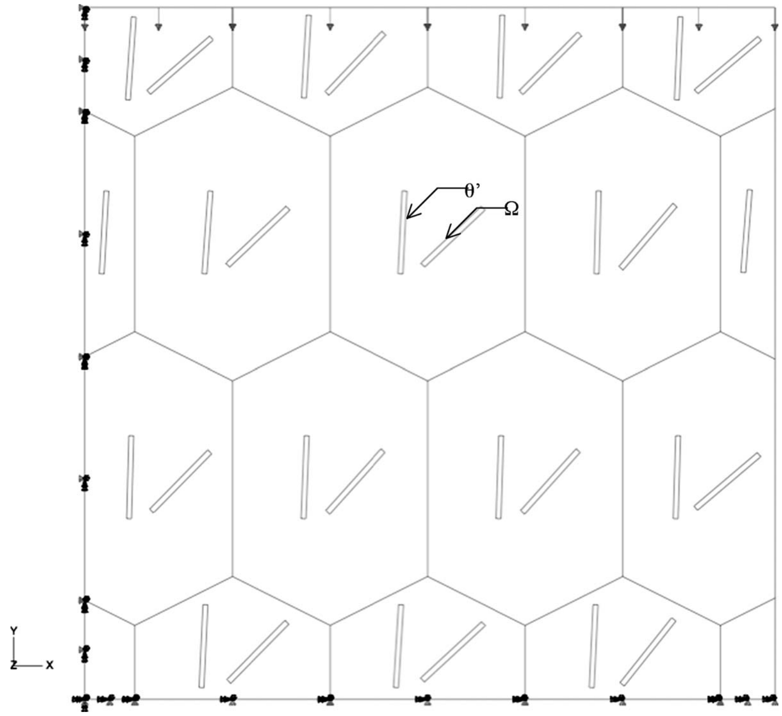

Fig. 5 An 18 grain aggregate with θ' and Ω precipitates, subject to an applied strain rate of 10^4 s^{-1} on the upper surface and with symmetry boundary conditions at the left and bottom edges

spect to each grain, and then projecting these directions in 2D). The material properties used in this study are summarized in Table 1 and accompanied by their respective references.

The aggregate was subjected to different nominal axial strain rates ranging from 10^{-3} s^{-1} to 10^4 s^{-1} by applying a velocity along the normal direction. Symmetry boundary conditions were applied for a 2D plane-strain deformation (Fig. 5) A convergent mesh of 6500 elements was used. Four-node bilinear plane-strain quadrilaterals, with one-point integration and enhanced assumed-strain hourglass control, were used. For representative behavior, the results for an applied strain rate of 10^4 s^{-1} will be presented in this paper.

5 Microstructural Finite Element Results

The contours of the accumulated plastic slip were shown in Fig. 6. The maximum accumulated plastic strain is 1.4 with most of the maximum accumulations occurring at the precipitate-matrix inter-

Table 1 Material properties for α-Al, Ω and θ'

Property	Description	Value: Al	Value: Ω, θ'	Reference
E(GPa)	Young's modulus	69	140	[35]
ν	Poisson's ratio	0.34	0.34	
τ_y (MPa)	Static yield stress	35	35	—
ρ (g/cm^3)	Mass density	2.70	4.36	—
Cp (J/kg K)	Specific heat	902	902	[36]
$\Delta H/k$ (K)	Activation enthalpy/Boltzmann constant	2500	3100	[37]
$\dot{\gamma}_{\mathrm{ref}}$(s^{-1})	Reference strain rate	0.001	0.001	[38]
$\dot{\gamma}_{\mathrm{crit}}$(s^{-1})	Critical strain rate	10^4	10^4	
ρ^0_{im}(m^{-2})	Initial immobile dislocation density	10^{12}	10^8	—
ρ^0_{mo}(m^{-2})	Initial mobile dislocation density	10^{10}	10^6	—
T_0 (K)	Reference temperature	293	293	—
m	Strain rate sensitivity	0.02	0.02	[39]
ξ	Thermal softening exponent	0.5	0.5	
χ	Fraction of plastic dissipation to heat	0.9	0.9	
g_{source}	Dislocation source coefficient	2.76×10^{-5}	2.76×10^{-5}	[38]
g_{immob}	Dislocation immobilization coefficient	0.0127	0.0127	
g_{minter}	Mobile dislocation interaction coefficient	5.53	5.53	
g_{recov}	Recovery coefficient	6.69×10^5	6.69×10^5	
a_i	Slip-system interaction coefficient	0.5	0.5	

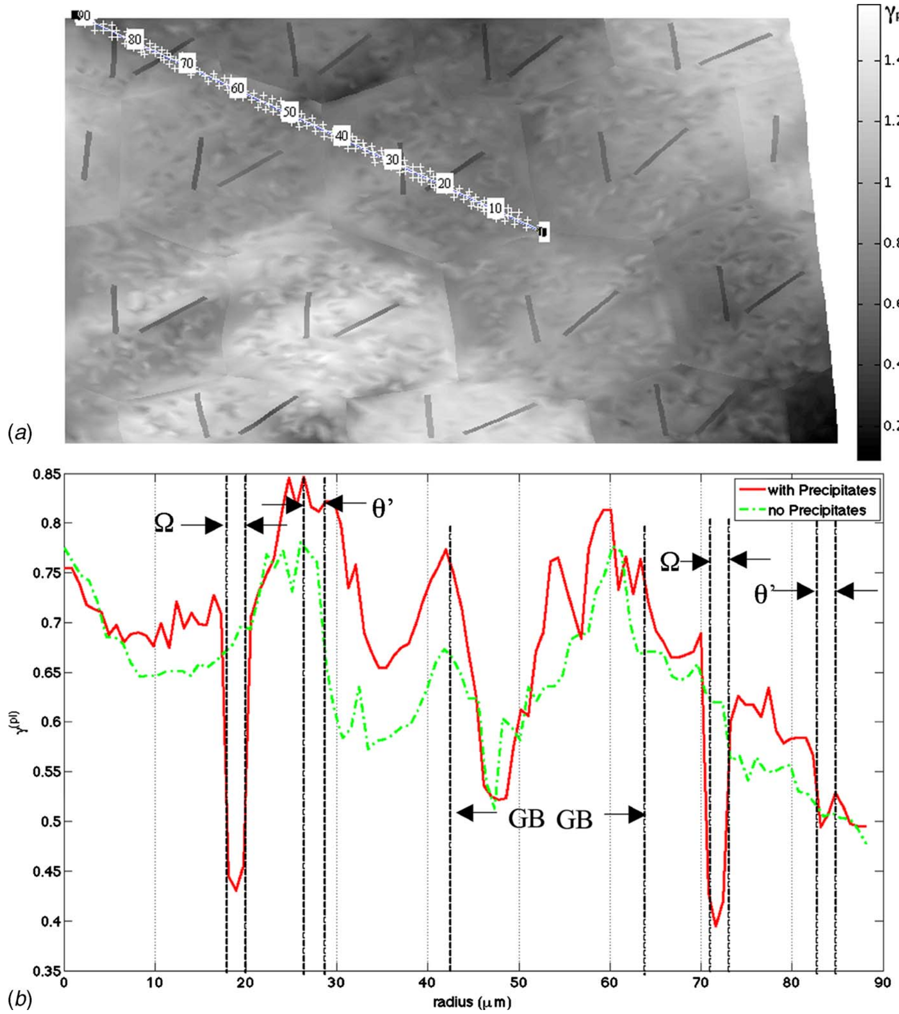

Fig. 6 (*a*) Contour plot of plastic slip at a nominal strain of 25%. (*b*) Plastic slip comparison between 2139-Al and precipitate-free Al along path shown in (*a*).

faces. The curves for the comparison between the precipitate-free aluminum and the 2139-Al indicate that the presence of precipitates has a significant effect on the plastic slip behavior and distribution. Specifically, the precipitates are clearly shear deformable. This is consistent with observations in Refs. [40–42]. The slip within the θ' and Ω precipitates has not resulted in slip concentration as was often observed with shearable particles [42–44]. This could be due to the precipitates continuing to harden and also acting as physical barriers that impede the matrix from forming large connected zones of intense plastic strain. Moreover, the FE model, though constrained in plane strain, showed plastic strain on multiple slip systems in the Ω and θ' precipitates. Therefore, slip in the precipitates was not planar, and shearing did not localize as would otherwise be expected [45].

The corresponding adiabatic temperature changes are shown in Fig. 7. The Ω precipitates along the selected evaluation path have a lesser increase in temperature than the θ' phase or the matrix, which indicates that these precipitates may delay thermal softening of the 2139-Al alloy. This, combined with the diffuse plastic slip accumulation, is another indication of 2139-Al's ductility and lack of susceptibility to shear-strain localization.

The contours in Fig. 8 show the immobile dislocation density corresponding to slip system $(111)[0\bar{1}1]$ in the matrix, which was the most active matrix system, and the immobile dislocation density corresponding to the most active system $(110)[\bar{1}12]$ for the precipitates. The contours indicate that the matrix slip system saturated to 10^{14} m^{-2} over most grains. This saturation actually occurred in most of the grains, at a nominal strain of approximately 12%, which was approximately equivalent to the true strain at which softening was first observed in the experimental stress-strain curves.

It was also seen that the dislocation densities attain maximum values at precipitate-free triple junction points and at precipitate-matrix interfaces. From the curve, it was seen that peaks in the immobile dislocation densities were at the matrix Ω interfaces. This accumulation at the precipitate interfaces further indicates the incompatibility of slip in the surrounding matrix with Ω precipitates, similar to the observations in Refs. [41,42,46] for $\{100\}_\alpha$ and $\{111\}_\alpha$ precipitates. This accumulation, however, does not occur for the θ' precipitates along the selected path. Furthermore, the largest immobile dislocation density for Ω precipitates was at 40% of the value in the matrix and θ', which have both saturated. This was therefore an indication that Ω precipitates can add further strength and ductility through the interrelated mechanism of material hardening and dislocation density generation.

The evolution of the reference shear stress values was shown in Fig. 9. It was clear from the contours that the Ω precipitates generally harden more than the surrounding matrix, and often more than the θ' precipitates. The curves in Fig. 9 show hardening peaks within the Ω precipitate well above those for the θ' precipitates or the matrix for the selected path. Hence, the Ω precipitates

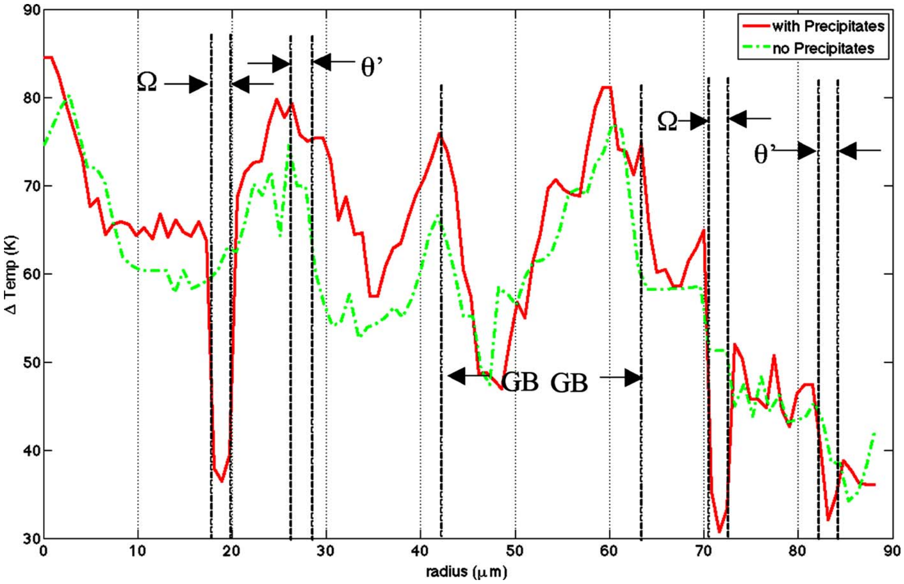

Fig. 7 Adiabatic temperature increase comparison between 2139-Al and precipitate-free Al along a selected path, showing the temperature build up to be the lowest inside the Ω precipitates

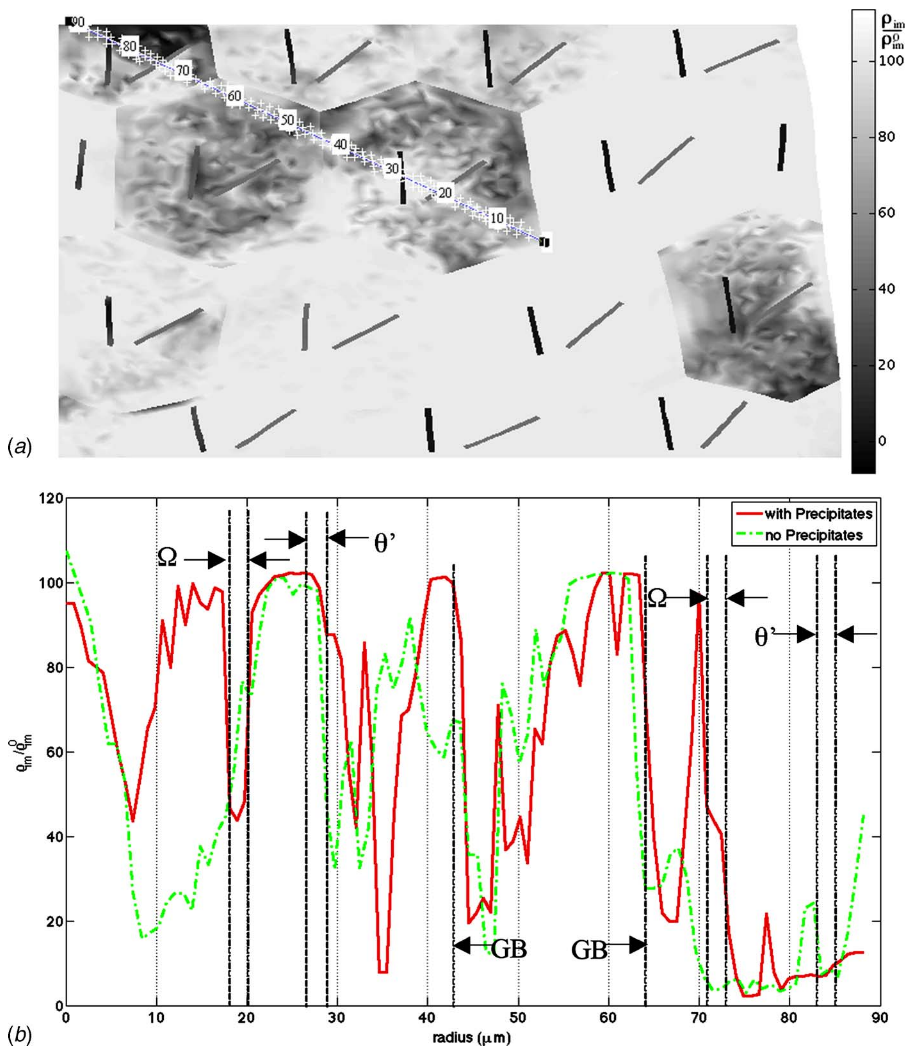

Fig. 8 (*a*) Contour plot of immobile dislocation density normalized by the initial density for $(111)[0\bar{1}\bar{1}]$ slip system in the matrix and $(110)[\bar{1}12]$ in the precipitates at a nominal strain of 25% (i.e., most active slip systems). (*b*) Comparison of dislocation densities for most active slip systems between 2139-Al and precipitate-free Al along path shown in (*a*).

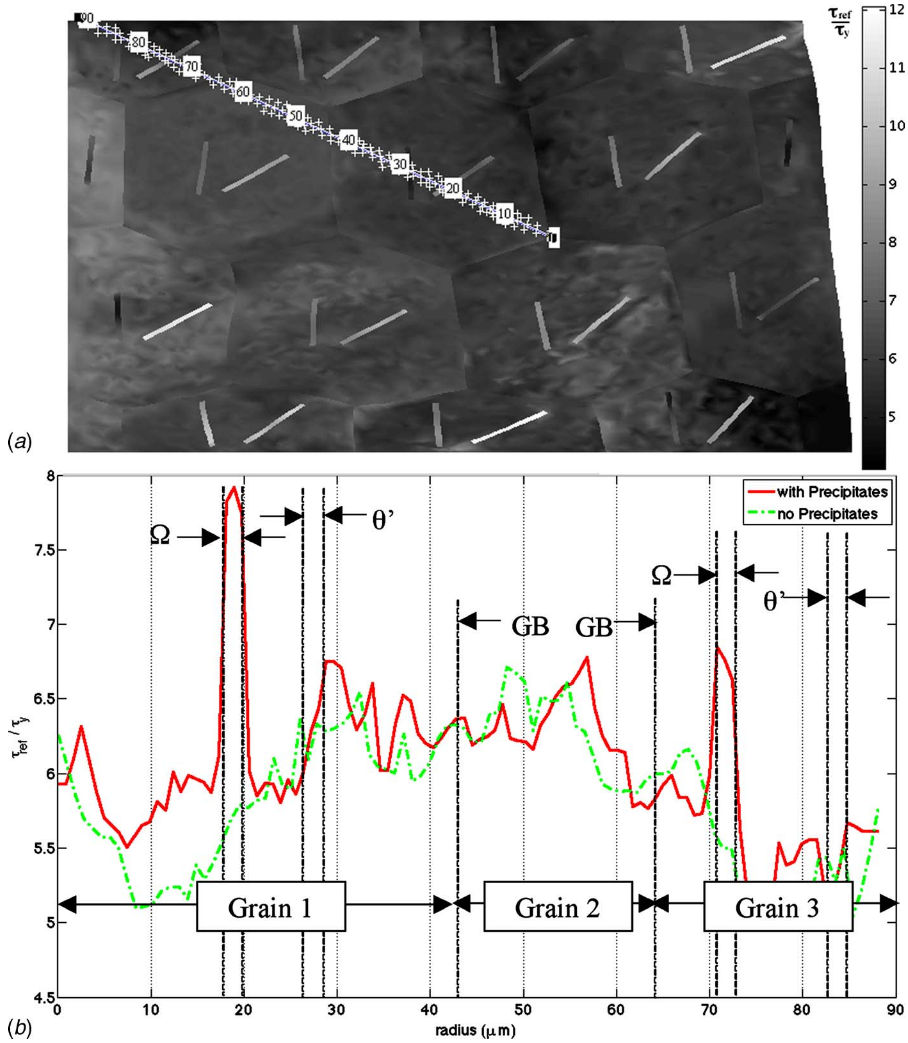

Fig. 9 (*a*) Contour plot of reference shear stress normalized by static yield at a nominal strain of 25%. (*b*) Comparison of reference shear stress (normalized by static yield) between 2139-Al and precipitate-free Al along the path shown in (*a*).

have a marked effect on strengthening the alloy, and it was more pronounced than that of the θ' precipitates. It was clear, however, that different grain orientations would align θ' and Ω differently, with respect to the loading direction, and could thus favor θ' hardening more than Ω. Hence, the effectiveness of precipitate strengthening of the alloy was dependent on the crystallographic orientation of the grains, which governs the relative precipitate orientations with respect to the loading of the aggregate, a dependence that was consistent with the observations and predictions in Refs. [46,47]. The presence, therefore, of both θ' and Ω, acting on different crystallographic orientations in the alloy, could be expected to enhance the strength and strain-hardening response [45] for the various grain orientations in the polycrystalline aggregate.

6 Summary

From the experiments, it was observed that the 2139-Al alloy exhibits considerable hardening at quasistatic strain rates ($\sim 10^{-3}\ s^{-1}$), can be deformed to large equivalent strains, and has a strength of approximately 800 MPa, which was significantly higher than most aluminum alloys. As the strain rate was increased to 8100/s, 2139-Al exhibited significant ductility of up to 80%. There was slight stress softening, but the strengths were only slightly lower than those observed in the quasistatic regime. The stress-strain response softened in the dynamic regime at true strains of approximately 12%. Moreover, 2139-Al exhibits considerable rate sensitivity, particularly at strain rates beyond $10^3\ s^{-1}$. These results are an indication of 2139-Al's high strength, significant ductility, and lack of susceptibility to shear strain localization under compressive strain rates.

First principles calculations, describing the structure of the Ω-Al interface, indicated that the strongest bonding, and hence the greatest stabilization of the interface, occurs when the Mg substitutes for the Al layer closest to Ω phase, and the Ag substitutes for the Al in the next layer into the Al, hence forming an interfacial bilayer like that observed experimentally [16]. The theoretically determined structure allows strong Ag–Al, Mg–Cu and Ag–Mg bonding, while excluding the weaker Ag–Cu bonds. The analysis of the charge density at the interface showed a net transfer of electrons to the Ω and Al matrix from the interface region that contributes to interface stabilization. Hence, the first principles modeling provides both a viable atom-resolved structure consistent with experiment and an insight into the driving force for the stability of the Ω phase in terms of bonding strengths and electron charge transfer.

The predictions from the microstructural finite element model indicated that the precipitates continue to harden, and also act as physical barriers that impede the matrix from forming large connected zones of intense plastic strain. This understanding was predicated on the accurate representation of the crystallography of the precipitates and the matrix. Moreover, the multiplicity of active slip systems resulted in the shearing of the precipitates, and this multiplicity also inhibited shear strain localization. As the predictions indicated, the combined effects of θ' and Ω, acting on different crystallographic orientations, enhance the strength and strain-hardening response of the alloy. The Ω precipitates had lower temperature increases than the matrix and therefore could delay thermal softening. Furthermore, dislocation densities in Ω have not saturated. Hence, Ω had the inherent capacity of increasing strength and ductility to the alloy through the interrelated mechanisms of hardening, and sustained ductility through precipitate shearing.

This integrated experimental and computational framework that spans different spatial and temporal scales provides a detailed understanding of the underlying mechanisms that delineate the high strength, ductility, and lack of susceptibility to shear strain localization of 2139-Al over a spectrum of dynamic compressive strain rates.

Acknowledgment

Support from the U.S. Army Research Office (Grant No. ARO W911 NF-06–1–0472) is gratefully acknowledged.

References

[1] Eschbach, L., Solenthaler, C., Uggowitzer, P. J., and Speidel, M. O., 1999, “Strength and Fracture Toughness of Spray Formed Al-Cu-Mg-Ag Alloys,” Mater. Sci. Technol., **15**(8), pp. 926–932.

[2] Polmear, I. J., and Couper, M. J., 1988, “Design and Development of an Experimental Wrought Aluminium-Alloy for Use at Elevated-Temperatures,” Metall. Trans. A, **19**(4), pp. 1027–1035.

[3] Hono, K., Sano, N., Babu, S. S., Okano, R., and Sakurai, T., 1993, “Atom Probe Study of the Precipitation Process in Al-Cu-Mg-Ag Alloys,” Acta Metall. Mater., **41**(3), pp. 829–838.

[4] Howe, J. M., Basile, D. P., Prabhu, N., and Hatalis, M. K., 1988, “Minimum Detectable Solute Concentration in Atomic-Resolution Transmission Electron-Microscopy,” Acta Crystallogr. A, **44**, pp. 449–461.

[5] Cho, A., and Bes, B., 2006, “Damage Tolerance Capability of an Al-Cu-Mg-Ag Alloy (2139),” Mater. Sci. Forum, **519–521**, pp. 603–608.

[6] Ma, J., Zikry, M., Ashamwi, W., and Brenner, D., 2007, “Hierarchical Modeling of Nanoindentation and Microstructural Evolution of Face-Centered Cubic Gold Aggregates,” J. Mater. Res., **22**(3), pp. 627–643.

[7] Ortiz, M., Cuitino, A. M., Knap, J., and Koslowski, M., 2001, “Mixed Atomistic Continuum Models of Material Behavior: The Art of Transcending Atomistics and Informing Continua,” MRS Bull., **26**(3), pp. 216–221.

[8] Kolsky, H., 1949, “An Investigation of the Mechanical Properties of Materials at Very High Rates of Loading,” Proc. Phys. Soc. London, Sect. B, **62**, pp. 676–700.

[9] Lifshitz, J., and Leber, H., 1994, “Data-Processing in the Split Hopkinson Pressure Bar Tests,” Int. J. Impact Eng., **15**(6), pp. 723–733.

[10] Kresse, G., and Hafner, J., 1993, “Ab Initio Molecular-Dynamics for Liquid-Metals,” Phys. Rev. B, **47**(1), pp. 558–561.

[11] Kresse, G., and Hafner, J., 1994, “Ab-Initio Molecular-Dynamics Simulation of the Liquid-Metal Amorphous-Semiconductor Transition in Germanium,” Phys. Rev. B, **49**(20), pp. 14251–14269.

[12] Perdew, J., Chevary, J. A., and Vosko, S. H., 1992, “Atoms, Molecules, Solids, and Surfaces-Applications of the Generalized Gradient Approximation for Exchange and Correlation,” Phys. Rev. B, **46**(11), pp. 6671–6687.

[13] Vosko, S., Wilk, L., and Nusair, M., 1980, “Accurate Spin-Dependent Electron Liquid Correlation Energies for Local Spin-Density Calculations—A Critical Analysis,” Can. J. Phys., **58**(8), pp. 1200–1211.

[14] Vanderbilt, D., 1990, “Soft Self-Consistent Pseudopotentials in a Generalized Eigenvalue Formalism,” Phys. Rev. B, **41**(11), pp. 7892–7895.

[15] Monkhorst, H. J., and Pack, J. D., 1976, “Special Points for Brillouin-Zone Integrations,” Phys. Rev. B, **13**(12), pp. 5188–5192.

[16] Hutchinson, C. R., Fan, X., Pennycook, S., and Shiflet, G., 2001, “On the Origin of the High Coarsening Resistance of ΩPlates in Al-Cu-Mg-Ag Alloys,” Acta Mater., **49**, pp. 2827–2841.

[17] Orsini, V., and Zikry, M., 2001, “Void Growth and Interaction in Crystalline Materials,” Int. J. Plast., **17**(10), pp. 1393–1417.

[18] Zikry, M. A., and Kao, M., 1996, “Inelastic Microstructural Failure Mechanisms in Crystalline Materials With High Angle Grain Boundaries,” J. Mech. Phys. Solids, **44**(11), pp. 1765–1798.

[19] Ashmawi, W., and Zikry, M., 2002, “Prediction of Grain-Boundary Interfacial Mechanisms in Polycrystalline Materials,” ASME J. Eng. Mater. Technol., **124**(1), pp. 88–96.

[20] Mughrabi, H., 1987, “A Tow Parameter Description of Heterogeneous Dislocation Distributions in Deformed Metal Crystals,” Mater. Sci. Eng., **85**, pp. 15–31.

[21] Kameda, T., and Zikry, M. A., 1998, “Three Dimensional Dislocation-Based Crystalline Constitutive Formulation for Ordered Intermetallics,” Scr. Mater., **38**(4), pp. 631–636.

[22] Wang, S. C., and Starink, M. J., 2005, “Precipitates and Intermetallic Phases in Precipitation Hardening Al-Cu-Mg-(Li) Based Alloys,” Int. Mater. Rev., **50**, pp. 193–215.

[23] Silcock, J., Heal, T. J., and Hardy, H. K., 1955, “The Structural Ageing Characteristics of Ternary Aluminium-Copper Alloys With Cadmium, Indium or Tin,” J. Inst. Met., **84**(1), pp. 23–31.

[24] Auld, J. H., 1972, “Structure of a Metastable Precipitate in an Al-Cu-Mg-Ag Alloy,” Acta Crystallogr., Sect. A: Cryst. Phys., Diffr., Theor. Gen. Crystallogr., **28**, p. S98.

[25] Auld, J. H., 1986, “Structure of Metastable Precipitate in Al-Cu-Mg-Ag Alloys,” Mater. Sci. Technol., **2**(8), pp. 784–787.

[26] Kerry, S., and Scott, V. D., 1984, “Structure and Orientation Relationship of Precipitates Formed in Al-Cu-Mg-Ag Alloys,” Meat Sci., **18**(6), pp. 289–294.

[27] Garg, A., and Howe, J. M., 1991, “Convergent-Bean Electron-Diffraction Analysis of the Omega Phase in an Al-4.0 Cu-0.5 Mg-0.5 Ag Alloy,” Acta Metall. Mater., **39**(8), pp. 1939–1946.

[28] Knowles, K. M., and Stobbs, W. M., 1988, “The Structure of (111) Age-Hardening Precipitates in Al-Cu-Mg-Ag Alloys,” Acta Crystallogr., Sect. B: Struct. Sci., **44**, pp. 207–227.

[29] Ringer, S., and Hono, K., 2000, “Microstructural Evolution and Age Hardening in Aluminium Alloys: Atom Probe Field-Ion Microscopy and Transmission Electron Microscopy Studies,” Mater. Charact., **44**(1–2), pp. 101–131.

[30] Bonnet, R., and Loubradou, M., 2002, “Crystalline Defects in a BCT Single Crystal Obtained by Unidirectional Solidification Along,” Phys. Status Solidi A, **194**(1), pp. 173–191.

[31] Ignat, M., and Durand, F., 1976, “Deformation Lines on Al_2Cu Single Crystals After Creep in Compression,” Scr. Metall., **10**(7), pp. 623–626.

[32] Giacovazzo, C., Monaco, H. L., Artioli, G., Viterbo, D., Ferraris, G., Gilli, G., Zanotti, G., and Catti, M., 2002, “Fundamentals of Crystallography,” *IUCr Texts on Crystallography*, C. Giacovazzo, ed., Oxford University, New York, pp. 74–76.

[33] Randle, V., 1993, *The Measurement of Grain Boundary Geometry* (Electron Microscopy in Materials Science Series) Institute of Physics, Bristol, UK.

[34] Garg, A., Chang, Y. C., and Howe, J. M., 1990, “Precipitation of the Phase in an Al-4.0Cu-0.5Mg Alloy,” Scr. Metall. Mater., **24**, pp. 677–680.

[35] Zhu, A. W., Shiflet, G. J., and Starke, E. A., 2006, “First Principles Calculations for Alloy Design of Moderate Temperature Age-Hardenable Al Alloys,” Mater. Sci. Forum, **519–521**, pp. 35–43.

[36] Smithells, C. J., 2004, *Smithells Metals Reference Book*, Vol. 1, 8th ed., W. F., Gale, and T. C., Totemeier, eds., Elsevier, New York.

[37] Ali, A. A., Podus, G. N., and Sirenko, A. F., 1979, “Determining the Thermal Activation Parameters of Plastic Deformation of Metals From Data on the Kinetics of Creep and Relaxation of Mechanical Stresses,” Strength Mater., **11**(5), pp. 496–500.

[38] Zikry, M., and Kao, M., 1997, “Inelastic Microstructural Failure Modes in Crystalline Materials: The S33A ANS S11 High Angle Grain Boundaries,” Int. J. Plast., **13**(4), pp. 403–434.

[39] Zikry, M., 1994, “An Accurate and Stable Algorithm for High Strain-Rate Finite Strain Plasticity,” Comput. Struct., **50**(3), pp. 337–350.

[40] Koda, S., Takahashi, S., and Matsuura, K., 1963, “Direct Observation of Interaction of Dislocations With W_{ij} Precipitates in an Aluminium-3.8 Wt.-Percent Copper Alloy,” J. Inst. Met., **91**(7), pp. 229–234.

[41] Li, B. Q., and Wawner, F. E., 1998, “Dislocation Interaction With Semicoherent Precipitates ($[M_{\mathrm{Cart}}^{\alpha *}][M_{\Omega}^{\mathrm{Cart}}]$ Phase) in Deformed Al-Cu-Mg-Ag Alloy,” Acta Mater., **46**(15), pp. 5483–5490.

[42] Nourbakhsh, S., and Nutting, J., 1980, “High-Strain Deformation of an Aluminium-4% Copper Alloy in the Supersaturated and Aged Conditions,” Acta Metall., **28**(3), pp. 357–365.

[43] Polmear, I. J., 2006, *Light Alloys: From Traditional Alloys to Nanocrystals*, Elsevier/Butterworth-Heinemann, Burlington, MA, pp. 153–154.

[44] Sanders, T., and Starke, E. A., 1982, “The Effect of Slip Distribution on the Monotonic and Cyclic Ductility of Al-Li Binary-Alloys,” Acta Metall., **30**(5), pp. 927–939.

[45] Polmear, I. J., 2006, *Light Alloys: From Traditional Alloys to Nanocrystals*, Elsevier/Butterworth-Heinemann, Burlington, MA, pp. 53–56.

[46] Nie, J. F., and Muddle, B. C., 2001, “On the Form of the Age-Hardening Response in High Strength Aluminium Alloys,” Mater. Sci. Eng., A, **319–321**, pp. 448–451.

[47] Nie, J. F., Muddle, B. C., and Polmear, I. J., 1996, “The Effect of Precipitate Shape and Orientation on Dispersion Strengthening in High Strength Aluminum Alloys,” Mater. Sci. Forum, **217–222**, pp. 1257–1263.

Energy and Momentum Transfer in Air Shocks

John W. Hutchinson
School of Engineering and Applied Sciences,
Harvard University,
Cambridge, MA 02138

A series of one-dimensional studies is presented to reveal basic aspects of momentum and energy transfer to plates in air blasts. Intense air waves are initiated as either an isolated propagating wave or by the sudden release of a highly compressed air layer. Wave momentum is determined in terms of the energy characterizing the compressed layer. The interaction of intense waves with freestanding plates is computed with emphasis on the momentum and/or energy transferred to the plate. A simple conjecture, backed by numerical simulations, is put forward related to the momentum transmitted to massive plates. The role of the standoff distance between the compressed air layer and the plate is elucidated. Throughout, dimensionless parameters are selected to highlight the most important groups of parameters and to reduce parametric dependencies to the extent possible. [DOI: 10.1115/1.3129773]

1 Introduction

Numerical analysis codes such as LS-DYNA, DYSMAS, and ABAQUS have been used for some time to model specific fluid-structure interactions (FSI) involving structures subject to blast loads generated in water and air environments. These powerful tools permit engineers to pose and solve complicated practical problems. In part, because of the availability of these codes, there has been little inclination in recent years to investigate some of the most elementary aspects of fluid-structure interaction relevant to structural design. Fundamental understanding of the role of intense blast loads on structures in water, which provided the momentum transferred to a plate struck by a planar wave, is grounded in results obtained years ago, such as those of Taylor [1] and Cole [2]. Recently, a significant advancement in basic knowledge became available through an extension of these results to intense air shocks by Kambouchev et al. [3,4], which will subsequently be referred to as the KNR theory. The study of basic one-dimensional fluid-structure interaction problems for air blasts is continued in this paper to elucidate behavior and to add to the store of relatively simple fundamental results.

Section 2 introduces some of the properties of intense planar waves. A standard device for bypassing detailed modeling of an explosive charge employing the sudden release of a highly compressed layer is introduced, and the connection between the source energy and wave momentum is established. The results of Taylor for a plate struck by an isolated planar wave are reviewed briefly in Sec. 3 with additional results for fluid-structure interactions in air supplementing those of KNR. The role of proximity of the compressed layer to the plate is studied in Sec. 4. The results for energy and momentum transfer to the plate are given as a function of the standoff distance between the plate and the compressed layer.

2 Isolated One-Dimensional Blast Waves

2.1 Linear Compression Waves in Water. Nonlinear compressibility effects of blast waves propagating in water are relatively small unless the peak pressures are in excess of 100 MPa, but they do give rise to a shocklike front and followed by exponentially decaying intensity. Valuable fluid-structure interaction results for water blast waves can be obtained using linear wave mechanics with cavitation modeled when the pressure in the water becomes negative. The result of Taylor [1] and Cole [2] for momentum transfer to a plate struck by a blast wave is such an example. An isolated planar wave propagating in the positive x-direction through water is modeled as being exponential in form with particle velocity $v=v_0 f(\xi)$ and overpressure $\Delta p=\Delta p_0 f(\xi)$, where $\xi=x-ct$ and

$$
\begin{aligned}
f(\xi) &= 0, \quad \xi > 0 \\
f(\xi) &= e^{\xi/\ell}, \quad \xi < 0
\end{aligned}
\tag{1}
$$

The peak overpressure and particle velocity are related by $\Delta p_0 = \rho c v_0$ with ρ as the ground state density, $c=\sqrt{B/\rho}$ as the wave speed, and B as the compressibility modulus. The decay time associated with the exponential shape is $t_0=c/\ell$. Generally, the ambient pressure in the water is very small compared with Δp_0, and it is neglected in the Taylor analysis. In this case, the total wave energy/area ΔE_0 is equally partitioned between the energy associated with the overpressure $\int \Delta p^2/(2B)dx$ and the kinetic energy $\int \rho v^2/2dx$ for isolated planar waves of any shape $f(\xi)$. The momentum/area is $I_0=\int \rho v dx$. For the exponential wave, these are

$$
I_0 = \Delta p_0 t_0 = \rho v_0 \ell, \quad \Delta E_0 = (\Delta p_0^2 \ell/B)/2 = \rho v_0^2 \ell/2 \tag{2}
$$

2.2 Nonlinear Compression Waves in Air. The nonlinear compressibility of air plays an essential role in the evolving shape changes experienced by intense planar waves. An intense wave propagating into quiescent ambient air develops a shock front with a shape that evolves as the wave advances. Because the wave speed increases with pressure due to nonlinear compressibility, the front of the wave propagates faster than rear portions of the wave such that as the wave propagates its width increases and its peak pressure decreases. Here, selected analytic results from the nonlinear theory of one-dimensional planar waves propagating in air [5] will be used along with numerical methods [6,7,3] to establish the results, which follow in the paper. Throughout, air is treated as an ideal gas with gas constant R and $\gamma=1.4$ as the ratio of the specific heats. Artificial viscosity will be introduced in the numerical simulations.

Let p_{atm}, ρ_{atm}, and $c_{\mathrm{atm}}=\sqrt{\gamma p_{\mathrm{atm}}/\rho_{\mathrm{atm}}}$ be the pressure, density, and wave speed in air under ambient atmospheric conditions, respectively. Consider adiabatic propagation of a rightward moving isolated planar wave with smooth velocity $v=f(x)$ at $t=0$. For $t>0$, prior to shock formation, the distributions of the velocity, pressure, density and wave speed are governed by the following nonlinear implicit equations [5]:

$$
v = f(x-(c+v)t)
$$

Contributed by the Applied Mechanics Division of ASME for publication in the JOURNAL OF APPLIED MECHANICS. Manuscript received July 28, 2008; final manuscript received January 27, 2009; published online June 15, 2009. Review conducted by Ashkan Vaziri.

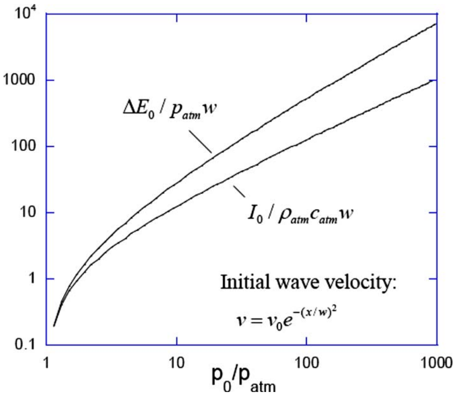

Fig. 1 Normalized wave energy/area and momentum/area for a isolated right-ward moving planar wave with an initial peak pressure p_0 in air and a prescribed velocity distribution

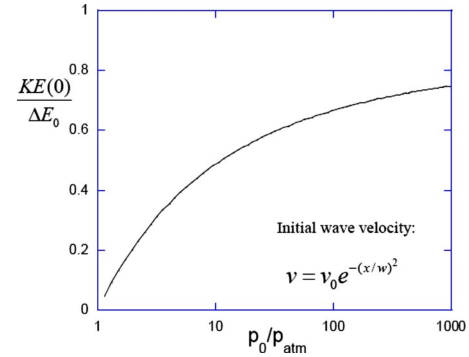

Fig. 2 Ratio of kinetic energy/area at t=0 to total wave energy/area as a function of initial peak pressure for a wave with a prescribed initial velocity distribution

$$\frac{p}{p_{\text{atm}}} = \left(\frac{\rho}{\rho_{\text{atm}}}\right)^{\gamma} = \left(\frac{c}{c_{\text{atm}}}\right)^{2\gamma/(\gamma-1)} = \left[1 + \frac{\gamma-1}{2}\frac{v}{c_{\text{atm}}}\right]^{2\gamma/(\gamma-1)} \tag{3}$$

This result will be used as an initial condition to initiate rightward moving waves with specified momentum and in some of the numerical simulations.

These results can also be used to establish the momentum and total wave energy for specific waves and the kinetic and internal energies at a given instant of time prior to shock formation. The momentum/area of the wave I_0 is independent of time as follows:

$$I_0 = \rho_{\text{atm}} c_{\text{atm}} \int_{-\infty}^{\infty} \left(\frac{\rho}{\rho_{\text{atm}}}\frac{v}{c_{\text{atm}}}\right) dx \tag{4}$$

The kinetic energy/area varies with time such that

$$\text{KE}(t) = \frac{1}{2}\gamma p_{\text{atm}} \int_{-\infty}^{\infty} \frac{\rho}{\rho_{\text{atm}}}\left(\frac{v}{c_{\text{atm}}}\right)^2 dx \tag{5}$$

The total wave energy/area is also independent of time; it is the sum of the kinetic energy and excess internal energy (the internal energy minus the ambient energy).

$$\Delta E_0 = \text{KE}(t) + \frac{p_{\text{atm}}}{\gamma-1}\int_{-\infty}^{\infty}\left[\frac{p}{p_{\text{atm}}} - \left(\frac{p}{p_{\text{atm}}}\right)^{1/\gamma}\right] dx \tag{6}$$

which is only valid prior to shock formation and with no dissipation. For example, for a wave with the velocity distribution at $t=0$,

$$v = v_0 e^{-(x/w)^2} \tag{7}$$

numerical integration provides the plots of momentum and total wave energy as a function of p_0/p_{atm} in Fig. 1, where p_0 is the maximum pressure at $t=0$ related to v_0 by Eq. (3). The ratio of the kinetic energy to total wave energy at $t=0$ is plotted as a function of p_0/p_{atm} in Fig. 2. The more intense the wave, the larger is the kinetic energy as a fraction of the total wave energy. These results depend on the details of the velocity distribution, but the trends expressed in term of peak pressure are representative. In Fig. 2, $\text{KE}(0)/\Delta E_0$ does not approach $\frac{1}{2}$ for low intensity waves, as seen for water blasts, because the ambient air pressure cannot be neglected for low intensity air waves.

The numerical method employed to analyze the series of one-dimensional problems presented below is based on the widely used von Neumann–Richtmyer algorithm [6], which incorporates artificial viscosity in the model of the gas to smoothen the shock discontinuities and to stabilize the solution procedure. The viscous contributions are added in a manner, which preserves energy conservation. The present formulation follows that are used in the KNR studies [3] and are detailed in the text [7]. The equations governing the constitutive behavior of the air are as follows. Let p, ρ, and T be the pressure, mass density, and temperature in the current state, respectively. The internal energy/mass is given by $e=RT/(\gamma-1)$. Denote the normal stress contribution due to viscosity by Q such that the ideal gas law is modified as

$$p = \rho RT - Q \tag{8}$$

Following Refs. [3,7], the artificial viscosity contribution is taken as $Q=0$ for $\dot{\varepsilon}>0$ and

$$Q = -\rho_i[(b_1\dot{\varepsilon}\Delta)^2 + b_2 c|\dot{\varepsilon}|\Delta], \quad \dot{\varepsilon}<0 \tag{9}$$

where $\dot{\varepsilon}$ is the strain-rate, ρ_i is the initial density, Δ is a measure of the smeared shock thickness related to the current mesh size, $c=\sqrt{\gamma(\gamma-1)e}$ is the current sound speed, and b_1 and b_2 are the dimensionless viscosity coefficients. The time rate of the internal energy is taken to be consistent with energy conservation ($-p\dot{\varepsilon}=\rho\dot{e}$) as

$$\dot{e} = \left[-(\gamma-1)e + \frac{Q}{\rho}\right]\dot{\varepsilon} \tag{10}$$

The regions on the x-axis occupied by the air at $t=0$ are divided into a uniform mesh. The plate is represented as a freestanding plane with mass/area m_p. The description is Lagrangian with the positions of the material points as independent variables. The equations for the nonlinear behavior of an ideal gas are discretized in a manner that conserves momentum and energy. The results presented in the paper have been computed with between 2000 and 5000 mesh points, depending on the problem, with time steps set in accord with the stability requirements of the algorithm [3,7]. The viscosity coefficients were set at $b_1=2$ and $b_2=1$.

2.3 Waves Generated by a Sudden Release of Highly Pressurized Air.

In numerical simulations, a useful device to simulate blast waves is to suddenly release a "container" of adiabatically compressed air that is initially at rest and that then pushes into quiescent ambient air. To this aim, consider a one-dimensional layer of air under ambient conditions of width h_{atm}, which is compressed adiabatically with no dissipation to thickness h. The excess energy/area in air in the compressed layer ΔE_0, excluding the energy of the air in its ambient state, is

$$\Delta E_0 = \frac{1}{\gamma-1}[p_0 h - p_{\text{atm}} h_{\text{atm}}] = \frac{p_{\text{atm}} h}{\gamma-1}\left[\frac{p_0}{p_{\text{atm}}} - \left(\frac{p_0}{p_{\text{atm}}}\right)^{1/\gamma}\right] \tag{11}$$

with $p_0/p_{\text{atm}}=(h_{\text{atm}}/h)^{\gamma}$. For example, a layer with $h_{\text{atm}}=0.27$ m that is squeezed to $h=0.01$ m produces $p_0/p_{\text{atm}}=100$ and $\Delta E_0=0.19$ MJ/m^2.

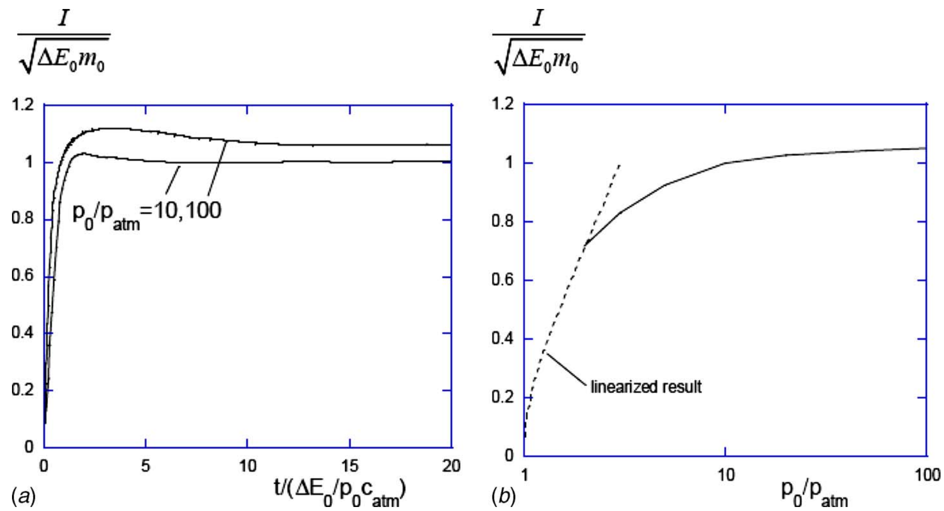

Fig. 3 Normalized momentum/area of rightward traveling wave produced by an initially compressed air layer with excess energy/area ΔE_0, mass/area m_0, and pressure p_0. (*a*) Momentum/area versus time for two initial pressures. (*b*) Momentum/area of the emerged wave.

Let $I(t)$ be the momentum/area of the rightward moving wave generated by the sudden release of the compressed air at $t=0$. The result will apply to a compressed layer of thickness h and excess energy/area ΔE_0 bounded by quiescent ambient air on its right and a rigid wall on the left or, equally, by symmetry, to a symmetrically placed compressed layer of thickness $2h$ and excess energy/area $2\Delta E_0$ bounded by quiescent air on both sides. As the wave propagates to the right, a shocklike front forms whose steepness is controlled by the artificial viscosity. The shape of the wave slowly evolves as described earlier. At any instant the wave energy is

$$\Delta E = \int \left[\frac{1}{2}\rho v^2 + \rho(e - e_{\text{atm}}) \right] dx \tag{12}$$

with integration in the current state for $0 \le x < \infty$ and $e_{\text{atm}} = p_{\text{atm}}/[(\gamma-1)\rho_{\text{atm}}]$. The wave energy is constant with $\Delta E = \Delta E_0$ given by Eq. (11), a feature that is preserved by the numerical scheme.

With $x=0$ at the edge of the rigid wall (or at the symmetry plane), $I=\int_0^\infty \rho v dx$ is the momentum/area of all the air occupying $x \ge 0$. By dimensional analysis, one can show that the entire parametric dependence for air modeled as an ideal gas is captured by the dimensionless form

$$\frac{I}{\sqrt{\Delta E_0 m_0}} = F\left(\frac{p_0}{p_{\text{atm}}}, \frac{t}{\Delta E_0/(p_0 c_{\text{atm}})} \right) \tag{13}$$

with a dependence on both γ and the viscosity coefficients being implicit. Here, $m_0=\rho_0 h=\rho_{\text{atm}} h_{\text{atm}}$ is the mass/area of the compressed air layer. Initially at $t=0$ when the compressed layer is released, $I=0$, but in a very short period of time ($t/[\Delta E_0/(p_0 c_{\text{atm}})] \approx 1$) an isolated compression wave forms and propagates to the right. Thereafter, I is nearly constant as can be seen in Fig. 3(*a*). The momentum in the air occupying $x \ge 0$ is not strictly constant because of interaction with the wall. After reaching a maximum, I decreases slightly as the pressure at the wall drops below p_{atm} and, subsequently, I increases slightly when the wall pressure rises again above p_{atm}. However, to a very good approximation, I is constant once an isolated wave emerges, and the normalized momentum of the wave $I/\sqrt{\Delta E_0 m_0}$ depends essentially only on p_0/p_{atm}. This dependence is plotted in Fig. 3(*b*) with I evaluated at its minimum value following the first maximum. The success of the particular normalization is evident in that $I/\sqrt{\Delta E_0 m_0} \approx 1$ for intense "explosions." Included in this figure is the result obtained by a linearized analysis in which p_0/p_{atm} is perturbed about unity as follows:

$$\frac{I}{\sqrt{\Delta E_0 m_0}} = \sqrt{\frac{1}{2}\left(\frac{p_0}{p_{\text{atm}}} - 1 \right)} \tag{14}$$

These results are not new, although the normalization given above seems to be particularly useful for the present objectives. The power of dimensional analysis to reduce the parametric dependencies is laid out in texts such as Ref. [8], and related results have been presented in various sources including Refs. [9,10].

3 Interaction Between Intense Isolated Waves and a Freestanding Plate

Kambouchev et al. [3] extended Taylor's linear theory of fluid-structure interaction in water to intense planar air blasts. Formulas for the momentum transfer to a freestanding plate were developed and calibrated by accurate numerical simulations. These authors generated a rightward moving wave by releasing a highly compressed layer well to the left of the plate. The wave propagates, forms a shock, and evolves in shape before striking the plate. The authors fit an exponential pressure distribution to the wave $p = p_0 e^{-t/t_0}$ with peak pressure p_0 and decay time t_0, in the period of time when the wave passes the plate (simulated with the plate removed). The interaction of the wave with the plate is computed with emphasis on the maximum momentum/area I transmitted to the plate as a function of the wave characteristics at the instant the plate is impacted.

Here, the KNR approach is modified in several ways. (1) The initial condition is taken as a rightward moving isolated wave (3) with precisely defined momentum/area I_0 and wave energy/area ΔE_0. (2) The momentum/area transmitted to the plate I is normalized by the incident momentum I_0 and it is conjectured based on numerical simulations that the limit for a massive plate is $I=2I_0$ for all incident blast waves. (3) The results are presented in dimensionless form using invariant measures I_0 and ΔE_0 of the wave intensity. (4) The plate interacts with ambient air on the side opposite the blast, which KNR neglects.

3.1 Wave Impinging on a Massive Plate. For massive plates ($m_p \to \infty$), many computations have been performed for different initial wave shapes (3) launched at a wide range of distances from the plate for initial pressure peaks p_0 ranging from several times p_{atm} to $1000 p_{\text{atm}}$. In all cases, it has been found that to within a few tenths of a percent the momentum/area transferred to the plate, or equivalently, the impulse/area acting on the plate is $I=2I_0$ with I_0 as the momentum/area of the incident wave (4). Concomitantly, within the same precision the momentum/area of the reflected wave is $-I_0$. As is well known, linear theory (e.g., Taylor's theory) gives precisely $I=2I_0$ for the limit of massive plates. Based on the above findings, it seems reasonable to conjecture that $I=2I_0$ holds for compressible air waves as well. The very small difference between the numerical results determined here and $I=2I_0$ is likely due to errors associated with the numerical method, but this has not been established.

To our knowledge there is no proof of this result for nonlinear compressible waves, nor does it appear to have been remarked upon in the literature. The fact that the reflected wave has momentum/area $-I_0$ is obviously consistent with equal and opposite propagating waves colliding subject to conservation of momentum and energy. By symmetry, this problem is the same as the wave impacting a massive plate. Moreover, the simple result $I=2I_0$ would be expected from a statistical mechanical model of an ideal gas with molecules represented as hard spheres that undergo perfectly elastic collisions. The constitutive equations of the continuum model of an ideal gas are derived from such a model. Nevertheless, it is not obvious that the solution to the full set of continuum equations governing the ideal gas preserves this simple result, especially with inclusion of artificial viscosity.

3.2 Wave Impinging Upon a Plate of Finite Mass/Area m_p. A rightward propagating wave prescribed by Eq. (7) is launched at $t=0$ in the direction of a plate whose surface directed toward the blast is initially located at $x=d$, with d/w sufficiently large such that there is no interaction between the plate and the wave at $t=0$. Ambient air exists on both sides of the plate. The region of the x-axis is taken to be sufficiently large such that no reflected waves impact the plate from either the left or the right. The plate accelerates upon impact of the blast wave, attaining a maximum velocity, and then begins a slow deceleration due to the fall-off in pressure on the blast side and the buildup of pressure on the back side of the plate as it plows into the air on that side. The objective is to determine the maximum momentum/area I transmitted to the plate as related to the incident momentum I_0.

One set of independent parameters determining I are m_p, v_0, w, d, p_{atm}, and ρ_{atm}, along with γ and the viscosity coefficients, which will be regarded as fixed. While $c_{\mathrm{atm}}=\sqrt{\gamma p_{\mathrm{atm}}/\rho_{\mathrm{atm}}}$ is not independent, it can be used when convenient. The momentum/area I_0 and wave energy/area ΔE_0 of the incident wave defined in Eqs. (4) and (6) can be used in place of v_0 and w. These variables have the advantage that they are invariant measures of the incident wave intensity in the sense that they remain constant as the wave propagates and, moreover, they are less tied to the specificity of the initial launching conditions. Based on the set of independent variables—m_p, I_0, ΔE_0, d, p_{atm} and ρ_{atm}—it follows from dimensional analysis that the general functional dependence of the maximum momentum/area imparted to the plate I depends on three dimensionless parameters as

$$\frac{I}{I_0}=F\left(\beta,\frac{\Delta E_0}{c_{\mathrm{atm}}I_0},\frac{p_{\mathrm{atm}}d}{c_{\mathrm{atm}}I_0}\right) \tag{15}$$

with

$$\beta=\frac{1}{2}\frac{I_0^2}{\Delta E_0 m_p} \tag{16}$$

The parameter β has been defined in terms of the wave invariants such that it coincides with Taylor's [1] fluid-structure interaction parameter for linear exponential waves (1) using the expressions in Eq. (2), i.e., $\beta=\rho\ell/m_p$ or, equivalently, $\beta=t_0/t_p$ with $t_p\equiv m_p/(\rho c)$. Taylor's result for the maximum momentum imparted to the plate in a water blast is

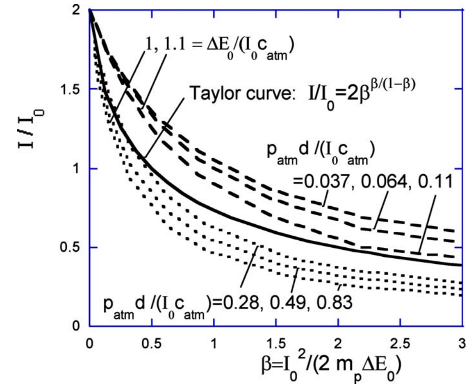

Fig. 4 Ratio of momentum/area transmitted to a plate to the momentum/area of the incident wave in terms of the generalized Taylor FSI parameter β in Eq. (16) and the two dimensionless parameters characterizing the wave. The values $\Delta E_0/I_0c_{\mathrm{atm}}=1$ and 1.1 correspond to a wave (7) released with $w=0.05$ m with $p_0/p_{\mathrm{atm}}=16$ and 127, respectively, at three distances from the plate ($d=0.4$ m, 0.7 m and 1.2 m.

$$\frac{I}{I_0}=2\beta^{\beta/(1-\beta)} \tag{17}$$

which is included in Fig. 4. In Taylor's water blast model, there is no restraint of water or air on the back side of the plate. The maximum momentum of the plate is attained when the pressure on the front side of the plate becomes negative, interpreted as the onset of cavitation.

Plots of I/I_0 as a function of the generalized β are presented in Fig. 4 for a range of initial conditions specified by the other two dimensionless parameters. An illustration in dimensional terms is included in the figure caption. It is seen that the fraction of the incident wave momentum transferred to the plate is primarily dependent on β with importance dependence on the other two parameters as well. Relatively small changes in $\Delta E_0/(c_{\mathrm{atm}}I_0)$ are associated with large changes in p_0/p_{atm}. In spite of the differences in modeling, the trends in Fig. 4 are similar to the more extensive results presented by KNR [3], who used other measures of the incident wave intensity evaluated at the moment of impact and who also developed formulas that accurately reproduce their numerical results. Specifically, KNR generalized the Taylor parameter to intensify air blasts according to $\beta=t_0/t_p^*$ where $t_p^*\equiv m_p/(\rho_s U_s)$ with ρ_s as the density directly behind the shock front and U_s as the velocity of the shock front, both measured at the instant just before the wave hits the plate.

Figure 4 provides a unified way to view fluid-structure interaction between blast waves in water and air and a freestanding plate. Substantial reductions in momentum transfer due to fluid-structure interaction will only be achieved if $I_0^2/\Delta E_0$ is comparable to m_p. For relatively thick metallic plates, this will only occur for very intense air blasts. In air blasts, most plates acquire the maximum possible momentum/area $2I_0$.

An advantage of using β as defined in Eq. (16) to describe the fluid-structure interaction behavior is that this dimensionless variable is defined using invariants of the incident wave, whereas, for example, the choice $\beta=t_0/t_p^*$ favored by KNR must be determined in some manner (computation or test measurements) at the instant the wave strikes the plate. For a wave launched with specific momentum/area and excess energy/area, $\beta=t_0/t_p^*$ depends on the distance the wave travels to reach the plate. Conversely, a disadvantage of the present choice of β in Eq. (16), as opposed to that of KNR, is that the present choice does not reflect the fact that the intensity of the traveling wave diminishes with distance traveled. This deficiency is due to the fact that the wave energy ΔE_0 defined initially by Eq. (6) and subsequently by Eq. (12), includes internal

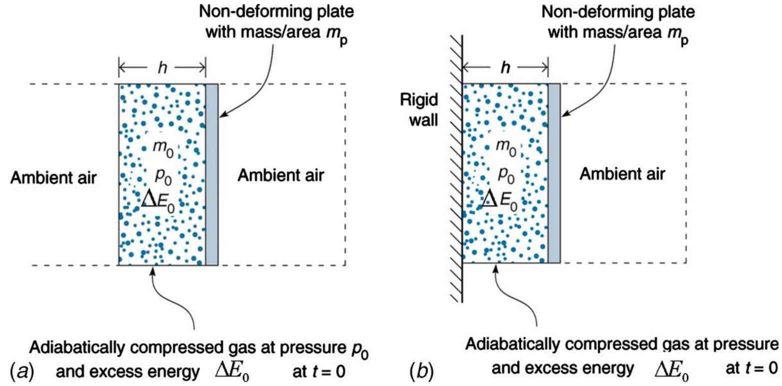

Fig. 5 Configuration and notation for simulations releasing compressed air layer at $t=0$ with no standoff distance to plate. (*a*) No backing to compressed layer. (*b*) Rigid backing to compressed layer.

energy (heat) in the "quiescent" air left behind the propagating wave. In the computational model, the remnant internal energy is set by the viscosity coefficients. In the absence of viscosity, the remnant energy is set by jump conditions across the shock. Thus, while the wave energy ΔE_0 is conserved, it does not faithfully measure the intensity available to accelerate the plate after the wave has traveled distances sufficient to leave behind an appreciable fraction of its initial energy as heat. These trends are made explicit in Fig. 4 through the dependence on $p_{atm}d/(c_{atm}I_0)$.

In conclusion, it has been noted that there are several ways to generalize Taylor's fluid-structure interaction parameter β for intense air blasts. The choice identified by KNR has the distinct advantage that it provides a measure of the relevant wave intensity at the instant the wave strikes the plate. As a consequence, it appears to reduce the dependence of I/I_0 on only one dimensionless parameter in addition to β, assuming wave has propagated far enough to have evolved into an exponential shape.

4 Energy and Momentum Imparted to a Plate by a Highly Compressed Layer of Air

4.1 The Role of Backing to the Compressed Air Layer for Plates With Zero Standoff. Consider the initial configurations in Fig. 5 wherein an adiabatically compressed air layer such as that introduced in Sec. 2.3 is released at $t=0$ and accelerates a plate in direct contact with the layer to the right. Two cases are considered: (a) no backing on the left of the layer other than ambient air and (b) rigid backing on the left. The plate flies into ambient air on its right. A specific example for the case of rigid backing in Fig. 6 shows the time evolution of the kinetic energy/area of the plate until the point that it attains its maximum velocity. In this example, almost 80% of the initial excess energy (11) in the compressed layer ΔE_0 is transferred to the plate. The figure also shows the evolution of the excess energy in the air to the left and right of the plate ΔE, defined as the sum of the kinetic energy and the excess internal energy in Eq. (12). The maximum velocity is attained after the plate has plowed into ambient air on its backside creating a pressure wave to the right of the plate.

It is no surprise that the role of the backing is enormous, as seen in Fig. 7. In this figure, the maximum kinetic energy/area transferred to the plate KE is normalized by the initial excess energy in the compressed layer ΔE_0 and plotted against m_p/m_0. As in Sec. 2.3, $m_0=h_{atm}\rho_{atm}=h\rho_0$ is the mass/area of the air in the compressed layer. The only other dimensionless parameter in this problem (other than γ and the viscosity coefficients) is $p_0/p_{atm} = (h_{atm}/h)^{\gamma}$. When the compressed layer has rigid backing, the plate acquires a significant fraction of the energy of the compressed layer, depending in detail on m_p/m_0 and p_0/p_{atm} as plotted in Fig. 7(*b*). With backing, highly compressed initial layers ($p_0/p_{atm}>100$) acting on relatively massive plates ($m_p/m_0>10$) transmit 80% or more of their energy to the plate. The maximum momentum/area transmitted to the plate can be obtained from $I = \sqrt{2m_p \mathrm{KE}}$. By contrast, a plate launched by a compressed layer with no backing acquires a small fraction of ΔE_0 (Fig. 7(*a*)).

4.2 Finite Standoff *d* With Rigid Backing. The effect of a finite standoff distance d between the plate and the compressed layer is now considered, as depicted in Fig. 8. The compressed air layer has rigid backing. At $t=0$, ambient air exists between the compressed layer and the plate and also to the right of the plate. The normalized maximum kinetic energy acquired by the plate $\mathrm{KE}/\Delta E_0$ is computed as a function of the standoff distance. In addition to the two dimensionless parameters introduced for the case of zero standoff p_0/p_{atm} and m_p/m_0, one new dimensionless standoff parameter comes into play. One possibility is d/h_{atm} and another is $p_{atm}d/\Delta E_0$; these parameters can be expressed in terms of one another using the other two dimensionless parameters. The choice d/h_{atm} is preferred because h_{atm} reflects the distance over which the highest pressures in the compressed layer will still persist as it expands. The results for one set of parameters p_0/p_{atm}

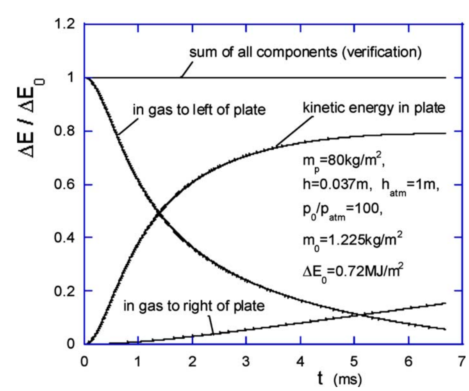

Fig. 6 An example for the case of the compressed layer with rigid backing and a plate with zero standoff distance. The evolution of the several components of the energy of the system with time is plotted until the time when the plate acquires its maximum velocity. The energy/area ΔE in the air to the left and right of the plate is the sum of the kinetic energy and the excess internal energy as defined in Eq. (12). As noted from the top curve, the numerical method conserves energy to a high degree of accuracy. In this example, value for m_p is equivalent to a 1 cm thick steel plate; the maximum velocity attained by the plate is 120 m/s.

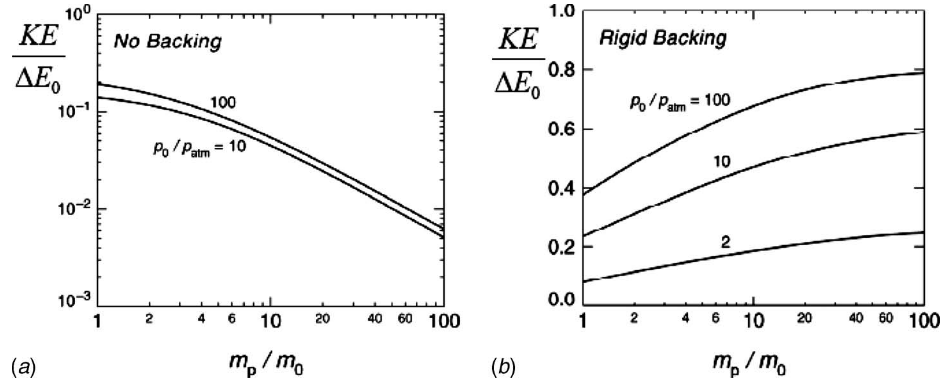

Fig. 7 Ratio of the maximum kinetic energy/area transmitted to plate to the initial excess energy/area in the compressed layer for the case with no standoff between the plate and the layer. (*a*) No backing to the compressed layer. (*b*) Rigid backing to the compressed layer.

$=100$ and $m_p/m_0=100$ are plotted as a function d/h_{atm} in Fig. 9. The exceptionally strong effect of the standoff distance is evident, as will now be discussed.

The kinetic energy transferred to the plate drops dramatically as the standoff distance increases. For the example given in the caption of Fig. 9 with a specific choice of dimensions, the kinetic energy transferred to the plate is already reduced substantially at the standoff $d \cong h_{\mathrm{atm}}=0.33$ m. The limit for large standoff labeled in Fig. 9 is readily understood using the result in Sec. 2.3 for the momentum of a wave generated by the release of the compressed air layer in a semi-infinite region in conjunction with the fluid-structure interaction results in Fig. 4. With reference to Fig. 3(*b*), note that the momentum/area of the rightward moving wave generated by a compressed layer with $p_0/p_{\mathrm{atm}}=100$ is $I \cong 1.05\sqrt{\Delta E_0 m_0}$, assuming the wave has been propagated sufficiently far to be fully developed with a well defined momentum. Assuming this is the case, identify I with the momentum/area I_0 of the wave hitting the plate and ΔE_0 as the wave energy/area. By Eq. (16), $\beta \cong 0.55(m_0/m_p)=0.0055$ and, thus, from Fig. 4, the momentum/area transferred to the plate is nearly $2I_0 \cong 2.1\sqrt{\Delta E_0 m_0}$. Then, because the kinetic energy/area of the plate is

$$\mathrm{KE}=(2I_0)^2/(2m_p) \cong 2.2\Delta E_0(m_0/m_p)$$

the large standoff limit is

$$\frac{\mathrm{KE}}{\Delta E_0} \cong 2.2\frac{m_0}{m_p} \tag{18}$$

For the set of parameters in Fig. 9 this limit is 0.022. The example in Fig. 9 is representative for any relatively massive plate (i.e., $m_p/m_0>10$) in any intense air blast.

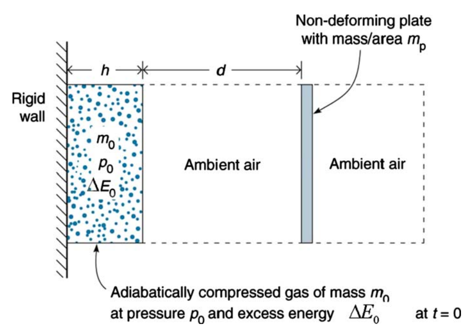

Fig. 8 Configuration for simulations of energy transferred to plate with standoff *d*. The compressed air layer has rigid backing.

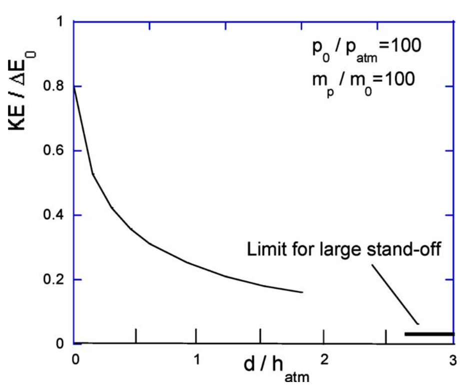

Fig. 9 The maximum kinetic energy/area transmitted to plate as a function of the standoff distance between the plate and the compressed air layer plotted for a specific set of dimensionless parameters. For reference, a set of dimensional parameters that corresponds to these results is: $h_{\mathrm{atm}}=0.33$ m, $h=0.012$ m, $\Delta E_0=0.24$ MJ/m^2, $m_p=40$ kg/m^2, $m_0=0.4$ kg/m^2 and $p_0=10.5$ MPa. The limit for large standoff is discussed in the text.

The standoff effect illustrated in Fig. 9 is one-dimensional. It is quite distinct from the more easily understood effect of standoff in two and three dimensions wherein the blast wave intensity, as measured by the momentum/area and/or energy/area, diminishes inversely as a function of distance as the wave propagates away from the source. In the one-dimensional situation considered here with backing and no standoff, a large fraction of the air layer energy is converted directly into the kinetic energy of the plate as the layer expands against the plate (c.f., Fig. 7(*b*)). At the other extreme, for large standoff, the energy in the compressed air layer is first converted into the energy of the propagating wave. When this wave hits the plate, a very small fraction of the wave energy is transferred to the plate because the wave bounces off the plate retaining much of its energy. In other words, with sufficient standoff (e.g., $d/h_{\mathrm{atm}}>1$) for intense waves ($p_0/p_{\mathrm{atm}}>10$) and relatively massive plates ($m_p/m_0>10$), most of the energy of the initial compressed layer remains trapped between the wall and the plate in the form of kinetic and internal energies of the air with waves reverberating back and forth between the wall and the plate.

5 Concluding Remarks

The study focused on one-dimensional waves in air modeled as an ideal gas. The main findings are as follows.

(a) For intense waves in air initiated by the sudden release of an adiabatically compressed layer, a relatively simple relation exists between the energy in the compressed layer and the momentum of the ensuing wave as presented in Fig. 3.

(b) A massive plate struck by an isolated wave acquires twice the momentum of the incident wave. It remains to establish this result theoretically—it has been verified to a high degree of numerical accuracy in this paper.

(c) A presentation is given of fluid-interaction curves for the fraction of the momentum transferred to a freestanding plate in intense air blasts using invariants of the impacting wave (Fig. 4). While more comprehensive results have been presented by KNR [3] using other variables to describe the incident wave, the results given here provide additional insights to the interaction and have certain advantages stemming from the invariance of the parameters.

(d) The enormous effect of backing to the compressed layer on the energy transmitted to a plate in direct contact with the layer is quantified.

(e) Standoff between the plate and the compressed layer also has a very large effect in a one-dimensional setting. If the standoff is sufficiently large such that a well developed wave forms prior to impacting the plate, relatively little of the initial energy in the compressed layer is transmitted to the plate.

Acknowledgment

This work was supported in part by the ONR through Grant No. N00014-07-1-0764 and in part by the School of Engineering and Applied Sciences, Harvard University.

References

[1] Taylor, G. I., 1963, "The Pressure and Impulse of Submarine Explosion Waves on Plates," *The Scientific Papers of Sir Geoffrey Ingram Taylor*, G. K. Batchelor, ed., Cambridge University Press, Cambridge, UK, Vol. 3, pp. 287–303.
[2] Cole, R. H., 1948, *Underwater Explosions*, Dover, New York.
[3] Kambouchev, N., Noels, L., and Radovitzky, R., 2006, "Nonlinear Compressibility Effects in Fluid-Structure Interaction and Their Implications on the Air-Blast Loading of Structures," J. Appl. Phys., **100**, p. 063519.
[4] Kambouchev, N., Noels, L., and Radovitzky, R., 2007, "Fluid-Structure Interaction Effects in the Dynamic Response of Free-Standing Plates to Uniform Shock Loadings," ASME J. Appl. Mech., **74**, pp. 1042–1045.
[5] Liepmann, H. W., and Roshko, A., 1957, *Elements of Gas Dynamics*, Wiley, New York.
[6] von Neumann, J., and Richtmyer, R., 1950, "A Method for the Numerical Computation of Hydrodynamic Shocks," J. Appl. Phys., **21**, pp. 232–237.
[7] Drumheller, D. S., 1998, *Introduction to Wave Propagation in Nonlinear Fluids and Solids*, Cambridge University Press, Cambridge, UK.
[8] Sedov, L. I., 1993, *Similarity and Dimensional Methods in Mechanics*, 10th ed., CRC, Boca Rotan, FL.
[9] von Neumann, J., 1943, "The Point Source Solution," *Collected Works*, Vol. 6, Pergamon, New York, pp. 219–237.
[10] Kambouchev, N., 2007, "Analysis of Blast Mitigation Strategies Exploiting Fluid-Structure Interaction," Ph.D. thesis, Department of Aeronautics and Astronautics, Massachusetts Institute of Technology, Cambridge, MA.

S. Chung Kim Yuen[1]
e-mail: steeve.chungkimyuen@uct.ac.za

G. N. Nurick

Blast Impact and Survivability Research Unit (BISRU),
Department of Mechanical Engineering,
University of Cape Town,
Private Bag,
Rondebosch 7701, South Africa

The Crushing Characteristics of Square Tubes With Blast-Induced Imperfections—Part I: Experiments

This two-part article presents the results of experimental and numerical work on the crushing characteristics of square tubes, with blast-induced imperfections, subjected to axial load. In Part I, the experimental studies are presented. The approach in the studies involves creating imperfections on opposite sides at midlength of a square tube by means of localized blast loads to create three types of imperfections; nontouching domes, rebound domes, and capped domes. These imperfections change the geometry and the material properties in the midsection of the tubes and hence affect the crushing characteristics. While the blast-induced imperfections enhance the energy absorption characteristics of the tubes they also affect the lobe formation process. In Part II, the finite element package ABAQUS/EXPLICIT *v6.5-6 is used to construct a $\frac{1}{2}$ symmetry model by means of shell and continuum elements to simulate the tube response to the localized blast loads followed by dynamic axial loading in the form of a rigid mass impacting at a specified initial velocity. The hydrodynamic code* AUTODYN *is used to characterize the localized blast pressure time and spatial history. The predictions show satisfactory correlation with experiments for both crushed shapes and crushed distance.*
[DOI: 10.1115/1.3005977]

Keywords: square tubes, imperfections, blast load, energy absorption

1 Introduction

If there is to be such an event as an ideal crash it would be no crash at all. However, with the ever-increasing demand for mass transport the potential for accidents is always on the rise. According to the 2004 World Health Organization report on road traffic injury prevention [1] approximately 1.2 million people are killed and 50 million people are injured in road traffic crashes each year. Nonetheless, in the event of a crash one wants the best possible chances of survival, and enduring a crash is all about absorbing kinetic energy. Tubular structural members of different geometries and materials have been widely established as energy absorbers as they have the ability to absorb and convert a large amount of kinetic energy into plastic strain energy when deforming under compression as in impact situations. These extruded thin-walled structures can sustain high impact loads with large geometric deformations, strain hardening effects, strain-rate effects, temperature effects, and various interactions between different deformation modes (such as bending and stretching). The studies on the behavior of thin-walled structures were initiated in the 1960s by Pugsley and Macaulay [2] and Alexander [3]. Since then, there has been continued interest on the axial crushing behavior of these structures, overviewed by numerous authors—Reid [4], Alghamdi [5], and Jones [6].

When loaded axially, these thin-walled structures fail into two distinct collapse modes, either Euler buckling or progressive buckling mode. While these collapse modes are highly influenced by the tube material and geometries (length, cross section, and wall thickness) the structure's response also depends on the loading conditions, boundary conditions, imperfections (also referred to as initiators or triggers), and fillers. In some cases a transition between these two modes of collapse is observed. For crashworthiness applications, the idea is to absorb a large amount of kinetic energy in a controllable and predictable manner or at a predetermined rate. The progressive buckling mode is hence more desirable than the Euler buckling mode.

When a tubular structure is crushed in progressive buckling mode, its initial peak force is greater than the subsequent peak force developed. For crashworthiness applications, this initial peak force is highly undesirable. The use of imperfections to initiate a specific collapse mode, stabilizing the collapse process and reducing the peak load magnitude, as explored by Thornton and Magee [7], has become very "common." These imperfections, can be either material or/and geometric modifications to the structure. Chung Kim Yuen and Nurick [8] recently presented an overview of the different imperfections used to improve crushing characteristics of tubular structures.

Examples of material imperfections are locally annealed regions generated by concentrated heating, or the heat-affected zone generated by a weld. Types of geometric initiators include naturally-formed and mechanically-induced modifications, structural additions, or deletions on the component and, for composite components, special end configurations and inserts. The imperfections based on the geometric modification of the component have the advantages of being visually detectable and controllable by dimension adjustment. Numerous authors have explored the effects of different types of imperfections. For instance, Langseth et al. [9], Lee et al. [10], DiPaolo et al. [11], and Mamalis et al. [12] have used triggering dents or parallel grooves to initiate the collapse of axially loaded thin-walled structures. Gupta and coworker [13,14], Toda [15], Kormi et al. [16], Marshall and Nurick [17], and Arnold and Altenhof [18] have reported on thin-walled structures with circular cut-outs.

In crashworthiness applications, other types of imperfections, such as triggers, cut-outs, and dents have to be preinduced, con-

[1]Corresponding author.

Contributed by the Applied Mechanics Division of ASME for publication in the Journal of Applied Mechanics. Manuscript received February 3, 2008; final manuscript received July 29, 2008; published online June 17, 2009. Review conducted by Ashkan Vaziri.

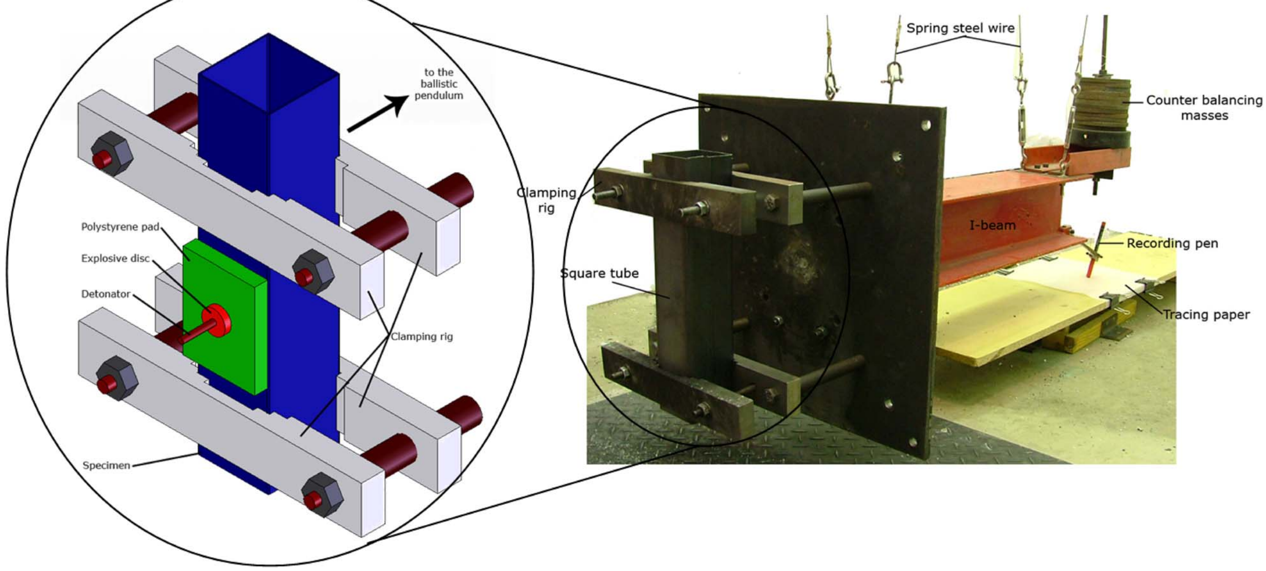

Fig. 1 Schematic and photo of the blast loading setup

sequently weakening the structure. Explosives, as used for air bag deployment in case of car crashes, can be applied to generate imperfections in tubular structures (car chassis) almost instantaneously. Thus helping to reduce crush peak forces. However, despite similar loading conditions, the response to the explosive charges does not necessarily result in imperfections of the same magnitude, which may lead to asymmetry. The latter is not ideal for crashworthiness because the Euler failure mode can be induced as opposed to progressive buckling.

This paper reports on the results of an investigation into the response of extruded square tubes with blast-induced imperfections subjected to dynamic axial impact load. The tube structure is weakened as a result of the change in geometry from the blast. The large inelastic response of the tube to the explosions occurs at high strain rates in a localized area, consequently affecting the material properties in that region. The combined effects of the change in geometry and material properties are investigated by dropping the different masses at different velocities to investigate the response of tubes to various impact energies and velocities after the explosions. A few quasistatic tests are also carried out to investigate the force-displacement characteristic.

2 Experiments

2.1 Blast Loading of Tubes. The blast loading experiments involve using small quantities of explosive positioned on the side of the square tubes to generate a localized blast load. The tubes, made from mild steel of 304 MPa in yield stress, 50×50 mm^2 in cross section, 1.5 mm in nominal thickness and 350 mm in length, are attached to a ballistic pendulum, as shown in Fig. 1, and the resulting impulse due to the explosive charge is recorded. The method of creating an impulsive load using a plastic explosive and the measurement of the impulse using a ballistic pendulum is similar to that used in many previous experimental investigations. The ballistic pendulum is the same as that used by Chung Kim Yuen and Nurick [19,20], Farrow et al. [21], Jacob et al. [22], Langdon et al. [23] and Nurick and co-workers [24–26] involving explosive loading on plates. This experimental technique has been proven to give consistent and reproducible results. The tests on the ballistic pendulum are carried out with a view to obtain an empirical relationship between the mass of the explosive and the impulse.

The square tubes are centrally loaded using plastic explosive (PE4), which has a burn speed of approximately 8200 m/s [27]. This explosive is laid out on a 14 mm thick polystyrene foam pad, which has the same width as the tube and is 100 mm in length. The explosive is spread evenly onto the polystyrene foam pad over the load diameters equivalent to one-third and one-half of the tube width (17 mm and 25 mm). A 1 g leader of explosive holding the detonator is attached to the center of the disk of explosive. The foam pad disintegrates up on detonation, but attenuates the shock transmitted to the square tube and prevents spallation of the specimen. The mass of explosive (ME) of the leader is kept constant for all the tests. Differing masses of explosives, ranging from 2 g to 6 g, are used, giving different impulses, resulting in different tube responses. The tube and blast load configuration is illustrated in Fig. 1.

Results from these blast tests together with additional data from past experiments [22,23,28,29] on localized blast loading (explosive mass ranging from 2 g to 6 g) of quadrangular structures are plotted in Fig. 2 with a view to obtaining an empirical relationship. Irrespective of the load diameter, there is a general trend that impulse increases with increasing mass of explosive. The empirical relationship shown in Eq. (1) is calculated from a least squares regression analysis. The equation is a good fit for the data, with a R^2 correlation coefficient of 0.91 for 200 data points. The resultant impulse is approximately twice the mass of explosive. However, deviations of up to 30% are observed in the experimental data. An error of ± 1 Ns to the empirical relationship is plotted in Fig. 2.

$$I = 2.0\mathrm{ME}^{0.97} \approx 2.0\mathrm{ME} \tag{1}$$

where I is the impulse (N s) and ME is the mass of the explosive for $1\ \mathrm{g} \leq \mathrm{ME} \leq 6\ \mathrm{g}$.

To create the blast-induced imperfections on opposing sides of the tube, two equal masses of explosives having the same load diameter are placed at the center on opposite sides of the square tube clamped onto an anvil. The explosive charges are always placed on the sides of the tube that do not contain the welded seam. The two detonators for the two explosive loads are connected to the same triggering wire for simultaneous blast.

The response of the tube to the localized blast loads show that the square tubes are affected in the central region (150 mm in length) and essentially exhibit two modes of failure: Mode I failure (permanent large deformation) and Mode IIc failure [tensile

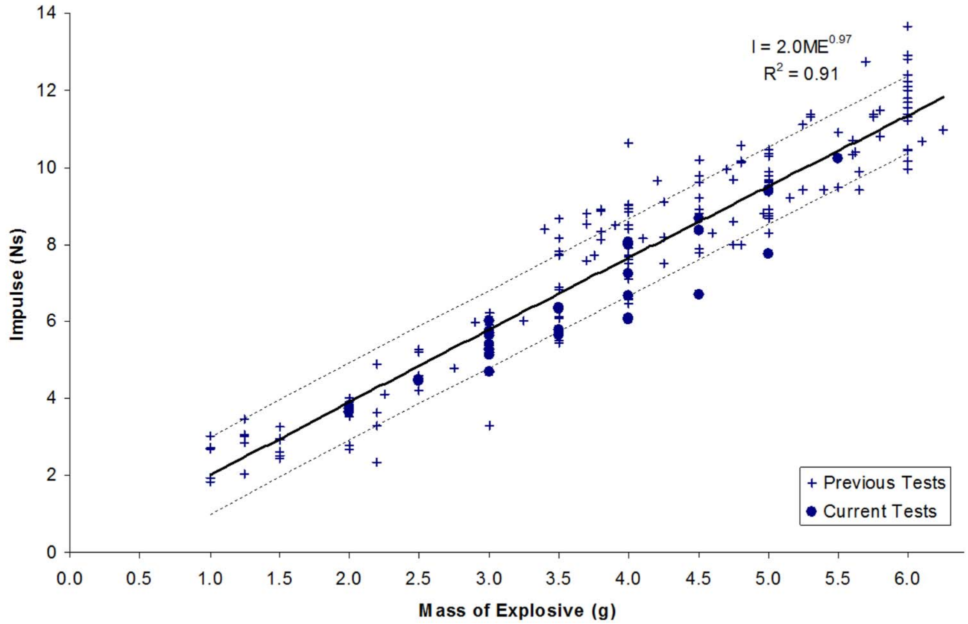

Fig. 2 Graph of the impulse versus mass of the explosive for ME ranging from 1 g to 6 g

tearing at in the central area of the tube where the load is applied—a fragment—in the shape of a disk (also referred to as cap) is released in the central area] as defined by Chung Kim Yuen Nurick [20], Langdon et al. [23], and Nurick and Radford [25] for plate response to localized blast load. Other phases in the Mode I and Mode II failure region are also exhibited. These include Mode Itc, which designate thinning in the central area of the tube side where the fragment is about to be released, and Mode IIc* which is defined where partial tearing of the central area of the tube's side. Three different types of imperfections, non-touching domes, rebound domes, and capped domes, shown in Fig. 3, are induced. The masses of explosive used (impulse) to induce these imperfections are listed in Table 1.

(a) *Simple Mode I (nontouching domes)*. The opposite tube sides plastically deform in an oval dome shape without touching each other.

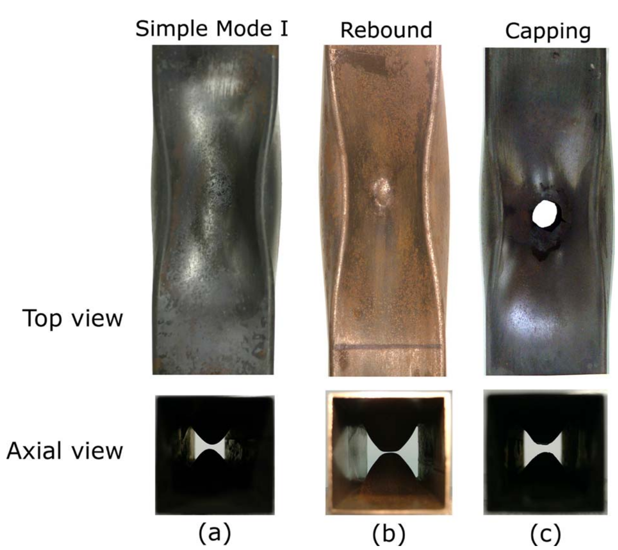

Fig. 3 Photograph showing the different modes of imperfections

(b) *Rebound domes*. The opposite tube sides plastically deform to such an extent that they make contact and rebound.

(c) *Capped domes (Mode IIc)*. The opposite tube sides plastically deform with a fragment (also referred to as cap), in the shape of a disk, and is released in the central area of the tube. This type of imperfection is similar to a circular cut-out with the region around the capped hole plastically deformed into a dish shape.

2.2 Quasistatic Axial Loading. The quasi-static crushing of the square tube is highly influenced by the geometry, boundary conditions, and material properties. A small set of experiments is carried out at a quasistatic rate on as-received and induced imperfections (blast and circular cut-outs) square tubes of the cross section 50×50 mm^2. These tests are performed, on a 200 kN rated Zwick testing machine that records the axial load-displacement histories at a constant preset cross-head speed, to provide a baseline to assess how the square tube would fold relative to their imperfections. The square tubes are 350 mm in length. The lower 50 mm end of the tube is fixed by means of a clamping rig, leaving a length of 300 mm to deform. The clamping rig is placed onto the moving bed of the test machine in such a way that the specimen is carefully positioned at the center of the cross-head with its end faces exactly perpendicular to the longitudinal axes. The specimen is then sandwiched against a flat stationary steel plug, which is parallel to the bottom clamping device to ensure a uniform distributed load. Fig. 4 shows a schematic of the quasistatic test setup.

Table 1 Range of masses of the explosive to induce imperfections

	∅17 mm		∅25 mm	
Simple Mode I (nontouching domes)	2.0–3.5 g	<6.7 N s	2.0–3.0 g	<5.8 N s
Rebound domes	N/A		3.5 g	6.7 N s
Capped domes (Mode IIc)	4.0–4.75 g	>7.6 N s	4.5 g	>8.6 N s

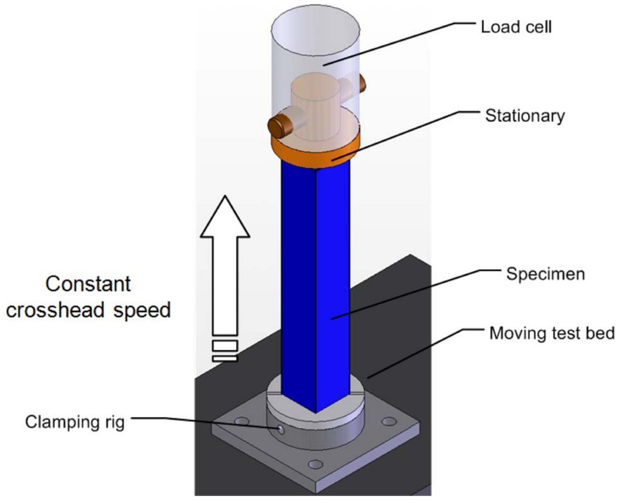

Fig. 4 Schematic of the quasistatic test setup

Table 2 Quasistatic crush test results for as-received square tubes

Specimen	Imperfection	CHS (mm/min)	P_{ult} (kN)	P_m (kN)	e_L (%)
Q001	None	15	103.37	32.73	31.66
Q002	None	15	104.52	36.38	34.81
Q003	None	15	105.58	37.39	35.41
Q004	None	30	107.34	34.99	32.59
Q005	None	45	109.62	33.06	30.16
Q006	None	60	104.75	33.52	32.00
Q007	None	75	111.12	33.17	29.85
Q008	None	90	108.85	33.36	30.65
Average			106.9	34.3	30.7

2.2.1 As-Received Square Tubes. Tests on the as-received tubes, listed in Table 2, are carried out at various cross-head speeds ranging from 15 mm/min to 90 mm/min. Tests on tubes with imperfections are performed at a constant cross-head speed of 15 mm/min. It is not considered necessary to vary the cross-head speed to crush the tubes with imperfections due to the minimal difference in buckling load. Crushing is stopped when the crushed distance reached 205 mm or when the collapse behavior becomes highly irregular.

Within the cross-head speed range, the ultimate buckling load and mean crushing load do not vary significantly (that is, within experimental variation). A nominal ultimate buckling load of 106.9 ± 5 kN and a nominal mean crushing load of 34.3 ± 3 kN are obtained for as-received square tubes. The load efficiency ($e_L = P_{\mathrm{ult}}/P_m$) average, as defined by Arnold and Altenhof [18], is 30.66%. It is also observed in Fig. 5 that the tubes crush progressively in a symmetric mode irrespective of the cross-head speed.

The sequential development of lobes in an as-received mild steel square tube subjected to a quasistatic axial load is shown in Fig. 6 with its corresponding axial force-displacement curve shown in Fig. 7. Sublabels (*a*)–(*e*) shown in Fig. 7 correspond to the different stages of the lobel development sublabelled (*a*)–(*e*) in Fig. 6. An ultimate peak load of 105.6 kN is reached prior to the formation of the first lobe. Thereafter, a repeated pattern of load-displacement behavior, which is associated with the sequential development of the lobe is exhibited, as expected. These subsequent "peak loads" are nominally 50% of the ultimate peak load. Each pair of peaks is associated with the development of a lobe. The mean crush load, calculated using the total area under the force-displacement curve divided by the crushed distance, is 37.39 kN.

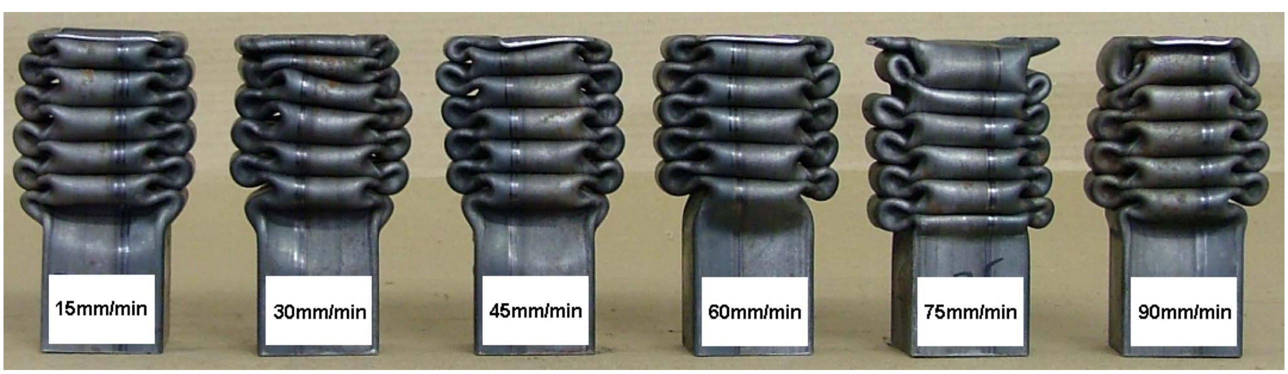

Fig. 5 Photograph showing as-received square tubes crushed quasistatically in the axial direction (increasing cross-head speed from left to right)

Fig. 6 Photograph showing the transient response of the quasistatically crushed as-received square tube

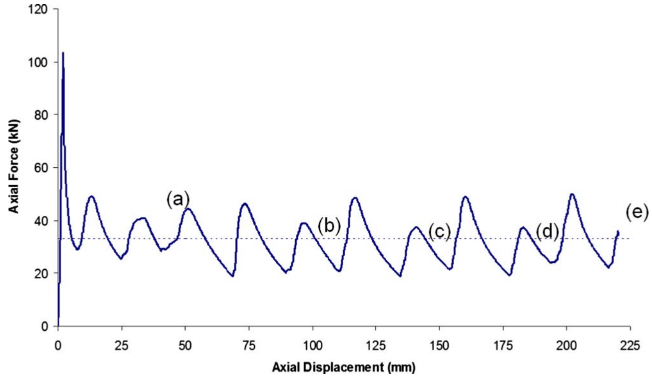

Fig. 7 Typical axial force-displacement graph for the quasistatically crushed as-received square tube

2.2.2 Induced Geometric Imperfection Square Tubes. Table 3 lists the results of the quasistatic tests performed on square tubes with induced imperfections. All the imperfections are induced using an explosive except for tubes with circular cut-outs.

2.2.2.1 Square tubes with circular cut-outs. The progressive development of lobes in a 50 mm square tube that has two holes cut-out subjected to quasistatic axial load is shown in Fig. 8. The holes are 12.5 mm in diameter and are located at the center of two opposite sides of the tube. The first lobe is developed at the center of the tube where the circular cut-outs are located. Thereafter, the tube buckles progressively toward the top end and later progresses toward the clamped end. Figure 9 shows its corresponding axial force-displacement curve obtained from the Zwick testing machine. Sublabels (*a*)—(*h*) shown in Fig. 9 correspond to the different stages of the lobel development sublabelled (*a*)–(*h*) in Fig. 8.

2.2.2.2 Square tubes with simple Mode I imperfections. Fig. 10 shows the transient response of a square tube with simple Mode I imperfections to a quasistatic axial load. The domes, a result of detonating two 3 g charges of explosives with a load diameter of 17 mm on two opposite sides of the tube, have a nominal depth of 16.5 mm. The tube starts to fold at its midlength where the dents are formed. Subsequent folds are developed in the top half of the tube before progressing at the lower end of the tube. The first lobe (at the tube midlength) is larger than the sub-

Table 3 Quasistatic crush test results for induced geometric imperfection square tubes

Specimen	Imperfection	CHS (mm/min)	Hole diameter (mm)	P_{ult} (kN)	P_m (kN)	e_L (%)
Q009	Circular cut-out	15	12.5	87.76	30.16	34.37
Q010	Circular cut-out	15	12.5	86.88	28.92	33.29
Average				87.3	29.5	32.8
Specimen	Imperfection (blast)	CHS (mm/min)	Dent depth [nominal] (mm)	P_{ult} (kN)	P_m (kN)	e_L (%)
S027	Dent	15	16.39	76.58	29.04	37.93
S046	Dent	15	16.55	76.11	31.54	41.44
S071	Dent	15	16.85	77.38	31.81	41.11
S070	Dent	15	17.42	76.27	32.51	42.62
S029	Dent	15	18.82	76.29	31.23	40.93
S073	Dent	15	21.02	73.42	30.30	41.27
Average				76.0	31.1	40.7
Specimen	Imperfection (blast)	CHS (mm/min)	Dent depth [nominal] (mm)	P_{ult} (kN)	P_m (kN)	e_L (%)
S077	Rebound	15	23.20	61.13	29.48	48.23
S041	Rebound	15	23.47	68.80	—	—
S025	Rebound	15	23.56	71.38	34.31	48.07
S078	Rebound	15	23.59	56.68	28.44	50.18
Average				64.5	30.8	48.8
Specimen	Imperfection (blast)	CHS (mm/min	Dent depth [nominal] (mm)	P_{ult} (kN)	P_m (kN)	e_L (%)
S040	Rebound (anneal)	15	24.53	57.40	27.03	47.1
Specimen	Imperfection (blast)	CHS (mm/min)	Cap diameter [nominal] (mm)	P_{ult} (kN)	P_m (kN)	e_L (%)
S045	Circular cap	15	11.5	71.83	32.40	45.10
S072	Circular cap	15	11.5	68.68	28.97	42.18
Average				70.3	30.7	43.6
S076	Oval cap	15	16	53.53	27.00	50.43
S079	Oval cap	15	16	54.03	25.19	46.62
Average				53.8	26.1	48.5

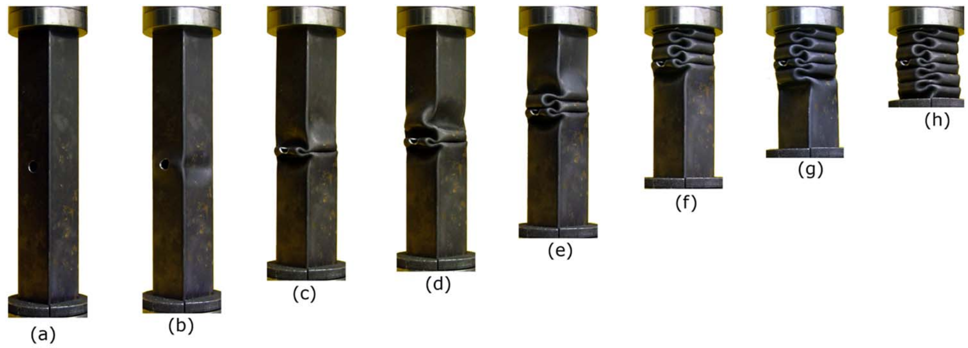

Fig. 8 Photograph showing the transient response of the quasistatically crushed square tube with circular cut-outs

sequent lobes as the domes collapse to touch each. Figure 11 shows the axial force-displacement curve obtained from the crush of the square tube shown in Figure 10. Sublabels (*a*)–(*h*) shown in Figure 11 correspond to the different stages of the lobe's development sublabelled (*a*)–(*h*) in Figure 10. An ultimate peak load of 76.1 kN is reached prior the formation of the first lobe. Thereafter, a repeated pattern of the load-displacement behavior of different load magnitudes which is associated with the sequential development of the lobe is exhibited. The mean crush load is 31.54 kN.

2.2.2.3 Square tubes with rebound imperfections. Figure 12 shows the transient folding mechanism of a square tube that has been subjected to two charges of 3.5 g explosive with a load diameter of 25 mm inducing rebound imperfections, with a maximum deflection of 23.5 mm. When the axial load is applied, the tube starts crushing at the imperfections. The rebounded domes touch each other forming two outward facing dimples. The first lobe is then developed at the top of the imperfection. Subsequent lobes progress to the top of the tube before continuing to the lower end of the tube. If the load is continually applied beyond the "stable" buckling, the crushing mode of the tube changes from progressive to Euler (tending to buckle to one side).

Figure 13 shows the axial force-displacement curve obtained from the crush of the square tube shown in Fig. 12. Sublabels (*a*)–(*g*) shown in Fig. 13 correspond to the different stages of the lobe's development sublabelled (*a*)–(*g*) in Fig. 12. The ultimate peak load, 71.38 kN, is reached before the formation of the first lobe. Thereafter, a repeated pattern of load-displacement behavior, which is associated with the sequential development of the lobe is exhibited. Unlike the as-received tube under a uniform axial load, the repeated peak loads for the tube with rebound imperfections are nominally 80% of the ultimate peak load. The mean load in this case is 34.31 kN.

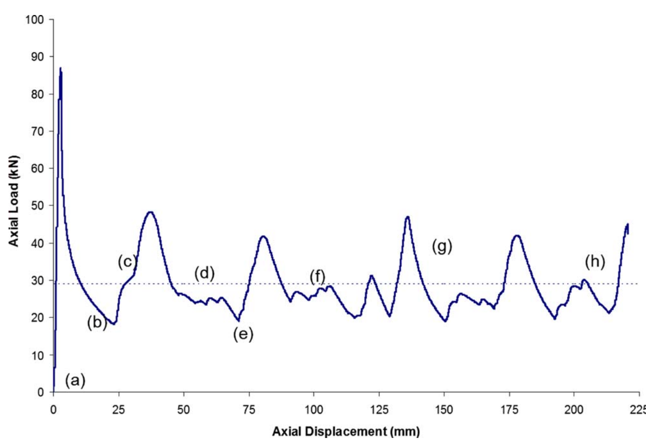

Fig. 9 Typical axial force-displacement graph for the quasistatically crushed square tube with circular cut-outs

2.2.2.4 Square tubes with capping imperfections. Figure 14 shows the transient folding mechanism of a square tube that has been subjected to two charges of 4.5 g of explosive with a load diameter of 17 mm, inducing capping imperfections. The holes are nominally 11.5 mm in diameter. When the axial load is applied, the tube starts crushing at the capped domes causing the two deformed sides to touch each other. The first lobe is then formed at the top of the imperfections. The lobe formation then progresses to the lower end of the tube. Any asymmetry in the tube imperfections causes the tube to buckle irregularly (in Euler mode).

The axial force-displacement curve obtained from the crush of the square tube shown in Fig. 14 is plotted in Fig. 15. Sublabels (*a*)–(*g*) shown in Fig. 15 correspond to the different stages of the lobe's development sublabelled (*a*)–(*g*) in Fig. 14. The ultimate peak load, 71.8 kN, is again reached before the formation of the first lobe. No clear repeated pattern of the load-displacement behavior, as observed for the as-received tube, is noticeable despite

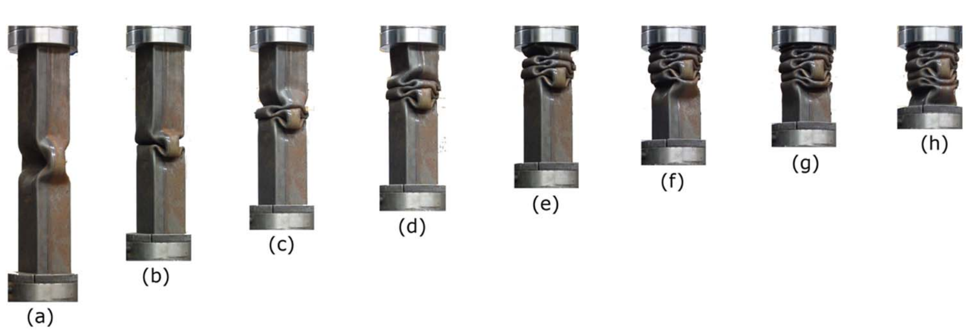

Fig. 10 Photograph showing the transient response of the quasistatically crushed square tube with simple Mode I imperfections (load diameter of 17 mm)

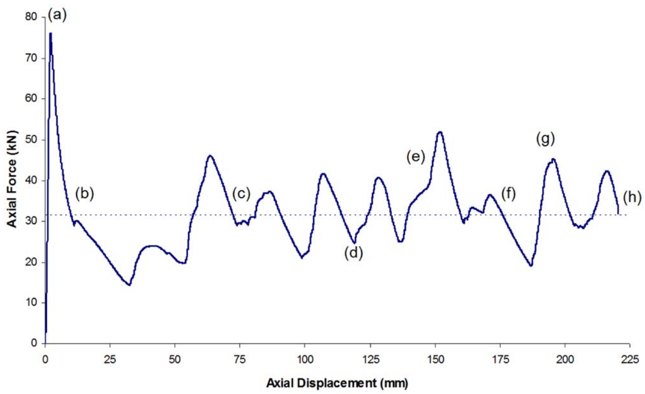

Fig. 11 Typical axial force-displacement graph for the quasistatically crushed square tubes with simple Mode I imperfections (load diameter of 17 mm)

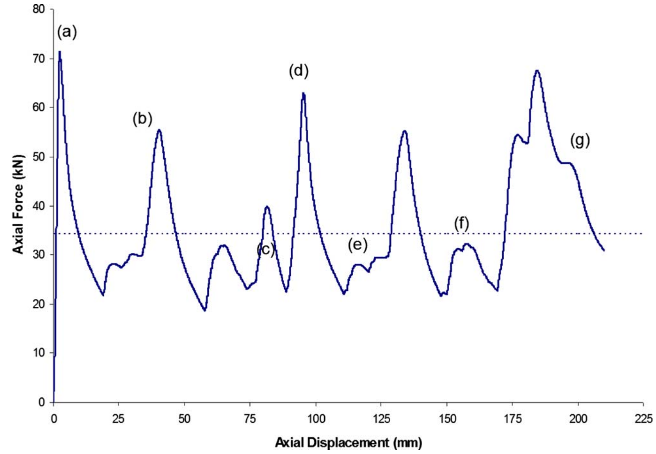

Fig. 13 Typical axial force-displacement graph for the crushed square tube with rebound dome imperfections

the subsequent development of lobes. However, the presence of "high" and "low" peaks of different magnitudes associated with lobe formation is observed. The mean crush load is 32.4 kN.

Not all the combined loading tests deform progressively. It is observed that numerous specimens start buckling progressively before showing signs of collapsing in either the Euler mode or askew, for example, specimens S079 and S029 shown in Fig. 16. The instability in the folding mechanism is the result of the asymmetric response to the blast loads despite the same blast loading condition. One side of specimen S079 caps while the other side of the tube is at the onset of capping. Upon buckling, the dome formed from the onset of capping folds into the cap causing the instability. The difference in the maximum deflection of the domes in specimen S029 is 0.65 mm. Whilst this difference in maximum deflection seems small the combined effect with its location and final deformed shape may have caused the skew lobe formation.

In cases where the imperfections are in the form of circular cut-outs and simple Mode I, lobe formation is initiated at the imperfections. In the cases of rebound and capping imperfections, the tube collapses in such a way that the dome first touches each other and compresses before the first lobe is formed at either above or below the dome induced by the blasts.

Figure 17 compares the deformed shape of 50 mm square tubes with and without imperfections that have been crushed quasistatically. All the tests are carried out at the same cross-head speed of 15 mm/min. The crushed as-received tube has the same number of lobes as the tube with circular cut-outs. Both tubes are crushed in symmetric mode. The tube with simple Mode I domes (nontouching "dome") has a similar crush shape to the tube with capping imperfections. The initial lobe (in the middle of the tube) of the tube with capping imperfections is larger than the simple Mode I dome tube. Skewed lobe formation is observed in the tube with capping imperfections as a result of the nonsymmetric imperfection. In contrast, the tube with the rebounded dome collapses symmetrically at the top and bottom of the tube. However, in the rebounded region of the tube, one side of the tube is observed to collapse outward while the other side collapses inward.

2.2.3 Mean Crushing Load. The total energy absorbed by the structure can be estimated by the product of the mean crushing load and the total crushed distance. It is therefore essential that the mean crushing load is not significantly reduced by the introduction of imperfections. The better energy absorber will have the higher mean crushing load (and the lower ultimate buckling load) over the same crushing distance.

Figure 18 compares the mean crushing load of the different tubes crushed quasistatically. There is no significant variation in the mean crushing force between the tubes with induced imperfection (average mean forces is shown by the dotted line in Fig. 18). The tube with oval cap imperfections that are nominally 16 mm in diameter has the lowest mean crushing load and the "as-received" tube, the highest. The mean crush load of the tube with circular cut-outs is less than those of the tubes with blast-induced imperfections by a magnitude of less than 1.6 kN (about 5% difference). In view of experimental scatter it is considered that the difference in magnitude is not high enough to draw any conclusions.

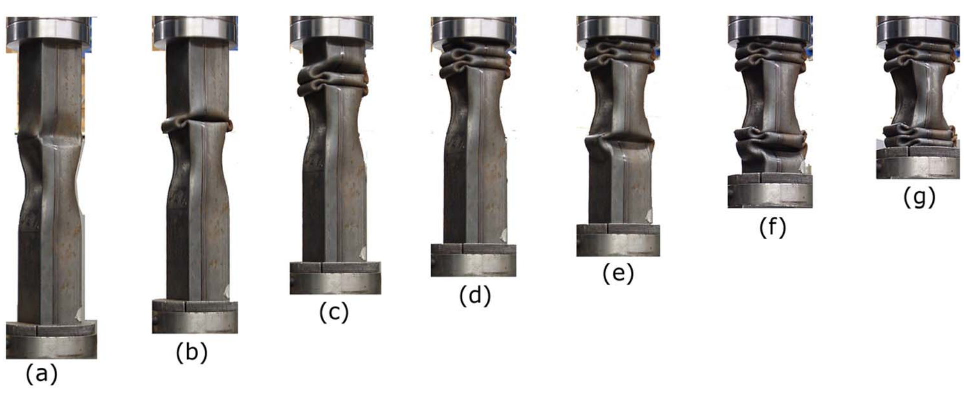

Fig. 12 Photograph showing the transient response of the quasistatically crushed square tube with rebound dome imperfections

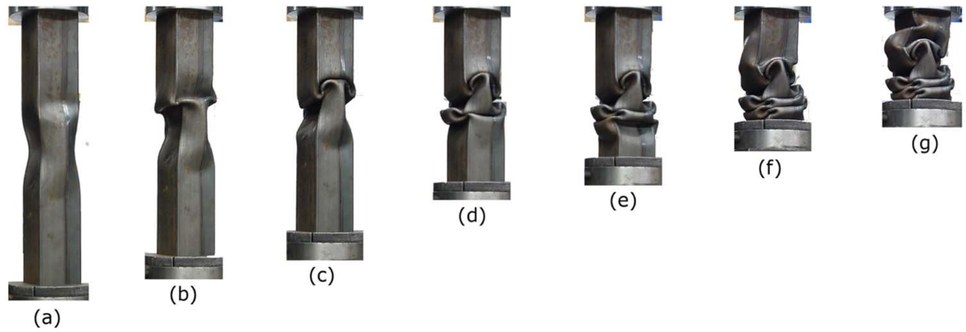

Fig. 14 Photograph showing the transient response of the quasistatically crushed square tube with capping imperfections (load diameter of 17 mm)

2.2.4 Ultimate Buckling Load. There are numerous theoretical calculations that enable the assessment of the energy absorbing capability of any structural design, which prohibit excessive damage in an impact event. In a crashworthiness application, while the duration of the impact and mean crushing load can be below the life-changing injury criteria threshold, the ultimate buckling load is often not the case. For better energy absorbers, it is ideal to have the ultimate buckling load below the injury threshold. Figure 19 compares the ultimate buckling load of the different tubes crushed quasistatically. There is a significant drop in the ultimate buckling load with the introduction of geometric imperfections, as expected. The tube with oval caps (nominal diameter of 16 mm) has the lowest ultimate buckling load. The tube with rebound imperfections has a lower ultimate buckling load than the tube with circular caps (nominal diameter of 11.5 mm).

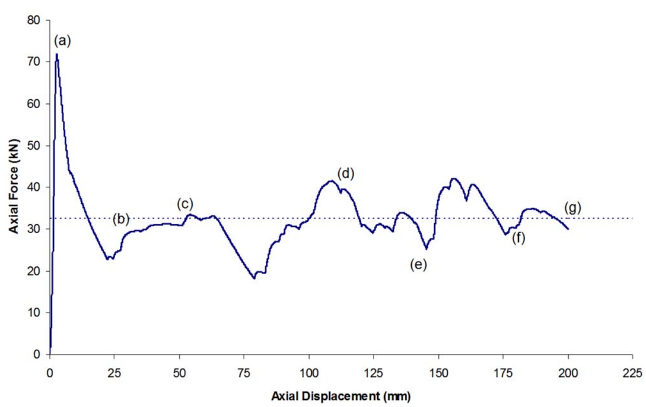

Fig. 15 Typical axial force-displacement graph of the quasistatically crushed square tube with capping imperfections (load diameter of 17 mm)

2.2.5 Load Efficiency, e_L. All the quasistatic tests are carried out until the tubes are crushed to the same distance, and hence have the same geometric efficiency as the tubes also having the same initial length. It is more meaningful, therefore, to evaluate the load efficiency (force efficiency) of each type of tube. The load efficiency, a measure of load fluctuations that occur during crushing, of the different tubes crushed quasistatically is shown in Fig. 20. High load efficiency denotes a low crushing force fluctuation, suggesting that the difference in the ultimate peak load and the mean crush force is not high. A high load efficiency thus is preferable as it suggests a constant deceleration of the impactor. The tubes with blast-induced imperfections, particularly those with oval caps or rebound domes, exhibit a high load efficiency. The tube with no imperfections has the lowest load efficiency.

2.3 Dynamic Axial Loading of Tubes. The test rig used for the dynamic impact testing is a 7 m high drop tester. The drop tester is located within the blast chamber to allow multiple loading conditions such as blast and axial impact loads.

The support arrangement (anvil) for the test specimens consists of two steel blocks of mass 430 kg each on the laboratory floor. The test specimens are clamped at the lower end by means of a clamping rig that is bolted to the top of one of the steel blocks by means of four bolts, as shown in Fig. 21. The clamping rig secures the bottom 50 mm of the specimens. To ensure a central impact, the striker and the anvil are aligned in such a way that the center of the striker matches the center bore hole of the anvil. The mass of the trolley can be varied. Prior to testing, the trolley is loaded

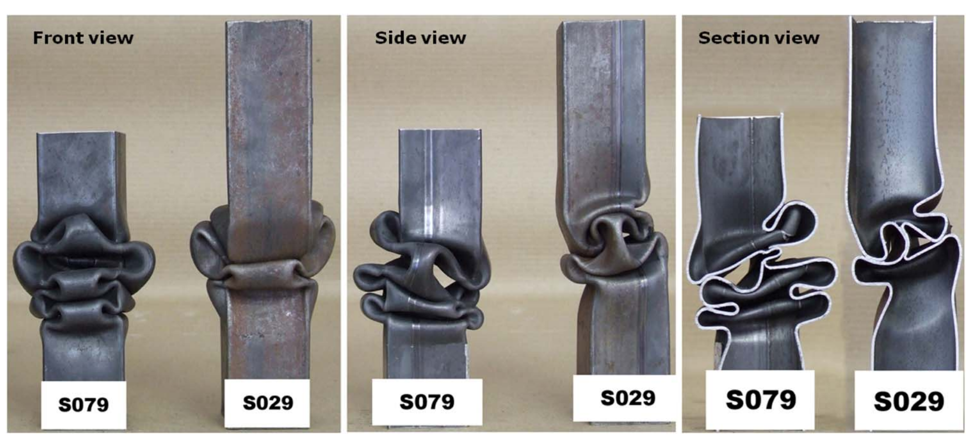

Fig. 16 Photographs showing the Euler buckling postprogressive collapse due to the skew lobe formation

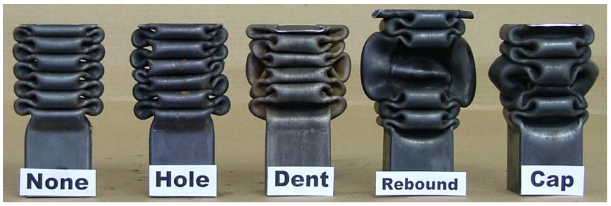

(a) Side view

(b) Front view

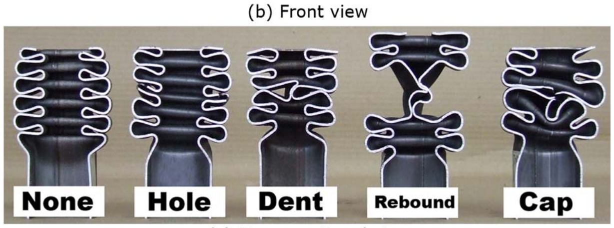

(c) Cross-sectional view

Fig. 17 Photograph showing square tubes with and without imperfections crushed quasistatically

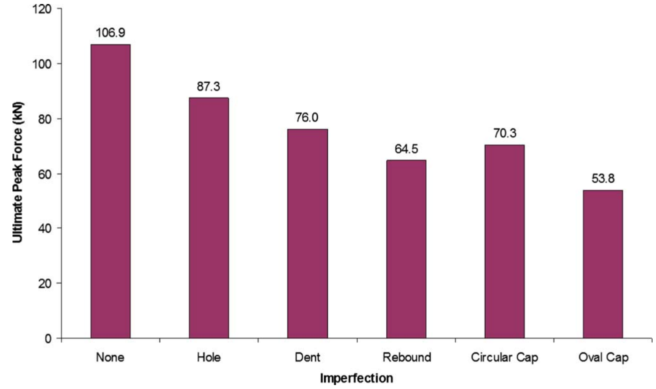

Fig. 19 Ultimate peak load of geometrically perfect and imperfect tubes crushed quasistatically

with the required drop mass and raised to the desired drop height. The trolley is released by a pneumatic piston and drops onto the free top edge of the tube under gravitational force.

Results from the dynamic axial loading tests are shown in Table 4 for the as-received tubes and in Tables 5–8 for tubes with induced imperfections. Figure 22 summarizes the results shown in Tables 3–8 by means of a graph of the crushed distance against the drop energy. Tubes with imperfections generally have a higher crushed distance than as-received tubes, shown by the trend line, for the same drop energy. Tubes that collapse in the unstable mode, as shown in Figure 23, are excluded in the tables of results. It should be noted that no experimental data measurement, for instance displacement, velocity, and acceleration history, is captured for the drop tests because the instrumentations required are expensive and unavailable. A qualitative analysis of the results is performed and compared with the quasistatic test results.

2.3.1 Simple Mode I Imperfection. Figure 24 shows the final buckled shape of three crushed tubes with different preblast imperfections. The two blast loads on opposite sides of the tube prior to the dynamic drop induces two simple Mode I imperfections. Figure 24(*a*) shows the final shape of an as-received tube crushed by a drop mass of 210 kg from a drop height of 5 m. Figures 24(*b*) and 24(*c*) show the final shape of two square tubes that are initially blast loaded with 3 g of explosives with load diameters of

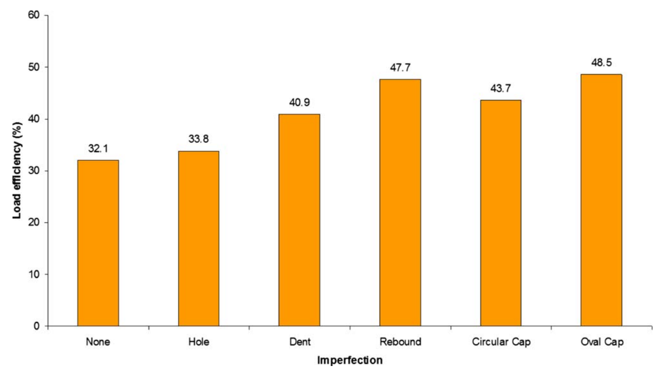

Fig. 20 Load efficiency of geometrically perfect and imperfect tubes crushed quasistatically

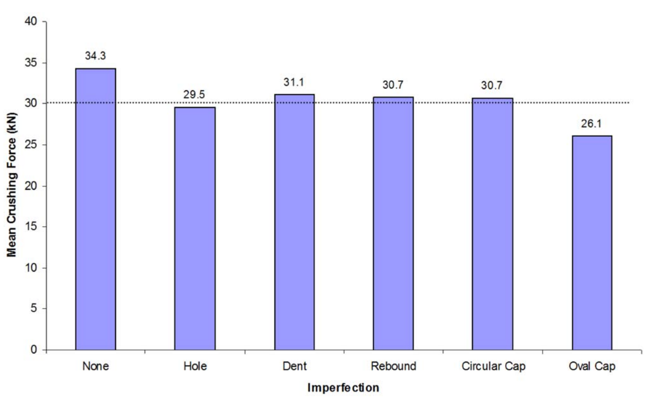

Fig. 18 Mean crush load of geometrically "perfect" and "imperfect" tubes crushed quasistatically

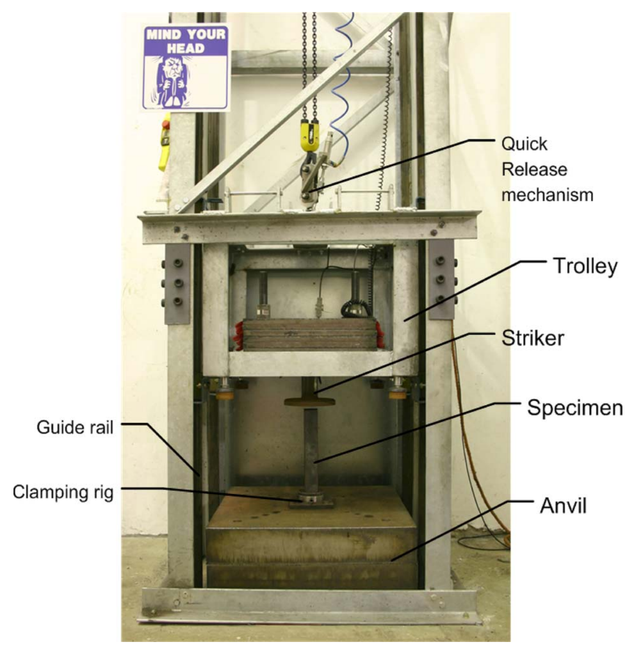

Fig. 21 Photograph of the dynamic axial crush setup

Table 4 Dynamic crush test results for as-received square tubes

Specimen	Width (mm)	Thickness (mm)	Drop mass (kg)	Drop height (m)	Calculated Impact velocity (m/)	Calculated Drop energy (kJ)	Measured crushed distance (mm)	Geometric effeciency (%)
S016	50	1.5	210.0	3.00	7.67	6.18	127.8	42.60
S014	50	1.5	210.0	5.00	9.90	10.30	235.5	78.50
S015	50	1.5	210.0	10.00	14.01	20.60	271.2	90.40
S022	50	1.5	214.0	1.00	4.43	2.10	39.1	13.04
S023	50	1.5	214.0	2.00	6.26	4.20	102.2	34.08
S024	50	1.5	214.0	3.00	7.67	6.30	110.8	36.92
S018	50	1.5	214.0	3.00	7.67	6.30	121.8	40.61
M001	50	1.5	265.3	2.19	6.55	5.70	116.6	38.87
M002	50	1.5	265.3	3.47	8.25	9.03	123.5	41.17
S060	50	1.5	265.3	3.47	8.25	9.02	133.2	44.40
S065	50	1.5	265.3	3.47	8.25	9.03	139.2	46.41
S064	50	1.5	265.3	3.49	8.28	9.09	143.7	47.90
M003	50	1.5	265.3	3.52	8.31	9.16	144.1	48.03
S062	50	1.5	265.3	3.52	8.31	9.17	144.2	48.08
S061	50	1.5	265.3	3.56	8.36	9.27	116.8	38.93
M004	50	1.5	265.3	4.21	9.09	10.96	175.2	58.40
M005	50	1.5	328.6	2.00	6.26	6.45	135.6	45.20
M009	50	1.5	328.6	3.00	7.67	9.66	182.2	60.73
M010	50	1.5	328.6	3.00	7.67	9.67	174.8	58.27
M016	50	1.5	328.6	3.00	7.67	9.67	176.8	58.93
M007	50	1.5	328.6	3.02	7.70	9.74	176.5	58.83
M008	50	1.5	328.6	3.05	7.74	9.83	187.5	62.50
M011	50	1.5	328.6	3.20	7.92	10.32	200.7	66.90
Q023	50	1.5	328.6	3.27	8.00	10.52	238.2	79.40
S082	50	1.5	328.6	2.51	7.01	8.08	190.5	63.51
M006	50	1.5	328.6	3.50	8.29	11.30	196.3	65.43
M012	50	1.5	328.6	3.50	8.29	11.29	200.8	66.93
M013	50	1.5	328.6	3.50	8.29	11.30	178.2	59.40
M014	50	1.5	328.6	3.51	8.30	11.31	196.5	65.49
M015	50	1.5	328.6	3.83	8.67	12.35	221.1	73.69
Q024	50	1.5	328.6	4.39	9.28	14.14	248.9	82.96
D006	50	1.5	329.8	3.26	8.00	10.56	220.1	73.36
D007	50	1.5	329.8	3.26	8.00	10.55	242.1	80.70
D009	50	1.5	329.8	3.26	8.00	10.55	239.5	79.83
D011	50	1.5	329.8	3.50	8.29	11.32	246.4	82.14
D013	50	1.5	329.8	3.50	8.28	11.32	245.1	81.69
D015	50	1.5	329.8	4.00	8.86	12.94	251.5	83.85

12.5 mm and 25 mm (equivalent to 5.8 Ns), respectively, before being axially crushed by a drop mass of 210 kg from a 4 m drop height. The difference in the crushed distance between tube (*b*) and the as-received tube (*a*) is insignificant despite the different drop heights hence suggesting that tube (*b*) is crushed with a lower mean force. Similar observation is made between tube (*b*) and tube (*c*). The bigger load diameter provided a dent over a bigger area (highlighted) making tube (*c*) a better energy absorber than tube (*b*). In the case of (*b*) and (*c*), the formation of the first lobe is accentuated by the imperfections causing the opposite

Table 5 Dynamic crush test results for square tubes with circular cut-outs imperfections

Specimen	Width (mm)	Thickness (mm)	Nominal hole diameter (mm)	Drop mass (kg)	Drop height (m)	Calculated Impact velocity (m/s)	Calculated Drop energy (kJ)	Crushed distance (mm)	Geometric efficiency (%)
D005	50	1.5	11.5	329.8	3.264	8.00	10.52	231.26	75.93
Q021	50	1.5	12.5	328.6	3.262	8.00	10.54	227.79	75.85
D003	50	1.5	12.5	329.8	3.262	8.00	10.56	231.47	72.72
D012	50	1.5	12.5	329.8	3.502	8.29	10.55	238.57	77.16
D017	50	1.5	12.5	329.8	3.751	8.58	10.56	242.60	77.09
D001	50	1.5	17	329.8	3.258	8.00	10.55	227.56	78.14
D016	50	1.5	17	329.8	3.504	8.29	10.55	236.12	72.57
D010	50	1.5	17.3	329.8	3.262	8.00	11.33	217.71	79.52
D008	50	1.5	25	329.8	3.262	8.00	11.32	234.42	77.43
D002	50	1.5	25	329.8	3.263	8.00	11.34	218.17	78.71
D014	50	1.5	25	329.8	3.498	8.28	12.14	232.30	80.87

Table 6 Dynamic crush test results for tubes with simple Mode I imperfections

Specimen	Width (mm)	Thickness (mm)	ME (g)	Load diameter (mm)	Nominal maximum deflection (mm)	Drop mass (kg)	Drop height (m)	Calculated Impact velocity (m/s)	Calculated Drop energy (kJ)	Measured crushed distance (mm)	Geometrice efficiency (%)
S002	50	1.5	2	12.5	9.34	210.0	5.00	9.90	10.30	233.4	77.80
S003	50	1.5	2	17	11.32	210.0	5.00	9.90	10.30	235.4	78.47
S011	50	1.5	3	17	17.94	210.0	5.00	9.90	10.30	238.6	79.53
S085	50	1.5	3	17	17.08	328.6	3.27	8.01	10.53	244.3	81.43
S009	50	1.5	3.5	17	21.34	210.0	4.00	8.86	8.24	185.5	61.83
S030	50	1.5	3.5	17	20.77	328.6	3.26	8.00	10.52	200.4	66.80
S074	50	1.5	4.5	17	21.99	328.6	3.26	8.00	10.52	236.6	78.88
S004	50	1.5	2	25	11.70	210.0	5.00	9.90	10.30	243.7	81.23
S012	50	1.5	3	25	19.97	210.0	4.00	8.86	8.24	233.8	77.93
S026A	50	1.5	3	25	21.79	328.6	3.27	8.01	10.53	245.2	81.73

sides of the tubes to touch. More contact between the opposite sides of the tube is visible for the specimen subjected to the bigger load diameter. In all cases, the tubes crush progressively, which is favorable to energy absorption.

The final buckling shape of the three tubes with blast-induced imperfections is shown in Fig. 25. The tube has different imperfections caused by different masses of explosives 17 mm in load diameter. The masses of the explosives used are 3.0 g, 3.5 g, and 4.5 g (equivalent to 5.8 N s, 6.7 Ns and 8.6 Ns) to induce simple Mode I imperfections that are 17.1 mm, 20.8 mm, and 22 mm in depth, respectively. An impact energy of 10.5 kJ (329 kg mass dropped from 3.26 m) is applied to each of these tubes. All three tubes crush progressively with a larger first lobe formed in the middle of the tube (at the location of the dome peak). Specimen S085, which has a dish dome with a depth less than 20 mm, exhibits a larger crush distance than the two tubes that have dish domes over 20 mm deep. The domes in specimen S085 are observed to rebound on the dynamic axial load to form two small outward facing dimples. The opposing domes in the other two tubes do not rebound onto each other but coalesce, causing an asymmetric collapse of the midsection of the tube. After the domes contact, specimen S030 is observed to collapse askew while specimen S074 collapses progressively.

2.3.2 Rebound Imperfections. The final buckling shapes obtained from the dynamic axial response of a tube that is crushed by a drop mass of 210 kg from a 4 m drop height (impact velocity 8.9 m/s) is shown in Fig. 26. The square tube is induced with blast imperfections using 3.5 g of explosives at a load diameter of 25 mm (equivalent to 6.7 Ns) to generate two rebound domes prior to the axial loading. When subjected to the dynamic axial load, the tube crushes symmetrically in a similar mode. The imperfections bounce outward to form two dimple shapes while symmetric lobes are progressively formed at both ends of the tubes.

2.3.3 Capping Imperfections. The final collapse shapes of square tubes with blast-induced imperfections crushed by a

Table 7 Dynamic crush test results for tubes with rebound imperfections

Specimen	Width (mm)	Thickness (mm)	ME (g)	Load diameter (mm)	Nominal rebound depth (mm)	Drop mass (kg)	Drop height (m)	Calculated Impact velocity (m/s)	Calculated Drop energy (kJ)	Measured crushed distance (mm)	Geometric efficiency (%)
S008	50	1.5	3.5	25	22.16	210.0	4.00	8.86	8.24	200.0	66.67
S091	50	1.5	3.5	25	23.1	329.8	3.26	7.99	10.54	230.0	76.65

Table 8 Dynamic crush test results for tubes with blast-induced cap imperfections

Specimen	Width (mm)	Thickness (mm)	ME (g)	Load diameter (mm)	Nominal cap diameter (mm)	Drop mass	Drop height (m)	Calculated Impact velocity (m/s)	Calculated Drop energy (kJ)	Measured crushed distance (mm)	Geometric efficiency
S010	50	1.5	4	17	11.1	210.0	4.00	8.86	8.24	201.7	67.24
S031	50	1.5	4	17	11.3	328.6	3.26	8.00	10.52	213.1	71.03
S013	50	1.5	4.25	17	11.2	210.0	4.00	8.86	8.24	203.0	67.67
S042	50	1.5	4.5	17	11.7	328.6	3.26	8.00	10.51	227.0	75.67
S043A	50	1.5	4.5	17	11.7	328.6	3.26	8.00	10.51	246.8	82.27
S044	50	1.5	4.5	17	11.5	328.6	3.27	8.00	10.53	226.0	75.33
S075	50	1.5	4.75	17	11.5	328.6	3.26	8.00	10.52	232.1	77.38
S086	50	1.5	4.75	17	11.9	328.6	3.26	8.00	10.52	239.2	79.72
S087	50	1.5	4.5	25	18.4	328.6	3.27	8.00	10.52	233.2	77.72
S089	50	1.5	4.5	25	18.0	328.6	3.27	8.00	10.53	247.8	82.58

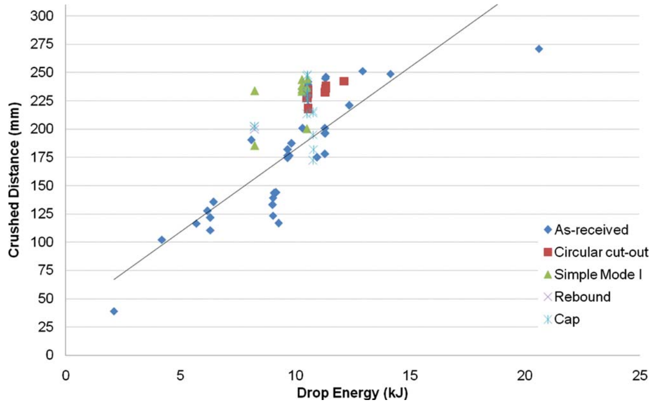

Fig. 22 Graph showing the crushed distance versus the drop energy for tubes with and without imperfections

Fig. 23 Photograph showing tubes collapsing in unstable mode (bolts included for photographic purposes)

329 kg mass dropped from a height of 3.26 m (impact velocity 8 m/s) are shown in Fig. 27. Prior to the dynamic axial load the square tube is subjected to two 17 mm localized blast loads of 4.5 g of PE4, equivalent impulses of 8.6 Ns each, to create two capping imperfections. Both specimens crush progressively which is very favorable to energy absorption with the same number of lobes that are similar in shape but different in size. The asymmetric collapse of the tube can be attributed to the asymmetric response to the blast loads.

2.3.4 Asymmetric Imperfections. Figure 28 shows the response of specimens S075 and S086 to two blast loads of 4.75 g of PE4 (equivalent to 9.1 Ns) followed a dynamic impact load of 329 kg dropped from 3.26 m. In both cases, the tube response after the blast is asymmetric with one side of the tube caps while the other side thins in the center (onset of capping) despite the same blast loading conditions. The size of the first lobe formed during the collapse of the specimen is bigger than the subsequent lobes. While the tube crushes progressively it buckles askew as a result of the initial asymmetric geometry caused by the blast loads. The number of lobes in both specimens is the same. There is, however, a difference in lobe size, which results in a 3% difference in crushed distance.

Figure 29 shows a photo of a series of drop tests carried out on 50 mm square tubes with induced geometric imperfections induced by circular cut-outs and 17 mm blast loads and without imperfections. The circular cut-outs are similar in size to that of the capping imperfections. All the tubes are subjected to having a 329 kg mass dropped from a nominal height of 3.26 m (impact

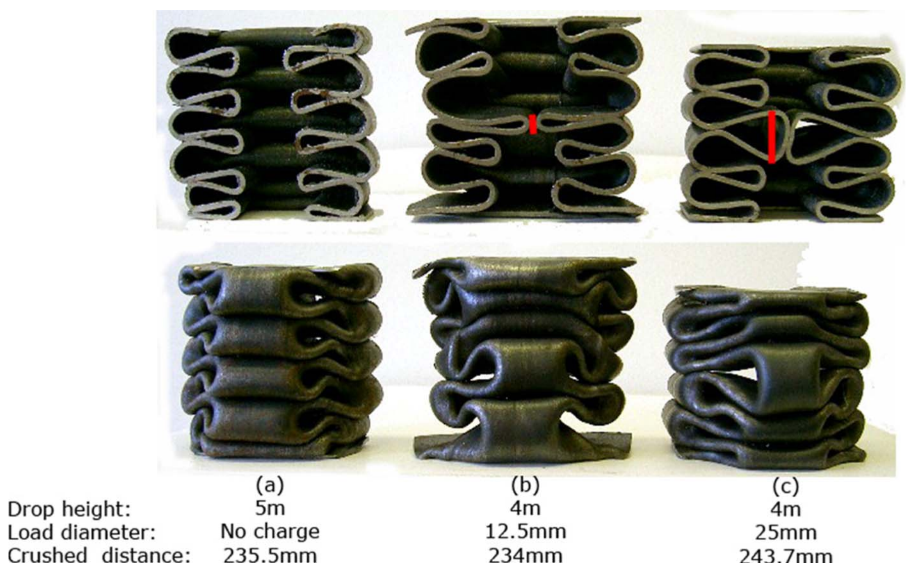

Fig. 24 Photographs showing dynamic axially crushed 50 mm square as-received and "blast-induced imperfections" tubes with drop mass of 210 kg (mass of explosive: 3 g)

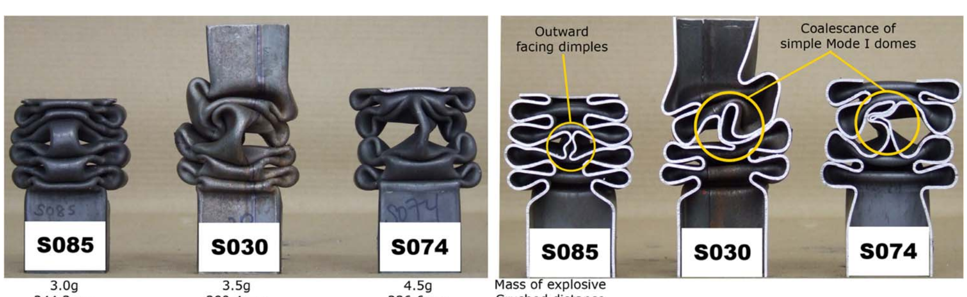

Fig. 25 Photograph showing dynamic axially crushed 50 mm square tubes, exposed to the explosive load 17 mm in diameter, from 3.26 m drop height with a drop mass of 329 kg

Fig. 26 Photographs showing the dynamic axially crushed blasted loaded 50 mm tube with a drop mass of 210 kg from a 4 m drop height (mass of explosive: 3.5 g, load diameter: 25 mm, crushed distance: 200 mm)

velocity 8 m/s). The tube with no imperfection is crushed 238.2 mm while the tube with the circular cut-outs is crushed 227.8 mm. There is an increase in crushed distance when imperfections created by 3 g of explosives (equivalent to 5.8 Ns) are induced. However, for tubes with imperfections induced by a mass of explosive greater than 3 g the crushed distance is less than the crushed distance of the as-received tube. Nonetheless, an increase in crushed distance with an increasing mass of explosive is observed for tubes with induced imperfections created by 3.5 g of explosives (equivalent impulse of 6.7 Ns) or higher. With the exception of tube S085, all the other tubes with explosively induced imperfections deform with skew lobe formation. The tube with the circular cut-outs is crushed by the same amount as the tube with imperfections caused by 4.5 g of explosives (equivalent to 8.6 Ns).

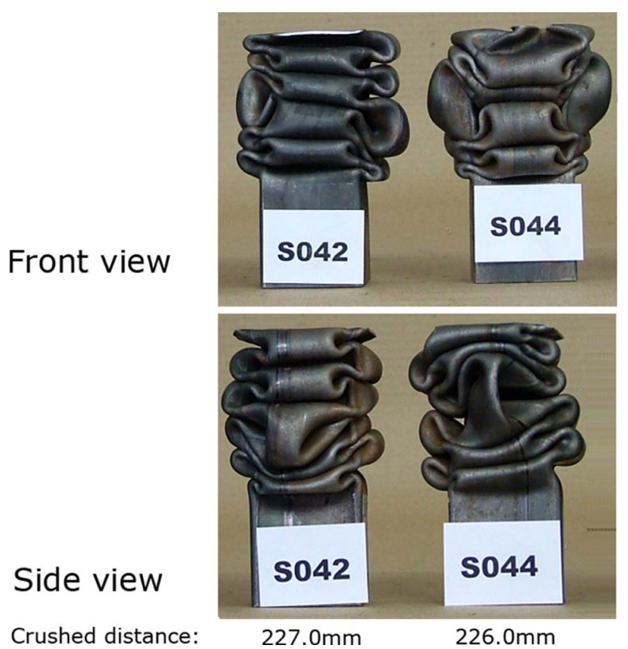

Fig. 27 Photographs showing the dynamic axial crushed 50 mm the square tubes with blast imperfection caused by a 4.5 g of PE4 at a load diameter of 17 mm (drop mass: 329 kg, nominal drop height: 3.26 m)

2.3.5 Geometric Efficiency, e_G. One way to assess the crashworthiness of the structures is to investigate its geometric efficiency. The geometric efficiency is the ratio of crushed distance to original length. Figure 30 shows the geometric efficiency of as-received tubes and tubes with different imperfections. In this case, all the tubes are subjected to the same impact load, 329 kg dropped from 3.26 m, to achieve an impact velocity of 8 m/s. For the same initial impact energy, the higher crushed distance or geometric efficiency suggests a lower mean crushed force. From Fig. 30, the tube with the simple Mode I imperfections (17.1 mm) in depth has the highest geometric efficiency as a result of the weakened structure. The tubes with rebound and capping imperfections are deformed to such an extent that collapse causes the opposite sides to contact each other and offer extra resistive force to the impact load. As a result the latter has a lower crushed distance, thus a lower geometric efficiency. It should be noted that the geometric efficiency will vary depending on the initial impact energy.

3 Discussion of Results

Figure 31 shows the final crush of quasistatic and dynamic loading of the tube with and without imperfections. All quasistatic tests are conducted at a nominal strain rate of 1.65×10^{-3} s^{-1} and stopped when the crushed distance reaches 205 mm. (The nominal strain rate is calculated using the equations suggested by Jones [30].) For the dynamic tests, the tube is crushed until the drop mass reaches equilibrium. The tube is subjected to an axial load resulting from a 329 kg mass dropped from a height of 3.26 m (impact velocity of 8 m/s) to obtain a nominal strain rate of 52.8 s^{-1}.

The quasistatic and dynamic tests can both be monitored in a controllable manner to achieve a desired final crush distance. While the quasistatic test can be stopped at any point during the crushing process, the dynamic test can be controlled by the loading conditions, drop height, and mass to crush by a specific amount. In Fig. 31, the global crush shape of the tubes subjected to either quasistatic or dynamic loads are compared. No significant difference is observed for the tube with similar imperfections.

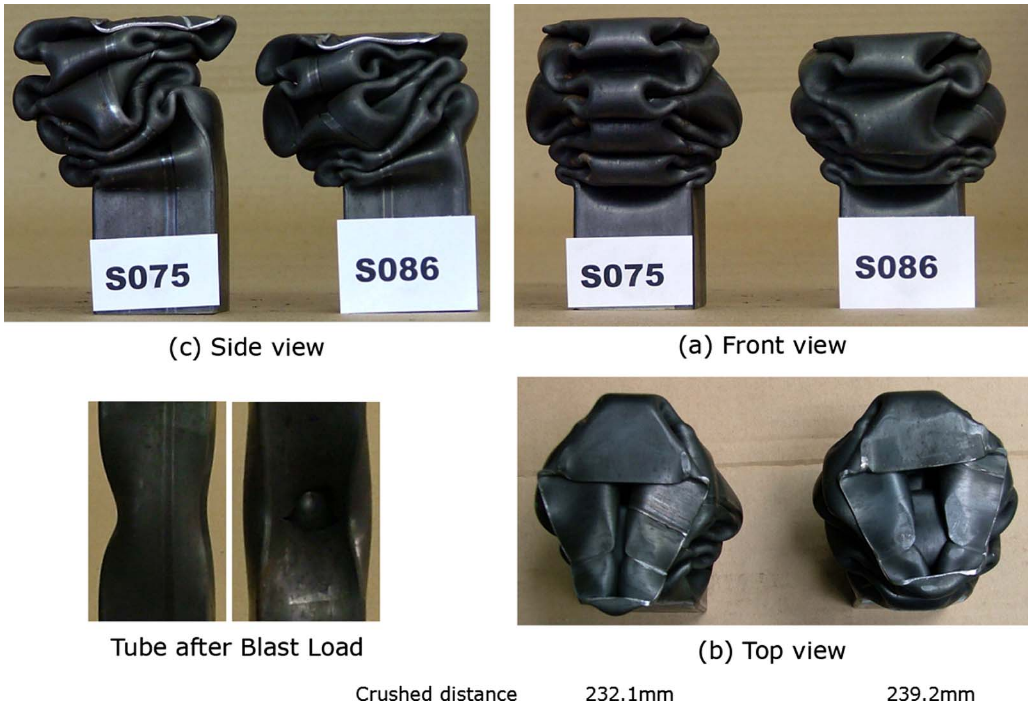

Fig. 28 Photographs showing the dynamic axial crushed 50 mm square tubes with blast imperfection caused by 4.75 g of PE4 at a load diameter of 17 mm (drop mass: 329 kg, nominal drop height: 3.26 m)

Fig. 29 Photographs showing dynamic axial crushed 50 mm square tubes with and without imperfections caused by an explosive of load diameter of 17 mm with a drop mass of 329 kg from a nominal height of 3.26 m (imperfections in tube Q021 are drilled holes)

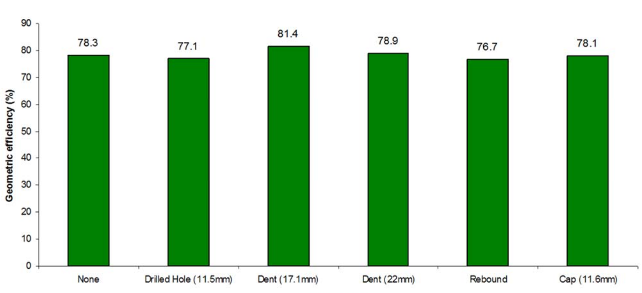

Fig. 30 Geometric efficiency of tubes with and without imperfections crushed dynamically

The transient response of the tube suggests from quasistatic tests and finite element simulations (see Part II) suggest that in both cases the crush is initiated at the imperfections.

4 Concluding Remarks

The introduction of the blast-induced imperfections at midpoints of the extruded tube affects its energy absorption characteristics but does not change its buckling mode (unless the blast-induced imperfections are asymmetrical). Irrespective of the size of the blast, as investigated, the magnitude of the first peak load is reduced. However, the mean crush force, crushed distance, and effective crushed distance are very dependent on the imperfections created by the blast loads. In all cases, the tubes with symmetric blast-induced imperfections buckle progressively.

Fig. 31 Photograph showing the comparison between quasistatically and dynamically crushed tubes

A tube with simple Mode I imperfections will start to collapse in such a way that the dome will try to touch each other, forming a lobe at the imperfection, before progressive lobes are formed alternatively at the impact end and clamp end of the tube. In the cases of rebound and capping imperfections, the domes are already in contact with each other. Progressive lobes are formed alternatively at both ends of the tube. If no more lobes can be developed and there is still more energy to absorb, the midsection of the tube tends to buckle in an Euler mode. The tubes with capping imperfections have, however, a higher tendency to changing buckling mode due to the different "cap" sizes and the location of the cap.

Acknowledgment

The authors are indebted to the workshop staff, in particular Mr. G. Newins, Mr. L. Watkins, and Mr. D. Jacobs of the Department of Mechanical Engineering of the University of Cape Town for manufacturing the test specimens and Mr. K. Balchin for his effort in designing and commissioning the drop tester. Thanks also go to Mr. P. Smith from the Department of Mechanical Engineering, Impact Research Center, University of Liverpool for his help with the initial drop test experiments. Participation in this project would not have been possible without the financial support from the National Research Foundation of South Africa (NRF), Technology Human Response Industry Programme (THRIP), and Armaments Corporation of South Africa (ARMSCOR).

Nomenclature

e_G = geometric efficiency
e_L = load efficiency
I = measured impulse
ME = mass of explosive
P = pressure
P_m = mean crush load
P_{ult} = ultimate peak force

References

[1] World Health Organization and World Bank, 2004, "World Report on Road Traffic Injury Prevention," Prevention, Geneva.
[2] Pugsley, A. G., and Macaulay, M., 1960, "The Large Scale Crumpling of Thin Cylindrical Columns," Q. J. Mech. Appl. Math., **13**(1), pp. 1–9.
[3] Alexander, J. M., 1960, "An Approximate Analysis of the Collapse of Thin Cylindrical Columns," Q. J. Mech. Appl. Math., **13**(1), pp. 10–15.
[4] Reid, S. R., 1993, "Plastic Deformation Mechanisms in Axial Compressed Metal Tubes Used as Impact Energy Absorbers," Int. J. Mech. Sci., **35**(12), pp. 1035–1052.
[5] Alghamdi, A. A. A., 2001, "Collapsible Impact Energy Absorbers: an Overview," Thin-Walled Struct., **39**(2), pp. 189–213.
[6] Jones, N., 2003, "Several Phenomena in Structural Impact and Structural Crashworthiness," Eur. J. Mech. A/Solids, **22**(5), pp. 693–707.
[7] Thornton, P. H., and Magee, C. L., 2008, "The Interplay of Geometric and Materials Variables in Energy Absorption," ASME J. Eng. Mater. Technol., **99**(2), pp. 114–120.
[8] Chung Kim Yuen, S., and Nurick, G. N., 2008, "The Energy Absorbing Characteristics of Tubular Structures with Geometric and Material Modifications: an Overview," Appl. Mech. Rev., **61**(2), pp. 020802-1–020802-15.
[9] Langseth, M., Berstad, T., Hopperstad, O. S., and Clausen, A. H., 1994, "Energy Absorption in Axially Loaded Square Thin-Walled Aluminium Extrusions," *Structures Under Shock Impact III (SUSI III)*, CMP, Southampton, pp. 401–410.
[10] Lee, S., Hahn, C., Rhee, M., and Oh, J. E., 1999, "Effect of Triggering on the Energy Absorption Capacity of Axially Compressed Aluminium Tubes," Mater. Des., **20**(1), pp. 31–40.
[11] DiPaolo, B. P., Monteiro, P. J. M., and Gronsky, R., 2004, "Quasi-Static Axial Crush Response of a Thin-Wall, Stainless Steel Box Component," Int. J. Solids Struct., **41**(14), pp. 3707–3733.
[12] Mamalis, A. G., Manolakos, D. E., Viegelahn, G. L., Vaxevanidis, N. M., and Johnson, W., 1986, "The Inextensional Collapse of Grooved Thin-Walled Cylinders of PVC Under Axial Loading," Int. J. Impact Eng., **4**(1), pp. 41–56.
[13] Gupta, N. K., and Gupta, S. K., 1993, "Effect of Annealing Size and Cutouts on Axial Collapse Behaviour of Circular Tubes," Int. J. Mech. Sci., **35**(7), pp. 597–613.
[14] Gupta, N. K., 1998, "Some Aspects of Axial Collapse of Cylindrical Thin-Walled Tubes," Thin-Walled Struct., **32**(1–3), pp. 111–126.
[15] Toda, S., 1983, "Buckling of Cylinders with Cut Outs Under Axial Compression," Exp. Mech., **23**, pp. 414–417.
[16] Kormi, K., Webb, D. C., and Montague, P., 1993, "Crash Behaviour of Circular Tubes with Large Side Openings," Int. J. Mech. Sci., **35**(3–4), pp. 193–208.
[17] Marshall, N., and Nurick, G. N., 1998, "The Effect of Induced Imperfections on the Formation of the First Lobe of Symmetric Progressive Buckling of Thin-Walled Square Tubes," *Structures Under Shock Impact V (SUSI V)*, Computational Mechanics, Southampton, pp. 155–168.
[18] Arnold, B., and Altenhof, W., 2004, "Experimental Observations on the Crush Characteristics of AA6061 T4 and T6 Structural Square Tubes With and Without Circular Discontinuities," Int. J. Crashworthiness, **9**(1), pp. 73–87.
[19] Chung Kim Yuen, S., and Nurick, G. N., 2005, "Experimental and Numerical Studies on the Response of Quadrangular Stiffened Plates—Part I—Subjected to Uniform Blast Load," Int. J. Impact Eng., **31**(1), pp. 55–83.
[20] Chung Kim Yuen, S., and Nurick, G. N., 2000, "The Significance of the Thickness of a Plate When Subjected to Localised Blast Load," 16th International Symposium on Military Aspects of Blast and Shock, (MABS 16), Oxford, UK,

pp. 491–499.
[21] Farrow, G. H., Nurick, G. N., and Mitchell, G. P., 1995, "Modelling of Impulsively Loaded Circular Plates Using the ABAQUS Finite Element Code," *Proceedings of the 13th Symposium Finite Element Methods in South Africa*, Stellenbosch, South Africa, Jan. 18–20, pp. 186–198.
[22] Jacob, N., Chung Kim Yuen, S., Bonorchis, D., Nurick, G. N., Desai, S. A., and Tait, D., 2004, "Quadrangular Plates Subjected to Localised Blast Loads—An Insight Into Scaling," Int. J. Impact Eng., **30**(8–9), pp. 1179–1208.
[23] Langdon, G. S., Chung Kim Yuen, S., and Nurick, G. N., 2005, "Experimental and Numerical Studies on the Response of Quadrangular Stiffened Plates—Part II—Subjected to Localised Load," Int. J. Impact Eng., **31**(1), pp. 85–111.
[24] Nurick, G. N., and Martin, J. B., 1989, "Deformation of Thin Plates Subjected to Impulsive Loading—A Review. Part II: Experimental Studies," Int. J. Impact Eng., **8**(2), pp. 171–186.
[25] Nurick, G. N., and Radford, A. M., 1997, "Deformation and Tearing of Clamped Circular Plates Subjected to Localised Central Blast Loads," *Recent Developments in Computational and Applied Mechanics: A Volume in Honour of John B. Martin*, International Centre for Numerical Methods in Engineering (CIMNE), Barcelona, Spain, pp. 276–301.
[26] Nurick, G. N., and Shave, G. C., 1996, "The Deformation and Tearing of Thin Square Plates Subjected to Impulsive Loads—An Experimental Study," Int. J. Impact Eng., **18**(1), pp. 99–116.
[27] Wharton, R. K., Formby, S. A., and Merrifield, R., 2000, "Airblast TNT Equivalence for a Range of Commercial Blasting Explosives," J. Hazard. Mater., **79**(1–2), pp. 31–39.
[28] Nurick, G. N., and Bryant, M. W., 1996, "Fragmentation Damage as a Result of an Explosion," International Symposium Plasticity and Impact Mechanics, New Delhi, India, pp. 484–498.
[29] Langdon, G. S., Cantwell, W. J., and Nurick, G. N., 2005, "The Response of Novel Thermoplastic-Based Fibre Metal Laminates—Some Preliminary Results and Observation," Compos. Sci. Technol., **65**(6), pp. 861–872.
[30] Jones, N., 1989, *Structural Impact*, Cambridge University Press, Cambridge.

The Crushing Characteristics of Square Tubes With Blast-Induced Imperfections—Part II: Numerical Simulations

S. Chung Kim Yuen[1]
e-mail: steeve.chungkimyuen@uct.ac.za

G. N. Nurick

Blast Impact and Survivability Research Unit (BISRU),
Department of Mechanical Engineering,
University of Cape Town,
Private Bag,
Rondebosch 7701, South Africa

This two-part paper presents the results of experimental and numerical work on the crushing characteristics of square tubes, with blast-induced imperfections, subjected to axial load. In Part I, the experimental studies are presented. The approach in the studies involves creating imperfections on opposite sides at midlength of a square tube by means of localized blast loads to create three types of imperfections: nontouching domes, rebound domes, and capped domes. These imperfections change the geometry and the material properties in the midsection of the tubes and hence affect the crushing characteristics. While the blast-induced imperfections enhance the energy absorption characteristics of the tubes they also affect the lobe formation process. In Part II, the finite element package ABAQUS/EXPLICIT *v6.5–6 is used to construct a $\frac{1}{2}$ symmetry model by means of shell and continuum elements to simulate the tube response to the localized blast loads followed by dynamic axial loading in the form of a rigid mass impacting at a specified initial velocity. The hydrodynamic code* AUTODYN *is used to characterize the localized blast pressure time and spatial history. The predictions show satisfactory correlation with experiments for both crushed shapes and crushed distance.*
[DOI: 10.1115/1.3005980]

Keywords: square tubes, imperfections, blast load, energy absorption

1 Introduction

Theoretical models of the response of tubular structures subjected to axial loading far outnumber experimental studies. Simple closed-form solutions can often provide a rapid and sufficiently accurate estimate of, for example, crushing distance and mean crushing load. According to Karagiozova and Jones [1], no clear classification on the influence of various parameters, such as geometries, loading conditions, and material properties, which cause the development of different dynamic buckling phenomena, has been made despite the numerous studies on both the static and dynamic responses of tubes. Finite element analysis has been widely applied to analyze the crushing of tubes, enabling parameters and boundary conditions, which are not accessible experimentally or analytically to be investigated. Consequently, this numerical tool has become an ideal instrument to gain a better understanding of the failure mechanism of tubular structures subjected to compressive loading conditions.

The different tubular response characteristics, such as peak load, fold length, axial compression, and energy absorption, have been studied using the numerous finite element techniques available. A few examples of the different finite element codes used to investigate these characteristics include the work of Langseth et al. [2,3], Otubushin [4], and Marsolek and Reimerdes [5] who used LS-DYNA. Abah et al. [6] and Markiewicz et al. [7] used PAM-CRASH. Miyazaki et al. [8] used the finite element package MARC K6.2. Nannucci et al. [9] and Karagiozova and co-worker [10–13] used ABAQUS. In most of the studies, an explicit integration scheme was used. However, the "implicit" finite element code MARC has also been used by Mamalis et al. [14] to simulate the crush behavior of cylindrical thin-walled composite tubes under static and dynamic axial compressions.

Karagiozova et al. [1,10,12,13,15–18], among others [3,4,7,19–21], have used numerical simulation to clarify the mechanics behavior and role of elastic and plastic stress waves and to explore the influence of the material properties, boundary conditions, and loading techniques on the energy absorbed and the buckling modes of axially crushed thin-walled structures. The influence of the material models, with respect to temperature effects at high strain rates, on the prediction of the response of aluminum alloy circular and square tubes was discussed by Karagiozova et al. [22].

Jensen et al. [23] and Karagiozova and Alves [24,25] have conducted numerous finite element studies to explore the transition between dynamic progressive buckling and global bending of thin-walled tubes, investigating the effects of geometry, material yield stress, strain hardening, and strain rate sensitivity.

The use of finite element techniques has also been extended to optimize different parameters with a view to obtain the ideal energy absorbers, with the aim to maximizing the specific energy absorption. Chiandussi and Avalle [26] and Nagel and Thambiratnam [27] optimized tapered tubular steel components. Other algorithms are carried out by Lust [28], Yamazaki and Han [29], and Avalle and co-workers [30,31] by applying structural optimization techniques using the response surface methodology. New types of trigger and multicell profiles with specific energy absorption 1.9 times larger than conventional square tubes in terms of energy absorbed and weight efficiency were developed by Kim [32]. Theobald and Nurick [33,34] numerically investigated the response of a novel lightweight panel, which comprised mild steel outer plates with thin-walled tubes as the core material to blast loads. The parametric study examined the effects and interaction between design variables (tube position, thickness and aspect ratio, and top plate thickness) in three different tube layouts.

[1]Corresponding author.

Contributed by the Applied Mechanics Division of ASME for publication in the JOURNAL OF APPLIED MECHANICS. Manuscript received February 3, 2008; final manuscript received July 29, 2008; published online June 17, 2009. Review conducted by Ashkan Vaziri.

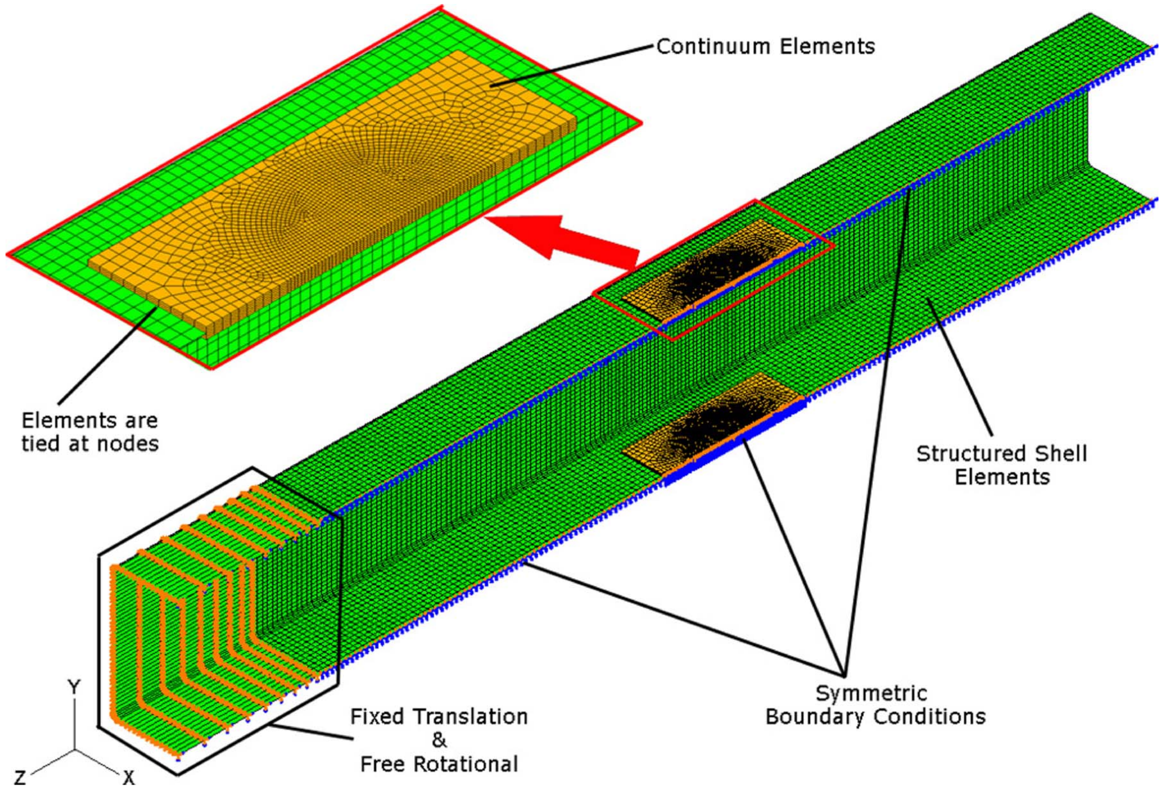

Fig. 1 $\frac{1}{2}$ **tube finite element (FE) model showing boundary conditions and assigned element type**

This paper presents the numerical simulation of square tubes with blast-induced imperfections subjected to dynamic axial load. With the lack of instrumentation in the experiments, the motivation for the numerical simulations was to obtain crushing axial force-displacement characteristics for square tubes with blast-induced imperfections. The numerical simulation is divided into two parts. First, an investigation using the hydrodynamic code AUTODYN to model the explosive interaction with a plane structure. The results obtained from the AUTODYN simulations are then applied to the explicit dynamic finite element program ABAQUS/EXPLICIT v6.5–6 to simulate the large inelastic deformation and tearing mode of the square tube due to the blast loads. The buckling mode of the square tube due to the dynamic impact load is also modeled using ABAQUS/EXPLICIT v6.5–6. The numerical predictions are compared with the experimental results reported in Part I.

2 Finite Element Formulation

The numerical analysis is carried out using the general-purpose finite element code ABAQUS/EXPLICIT v6.5–6, which incorporates nonlinear geometry, strain rate sensitivity, and temperature effects.

2.1 Model Geometry. A half-symmetric model of the tube is generated in such a way to capture a solution that would approach the exact solution within "reasonable" computational expenses. Four-noded shell elements (S4R) are used to model the tube as they have been proven, for example, by Langseth et al. [3] and Karagiozova [10–12], to provide results that correlate well with experiments for the crushing of tubes when subjected to dynamic and static axial loads. The shell elements, nonetheless, fall short to capture material data through the tube thickness.

An eight-noded, linear brick, 3D continuum element with reduced integration and hourglass control (C3D8R) as used by Wiehahn et al. [35,36] and Nurick and co-workers [37,38] is thus applied on two midsections of the square tube to capture not only the deformation of the tube as a result of the blast load but also the shear band failure through the tube thickness when "capping" occurs. The 3D continuum elements are developed in such a way that a finer mesh size is obtained in areas where capping is more like to occur and a coarser mesh is obtained to match the shell elements of the tube where the shell and 3D continuum elements are "tied" together at the nodes. Six layers of 3D continuum elements are used.

An assembly of the different elements used to model the tube with its assigned elements and boundary conditions is shown in Fig. 1. At the interface, the continuum elements are tied to the shell elements at the nodal points. Symmetric conditions are applied in the Y-Z plane. The lower part of the tube, which is clamped in the experiment, is fixed in the translational degree of freedom but is allowed to rotate.

2.2 Material Properties. Standard uniaxial tensile test specimens extracted from the mild steel tube profile, as shown in Fig. 2, are tested at different strain rates to give a static yield stress of 304 MPa. For an isotropic material, mild steel in the case of this study, the nominal stress-strain data obtained from uniaxial tests are converted to true stress and logarithmic plastic strain using

$$\sigma_{\text{true}} = \sigma_{\text{nom}}(1 + \varepsilon_{\text{nom}}) \tag{1}$$

$$\varepsilon_{\ln}^{\text{pl}} = \ln(1 + \varepsilon_{\text{nom}}) - \frac{\sigma_{\text{true}}}{E} \tag{2}$$

where σ_{true} is the true stress, σ_{nom} is the nominal stress, ε_{nom} is the nominal strain, $\varepsilon_{\ln}^{\text{pl}}$ is the logarithmic plastic strain, and E is Young's modulus.

As a result of necking, uniaxial stress-strain data obtained from tensile tests for mild steel are not valid beyond the necking point because of its large postnecking deformation. Bridgman [39] developed an analytical expression in order to obtain the effective stress and strain in the necked region. Bridgman's analysis uses geometric dimensions of the necked region to relate effective stress and strain to the measured values. Mirone [40] suggested a

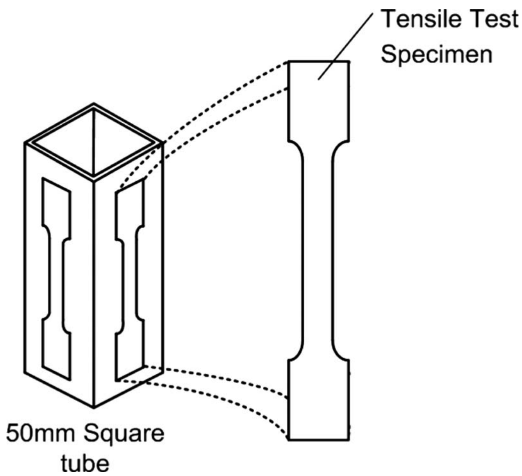

Fig. 2 Tensile test specimen extraction from the mild steel extrusion

similar analysis that achieves an error level less than half that obtainable with the Bridgman method. This method referred to as a MLR_σ function is dependent on the current value of the logarithmic strain and strain at necking initiation, which is a material constant.

The MLR_σ function is, thus, used to transform the true stress obtained from the tensile tests into an estimation of the equivalent stress averaged onto the neck cross section. The MLR_σ function is given by

$$MLR_\sigma(\varepsilon_{eq},\varepsilon_N) = 1 - 0.6058(\varepsilon_{eq} - \varepsilon_N)^2 + 0.6317(\varepsilon_{eq} - \varepsilon_N)^3 - 0.2107(\varepsilon_{eq} - \varepsilon_N)^4 \quad (3)$$

where ε_{eq} is the current value of the logarithmic strain and ε_N is the strain at necking initiation.

Typical result of uncorrected and corrected true stress versus logarithmic strain is shown in Fig. 3. Strain rate effects on the material properties are incorporated using the Cowper–Symonds relationship given by

$$\frac{\sigma_y^1}{\sigma_0} = 1 + \left(\frac{\dot{\varepsilon}}{\dot{\varepsilon}_0}\right)^{1/\eta} \quad (4)$$

where σ_y^1 is the dynamic yield stress, σ_0 is the static yield stress, $\dot{\varepsilon}$ is the strain rate, $\dot{\varepsilon}_0$ and η are material constants, and $\dot{\varepsilon}_0 = 844\ s^{-1}$ and $\eta = 2.207$ are the values for common South African mild steel obtained by Marais et al. [41] from split-Hopkinson bar tests.

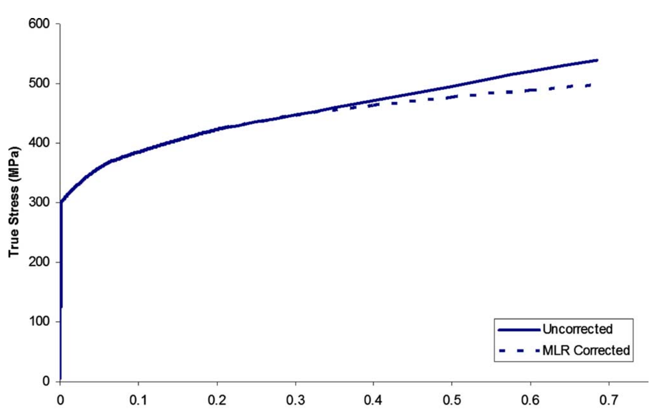

Fig. 3 Graph of true stress versus logarithmic strain

Temperature effects are incorporated using the variations of Young's modulus and yield stress as functions of temperature as proposed by Masui et al. [42] and applied by Nurick and coworkers [37,38]. The model is assumed to be adiabatic due to the very short duration of the blast ($\pm 2\ \mu s$) and the subsequent deformation ($\pm 300\ \mu s$) allowing very little heat to be transferred from the structure. It is assumed during adiabatic analyses that 90% of the plastic work is converted to heat (this is the default recommended by the ABAQUS/EXPLICIT user manual). A specific heat capacity of 450 J/kg °C is used in the model. The von Mises yield criterion with isotropic hardening is the constitutive model used. Moreover it is assumed that the density and the specific heat of the material do not change with temperature.

2.3 Modeling the Blast Load. The blast load, generated by the use of plastic explosive in the experiments, is modeled as a pressure applied to the exposed area of the square tube over a given time in the finite element model. The time is fixed by the explosive properties and geometry, but the pressure distribution and area over which it acts are complex. The modeling of the blast load is, however, simplified by certain assumptions.

The duration of the pressure distribution, t_{blast}, is calculated from the burn time of the explosive and the radius of the disk of explosive.

$$t_{blast} = \frac{R_0}{V_b} \quad (5)$$

where R_0 is the load radius, and V_b is the burn speed of the explosive, assumed to be 8200 m/s [43].

While Grobbelaar and Nurick [44] showed that an equation of state for the explosive can be incorporated into the model to simulate the pressure wave, it is also possible to approximate the pressure distribution. Within this approximation of the pressure distribution it is assumed that the pressure is applied for the blast duration, and that the pressure is constant over the area of the explosive and decays exponentially over the rest of the plate as reported by Bimha [45].

The pressure conditions are given as

$$P(r) = P_0 \quad \text{for} \quad 0 \le r \le r_{explosive} \quad \text{and} \quad 0 \le t \le t_{blast}$$

$$P(r) = P_0 e^{-k(r - r_{explosive})} \quad \text{for} \quad r_{explosive} \le r \le r_{plate} \quad \text{and} \quad 0 \le t \le t_{blast} \quad (6)$$

where $P(r)$ is the pressure as a function of the radial position r, P_0 is the pressure magnitude, and k is the exponential decay constant derived from empirical data.

Similar pressure-time loading characteristics were reported by Balden and Nurick [46] when the blast load is simulated using the hydrodynamic code AUTODYN 2D. However, unlike Bimha [45], Balden and Nurick [46] found that the constant pressure was distributed over a "burn radius" that is slightly smaller than the load radius. It was also found that the pressure decayed to a radius, referred to as r_p, which is less than the plate radius. In this paper a similar procedure to Balden and Nurick [46] is adopted.

Two Eulerian spaces to represent air and explosive interacting with a Lagrangian mesh occupied by the deformable plate, as shown in Fig. 4, are assembled as axisymmetric AUTODYN model to obtain the pressure-time loading characteristics. The air media is assumed to behave as an ideal gas. The Jones–Wilkins–Lee equation of state (JWL EOS) is specified for the C4/PE4 (plastic) explosive (as used in the experiments) material as defined in the AUTODYN material library. The response of the mild steel plate is of little significance in these simulations and is therefore simulated using the shock equation of state and Johnson–Cook strength models. These models are readily available in the AUTODYN extensive material library. Axisymmetry simulations for different load diameters are carried out to obtain the pressure distribution as a function of radius of the plate.

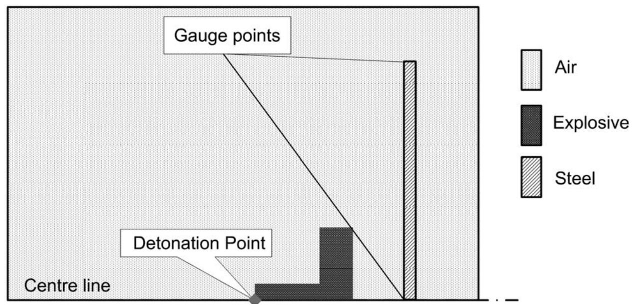

Fig. 4 Axisymmetric schematic of the localized blast of PE4 explosive, using AUTODYN 2D

During the simulation, the pressure history on the mild steel plate is recorded at 1 mm intervals along the plate radius. The pressure at discrete points along the plate radius increases sharply and thereafter decays in a more gradual fashion. The resulting plot of the normalized maximum pressure at the gauge points along the plate radius from the explosive center shows a pressure profile that resembles a constant pulse coinciding with the burn radius and subsequently decays in the assumed exponential manner and is described by Eq. (7), which is similar to Bimha's [45] approximation. This blast pressure, $P(r)$, is applied to the opposite sides of the square tube to simulate the blast load.

$$\begin{aligned} P(r) &= P_0 \quad \text{for} \quad 0 \le r \le r_b \quad \text{and} \quad 0 \le t \le t_{\text{blast}} \\ P(r) &= P_0 e^{-k(r-r_b)} \quad \text{for} \quad r_b \le r \le r_p \quad \text{and} \quad 0 \le t \le t_{\text{blast}} \end{aligned} \tag{7}$$

The burn radius, r_b, the exponential decay constant, k, and the zero pressure radius, r_p, are extracted from AUTODYN simulations. r_b, r_p, and k are found to be a function of the explosive radius and not mass. Table 1 shows the different values obtained for the different load diameters used.

The blast pressure distributed over the entire exposed surface related to the measured impulse is given by

$$I = 2\pi \int_{t=0}^{t_{\text{blast}}} \int_{r=0}^{r_p} P(r,t) r dr dt \tag{8}$$

where I is the measured blast impulse from experiment, and $P(r,t)$ is the axisymmetrical blast pressure as a function of radius, r, and time, t. The integration limits in Eq. (6) are for radius $r=0$ to $r=r_p$ and for the time interval $t=0$ to $t=t_{\text{blast}}$. The magnitude of the peak pressure, P_0, is solved by integrating and rearranging Eq. (6) and is given by

$$P_0 = \frac{I}{\pi t_{\text{blast}} \left[r_b^2 + 2\left\{ \left(\frac{r_b}{k} + \frac{1}{k^2} \right) - \left(\frac{r_p}{k} + \frac{1}{k^2} \right) e^{k(r_b - r_p)} \right\} \right]} \tag{9}$$

2.4 Loading Conditions. To model the response to blast loading, ABAQUS/EXPLICIT employs a multiple step concept to which the model is exposed. The model is first exposed to the blast pressure loaded followed by an unloading phase during which the tube deforms elastically as a result of inertia effects. To simulate the combined loading conditions, the finite element model is run in three different sequential steps:

(1) blast loading (apply blast pressure load)
(2) inertia effect due to blast loading (inertial response of tube)
(3) dynamic axial load (crushing of tube)

In the model, the rigid mass is set up in such a way to provide a space gap between the rigid body representing the mass and the strike end of the tube. The gap is set depending on the striking velocity to prevent the drop mass from contacting the tube while the tube is being subjected to the first two loading steps representing the two opposite blast loads.

2.5 Contacts. In order to simulate the interactions between the tube walls and the rigid drop mass, contact in the form of "self-contact" is defined for the whole model to allow both the inside and outside walls of the tubes to interact with each other and the drop mass with the tube.

Self-contact is generally available in the context of surface folding and touching itself in ABAQUS/EXPLICIT. Contact elements are internally generated for each node on the contact surfaces to allow contact of all surface segments. A penalty is used to avoid overconstraining that will occur, for example, if the meshes on both sides of the interface match exactly since a node is simultaneously a master and a slave. The penalty contact algorithm has a weaker enforcement of contact constraints but allows for treatment of more general types of contact. The algorithm, nevertheless, conserves momentum between the contacting bodies.

Table 1 Values of r_b, r_p, and k obtained for different load diameters

Load diameter (mm)	r_b (mm)	r_p (mm)	k
17	6	18	328
25	11	23	307

3 Results of the Finite Element Simulations

3.1 Blast Loading. The transient response of the tubes to the two localized blast loads is illustrated in Fig. 5. The midsections of the tube are deformed creating the different blast-induced imperfections depending on the loading conditions. Figure 6 shows the results of finite element simulation and experiment for three types of imperfections. Good correlation is obtained for all types of imperfections. For the cases, of simple Mode I (Fig. 6(*a*)) and rebound dome (Fig. 6(*b*)) imperfections, the simulations predict similar deformed shapes and final maximum deflection. A range of temperature and strain values is used to categorize the tearing mode of failure as a result of the severe temperature rise in the region of fracture. A band of high temperatures as a result of greater adiabatic heating due to the increased strain rate and strain is formed in the region of fracture. In this regard, elements with temperatures above 500°C and strain exceeding 140% throughout the wall thickness are considered as torn. Similar criteria were used by Nurick and co-workers [37,38]. Figure 6(*c*) shows good agreement with the experiment for capping imperfections. Because of the symmetry conditions applied in the model, the prediction fails to show any asymmetric responses observed in the experiments.

The numerical simulations also failed to predict capping imperfections for the 25 mm load diameter as observed in the experiments. Rebound imperfections are predicted in these cases.

3.2 Combined Loading

3.2.1 Simple Mode I Imperfections. The final buckling shape for a 50 mm square tube subjected to a dynamic axial load of 210 kg dropped from 5 m (impact velocity 9.9 m/s) is compared with that obtained from numerical predictions in Fig. 7. Prior to the axial impact, the tube is induced with imperfections created by two 25 mm localized blast loads of 2 g of PE4 (equivalent to 3.9 Ns). The overall buckling shape is well described by the finite element prediction, showing the same number of lobes in the two cases shown. In Fig. 7(*a*) the model is simulated with a clamping area and in Fig. 7(*b*) the clamping area is omitted as in the ex-

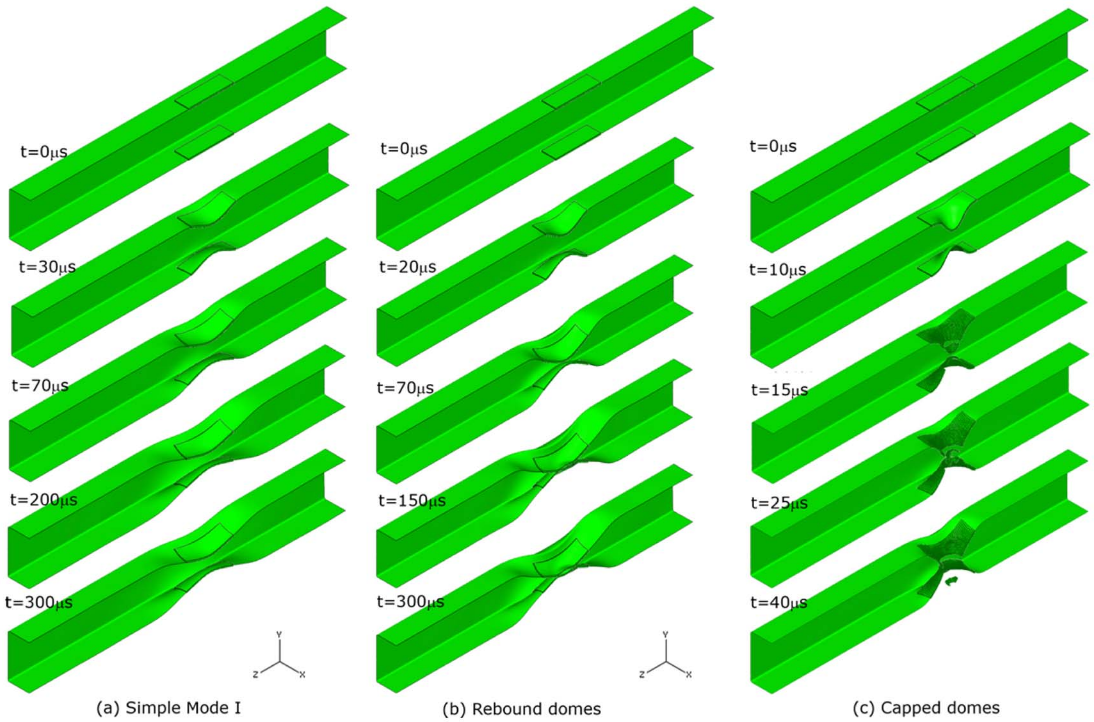

Fig. 5 Transient response of the tube to two localized blast loads (for all types of imperfections)

periment. The predicted result shows a crushed distance within 5% of the experiments, hence showing good correlation. Rebound of the opposing domes is predicted but not observed experimentally.

Figure 8 shows the buckling progression of the tube with simple Mode I imperfections. The impacting mass causes the tube to first collapse in such a way that opposing Mode I domes touch each other and then rebound before the first lobe is formed below the imperfection (relative to the impact end—top) at point *A*. Subsequently two lobes are formed above the Mode I dome followed by a fourth lobe beneath the first one. The impact event lasts for 51 ms.

3.2.2 Rebound Imperfections. The experimentally and numerically predicted buckling shapes are shown in Fig. 9 for a square tube subjected first to two opposing 3 g of PE4 blast (impulse per blast: 5.8 Ns) followed by the axial impact of 329 kg rigid mass at 8 m/s. The numerical prediction shows the bulging outwards of the blast-induced imperfection (referred to as a "rebound dome") and two sets of lobes at either side, in agreement with the deformed shape observed experimentally. The numerical prediction shows good correlation for crushed distance subsequent to axial loading but overpredicts the size of the rebound domes.

The transient predicted collapse mechanism of the square tube, shown in Fig. 9, is shown in Fig. 10. Prior to the dynamic axial load, two blast-induced imperfections form on opposite sides of the tube as a result of the applied impulsive loading. The first lobe is formed at point *A*, below the rebound dome (relative to the impact position). The second and third lobes are formed from point *B*, above the rebound dome at the impacted end. A fourth lobe is then formed beneath the first. Thereafter, the tube crushed in the middle region around the imperfections between points *A* and *B*. The rebound dome folds and increases in maximum deflection between 30 ms and 65 ms. The impact event is completed in 65 ms.

The comparison in final buckling shapes obtained from numerical predictions with the axial dynamic loading of a 50 mm square tube with a mass of 210 kg dropped from a height of 4 m (impact velocity of 8.9 m/s) is shown in Fig. 11. The square tube is in-

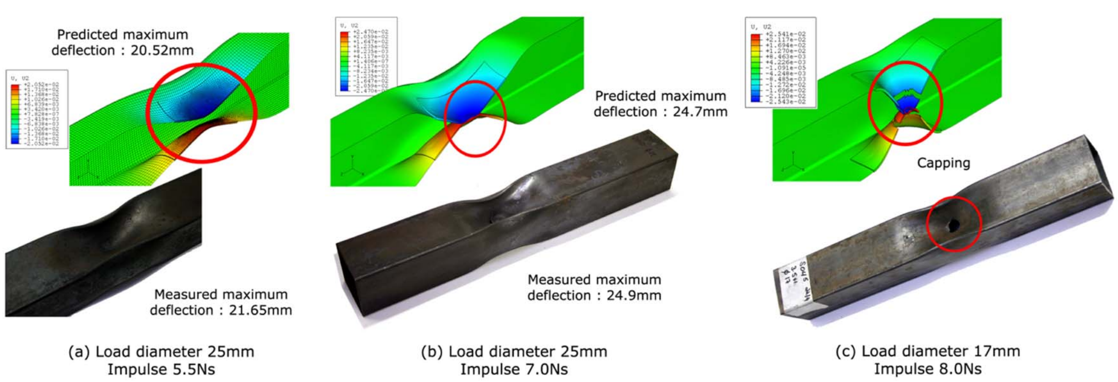

Fig. 6 Comparison of tube response to two localized blast loads (for all types of imperfections)

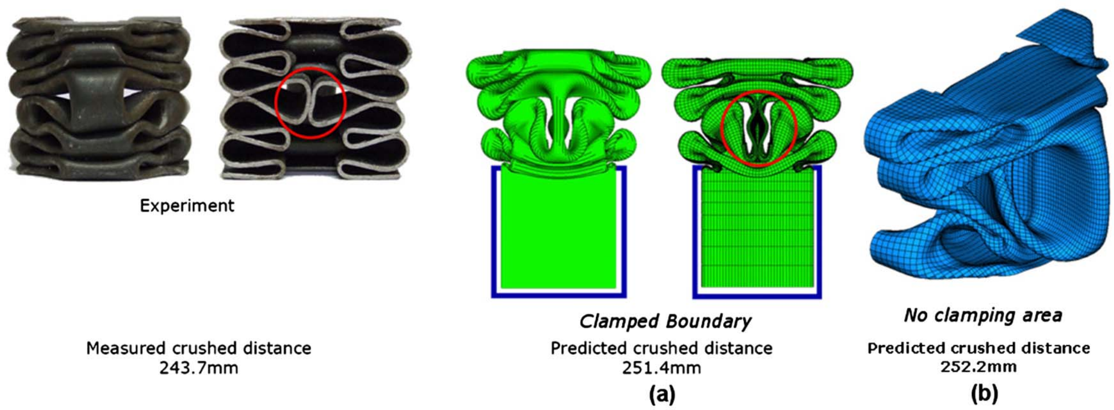

Fig. 7 Predicted collapse mode of a 50 mm square tube with simple Mode I imperfections created by two 25 mm blast loads (drop mass: 210 kg; drop height: 5 m)

duced with blast imperfections using 3.5 g of explosive at a load diameter of 25 mm (equivalent to 6.7 Ns) to generate two rebound domes prior to the axial loading. The numerical model predicts a rebound deflection of 23.22 mm, which compares favorably to the 22.16 mm obtained from the experiment. The overall crush behavior is well described by the numerical model irrespective of the inclusion or exclusion of clamping area as illustrated in Figs. 9(*a*) and 9(*b*) for both crushed shape and crushed distance.

The predicted transient collapse response is similar to that predicted for the 17 mm load diameter and to that observed during quasistatic loading of a tube with comparable imperfections.

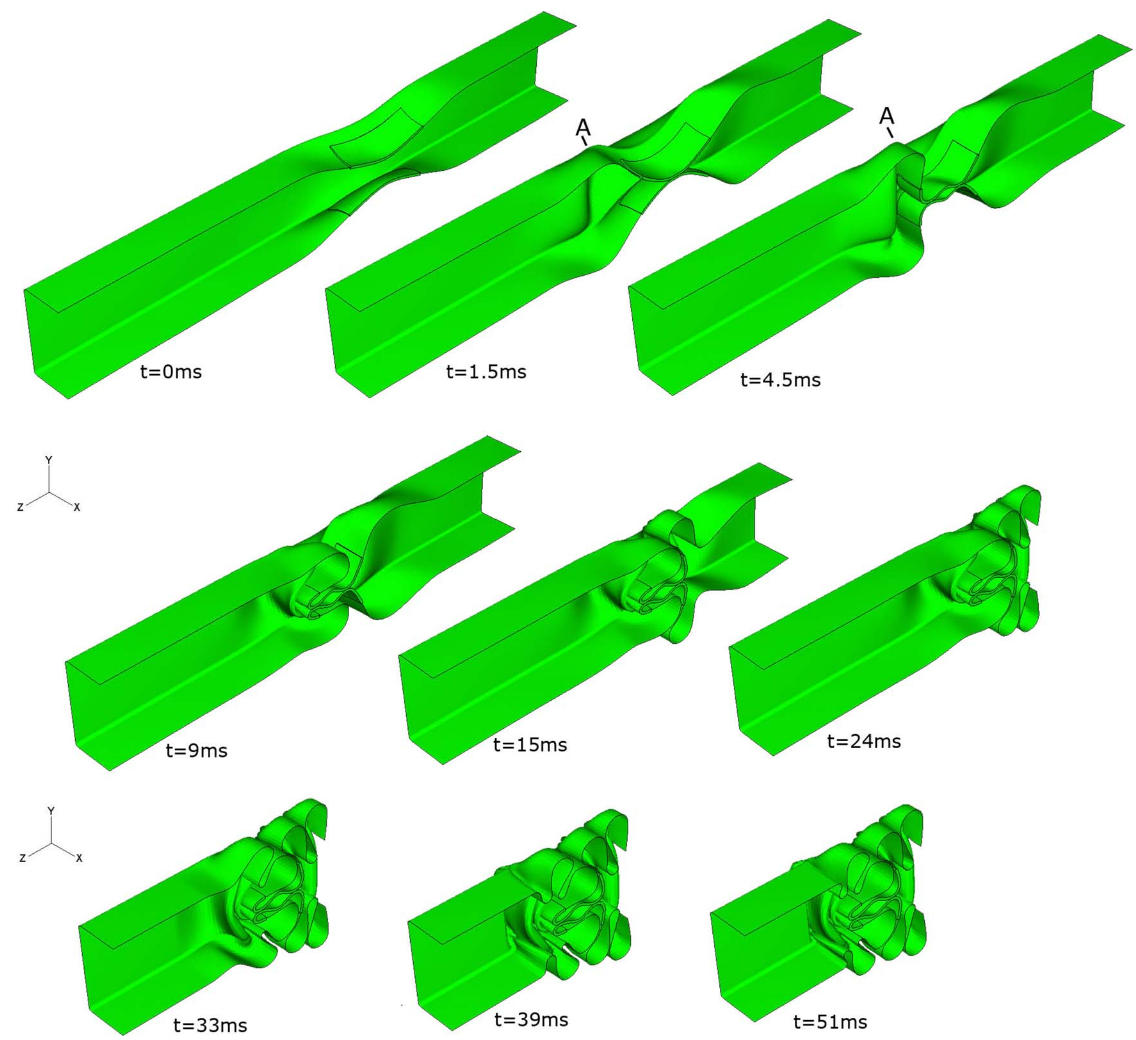

Fig. 8 Collapse sequences of a 50 mm square tube with simple Mode I imperfections created by two 25 mm blast loads (drop mass: 210 kg; drop height: 5 m)

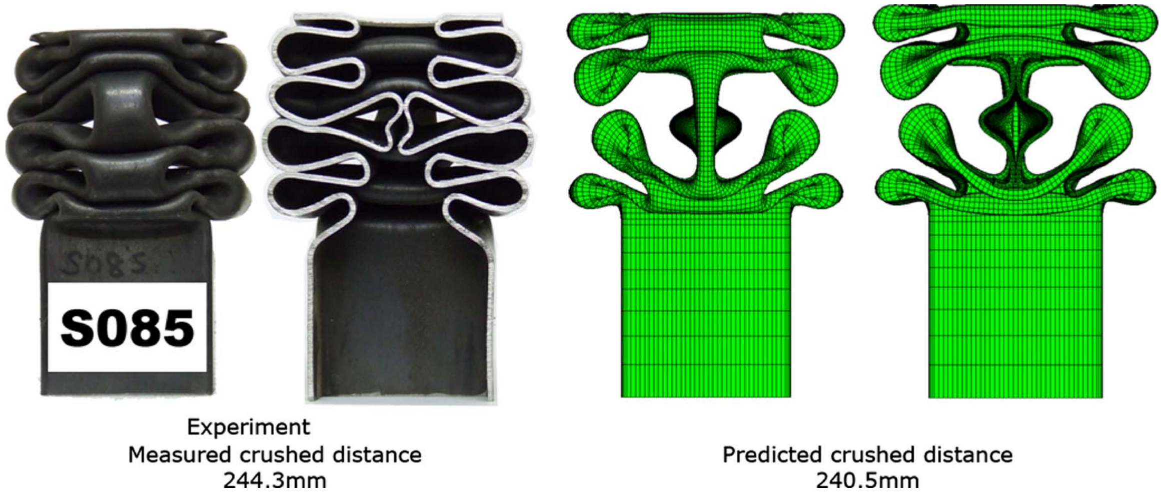

Fig. 9 Comparison of predicted collapse mode of a 50 mm square tube with induced rebound imperfections created by two 17 mm blast loads (drop mass: 329 kg; drop height: 3.27 m)

3.2.3 Capping Imperfections. The predicted folded shape of a square tube with blast-induced imperfections impacted by a 329 kg rigid mass at an impact velocity of 8 m/s (drop height of 3.27 m) is shown in Fig. 12. Prior to the dynamic axial load the square tube is subjected to two localized blast loads equivalent to 7.7 Ns impulses each at a load diameter of 17 mm, to induce capping imperfections. In the experiments, the tube is subjected to the same dynamic load but the capping imperfections are induced by two localized blast loads of 4.5 g of PE, each equal to 8.6 Ns at a load diameter of 25 mm. It should be noted that modeling capping imperfections followed by dynamic axial crushing is computationally very expensive despite element deletion for the solver in that particular version of ABAQUS/EXPLICIT. Only the elements that meet the failure criteria ($T > 500°\mathrm{C}$ and PEEQ $> 140\%$) are deleted. Within the cap there are elements that do not meet the failure criteria traveling away from the tube preventing the solution convergence within reasonable timeframe. Regardless of the blast loading parameters, the numerical simulation shows good correlation for the crushed shape and crushed distance for capping imperfections.

Figure 13 shows the predicted collapse mechanism of the square tube. The transient collapse response is similar to that observed for quasistatic loading of a tube with comparable imperfections. The tube first collapses in such a way that the capped

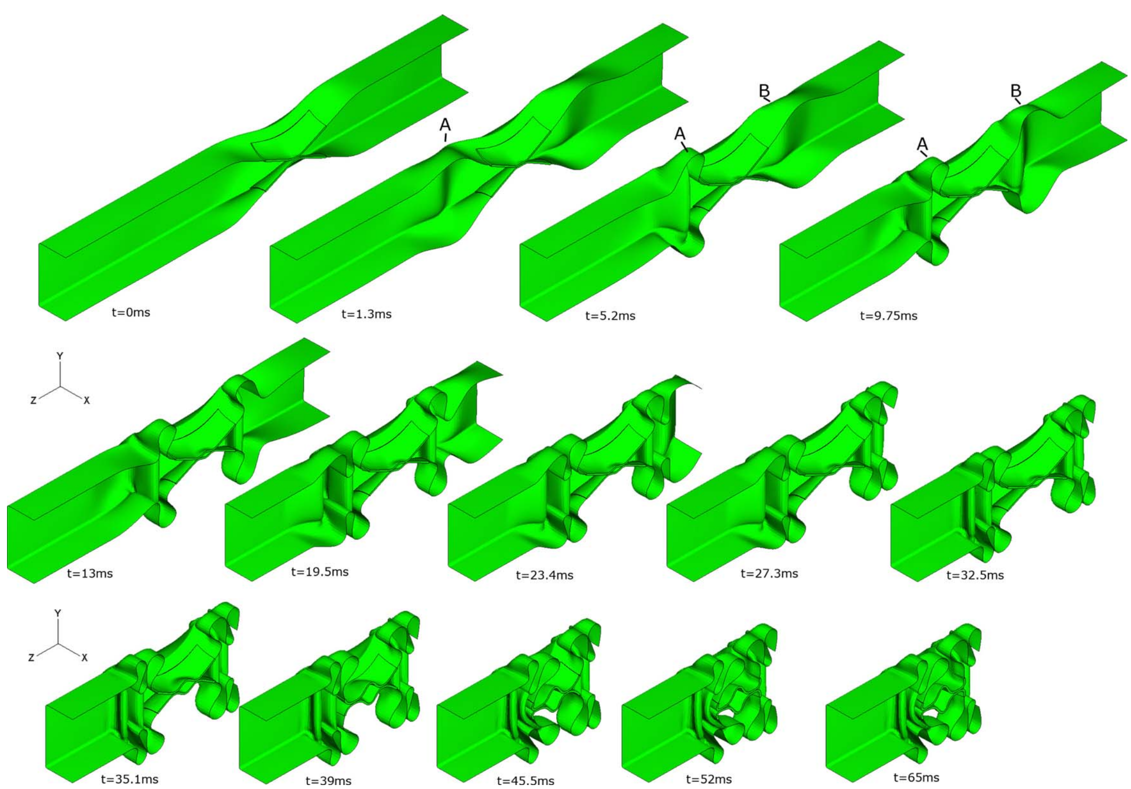

Fig. 10 Collapse sequences of a 50 mm square tube with induced rebound imperfections created by two 17 mm blast loads (drop mass: 329 kg; drop height: 3.27 m)

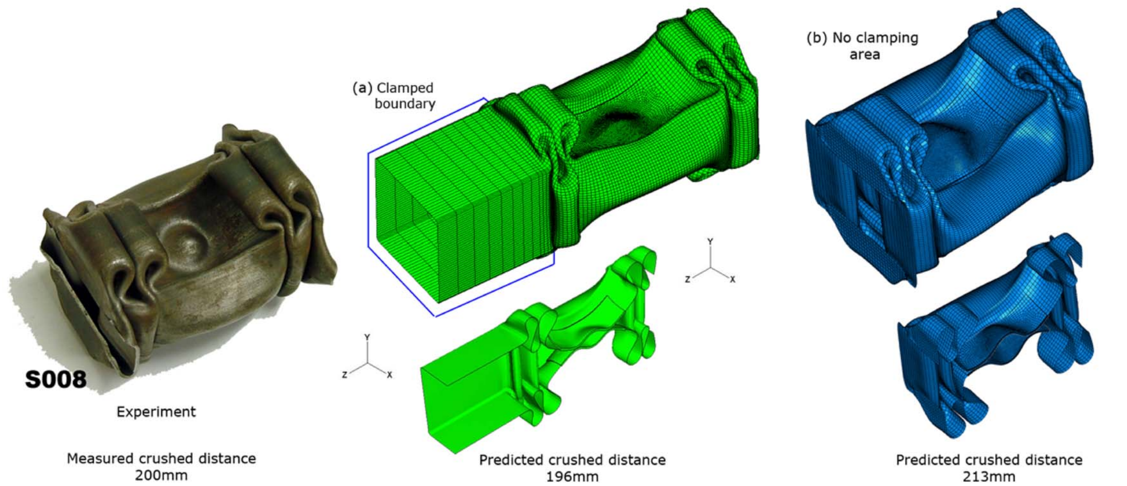

Fig. 11 Final collapse mode of a 50 mm square tube with rebound induced imperfections created by two 25 mm blast loads (drop mass: 210 kg; drop height: 4 m)

domes touch each other (as observed for simple Mode I imperfections) before the first lobe is developed below the capped dome at point *A* (relative to the impacted end). Subsequent progressive lobes are formed above and below the imperfection in alternate order. The impact event is completed in 63 ms.

Additional simulation predicting folded shape of tubes with capping induced imperfections, in which Cowper–Symond constants used to describe the strain rate sensitivity are $\dot{\varepsilon}_0=40.4\ \mathrm{s}^{-1}$ and $\eta=5$ [47], is shown Fig. 14. The tube is impacted by a 329 kg rigid mass at an impact velocity of 8 m/s (drop height of 3.27 m). Prior to the dynamic axial load the square tube is subjected to two localized blast loads of 4.5 g of PE4, equivalent impulses of 8.6 Ns each, to create capping imperfections. The numerical simulation is equivalent to experiments S042 and S044, with the experimental buckling shapes shown in Fig. 14(*a*). The finite element simulation, however, predicts buckled shape (shown in Fig. 14(*c*)) similar to that observed in experiment S086 for a slightly higher charge mass of 4.75 g PE4, shown in Fig. 14(*b*). The slight asymmetry is due to the element deletion process within the numerical solution, but it correlates favorably with "real" material failure. The predicted crushed distance is 225.1 mm compared with 239.2 mm obtained from experiments.

4 The Influence of Asymmetric Blast-Induced Imperfections

From experiments it is observed that several tubes displayed asymmetric response to blast loading despite applying the same loading conditions. This is most likely due to very small differences in the explosive charge location (relative to the tube walls) or minimal differences in the tube thickness and cross section caused by the extrusion process or small differences in applied impulse. Furthermore the mass of explosive at the same loading conditions does not result in identical impulse (experimental variation). Three examples of tubes exhibiting asymmetric response are shown in Fig. 15.

The results from the finite element model, hitherto, have shown symmetric response to the blast and axial loadings because any small variations in the loading or tube geometry that are found in practice are not modeled. In an attempt to model the asymmetric tube response three tubes are simulated and subjected to different localized blast loading conditions on the opposing sides. On the one side, the decaying pressure function (blast load 1) as described in Sec. 2.3 is applied. On the opposing side, a rectangular pressure pulse (blast load 2) is applied over the explosive radius.

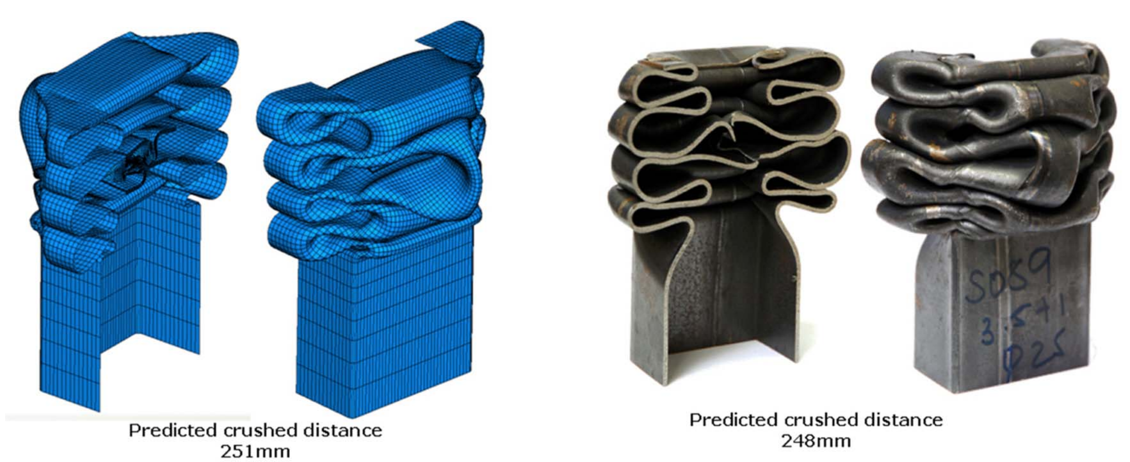

Fig. 12 Final collapse mode of a 50 mm square tube with capping induced imperfections (drop mass: 329 kg; drop height: 3.27 m)

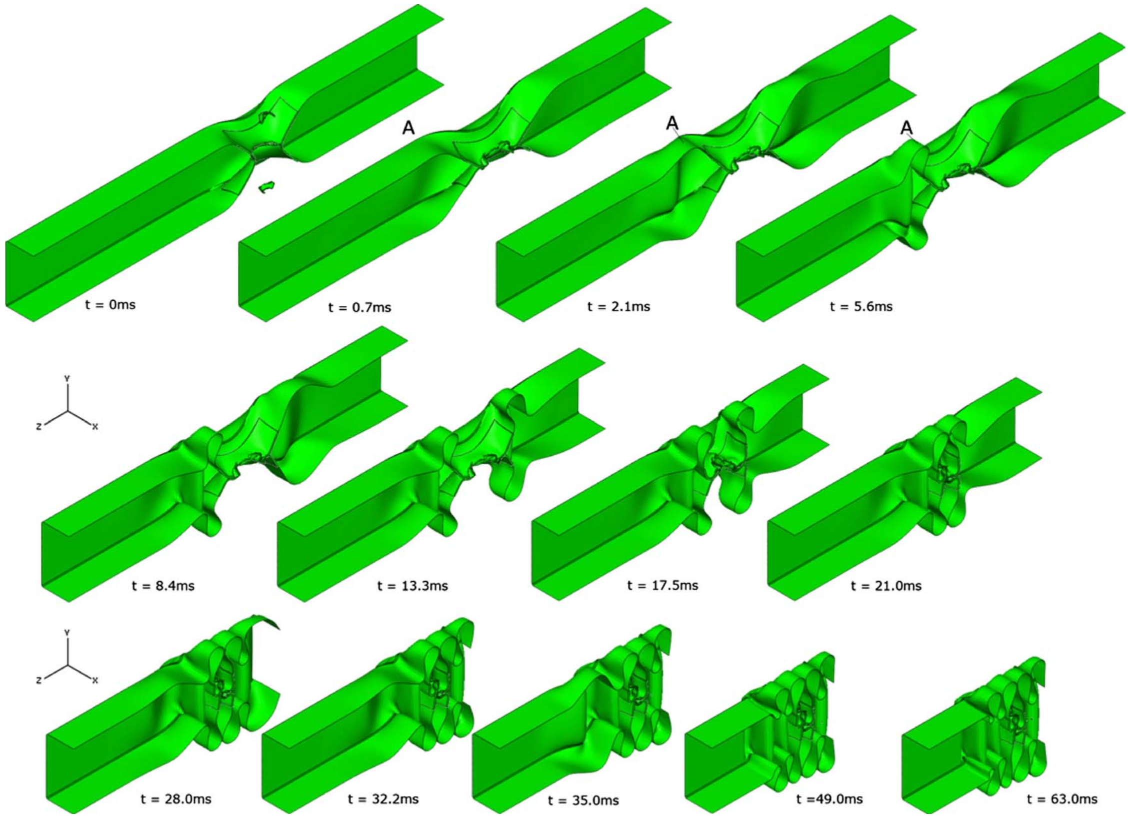

Fig. 13 Collapse sequences of a 50 mm square tube with induced capping imperfections (drop mass: 329 kg; drop height: 3.27 m)

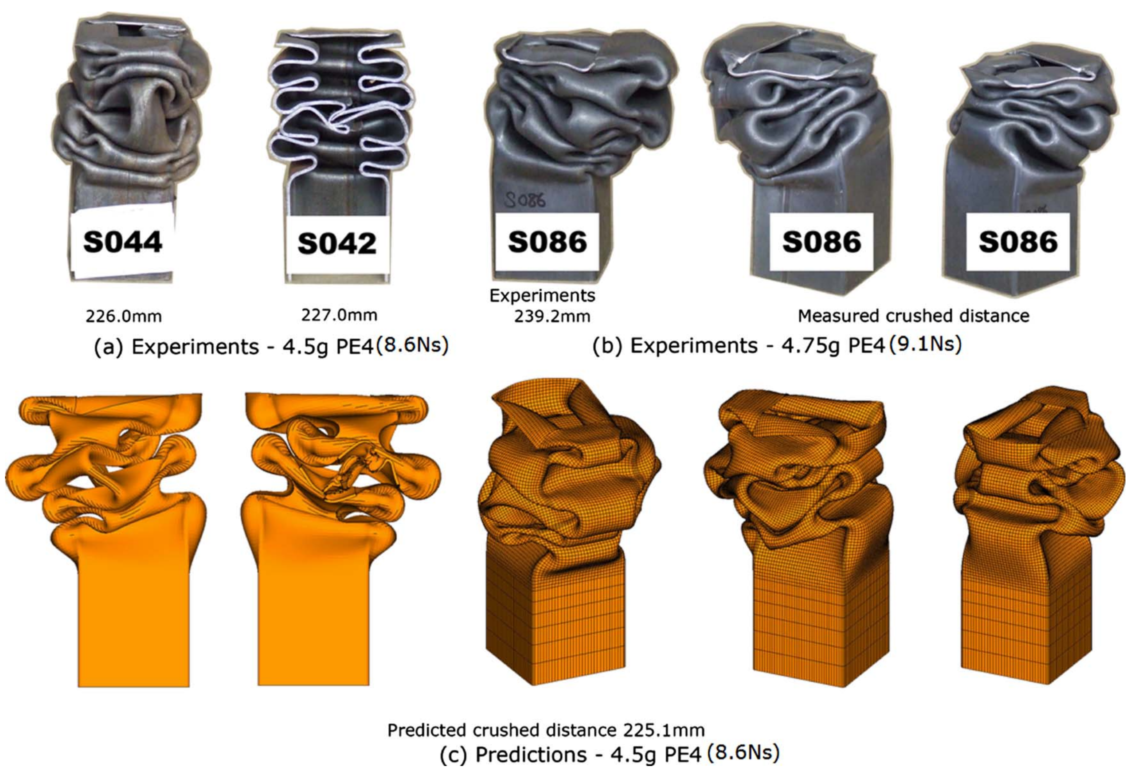

Fig. 14 Comparison of predicted collapse mode of a 50 mm square tube with induced capping imperfections created by two 17 mm blast loads (drop mass: 329 kg; drop height: 3.27 m)

Fig. 15 Crushed 50 mm tubes with asymmetric blast response

The pulse is applied over a duration equal to the explosive burn time. For the impulse applied using the rectangular pulse (blast load 2), the magnitude of the applied pressure is calculated using

$$P_0 = \frac{I}{At_{\text{blast}}} \tag{10}$$

where I is the measured blast impulse, A is the explosive area, and t_{blast} is the burn time of explosive.

Figure 16 shows the different loading conditions, asymmetric localized blast loads followed by dynamic axial load. It is, however, difficult to compare experiments with finite element predictions in these asymmetric cases because the response of the tubes in the experiments results from the combination of blast and impact. The purpose of the finite element simulations in this section is to illustrate the sensitivity of the tube response to small variations in the blast loading conditions.

Finite element analyses for three tubes with asymmetric blast loading conditions are performed and their predicted final buckling shapes are shown in Fig. 17. It can be seen by comparing the predicted buckling shapes with the tubes shown in Fig. 15 that they have similar characteristics.

The prediction, shown in Fig. 17(*a*), has the same applied impulse for both blast loads but different spatial distributions. The asymmetric response shown in Figs. 17(*b*) and 17(*c*) is carried out using different spatial distributions and impulse magnitudes. In both cases, blast load 1, the decaying pressure function, has an impulse of 7 Ns. The pressure magnitude in blast load 2, the rectangular pulse, is slightly varied to give small differences in impulse. In Fig. 17(*b*), the rectangular pulse has an applied impulse of 6.5 Ns and in Fig. 17(*c*), the applied impulse is 7.4 Ns. This sensitivity is important in cases where it could lead to Euler buckling mode, which is highly inefficient as an energy absorber.

5 The Influence of Impulse and Load Diameter

5.1 Blast-Induced Imperfection Type. The influence of load diameter and impulse on the imperfection geometry is investi-

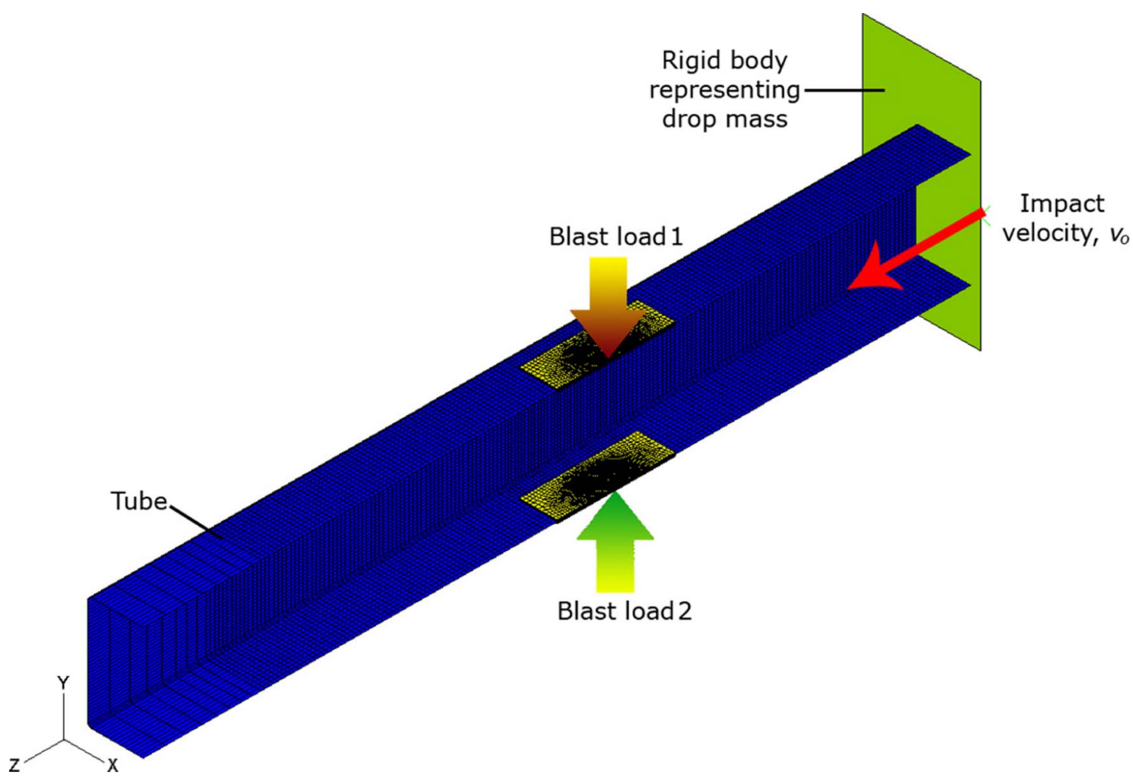

Fig. 16 $\frac{1}{2}$ tube FE model showing different loading conditions

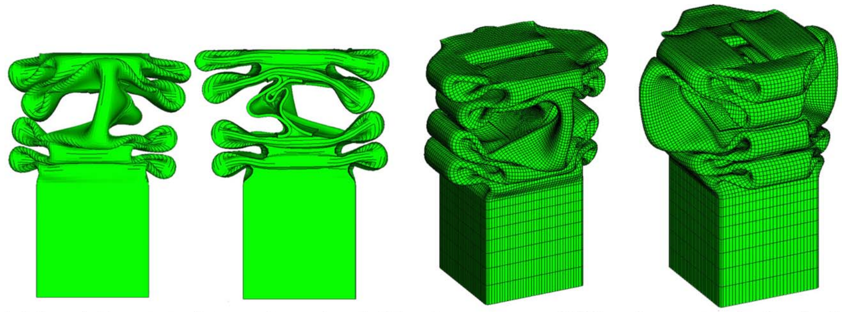

(a) Load diameter 17mm, Impulse 6.4Ns, Drop mass : 329kg, Impact velocity 8m/s

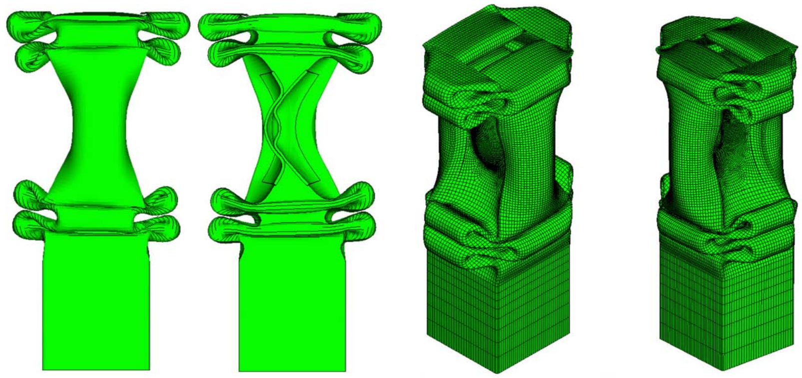

(b) Load diameter 25mm, Nominal impulse 6.75Ns, Drop mass 329kg, Impact velocity 6.62m/s

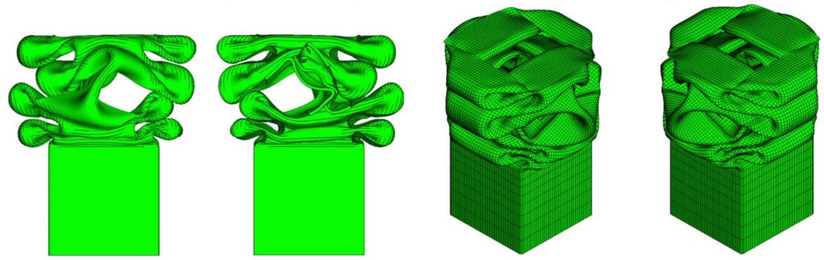

(c) Load diameter 25mm, Nominal impulse 7.2Ns, Drop mass 329kg, Impact velocity 8m/s

Fig. 17 Predicted collapse mode of a 50 mm square tube with blast-induced asymmetric imperfections

gated numerically. Two load diameters (17 mm and 25 mm) and different impulses per load diameter are investigated. Some typical predicted imperfections induced by blast load of different charge diameters are shown in Fig. 18. It should be noted that capping imperfection is excluded in this discussion because of its expensive computational time.

For both load diameters, tube deforms in the midsection (150 mm in length) with the maximum deflection of the tube side increases with increasing impulse, as expected. The maximum deflection is similar in magnitude for the same impulse indifferent to load diameter, as shown in Fig. 18 and Table 2. For a 50 mm tube, the maximum deflection is limited to 23.5 mm (accounting for tube thickness) without contact occurring between the opposite sides. From Figs. 18(*a*), 18(*b*), 18(*e*), and 18(*f*), it is observed that for impulses of 3.7 Ns and 4.7 Ns, the tube walls do not contact and simple Mode I domes with nominal maximum deflection of 15.2 mm and 19.5 mm are induced for both load diameters, respectively. At impulse of 5.7 Ns, the 17 mm load diameter charge induces simple Mode I domes that are just touching (Fig. 18(*c*)). The 25 mm load diameter charge produces domes that have just contacted and rebounded with a maximum deflection of 23.4 mm after elastic recovery (Fig. 18(*g*)).The "peak" of the dome is slightly flattened after contact and rebound. Rebound imperfections are predicted for both load diameters at impulse of 6.7 Ns, as shown in Fig. 18(*d*) and 18(*h*). Upon contact and rebound, outward facing dimples are predicted at the center of the imperfections. The size of the dimple increases with increasing impulses.

The predicted deformed profile of the central longitudinal axis of the tubes for different load charges and diameters is shown in Fig. 19. The 25 mm load diameter exhibits profiles that are "squarer" than the 17 mm load diameter, as expected because of the larger loaded area. It is anticipated that the squarer profiles would result in larger contact area upon dynamic loading and would thus affect the crush response. While no significant deformation is observed in the bottom and top ends of the tubes between the 50–120 mm and 280–350 mm marks, there exists some structural "imperfections" as a result of the changes in eigenmode of the tube. These changes in eigenmodes are believed to affect the crushing characteristics of the tube and the location of the first lobe is formed. The influence of eigenmode is not investigated in this paper.

5.2 Predicted Collapse Mode. Numerical simulations of dynamic axial loading of tubes with blast-induced imperfections are performed to investigate the influence of impulse and load diameter on the crush behavior of the tubes. The tubes are subjected to a 329 kg rigid mass impacted at 8 m/s. The crushing performance

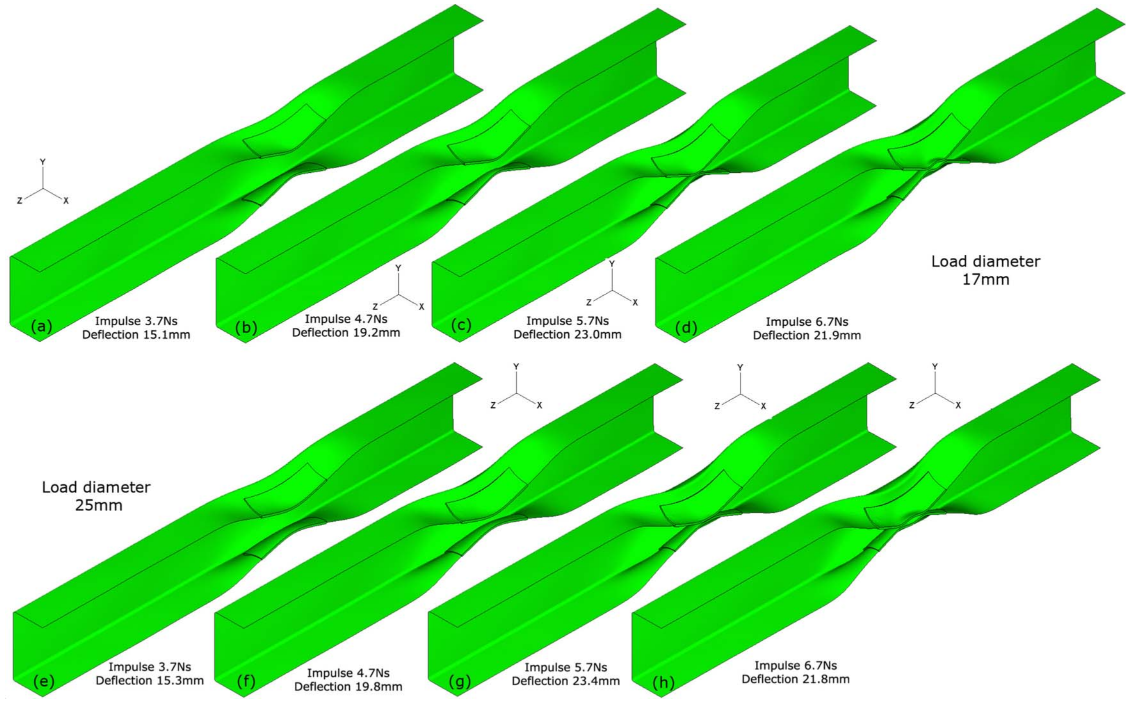

Fig. 18 Predicted blast-induced imperfections for a 50 mm tube at various impulses

is given in Table 3 in terms of ultimate peak load, mean crush force, and crushed distance. The predicted buckling shapes are shown in Fig. 20 with the axial force-displacement curves shown in Fig. 21.

All the tubes exhibit similar final collapse shapes, with the same number of lobes. The geometrically "as-received" tube shows uniform lobe formation, as expected. The tubes with the blast-induced imperfections develop lobes on either side of the deformed geometrical modifications.

From Table 3, it is observed that the simulations with the 25 mm blast load generally predict higher mean crush force and lower crushed distance than the 17 mm blast load. The ultimate peak load, for the 17 mm blast load diameter, appears to have reached a maximum when the domes are just touching at impulse of 5.7 Ns and decreases for higher load. For the 25 mm blast load diameter, the ultimate peak load increases with increasing blast load for the range of impulses investigated. The mean crushed force appears to slightly increase and the crushed distance appears to decrease with increasing blast load for both blast load diameters.

From Fig. 21, it is observed that the ultimate peak loads for tubes with blast-induced imperfections are less than for the "as-received" tube. The tubes with nontouching simple Mode I domes (impulse of 4.7 Ns) have generally lower crushed forces but higher crushed distance than the tubes with rebound imperfections (impulse of 6.7 Ns). This can be attributed to the fact that the nontouching simple Mode I domes offer less resistance force than the tubes with rebound imperfections to crushing. The larger

Table 2 Predicted maximum deflection of blast-induced imperfections for a 50 mm tube at various impulses

Deflection of imperfections (mm)					
Impulse (N s)	3.7	4.7	5.7	6.7	7.7
Load diameter (mm)					
17	15.1	19.2	23.0	21.9	19.2
25	15.3	19.8	23.4	21.8	—

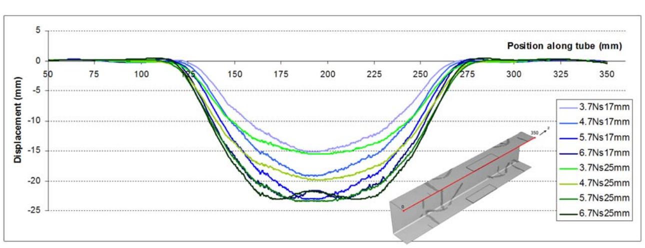

Fig. 19 Predicted deformation profile along central longitudinal axis of a 50 mm tube at various impulses

Table 3 Summary of predicted results for dynamic axial load of 50 mm square tubes with imperfections induced by different blast loads

Ultimate peak load, P_{ult} (kN)						
Impulse (N s)	0	3.7	4.7	5.7	6.7	7.7
Load diameter (mm)						
—	139.9					
17		92.9	83.9	119.6	108.6	100.6
25		95.0	98.3	102.1	104.9	
Mean crush force, P_m (kN)						
Impulse (N s)	0	3.7	4.7	5.7	6.7	7.7
Load diameter (mm)						
—	44.0					
17		41.7	41.7	44.1	44.3	44.4
25		42.0	43.7	44.1	45.7	
Crush distance, δ (mm)						
Impulse (N s)	0	3.7	4.7	5.7	6.7	7.7
Load diameter (mm)						
—	237.9					
17		252	253.8	241.6	238.0	236.8
25		253.5	244.8	241.3	231.3	

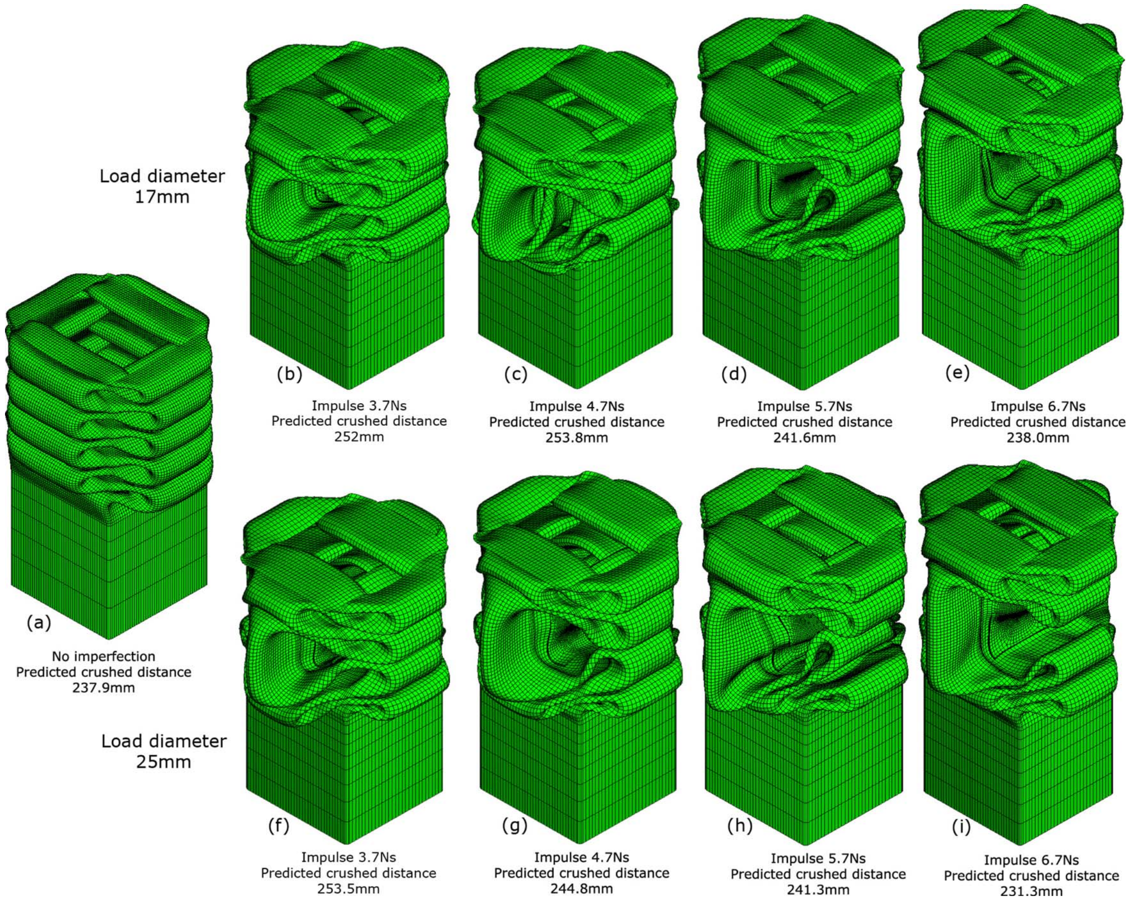

Fig. 20 Predicted buckling shapes for dynamic axially loaded 50 mm tubes with imperfections induced by different blast loads

crushed distance, however, makes the tube denser as the folds are compressed to their maximum and crushing takes place in a stiffer region where the imperfections are located. This results in undesirably high crushed peak force, as highlighted by the ellipse in Fig. 21.

6 Conclusions

The introduction of the blast-induced imperfections at midpoints of the extruded tube affects the final crushed shape. The different types of blast-induced imperfections affect the crushing mechanism of the tubes differently. The numerical predictions of axial loading of square tubes with blast-induced imperfections have been presented. Good correlations are obtained for overall buckling shape and crushed distance.

While the numerical simulations, presented in this paper, predict the tube response to two localized blast loads forming the imperfections followed by the dynamic axial load, in the experiments, these two loading conditions are not carried out almost simultaneously. Further experimental investigation is planned to carry out the two loading conditions simultaneously with a view to investigate the effect of material property changes with the help of numerical simulations.

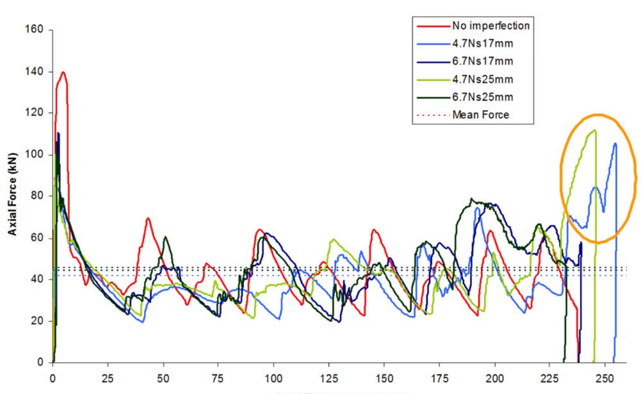

Fig. 21 Predicted axial force-displacement curves for some dynamic axial load of 50 mm square tubes with imperfections induced by different blast loads

Acknowledgment

Participation in this project would not have been possible without the financial support from the National Research Foundation of South Africa (NRF), Technology Human Response Industry Programme (THRIP), and Armaments Corporation of South Africa (ARMSCOR).

Nomenclature

$\dot{\varepsilon}$ = strain rate
$\dot{\varepsilon}_0$ = strain rate material constant
ε_{eq} = current value of logarithmic strain
ε_N = strain at necking initiation
η = material constant
σ_0 = static yield stress
σ_y^1 = dynamic yield stress
I = measured impulse
k = decay constant

P = pressure
P_m = mean crush load
P_{ult} = ultimate peak force
R_0 = load radius
t_{blast} = duration of pressure distribution
V_b = burn speed of explosive

References

[1] Karagiozova, D., and Jones, N., 2001, "Influence of Stress Waves on the Dynamic Progressive and Dynamic Plastic Buckling of Cylindrical Shells," Int. J. Solids Struct., **38**(38/39), pp. 6723–6749.

[2] Langseth, M., Berstad, T., Hopperstad, O. S., and Clausen, A. H., 1994, "Energy Absorption in Axially Loaded Square Thin-Walled Aluminium Extrusions," *Structures Under Shock Impact III (SUSI III)*, CMP, Southampton, pp. 401–410.

[3] Langseth, M., Hopperstad, O. S., and Berstad, T., 1999, "Crashworthiness of Aluminium Extrusion: Validation of Numerical Simulation, Effect of Mass Ratio and Impact Velocity," Int. J. Impact Eng., **22**(9/10), pp. 829–854.

[4] Otubushin, A., 1998, "Detailed Validation of a Non-Linear Finite Element Code Using Dynamic Axial Crushing of a Square Tube," Int. J. Impact Eng., **21**(5), pp. 349–368.

[5] Marsolek, J., and Reimerdes, H. G., 2003, "Energy Absorption of Metallic Cylindrical Shells With Induced Non-Axisymmetric Folding Patters," Eighth International Symposium on Plasticity and Impact Mechanics, IMPLAST 2003, New Delhi, India, Phoenix Publishing House, Mar. 16–19, pp. 454–464.

[6] Abah, L., Limam, A., and Dejeammes, M., 1998, "Effects of Cutouts on Static and Dynamic Behaviour of Square Aluminium Extrusions," Fifth International Conference on Structures Under Shock and Impact (SUSI V), Computational Mechanics, Southampton, UK, pp. 133–142.

[7] Markiewicz, E., Ducrocq, P., and Drazetic, P., 1998, "An Inverse Approach to Determine the Constitutive Model Parameters From Axial Crushing of Thin-Walled Square Tubes," Int. J. Impact Eng., **21**(6), pp. 433–449.

[8] Miyazaki, M., Endo, H., and Negishi, H., 1999, "Dynamic Axial Plastic Buckling of Square Tube," J. Mater. Process. Technol., **85**(1/3), pp. 213–216.

[9] Nannucci, P. R., Marshall, N. S., and Nurick, G. N., 1999, "A Computational Investigation of the Progressive Buckling of Square Tubes With Geometric Imperfections," Third Asia-Pacific Conference on Shock and Impact Loads on Structures, Singapore, Nov. 24–26, pp. 335–342.

[10] Karagiozova, D., 2003, "Velocity and Mass Sensitivity of Circular and Square Tubes Under Axial Impact," *Proceedings of the Eighth International Symposium on Plasticity and Impact Mechanics (IMPLAST 2003)*, New Delhi, Phoenix Publishing House, pp. 403–410.

[11] Karagiozova, D., 2003, *On the Dynamic Collapse of Circular and Square Tubes Under Axial Impact, Advances in Dynamics and Impact Mechanics*, WIT, Southampton, pp. 1–22.

[12] Karagiozova, D., 2004, "Dynamic Buckling of Elastic-Plastic Square Tubes Under Axial Impact-I: Stress Wave Propagation Phenomenon," Int. J. Impact Eng., **30**(2), pp. 143–166.

[13] Karagiozova, D., and Jones, N., 2004, "Dynamic Buckling of Elastic-Plastic Square Tubes Under Axial Impact-II: Structural Response," Int. J. Impact Eng., **30**(2), pp. 167–192.

[14] Mamalis, A. G., Manolakos, D. E., Ioannidis, M. B., Kostazos, P. K., and Chirwa, E. C., 2003, "Static and Dynamic Axial Collapse of Fibreglass Composite Thin-Walled Tubes: Finite Element Modelling of the Crush Zone," Int. J. Crashworthiness, **8**(3), pp. 247–254.

[15] Karagiozova, D., and Jones, N., 2000, "Dynamic Elastic-Plastic Buckling of Circular Cylindrical Shells Under Axial Impact," Int. J. Solids Struct., **37**(14), pp. 2005–2034.

[16] Karagiozova, D., and Jones, N., 2001, "Dynamic Effects on Buckling and Energy Absorption of Cylindrical Shells Under Axial Impact," Thin-Walled Struct., **39**(7), pp. 583–610.

[17] Karagiozova, D., and Jones, N., 2002, "On Dynamic Buckling Phenomena in Axially Loaded Elastic-Plastic Cylindrical Shells," Int. J. Non-Linear Mech., **37**(7), pp. 1223–1238.

[18] Karagiozova, D., Alves, M., and Jones, N., 2000, "Inertia Effects in Axisymmetrically Deformed Cylindrical Shells Under Axial Impact," Int. J. Impact Eng., **24**(10), pp. 1083–1115.

[19] Gupta, N. K., Sekhon, G. S., and Gupta, P. K., 2002, "A Study of Fold Formation in Axisymmetric Axial Collapse of Round Tubes," Int. J. Impact Eng., **27**(1), pp. 87–117.

[20] Huh, H., Kim, K. P., and Kim, H. S., 2001, "Collapse Simulation of Tubular Structures Using a Finite Element Limit Analysis Approach and Shell Elements," Int. J. Mech. Sci., **43**(9), pp. 2171–2187.

[21] Mamalis, A. G., Manolakos, D. E., Ioannidis, M. B., and Kostazos, P. K., 2003, "Crushing of Hybrid Square Sandwich Composite Vehicle Hollow Bodyshells With Reinforced Core Subjected to Axial Loading: Numerical Simulation," Compos. Struct., **61**(3), pp. 175–186.

[22] Karagiozova, D., Nurick, G. N., and Chung Kim Yuen, S., 2005, "Energy Absorption of Aluminium Alloy Circular and Square Tubes Under an Axial Explosive Load," Thin-Walled Struct., **43**(6), pp. 956–982.

[23] Jensen, O., Langseth, M., and Hopperstad, O. S., 2002, "Transition Between Progressive and Global Buckling of Aluminium Extrusions," *Structures Under Shock and Impact VII (SUSI VII)*, WIT, Southampton, pp. 269–277.

[24] Karagiozova, D., and Alves, M., 2004, "Transition From Progressive Buckling to Global Bending of Circular Shells Under Axial Impact—Part II: Theoretical Analysis," Int. J. Solids Struct., **41**(5/6), pp. 1581–1604.

[25] Karagiozova, D., and Alves, M., 2004, "Transition From Progressive Buckling to Global Bending of Circular Shells Under Axial Impact—Part I: Experimental and Numerical Observations," Int. J. Solids Struct., **41**(5/6), pp. 1565–1580.

[26] Chiandussi, G., and Avalle, M., 2002, "Maximisation of the Crushing Performance of a Tubular Device by Shape Optimization," Comput. Struct., **80**(27/30), pp. 2425–2432.

[27] Nagel, G. M., and Thambiratnam, D. P., 2004, "Dynamic Simulation and Energy Absorption of Tapered Tubes Under Impact Loading," Int. J. Crashworthiness, **9**(4), pp. 389–399.

[28] Lust, R., 1992, "Structural Optimization With Crashworthiness Constraints," Struct. Optim., **4**(2), pp. 85–89.

[29] Yamazaki, K., and Han, J., 2000, "Maximization of the Crushing Energy Absorption of Cylindrical Shells," Adv. Eng. Software, **31**(6), pp. 425–434.

[30] Belingardi, G., and Avalle, M., 1998, "Optimization of a Passive Safety Device by Means of the Response Surface Methodology," *Proceedings of the Second Integrated Design and Manufacturing in Mechanical Engineering Conference (IDMME)*, Compiegne, France, pp. 85–92.

[31] Avalle, M., Chiandussi, G., and Belingardi, G., 2002, "Design Optimization by Response Surface Methodology: Application to Crashworthiness Design of Vehicle Structures," Struct. Multidiscip. Optim., **24**(4), pp. 325–332.

[32] Kim, H. S., 2002, "New Extruded Multi-Cell Aluminum Profile for Maximum Crash Energy Absorption and Weight Efficiency," Thin-Walled Struct., **40**(4), pp. 311–327.

[33] Theobald, M. D., and Nurick, G. N., 2005, "Numerical Investigation of the Response of Sandwich Panels Subject to Blast Loads," International Conference on Impact Loading of Lightweight Structures, WIT, Brazil, pp. 521–534.

[34] Theobald, M. D., and Nurick, G. N., 2007, "Numerical Investigation of the Response of Sandwich-Type Panels Using Thin-Walled Tubes Subject to Blast Loads," Int. J. Impact Eng., **34**(1), pp. 134–156.

[35] Wiehahn, M. A., Nurick, G. N., and Bowles, H. C., 2000, "Thin Plate Fragmentation Due to Blast Loading: A Simulation Using Temperature Dependent Material Properties," *Proceedings of the Third International Conference on Applied Mechanics (SACAM 2000)*, Durban, South Africa, pp. 567–572.

[36] Wiehahn, M. A., Nurick, G. N., and Bowles, H. C., 2000, "Some Insights Into the Mechanism of the Deformation and Tearing of Thin Plates at High Strain Rates Incorporating Temperature Dependent Material Properties," *Structures Under Shock and Impact VI SUSI VI*, Computational Mechanics, UK, pp. 207–220.

[37] Chung Kim Yuen, S., and Nurick, G. N., 2005, "Experimental and Numerical Studies on the Response of Quadrangular Stiffened Plates: Part I—Subjected to Uniform Blast Load," Int. J. Impact Eng., **31**(1), pp. 55–83.

[38] Langdon, G. S., Chung Kim Yuen, S., and Nurick, G. N., 2005, "Experimental and Numerical Studies on the Response of Quadrangular Stiffened Plates: Part II—Subjected to Localised Load," Int. J. Impact Eng., **31**(1), pp. 85–111.

[39] Bridgman, P. W., 1956, *Studies in Large Flow and Fracture*, McGraw-Hill, New York.

[40] Mirone, G., 2004, "A New Model for the Elastoplastic Characterization and the Stress-Strain Determination on the Necking Section of a Tensile Specimen," Int. J. Solids Struct., **41**(13), pp. 3545–3564.

[41] Marais, S. T., Tait, R. B., Cloete, T. J., and Nurick, G. N., 2004, "Material Testing at High Strain Rate Using the Split Hopkinson Pressure Bar," Latin American Journal of Solids and Structures, **1**(3), pp. 319–338.

[42] Masui, T., Nunokawa, T., and Hiramatsu, T., 1987, "Shape Correction of Hot Rolled Steel Using an on Line Leveller," J. Jpn. Soc. Technol. Plast., **28**(312), pp. 81–87.

[43] Wharton, R. K., Formby, S. A., and Merrifield, R., 2000, "Airblast TNT Equivalence for a Range of Commercial Blasting Explosives," J. Hazard. Mater., **79**(1–2), pp. 31–39.

[44] Grobbelaar, W. P., and Nurick, G. N., 2000, "An Investigation of Structures Subjected to Blast Loads Incorporating an Equation of State to Model the Material Behaviour of the Explosive," *Proceedings of the Seventh International Symposium on Structural Failure and Plasticity (IMPLAST 2000)*, Melbourne, Australia, Oct. 4–6, pp. 185–194.

[45] Bimha, R. E., 1996, "Response of Thin Circular Plates to Blast Loading," M.S. thesis, University of Cape Town, Rondebosch, South Africa.

[46] Balden, V. H., and Nurick, G. N., 2005, "Numerical Simulation of the Post Failure Motion of Steel Plates Subjected to Blast Loading," Int. J. Impact Eng., **32**(1–4), pp. 14–34.

[47] Jones, N., 1989, *Structural Impact*, Cambridge University Press, Cambridge, England.

The Effects of Strong Cubic Nonlinearity on the Existence of Periodic Solutions of the Mathieu–Duffing Equation

Ivana Kovacic
e-mail: ivanakov@uns.ac.rs

Livija Cveticanin
e-mail: cveticanin@uns.ns.ac.yu

Department of Mechanics,
Faculty of Technical Sciences,
University of Novi Sad,
21121 Novi Sad, Serbia

This paper deals with systems governed by the Mathieu–Duffing equation, with a time-dependent coefficient of the linear term and a constant, not necessarily small coefficient of the cubic term. This coefficient can be positive or negative. The method of strained parameters applied to a linear system governed by the Mathieu equation is extended to a strongly nonlinear system. As a result, the curves corresponding to the parameter values at which periodic solutions exist are obtained. It is shown that they strongly depend on the value of the coefficient of nonlinearity and the initial conditions. The corresponding parameter planes are plotted. Numerical integrations are carried out to confirm the analytical results. [DOI: 10.1115/1.3112722]

Keywords: Mathieu–Duffing equation, strong nonlinearity, periodic solution

1 Introduction

The first recorded parametric behavior was that of Faraday in 1831 [1], when he noted that surface waves in a fluid-filled cylinder under vertical excitation exhibited twice the period of the excitation itself. Since then, parametric phenomena have been recognized in many problems of physics and engineering (see, for example, Refs. [2–9]).

The simplest mathematical model of a parametrically excited system is the Mathieu equation

$$\ddot{x} + (\delta + 2\varepsilon \cos 2t)x = 0 \tag{1}$$

where δ and ε are constants. The majority of studies devoted to this equation has been aimed at defining the regions of stable (bounded) and unstable (unbounded) motions in a parameter plane, i.e., in the $\delta\varepsilon$-plane. These regions are separated by the transition curves along which the zero-solution is periodic and the expressions for which are independent of the initial conditions.

The Mathieu equation with cubic nonlinearity (the Mathieu–Duffing equation),

$$\ddot{x} + (\delta + 2\varepsilon \cos 2t)x + cx^3 = 0 \tag{2}$$

where c is a constant, has recently been of interest to researchers due to its numerous applications. The method of multiple scales [10] was used to obtain the conditions for the existence of nontrivial steady-state amplitudes and phases and for investigating their stability. Rand [11] showed that the nonlinearity causes bifurcations to occur as the transition curves corresponding to the linear Mathieu equation are crossed. Namely, the question of the stability of the trivial solution $x=0$ is the same both for the weakly nonlinear equation (2) and for the linear Mathieu equation (1). However, for the nonlinear equation, as δ changes through the tongue formed by the transition curves emanating from $(\delta,\varepsilon)=(1,0)$, the trivial solution $x=0$ changes its stability and simultaneously subharmonic motions appear. Esmailzadeh and Nakhaie-Jazar [12] stated the necessary and sufficient conditions for the existence of at least one periodic solution of the Mathieu–Duffing equation. Zounes and Rand [13] derived analytical expressions for the resonance bands that are associated with some subharmonic periodic solutions.

In this work, the Mathieu–Duffing equation (2) is studied with a view to obtain the values of the parameters of the system which lead to the periodic solutions corresponding to different frequencies for the case when the magnitude of the parametric forcing ε is assumed to be small, while the coefficient of the cubic term c can have an arbitrary sign: negative (softening nonlinearity) or positive (hardening nonlinearity) and it is not necessarily small. This assumption implies that the coefficient c is not of the same or of a smaller order with respect to the parameter ε. The method of strained parameters [10] is adapted in such a way that the use of elliptic functions is introduced. The graphical presentation of the expressions for the parameters of the system yielding the periodic solutions generates the parameter plane, the configuration of which is the main task of this study.

2 The Elliptic Method of Strained Parameters

In accordance with the method of strained parameters, the perturbation expansions of the coordinate x and the parameter δ are introduced as follows:

$$x(t,\varepsilon) = x_0(t) + \varepsilon x_1(t) + O(\varepsilon^2) \tag{3}$$

$$\delta = \delta_0 + \varepsilon\delta_1 + O(\varepsilon^2) \tag{4}$$

Substituting Eqs. (3) and (4) into Eq. (2) and equating coefficients of the same powers of ε, one obtains

$$\ddot{x}_0 + \delta_0 x_0 + cx_0^3 = 0 \tag{5}$$

$$\ddot{x}_1 + \delta_0 x_1 + 3cx_0^2 x_1 = -\delta_1 x_0 - 2x_0 \cos 2t \tag{6}$$

The solution of Eq. (5) can be assumed as

$$x_0 = A_0 ep(\omega_0 t + \alpha_0, k) \tag{7}$$

where $ep(\omega_0 t+\alpha_0,k)$ denotes a convenient Jacobian elliptic function, A_0 and α_0 are constants dependent on the initial conditions, ω_0 is a frequency, and k is an elliptic modulus [14,15]. There are two possible types of the solution (7), and accordingly, two possible values of the parameters A_0, α_0, ω_0, and k. In Table 1, the form of the zero-solutions (7) and the quantities ω_0 and k are given, depending on which type of the equation they refer to (softening or hardening nonlinearities). It should be noted that for the initial condition prescribed as $x(0)=X_0$, $\dot{x}(0)=\dot{X}_0$, one has $x_0(0)=X_0$, $\dot{x}_0(0)=\dot{X}_0$, $x_1(0)=\dot{x}_1(0)=0$; the constants A_0 and α_0 can be calculated accordingly.

Thus, Eq. (6) turns to a new equation with a time-varying coefficient next to the linear term as follows:

$$\ddot{x}_1 + (\delta_0 + 3cA_0^2 ep^2(\omega_0 t + \alpha_0, k_0))x_1 = -\delta_1 A_0 ep(\omega_0 t + \alpha_0, k) - 2A_0 ep(\omega_0 t + \alpha_0, k)\cos 2t \tag{8}$$

The second coefficient of the linear term x_1 in Eq. (8) is time-varying, which means that this equation represents a modified Mathieu equation. In order to solve it, the product cA_0^2 is assumed to be small, and a new small parameter ε_1 is introduced (Table 2). Hence, the standard approach of the method of strained parameters is to be used with the following series expansions for the

Manuscript received March 12, 2008; final manuscript received February 4, 2009; published online June 16, 2009. Review conducted by Wei-Chau Xie.

Table 1 Solutions of Eq. (5) depending on the sign of the constant c

Type of nonlinearity	Zero-solution	Frequency	Elliptic modulus
Softening $c<0$	$x_0=A_0 sn(\omega_0 t+\alpha_0,k)$	$\omega_0^2=\delta_0-\frac{cA_0^2}{2}$	$k^2=\frac{cA_0^2}{2\left(\delta_0-\frac{cA_0^2}{2}\right)}$
Hardening $c>0$	$x_0=A_0 cn(\omega_0 t+\alpha_0,k)$	$\omega_0^2=\delta_0+cA_0^2$	$k^2=\frac{cA_0^2}{2(\delta_0+cA_0^2)}$

coordinate and parameter δ_1 with respect to the small parameter ε_1:

$$x_1(t,\varepsilon_1)=x_{10}(t)+\varepsilon_1 x_{11}(t)+O(\varepsilon^2) \tag{9}$$

$$\delta_1=\delta_{10}+\varepsilon_1\delta_{11}+O(\varepsilon^2) \tag{10}$$

Furthermore, it can be seen that Eq. (8) contains both elliptic and circular functions. The application of the standard method of strained parameters requires re-expressing the elliptic functions by using the additional formulas for Jacobian elliptic functions [14], which are given in Table 2. Besides, in this table, the approximations of these expressions based on the fact that the quantity cA_0^2 is small (which means that k is small) are included.

Substituting Eqs. (9) and (10) and the appropriate approximations from Table 2 into Eq. (8), and separating the terms with the same order of the small parameter ε_1, the following equations, presented in the general form, are obtained:

$$\ddot{x}_{10}+\Delta(S_0,C_0,D_0)x_{10}=F_1(S_0,C_0,D_0,A_0,\delta_{10})\cos\sqrt{\Delta}t + F_2(S_0,C_0,D_0,A_0,\delta_{10})\sin\sqrt{\Delta}t+\mathrm{NST} \tag{11}$$

$$\ddot{x}_{11}+\Delta(S_0,C_0,D_0)x_{11}=G_1(S_0,C_0,D_0,A_0,\delta_{11})\cos\sqrt{\Delta}t + G_2(S_0,C_0,D_0,A_0,\delta_{11})\sin\sqrt{\Delta}t+\mathrm{nst} \tag{12}$$

where NST and nst stand for nonsecular terms, while Δ, F_1, F_2, G_1, and G_2 denote the functions of the variables shown. On the basis of the requirement of the nonsecular terms in Eq. (11), the component δ_{10} is to be found. Then, integrating Eq. (11), the solution for x_{10} can be obtained. Similarly, eliminating secular terms from Eq. (12), the component δ_{11} is to be calculated. The values of δ_0, δ_{10}, and δ_{11} depend on the frequency (see Table 1), which relates to the period of the solution (7). Since the fundamental Jacobian elliptic functions have the period $4K(k)$, where $K(k)$ is the complete elliptic integral of the first kind [14], two cases will be analyzed separately: the solution (7) is of the period $4K(k)$, the frequency is $\omega_0=1$; and the solution (7) is of the period $2K(k)$, the frequency is $\omega_0=2$. The details of the whole procedure will be omitted for brevity and just the results will be given (the details can be found in Ref. [16]).

2.1 Softening Nonlinearity: $c<0$. The parameter values yielding the solution of the period $4K(k)$ are given by

$$\delta=1+\frac{\varepsilon_1}{6}-\varepsilon, \quad \delta=1+\frac{\varepsilon_1}{6}+\varepsilon\left(1-\frac{\varepsilon_1}{8\left(1-\frac{\varepsilon_1}{3}\right)}\right) \tag{13}$$

The parameter values, which lead to the solution of the period $2K(k)$ are defined by

$$\delta=4+\frac{\varepsilon_1}{6}-\frac{\varepsilon\varepsilon_1}{24-2\varepsilon_1}, \quad \delta=4+\frac{\varepsilon_1}{6}+\frac{\varepsilon\varepsilon_1}{24-2\varepsilon_1} \tag{14}$$

2.2 Hardening Nonlinearity: $c>0$. The expressions for the parameter values for which the solutions of the period $4K(k)$ exist are

$$\delta=1-\frac{2}{3}\varepsilon_1-\varepsilon, \quad \delta=1-\frac{2}{3}\varepsilon_1+\varepsilon\left[1+\frac{\varepsilon_1(3-\varepsilon_1)}{4(3+\varepsilon_1-\varepsilon_1^2)}\right] \tag{15}$$

while those leading to the solutions of the period $2K(k)$ read as follows:

$$\delta=4-\frac{2}{3}\varepsilon_1-\frac{12\varepsilon\varepsilon_1}{12+\varepsilon_1}, \quad \delta=4-\frac{2}{3}\varepsilon_1+\frac{\varepsilon\varepsilon_1(12-\varepsilon_1)}{144+12\varepsilon_1-3\varepsilon_1^2} \tag{16}$$

3 Numerical Results and Discussion

In the special case when $\varepsilon_1=0$, i.e., $c=0$ the expressions given by Eqs. (13)–(16) correspond to the expressions for the transition curves of the Mathieu equation [10], which are

$$\delta=1-\varepsilon+O(\varepsilon^2), \quad \delta=1+\varepsilon+O(\varepsilon^2), \quad \delta=4+O(\varepsilon^2) \tag{17}$$

When $c=0$, the elliptic modulus k is equal to zero, as a result of which the elliptic functions in Table 2 are simplified to the sine and cosine functions for the softening and hardening types of nonlinearity, respectively. These solutions of motion along the curves (17) agree with those given in Ref. [10].

The transition curves of the Mathieu equation emanate from the critical points $\delta_0=1$ and $\delta_0=4$. However, in the case of the Mathieu–Duffing equation, the values corresponding to the critical points, as well as the geometry of the curves along which periodic solutions exist, change with the values of the parameter of nonlinearity and the initial conditions, i.e., with the value of the quantity ε_1. Using Eqs. (13)–(16), the parameter $\delta\varepsilon$-plane for the Mathieu–Duffing equation is plotted in Fig. 1 for various values of the quantity ε_1. For the equation with softening nonlinearity, the values of the critical points are higher for $\varepsilon_1/6$ than the critical values of the Mathieu equation. Consequently, the curves along which periodic solutions exist are shifted to the right (Fig. 1(*a*)). For the equation with hardening nonlinearity, the critical values for the Mathieu–Duffing are lower than the critical values of the

Table 2 Transformation of the solution (7) depending on the sign of the constant c

Type of nonlinearity	Small parameter	Addition formula	Approximation	Notation
Softening $c<0$	$\varepsilon_1=3cA_0^2$	$x_0=A_0\frac{sn_0C_0D_0+cn_0dn_0S_0}{1-k^2sn_0^2S_0^2}$	$x_0\approx A_0\sin(\omega_0 t)C_0D_0+\cos(\omega_0 t)S_0$	$sn_0\equiv sn(\omega_0 t,k)$ $cn_0\equiv cn(\omega_0 t,k)$ $dn_0\equiv dn(\omega_0 t,k)$
Hardening $c>0$	$\varepsilon_1=\frac{3cA_0^2}{2}$	$x_0=A_0\frac{cn_0C_0-sn_0dn_0S_0D_0}{1-k^2sn_0^2S_0^2}$	$x_0\approx A_0\cos(\omega_0 t)C_0-\sin(\omega_0 t)S_0D_0$	$S_0=sn(\alpha_0,k)$ $C_0=cn(\alpha_0,k)$ $D_0=dn(\alpha_0,k)$

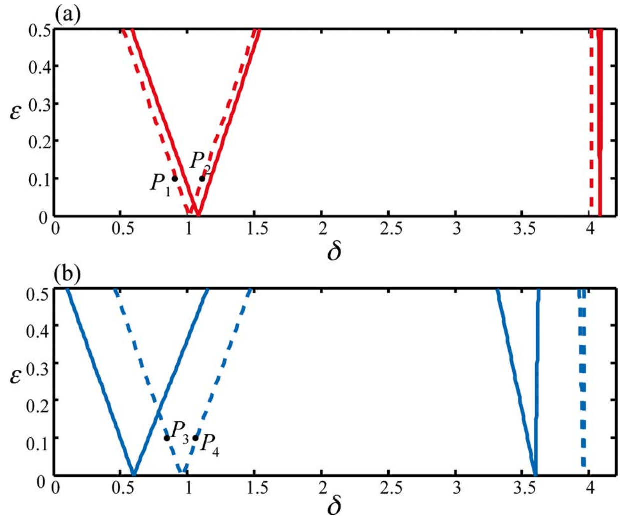

Fig. 1 Parameter $\delta\varepsilon$-plane for (*a*) softening nonlinearity $\varepsilon_1 = 0.5$ (solid line), $\varepsilon_1 = 0.12$ (dashed line), and (*b*) hardening nonlinearity $\varepsilon_1 = 0.5$ (solid line), $\varepsilon_1 = 0.06$ (dashed line)

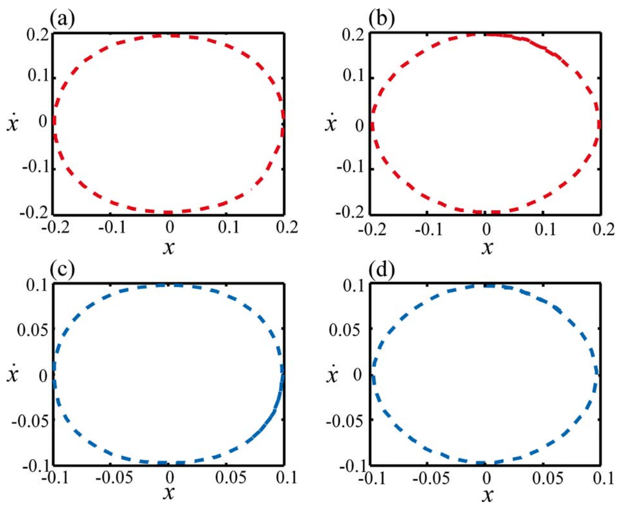

Fig. 2 Phase projections for $|c| = 1$ and $\varepsilon = 0.1$: (*a*) point P_1, (*b*) point P_2, (*c*) point P_3, and (*d*) point P_4

linear Mathieu equation, as a result of which the curves corresponding to periodic solutions are shifted to the left (Fig. 1(*b*)).

In order to check the validity of the results regarding the periodicity of the response for the particular relationships between the system parameters, a direct numerical integration of the equation of motion (2) was done. The numerical simulations were carried out by using the MATLAB code 45 function for the fixed values of the parameters $|c| = 1$ and $\varepsilon = 0.1$. The parameter δ was calculated on the basis of the analytically obtained values defined by Eqs. (13)–(16), where the parameter ε_1 is equal to 0.12 for the softening nonlinearity and 0.06 for the hardening nonlinearity. Figure 2 shows that the numerically computed response corresponding to the points P_1-P_4 labeled in Fig. 1 is periodic, as it has been predicted analytically.

4 Conclusions

The Mathieu–Duffing equation has been treated by using the method of strained parameters and assuming the zero-solution in the form of Jacobian elliptic functions. The parameter values for which the periodic solutions with period $2K(k)$ and $4K(k)$ exist, have been obtained. In the special case when the value of the parameter of nonlinearity c is chosen to be zero, these curves in the first approximation are equivalent to the transient curves of the linear Mathieu equation. In comparison to the location of the transition curves, the curves along which the periodic solutions of the nonlinear equation appear are shifted to the right for softening nonlinearity $c < 0$ and to the left for hardening nonlinearity $c > 0$.

Acknowledgment

This study has been financially supported by the Ministry of Science and Environmental Protection, Republic of Serbia (Project No. 144008).

References

[1] Faraday, M., 1831, "On a Peculiar Class of Acoustical Figures; and on Certain Forms Assumed by a Group of Particles Upon Vibrating Elastic Surfaces," Philos. Trans. R. Soc. London, **121**, pp. 299–318.
[2] Mond, M., and Cederbaum, G., 1993, "Stability Analysis of the Non-Linear Mathieu Equation," J. Sound Vib., **167**(1), pp. 77–89.
[3] Esmailzadeh, E., Jazar, G. N., and Mehri, B., 1997, "Existence of Periodic Solution for Beams With Harmonically Variable Length," ASME J. Vibr. Acoust., **119**(3), pp. 485–488.
[4] Esmailzadeh, E., and Jalili, N., 1998, "Parametric Response of Cantilever Timoshenko Beams With Tip Mass Under Harmonic Support Motion," Int. J. Non-Linear Mech., **33**(5), pp. 765–781.
[5] Esmailzadeh, E., and Goodarzi, A., 2001, "Stability Analysis of a CALM Floating Offshore Structure," Int. J. Non-Linear Mech., **36**(6), pp. 917–926.
[6] El-Dib, Y. O., 2001, "Nonlinear Mathieu Equation and Coupled Resonance Mechanism," Chaos, Solitons Fractals, **12**(4), pp. 705–720.
[7] Ng, L., and Rand, R., 2002, "Bifurcations in a Mathieu Equation With Cubic Nonlinearities," Chaos, Solitons Fractals, **14**, pp. 173–181.
[8] Abraham, G. T., and Chatterjee, A., 2003, "Approximate Asymptotic Solution for Nonlinear Mathieu Equation Using Harmonic Balance Based Averaging," Nonlinear Dyn., **31**, pp. 347–365.
[9] Rhoads, J. F., Shaw, S. W., Turner, K. L., Moehlis, J., De Martini, B. E., and Zhang, W., 2006, "Generalized Parametric Resonance in Electrostatically Actuated Microelectromechanical Oscillators," J. Sound Vib., **296**, pp. 797–829.
[10] Nayfeh, A. H., and Mook, D. T., 1979, *Nonlinear Oscillations*, Wiley, New York.
[11] Rand, R. H., "Lecture Notes on Non-Linear Vibrations," Version 45, http://tam.cornell.edu/randdocs/nlvibe45.pdf.
[12] Esmailzadeh, E., and Nakhaie-Jazar, G., 1997, "Periodic Solution of a Mathieu-Duffing Type Equation," Int. J. Non-Linear Mech., **32**(5), pp. 905–912.
[13] Zounes, R. S., and Rand, R. H., 2002, "Subharmonic Resonance in the Non-Linear Mathieu Equation," Int. J. Non-Linear Mech., **37**, pp. 43–73.
[14] Byrd, P. F., and Friedman, M. D., 1954, *Handbook of Elliptic Integrals for Engineers and Physicists*, Springer-Verlag, Berlin.
[15] Abramowitz, M., and Stegun, I. A., 1979, *Handbook of Mathematical Functions With Formulas, Graphs and Mathematical Tables*, Nauka, Moscow.
[16] Cveticanin, L., and Kovacic, I., 2007, "Parametrically Excited Vibrations of an Oscillator With Strong Cubic Negative Non-Linearity," J. Sound Vib., **304**(1–2), pp. 201–212.

Erratum: “A Momentum Transfer Measurement Technique Between Contacting Free-Falling Bodies in the Presence of Adhesion” [Journal of Applied Mechanics, 2008, 75(1), p. 011016]

M. Benedetti, D. Bortoluzzi, and S. Vitale

The complete affiliation of the authors is the following:

M. Benedetti
Department of Materials Engineering and Industrial Technologies and Italian Institute of Nuclear Physics INFN,
University of Trento, 38050 Trento, Italy
e-mail: matteo.benedetti@ing.unitn.it

D. Bortoluzzi
Department of Mechanical and Structural Engineering and Italian Institute of Nuclear Physics INFN,
University of Trento, 38050 Trento, Italy

S. Vitale
Department of Physics, University of Trento and Italian Institute of Nuclear Physics INFN, 38050 Trento, Italy

